

hardening, deformation rate effects and thermal softening. Each parameter is multiplied to characterize the cumulative effect of each effect.

$$\sigma_y = \left[A + B \left(\varepsilon_{eff}^p \right)^n \right] (1 + C \ln \varepsilon) [1 - (T_H)^m] \tag{7}$$

In Equation (7), ε_{eff}^p is the effective plastic strain; $\varepsilon = \frac{\varepsilon_{eff}^p}{\varepsilon_0}$, where ε_0 is the strain rate used to determine A , B , and n ; $T_H = \frac{T - T_R}{T_M - T_R}$ is the homologous temperature; T_M is the melting temperature; T_R is the reference temperature; $\Delta T = \frac{1}{\rho C_p} \int \sigma d\varepsilon_{eff}^p$, where ρ is the density, and C_p is the specific heat. The five parameters A , B , n , m and C in the model are basic parameters for characterizing the yield strength, where A is the initial yield strength of the material under the quasi-static strain rate, B and n are the flow stress of the strain-hardening behavior under the quasi-static strain rate, C is the strain rate effect, and m is the thermal softening effect. In addition to the material properties ρ , C_p , and T_M , there are also elastic parameters. Usually, the pressure is defined as a function of the volume strain response, and the shear modulus is integrated along the equation of state [11].

The cumulative damage of the material is used to characterize the failure of the material in the J-C constitutive, as shown in Equation:

$$\varepsilon^F = \left(D_1 + D_2 \exp \left[D_3 \frac{P}{\sigma_{eff}} \right] \right) (1 + D_4 \ln \varepsilon) (1 + D_5 T_H) \tag{8}$$

where $D = \sum \frac{\Delta \varepsilon_{eff}^p}{\varepsilon^F}$ the material failure occurs when $D = 1$ where ε_{eff} is the effective stress, P is the average stress. The parameters of the Johnson–Cook model for the Al7075-T6Al alloy and the parameters of the Mie–Gruneisen equation of state are shown in Table 1 [12].

Table 1. Al7075-T6 Johnson–Cook model and Mie–Gruneisen EOS parameters.

Parameters	Symbol	7075-T6
Johnson–Cook model parameters		
Density (kg/m ³)	R0	2.81
Poisson’s ratio	PR	0.33
Shear modulus (GPa)	E	0.717
Static yield limit (MPa)	A	0.00546
Strain hardening modulus [13]	B	0.00678
Strain hardening exponent	n	0.71
Strain rate coefficient	C	0.35
Spall type	SPALL	3
Failure parameters D ₁	D1	−0.068
Failure parameters D ₂	D2	0.451
Failure parameters D ₃	D3	−0.952
Failure parameters D ₄	D4	0.036
Failure parameters D ₅	D5	0.697
Mie–Gruneisen EOS parameters		
Constants C	C	0.535
Constants S ₁	S1	1.34
Constants γ	GAMAO	2.17

T300/QY8911 related material parameters are shown in Table 2.

Table 2. T300/QY8911 material parameters [14].

Parameter	Symbol	T300/QY8911
Density	R0	1.6
Elastic modulus along the a direction	EA	1.32
Elastic modulus along the b direction	EB	0.073
Elastic modulus along the c direction	EC	0.073
ba/ca Poisson's ratio	PRBA/PRCA	0.03
cb Poisson's ratio	PRCB	0.31
Shear strength	SC	0.00079
Tensile strength along the a direction	XT	0.049
Tensile strength along the b direction	YT	4.8
Compressive strength along the b direction	YC	0.002

The simulated spherical fragments are divided by a uniform mesh with a mesh size of about 0.3 mm, using hexahedral eight-node units with a total number of 56,000 units, as shown in Figure 19.

**Figure 19.** Finite element model of spherical fragments.

The structural metal part of the model mesh uses a hexahedral deca-node unit, and the composite part of the model consists of a 2D shell unit, with a single sub-layer containing three layers of actual layup information. *CONTACT_SURFACE_TO_SURFACE_TIEBREAK [15,16] is used between layers. The total number of model units for the air inlet Al alloy I-beam riveted structure is 241,437, and the total number of model units for the wing composite/Al alloy spacer structure is 1,099,060. In order to improve the overall computational efficiency and ensure the computational accuracy, the local mesh refinement method is used to divide the model into two density meshes, where the impact penetration part is encrypted mesh, and the two are connected by the trapezoidal transition mesh co-node method, as shown in Figure 20.

The fragment is set up with *CONTACT_AUTOMATIC_SURFACE_TO_SURFACE automatic face-to-face contact and *CONTACT_AUTOMATIC_SINGLE_SURFACE automatic single-sided contact between the fragment and the structure.

Typical damage modes of the composite bottom skin and stringer obtained by experiments and simulation are shown in Figures 21 and 22, respectively. In terms of characteristic damage size, the diameter of openings and penetrations obtained from the simulation is close to that of the test. Since the composite simulation model uses 2D shell unit modeling, it cannot simulate the damage morphology of fiber fracture and spalling, and the Mat_Composite_Damage model does not consider the effect of temperature on overall damage. However, there is a small amount of fiber-melting phenomena in the actual test. Therefore, the characteristic damage size of a composite obtained from simulation is relatively small compared with the actual one, but the relative error is not big, and it can meet the requirements of battle damage size prediction to some extent. In terms of the Al alloy side damage morphology, the simulated results are in high agreement with the test, and the difference in feature size is small, as shown in Figure 23.

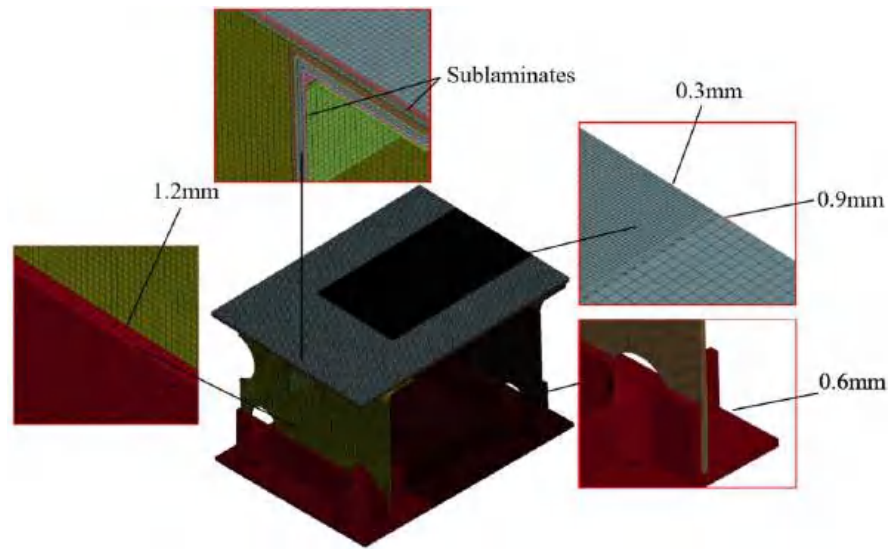


Figure 20. Finite element model of the structure.

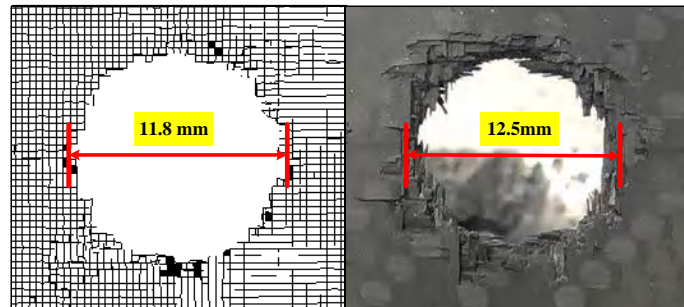


Figure 21. Damages of composite bottom skin damage.



Figure 22. Damages of composite stringer.

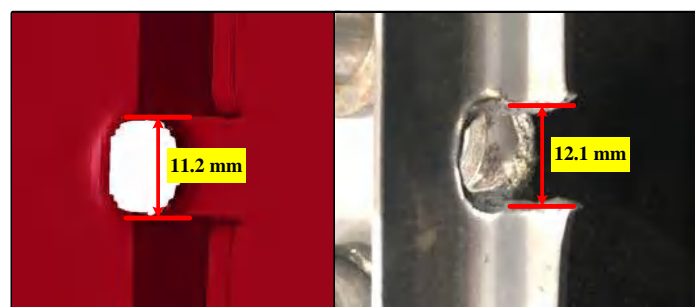


Figure 23. Damages of metallic top skin.

Figure 24 shows the kinetic energy curve of the fragment at a speed of 2400 m/s (kinetic energy = 6 kJ) from the composite side (Situation 2) and the metal side (Situation 3), respectively. The fragment is almost always linearly decaying during the intrusion. At a constant thickness, the kinetic energy dissipation of the fragment is greater for the carbon fiber composite layer, while the Al alloy layer is insensitive to the kinetic energy dissipation of the secondary penetration of the fragment, and the kinetic energy of the fragment decays rapidly to 0 during the secondary penetration of the composite layer.

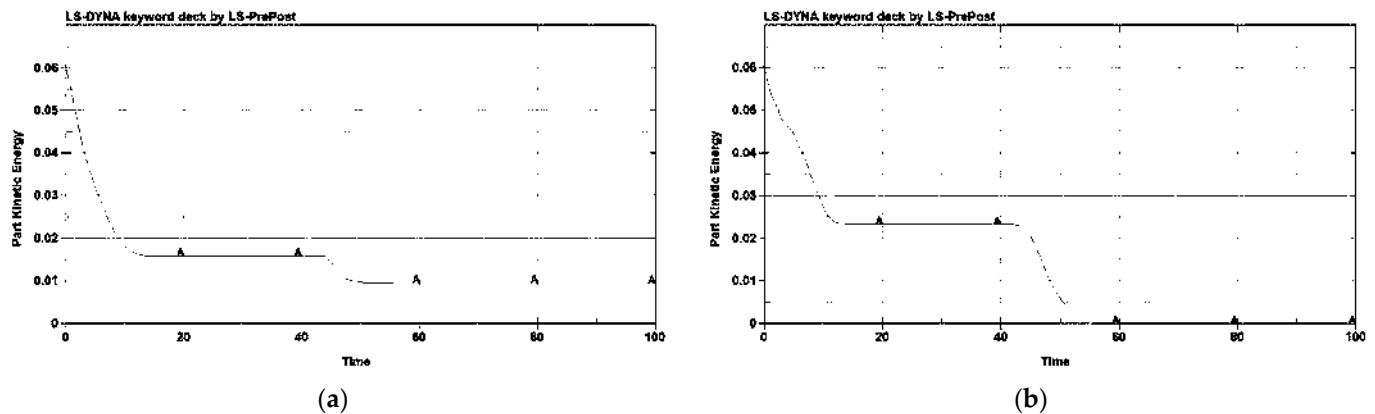


Figure 24. Curve of kinetic energy of fragments. (a) Curve of kinetic energy of fragments in Situation 2; (b) Curve of kinetic energy of fragments in Situation 3.

4. Conclusions

A high-velocity impact test based on a two-stage light gas gun was carried out on an aircraft-typical composite/metal connecting structure (CFRP/AL). The simulated battle damage impact on the typical composite/metal connecting structure of the aircraft under different rendezvous conditions was achieved. This study aims to provide a reference for the rapid repair and assessment of aircraft battle damage and the design of aircraft structural survivability. The following conclusions are drawn from the study:

1. The composite laminate damage is characterized by stages, and its regional profile is mainly in the pattern of a combination of cylindrical (shear failure zone) and circular truncated cones (tensile failure zone), and the upper and lower surfaces will produce different degrees of random spalling phenomena under the action of impact.
2. The established numerical model can well characterize the real damage morphology of both composites and the Al alloy. The damage sizes of predicted results are generally smaller than experimental results, which is within 8% on average.
3. The energy of carbon fiber debris dissipates quickly, while metal debris clouds contain considerable penetration capability, which will cause widely distributed secondary damage to the structure.
4. Different structural components have different energy dissipation capabilities. The kinetic energy of fragments decays by 4.3 kJ and 3.7 kJ, respectively, on the composite part and Al part at the first impact, and decays by 2.3 kJ and 0.4 kJ, respectively, on the composite part and Al part at the second impact. The composite part show stronger energy absorption properties, at the same thickness, than an Al alloy.

Author Contributions: Conceptualization, Y.W. and Y.H.; methodology, Y.W.; software, J.Y.; validation, Y.W.; formal analysis, J.Y.; investigation, T.Z.; resources, T.Z.; data curation, T.Z.; writing—original draft preparation, Y.W.; writing—review and editing, Y.W.; visualization, Y.W. and X.F.; supervision, H.Z.; project administration, Y.H.; funding acquisition, Y.H. All authors have read and agreed to the published version of the manuscript.

Funding: This research received no external funding.

Institutional Review Board Statement: The study was conducted in accordance with the Declaration of Helsinki, and approved by the Institutional Review Board (or Ethics Committee) of Aviation Engineering School, Air Force Engineering University.

Informed Consent Statement: Informed consent was obtained from all subjects involved in the study.

Data Availability Statement: Data will be made freely available on request.

Conflicts of Interest: The authors declare no conflict of interest.

References

1. Horsfall, I.; Austin, S.J.; Bishop, W. Structural ballistic armour for transport aircraft. *Mater. Des.* **2000**, *21*, 19–25. [CrossRef]
2. Sweetman, B. *f-22 Raptor*; Zenith Imprint: Neunkirchen, Germany, 1998.
3. Appleby-Thomas, G.J.; Hazell, P.J. The impact of structural composite materials. Part 2: Hypervelocity impact and shock. *J. Strain Anal. Eng. Des.* **2012**, *47*, 406–418. [CrossRef]
4. Miao, C.; Du, M.; Huang, L.; Zu, Z. Experimental research on hypervelocity impact characteristics of flexible anti-debris multi-shields structure. *Manned Spacefl.* **2017**, *23*, 173–176.
5. Wang, Y.T.; He, Y.T.; Zhang, T.; Fan, X.H.; Zhang, T.Y. Damage analysis of typical structures of aircraft under high-velocity fragments impact. *Alex. Eng. J.* **2022**, *62*, 431–443. [CrossRef]
6. Moritoh, T.; Kawai, N.; Matsuoka, S.; Nakamura, K.G.; Kondo, K.I.; Katayama, M. Hypervelocity impact experiments up to 9 km/s by a compact multi-stage light-gas gun. *Int. J. Impact Eng.* **2003**, *29*, 459–467. [CrossRef]
7. Reddy, P.R.S.; Reddy, T.S.; Srikanth, I.; Madhu, V.; Gogia, A.K.; Rao, K.V. Effect of viscoelastic behaviour of glass laminates on their energy absorption subjected to high velocity impact. *Mater. Des.* **2016**, *98*, 272–279. [CrossRef]
8. Reddy, P.R.S.; Reddy, T.S.; Mogulanna, K.; Srikanth, I.; Madhu, V.; Rao, K.V. Ballistic impact studies on carbon and e-glass fibre based hybrid composite laminates. *Procedia Eng.* **2017**, *173*, 293–298. [CrossRef]
9. Cantwell, W.J.; Morton, J. Comparison of the low and high velocity impact response of CFRP. *Composites* **1989**, *20*, 545–551. [CrossRef]
10. Johnson, G.R.; Cook, W.H. Fracture characteristics of three metals subjected to various strains, strain rates, temperatures and pressures. *Eng. Fract. Mech.* **1985**, *21*, 31–48. [CrossRef]
11. He, Q.G.; Chen, X.W.; Chen, J.F. Finite element-smoothed particle hydrodynamics adaptive method in simulating debris cloud. *Acta Astronaut.* **2020**, *175*, 99–117. [CrossRef]
12. Brar, N.; Joshi, V.; Harris, B. Constitutive model constants for Al7075-t651 and Al7075-t6. In Proceedings of the Aip Conference Proceedings, Nashville, TN, USA, 28 June–3 July 2009; pp. 945–948.
13. Vignjevic, R.; Campbell, J.; Hughes, K.; Orłowski, M.; Garcea, S.; Withers, P.; Reed, J. Soft body impact resistance of composite foam core sandwich panels with unidirectional corrugated and tubular reinforcements. *Int. J. Impact Eng.* **2019**, *132*, 103320. [CrossRef]
14. Zhu, W.; Xu, X. Experiment and finite element simulation in T300/QY8911 laminate under low-velocity impact. *J. Mater. Sci. Eng.* **2013**, *31*, 68–73.
15. Dogan, F.; Hadavinia, H.; Donchev, T.; Bhonge, P.S. Delamination of impacted composite structures by cohesive zone interface elements and tiebreak contact. *Cent. Eur. J. Eng.* **2012**, *2*, 612–626. [CrossRef]
16. Hallquist, J.O. *LS-DYNA Keyword User's Manual*; Livermore Software Technology Corporation: Livermore, CA, USA, 2003; Volume 970, pp. 299–800.

Article

Hybrid Shielding for Hypervelocity Impact of Orbital Debris on Unmanned Spacecraft

Kayleigh Fowler and Filipe Teixeira-Dias * 

Institute of Infrastructure and Environment (IIE)—School of Engineering, The University of Edinburgh, The King's Buildings, Edinburgh EH9 3FG, UK; k.r.fowler@sms.ed.ac.uk

* Correspondence: f.teixeira-dias@ed.ac.uk

Abstract: The passive shielding of space craft structures is critical due to the increase in demand for lightweight protection, which is required to counter the damaging effects of micro-meteoroid orbital debris (MMOD) on unmanned spacecraft, which have steeply increased in recent years. Research on hypervelocity impact (HVI) led to the development of shield configurations such as the conventional Whipple shield, which consists of two plates separated by a stand-off distance to allow for the fragmentation and dispersion of the debris from the impact. Variations in the Whipple shield have been proposed, where additional layers are included for increased energy dissipation efficiency. In this work, the authors develop, validate and test a numerical model of an orthogonally loaded hybrid Whipple shield, incorporating an aluminium honeycomb core, orientated with hexagonal tubes perpendicular to the direction of proposed debris travel, to mitigate the well-known channelling effect. The debris threat is an A2024-T3 projectile, impacting the structure at a velocity of 6.5 km/s. The proposed model is validated with experimental observations of the debris spread at half-angle and the efficiency of the proposed topology is assessed against a conventional two-plate A2024-T3 shield. The honeycomb core cell density, its position relative to the point of impact, the thickness of the honeycomb shell, and the material of the honeycomb are thoroughly analysed. A hybrid honeycomb structure concept is proposed, which provides a highly efficient alternative to a standard Whipple shield design, without significantly compromising the weight of the structure. The obtained results clearly show that the hybrid Whipple shield exhibits significantly increased the kinetic energy dissipation of the debris from the impactor and shield front plate, with an increase in the dissipated kinetic energy that can reach 86.8% relative to the conventional shield.

Citation: Fowler, K.; Teixeira-Dias, F. Hybrid Shielding for Hypervelocity Impact of Orbital Debris on Unmanned Spacecraft. *Appl. Sci.* **2022**, *12*, 7071. <https://doi.org/10.3390/app12147071>

Academic Editors: Lina M. López, Ricardo Castedo and Anastasio P. Santos

Received: 12 May 2022

Accepted: 12 July 2022

Published: 13 July 2022

Publisher's Note: MDPI stays neutral with regard to jurisdictional claims in published maps and institutional affiliations.



Copyright: © 2022 by the authors. Licensee MDPI, Basel, Switzerland. This article is an open access article distributed under the terms and conditions of the Creative Commons Attribution (CC BY) license (<https://creativecommons.org/licenses/by/4.0/>).

Keywords: hypervelocity impact; whipple shield; honeycomb passive shielding; micro-meteoroid and orbital debris (MMOD); Smoothed Particle Hydrodynamics (SPH); finite-element analysis; LSDyna

1. Introduction

Research into the passive shielding of spacecraft structures has heightened over recent decades owing to an increase in demand for lightweight, cost-effective technology, which is required to counter the damaging effects of micro-meteoroid orbital debris (MMOD) [1]. The amount of MMOD in space has been “steadily rising since the beginning of the space age”, as stated in the European Space Agency’s Annual Space Environment Report in 2020 [2]. In 2007 alone, a further 32% increase in MMOD was observed as a result of major low-earth-orbit (LEO) collisions [3]. The rise in MMOD significantly increased the risk associated with space exploration and, as a result, the Inter-Agency Space Debris Coordination Committee (IDAC) was established in 1993 to mitigate the damage caused by micro-meteoroid orbital debris.

The design of the International Space Station (ISS) in the 1990s prompted the further development of protective shielding methods. Hypervelocity impact (HVI) research, along with the hydrocode simulations conducted by NASA and other research facilities and

groups, led to the development of numerous shield configurations, such as the Whipple, Stuffed Whipple, and metallic foam sandwich Whipple shields [4]. These protective structures are designed with the main aim of mitigating the effects of hypervelocity impacts that, due to their extremely high energy, have the potential to perforate shields in space structures.

The conventional Whipple shield design consists of two plates, usually made of aluminium, separated by a stand-off distance to allow for the fragmentation and dispersion of debris from the impact on the first plate. A schematic illustration of this design principle is shown in Figure 1.

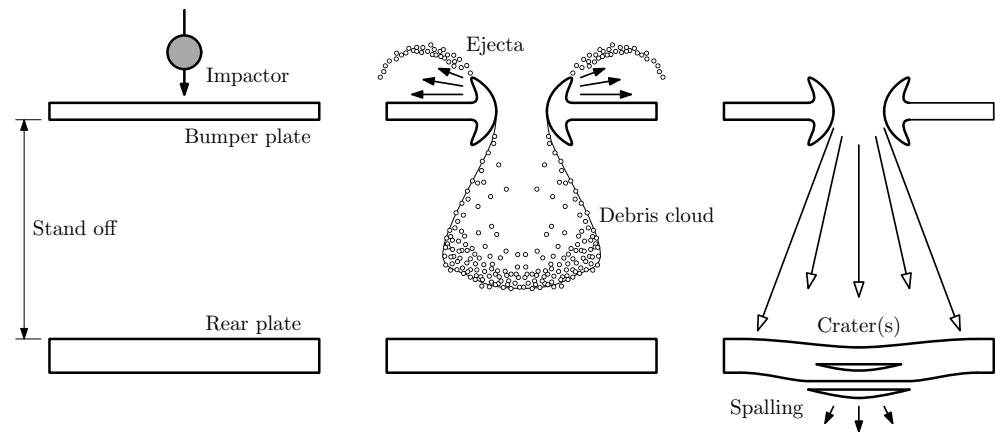


Figure 1. Conventional Whipple shield design: (left) Whipple shield configuration, (centre) post-impact debris cloud formation and (right) effects of impact on rear plate (adapted from [5]).

The Stuffed Whipple, as shown in Figure 2a, incorporates an additional layer, commonly a combination of Nextel or Kevlar/Epoxy, to improve overall shield performance and energy dissipation [6]. The incorporation of metal foams into the Whipple shield design has also been studied in 2017 by Cherniaev and Telichev [6], as shown schematically in Figure 2b. Ryan and Christiansen [5] also demonstrated the potential of such design approaches for space applications, owing to ability to significantly increase the absorption of impact energy compared to more conventional shielding structures. In these studies, it was clearly demonstrated that the two main design characteristics affecting the dissipation of kinetic energy and debris fragmentation are the choice of material(s) (and corresponding material properties) and the geometry of the shield design [1].

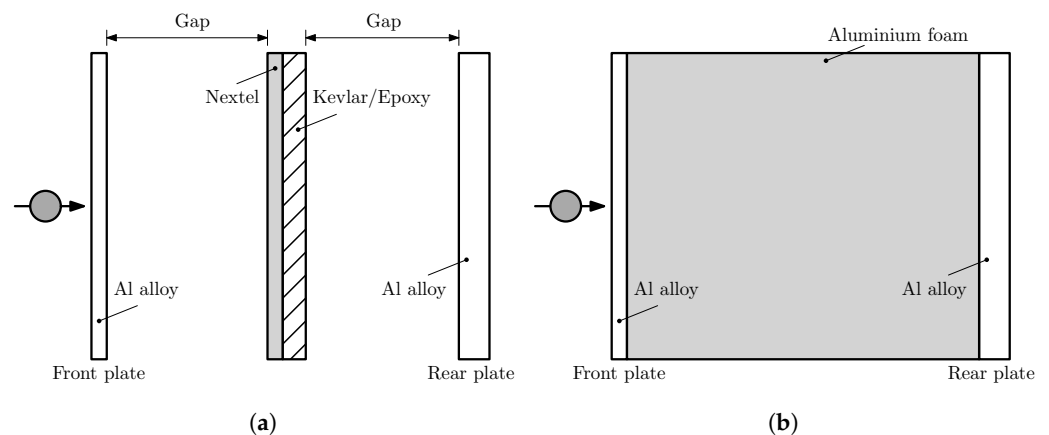


Figure 2. Schematics of alternative Whipple shield designs: (a) Stuffed Whipple and (b) aluminium foam sandwich (adapted from [6]).

In the late 1990s, Christiansen et al. [7] proposed the use of lightweight, non-metallic materials, such as Nextel ceramic cloth and Kevlar, for the Whipple shield. These materials

were configured in a number of different flexible multi-layer designs. Christiansen et al. tested the penetration resistance in terms of hypervelocity impact and successfully demonstrated the potential for this lightweight shielding, going as far as deriving a set of ballistic limit equations for the proposed shields for orthogonal and non-orthogonal low ($v < 2700$ [m/s]), intermediate ($2700 < v < 6500$ [m/s]) and high velocity impacts ($v > 6500$ [m/s]).

Plassard et al. [8] conducted HVI experiments using a two-stage light gas gun. A 3-mm aluminium projectile was fired with a velocity of 4119 m/s at a Whipple shield consisting of an aluminium target plate and a witness plate positioned 30 mm apart. The experimental observations were compared to numerical simulation results in LS-DYNA. The proposed numerical model was found to be a sufficiently accurate representation of the experiment, justifying the use of the hydrocode in further analysis and the shielding design for the hypervelocity impact of orbital debris on unmanned spacecraft.

Research into the material properties of the Whipple shield was more recently conducted by Zhang et al. [9], where the energy absorption efficiency of the combination of a homogeneous aluminium sheet with a Ti-Al-nylon impedance-graded material (IGM) was compared using both laboratory testing and numerical simulations. The experiments were performed using a two-stage light gas gun and focussed on post-impact effects, using 3D scanners to detect physical damage in detail. Zhang et al. proposed a smooth particle hydrodynamics (SPH) numerical model, developed in AUTODYN, and performed a detailed analysis of the relevant kinetic energy dissipation, fragmentation, and pressure distribution. Their results revealed a significant improvement in shield performance using the IGM with regards to both fragmentation and energy dissipation. The increased shock pressure that was experienced, achieved through the interaction between travelling shock waves and reflected rarefactions, allowed for an optimised shield design. The increase in debris spread angle was further confirmation that the material properties of the IGM were suited to HVI shield design.

Recently, the addition of a honeycomb structure to Whipple shield design has been extensively explored by authors such as Carriere and Cherniaev [10,11] and Aslebagh and Cherniaev [12], among others. These researchers adopted an orientation of the honeycomb, where the cells' axis is perpendicular to the front and bumper plates. This allows for a significant reduction in the debris spread angle, but creates a channelling effect, as the honeycomb is orientated parallel to the direction of debris travel, as shown in Figure 3. Although the reduction in the debris spread angle is significant, it creates the adverse effect of concentrating the impact on a smaller area, adversely affecting the energy dissipation of the projectile. Double/multi-honeycomb core configurations were noted as being less prone to channelling effects due to the implementation of a staggered design [10].

More recently, Pai and Shenoy [13] presented a detailed review of recent advances in the Whipple shield design, noting that debris channelling (also referred to as ejection-tunnelling effect) should be considered in the design process of Whipple shields, and can be detrimental to the energy dissipation and mechanisms.

A solution to the channelling effects, however, would be to change the orientation of the honeycomb cells from parallel to perpendicular to debris travel, with the added advantages that the weight of the structure could remain unchanged. In 2009, Ryan et al. [14] conducted a comparative study between the use of a parallel-orientated honeycomb core and metallic open-cell foam for Whipple shield application. These authors found that the foam had several advantages over the honeycomb due to the elimination of channelling.

Very few studies have been dedicated to determining the effectiveness of a perpendicular honeycomb cell orientation regarding the energy absorption of Whipple shields. Therefore, the proposed research aims to explore the potential benefits of implementing a perpendicularly orientated honeycomb core in relation to the energy dissipation of an impact projectile at hypervelocity, and exploring the effects of the topology of the honeycomb structure on the energy absorption of the shield as a whole.

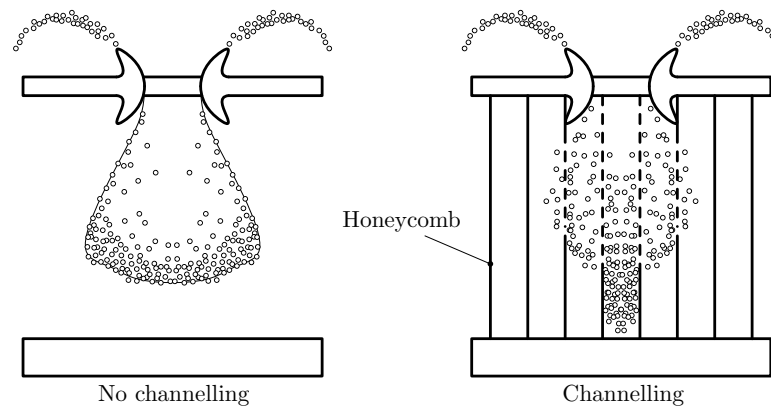


Figure 3. Illustration of the channelling effect on honeycomb core Whipple shields: without honeycomb core (left) and with honeycomb core (right).

2. Numerical Modelling

The main aim of the proposed research is to explore and optimise the benefits of using lightweight honeycomb structures in the Whipple shield design, with potential application in unmanned spacecraft. A set of numerical models is developed and validated, based on an aluminium honeycomb Whipple shield. These passive shielding models are implemented in LS-DYNA and described in detail in the following paragraphs. The validated models are then used to perform a thorough analysis of the effects of different shield parameters (core density, impact location, etc.) on the energy absorption performance and impact protection of the Whipple shield.

2.1. Model Configuration

The proposed modified Whipple shield has a honeycomb layer—the shield core—between the bumper plate and the rear wall. The honeycomb is orientated with the axis of the cells perpendicular to the impact direction, as shown in Figure 4. The main design principle is that this allows for the sides of the honeycomb cells to maximise the dispersion of fragments at wider angles, also maximising the dissipation of energy further from the back plate and onto a larger area. This orientation also fully eliminates the possibility of channelling effects, which, as previous research suggests, has a highly detrimental effect on reducing the impact kinetic energy of the debris particle [10].

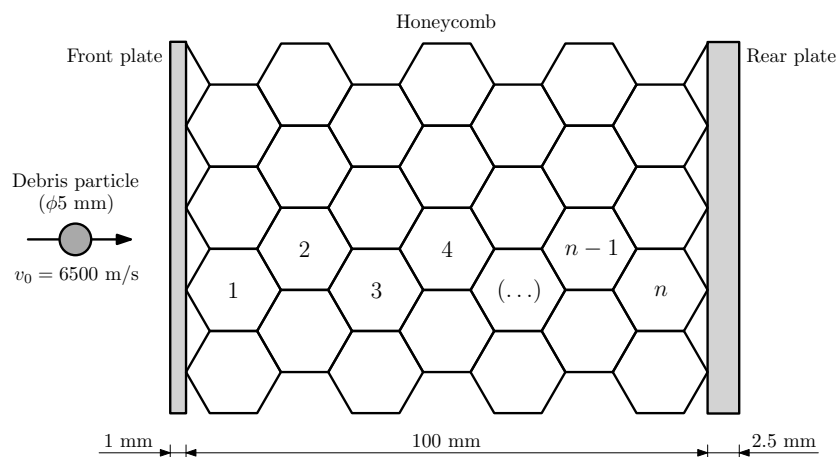


Figure 4. Honeycomb Whipple shield configuration with cell numbering, sequentially from the front towards the back plate.

The numerical models include a spherical projectile, and front and back plates with 1 and 2.5 mm thickness, respectively. The diameter of the projectile is 5 mm, which is

consistent with the lower end of the equivalent sphere diameter (ESD) distribution, as reported by a number of different authors [15–17]. The model developed by the authors is validated and optimised based on the effects of a number of design parameters on the energy absorption capacity of the shield. These include the density of the honeycomb (i.e., number of honeycomb cells per unit length), the thickness of the honeycomb shell, the choice of honeycomb material, and the location of impact relative to the honeycomb.

2.2. Finite Elements and SPH Model

The finite-element method is used to model the impact response of the whole system, including the front (bumper) and back plates, and all models were set up in LS-DYNA.

Solid constant stress solid elements are used to model the bumper plate and black wall, and four-node constant thickness shell elements are used in the honeycomb structure. The same mesh size is used in both the bumper and back plates and a thorough mesh convergence analysis is carried out to determine the optimal mesh size. The spherical projectile and the impact area on the front plate are modelled using Smoothed Particle Hydrodynamics (SPH). The convergence analysis was also extended into the SPH domain to determine the optimal particle density, especially as this method is highly computationally heavy and often leads to high CPU times. Specific contacts were implemented to model the interaction between the different model components: (i) tied contacts between the finite element and the SPH particles in the bumper plate, and (ii) automatic contacts between all SPH particles—both from the impactor and the impacted area—and all other finite-element components in the model (the back plate, the front plate and the honeycomb). In LS-DYNA, these contacts were implemented with the keywords `*CONTACT_AUTOMATIC_NODES_TO_SURFACE` and `*CONTACT_TIED_NODES_TO_SURFACE`, respectively.

To optimise computational efficiency the proposed models explored symmetries when possible, that is, when all impact, geometrical and boundary conditions were symmetrical. Oxz and Oyz are the two symmetry planes of this model, as can be seen in Figure 5a. One of these planes—symmetry plane Oxz —is used in this research, as shown in Figure 5b. Symmetry plane Oyz , however, cannot be used, as it is not a symmetry plane for the impact location analyses, where symmetry is broken when the debris particle impacts at different locations.

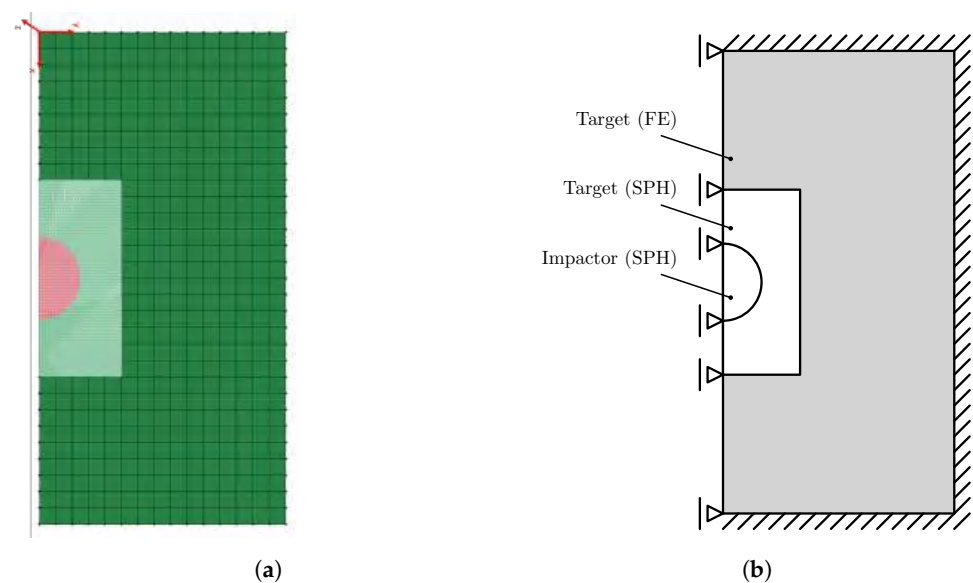


Figure 5. Simulation set-up showing (a) FE mesh, SPH regions and coordinate system; and (b) boundary conditions.

The HVI problem being analysed is a kinematics-dominated problem; thus, imposing fixed boundary conditions on the Whipple plates is not strictly necessary. This is supported by the progression of the post-impact radial stress wave on the Whipple front plate. To

ensure the consistency of analysis with the experimental results of Zhang et al. [9], these boundary conditions were imposed. The implemented boundary conditions are shown in Figure 5. The external edges of the finite-element meshes on the front and back plate, as well as the honeycomb core, are fixed in all degrees of freedom (linear and rotational). The motion of all SPH particles on the plane of symmetry was also restricted to in-plane motion, that is, fixed in the y-direction, as shown in Figure 5.

An initial constant velocity of 6500 m/s is imposed on the spherical projectile along the direction perpendicular to the bumper plate (z-direction in Figure 5). This velocity is representative of a generic micro-meteoroid orbital debris particle impacting the shield.

2.3. Constitutive Modelling

Due to the high energy involved in the hypervelocity impact, all Whipple shield components, including the honeycomb core and debris particle, were modelled with the Johnson–Cook constitutive law to ensure adequate plasticity, strain-rate and temperature material behaviour is captured. These three terms are explicitly and separately described in Johnson–Cook’s constitutive equation

$$\bar{\sigma} = \left[A + B \left(\bar{\epsilon}^{pl} \right)^n \right] \left[1 + C \ln \left(\frac{\dot{\bar{\epsilon}}^{pl}}{\dot{\bar{\epsilon}}_0^{pl}} \right) \right] \left[1 - \left(T^* \right)^m \right] \quad (1)$$

where $\bar{\sigma}$ is the flow stress, $\bar{\epsilon}^{pl}$ is the equivalent plastic strain, n is the strain hardening exponent, A , B , C and m are material constants that can be determined experimentally, $\dot{\bar{\epsilon}}^{pl}$ is the equivalent plastic strain rate [18], and T^* is the non-dimensional homologous temperature, defined as

$$T^* = \frac{T - T_t}{T_m - T_t} \quad (2)$$

where T is the current temperature, T_m is the melting temperature and T_t is the transition temperature, at or below which there is no temperature dependence for the yield stress.

Damage caused by the impact is modelled using the associated Johnson–Cook damage model, which similarly considers the effects of plasticity, strain-rate and temperature, and can be described by the equation

$$\bar{\epsilon}_D^{pl} = \left[D_1 + D_2 \exp(-D_3 \eta) \right] \left[1 + D_4 \ln \left(\frac{\dot{\bar{\epsilon}}^{pl}}{\dot{\bar{\epsilon}}_0^{pl}} \right) \right] \left(1 + D_5 T^* \right) \quad (3)$$

where D_i ($i = 1, \dots, 5$) are the damage parameters measured at or below the transition temperature and η is the stress triaxiality, which represents the ratio of pressure to von Mises stress. The damage parameter is then calculated as

$$D = \sum \frac{\bar{\epsilon}_D}{\bar{\epsilon}_D^{pl}} \quad (4)$$

and damage occurs when the damage parameter D reaches a value of 1.0. After damage initiation, the material stiffness is progressively degraded according to the damage evolution relationship [18].

The developed models of the Whipple shield honeycomb core were tested with two different lightweight materials: an aluminium alloy (AL2024-T3) and a titanium alloy (Ti-6Al-4V). The impact energy absorption efficiency of both materials is analysed and compared. The front plate, the back plate and the debris particle (projectile) are aluminium (AL2024-T3) throughout. The material parameters for all materials in the models are listed in Table 1 [19,20].

Due to the high energy involved in the hypervelocity impact, the compressibility of the materials is modelled using the non-linear Mie–Grüneisen equation of state

$$p = \frac{\rho_0 G^2 \mu [1 + (1 - \frac{\gamma_0}{2})\mu - \frac{a}{2}\mu^2]}{[1 - (S_1 - 1)\mu]^2} + (\gamma_0 + a\mu)E \tag{5}$$

where E is the internal energy, $\mu = \rho/\rho_0 - 1$ is the relative density, γ_0 is the non-dimensional Grüneisen constant, a is the volume correction for γ_0 and G, S_1 are material constants that depend on the shock wave and particle velocities. The corresponding parameters are listed in Table 1. This simplified version of the non-linear Mie–Grüneisen equation of state in Equation (5) only considers the first-order dependency of the pressure on the material density ($S_2 = S_3 = 0$).

Table 1. Johnson–Cook constitutive and damage models, and Mie–Grüneisen equation of state parameters for AL2024-T3 (debris particle, shield and honeycomb core) and Ti-6Al-4V (honeycomb core) [21,22].

Constitutive Equation	Material Parameter	AL2024-T3	Ti-6Al-4V
Johnson–Cook	A (MPa)	167	862
	B (MPa)	684	331
	n	0.551	0.34
	C	0.001	0.012
	m	0.859	0.8
Johnson–Cook (damage)	D_1	0.112	−0.09
	D_2	0.123	0.25
	D_3	1.5	−0.5
	D_4	0.007	0.014
	D_5	0	3.87
Mie–Grüneisen (EoS)	G	5240	5130
	γ_0	1.97	1.23
	S_1	1.400	1.028
	a	0.48	0.17

2.4. Convergence and Validation

A standard two-plate Whipple shield was used to validate the methodology and models in this research. To achieve this, the numerical results from the standard Whipple shield (SWS) were compared to experimental observations by Zhang et al. [9], where all model parameters were kept the same to allow for a direct comparison. The SWS simulation setup is shown in Figure 6. A 5-mm aluminium projectile was fired with a velocity of 6500 m/s at a Whipple shield with a front plate of thickness 1 mm and a back plate thickness of 2.5 mm. Figure 7 shows the progression of the simulation in approximately 2- μ s intervals.

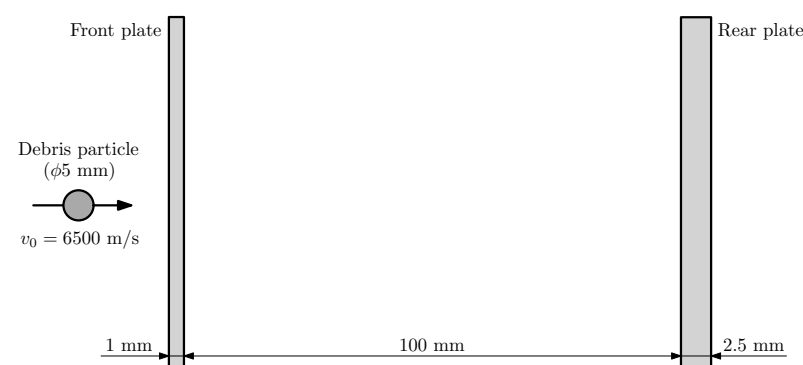


Figure 6. Standard Whipple shield configuration.

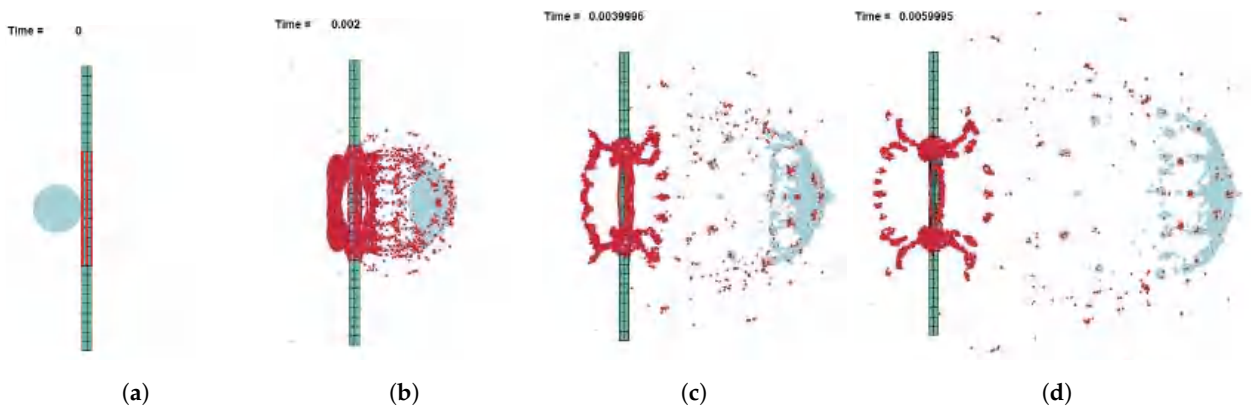


Figure 7. Simulation of standard Whipple shield model shown at: (a) $t = 0 \mu\text{s}$, (b) $t = 2 \mu\text{s}$, (c) $t = 4 \mu\text{s}$, and (d) $t = 6 \mu\text{s}$.

2.4.1. SPH Particle Density

Zhang et al. [9] published the results of a pressure analysis conducted on an AL2024 standard Whipple shield. These authors used pressure gauges applied to the front of the projectile to calculate the average impact pressure on the front plate on the first $0.5 \mu\text{s}$ of the impact. A similar procedure is followed in the numerical model developed in this work. The simulation was run with varying SPH particle densities and the results obtained for $t \in [0, 0.5] \mu\text{s}$ are shown in Figure 8. Datapoints were extracted from the work of Zhang et al. [9] and have also been included in Figure 8 to allow for a comparison and validation to be made, where the average impact pressure p was determined as the average of the pressure distribution for $t \in [0, 0.5] \mu\text{s}$, for a range of selected SPH particles on the front side (towards the direction of impact) of the projectile, to match the data recorded by Zhang et al. [9].

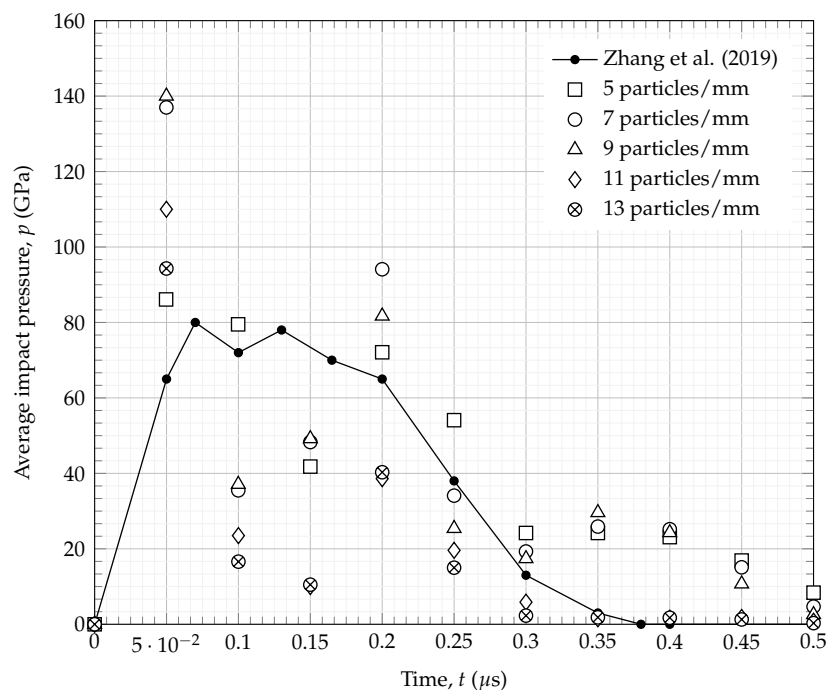


Figure 8. Average impact pressure p for varying SPH density and comparison with observations by Zhang et al. [9].

The general trend of the impact pressure results is similar to the experimental observations of Zhang et al., albeit with a relatively high level of scatter—the largest relative difference in peak average impact pressure between the numerical model and the obser-

variations of Zhang et al. [9] is below 43%. The results in Figure 9, showing the average impact pressure p and computational runtime against the SPH particle density, allow for a converging solution to be more easily identified. A clear convergence can be observed from an SPH particle density of 5 particles/mm to 13 particles/mm. The computational runtime is shown to exponentially increase with an increase in the SPH particle density. This clearly suggests that using fewer SPH particles within the model is a more efficient approach. The intersection of best-fit curves in Figure 9 can be used to select the optimum modelling approach and SPH particle density, which, in this case, is below 10 particles/mm. Optimising the computational runtime for the available resources was necessary, leading to an optimal particle density of 5 particles/mm.

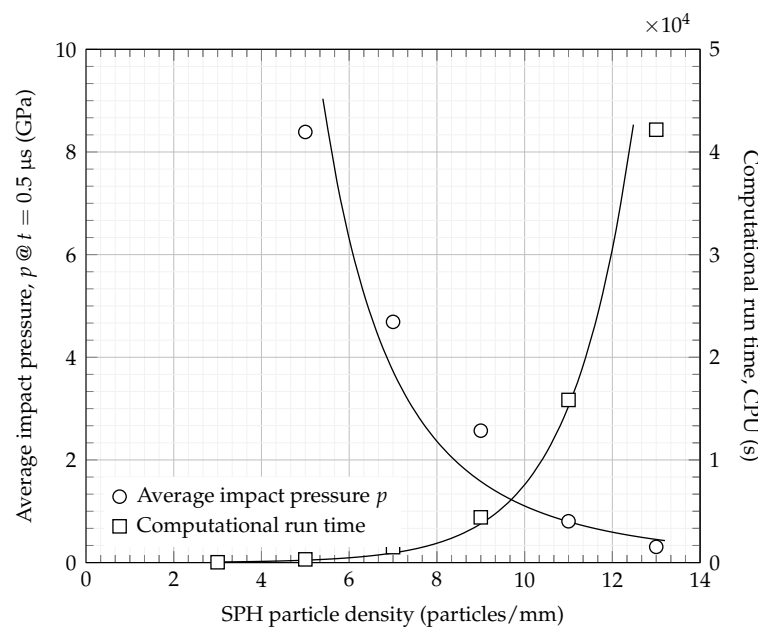


Figure 9. Average impact pressure p at time $t = 0.5 \mu\text{s}$ and computational run time (CPU) against the SPH particle density, with corresponding trendlines.

To more robustly validate the proposed models, a thorough comparison of the debris spread angle was also done. Zhang et al. [9] reported that the half-angle obtained using the aforementioned parameters to be 19.8° . The debris spread half-angle for the LS-DNYA model was measured on the Whipple shield model at multiple time intervals and averaged to obtain a half-angle of 21.5° . This corresponds to a relative difference of 7.9%, and is thus considered accurate, further validating the use of the proposed SPH particle density in the model for further analysis.

2.4.2. Honeycomb Mesh Convergence

A detailed mesh convergence analysis was also performed on the honeycomb core structure. The computational run time (CPU) was monitored for finite element meshes of the honeycomb with different element sizes, ranging from 0.4 to 3.2 mm, with the corresponding results shown in Figure 10. The convergence analysis simulation was set up with an SPH density of 5 particles/mm to minimise computational run time, and all remaining models were set up with the optimal 7 particles/mm density. Al2024-T3 was used for all components of the shield, and all parameters other than the mesh element size of the honeycomb shell were kept constant. The results in Figure 10 indicate that the optimum solution in terms of reducing CPU time whilst retaining an accurate solution, is to use a 1 mm element size.

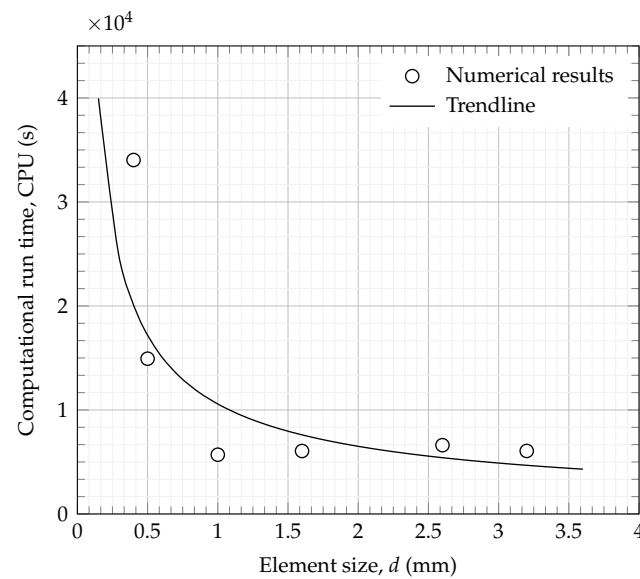


Figure 10. Computational run time (CPU) against finite element mesh element size of the honeycomb core structure.

3. Results and Discussion

This section discusses the results of further analyses done with the models described and validated in the previous sections. These include a number of critical design parameters of the Whipple shield, such as (i) the density of the honeycomb core (i.e., the number of honeycomb cells along the width of the core); (ii) the thickness of the honeycomb shell, both of which will directly impact the weight (areal density) of the final shield; (iii) the honeycomb base material; and (iv) the exact location of the impact relative to the honeycomb. The capacity for the shield to dissipate the kinetic energy of the impact was used as the main design parameter in these studies. The labels and specifications of the developed models are listed in Table 2, along with the key results from each parameter study to analyse the effectiveness of the honeycomb core shield. As an example, Figure 11 shows a 3-dimensional view of the T-50 model, with a core cell density of 6 and a shell thickness $t_h = 0.5$ mm. Table 3 and Figure 12 summarise the main results from all the tests. In order to record the energy dissipated before particles bounce back off the back plate, some results are captured at different times, $t = 17.5 \mu\text{s}$ for the honeycomb shell thickness simulations and $t = 20 \mu\text{s}$ for all remaining ones.

Table 2. Characteristics and labels of the developed Whipple shield numerical models.

Test	Model Label	Material	Cells	Thickness t_h (mm)	Impact Location
Standard shield	C-0	–	0	–	–
Cell density	C-2	AL2024-T3	2	0.5	Single edge
	C-4		4	0.5	
	C-6		6	0.5	
	C-8		8	0.5	
	C-10		10	0.5	
Shell thickness	T-01	AL2024-T3	6	0.01	Single edge
	T-05		6	0.05	
	T-10		6	0.1	
	T-15		6	0.15	
	T-20		6	0.2	
	T-30		6	0.3	
	T-50		6	0.5	

Table 2. Cont.

Test	Model Label	Material	Cells	Thickness t_h (mm)	Impact Location
Material	M-AL	AL2024-T3	6	0.3	Single edge
	M-TI	Ti-6Al-4V	6	0.3	
Impact location	L-SE	AL2024-T3	6	0.3	Single edge
	L-MP		6	0.3	Mid point
	L-DP		6	0.3	Double point

Table 3. Summary of main results and dissipation of kinetic energy for all numerical simulations.

Model Label	Kinetic Energy E_k (kNmm)	Time Stamp t (μ s)	Energy Dissipation
C-0	575	20	Reference @ 20 μ s
C-2	330	20	42.6%
C-4	202		64.9%
C-6	164		71.5%
C-8	162		71.8%
C-10	146		74.6%
T-0	1286	17.5	Reference @ 17.5 μ s
T-01	1285	17.5	0.1%
T-05	1230		4.8%
T-10	1040		19.5%
T-15	773		40.2%
T-20	432		66.6%
T-30	280		78.4%
T-50	172		86.8%
M-AL	244	20	57.6%
M-TI	177		69.2%
L-DP	255	20	55.7%
L-SE	244		57.6%
L-MP	225		60.9%

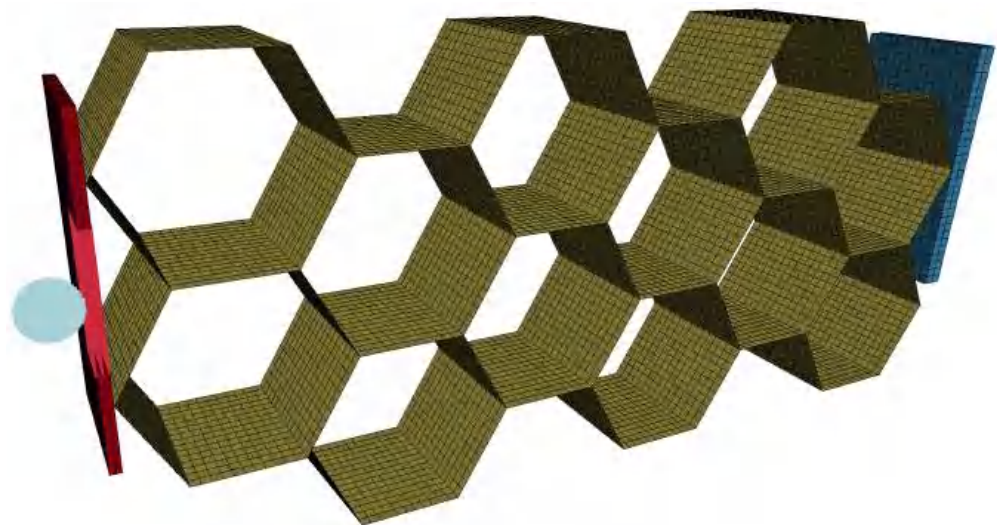


Figure 11. 3-dimensional view of model T-50, with a core cell density of 6 and a shell thickness $t_h = 0.5$ mm (see Table 2).

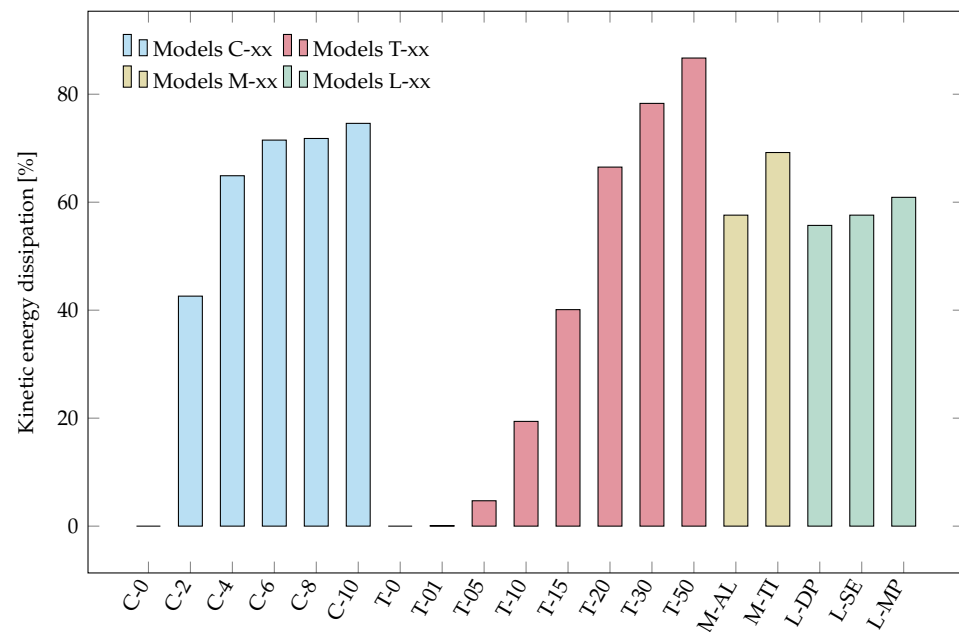


Figure 12. Kinetic energy dissipation for the honeycomb core density, shell thickness, material and impact location models, relative to reference cases (see Table 3).

3.1. Honeycomb Core Cell Density

It was anticipated that the honeycomb core cell density, i.e., the number of cells per unit length across the width of the shield gap, would be a critical parameter influencing the energy absorption efficiency of the shield. In order to test this hypothesis and quantify the influence of the honeycomb core cell density, a number of models were developed using an SPH particle density of 7 particles/mm for the projectile and region of impact, as discussed in Section 2.4.1, and different cell densities. All model parts, including the honeycomb, were set as AL2024-T3 and a finite-element mesh element size of 1 mm was used.

The results in Figure 13 show how the total kinetic energy of the debris particle was dissipated to increase the honeycomb core cell densities (models C-0 to C-10). Model C-0 is included as it represents the standard Whipple shield, i.e., without a honeycomb core. It can be clearly observed that the kinetic energy of the debris particle significantly decreases when a honeycomb component is introduced, corresponding to an increase in the energy dissipation ranging from a minimum of 42.6% to a maximum of 74.6%, as shown in Table 3. Figure 13 also shows that the change in kinetic energy of the debris particle for cores with more than six cells across the width is minimal. The difference in energy dissipation between model C-6 and model C-10 is only 3.1%. Therefore, for the modelled impact conditions, increasing the core cell density above six cells (model C-6) is not beneficial in terms of energy absorption and will clearly be detrimental to the weight of the structure.

The simulation frames in Figure 14, showing the numerical model of each honeycomb configuration at time $t = 16.2 \mu\text{s}$, further support these observations and conclusions, clearly showing that the dispersion of particles becomes more evident when increasing honeycomb core cell density. There is some visible penetration of rogue SPH particles, which is a known issue with SPH modelling. Common strategies to try to mitigate these nonphysical effects include changing the contact algorithm and/or refining the finite-element mesh of the impacted part. In the present case, however, these two strategies were tested and proved to not decrease rogue particle penetration without significantly increasing the cost of the computation. Additionally, the energy of these rogue particles was estimated to be insignificant (less than 1%) compared to the total energy of the problem. A higher level of fragmentation and damage to the honeycomb shell occurred closer to the front plate, which further supports the results shown in Figure 13. A complete absence of channelling effects is also visible.

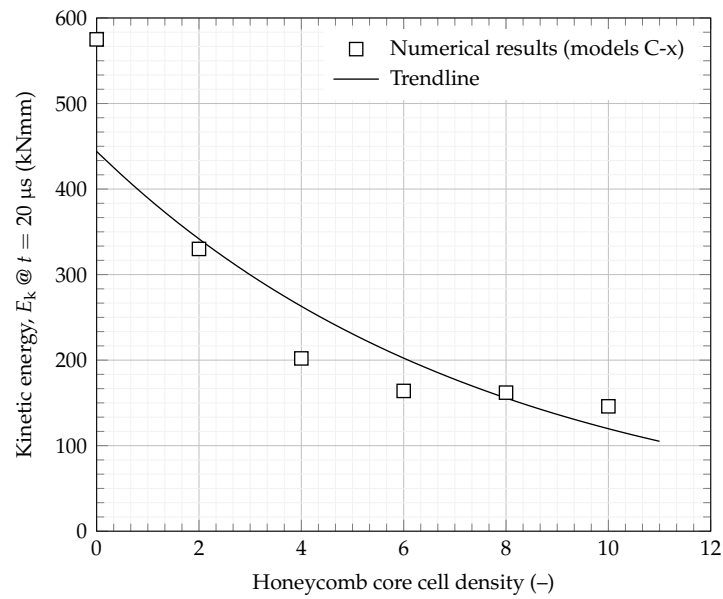


Figure 13. Kinetic energy of the debris particle at $t = 20 \mu s$ against the number of cells across the width of honeycomb core.

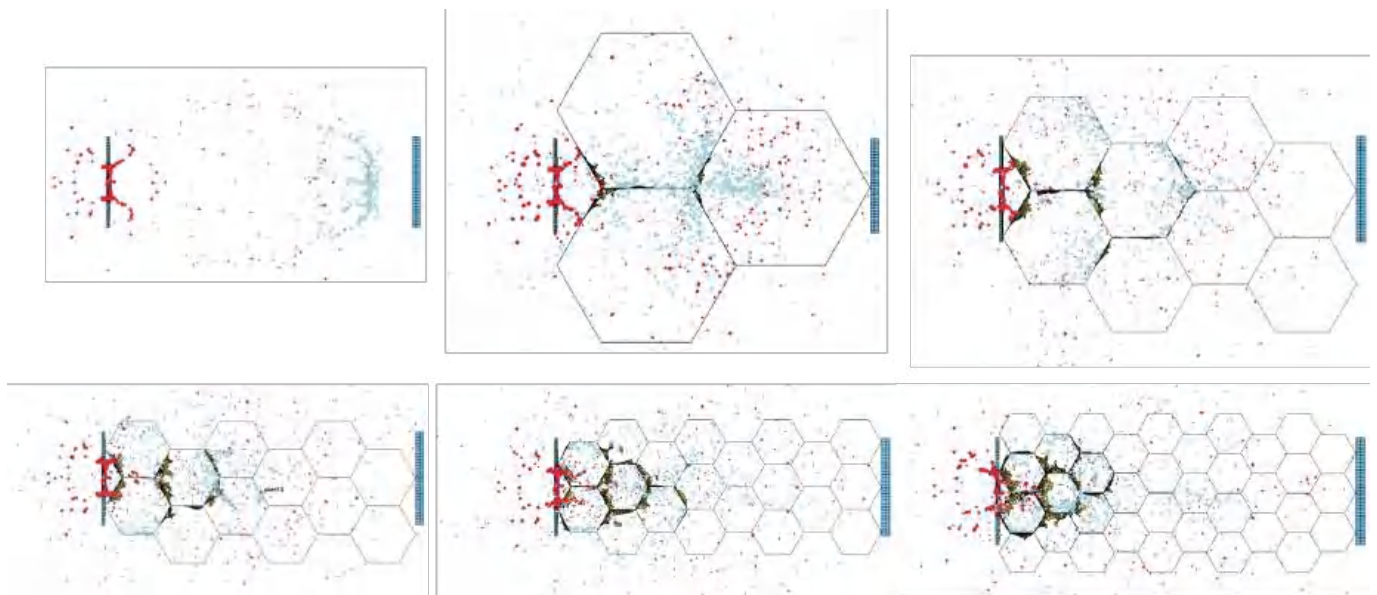


Figure 14. Simulation progress at $t = 16.2 \mu s$ for an increasing number of cells across the width of honeycomb core for model C-0 (top left) to model C-10 (bottom right).

3.2. Honeycomb Shell Thickness

The impact of the thickness of the honeycomb core shell on the energy dissipation efficiency is analysed by simulating varying values of shell thickness, t_h . Following the conclusions regarding the optimisation of the honeycomb core cell density in Section 3.1 above, model C-6 is used, with an AL2024-T3 honeycomb, and a shell thickness t_h ranging from 0.01 to 0.5 mm, as listed in Table 2. The debris particle and impact zone have an SPH particle density of 7 particles/mm. The results in Figure 15 show a significant decrease in the kinetic energy of the debris particle at 17.5 μs for increasing t_h . This trend shows that, for thicknesses above 0.3 mm, the increase in energy dissipation becomes less evident. The energy dissipation increases only 8.4% for thicknesses between 0.3 and 0.5 mm, compared to a 78.3% increase between 0.01 and 0.3 mm, which corresponds to model T-30 in Table 3.

To further support these conclusions, the simulation images in Figure 16 clearly show that, for shell thicknesses above 0.3 mm, there is no clustering of SPH particles (i.e., debris) reaching the back plate of the Whipple shield. A clear increase in debris fragmentation can also be observed from model T-01 to model T-50 at $t = 16.2 \mu\text{s}$. Models with a smaller shell thickness exhibit a more tightly packed particle spread than models with a larger shell thickness, showing fewer particle clusters. The particle spread also appears much closer to the back plate for a smaller shell thickness. This further supports the results in Figure 15, as the increasing thickness of the honeycomb shell could be expected to positively influence the spread of debris fragments.

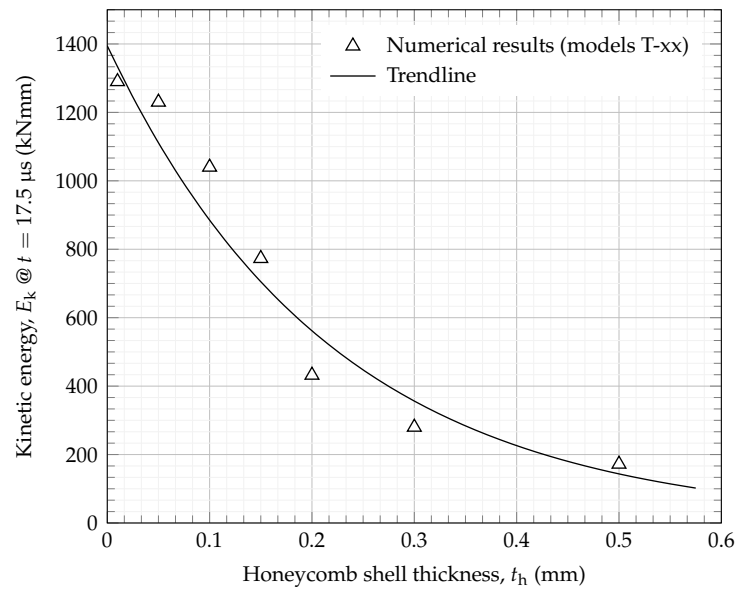


Figure 15. Kinetic energy of the debris particle at $t = 17.5 \mu\text{s}$ against thickness of the honeycomb shell.

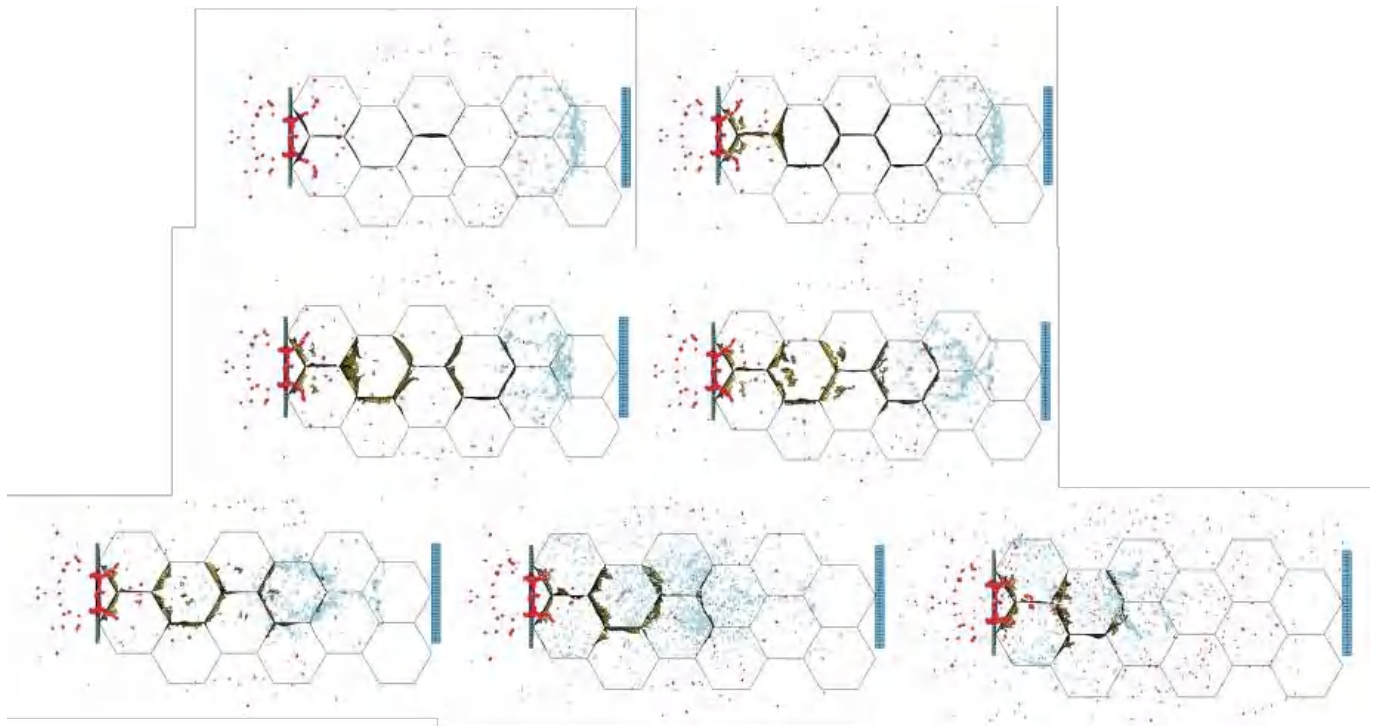


Figure 16. Simulation progress at $16.2 \mu\text{s}$ for an increasing thickness of honeycomb core from top left (model T-01) to bottom right (model T-50).

3.3. Honeycomb Material

The honeycomb material is a critical design aspect for the optimised Whipple shield as this will not only have a direct impact on the energy absorption, but also on the weight of the structure. Two different numerical models were developed using aluminium alloy (AL2024-T3) and titanium alloy (Ti-6Al-4V) honeycomb cores, corresponding to models M-AL and M-TI in Table 2, respectively. These models are compared to determine the effect that changing the material of the honeycomb core has on the energy dissipation of the debris particle. Figure 17 shows how the kinetic energy is dissipated for both models in the first 20 μs of the impact. These results clearly show that, from early in the impact ($t \approx 1 \mu\text{s}$), model M-TI is more efficient at dissipating the kinetic energy of the debris particle when compared with model M-AL. Although a 27.8% difference can be observed in the kinetic energy of the debris particle between the two different materials at $t = 20 \mu\text{s}$, when comparing to the standard Whipple shield, the energy dissipation efficiency is significantly higher, at 57.6% and 69.2% for the M-AL and M-TI models, respectively.

Figure 18 shows a comparison in debris fragmentation and honeycomb perforation between the two material models, M-AL and M-TI. Although the perforation pattern of the honeycomb is similar between the two models, there is an evident variation, albeit slight, in the distribution of the debris going through the honeycomb structure, with a larger fraction of particles appearing further toward the back plate in model M-AL compared with model M-TI. This agrees with the results in Figure 17, and suggests that the titanium alloy Ti-6Al-4V honeycomb is more effective in dissipating the kinetic energy from the hypervelocity impact.

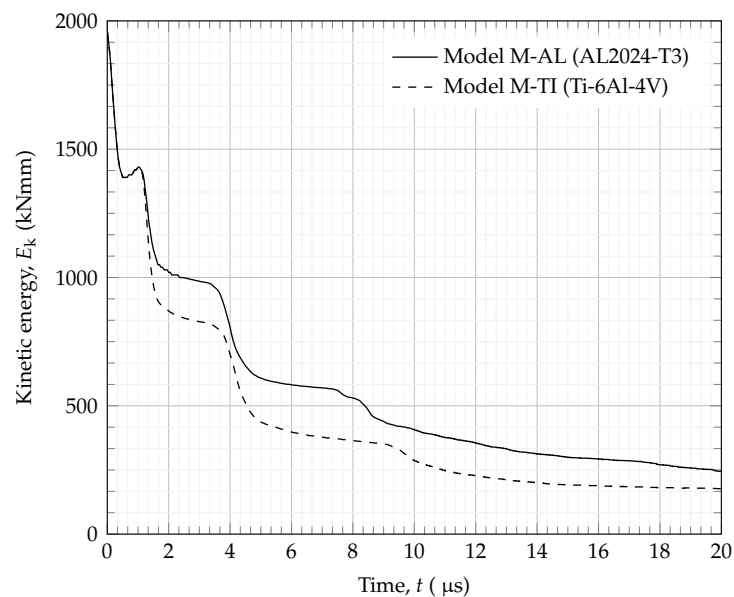


Figure 17. Kinetic energy comparison using AL2024-T3 and Ti-6Al-4V honeycombs.

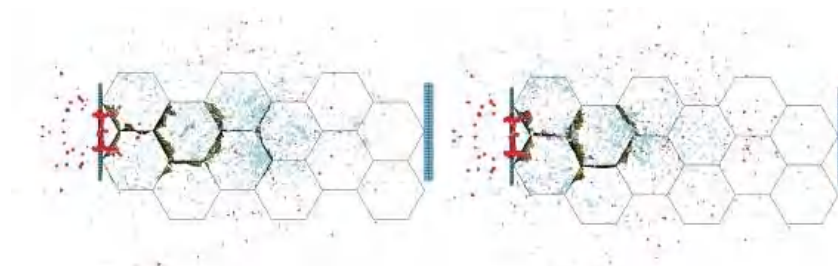


Figure 18. Numerical simulation comparing honeycomb shell materials: Al2024-T3 (model M-AL, left) and Ti-6Al-4V (model M-TI, right).

3.4. Location of Impact

Given the hexagonal geometry of the honeycomb core when orientated perpendicular to the impact direction, it could be expected that the exact location of the impact might lead to different energy dissipation patterns. To explore this, three distinct models were developed where the location of impact is changed according to the schematics in Figure 19. Model T-30, with an Al2024-T3 alloy honeycomb core, was used to analyse the effect of changing the location of impact on the dissipation of kinetic energy of the debris particle. The debris particle was fired at a velocity of 6500 m/s at a single edge of the honeycomb structure, a double point and at the mid-point. The details of these models are listed in Table 2. The results in Table 3 show that the highest kinetic energy dissipation occurs for model L-MP, where the debris particle impacts the mid-point of the honeycomb. However, the energy absorption history is similar across all three models, as can be seen in Figure 20, which indicates that very little variation is seen between simulations at different debris impact locations. This is additionally supported by the maximum difference in energy dissipation of 5.2% between the three models. Further, Figure 21 shows little visible variation in particle fragmentation, demonstrating that using the honeycomb structure in this orientation is a suitable method for dissipating kinetic energy, irrespective of the exact location of the impact.

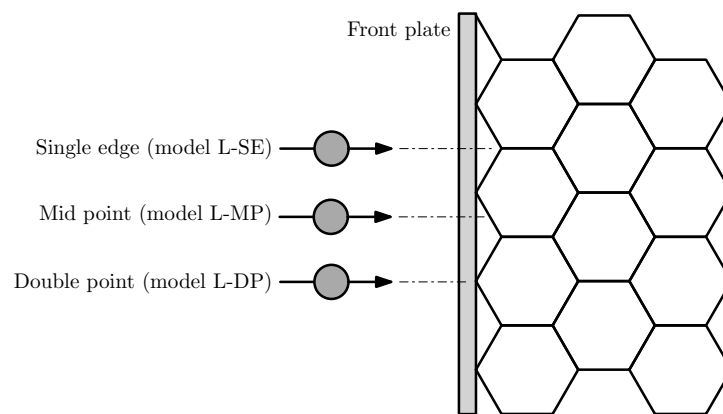


Figure 19. Location of impact on Whipple shield relative to honeycomb.

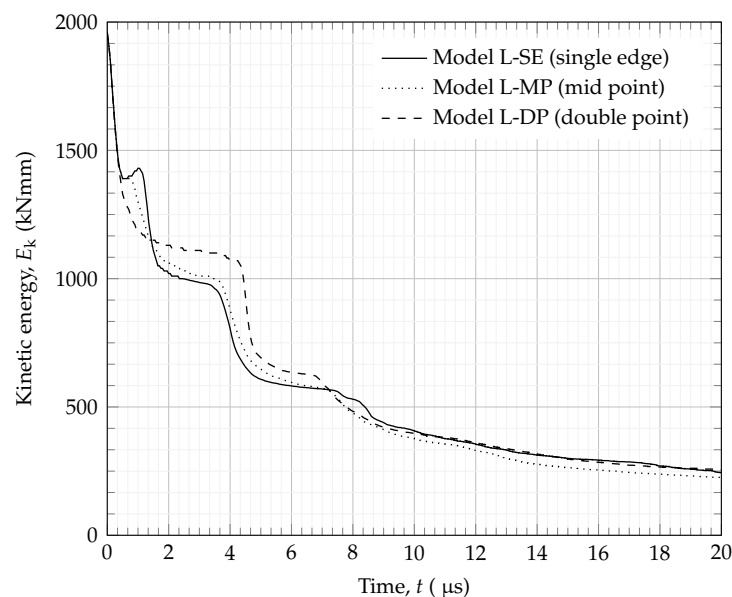


Figure 20. Kinetic energy of debris particle against time for varying debris impact locations.

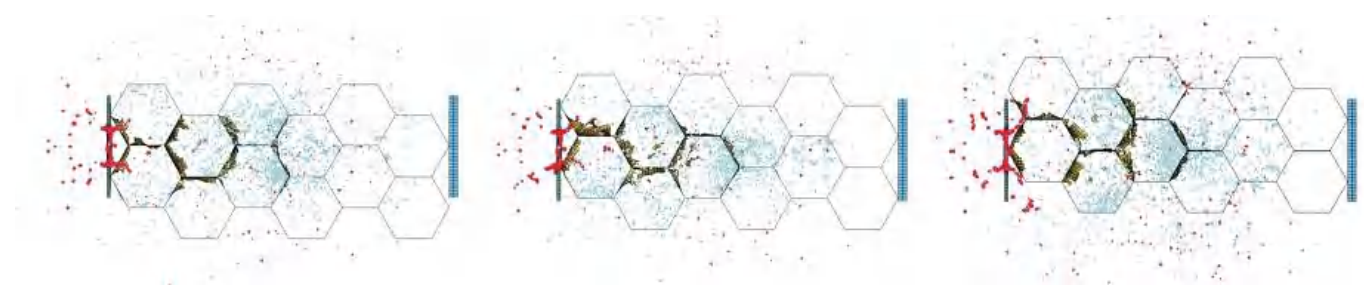


Figure 21. Comparison between varying points of impact: single edge (model L-SE, left), mid-point (model L-MP, centre) and double point (model L-DP, right).

4. Conclusions

This research proposes a set of numerical models to improve the design practice of unmanned hypervelocity impact shields. These are validated with experimental observations, including the debris-spread half-angle. Critical design parameters such as the honeycomb core cell density (i.e., the number of cells per unit length of the standoff gap), the thickness of the honeycomb core shell, the material of the honeycomb and the location of the impact relative to the honeycomb, are thoroughly analysed. The observations and results from this research clearly show that the proposed hybrid Whipple shield exhibits a significantly increased kinetic energy dissipation of the debris from the impactor and shield front plate.

The extent of the effect of altering both the material properties and the location of impact is not comparable to the cases in which the geometry of the honeycomb core was altered (the number of honeycomb cells and the thickness of the honeycomb shell). The dissipation of the kinetic energy of the debris particle is more sensitive to geometrical changes than to changes in the material properties and location of impact. The observed relative increase in energy dissipation can reach 86.8% by including the honeycomb core and increasing the thickness of its shell.

From a shield design perspective, however, there are a number of other factors that cannot be accounted for in the present work. These include, for example, component and assembly level cost, component and assembly level weight and geometrical constraints beyond those considered in this research. The work presented here is not intended to be a multi-parameter optimisation study, but instead a detailed analysis of the main design parameters affecting the shielding performance under hypervelocity impact. With these constraints, the following conclusions can be drawn:

- Adding a honeycomb core can significantly improve the shielding ability.
- Increasing the honeycomb core density also improves the performance of the shield, although these effects are significantly less pronounced for cell densities beyond 4, as can be seen in Table 3 and Figures 12 and 14.
- Increasing the thickness of the honeycomb core shell also increases efficiency, although this parameter has the opposite effect on the cost and weight of the shield.

It should be added that no definite conclusion should be drawn regarding the location of the impact, as this parameter cannot be controlled by design. These observations clearly suggest that the proposed hybrid honeycomb structure concept provides a highly efficient alternative to a standard Whipple shield design without significantly compromising the weight of the structure.

Author Contributions: Conceptualization, K.F. and F.T.-D.; methodology, K.F. and F.T.-D.; validation, K.F. and F.T.-D.; formal analysis, K.F. and F.T.-D.; resources, F.T.-D.; writing—original draft preparation, K.F.; writing—review and editing, K.F. and F.T.-D.; supervision, F.T.-D. All authors have read and agreed to the published version of the manuscript.

Funding: This research received no external funding.

Data Availability Statement: Not applicable.

Acknowledgments: For the purpose of open access, the authors have applied a Creative Commons Attribution (CC BY) licence to any Author Accepted Manuscript version arising from this submission.

Conflicts of Interest: The authors declare no conflict of interest.

Abbreviations

The following abbreviations are used in this manuscript:

CPU	Central Processing Unit
ESD	Equivalent Sphere Diameter
FEM	Finite-Element Method
HVI	Hypervelocity impact
IDAC	Inter-Agency Space Debris Coordination Committee
IGM	Impedance-graded material
ISS	International Space Station
LEO	Low earth orbit
MMOD	Micro-meteoroid orbital debris
NASA	National Aeronautics and Space Administration
SPH	Smoothed Particle Hydrodynamics
SWS	Standard Whipple Shield

References

1. Astromaterials Research and Exploration Science Directorate. *Handbook for Designing MMOD Protection*; Technical Report JSC-64399; National Aeronautics and Space Administration (NASA): Washington, DC, USA, 2009.
2. European Space Agency (ESA) Space Debris Office. *European Space Agency's Annual Space Environment Report*; European Space Agency (ESA) Space Debris Office: Darmstadt, Germany, 2020.
3. National Research Council. *Limiting Future Collision Risk to Spacecraft: An Assessment of NASA's Meteoroid and Orbital Debris Programs*; The National Academies Press: Washington, DC, USA, 2011.
4. Astromaterials Research & Exploration Science, Hypervelocity Impact Technology, Shield Development. National Aeronautics and Space Administration (NASA). Available online: <https://hvit.jsc.nasa.gov/shield-development/> (accessed on 2 February 2021).
5. Ryan, S.; Christiansen, E. *Hypervelocity Impact Performance of Open Cell Foam Core Sandwich Panel Structures*; Technical Report TM-2015-218593; National Aeronautics and Space Administration (NASA): Washington, DC, USA, 2015.
6. Cherniaev, A.; Telichev, I. Weight-Efficiency of Conventional Shielding Systems in Protecting Unmanned Spacecraft from Orbital Debris. *J. Spacecr. Rocket.* **2017**, *54*, 1–15. [CrossRef]
7. Christiansen, E.; Kerr, J.; de la Fuente, H.; Schneider, W. Flexible and deployable meteoroid/debris shielding for spacecraft. *Int. J. Impact Eng.* **1999**, *23*, 125–136. [CrossRef]
8. Plassard, F.; Mespoulet, J.; Hereil, P. Hypervelocity impact of aluminium sphere against aluminium plate: Experiment and LS-DYNA correlation. In Proceedings of the 8th European LSDYNA Users Conference, Strasbourg, France, 23–24 May 2011; pp. 142–149.
9. Zhang, P.; Gong, Z.; Tian, D.; Song, G. Study of the shielding performance of Whipple shield enhanced by impedance-graded materials. *Int. J. Impact Eng.* **2019**, *124*, 23–30. [CrossRef]
10. Carriere, R.; Cherniaev, A. Hypervelocity impacts on satellite sandwich structures—A review of experimental findings and predictive models. *Appl. Mech.* **2021**, *2*, 25–45. [CrossRef]
11. Carriere, R.; Cherniaev, A. Honeycomb parameter-sensitive predictive models for ballistic limit of spacecraft sandwich panels subjected to hypervelocity impact at normal incidence. *J. Aerosp. Eng.* **2022**, *35*, 04022039. [CrossRef]
12. Aslebagh, R.; Cherniaev, A. Projectile shape effects in hypervelocity impact of honeycomb-core sandwich structures. *J. Aerosp. Eng.* **2022**, *35*, 04021112. [CrossRef]
13. Pai, A.; Divakaran, R.; Anand, S.; Shenoy, S.B. Advances in the Whipple shield design and development: A brief review. *J. Dyn. Behav. Mater.* **2022**, *8*, 20–38. [CrossRef]
14. Ryan, S.; Hedman, T.; Christiansen, E. Honeycomb vs. foam: Evaluating potential upgrades to ISS module shielding. *Acta Astronaut.* **2010**, *67*, 818–825. [CrossRef]
15. Lambour, R.; Rajan, N.; Morgan, T.; Kupiec, I.; Stansbery, E. Assessment of orbital debris size estimation from radar cross-section measurements. *Adv. Space Res.* **2004**, *34*, 1013–1030. [CrossRef]
16. Rajan, N.; Morgan, T.; Lambour, R.; Kupiec, I. Orbital debris size estimation from radar cross section measurements. In Proceedings of the 3rd European Conference on Space Debris, Darmstadt, Germany, 19–21 March 2001.
17. Cowardin, H.M.; Hostetler, J.M.; Murray, J.I.; Reyes, J.A.; Cruz, C.L. Optical characterization of DebrisSat fragments in support of orbital debris environmental models. *J. Astronaut. Sci.* **2021**, *68*, 1186–1205. [CrossRef]
18. Wang, X.; Shi, J. Validation of Johnson-Cook plasticity and damage model using impact experiment. *Int. J. Impact Eng.* **2013**, *60*, 67–75. [CrossRef]

19. Venkatesan, J.; Iqbal, M.; Gupta, N.; Bratov, V. Ballistic characteristics of bi-layered armour with various aluminium backing against ogive nose projectile. *Procedia Struct. Integr.* **2017**, *6*, 40–47. [CrossRef]
20. Zhang, Y.; Outeiro, J.; Mabrouki, T. On the selection of Johnson-Cook constitutive model parameters for Ti-6Al-4V using three types of numerical models of orthogonal cutting. In Proceedings of the 15th Conference on Modelling of Machining Operations, Karlsruhe, Germany, 11–12 June 2015.
21. Nor, M.K.M.; Ho, C.S.; Ma'at, N. Modelling shock waves in composite materials using generalised orthotropic pressure. *Contin. Mech. Thermodyn.* **2020**, *32*, 1217–1229.
22. Olleak, A.A.; El-Hofy, H.A. SPH Modelling of cutting forces while turning of Ti6Al4V alloy. In Proceedings of the 10th European LS-DYNA Conference, Wurzburg, Germany, 15–17 June 2015.

Article

Numerical Analysis and Experimental Test for the Development of a Small Shaped Charge

Piotr Malesa ^{1,*} , Grzegorz Sławiński ¹ and Karolina Pęcherzewska ²

¹ Faculty of Mechanical Engineering, Military University of Technology, Gen. Sylwestra Kaliskiego Street 2, 00-908 Warsaw, Poland; grzegorz.slawinski@wat.edu.pl

² Ministry of National Defence, 00-911 Warsaw, Poland; kpecherzewska@ron.mil.pl

* Correspondence: piotr.malesa@wat.edu.pl; Tel.: +48-261-83-78-18

Abstract: Currently, shaped charges are widely used in many fields of science and industry. Due to the high efficiency of piercing materials with high strength and hardness, shaped charges are commonly used in mining, military and for structural damage. The main application area of shaped charges is the military industry, where they are used in missiles with warheads (torpedoes, rocket launchers) and for piercing vehicle armor or bunker walls. When analyzing the existing solutions of shaped charges, one can find many typical solutions designed for specific applications. However, there are no universal constructions which, after appropriate regulation, will fulfil their role in a wide range of applications. The subject of this article is a new solution for a shaped charge that is characterized by compact dimensions and a short preparation time. This article presents the results of experimental research and the numerical analyses of such a charge.

Keywords: shaped charge; jet; cumulative charge; numerical simulation; LS-Dyna

Citation: Malesa, P.; Sławiński, G.; Pęcherzewska, K. Numerical Analysis and Experimental Test for the Development of a Small Shaped Charge. *Appl. Sci.* **2021**, *11*, 2578. <https://doi.org/10.3390/app11062578>

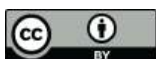
Academic Editor: Ricardo Castedo

Received: 18 February 2021

Accepted: 9 March 2021

Published: 13 March 2021

Publisher's Note: MDPI stays neutral with regard to jurisdictional claims in published maps and institutional affiliations.



Copyright: © 2021 by the authors. Licensee MDPI, Basel, Switzerland. This article is an open access article distributed under the terms and conditions of the Creative Commons Attribution (CC BY) license (<https://creativecommons.org/licenses/by/4.0/>).

1. Introduction

Cumulative charges have been widely used for many years, including in military technology [1,2] (mainly in anti-tank weapons) and in the mining industry (drilling holes) [3]. The nature of this phenomenon also allows for its use in the process of developing new design solutions intended for special applications [4].

The analyses carried out in 2017, aimed at identifying the optimal design solution for one such application, showed the need to use a shaped charge which, depending on the need, will enable the pierceability of approximately 80 mm to 200 mm to be obtained. Additionally, such a charge should be as small as possible in weight and dimensions, with a short time to prepare for use and the possibility of detonation with a time fuse.

The analysis of the state of the art in this field has shown that there are known design solutions that enable the adjustment of the distance between the base of the cumulative insert from the surface being destroyed by means of feet (these solutions are protected by patent law) [5]. However, they did not meet the requirements due to the lack of a fuse with a timed electronic system and because of the extended amount of time that it took to prepare the charge for use. Therefore, there was a need to develop a new design solution.

The developed conceptual design assumed the achievement of the required pierceability through the use of a conical, copper shaped liner and a pressed octogen (HMX) explosive in the structure of the charge. The quick adjustment of the height of the load and the distance from the base of the accumulation insert to the destroyed surface was to be ensured by placing the load casing in an additional sleeve in a way that allowed for an abrupt change of the position of both elements in relation to each other. An additional advantage of this solution was the minimization of the dimensions of the load in the transport position. Neodymium magnets, placed in the flange at the base of the sleeve (in the case of mounting the load on steel structures), or the use of a special, universal tape

(in the case of the need to mount the load on other types of surfaces), were to ensure the possibility of quick fastening of the load to the destroyed element.

The developed conceptual design also included the construction of a time-type fuse with a self-destruction function. Its block diagram is shown in Figure 1.

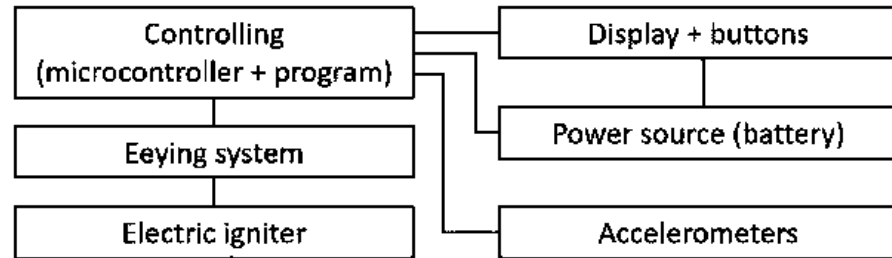


Figure 1. Block diagram of the time-type fuse.

On the basis of the developed conceptual design, a 3D CAD (Computer Aided Design) model of the cargo casing was created, which was then produced using the FDM (Fused Deposition Modeling) 3D printing technique in Figure 2a.

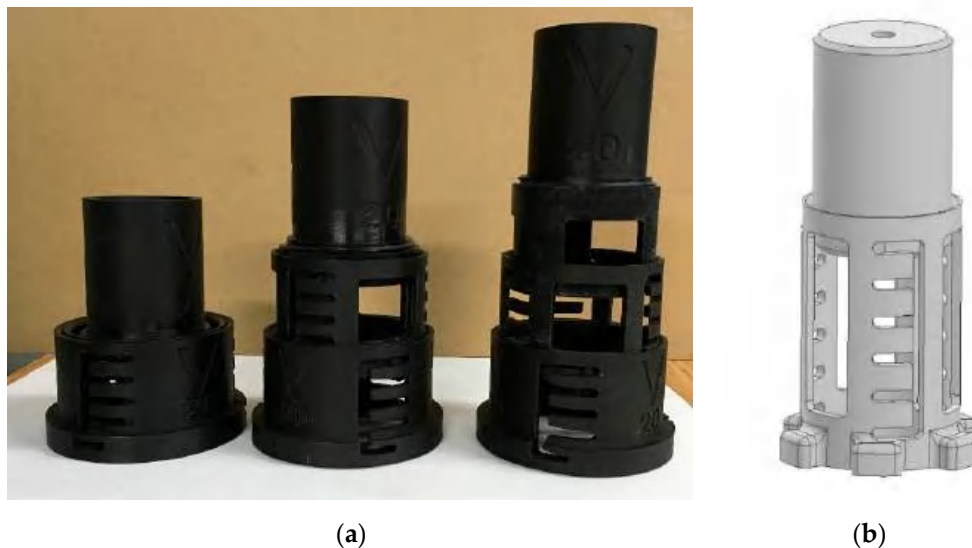


Figure 2. View of the structure of shaped charges: (a) first design of the shaped charge prototype and (b) final design of the shaped charge construction.

In 2018, the first preliminary tests were conducted at the Military University of Technology to verify the developed cargo design concept, which confirmed its correctness.

The next stage of work was the optimization of the structure, aimed at minimizing the weight and dimensions of the load. As a result, modifications to the housing structure were introduced. The number of components was reduced so that the structure consists of a spacer sleeve and a housing. The view of the final cargo structure after the modification is shown in Figure 2b.

The developed solution of the final shaped charge was then subjected to experimental tests and multi-variant numerical analyses, which are presented in the following chapters.

2. Materials and Methods

With the use of modern technologies, it is possible to model many physical processes, the observation and research of which are hampered by various factors, such as process dynamics. All kinds of issues related to research with the use of explosives [6,7] or shaped charges, which are the main topic of this paper [8,9], constitute an example of such processes.

One of the main factors determining the choice of a research method is undoubtedly the economic factor. Computer modeling is usually much cheaper than the corresponding experiment. For this reason, FEM has found wide application in many fields of science, and this proves that it is a method as useful as experimental research.

Modeling of dynamic interactions of bodies [10–12] with the use of numerical analyses has been developed over many years. As a result of the work carried out so far, a set of mathematical and physical models and computer codes has been developed that can be effectively adapted to the research, optimization and evaluation of parameters of various types of loads.

For metal charge elements, i.e., a shaped charge liner, mathematical–physical models are used based on the theory of elastic plasticity supplemented with semi-empirical equations of state and dependencies describing the changes of the plastic flow limit as a function of temperature, pressure, density, plastic deformation and plastic deformation velocity (Johnson–Cook model) [13]. The Johnson–Cook material model is one of the most popular and most frequently used material model for the problems of modeling the cumulation process [14,15].

Reference [16] is one of the most interesting collective works devoted to the modeling of dynamic processes in the LS-Dyna program with the use of axisymmetric models, including the cumulative charge. The model presented in the paper is a 2D axisymmetric model, with an innovative use of a new formulation of elements in this field. The authors of this publication point to the possibility of modeling the problems of cumulation in an easy way, using for this purpose axisymmetric models and the 2D Arbitrary Lagrangian–Eulerian (ALE) element in the Eulerian formulation.

Multi-Material Arbitrary Lagrangian–Eulerian (MM-ALE) formulation is a two-step process [17–19]. The first step of the ALE procedure consists in carrying out the classical Lagrange step, which describes the deformation of the solid state (stiffness matrix with new initial-boundary conditions). The mesh moves with the flowing matter (fluid), thus fulfilling the principle of conservation of mass. The velocity and displacements of the mesh are determined, and the nodes of the deformed elements return to their original position [18,19].

The second stage of the procedure is to carry out the advection step, which includes:

1. Deciding which nodes to move.
2. Displacement of extreme nodes.
3. Displacement of nodes inside.
4. Recalculating all variables related to the elements.
5. Recalculating momentum values and updating speed.

When determining the velocity and fluid displacements, the equations of the conservation of mass, torque and energy are implemented [18,19]:

$$\frac{dM}{dt} = \frac{d}{dt} \int_{V(t)} \rho dV = \int_{S(t)} \rho (\omega - v) \cdot n dS, \quad (1)$$

$$\frac{dQ}{dt} = \frac{d}{dt} \int_{V(t)} \rho v dV = \int_{S(t)} \rho v (\omega - v) \cdot n dS - \int_{V(t)} \nabla p dV + \int_{V(t)} v g dV, \quad (2)$$

$$\frac{dE}{dt} = \frac{d}{dt} \int_{V(t)} \rho e dV = \int_{S(t)} \rho e (\omega - v) \cdot n dS - \int_{S(t)} p v \cdot n dS + \int_{V(t)} p g \cdot v dV. \quad (3)$$

where ρ is fluid mass density, p is pressure, g is acceleration of gravity and e is the total specific energy. The quantities M , Q and E are total mass, total momentum and total energy, respectively, of control volume $V(t)$, bounded by surface S , which moves in the fluid (gas–air) with arbitrary velocity ω which may be zero in Eulerian coordinates or v in Lagrangian coordinates. The vector n is the outwards normal to the surface S .

The Johnson–Cook (JC) constitutive model was used to describe the proper dynamic behavior of the cumulative insert and the steel block affected by the insert. It is an elastic–plastic model of the material. Plastic deformation in the material is modeled using isotropic material hardening. The yield point of the material is described by the following relationship:

$$\sigma_Y = (A + B\varepsilon_p^n) (1 + C \ln \dot{\varepsilon}^*) (1 - T^{*m}) \tag{4}$$

where:

A —static yield point,

ε_p —plastic deformation,

$\dot{\varepsilon}^*$ —dimensionless strain rate, $\dot{\varepsilon}^* = \dot{\varepsilon} / \dot{\varepsilon}_0$

$\dot{\varepsilon}_0$ —reference strain rate,

T^* —the ratio of the absolute temperature of the sample to its melting point, which is determined by the following relationship:

$$T^* = \begin{cases} 0 & dT < T_{room} \\ \frac{T - T_{room}}{T_{melt} - T_{room}} & dT \leq T \leq T_{melt} \\ 1 & dT > T_{melt} \end{cases} \tag{5}$$

T_{room} —temperature at which the experiment was carried out,

T_{melt} —material melting point,

n —parameter determining the material’s susceptibility to hardening by deformation,

m —thermal plasticization exponent,

B —hardening constant,

C —strain rate constant.

Johnson and Cook proposed that fracture strain typically depends on the stress triaxiality ratio, the strain rate and the temperature. The strain at fracture is given by:

$$\varepsilon^f = \max\left([D_1 + D_2 \exp D_3 \sigma^*] [1 + D_4 \ln \dot{\varepsilon}^*] [1 + D_5 T^*], EFMIN\right) \tag{6}$$

where σ^* is the ratio of pressure divided by effective stress:

$$\sigma^* = \frac{p}{\sigma_{eff}} \tag{7}$$

Fracture occurs when the damage parameter:

$$D = \sum \frac{\Delta \bar{\varepsilon}^p}{\varepsilon^f} \tag{8}$$

reaches the value of 1.

The data of the copper insert material [20] with the EOS (Equation of State) model, and the steel material model [21] with the EOS data [22] from which the target was made, are presented in Table 1.

Table 1. Material data for cumulative insert and steel target [20–22].

Parameter	Symbol	Unit	Shaped Charge Liner	Steel Target
Density	ρ	Kg/m ³	8940	7860
Shear modulus	G	GPa	-	81.8
Young modulus	E	GPa	126	209
Poisson’s ratio	ν	-	0.335	0.28
Yield stress	A	MPa	99.7	792
Hardening constant	B	MPa	262.8	510
Hardening exponent	N	-	0.23	0.26
Strain rate constant	C	-	0.029	0.014
Thermal softening exponent	M	-	0.98	1.03
Room temperature	Tr	K	293	300
Melting temperature	Tm	K	775	1790
Ref. strain rate	EPSO	s ⁻¹	1.0	1.0
Specific heat	Cp	J/kgK	875	477
Johnson Cook failure				
Failure parameter	D ₁	-	0.13	0.05
Failure parameter	D ₂	-	0.13	3.44
Failure parameter	D ₃	-	-1.5	-2.12
Failure parameter	D ₄	-	0.011	0.002
Failure parameter	D ₅	-	0	0.61
EOS_LINEAR_POLYNOMIAL				
	C ₀	-	20.790	-
	C ₁	-	1.337 × 10 ⁵	-
	C ₂	-	1.256 × 10 ⁵	-
	C ₃	-	1.454 × 10 ⁵	-
	C ₄	-	1.940	-
	C ₅	-	0.585	-
	C ₆	-	1.125	-
EOS_GRUNEISEN				
	C	m/s	-	4570
	S ₁	-	-	1.49
	γ_0	-	-	1.93
	A	-	-	0.5

For the JC model, it is necessary to define a polynomial equation of state describing the relationship between pressure, volume and the internal energy in a material. The linear polynomial equation of state was used for the model of the copper insert material. This equation is expressed as:

$$P = c_0 + c_1\mu + c_2\mu^2 + c_3\mu^3 + (c_4 + c_5\mu + c_6\mu^2)E_0 \tag{9}$$

where: $c_0 \div c_6$, state equation parameters; μ , compression factor $\mu = \rho/\rho_0$ expressed as the ratio of the actual density ρ to the original density ρ_0 ; E_0 , internal energy.

The polynomial equation of state in a simplified form is used to describe the gas (air) medium surrounding the explosive charge and the tested object:

$$P = (c_4 + c_5\mu)E \tag{10}$$

where: $\mu = \rho/\rho_0$, C_4 and C_5 , equation coefficients; ρ , density; ρ_0 , starting density; E , internal energy.

The Grüneisen equation of state was defined for the steel material model. The equation defines the pressure in the shock-compressed material as:

$$p = \frac{\rho_0 C^2 \mu [1 + (1 - \frac{\gamma_0}{2})\mu - \frac{a}{2}\mu^2]}{\left[1 - (S_1 - 1)\mu - S_2 \frac{\mu^2}{\mu + 1} - S_3 \frac{\mu^3}{(\mu + 1)^2}\right]^2} + (\gamma_0 + a\mu)E \tag{11}$$

whereas for the expanded material as:

$$p = \rho_0 C^2 \mu + (\gamma_0 + a\mu)E \tag{12}$$

- C—bulk speed of sound,
- γ_0 —Grüneisen gamma,
- S_1 —linear coefficient,
- S_2 —quadratic coefficient,
- S_3 —cubic coefficient,
- a —first order volume correction to γ_0 ,
- μ —volume parameter, expressed as $\mu = (\rho/\rho_0) - 1$,
- ρ —actual density,
- ρ_0 —initial density,
- E —internal energy per unit of mass.

The MAT_HIGH_EXPLOSIVE_BURN material model was selected to describe the octogen (HMX) explosive. The material data for the HMX explosive and presented in Table 2.

Table 2. Pressed octogen (HMX) explosive data with equation of state [23].

Parameter	Symbol	Unit	Value
MAT_HIGH_EXPLOSIVE_BURN			
Density	ρ	Kg/m ³	1890
Detonation velocity	D	m/s	9110
Chapman–Jouget pressure	PCJ	GPa	42
EOS_JWL			
	A	GPa	778.3
	B	GPa	7.071
	R_1	-	4.2
	R_2	-	1
	ω	-	0.3

The Jones–Wilkins–Lee (JWL) equation of state was used to describe the relationship between the parameters of the thermodynamic system for the explosive. The equation of state of gaseous products of detonation of condensed explosives takes the following form:

$$p = A \left(1 - \frac{\omega}{R_1 V} \right) e^{-R_1 V} + B \left(1 - \frac{\omega}{R_2 V} \right) e^{-R_2 V} + \frac{\omega E}{V}, \tag{13}$$

A , B and E have units of pressure. R_1 , R_2 , ω , and V_0 are dimensionless. E —internal energy per unit volume and ω —the relative volume of the explosive.

The air domain was modeled using the MAT_NULL material model and the EOS_LINEAR_POLYNOMIAL equation of state, for which the material data summarized in Table 3 were used.

Table 3. Air material data with the equation of state [24].

Parameter	Symbol	Unit	Value
MAT_NULL			
Density	ρ	Kg/m ³	1.29
EOS_LINEAR_POLYNOMIAL			
	C_4	GPa	0.4
	C_5	GPa	0.4
	E_0	GPa	2.5×10^{-4}
	V_0	-	1

The explosive casing, which in real conditions was made of Acrylonitrile Butadiene Styrene (ABS) was modeled using the MAT_PIECEWISE_LINEAR_PLASTICITY material model, for which the data are summarized in Table 4.

Table 4. Acrylonitrile Butadiene Styrene (ABS) material data [25].

ρ [Kg/m ³]	E [GPa]	ν [–]	SIGY [MPa]
1040	2.2	0.35	34.17
EPS1 [%]	EPS2 [%]	EPS3 [%]	EPS4 [%]
0	0.8	1.4	2.8
EPS5 [%]	EPS6 [%]	EPS7 [%]	EPS8 [%]
5.7	6.5	7.1	7.7
ES1 [MPa]	ES2 [MPa]	ES3 [MPa]	ES4 [MPa]
34.17	34.52	34.72	35.13
ES5 [MPa]	ES6 [MPa]	ES7 [MPa]	ES8 [MPa]
35.49	35.53	35.54	35.55

All numerical simulations were performed using the LS-Dyna code with an implementation of the Multi-Material Arbitrary Lagrangian–Eulerian (MM-ALE) formulation.

3. Subject and Scope of the Tests

The numerical model of the stand for the penetration test with the use of the shaped charge was developed based on the solid model of the analyzed system. During the experimental tests, a charge consisting of a casing in which the explosive was compressed, a sleeve regulating the distance between the target and the charge and a shaped charge liner were used. The view of the analyzed system for extreme variants of the distance between the load and the target is shown in Figure 3.

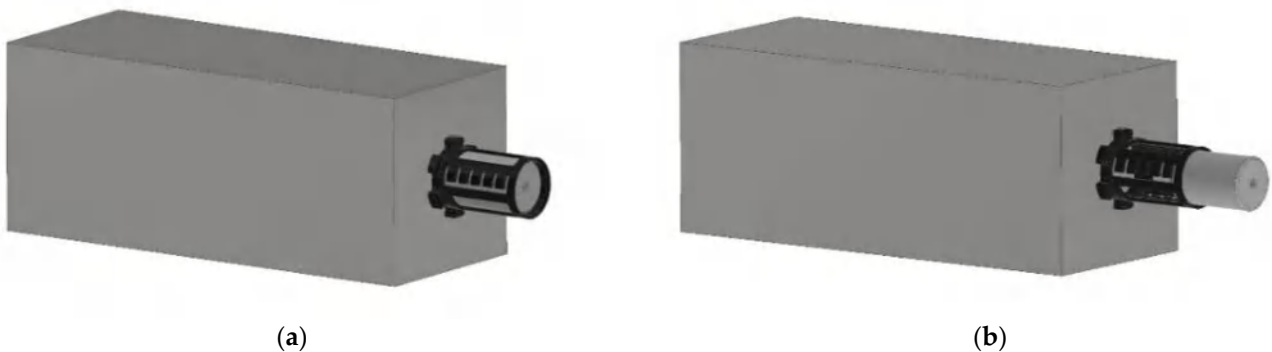


Figure 3. View of two variants of shaped charges: (a) charge closest to the target and (b) charge farthest from the target.

The distance between the face of the casing with the explosive and the liner insert was adjusted with the use of a solution based on a system of five serrations enabling insertion and locking of the sleeve within them. The solution allows for a six-step adjustment of the distance of the load from the target, with the minimum distance in step 1 being 7.5 mm and changing every 12.5 mm up to the maximum distance of 70 mm.

Based on the solid model, an axially symmetric shell model was developed, consisting of a steel block, housing, charge and a shaped charge liner placed in the air domain. The axisymmetric model covered half of the whole system due to the applied axial symmetry.

The discretization of the geometry made it possible to freely change the distance between the load and the target. In the initial phase of the analysis, two models were built for the two extreme distances as shown in Figure 4.

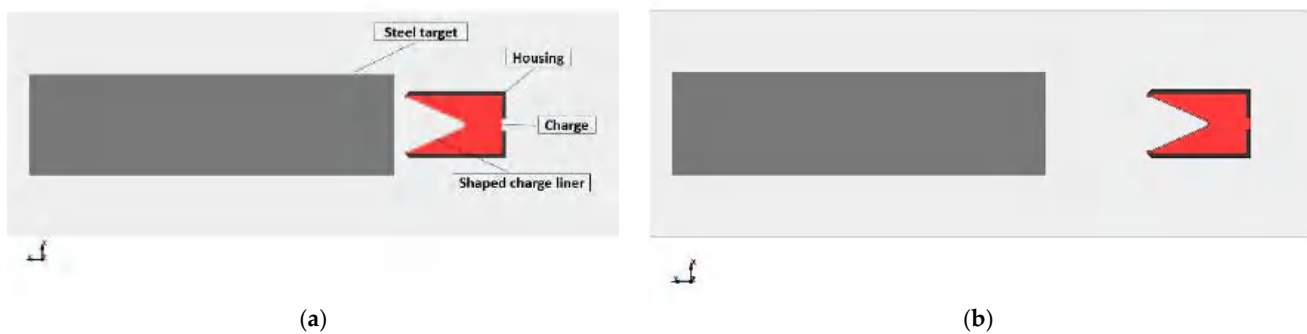


Figure 4. View of two variants of the shaped charge model: (a) charge closest to the target and (b) charge farthest from the target.

The ALE procedure requires that the finite element mesh be constructed from the smallest possible elements to properly implement the explosion phenomenon. For this reason, the models consist of many elements, which translates into a time-consuming calculation. The analyzed models consisted of finite elements with the dimensions of $0.25 \text{ mm} \times 0.25 \text{ mm}$ —158,455 for the model with the load closest to the target and 199,351 for the load farthest from the target.

The calculations were performed at time $t = 0.5 \text{ ms}$. For numerical calculations, an explicit type of algorithm was used to solve the structure dynamics equations in the non-linear range.

4. Model Validation, Results and Discussion

At the beginning, numerical analyses were carried out for two extreme variants of the shaping charge displacement against the target. Numerical analyses of the propagation of the shaped charge in the Euler domain and for the penetration of the steel block were carried out. A graphical summary of the subsequent steps of the analysis for two variants was obtained. The results are presented in Table 5.

Table 6 shows a cross-sectional comparison view of a steel block that has been subjected to a shaped charge for experimental and numerical tests. The obtained values of the penetration depth of the shaped charge in the steel block were compared with the results of the experimental study. Table 7 presents the quantitative results of the penetration depth obtained through numerical analyses and experimental tests.

For the charge placed closest to the target, a large-diameter hole was obtained at the entrance of the charge into the material, with a small diameter at its end. In the case of the load placed over the longest standoff from the target, the hole has a more regular shape with a diameter taper toward its end. As can be seen from the obtained cross-sections and numerical analyses, the displacement of the charge from the target causes the shaped charge that hits the target to be formed better, which translates directly into the effectiveness of its penetration.

Table 5. View of the propagation process of detonation products and the penetration process of the shaped charge inside the steel target.

Time	Penetration Process for 7.5 mm Standoff	Penetration Process for 70 mm Standoff
T = 0 ms		
T = 0.01 ms		
T = 0.05 ms		
T = 0.1 ms		
T = 0.5 ms		

Table 6. View of the section of the steel block after shooting with the shaped charge for experimental and numerical tests.

Cross-Section of Steel Target for 7.5 mm Standoff	Cross-Section of Steel Target for 70 mm Standoff

Table 7. The values of the penetration depth of the steel block with the shaped charge.

	Depth of Penetration for 7.5 mm Standoff	Depth of Penetration for 70 mm Standoff
Experimental test	110 mm	220 mm
Numerical analysis	106 mm	244 mm
Difference	4%	8%

By analyzing the obtained results of the hole depth in the steel block material, it is possible to notice a double penetration value for the charge away from the target. This difference results from the different focusing of the stream of the shaped charge. The distance of the cumulative charge from the target is a very important parameter because its proper selection makes it possible to maximize the energy transferred to the obstacle by the cumulative flux [26] and at the same time reduce energy losses to the environment, thus increasing the effectiveness of the work done by the charge.

To investigate more accurately the effect of moving the charge away from the target on the penetration capabilities of the shaped charge, numerical simulations were carried out for all six variants of the removal of the charge from the target. The variants corresponded to a six-step adjustment by means of a system of teeth and sleeves connecting the load casing with the distance sleeve.

The following variants of the analyses were implemented:

- Variant 1—7.5 mm standoff closest to the target.
- Variant 2—20 mm standoff.
- Variant 3—32.5 mm standoff.
- Variant 4—45 mm standoff.
- Variant 5—57.5 mm standoff.
- Variant 6—70 mm standoff farthest from the target.

Table 8 shows the results of the impact of the shaped charge for all six variants for the analysis times $t = 0.1$ ms, 0.25 ms and 0.5 ms.

Based on the obtained values of the maximum penetration of the shaped charge in the steel block, the characteristics of the dependence of the puncture efficiency depending on the distance between the charge and the target were determined. The results are shown in Figure 5.

Depending on the distance between the charge and the target, the value of the velocity of the cumulative stream front changes. For the charge in question, the value of the maximum speed at the time of formation of the cumulative stream was 7180 m/s. Figure 6 shows the view of the cumulative flux with a map of the resultant velocity value at the moment of contact between the flux front and the target.

The following values of the cumulative flux velocity at the moment of contact with the target and the diameter of the holes formed in the steel block were obtained for the individual variants of moving the charge from the target.

Table 8. View of the propagation process of detonation products and the penetration process of the shaped charge.

Variant	Penetration Process for Theanalysis Time of 0.1 ms	Penetration Process for Theanalysis Time of 0.25 ms	Penetration Process for Theanalysis Time of 0.5 ms
Standoff = 7.5 mm			
Standoff = 20 mm			
Standoff = 32.5 mm			
Standoff = 45 mm			
Standoff = 57.5 mm			
Standoff = 70 mm			

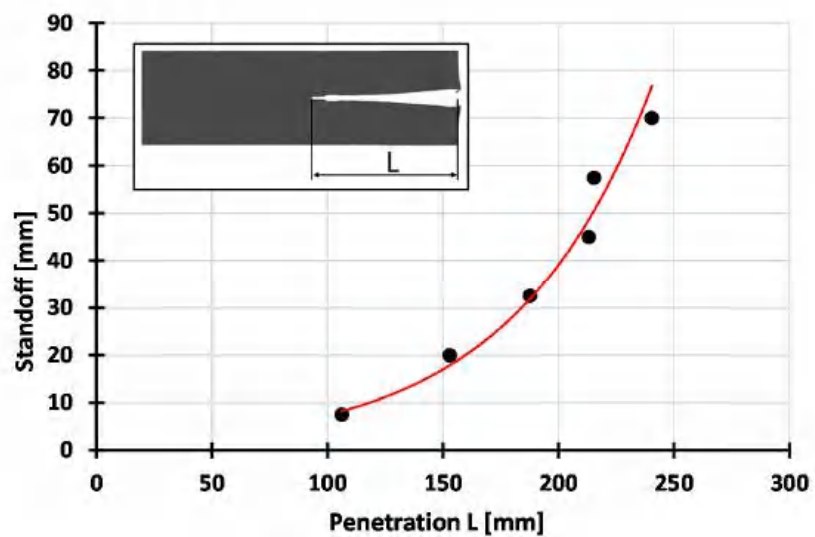


Figure 5. Characteristics of the change of penetration depth of the shaped charge in the steel block depending on the distance from the target.

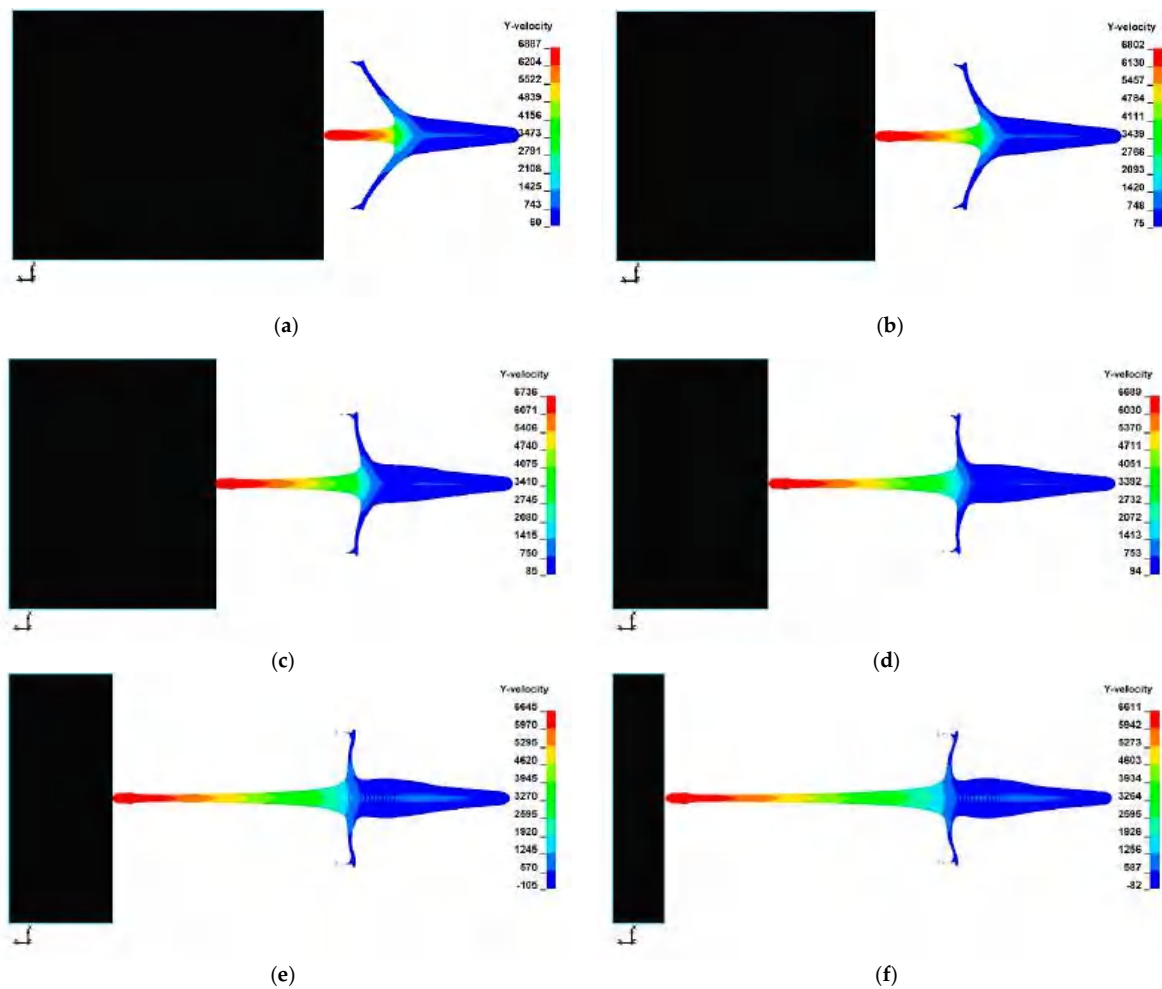


Figure 6. View of the shaped charge jet with the marked map of the resultant velocity at the moment of contact with the target: (a) 7.5 mm standoff, (b) 20 mm standoff, (c) 32.5 mm standoff, (d) 45 mm standoff, (e) 57.5 mm standoff and (f) 70 mm standoff.

5. Conclusions

The main purpose of the paper was to test and analyze the effectiveness of small-shaped charges in terms of their ability to penetrate a steel block. The conducted experimental tests allowed us to determine the real ability to penetrate a steel target with a shaped charge at a variable value of its distance from the target. On the basis of the experimental test, the breakthrough values of 110 and 220 mm were obtained for two variants of the charge standoff from the target, determined by the proprietary solution in the form of a spacer sleeve.

As a result of the numerical analyses carried out, the process of validation of the numerical model in the axisymmetric approach was conducted using the Multi-Material Arbitrary Lagrangian–Eulerian (MM-ALE) formulation method. The performed numerical model made it possible to regulate the distance of the charge from the target in accordance with the actual conditions, while maintaining all dimensions of the components of the load, i.e., casing, cumulative insert and the explosive used there. The obtained results of the penetration depth obtained by means of numerical analyses and experimental tests were characterized by a difference at the level of 4–8%, which made it possible to adopt the method used as effective for modeling the cumulative charge.

After a successful validation process, further numerical analyses were carried out for the remaining variants of the load positioning in relation to the target, using the distance adjustment system of the sleeve. The method of formation of the cumulative flux and

the ability to break through another material in terms of the distance between them were checked via numerical analyses. A graph of the change of the penetration capacity of a shaped charge jet in a steel block depending on the distance between it and the target was developed. The exponential trend line shown in Figure 3 illustrates this relationship. Another phenomenon that was verified by numerical analysis was the velocity of the jet reached at the moment when the top of it contacts the target. Based on the conducted analyses, the results for all tested variants of the retraction were collected, as shown in Table 9.

Table 9. Summary of the shaped charge jet velocity at the moment of contact with the target.

Variant	Jet Velocity [m/s]	Hole Diameter [mm]
Standoff = 7.5 mm	6887	12.5
Standoff = 20 mm	6802	12.5
Standoff = 32.5 mm	6736	12.5
Standoff = 45 mm	6689	12
Standoff = 57.5 mm	6645	12
Standoff = 70 mm	6611	11.5

To sum up, the assumption of this paper was to carry out the modeling and validation process of the shaped charge initiation and propagation process in interaction with a steel target. The method of modeling the phenomenon of this problem in the axisymmetric approach was used, which faithfully reflects the conditions of real experimental research. The obtained results constitute the basis for further numerical research based on a correctly functioning and validated numerical model. Subsequent papers will focus on analyzing the effectiveness of a small-shaped charge jet penetration with other types of materials.

Author Contributions: Conceptualization, P.M., G.S. and K.P.; methodology, P.M., G.S. and K.P.; software, P.M. and G.S.; validation, P.M. and G.S.; formal analysis, P.M., G.S. and K.P.; investigation, P.M., G.S. and K.P.; resources, P.M., G.S. and K.P.; data curation, P.M., G.S. and K.P.; writing—original draft preparation, P.M., G.S. and K.P.; writing—review and editing, P.M., G.S. and K.P.; visualization, P.M., G.S. and K.P.; supervision, P.M., G.S. and K.P.; project administration, G.S.; funding acquisition, G.S. All authors have read and agreed to the published version of the manuscript.

Funding: The article was written as part of the implementation of the university research grant supported by the Military University of Technology (No. UGB 22-746/2020).

Institutional Review Board Statement: Not applicable.

Informed Consent Statement: Not applicable.

Data Availability Statement: Not applicable

Acknowledgments: Special thanks for organizing and conducting experimental studies of the impact of the shaped charge on the steel block to Waldemar Trzciński from Military University of Technology.

Conflicts of Interest: The authors declare no conflict of interest.

References

1. Cui, P.; Wang, D.; Shi, D.; Gao, X.; Xu, J.; Zhen, J. Investigation of penetration performance of Zr-based Amorphous Alloy Liner Compared with Copper. *Materials* **2020**, *13*, 912. [CrossRef] [PubMed]
2. Wu, H.; Hu, F.; Fang, Q. A comparative study for the impact performance of shaped charge JET on UHPC targets. *Def. Technol.* **2019**, *15*, 4. [CrossRef]
3. Wilk, Z.; Zygmunt, B. Zastosowanie ładunków kumulacyjnych do perforacji odwiertów geologicznych. *Biul. Wojsk. Akad. Tech.* **2007**, *56*, 245–258.
4. Available online: <http://cama.pl/realizacje/wybuchowe-ciecie-stalowej-konstrukcji-zwalowarki-turow> (accessed on 20 January 2021).
5. Śliwiński, J.; Ludas, M.; Czuby, Ł. Opis ochronny wzoru użytkowego nr. 68492. In *Urząd Patentowy Rzeczypospolitej Polskiej*; data zgłoszenia: 12.03.2014; 2014.

6. Sławiński, G.; Malesa, P.; Świerczewski, M. Analysis regarding the risk of injuries of soldiers inside a vehicle during accidents caused by improvised explosive devices. *Appl. Sci.* **2019**, *9*, 4077. [CrossRef]
7. Baranowski, P.; Małachowski, J. Numerical study of selected military vehicle chassis subjected to blast loading in terms of tire strength improving. *Bull. Pol. Acad. Sci. Tech. Sci.* **2015**, *63*. [CrossRef]
8. Pyka, D.; Kurzawa, A.; Bocian, M.; Bajkowski, M.; Magier, M.; Sliwinski, J.; Jamroziak, K. Numerical and Experimental Studies of the ŁK Type Shaped Charge. *Appl. Sci.* **2020**, *10*, 6742. [CrossRef]
9. Panowicz, R.; Nowak, J.; Konarzewski, M.; Niezgoda, T. Parametric studies of directed fragmentation warhead used for combat shaped charges. *Eng. Trans.* **2015**, *63*, 181–190.
10. Malachowski, J.; Baranowski, P.; Gieleta, R.; Mazurkiewicz, Ł. Rubber structure under dynamic loading—Computational Studies. *Eng. Trans.* **2013**, *61*, 33–46.
11. Morka, A.; Kędzierski, P.; Gieleta, R. Selected aspects of numerical analysis of layered flexible structures subjected to impact of soft core projectile. *Arch. Mech. Eng.* **2015**, *62*. [CrossRef]
12. Sybilski, K.; Małachowski, J. Impact of disabled driver’s mass center location on biomechanical parameters during crash. *Appl. Sci.* **2021**, *11*, 1427. [CrossRef]
13. Johnson, G.R.; Cook, W.H. A constitutive model and data for metals subjected to large strains and high temperatures. In Proceedings of the 7th International Symposium on Ballistics, Hague, The Netherlands, 19–21 April 1983.
14. Huang, J.; Wang, W.; Zhang, W.; Huang, K. The 3D numerical simulation of the shaped charge jet penetration through the steel target. In Proceedings of the 2nd International Conference on Computer Application and System Modeling, Cochin, India, 20–21 October 2012. [CrossRef]
15. Costa, E.; Ferrante, E.; Trevisi, A.; Bozzolo, A. Shaped charge: A comparative study of jet penetration into a multi-layered target. In Proceedings of the International CAE Conference and Exhibition, Vicenza, Italy, 8–9 October 2018.
16. Van Dorsselaer, N.; Lapoujade, V. A contribution to new ALE 2D Method Validation. In Proceedings of the 11th International LS-Dyna Users Conference, Dearborn, Michigan, 6–8 June 2010.
17. Małachowski, J. *Modelowanie i badania interakcji ciało stałe-gaz przy oddziaływaniu impulsu ciśnienia na elementy konstrukcji rurociągu*; Bel studio: Warszawa, Poland, 2010.
18. Baranowski, P.; Małachowski, J.; Mazurkiewicz, Ł. Numerical and experimental testing of vehicle tyre under impulse loading conditions. *Int. J. Mech. Sci.* **2016**, *106*. [CrossRef]
19. Hallquist, J. *LS-Dyna: Theory Manual*; Livemore Software Technology Corporation (LSTC): Livermore, CA, USA, 2019.
20. Kołodziejczyk, D. Numeryczno-eksperymentalne badanie wpływu uszkodzeń lub deformacji wkładki kumulacyjnej na tworzenie się strumienia kumulacyjnego. Rozprawa Doktorska, Wojskowa Akademia Techniczna, Warszawa, Poland, 2015.
21. Rashed, A.; Yazdani, M.; Babaluo, A.; Hajizadeh, P.P. Investigation on high-velocity impact performance of multi-layered alumina ceramic armors with polymeric interlayers. *J. Compos. Mater.* **2015**, *50*, 25. [CrossRef]
22. Kędzierski, P.; Morka, A.; Sławiński, G.; Niezgoda, T. Optimization of two-component armour. *Bull. Pol. Acad. Sci. Tech. Sci.* **2015**, *63*. [CrossRef]
23. Panowicz, R.; Trypolin, M.; Konarzewski, M. Numerical comparison of blast waves generated by cylindrical explosive charges with varying shapes and materials. *Comput. Assist. Methods Eng. Sci.* **2016**, *23*, 4.
24. Sławiński, G.; Malesa, P.; Niezgoda, T.; Świerczewski, M. A comparison between two different methods of blast modelling. *Lect. Notes Mech. Eng.* **2017**. [CrossRef]
25. Kucewicz, M.; Baranowski, P.; Małachowski, J.; Popławski, A.; Płatek, P. Modelling, and characterization of 3D printed cellular structures. *Mater. Des.* **2018**, *142*. [CrossRef]
26. Wojewódka, A.; Witkowski, T. Metodyka modelowania procesu formowania strumienia kumulacyjnego wydłużonych ładunków materiałów wybuchowych. *Chemik* **2011**, *65*, 28–35.

Article

SimEx: A Tool for the Rapid Evaluation of the Effects of Explosions

Juan Sánchez-Monreal [†] , Alberto Cuadra , César Huete  and Marcos Vera ^{*} 

Departamento de Ingeniería Térmica y de Fluidos, Escuela Politécnica Superior, Universidad Carlos III de Madrid, 28911 Leganés, Spain

^{*} Correspondence: marcos.vera@uc3m.es; Tel.: +34-91-624-99-87

[†] Current address: Institute of Engineering Thermodynamics, German Aerospace Center (DLR), Pfaffenwaldring 38–40, 70569 Stuttgart, Germany.

Abstract: The dynamic response of structural elements subjected to blast loading is a problem of growing interest in the field of defense and security. In this work, a novel computational tool for the rapid evaluation of the effects of explosions, hereafter referred to as SimEx, is presented and discussed. The classical correlations for the reference chemical (1 kg of TNT) and nuclear (10⁶ kg of TNT) explosions, both spherical and hemispherical, are used together with the blast wave scaling laws and the International Standard Atmosphere (ISA) to compute the dynamic response of Single-Degree-of-Freedom (SDOF) systems subject to blast loading. The underlying simplifications in the analysis of the structural response follow the directives established by UFC 3-340-02 and the Protective Design Center Technical Reports of the US Army Corps of Engineers. This offers useful estimates with a low computational cost that enable in particular the computation of damage diagrams in the Charge Weight–Standoff distance (CW–S) space for the rapid screening of component (or building) damage levels. SimEx is a computer application based on Matlab and developed by the Fluid Mechanics Research Group at University Carlos III of Madrid (UC3M). It has been successfully used for both teaching and research purposes in the Degree in Security Engineering, taught to the future Guardia Civil officers at the Spanish University Center of the Civil Guard (CUGC). This dual use has allowed the development of the application well beyond its initial objective, testing on one hand the implemented capacities by undergraduate cadets with the end-user profile, and implementing new functionalities and utilities by Masters and PhD students. With this experience, the application has been continuously growing since its initial inception in 2014 both at a visual and a functional level, including new effects in the propagation of the blast waves, such as clearing and confinement, and incorporating new calculation assistants, such as those for the thermochemical analysis of explosive mixtures; crater formation; fragment mass distributions, ejection speeds and ballistic trajectories; and the statistical evaluation of damage to people due to overpressure, body projection, and fragment injuries.

Keywords: effects of explosions; blast loading; SDOF systems; thermochemistry of explosives; fragments; crater formation; damage to people

Citation: Sánchez-Monreal, J.; Cuadra, A.; Huete, C.; Vera, M. SimEx: A Tool for the Rapid Evaluation of the Effects of Explosions. *Appl. Sci.* **2022**, *12*, 9101. <https://doi.org/10.3390/app12189101>

Academic Editors: Ricardo Castedo, Lina M. Lopez and Jeong Ik Lee

Received: 22 July 2022

Accepted: 6 September 2022

Published: 10 September 2022

Publisher's Note: MDPI stays neutral with regard to jurisdictional claims in published maps and institutional affiliations.



Copyright: © 2022 by the authors. Licensee MDPI, Basel, Switzerland. This article is an open access article distributed under the terms and conditions of the Creative Commons Attribution (CC BY) license (<https://creativecommons.org/licenses/by/4.0/>).

1. Introduction

Unlike the slow energy release exhibited by deflagrations, the instantaneous energy deposition associated with the detonation of a high explosive produces an extremely rapid increase in temperature and pressure due to the sudden release of heat, light, and gases [1]. The gases produced by the explosion, initially at extremely high temperatures and pressures, expand abruptly against the surrounding atmosphere, vigorously pushing away any other object that may be found in their path. This gives rise to the two most notable effects of explosions: the aerial, or blast, wave [2], and the projection of shell fragments or other items (i.e., secondary fragments) located in the surroundings of the charge [3].

If the explosive device is located at a ground level, a fraction of its energy is effectively coupled to the ground, generating seismic waves and a well distinguished surface crater that results from the ejection of the shattered ground materials in direct contact with the charge [4]. Quantifying these phenomena and assessing their effect on the environment, including structural elements, vehicles, objects, or people located around the blast site, is a highly complex task that requires a thorough knowledge of the physical-chemistry of explosions [1,5–7] and their dynamic interactions with nearby structures [8] or the human body [9].

As a result of the growing terrorist threat experienced in the last few decades [10], estimating the effects of explosions has become a critical issue in the design, protection, and restoration of buildings and infrastructures, both civil and military [11]. However, this task is far from trivial, in that it involves transient compressible flows, nonlinear structural response, and highly dynamic fluid–structure interactions. These phenomena can be described with some accuracy using multiphysics computational tools, also known as hydrocodes [12], such as Ansys Autodyn, LS-Dyna, or Abaqus, based on the explicit finite element method [13]. In the simulations, all the critical components are modeled, including the detonation of the explosive charge, the resulting blast wave, the induced dynamic loads, and the nonlinear structural response. However, the enormous computational effort required to complete detailed computational analyses, which includes not only the calculation time itself, but also complex pre- and post-processing stages, remains a critical issue. For instance, simulating the effect of an explosive charge on a full-scale bridge may require more than 10 million finite elements [14]. For this reason, most engineering analyses still make use of simplified models for determining the explosive loads and estimating the resulting dynamic structural response in a timely manner. This enables the fast computation of damage diagrams in the Charge Weight–Standoff distance (CW–S) space, of utility to determine the level of protection provided by an input structural component loaded by blast from an input equivalent TNT charge weight and standoff [15].

In this regard, the American Unified Facilities Criteria UFC 3-340-02 [16], which supersedes the former ARMY TM 5-1300, establishes the requirements imposed by the US Department of Defense in the tasks of planning, design, construction, maintenance, restoration, and modernization of those facilities that must be protected against explosive threats. In the absence of similar regulations in other countries, UFC 3-340-02 [16] is widely used by engineers and contractors outside the US, as it provides a valuable guide for calculating the effects of blast-induced dynamic loads, including step-by-step procedures for the analysis and design of buildings to resist the effects of explosions.

To facilitate the application of the procedures set forth in the UFC 3-340-02 [16], as well as other analyses established in classic references of explosives engineering [3,5,6,9,17–19], fast evaluation software tools have been developed that incorporate the vast amount of data available as tables or graphs in the literature [7]. For instance, the United States Army Corps of Engineers (USACE) has developed and provides support for a series of software packages related to the design of explosion-resistant buildings [20]. Those tools were developed with public funding, and therefore there are regulations that restrict distributing those products outside of the United States. In addition, given the critical nature of this knowledge, access to these packages is severely limited to US government agencies and their contractors, with use only authorized to US citizens.

The inability to access these software packages motivated the authors to develop their own computational toolbox for the rapid evaluation of the effects of explosions. The result was the SimEx platform to be presented in this work. Conceived initially for educational purposes, the main goal was to develop a virtual software platform with an easy and intuitive Graphical User Interface (GUI) to be used in the computer lab sessions of the Explosion Dynamics course of the Degree in Security Engineering, taught at the University Center of the Civil Guard (CUGC) in Aranjuez, Spain. The Civil Guard is the oldest and biggest law enforcement agency in Spain. Of a military nature, its competencies include delinquency prevention, crime investigation, counter-terrorism operations, coastline and

border security, dignitary and infrastructure protection, as well as traffic, environment or weapons and explosives control using the latest research techniques. The paradigm of the Civil Guard’s capacity is its outstanding role in the defeat of the terrorist group ETA, the longest-running terrorist group in Europe and the best technically prepared. In this context, the main target of the Degree in Security Engineering is the training of Guardia Civil cadets (i.e., the Guardia Civil’s future officer leadership) in the development, integration, and management of last generation civil security systems.

The purpose of SimEx was initially limited to the blast damage assessment on simple structural elements [21], such as beams, columns, pillars, or walls, following the Single-Degree-of-Freedom (SDOF) system analysis established by UFC 3-340-02 [16]. The tool has been successfully used since its initial inception in 2014 in both the computer lab sessions of the Explosion Dynamics course, and as a research tool for the development of a number of Bachelor and Master’s theses on explosion dynamics and blast effects. This double use as end-users and software developers by the Civil Guard cadets and students from other UC3M degrees has enabled the development of the application well beyond the initially planned objectives [22]. As a result, the current version of SimEx incorporates advanced topics in blast wave propagation, such as the prediction of cleared blast pressure loads due to the generation of rarefaction waves, as well as confined blast loading in vented structures [23]. It also includes several other calculation assistants for the thermochemical analysis of explosive mixtures [5,7,24]; crater formation [4,6,25]; fragment mass distributions, ejection speeds and ballistic trajectories [3,26–28]; and the statistical evaluation of damage to people due to overpressure, body projection and fragment injuries [9,29,30].

2. SimEx Capabilities

This section presents the current capabilities of SimEx, starting with the main interface used for computing the dynamic response of SDOF systems subjected to blast loading, and following with the description of the remaining calculation assistants.

2.1. Single-Degree-of-Freedom System Analysis

In many situations of practical interest, the response of structural elements to blast loading can be reduced, in first approximation, to that of an equivalent spring-mass SDOF system. As sketched in Figure 1, this system is made up of a concentrated mass subject to external forcing and a nonlinear weightless spring representing the resistance of the structure against deformation [8]. The mass of the equivalent system is based on the component mass, the dynamic load is imposed by the blast wave, and the spring stiffness and yield strain on the component structural stiffness and load capacity. Generally, a small viscous damping is also included to account for all energy dissipated during the dynamic response that is not accounted by the spring-mass system, such as slip and friction at joints and supports, material cracking, or concrete reinforcement bond slip [31].

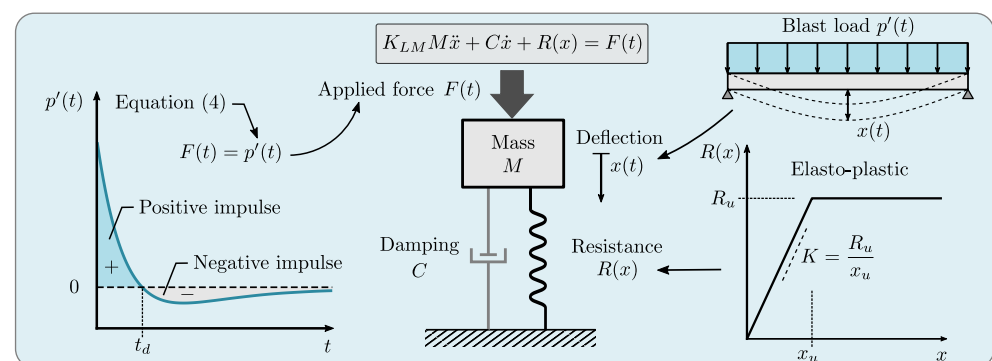


Figure 1. Sketch of the equivalent SDOF system showing the different terms involved in its mathematical description. **Left:** forcing term; **right:** resistance term; **center:** equivalent spring-mass SDOF system and its associated differential equation.

If the system properties are properly defined, the deflection of the spring–mass system, $x(t)$, will reproduce the deflection of a characteristic point on the actual system (e.g., the maximum deflection). The system properties required for the determination of the maximum deflection are the effective mass of the equivalent SDOF system, M_e , the effective viscous damping, C_e , the effective resistance function, $R_e(x)$, and the effective load history acting on the system, $F_e(t)$. To systematize the calculations, the effective properties are obtained using dimensionless transformation factors that multiply the actual properties of the blast-loaded component, respectively, M , C , $R(x)$, and $F(t)$ [32]. These factors are obtained from energy conservation arguments in order to guarantee that the equivalent SDOF system has the same work, kinetic, and strain energies as the real component for the same deflection when it responds in a given, assumed mode shape, typically the fundamental vibrational mode of the system [31].

In the analysis of blast-loaded SDOF systems, it is therefore of prime importance to identify the fundamental vibrational mode of the structural element. This procedure is not trivial, since obtaining the fundamental mode can entail certain difficulties, in which case its shape must be approximated in some way [32]. To determine the equivalent properties of the SDOF system, it is also necessary to determine the type of structure (beam, pillar, frame, etc.) and how the load is applied (typically, a uniform load is assumed). The elastic behavior of the material is often modeled as perfect elasto-plastic, probably the simplest of all nonlinear material models. This assumes that the initial response follows a linear elastic behavior described by an apparent elastic constant K , but once the yield strain is reached, $x \geq x_u$, the material behaves as plastic, flowing at a constant stress with an ultimate resistance $R_u = Kx_u$, i.e.,

$$R(x) = \begin{cases} Kx & \text{for } |x| < x_u \\ R_u & \text{for } |x| \geq x_u \end{cases} \quad (1)$$

Although more complex models could be used, they are not considered here due to the heavy simplifications introduced in the formulation of the problem.

The mass transformation factor, K_M , is defined as the ratio between the equivalent mass M_e and the real mass M of the blast-loaded component; the load transformation factor K_L is defined as the ratio between the equivalent load $F_e(t)$ and the actual load $F(t)$, and usually coincides with the resistance and damping transformation factors; and finally the load-mass factor K_{LM} is defined as the ratio between the mass factor and the load factor

$$K_M = \frac{M_e}{M}; \quad K_L = \frac{F_e(t)}{F(t)} = \frac{R_e(x)}{R(x)} = \frac{C_e}{C}; \quad K_{LM} = \frac{K_M}{K_L} = \frac{M_e}{M} \cdot \frac{F(t)}{F_e(t)} \quad (2)$$

Although all these factors are easy to obtain, even through analytical expressions in some cases, most of them can be found tabulated in the UFC-3-340-02 [16].

The linear momentum equation for the equivalent SDOF system then takes the form [32]

$$K_{LM}M\ddot{x} + C\dot{x} + R(x) = F(t) \quad (3)$$

where, as previously discussed, C represents the viscous damping constant of the blast-loaded component. This constant is often specified as a small percentage, z , of the critical viscous damping, $C = (z/100)C_{cr}$, with a damping coefficient $z = 2$ being a good value when not otherwise known (for further details see [31]). Note, however, that damping has very little effect on the maximum displacement, which typically occurs during the first cycle of oscillation, so the actual value of z is not of major relevance. The inhomogeneous term, $F(t)$, appearing on the right-hand side of Equation (3) represents the dynamic load associated with the blast wave, to be discussed in Section 2.1.1 below.

SimEx provides an easy and intuitive GUI environment for the study of the dynamic response to blast loadings of a variety of structural elements that can be modeled as SDOF systems. Figure 2 shows the main SimEx interface, divided into three calculation

assistants for the three basic elements that make up the SDOF system: a module for calculating the properties of the blast wave (forcing term, $F(t)$), a module for calculating the equivalent mechanical properties (resistance term, $R(t)$), and a module for the numerical integration of the problem, which includes the post-processing of the results and their graphic representation in the form of displacements, forces, and deformation diagrams (see the bottom plots of Figure 2) and of CW-S damage charts, to be discussed in Section 3.3.

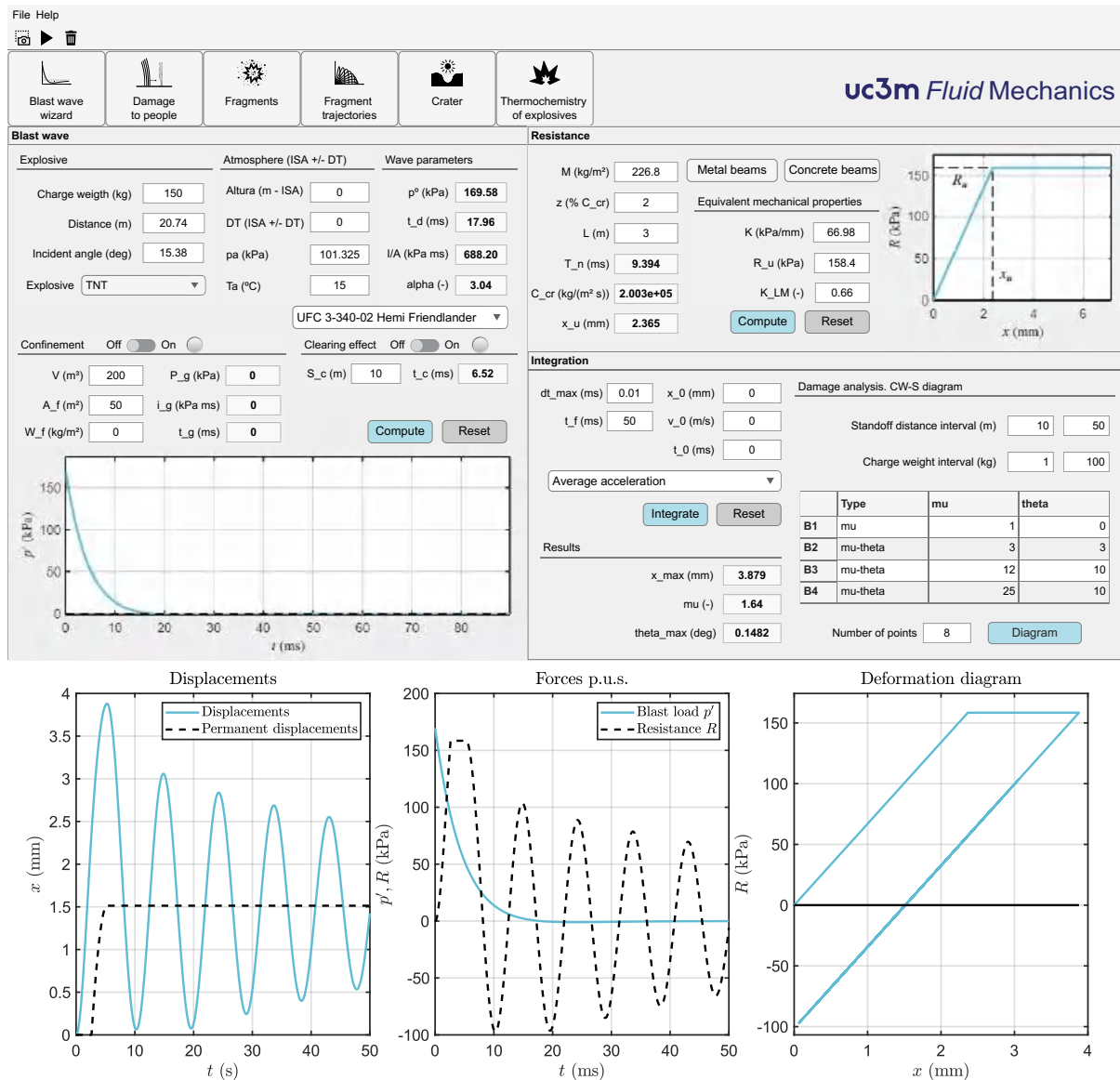


Figure 2. Main interface of SimEx showing the “Blast wave”, “Resistance”, and “Integration” assistants for the computation of the structural response of perfect elasto-plastic SDOF systems under blast loading. The access buttons to the other calculation assistants are seen under the top toolbar. The bottom plots show the post-processing pop-up window that displays the results of the numerical integration in terms of displacements, forces, and deformation diagrams (for a detailed discussion of these diagrams, see Section 2.1.4).

As a final remark, it is important to note that, following standard practice, the SDOF analysis carried out by SimEx uses the load defined in terms of pressure, $F(t) = p'(t)$ (Pa), so that both the mass M (kg/m²), the damping coefficient C (kg/(m² s)) and the ultimate resistance R_u (Pa) must all be introduced as distributed values per unit surface (p.u.s.) in the different calculation assistants.

2.1.1. Forcing Term

As previously discussed, the blast wave overpressure defined in Equation (4) below can be used directly in Equation (3) as forcing term, $F(t) = p'(t)$, as long as the analysis is formulated per unit surface and uses distributed masses and forces. In order to determine the blast parameters (arrival time, peak overpressure, positive phase duration, impulse per unit area, waveform parameter, etc.), classical correlations [1,2,17–19,33,34] in terms of scaled distance are used together with the scaling laws for spherical or hemispherical blast waves [1,17,35,36], which allow their evaluation for arbitrary CW–S pairs. It is interesting to note that the standoff distance is defined as the minimum distance from the charge to the structural element under study (e.g., a wall). However, the actual distance to a given point of that element, e.g., the centroid (or geometric center), which may be considered the most representative point of the structure, may be slightly different due to the incidence angle being larger than 0 at that point.

The local atmospheric pressure, p_a , and temperature, T_a , are determined using the International Civil Aviation Organization (ICAO) Standard Atmosphere (ISA) [37] with a temperature offset ($ISA \pm \Delta T$). The user must specify the geopotential height, in meters, and the non-standard offset temperature $\pm \Delta T$, although arbitrary ambient temperature and pressure can also be introduced directly [38]. TNT is used as reference explosive, although the results can be extrapolated to other compositions using either the equivalence tables included in SimEx for selected explosives [39], or the thermochemical calculation assistant, to be presented in Section 2.2.1, for less conventional formulations or explosive mixtures.

To estimate the dynamic load exerted by the blast wave, the angle of incidence of the incoming shock wave must be considered, the worst-case conditions being usually those of normal incidence. UFC 3-340-02 [16] contains scaled magnitude data for both spherical and hemispherical blast waves. It also provides methods to calculate the properties of the blast wave with different incidence angles, including both ordinary and Mach reflections for oblique shocks. The time evolution of the blast wave overpressure $p'(t')$ at a fixed distance, d , sufficiently far from the charge (at least, larger than the fireball scaled distance) is approximated using the modified Friedlander's equation, which captures also the negative overpressure phase [1,17,40]

$$p'(t') = p(t') - p_1 = p^\circ \left(1 - \frac{t'}{t_d}\right) \exp\left(-\alpha \frac{t'}{t_d}\right) \quad (4)$$

where $p^\circ = p_2 - p_1$ represents the peak overpressure measured from the undisturbed atmospheric pressure $p_1 = p_a$, with p_2 denoting the peak post-shock pressure, $t' = t - t_a$ is time measured from the blast arrival time, t_d is the positive phase duration, and α is the waveform parameter, closely related to the impulse per unit area of the positive phase $I/A = \int_0^{t_d} p'(t') dt'$ (area under the positive phase of the overpressure-time curve) according to $I/A = p^\circ t_d [1/\alpha - (1 - e^{-\alpha})/\alpha^2]$. SimEx performs by default the complete integration of the Friedlander waveform, but the equivalent triangular pressure pulse can also be used without significant errors [32]. This simplified waveform has the same maximum peak overpressure, p° , but a fictitious positive duration computed in terms of the total positive impulse and the peak over pressure, $t_d = 2(I/A)/p^\circ$.

The "Blast wave" calculation assistant allows the activation of the effects of clearing and confined explosions, which increases the computational capabilities to more realistic situations. The clearing effect takes into account the time required for reflected pressures to clear a solid wall that has received the impact of a blast wave as a result of the propagation of rarefaction waves from the edges of the wall. In the case of confined explosions, SimEx implements the procedure outlined in UFC 3-340-02 [16] to estimate the gas phase peak overpressure and duration of the equivalent triangular pressure pulse in terms of the chamber's total vent area and free volume. These effects can be activated on the lower part of the "Blast wave" calculation assistant.

2.1.2. Resistance Term

The “Resistance” calculation assistant provides a means to define the equivalent mechanical properties (i.e., structural mass, damping coefficient, and structural strength) of the SDOF system under study modeled as a perfectly elasto-plastic system with elastic stiffness K until the yield strain, as given in Equation (1). The characteristic length, L , of the structural element must also be provided, as it is required to determine the maximum rotation angle at its boundaries, often referred to as support rotation, θ . For the equivalent SDOF system, the assistant computes the fundamental natural period, $T_n = 2\pi\sqrt{K_{LM}M/K}$, the critical damping, $C_{cr} = 2\sqrt{K_{LM}KM}$, and the deflection at which plastic deformation initiates in the system, x_u . Direct access to calculation assistants that compute the equivalent properties (M , K , K_{LM} , R_u) required for the calculations is also provided for various types of systems. Currently, standard European wide flange “metal beams” [41] and reinforced “concrete beams” are included (see Section 3.2), although it could be possible to incorporate additional assistants for other elements, such as metal panels/plates, open-web steel joists, reinforced concrete slabs, reinforced/unreinforced masonry, or wood panels/beams. The metal beams assistant also provides the possibility of studying custom (i.e., non-normalized) profiles and materials in order to widen the computation capabilities.

2.1.3. Numerical Integration

Once the characteristics of the equivalent SDOF system have been defined, the resulting ordinary differential equation that models the transient nonlinear response of the equivalent structural system (3) must be integrated numerically. The integration module implements the two numerical methods recommended by UFC-3-340-02 [16], namely the “Acceleration-Impulse-Extrapolation Method” and the “Average Acceleration Method” [16], which can be selected from a drop-down menu. Text boxes are also included to set the initial conditions (displacement and initial speed, which are zero by default) as well as the final integration time. Since both numerical methods use constant time steps, a sufficiently short time increment, typically of the order of a few percentage of the natural period or the positive phase duration (usually, fractions of a millisecond), should be used in order to ensure the numerical convergence of the integration.

2.1.4. Post-Processing

After integration, three plots appear in a pop-up window and a summary table is provided at the bottom left corner of the main window. The left plot shows the instantaneous displacement (solid line) and the permanent displacement, or deformation (dashed line). The central plot shows the temporal variation of the forcing term (i.e., the blast pressure wave, solid line) together with the resistance strength of the SDOF system (dashed line). The right plot shows the displacement–resistance graph, in which it is possible to determine more clearly whether permanent deformations occur or not. Finally, the table of results shows the maximum displacement obtained, x_{max} , along with two damage indicators: the ductility ratio, $\mu = x_{max}/x_u$, defined as the ratio of the peak deflection to the ultimate elastic deflection, and the maximum support rotation, θ , whose calculation depends on the type of structure under study.

By integrating different combinations of charge weights and standoff distances for the same structural element, damage level diagrams can be rapidly obtained in the CW–S distance space. SimEx has a function for it located in the central part of the integrator module. One can select the range of charge weights and standoff distances, the number of intermediate values and the type of damage in terms of the quantitative indicators μ and θ [15]. From the two quantitative indicators, the structural damage level can be classified qualitatively into: superficial, moderate, heavy, hazardous failure, and blowout, with response limit boundaries between these levels denoted respectively by B1 (superficial to moderate), B2 (moderate to heavy), B3 (heavy to hazardous failure), and B4 (hazardous failure to blowout). Convenient limits for the boundaries of component damage levels for common structural components in terms of μ and θ are provided in [15]. An example of a

damage level diagram for the façade of a conventional building subject to blast loading computed with SimEx will be presented in Section 3.3.

2.2. Other Calculation Assistants

The main SimEx interface gives access to several other calculation assistants. These include: a module for the calculation of the theoretical (i.e., thermochemical) properties of explosives and explosive mixtures; a module for estimating the initial velocity, mass distribution and ballistic trajectories of primary fragments; a crater formation calculator; and a module for estimating damage to people, including both primary and tertiary injuries. The fragment assistant also provides estimations of the secondary injuries due to the impact of primary fragments on people. In this section, we shall briefly present and discuss the above-mentioned assistants.

2.2.1. Assistant for the Calculation of the Thermodynamic Properties of Explosives

For the calculation of the theoretical thermodynamic properties of explosives and explosive mixtures, SimEx includes an extensive database of pure CHNO propellants and explosives extracted from Kinney and Graham [1], updated with data from Meyer [7] and Akhavan [5] for more recent explosives. From the properties of pure explosives, the thermochemical assistant estimates the properties of explosive mixtures formed by two or more components by specifying the mass fractions and the density of the mixture.

First, it computes the apparent chemical formula of the explosive mixture along with its molecular weight and maximum density. For the calculation of the decomposition reaction in nominal products, which provides the heat of explosion and the volume of gases generated, one can choose different calculation hypotheses: Kamlet–Jacobs (KJ), Kistiakowsky–Wilson (KW), Modified Kistiakowsky–Wilson (modified KW), Springall–Roberts (SR), or chemical equilibrium [5]. In the latter case, SimEx determines the composition of the product mixture following the chemical equilibrium approach considering a constant–volume explosion transformation that uses the ideal gas Equation of State (EoS) for the products according to the norm UNE 31-002-94 [42], as illustrated in Figure 3.

Reactants		Equation of State		Parameters		Composition	
UNE 31-002-94		Ideal					
Components	Mass fraction			Reactants		Products	
NG	0.0350	298.1	Temperature [K]	3030			
EGDN	0.0350	1	Pressure [bar]	1.164e+05			
N2O3H4	0.7200	1100	Density [kg/m3]	1100			
TNT	0.1400	-3964	Enthalpy [kJ/kg]	-2961			
C6H10O5	0.0500	-3840	Internal energy [kJ/kg]	-3840			
CaCO3	0.0100	95.83	Mean Molecular Weight [g/mol]	25.12			
TALC	0.0100		Entropy [kJ/(kg K)]	8.81			
C 7.1885 CA 0.0999 H 43.9106 MG 0.0791 N 20.7720 O 35.6249 SI 0.1055			Volume gases [m3/kg]	0.8924			
Charge weight [kg]	1		cp [kJ/(kg K)]	2.074			
Density [kg/m3]	1100		gamma = cp/cv [-]	1.19			
Oxygen Balance [%]	-1.756		Sound speed [m/s]	1093			
Compute Reset			Detonation speed [m/s]	6097			
			Heat release [kJ/kg]	4003			
			Gurney constant [m/s]	2830			
			Explosive force [kJ/kg]	1003			

Figure 3. Interface of the assistant for the calculation of the theoretical thermodynamic properties of explosives and explosive mixtures.

More complex computations based on the European Standard EN 13631-15 [43], which use the semi-empirical Becker–Kistiakowsky–Wilson (BKW) EoS [44–46] or the Heuzé (H9) EoS [47] for the products, are also supported in the last version of SimEx. As sample results of these computations, Table 1 shows the detonation properties obtained by SimEx for different explosive mixtures (see Table 2 for its composition) compared with the results

reported in the European Standard EN 13631-15 [43], and obtained with the W-DETCOM code [48,49], which computes directly the Chapman–Jouguet state.

Table 1. Comparison of the calculated temperature at constant volume, T , detonation pressure, p_{CJ} , detonation velocity, v_{CJ} , heat release at constant volume, Q_v , and explosive force, F_e , with the results provided by the European Standard EN 13631-15 [43] and by the thermochemical code W-DETCOM [49] for different explosive mixtures using the BKW–S EoS.

Explosive	Source	T [K]	p_{CJ} [GPa]	v_{CJ} [m/s]	Q_v [kJ/kg]	F_e [kJ/kg]
ANFO	CT	2592	7.14	5353	3845	943
	EN 13631-15	2586	-	-	3820	945
	W-DETCOM ¹	2919	6.62	5326	3849	-
ANFO-Al	CT	3026	7.38	5442	4666	1009
	EN 13631-15	3060	-	-	4642	1020
	W-DETCOM ¹	3370	6.55	5215	4655	-
Emulsion	CT	2112	15.3	6549	3263	766
	EN 13631-15	2099	-	-	3236	771
	W-DETCOM ¹	2438	13.9	6758	3214	-
Dynamite I	CT	4173	25.03	7960	6452	1147
	EN 13631-15	4130	-	-	6338	1138
Dynamite II	CT	3165	23.58	7729	5049	987
	EN 13631-15	3151	-	-	4989	984

¹ Calculation performed assuming Chapman–Jouguet detonation.

Table 2. Composition [mass %], density, and oxygen balance of different explosive mixtures tested.

Component	ANFO	ANFO-Al	Emulsion	Dynamite I	Dynamite II
Aluminium	-	5	-	-	-
Ammonium nitrate	94	91	80	-	49
Cellulose	-	-	-	-	3
2,4-Dinitrotoluene	-	-	-	-	4
Nitrocellulose 12%	-	-	10	-	4
Nitroglycerin	-	-	-	45	20
Nitroglycol	-	-	-	45	20
Fuel oil	6	4	7	-	-
Sodium nitrate	-	-	5	-	-
Water	-	-	8	-	-
Density [kg/m³]	850	850	1300	1500	1500
Oxygen balance [%]	-1.7	0.08	-5.57	-2.26	0.84

The equilibrium calculations are carried out using Combustion Toolbox (CT), an in-house thermochemical equilibrium package developed at UC3M [24,50]. CT determines the equilibrium composition of the product mixture through the Gibbs free energy minimization method by using Lagrange multipliers combined with a multidimensional Newton–Raphson method. The thermodynamic properties (specific heat, enthalpy, and entropy) are

computed as a function of temperature derived from NASA's 9-coefficient polynomial fits for combustion of ideal and non-ideal gases and condensed phases.

From the resulting composition of the product mixture at equilibrium, the assistant computes the volume of gases generated, the heat of explosion, the Gurney constant, the detonation pressure, the detonation velocity, and the explosive force (or power index). To estimate the detonation pressure and velocity, the approximate expressions of Kamlet & Jacobs [51,52] are used, whereas the explosive force is estimated using the well-known Berthelot approximation [1]. These data are subsequently used to calculate the TNT equivalent of the explosive composition under study.

2.2.2. Crater

SimEx also has an assistant for the direct and inverse calculation of craters based on the classical correlations for craters reviewed by Cooper [6] (see also Refs. [4,25]), whose interface is shown in Figure 4. With this assistant, one can calculate the radius of the crater generated by the detonation of a certain amount of a given explosive at a certain height above the ground, considering different types of soil. It is also possible to calculate the explosive charge required to produce a crater of a certain size, which may be useful for the forensic analysis of explosions [53]. Buried craters are not yet included in the assistant, but could be incorporated in future versions following the work of Westine [54], as reviewed by Baker et al. [55].

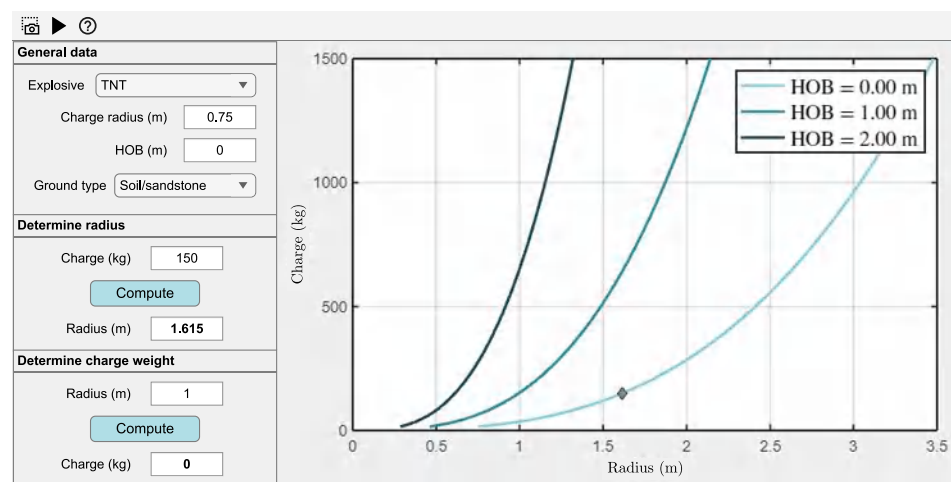


Figure 4. Interface of the assistant for the calculation of craters. HOB denotes the height of burst.

2.2.3. Primary Fragments

SimEx incorporates assistants for calculating the mass distribution, ejection velocity, and ballistic trajectory of primary fragments. The corresponding interfaces are shown in Figures 5–7. The fragment size distribution is estimated using Mott's statistical theory for fragmentation of steel cylindrical shells [3,26–28], as suggested by UFC-3-340-03 [16]. As shown in Figure 5, this model determines the average number of fragments and their average weight. It also provides the size of the largest fragment corresponding to a given Confidence Level (CL). SimEx also includes a ballistic trajectory assistant for primary fragments that, in addition to the flight path, provides the flight time, velocity, and maximum distance, as illustrated in Figure 6. The initial velocity of primary fragments is computed using Gurney's analysis [56] for cylindrical, spherical, and symmetrical/asymmetrical sandwich charges. Although this analysis assumes that all fragments have the same the initial velocity, given the different fragment sizes, both their initial kinetic energy and their subsequent aerodynamic deceleration are different. The assistant thus includes an initial aerodynamic deceleration chart, shown in Figure 7, that provides the fraction of the initial velocity achieved at a certain distance, given the fragment mass and material, and the local air density, specified through the ISA $\pm \Delta T$ model. The aerodynamic assistants assume

spherical fragments with a variable drag coefficient for all Mach numbers [57], although the model could be extended to account for more realistic (i.e., irregular) fragment shapes in future versions [58]. The results of these models are also used to estimate the lethality risk by the impact of primary fragment in the event of a strike on a person, which is found to depend on the speed and the mass of the fragment, as illustrated by Figure 5.

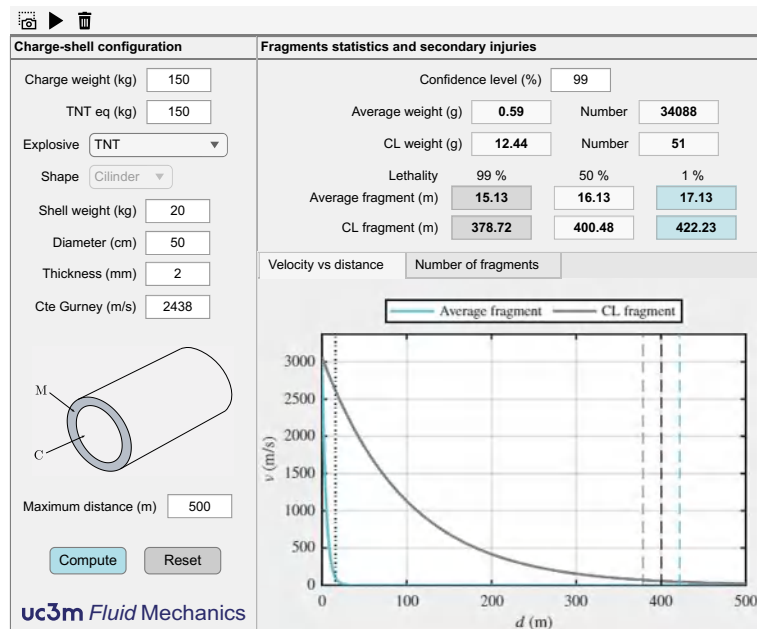


Figure 5. Interface of the primary fragment mass distribution and lethality assistant.

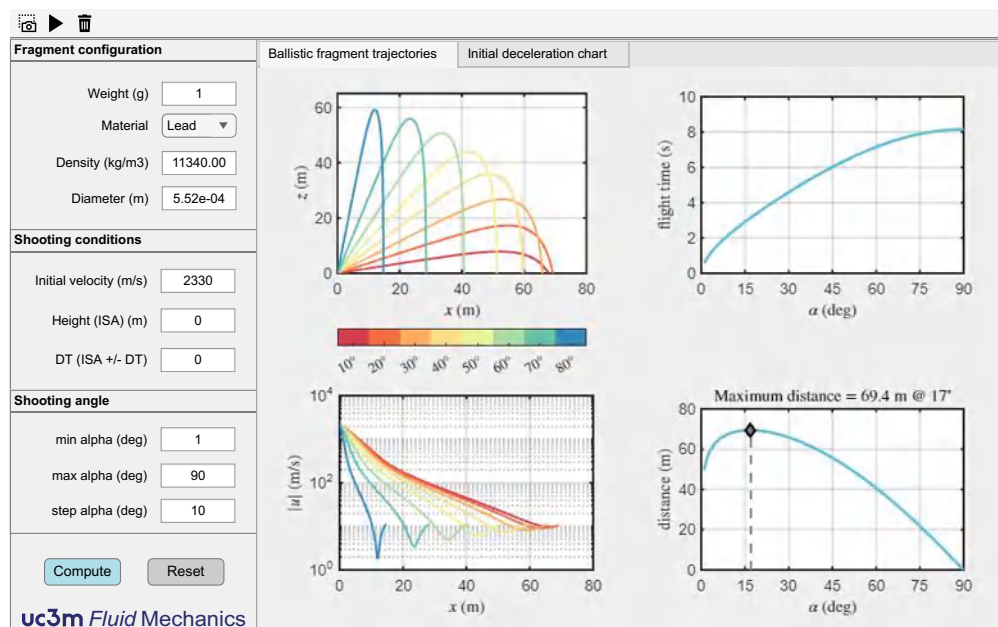


Figure 6. Interface of the primary fragment calculation assistant showing the ballistic fragment trajectory, flight time, velocity, and maximum distance charts. Fragments are assumed spherical.

Non-tabulated explosives or explosive mixtures can also be considered, with the Gurney constant being computed by the thermochemical assistant presented in Section 2.2.1. In this case, the user must select a “custom” explosive, and the thermochemical assistant will open to specify the desired explosive composition. Once the wizard is closed, the Gurney constant is automatically exported to the fragment wizard.

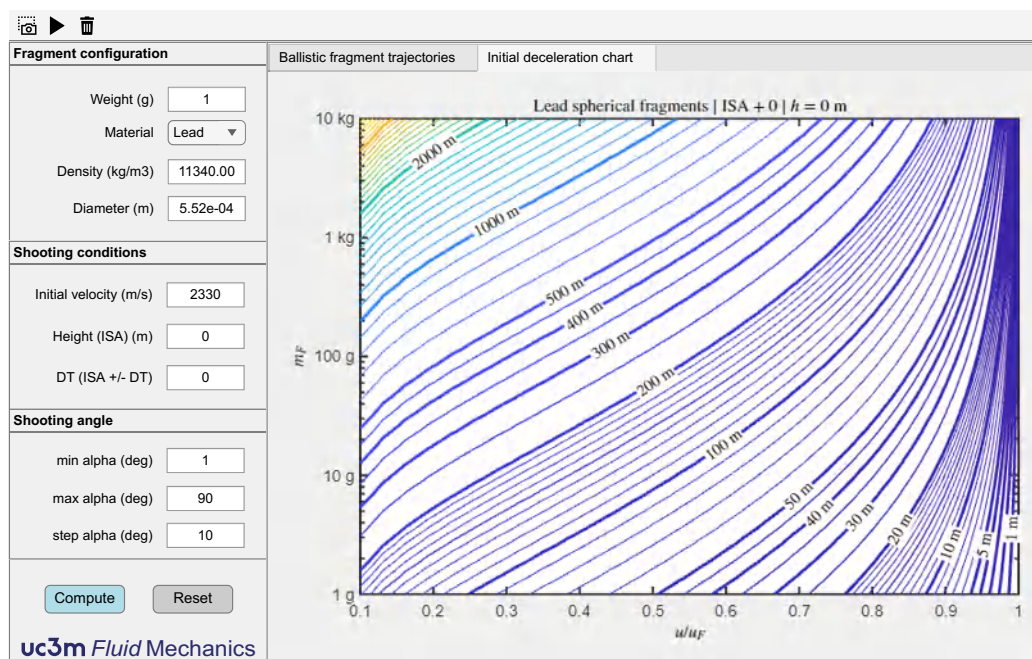


Figure 7. Interface of the primary fragment calculation assistant showing the initial deceleration chart, which provides the fraction of the initial velocity, u/u_f , achieved at a certain distance (contour lines), given the fragment mass, m_f , and material (e.g., lead), and the atmospheric conditions (e.g., ISA mean sea level). Fragments are assumed spherical.

2.2.4. Damage to People

SimEx includes an assistant for estimating damage to people using the widely accepted probit (*probability unit*) functions [58,59] provided by the TNO’s Green Book [9] and summarized in Table 3. For each type of injury or cause of death (eardrum rupture, lung injury, etc.), a probit function is defined that depends on the blast parameters: side-on, dynamic or reflected peak overpressure (depending on the body position), impulse per unit area, etc. For primary injuries, lethality due to lung damage is evaluated together with the probability of eardrum rupture. For tertiary injuries, lethality is evaluated for shock-induced body displacement and subsequent direct impact, either with the head or the whole body [29].

Table 3. Probit functions used to estimate the probability of different types of primary and tertiary injuries. Pr is the probit value, p° [Pa] the peak overpressure, p_{ef}° [Pa] the maximum effective overpressure, depending on the relative orientation of the person with respect to the shock wave, p_1 [Pa] the atmospheric pressure, I/A [$\text{Pa} \cdot \text{s}$] the impulse per unit area and m [kg] the weight of the person [9].

Effect	Probit Function
Primary injuries	
Eardrum rupture	$Pr = -12.6 + 1.52 \ln p^\circ$
Death due to lung damage	$Pr = 5 - 5.74 \ln \left(\frac{4.2}{p_{ef}^\circ/p_1} + \frac{1.3}{i/(p_1^{1/2}m^{1/3})} \right)$
Tertiary injuries	
Death due to displacement and whole-body impact	$Pr = 5 - 2.44 \ln \left(\frac{7380}{p^\circ} + \frac{1.3 \times 10^9}{p^\circ i} \right)$
Death due to displacement and skull impact	$Pr = 5 - 8.49 \ln \left(\frac{2430}{p^\circ} + \frac{4 \times 10^8}{p^\circ i} \right)$

The appearance of the interface is shown in Figure 8. All necessary parameters can be selected on the left: size, type, and geometry of the explosive charge, as well as the body position relative to the incoming pressure wave, which determines whether side-on, dynamic, or reflected pressure is used to compute the peak overpressure and impulse. The rest of the window presents the results both numerically and graphically, using overpressure–impulse diagrams on the left and CW–S diagrams on the right, with primary injuries shown above and tertiary injuries below. Overpressure–impulse diagrams display the characteristic overpressure–impulse–distance curve for the selected charge weight to facilitate the interpretation of results [60], while CW–S diagrams include a diagonal dashed line indicating the approximated position of the fireball radius, corresponding roughly to an scaled distance $Z = d/W^{1/3} = 1$ m. Above this line, the Freidlander waveform is not valid, and the blast wave parameters are increasingly imprecise [1].

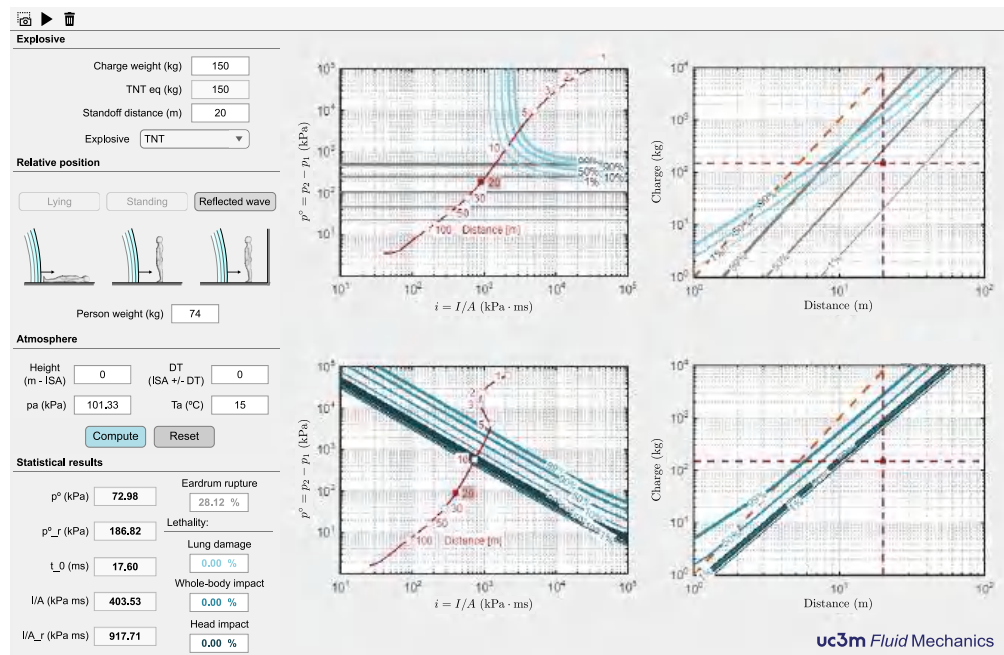


Figure 8. Interface of the assistant for estimating blast-induced damage to people. The CW–S and atmospheric data, along with the body position relative to the incoming pressure wave, are introduced in the top-left corner, the blast wave parameters and the statistical damage indicators for the chosen CW–S combination appear in the bottom left corner. The right plots represent graphically the statistical damage indicators in the form of overpressure–impulse and CW–S diagrams. Both show the conditions corresponding to the specified CW–S combination with a solid red dot, while the CW–S diagrams include also a diagonal dashed line indicating the approximated position of the fireball radius. Above this line, the Freidlander waveform is not valid, and the blast wave parameters are increasingly imprecise [1].

3. Example of Application: Façade of a Building under Blast Loading

To illustrate the capabilities of SimEx, this section presents a preliminary study to assess the ability of a conventional three-story steel frame building, such as the one shown in Figure 9, to resist three different combinations of charge weight, W , and standoff distance, d , preserving a similar scaled distance, $Z = d/W^{1/3}$. The three CW–S combinations are summarized in Table 4. For simplicity, we assume mean sea level ISA conditions for all the calculations. For illustrative purposes, the figures quoted below show results corresponding to the first floor of the building (hereafter referred to as Level 1) and Case 2 conditions. That is, we shall consider as reference conditions a ground explosion of 150 kg of TNT at a 20 m standoff distance from the front façade of the building, as depicted in Figure 9a.

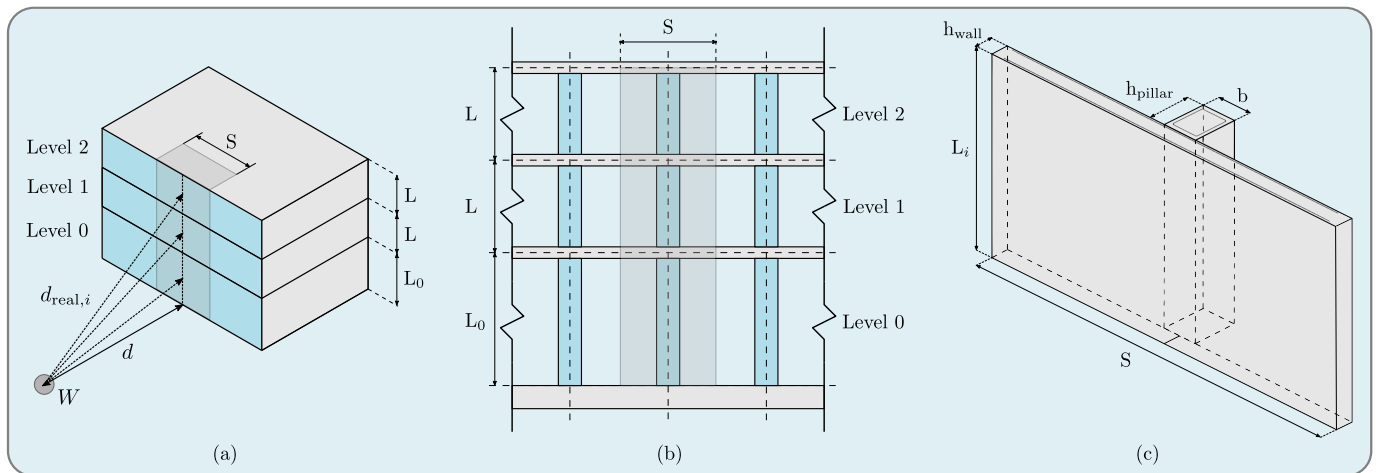


Figure 9. Schematic diagram of the three-story building under study, composed of equally spaced pillars and an outer enclosure wall, including: (a) the distances and angles used for the different floor levels ($i = 0, 1,$ and 2), including the standoff distance, d , the real distance to the midpoint of the different levels, $d_{real,i}$, and the corresponding angles of incidence, $\delta_{real,i}$; (b) schematic of the façade constructive details and dimensions; and (c) diagram of the equivalent façade element used in the SDOF analysis. L_i denotes the height of Level i , representing the length of the pillars, and S is the spacing between pillars, representing the tributary loaded width.

Table 4. Standoff distance, d , explosive charge, W , and scaled distance, Z , of the different case studies. The reference case is shown in blue.

Variables	Case 1	Case 2	Case 3
d (m)	12	20	25
W (kg)	30	150	300
Z (m/kg ^{1/3})	3.86	3.76	3.73

3.1. Incident Load

As previously discussed, SimEx allows the user to enter directly the desired CW-S combination to define the incident blast load. Figure 2 shows the results corresponding to the reference conditions (Level 1, Case 2). For a more detailed analysis of the load induced by the blast wave, the “Blast Wave” calculation assistant shown in Figure 10 allows a fast evaluation of all blast parameters as a function of the standoff distance. To this end, the user must provide the following input data: the ground distance from the explosion to the point of calculation, d , the elevation of the explosive charge, h_c , and the elevation of the calculation point, h_0 , both measured from the ground.

For $h_c = 0$, a hemispherical surface burst computed from Kingery and Bulmash parameters for TNT [18] is considered, although other correlations for hemispherical explosions [1] could also be selected. For $h_c > 0$, hemispherical or spherical blasts are both available, letting the user decide what is the best option based on the height of burst. The code does not include correlations for more complex configurations, such as air bursts producing regions of regular and Mach reflections that eventually modify the incident shock wave. The user must also introduce the angle formed by the normal to the structural element at the point of calculation with the horizontal projection of the line joining the center of the explosion with that point, δ , which is identically zero in our case studies if we assume a symmetric configuration with a pillar in the center of the front façade. These distances and angles are employed for simplicity in obtaining in-field measurements.

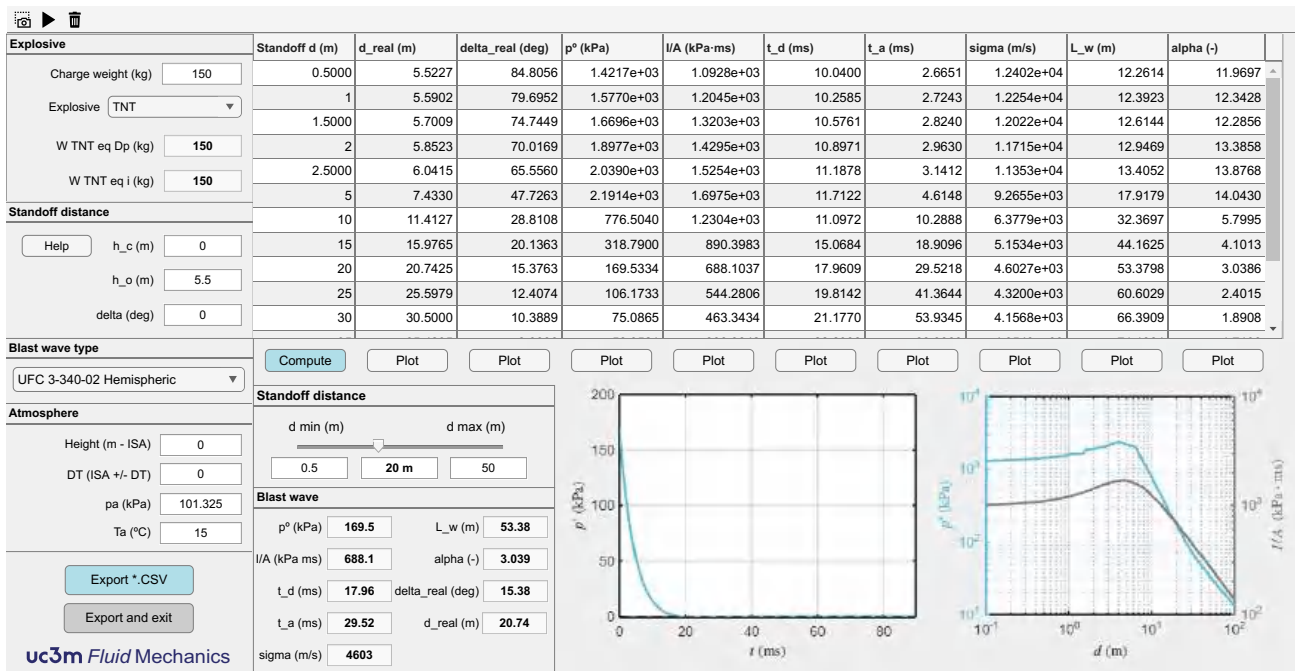


Figure 10. Interface of the Blast Wave calculation assistant for a charge weight of 150 kg of TNT at the ISA mean sea level, showing the variation of the blast parameters with the standoff distance from the front façade (top table). The lower part of the assistant shows the blast parameters calculated at a point located at $d = 20$ m standoff distance and $h_0 = 5.5$ m above the charge.

With these data, the wizard is able to compute the real distance and incidence angle, thereby providing the peak overpressure, p° , the impulse per unit area, I/A , the duration of the positive phase, t_d , the blast arrival time, t_a , the average speed of the pressure front, $\sigma = d_{\text{real}}/t_a$, the positive phase length, L_w , and the waveform parameter, α . The results are presented in a table for several standoff distances, d , which also gives the real distances, d_{real} , and angles of incidence, δ_{real} . The maximum and minimum distances that appear in the table can be easily modified by the user, who can select any intermediate value using a slider bar to compute the blast parameters at a fixed specified distance. A button has also been included to graphically represent the variation of any of the blast parameters as a function of the distance to the center of the explosion. The results are also exportable as a "comma-separated-value" format for further postprocessing.

For more qualitative information, two exportable graphs are presented in the lower part. The graph on the left displays the time evolution of the overpressure at a fixed horizontal distance. The user can change this distance easily with the slider bar. All the characteristics of the blast wave are shown for the particular distance chosen by the user. The graph on the right represents the maximum overpressure and the impulse per unit area as a function of the horizontal distance. As previously indicated, the range of distances is also adjustable by the user. Using the "Export and exit" button, the module is closed and the weight and type of explosive, the distance to the charge, and the real angle of incidence to be used in the integration of the SDOF system are exported to the main SimEx module. Figure 10 shows the calculation of the blast parameters for an explosive charge of 150 kg of TNT on a point at a height of 5.5 m above the horizontal, i.e., the geometric center of the façade of the first floor, corresponding to the reference case (Level 1, Case 2). Other distances are also included in the top table, showing how the angle of incidence tends to become normal as the charge moves away from the target.

3.2. Estimation of the Equivalent SDOF System Response

To study the structural response to an explosive charge, it is necessary to know in detail the type of construction. However, when using a simplified SDOF model, the study

can be simplified and generalized for many different cases. In the present example, we will analyze a façade structure like the one in Figure 9b, composed of equally spaced pillars and an outer enclosure wall.

The first element that receives the blast wave is the enclosure of the façade. This, in turn, transmits the load to the rest of the structure. In most constructions, the façade is only an enclosure without structural function (glass façades, brick, etc.). In first approximation, it can be considered that the exterior enclosure transmits the full load received directly to the pillars. The pillars are structural elements whose integrity is considered critical. It will therefore be the first element to be studied since the protection of the supporting structure is pivotal to avoid the potential collapse of the building. The enclosure can be considered as a secondary element in most constructions and therefore a significantly higher level of damage than in primary elements can be allowed.

Figure 9c shows the simplest element in which the façade is to be divided. Each pillar receives loads from a part of the façade corresponding to the distance between pillars and the height between floors. The load generated by the explosion is applied to the pillars crosswise, so they behave in first approximation as bending elements. For the calculation of the equivalent properties, the beam assistants available in SimEx are employed. Either for metal or concrete beams, the length corresponds to the height between floors, while the span is the spacing between pillars. In the case of pillars, the boundary condition between floors is that of embedment on both sides, whereas a free condition is preferred at the roof. As a result, we use fixed-fixed conditions for Levels 0 and 1 and cantilever (or fixed-free) for Level 2. The presence of a roof diaphragm element may require additional considerations regarding the boundary condition at the roof top, but we prefer to use a fixed-free boundary condition for the second floor both for simplicity and for illustrating the effect of considering different boundary conditions on different floors.

In the case of metal beams, it is only necessary to indicate the standard shape of the profile and the size. SimEx uses European cross-section profiles HEB, IPE, and IPN in accordance with Euronorm 53–62 (DIN 1025) [41]. Figure 11 shows the result for a HEB 340 profile with a length of 3 m and a separation between pillars of 5 m. The assistant uses standardized profiles, so if a non-existent measure is introduced, it corrects down to the nearest lower normalized profile. However, it is also possible to select custom profiles and materials. In this case, the area, first moment of area about the bending axis, moment of inertia about the bending axis, density, Young's modulus, and resistance must be provided by the user. Once the structural properties have been introduced, closing the assistant incorporates the computed data into the main SimEx interface. Figure 2 shows the result for the case under study. It should be noted that the additional enclosure mass supported by the pillar when flexed must also be included in the mass of the equivalent SDOF system in the main interface.

If a rectangular reinforced concrete pillar is considered, SimEx requires that the external measurements b and h (perpendicular and parallel to the direction of application of the load, respectively) be introduced. In addition, the properties of the reinforcement should be indicated in a simplified manner, that is, interior spacing, d_c , and reinforcement area, $A_s = n\pi d_{\text{bar}}^2/4$, where n represents the number of steel reinforced bars per side. Figure 12 shows results for a pillar of $45 \times 45 \text{ cm}^2$ with 5 A36 steel reinforcement bars of #7 (approximately 22.5 mm in diameter) per side, for a length of 3 m and a spacing between pillars of 5 m. The distance d_c must be estimated according to the constructive detail. In this particular case, it is assumed that the reinforcement centers are located at 4 cm from the edge, resulting in an interior reinforcement spacing of $d_c = 37 \text{ cm}$.

It is worth noting that neglecting axial load can be considered a conservative approach, particularly in the case of columns or pillars. These elements are initially subjected to a significant compression load due to the weight of the supported structure, which reduces the tensile stresses caused by bending. This simplification constitutes a first approximation in the study of the structural response. For a more detailed analysis, the wall should be the next element to be analyzed in order to assure that it is able to fully transmit the blast load

to the load-bearing element. If the wall was made of concrete, this could be done using the concrete beam assistant with $b = S$. In this case, the mass of the element under study would be the total mass of the equivalent SDOF system. However, in the case considered here of load-bearing elements (beams or columns/pillars), the total mass can be significantly larger than the mass of the element.

Figure 11. Metal beam calculation assistant showing results for a HEB 340 pillar with a length of 3 m and a spacing between pillars of 5 m. Note that, even though a HEB 350 is requested, which is not included in the norm, the assistant corrects down to the nearest normalized value, HEB 340.

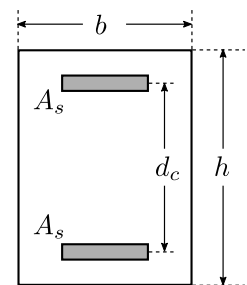


Figure 12. Reinforced concrete beam calculation assistant showing results for a pillar of $45 \times 45 \text{ cm}^2$ with a length of 3 m and a spacing between pillars of 5 m. The pillar is reinforced using 5 A36 steel reinforcement bars of 22.5 mm of diameter per side spaced apart 37 cm.

3.3. SDOF System Integration and CW–S Damage Diagrams

Once the user sets the explosive charge and the properties of the equivalent SDOF system, SimEx is ready to integrate the resulting mathematical problem. Figure 2 shows the results for the case of a HEB 340 profile with a 5 m span between pillars. The main results are the maximum deflection, x_{max} , the ductility ratio, μ , and the maximum rotation angle, θ . The two latter parameters are used as indicators to quantify the component damage levels [15]. Assuming that the Level of Protection (LOP) required is very low, in case of a hot rolled compact steel shape for the columns, according to [15], the allowable component damage is heavy (response between B2–B3).

For fixed values of the structural parameters, a parametric sweep can be carried out in CW–S space to obtain damage diagrams such as the ones shown in Figure 13. To this end, it is enough to indicate in the assistant the charge weight and standoff distance ranges to be analyzed and the number of intervals to be used for each parameter. In addition, the desired damage level criteria must be indicated to separate the zones. Figure 2 shows characteristic values of μ and θ for metallic elements, although other values could be selected from [15] for other structural elements and materials. Note that CW–S damage diagrams are presented both in linear and log-log scales.

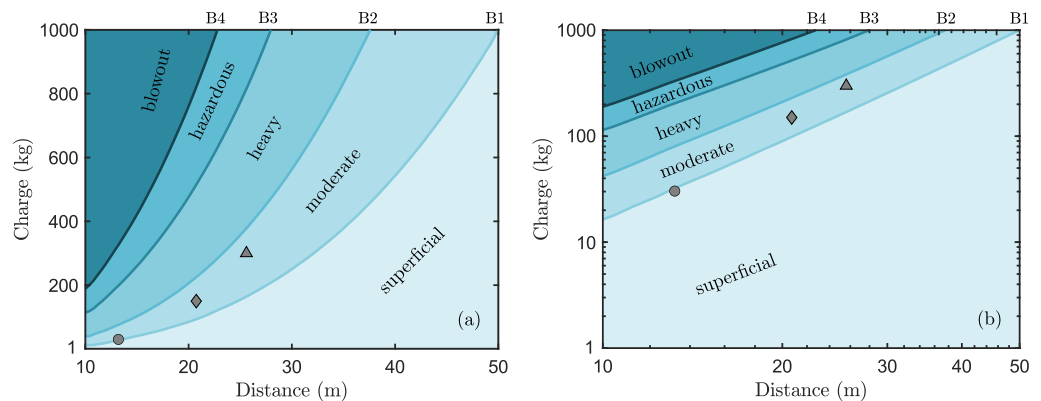


Figure 13. CW–S linear (a) and log-log (b) damage diagrams for reflected blast load on the façade of the first floor (Level 1): Case 1 (○), Case 2 (◇), Case 3 (△).

As can be seen, the CW–S damage diagrams shown in Figure 13 include three points corresponding to the three cases considered in Table 4. As the three scaled distances are almost equal, then the damage levels are also very similar, although differences in real distances and incidence angles make them grow from superficial-moderate (B1) to (almost) moderate-heavy (B2) for increasing charge weights and standoff distances. According to the PDC-TR 06-08 [15], a superficial damage level implies “no visible permanent damage”, whereas a moderate damage level implies “some permanent deflection” that generally can be repaired. By way of contrast, a heavy damage is associated with “significant permanent deflections” that cause the component to be unreparable.

To summarize the results obtained in the different case studies, Table 5 reports the incident blast load parameters and the corresponding component damage indicators per floor for Cases 1, 2, and 3. The reference case (Level 1, Case 2) and the worst-case scenario (Level 2, Case 3) are both highlighted for clarity. As can be seen, damage levels are significantly higher in the upper floor (Level 2) as a result of the lowest rigidity imposed by the cantilever boundary condition at the roof top, resulting in heavy damage levels for cases 2 and 3.

3.4. Crater, Fragments, and Damage to People

Figure 4 presents an estimation of the crater generated in the reference case on a sandstone soil, with an approximated radius of 1.6 m. For surface bursts, HOB = 0 m, as the one considered here, the equivalent charge radius is irrelevant, as it is only used to determine the dimensionless height of burst, which is identically zero in our example. The figure also shows that, for above-surface bursts, HOB > 0 m, the crater radius is significantly smaller for the same amount of explosive due to the air cushion that exists between the load and the ground, which reduces to a great extent the pressure that reaches the ground surface [6].

Figure 5 shows the interface of the fragment assistant using the input data of the reference case. For the application of Mott’s statistical theory for fragmentation of steel cylindrical shells [3,26–28], the explosive charge is approximated to a cylinder of approximately 50 cm diameter surrounded by a steel fragmentation shell with a mass of the order of about 13% of the charge and a thickness of 2 mm.

Table 5. Incident load parameters and component damage indicators per floor. According to the PDC-TR-06-08 [15], the response limits for hot rolled structural steel can be defined in terms of the ductility ratio, μ , and support rotation angle, θ , as follows: B1—superficial $\{\mu, \theta\} = \{1, -\}$; B2—moderate $\{\mu, \theta\} = \{3, 3^\circ\}$; B3—heavy $\{\mu, \theta\} = \{12, 10^\circ\}$; B4—hazardous $\{\mu, \theta\} = \{25, 20^\circ\}$. The reference case and worst-case scenario are indicated in blue and gray, respectively.

Level	Type	Variables	Case 1	Case 2	Case 3
0	Incident load parameters	Δp (kPa)	168.30	182.50	186.80
		I/A (kPa · ms)	406.70	724.40	922.20
		d_{real} (m)	12.17	20.10	25.08
		δ_{real} (deg)	9.46	5.71	4.57
	Damage level indicators	μ (-)	1.60	3.26	4.40
		θ (deg)	0.19	0.39	0.53
1	Incident load parameters	Δp (kPa)	139.40	169.50	178.00
		I/A (kPa · ms)	349.90	688.10	893.00
		d_{real} (m)	13.20	20.74	25.60
		δ_{real} (deg)	24.62	15.38	12.41
	Damage level indicators	μ (-)	0.90	1.64	2.10
		θ (deg)	0.08	0.15	0.19
2	Incident load parameters	Δp (kPa)	110.20	152.00	165.40
		I/A (kPa · ms)	293.00	630.50	845.50
		d_{real} (m)	14.71	21.73	26.41
		δ_{real} (deg)	35.31	23.03	18.78
	Damage level indicators	μ (-)	1.67	5.85	9.26
		θ (deg)	0.87	3.05	4.83

Finally, Figure 8 shows the calculating assistant for estimating damage to people in the reference case. As an illustrative example, the figure presents the results of lethality due to different types of injuries at a distance of 20 m from the origin of the explosion, assuming the worst-case scenario of an average person located close to the façade of the building being attacked. In the pressure-impulse graphs, representative distances are indicated using red dots plotted along the characteristic overpressure-impulse-distance curve [60]. As can be seen, at 20 m standoff distance, lethality due to lung damage or whole-body projection is negligible, but large primary fragments (e.g., CL 99%) may still produce secondary injuries with fatal results, as indicated by Figure 5.

4. Conclusions

SimEx is a computational tool that allows a rapid and easy estimation of the effects of explosions on structural elements and their damage to people. It has been developed in accordance with the specifications of American standard UFC-3-340-02 and other widely accepted directives published in the open literature. It provides assistants for the calculation of the blast-wave load; SDOF dynamic response, including the calculation of the equivalent structural properties of standardized metal and reinforced concrete beams; thermodynamic properties of explosive mixtures; crater formation; projection of primary fragments; and damage to people.

After presenting the main calculating assistants, a preliminary study has been presented to illustrate the full capabilities of SimEx in the assessment of the ability of a building to resist a given explosive charge. The analysis enables the determination of component damage levels for the main structural components, and a further study of the reference case has led to the computation of CW-S damage diagrams for a pillar of the first floor. These diagrams are very useful to provide design guidelines for those facilities that must be protected against explosive threats.

Although still under development, SimEx is being successfully used for research and teaching activities at the Spanish University Center of the Civil Guard. Due to its

advanced stage of maturation, it could also be used in other areas within the Army and Law enforcement Agencies involved in the fight against terrorism and the design of blast resistant buildings and structures.

Author Contributions: Conceptualization, J.S.-M. and M.V.; methodology, J.S.-M. and M.V.; software, J.S.-M. and A.C.; validation, all authors; formal analysis, J.S.-M. and M.V.; investigation, all authors; resources, C.H. and M.V.; data curation, J.S.-M. and A.C.; writing—original draft preparation, J.S.-M., A.C. and M.V.; writing—review and editing, C.H. and M.V.; visualization, J.S.-M. and A.C.; supervision, C.H. and M.V.; project administration, M.V.; funding acquisition, C.H. and M.V. All authors have read and agreed to the published version of the manuscript.

Funding: This research was partially funded by UE (H2020-SEC-2016-2017-1) Grant No. SEC-08/11/12-FCT-2016 and by project H2SAFE-CM-UC3M awarded by the Spanish Comunidad de Madrid. The authors would like to thank Henar Miguelez from University Carlos III of Madrid and Col. Fernando Moure from the University Center of the Civil Guard for their continuous support, as well as Com. Miguel Ángel Albeniz from the SEDEX-NRBQ (EOD-CBRN) service of the Civil Guard for many enlightening discussions. Fruitful discussions with Dr. Lina López from the School of Mines at Technical University of Madrid are also gratefully acknowledged.

Institutional Review Board Statement: Not applicable.

Informed Consent Statement: Not applicable.

Acknowledgments: The authors would like to thank Henar Miguelez from University Carlos III of Madrid and Col. Fernando Moure from the University Center of the Civil Guard for their continuous support, as well as Com. Miguel Ángel Albeniz from the SEDEX-NRBQ (EOD-CBRN) service of the Civil Guard for many enlightening discussions. Fruitful discussions with Lina López from the School of Mines at Technical University of Madrid are also gratefully acknowledged.

Conflicts of Interest: The authors declare no conflict of interest. The funders had no role in the design of the study; in the collection, analyses, or interpretation of data; in the writing of the manuscript, or in the decision to publish the results.

SimEx License & Distribution: SimEx is a closed-source proprietary software that may be licensed by the copyright holders, UC3M & Guardia Civil, under specific conditions. Please contact the corresponding author for further information.

Abbreviations

The following abbreviations are used in this manuscript:

BKW	Becker–Kistiakowsky–Wilson EoS
CL	Confidence Level
CT	Combustion Toolbox
CUGC	Centro Universitario de la Guardia Civil
CW-S	Charge Weight–Standoff
EoS	Equation of State
GUI	Graphical User Interface
H9	Heuzé EoS
HOB	Height of Burst
IED	Improvised Explosive Device
ISA	International Standard Atmosphere
LOP	Level of Protection
PDC	Protective Design Center
SDOF	Single Degree of Freedom
SEDEX-NRBQ	Explosive Ordnance Disposal (EOD) and CBRN Defense Service
UC3M	University Carlos III of Madrid
UFC	Unified Facilities Criteria
US	United States
USACE	United States Army Corps of Engineers

References

- Kinney, G.F.; Graham, K.J. *Explosive Shocks in Air*, 2nd ed.; Springer: New York, NY, USA, 1985.
- Brode, H.L. Numerical solutions of spherical blast waves. *J. Appl. Phys.* **1955**, *26*, 766–775. [CrossRef]
- Grady, D. *Fragmentation of Ring and Shells, the Legacy of N.F. Mott*; Springer: Berlin/Heidelberg, Germany, 2006.
- Ambrosini, R.D.; Luccioni, B.M. Craters produced by explosions on the soil surface. *J. Appl. Mec.* **2006**, *73*, 890–900. [CrossRef]
- Akhavan, J. *The Chemistry of Explosives*, 3rd ed.; Royal Society of Chemistry: Cambridge, UK, 2011.
- Cooper, P.W. *Explosives Engineering*; Wiley-VCH, Inc.: New York, NY, USA, 1996.
- Meyer, R.; Köhler, J.; Homburg, A. *Explosives*, 6th ed.; Wiley-VCH Verlag GmbH: Weinheim, Germany, 2007.
- Ngo, T.; Mendis, P.; Gupta, A.; Ramsay, J. Blast loading and blast effects on structures—An overview. *Electron. J. Struct. Eng.* **2007**, *1*, 76–91. [CrossRef]
- TNO Green Book Methods for the Determination of Possible Damage to People and Objects Resulting from Releases of Hazardous Materials (CPR 16E); CIP-data of the Royal Library: The Hage, The Netherlands, 1992.
- START. National Consortium for the Study of Terrorism and Responses to Terrorism. Global Terror-Isms Database. 2017. Available online: <https://www.start.umd.edu/gtd> (accessed on 3 September 2022).
- US Department of Homeland Security (DHS). *Reference Manual to Mitigate Potential Terrorist Attacks Against Buildings*, 2nd ed.; Federal Emergency Management Agency: Washington, DC, USA, 2011.
- Luccioni, B.; Ambrosini, D.; Danesi, R. Blast load assessment using hydrocodes. *Eng. Struct.* **2006**, *28*, 1736–1744. [CrossRef]
- Anderson, C.E., Jr. An overview of the theory of hydrocodes. *Int. J. Impact Eng.* **1987**, *5*, 33–59. [CrossRef]
- Han, Y.; Liu, H. Finite element simulation of medium-range blast loading using LS-DYNA. *Shock Vib.* **2015**, *2015*, 631493. [CrossRef]
- Protective Design Center Technical Report PDC-TR 06-08; Single Degree of Freedom Structural Response Limits for Antiterrorism Design. US Army Corps of Engineers: Washington, DC, USA, 2008.
- Unified Facilities Criteria (UFC) 3-340-02; Structures to Resist the Effects of Accidental Explosions. US Department of Defense: Washington, DC, USA, 2008.
- Baker, W.E. *Explosions in Air*; University of Texas Press: Austin, TX, USA, 1973.
- Kingery, C.N.; Bulmash, G. *Airblast Parameters from TNT Spherical Air Burst and Hemispherical Surface Burst*; US Technical Report ARBRL-TR-02555; Aberdeen Proving Ground, Ballistic Research Laboratories (BRL): Aberdeen, MD, USA, 1984.
- Needham, C.E. *Blast Waves*; Springer: Berlin/Heidelberg, Germany, 2010.
- Protective Design Center Software, US Army Corps of Engineers. Available online: <https://www.nwo.usace.army.mil/About/Centers-of-Expertise/Protective-Design-Center/PDC-Software> (accessed on 3 September 2022).
- Sánchez-Monreal, J.; Vera, M. SimEx: SIMulador de EXPlosiones mediante sistemas SDOF. In Proceedings of the III National Congress of R&D in Defense and Security (DESEi+d 2015), Naval Military School of Marín, Pontevedra, Spain, 19–20 November 2015; pp. 993–1000.
- Sánchez-Monreal, J.; Vera, M. SIMulador de EXPlosiones mediante sistemas SDOF (SimEx): Desarrollo de la aplicación y nuevas funcionalidades. In Proceedings of the IV National Congress of R&D in Defense and Security (DESEi+d 2016), University Defense Center, General Air Academy, San Javier, Spain, 16–18 November 2016; pp. 949–955. Available online: https://www.tecnologiaeinnovacion.defensa.gob.es/.../Actas_DESEi+d2016_1.pdf (accessed on 3 September 2022).
- Sánchez-Monreal, J.; Vera, M. SimEx: Una herramienta para la evaluación rápida de los efectos de explosiones. *Bol. Obs. Tecnol. Def.* **2017**, *55*, 23–27. Available online: https://publicaciones.defensa.gob.es/.../bot_55.pdf (accessed on 3 September 2022).
- Cuadra, A.; Huete, C.; Vera, M. *Combustion Toolbox: A MATLAB-GUI Based Open-Source Tool for Solving Gaseous Combustion Problems (v0.9.7)*; Zenodo: Geneva, Switzerland, 2022.
- Ambrosini, R.D.; Luccioni, B.M.; Danesi, R.F.; Riera, J.D.; Rocha, M.M. Size of craters produced by explosive charges on or above the ground surface. *Shock Waves*, **2002**, *12*, 69–78. [CrossRef]
- Mott, N.F. *A Theory of Fragmentation of Shells and Bombs*; AC4613; Ministry of Supply: Great Britain, UK, 1943.
- Mott, N.F. *Fragmentation of H.E. Shells; A Theoretical Formula for the Distribution of Weights of Fragments*; AC3642; Ministry of Supply: Great Britain, UK, 1943.
- Mott, N.F. Fragmentation of shell cases. *Proc. R. Soc.* **1947**, *A189*, 300–308.
- Sánchez-Monreal, J.; Llamazares-Mendo, F.; Vera, M. Estimación de daños de explosiones sobre personas. In Proceedings of the V National Congress of R&D in Defense and Security (DESEi+d 2017), Toledo, Spain, 22–24 November 2017; pp. 1689–1697. Available online: https://publicaciones.defensa.gob.es/.../actas_v_congreso_id_2017.pdf (accessed on 3 September 2022).
- González Duperón, E.; Martínez Gil, M.; Giménez Francés, B.; González Ferradás, E. Analysis of effects of detonation of explosive substances on humans from characteristic curves explosive mass-distance from the origin of the explosion. *Process. Saf. Prog.* **2016**, *35*, 233–240. [CrossRef]
- Protective Design Center Technical Report PDC TR 06-01; Rev 1, Methodology manual for the Single-Degree-of-Freedom Blast Effects Design Spreadsheets (SBEDS). US Army Corps of Engineers: Washington, DC, USA, 2008.
- Biggs, J.M. *Introduction to Structural Dynamics*; McGraw-Hill College: New York, NY, USA, 1964.
- Brode, H.L. Blast wave from a spherical charge. *Phys. Fluids* **1959**, *2*, 217–229. [CrossRef]
- Needham, C.E.; Crepeau, J.E. *The DNA Nuclear Blast Standard (1 kT)*; Report No. DNA 5648-T; Systems, Science and Software, Inc.: Alburquerque, Spain, 1981.

35. Hopkinson, B. *British Ordnance Board Minutes 13565*; The National Archives: Richmond, UK, 1915.
36. Sachs, R.G. *The Dependence of Blast on Ambient Pressure and Temperature*; Technical Report 466; Ballistic Research Laboratories: Aberdeen, MD, USA, 1944.
37. *ISO 2533:1975*; Standard Atmosphere. International Organization for Standardization: Geneva, Switzerland, 1975.
38. Gallo, E. Quasi static atmospheric model for aircraft trajectory prediction and flight simulation. *arXiv* **2021**, arXiv:2101.10744.
39. *International Ammunition Technical Guideline (IATG) 01.80 Formulae for Ammunition Management*; UNODA Office for Disarmament Affairs: New York, NY, USA, 2013.
40. Friedlander, F.G. The diffraction of sound pulses I. Diffraction by a semi-infinite plane. *Proc. R. Soc. London Ser. Math. Phys. Sci.* **1946**, *186*, 322–344.
41. *Euronorm 53–62*; European Wide Flange Beams. CEN: Brussels, Belgium, 1993.
42. *Norma UNE 31-002-94*; Cálculo de las Principales Características Teóricas de los Explosivos. Asociación Española de Normalización UNE: Biddeford, Maine, 1994.
43. *European Standard EN 13631-15*; Explosives for Civil Use—High Explosives—Part 15: Calculation of the Thermodynamic Properties. UNE: Biddeford, Maine, 2005.
44. Arnold, W.; Rottenkolber, E.; Hartmann, T. DRAGON—The German Thermo-Chemical Code Based on the Becker-Kistiakowsky-Wilson Equation of State. *Propellants Explos. Pyrotech.* **2022**, e202100329. [CrossRef]
45. Hobbs, M.L.; Baer, M.R. Nonideal thermoequilibrium calculations using a large product species data base. *Shock Waves* **1992**, *2*, 177–187. [CrossRef]
46. Mader, C.L. *Detonation Properties of Condensed Explosives Computed Using the Becker-Kistiakowsky-Wilson Equation of State*; Report LA-2900; Los Alamos Scientific Laboratory: Los Alamos, NM, USA, 1963.
47. Heuzé, O. Equations of state of detonation products: Influence of the repulsive intermolecular potential. *Phys. Rev. A* **1986**, *34*, 428–432. [CrossRef] [PubMed]
48. López, L.M. Evaluación de la Energía de los Explosivos Mediante Modelos Termodinámicos de Detonación. Ph.D. Thesis, Universidad Politécnica de Madrid, ETSI Minas, Madrid, Spain, 2003.
49. Sanchidrián, J.A.; López, L.M. Calculation of the energy of explosives with a partial reaction model. Comparison with cylinder test data. *Propellants Explos. Pyrotech.* **2006**, *31*, 24–32. [CrossRef]
50. Cuadra A.; Huete, C.; Vera M. Desarrollo de un código termoquímico para la evaluación de las propiedades teóricas de explosivos (CT-EXPLO) y la estimación del rendimiento de motores cohete (CT-ROCKET). In Proceedings of the IX National Congress of R&D in Defense and Security (DESEi+d 2022), Army's "General Morillo" Base, Pontevedra, Spain, 15–17 November 2022, *accepted*.
51. Kamlet, M.J.; Jacobs, S.J. Chemistry of detonations. I. A simple method for calculating detonation properties of CHNO explosives. *J. Chem. Phys.* **1968**, *48*, 23–55. [CrossRef]
52. Politzer, P.; Murray, J.S. Some perspectives on estimating detonation properties of C, H, N, O compounds. *Cent. Eur. J. Energetic Mater.* **2011**, *8*, 209–220.
53. Beveridge, A. *Forensic Investigation of Explosions*, 2nd ed.; CRC Press: Boca Raton, FL, USA; Taylor & Francis Group: Boca Raton, IL, USA, 2012.
54. Westine, P.S. Explosive cratering. *J. Terramechanics* **1970**, *7*, 9–19. [CrossRef]
55. Baker, W.E.; Westine, P.S.; Dodge, F.T. *Similarity Methods in Engineering Dynamics: Theory and Practice of Scale Modeling*; Fundamental Studies in Engineering No. 12; Elsevier Science Limited: Amsterdam, The Netherlands, 1991.
56. Gurney, R.W. *The Initial Velocities of Fragments from Bombs, Shells and Grenades*; Report No 405; Aberdeen Proving Ground, Ballistic Research Laboratories (BRL): Aberdeen, MD, USA, 1943.
57. Carter, R.T.; Jandir, P.S.; Kress, M.E. Estimating the drag coefficients of meteorites for all Mach number regimes. In Proceedings of the 40th Lunar and Planetary Science Conference, (Lunar and Planetary Science XL), The Wood-Lands, TX, USA, 23–27 March 2009.
58. Häring, I. Damage Analysis I: Probit Functions and Probability Distributions. In *Risk Analysis and Management: Engineering Resilience*; Springer: Singapore, 2015; pp. 187–204.
59. Finney, D.J. *Probit Analysis*, 3rd ed.; Cambridge University Press: Cambridge, UK, 1971.
60. Alonso, F.D.; Ferradás, E.G.; Pérez, J.F.S.; Aznar, A.M.; Gimeno, J.R.; Alonso, J.M. Characteristic overpressure–impulse–distance curves for the detonation of explosives, pyrotechnics or unstable substances. *J. Loss Prev. Process. Ind.* **2006**, *19*, 724–728. [CrossRef]

Article

Numerical Analysis of Blast Effects and Mitigation in the Far-Field from Small Explosions

Adam G. Taylor 

Lawrence Livermore National Laboratory, Computational Engineering Division, Livermore, CA 94550, USA;
taylor265@llnl.gov

Abstract: Requirements for explosive safety are often given in terms of a “K-Factor”, correlating incident blast effects with the distance and TNT equivalent weight of an explosion. Traditionally, this is conducted using empirical correlations to experimental measurements (e.g., the Kingery–Bulmash equations). In the far-field, empirical verification of incident overpressure and impulse magnitudes can be difficult; extrapolations from data give expected values at reasonable standoff distances that sometimes are too small to measure on available equipment but are larger than some regulations require. The present paper describes the results of numerical hydrocode analysis to verify the expected incident overpressure and impulse from small hemispherical ground charges of TNT at these relatively large distances. Furthermore, the dynamic effect of incident blast waves on lightweight, modular mitigation barriers is studied to gauge their effectiveness at providing safety standard compliance.

Keywords: blast effects; mitigation; hydrocode analysis

Citation: Taylor, A.G. Numerical Analysis of Blast Effects and Mitigation in the Far-Field from Small Explosions. *Appl. Sci.* **2022**, *12*, 8824. <https://doi.org/10.3390/app12178824>

Academic Editors: Ricardo Castedo, Lina M. López and Anastasio P. Santos

Received: 16 July 2022

Accepted: 29 August 2022

Published: 2 September 2022

Publisher’s Note: MDPI stays neutral with regard to jurisdictional claims in published maps and institutional affiliations.



Copyright: © 2022 by the author. Licensee MDPI, Basel, Switzerland. This article is an open access article distributed under the terms and conditions of the Creative Commons Attribution (CC BY) license (<https://creativecommons.org/licenses/by/4.0/>).

1. Introduction

Understanding the structure of blast waves and the dynamics of their interactions with structures is key for mitigation and safety. The formation and propagation of these shock waves is a highly nonlinear dynamic process; thus, prediction of the incident waveforms and their corresponding blast overpressure and impulsive loads for a given scenario can be difficult. It is common for various government, military, and scientific institutions to prescribe criterion for safety from blast effects in terms of “K factors”:

$$K = R/W^{1/3} \quad (1)$$

Here, R is the distance from the explosive source and W is the net explosive (TNT equivalent) weight. Allowable exposure for personnel, nearby structures, and withdrawal distances can be given in terms of these K factors, which have been empirically correlated to values of incident overpressure and impulse. A figure regularly encountered in explosive safety documentation is the K328 criterion, often referred to as the “Public Withdrawal Distance”; calculated using units of $\text{ft}/\text{lb}^{1/3}$ this corresponds to a peak incident overpressure of 0.0655 psi, (0.4516 kPa) and is said to be a condition under which there is no probability of harm. Different safety guidelines have different requirements for personnel, but they are very commonly given in terms of these K factors.

The empirical nexus of K factor correlation appears to be the work of Kingery [1,2]. The original data came from quite large (5, 20, 100, and 500 ton) hemispherical TNT events. Instrumentation at various distances measured arrival time, peak overpressure, and the duration of the positive pressure phase and the positive impulse. This same data set was later reinterpreted and extrapolated to include reflected pressures/impulse and shock velocities by Kingery and Bulmash [3]. It is these fits which became the basis for more widespread application, and thus the empirical equations are often referred to as Kingery–Bulmash (KB) curves. Swisdak [4] provides a good overview of this history, along with

improved equations fitting the same data. More recent fits by Jeon et al. [5] claim to further simplify the curves with the same accuracy.

There is definite uncertainty in the accuracy of the KB curves and other analytical and empirical tools for predicting blast overpressure in a given case. Karlos et al. [6–8] have investigated the structure of blast waves and their parameters for scaling and decay, including variations in explosive type, weight, and configuration on the resulting incident pulses. A recent review of analytical and empirical prediction methods by Ullah et al. [9] shows a very large spread in the predicted blast overpressures and wave structures from various accepted sources. Recent repeated blast measurements from Stewart et al. [10] show large variability in the measured results from what are ostensibly the same experiments. The recent experiment of Filice et al. [11] provides more data and KB comparisons and variances for relatively nearby (2–5 m) and relatively small (100–400 g) explosives. In a review of the experimental literature vs. KB predictions, Rigby et al. [12] state that the variation in experimental predictions is so large in nominally similar experiments that there is a valid question as to whether blast phenomena are inherently deterministic, or whether they should be viewed as fundamentally stochastic processes. Under this lens, KB and others may be viewed as useful only at predicting the order of magnitude of blast effects.

The question arises: can direct physics-based calculation of blast wave parameters provide more detailed and accurate predictions for a given case of interest?

The classical analytical result for the prediction of the evolution of a very strong explosion is the so-called Taylor–von Neumann–Sedov solution [13–16]. This applies only to spherical (1D) blasts and is derived under assumptions (point source, zero ambient pressure) that leave it applicable only for intermediate distances. Some of the earliest published attempts to simulate explosions under real conditions (i.e., into non-zero ambient pressure conditions) were performed by Brode [17,18] and Goldstine and von Neumann [19].

More recently there have been various simulations performed in modern software packages aimed at the prediction of the evolution of blast waves. Ding et al. [20,21] recently presented the results of numerical simulations of very large TNT equivalent blasts and their resulting effects on near and far-field structures. Xue et al. [22] modeled the whole process of explosive shockwave formation and propagation from relatively smaller blasts over larger distances. Sung and Chong have produced a fast-running semi-empirical method for the prediction of blast effects behind shielding barriers; this work includes uncertainty estimations when using KB-type charts [23]. Giodo et al. compared empirical and numerical approaches to investigating the effects of free far-field blasts on masonry wall [24]. Vannucci et al. [25] provide analysis of a blast and shock propagation inside a monumental structure. Draganic and Varevac [26] have provided a useful parametric study on the effects of numerical mesh size on the blast wave parameters.

It is easy to imagine situations (involving explosive training, demolitions, etc.) where relatively small explosions (comparable to 1 kg TNT) send overpressure waves towards personnel relatively far away (30–40 m). These blasts are very small compared to the conditions studied in the published literature or in the data informing KB-type predictions, but nevertheless may induce pressures and impulses in excess of safety guidelines (e.g., the Public Withdrawal Distance). Furthermore, the incident overpressure will be far below the ambient atmospheric pressures and will be difficult or impossible to accurately measure using easily available pressure gauges. Given that there are reasons to question the accuracy of KB-type predictions under these circumstances, research is needed to clarify the situation.

The purpose of this paper is to use numerical tools to investigate cases where very small charges produce relatively small incident overpressure at large distances which still exceed the safety guidelines of public withdrawal distance. The goals here are two-fold:

1. to predict the structure and magnitude of the incident pressure waves in these cases and to compare to the available empirical blast curves;
2. to investigate the efficacy of lightweight, modular barriers at mitigating incident overpressure waves to the desired levels.

Towards the first goal, free-field explosions of small hemispherical ground TNT charges into air are simulated out to a range of 40 m. Wave profiles obtained from the free-field simulations are subsequently employed as boundary conditions for dynamic wave-structure interaction models which investigate the second goal.

It is noted that a few different sets of units were used in the preparation of this work. Much of the original work conducted in blast load estimation was conducted in English units (ft/lb/ms/psi) (see for example the original Kingery report [1]). For that reason, explosive range operators and field experts tend to think in terms of these units, and regulations often give quantities such as *K* factors in these units. On the other hand, ALE3D hydrocode analyses are traditionally conducted in a special set of units (cm/g/μs/Mbar). The simulations described herein follow in this tradition. For the sake of consistency, all units in this paper will be given in terms of SI units (m/kg/ms/kPa). In some cases, English units will be listed concurrently.

2. Materials and Methods

Simulations presented in this work were performed in ALE3D, a multi-physics software package which utilizes an Arbitrary Lagrangian/Eulerian (ALE) numerical scheme [27]. The numerical simulations performed are of two types: (i) free-field explosions of various weights of TNT in air at atmospheric pressure, and (ii) the dynamic interaction of incident blast waves with simple mitigation barriers. The remainder of this section will describe the material models implemented, and provide further details into the setup of each type of simulation.

2.1. Material Models

Three material models were employed for the three separate material components simulated in this work, namely the TNT explosive, the surrounding air, and the Lexan structural barrier. Only the TNT and air appear in the free-field simulations, and only the air and Lexan appear in the blast mitigation simulations. For the explosive TNT, a simple Jones–Wilkins–Lee (JWL) equation of state [28] is used:

$$P(v, e) = A \left(1 - \frac{\omega}{R_1 v} \right) \exp(-R_1 v) + B \left(1 - \frac{\omega}{R_2 v} \right) \exp(-R_2 v) + \frac{\omega}{v} e \quad (2)$$

Here, *P* is the pressure, $v = V/V_0 = \rho_0/\rho$ the relative volume, and *e* is the material energy per reference volume. *V*, ρ are the volume and density, respectively, while V_0, ρ_0 are the initial (reference) values of these properties. The parameter ω is the Grüneisen coefficient; *A*, *B*, R_1 , and R_2 are free parameters. ω, R_1 and R_2 are dimensionless, while *A* and *B* have units of pressure. The parameter values used in simulations for Equation (2) are given in Table 1.

Table 1. JWL parameters for TNT.

<i>A</i> (kPa)	<i>B</i> (kPa)	R_1	R_2	ρ_0 (g/cm ³)	ω
3.712×10^8	3.231×10^6	4.150	0.950	1.630	0.30

The equation of state of air is given by a simple Gamma-law:

$$P(\rho, e) = (\gamma - 1) \frac{\rho}{\rho_0} e \quad (3)$$

The only free parameter γ is dimensionless and typically has a value of 1.4 for air. The initial (atmospheric) pressure P_0 is obtained through Equation (3) by prescribing an initial energy per unit volume:

$$e_0 = \frac{P_0}{\gamma - 1}$$

The parameter values used in simulations for Equation (3) are given in Table 2.

Table 2. Gamma law parameters for air.

γ	ρ_0 (g/cm ³)	P_0 (kPa)
1.40	1.225×10^{-3}	1.0135×10^2

The Lexan mitigation barrier is modeled using a power law constitutive model:

$$\sigma = k(\epsilon_0 + \epsilon)^{y_c}, \tag{4}$$

$$\epsilon_0 = \left(\frac{E}{k}\right)^{\frac{1}{y_c-1}} \tag{5}$$

Here, σ is the current yield stress and ϵ an equivalent plastic strain. ϵ_0 is an initial yield strain determined by parameters k, E and y_c . E is a standard Young’s modulus with dimensions of pressure, k the yield stress coefficient with dimensions of pressure, and y_c is a dimensionless strain-hardening coefficient. An additional equation of state relates pressure P to the bulk modulus K and the relative volume v :

$$P = K\mu \tag{6}$$

Here, $\mu = (1/v) - 1$, and the bulk modulus is derived from the Young’s modulus and Poisson ratio ν :

$$K = \frac{E}{3(1 - 2\nu)}$$

The values used for Lexan in the present work are given in Table 3. Given the nature of the low pressure incident waves studied in this paper, only small (elastic) deformations of the barrier are expected. Therefore the values used for the barrier material are not expected to have significant effect on the analysis results.

Table 3. Power law parameters for Lexan.

E (kPa)	k (kPa)	ν	ρ_0 (g/cm ³)	y_c
2.344×10^6	1.119×10^5	0.4	1.218	2.086×10^{-1}

2.2. Free-Field Detonation of TNT

The free-field detonation of hemispherical TNT was simulated under 2D axisymmetric conditions. Figure 1 depicts a cartoon of the setup. The $x = 0$ axis is the axis of rotational symmetry, while the $y = 0$ has symmetry boundary conditions which are used to crudely approximate the ground; however, this approximation causes the simulation to be equivalent to a spherical charge of the same radius exploding in air. The air domain extends from the origin to 40 m in the x and y directions. The outer boundaries have three different boundary conditions applied; “pressure continuous” provides ghost nodes external to the boundary which keeps the pressure constant on the other side, which keeps the initially pressurized gas from expanding and depressurizing as soon as the simulation starts. “Non-reflecting” boundary conditions dampen out any reflected incident waves to minimize boundary effects. The “outflow” condition allows material given outbound velocity to leave the domain.

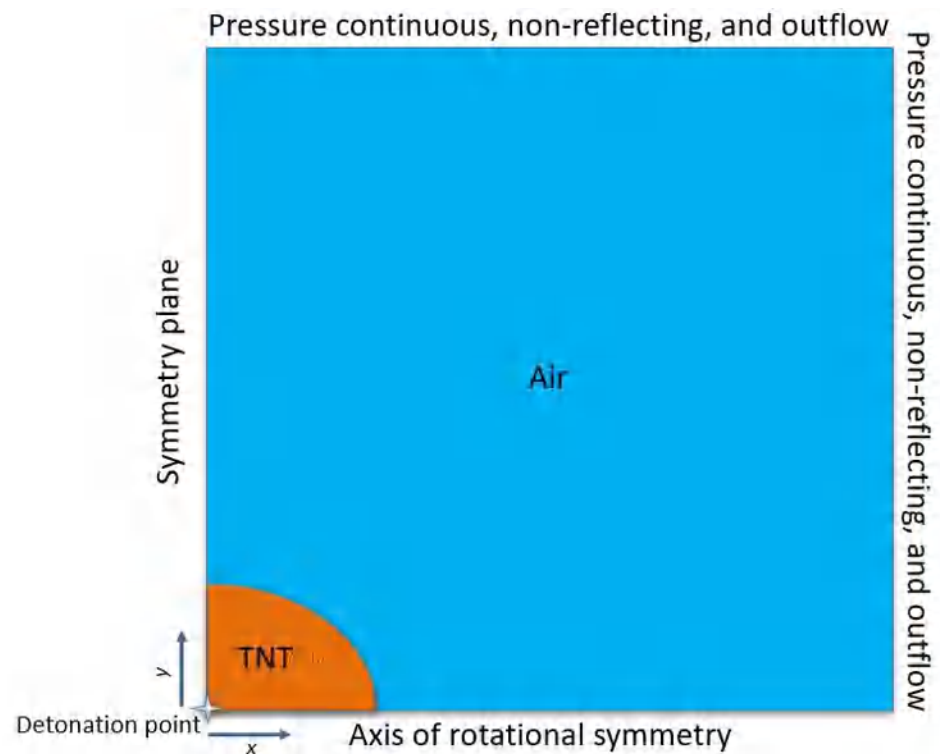


Figure 1. A “cartoon” depiction of the setup of the free-field TNT detonation simulations with materials and boundary conditions labeled (Not to scale).

Four simulations in total were performed with charges with radius 0.0261 m, 0.051 m, 0.0643 m, and 0.081 m, yielding hemispherical charge weights of approximately 0.06123 kg (0.135 lb), 0.45359 kg (1 lb), 0.90718 kg (2 lb), and 1.81436 kg (4 lb), respectively. Note that the charge radius is around 3 orders of magnitude smaller than the domain length; even in 2D, a uniform Cartesian mesh small enough to adequately resolve the TNT would lead to an intractably-large numbers of zones. Instead, a graded mesh approach was used, coarsening with distance from the origin. Initial zone sizes range from approximately 4.5×10^{-3} m at the center of the charge out to 5.4×10^{-2} m at the outer edge of the domain. The simulations ultimately contained around 7.1 million zones.

Figure 2 shows representative temporal snapshots of pressure in the system as the explosive wave propagates in air. The peak overpressure occurs near the wavefront but rapidly decreases to the ambient pressure and then dips below it for some time before returning. The magnitude of this peak pressure decreases as the wave propagates further from the source. Fixed (Eulerian) pressure tracers were placed every 2 m in the domain just off the y -axis in order to study the structure and evolution of the blast wave. Figure 3 shows the results of these pressure tracer time histories. Each tracer shows a pronounced positive overpressure phase followed by a negative phase where pressure dips below ambient. The effects of these negative pressure phases have been studied and are in general not negligible [29,30].

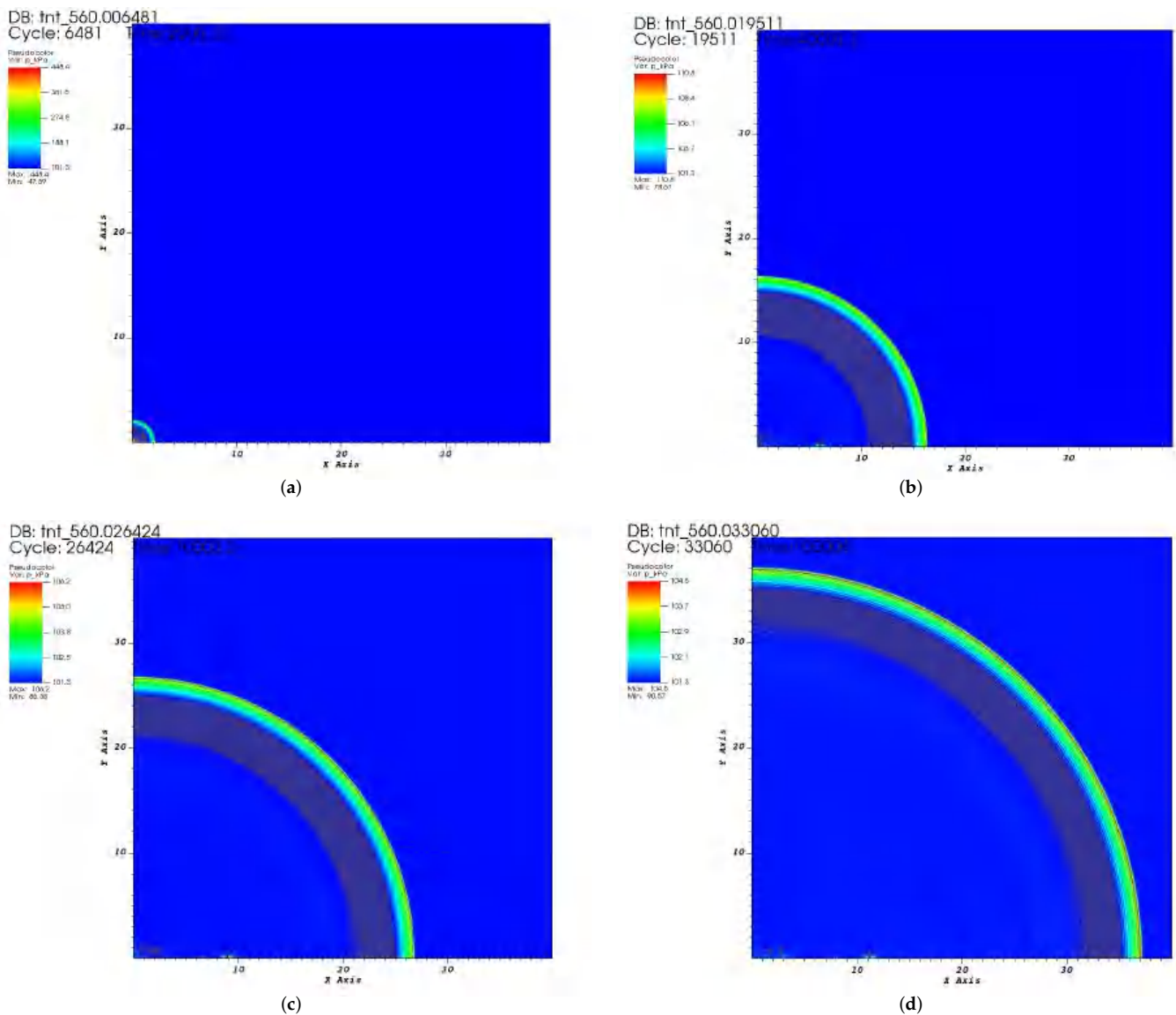
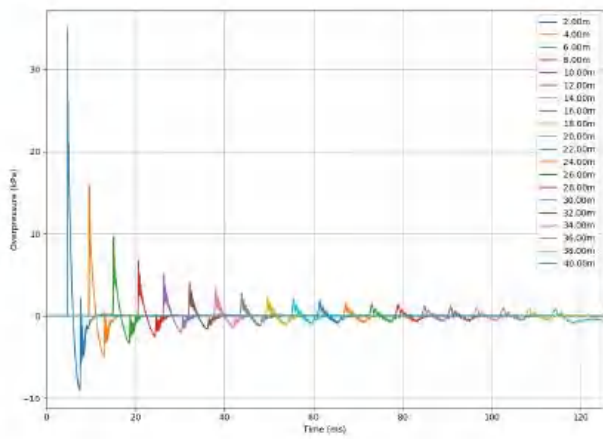
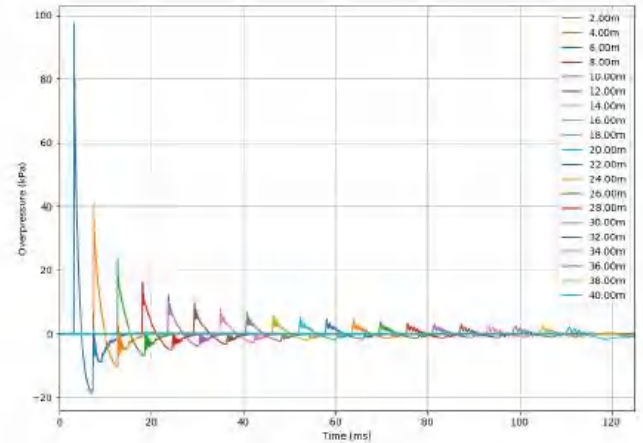


Figure 2. Snapshots of the pressure wave from the 0.90718 kg explosion of hemispherical TNT into air at atmospheric pressure (approximately 101.35 kPa): (a) 2 ms, (b) 40 ms, (c) 70 ms, and (d) 100 ms after programmed detonation.

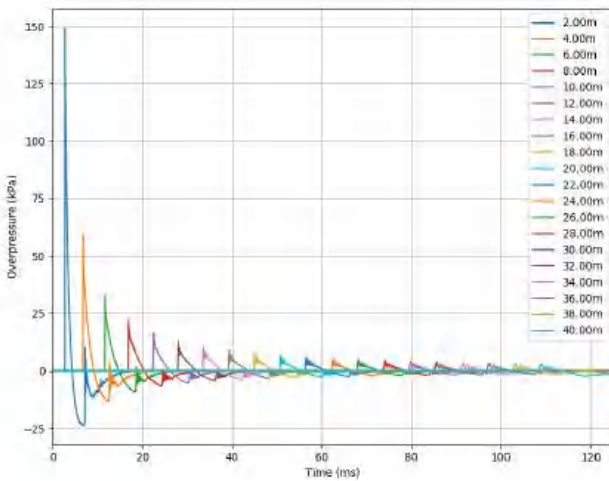
Figure 4 shows the pressure waves recorded at 36.576 m (120 ft) from the source. Note that when compared to some of the larger pressure, early time pressure waves on the left-hand side of the plots in Figure 3, these waves are relatively smooth and have a shallower initial slope as they ramp up to maximum incident overpressure. This corresponds to the fact that at this distance the waves are no longer proper shock waves. In fact, the wave velocity is approximately that of the speed of sound in air. The area under the positive portion of the overpressure wave is the total incident impulse at this point. As will be shown in the next section, pressure time histories of this type are useful in that they can be used as boundary conditions in subsequent simulations to study the dynamic effects of realistic incident waves on structures.



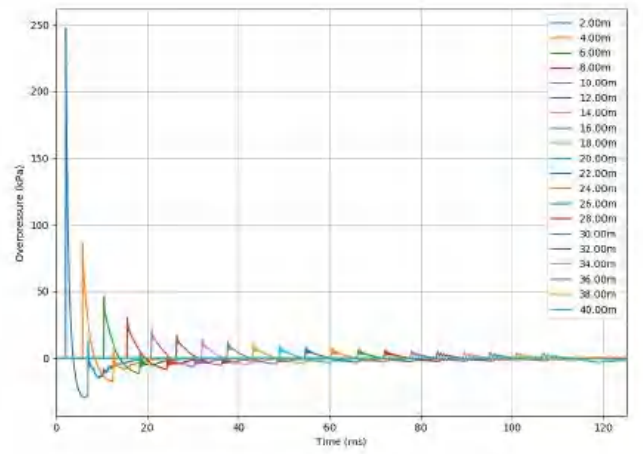
(a)



(b)

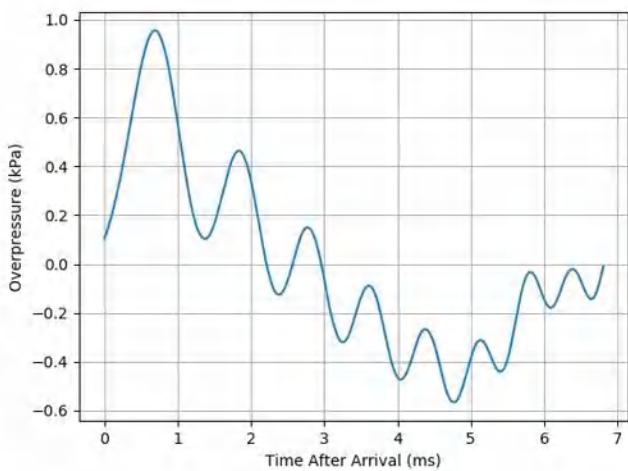


(c)

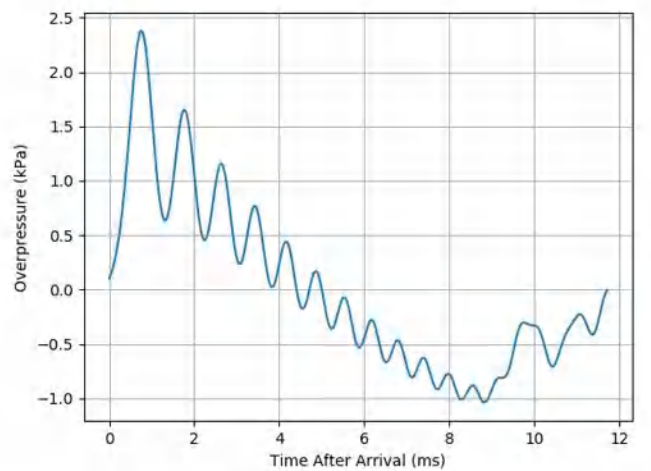


(d)

Figure 3. Pressure time histories from four simulations of hemispherical TNT detonation of different weights: (a) 0.06123 kg (0.135 lb), (b) 0.45359 kg (1 lb), (c) 0.90718 kg (2 lb), and (d) 1.81436 kg (4 lb).



(a)



(b)

Figure 4. Cont.

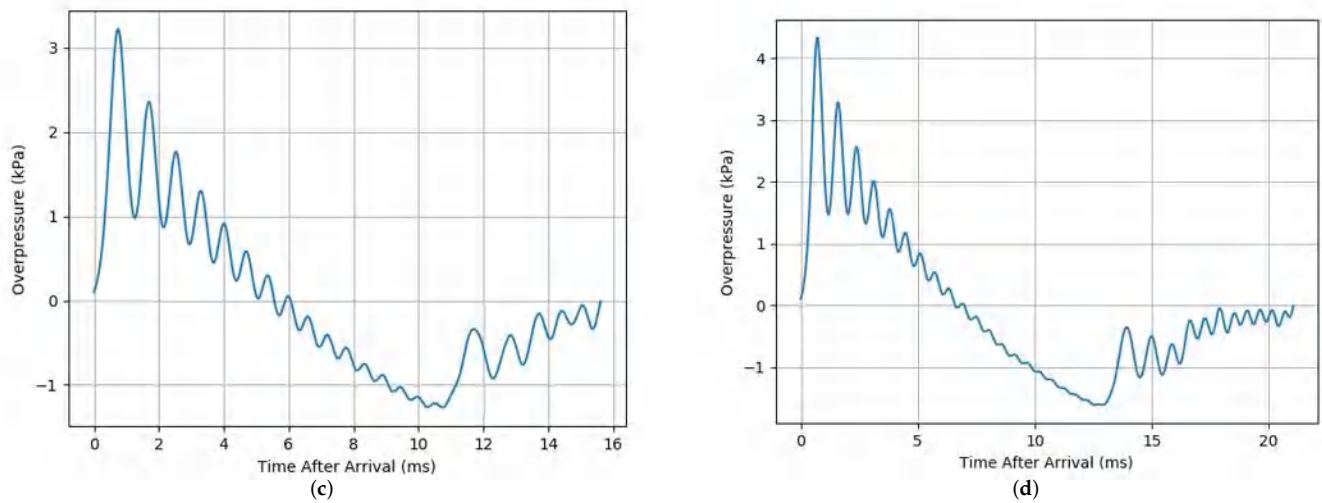


Figure 4. Pressure time histories from four simulations of hemispherical TNT detonation at 36.576 m (120 ft): (a) 0.06123 kg (0.135 lb), (b) 0.45359 kg (1 lb), (c) 0.90718 kg (2 lb), and (d) 1.81436 kg (4 lb).

Simulation of Detonation Cord

Further simulations were performed in order to study the variation of effects due to geometry. In particular 1.829 m of detonation cord suspended 1.524 m and parallel to the ground was detonated in a 4.5 m × 4 m × 3 m domain of air under atmospheric pressure (Figure 5). The cord is comprised of a 0.18 cm radius cylinder of TNT, so that ultimately 32.27 g is detonated. Pressure tracers are placed at regular distances from the center of the cord at a height of 1.524 m. Figure 5 shows snapshots of the resulting pressure waves in time.

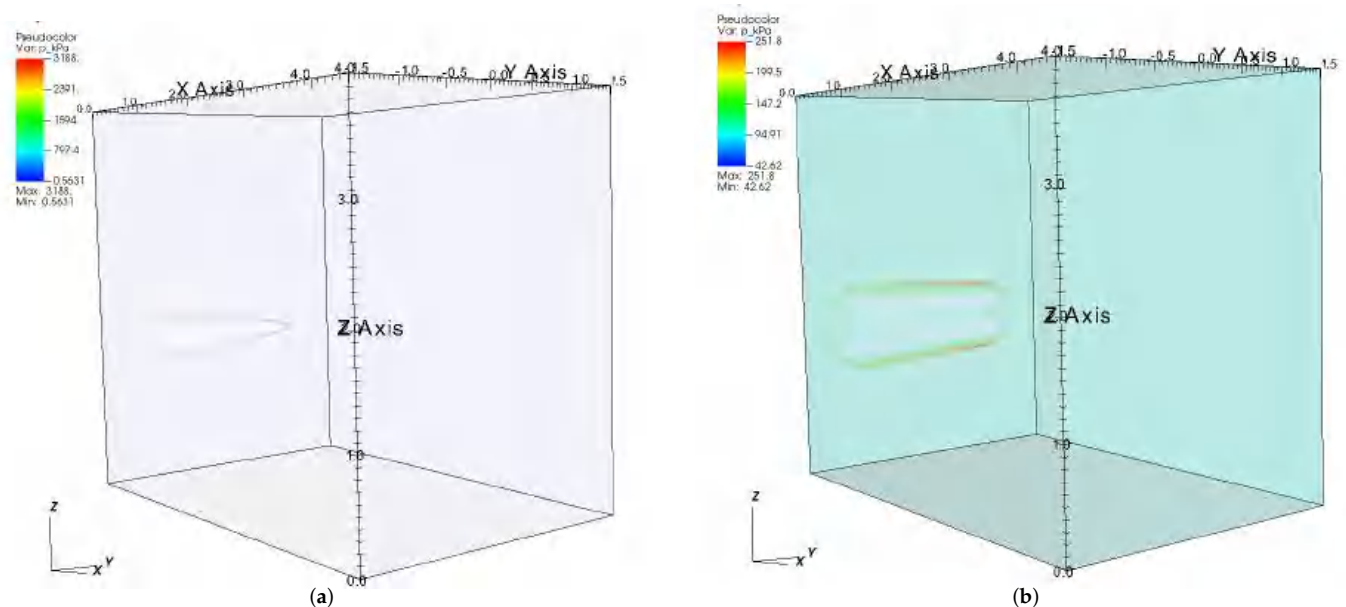


Figure 5. Cont.

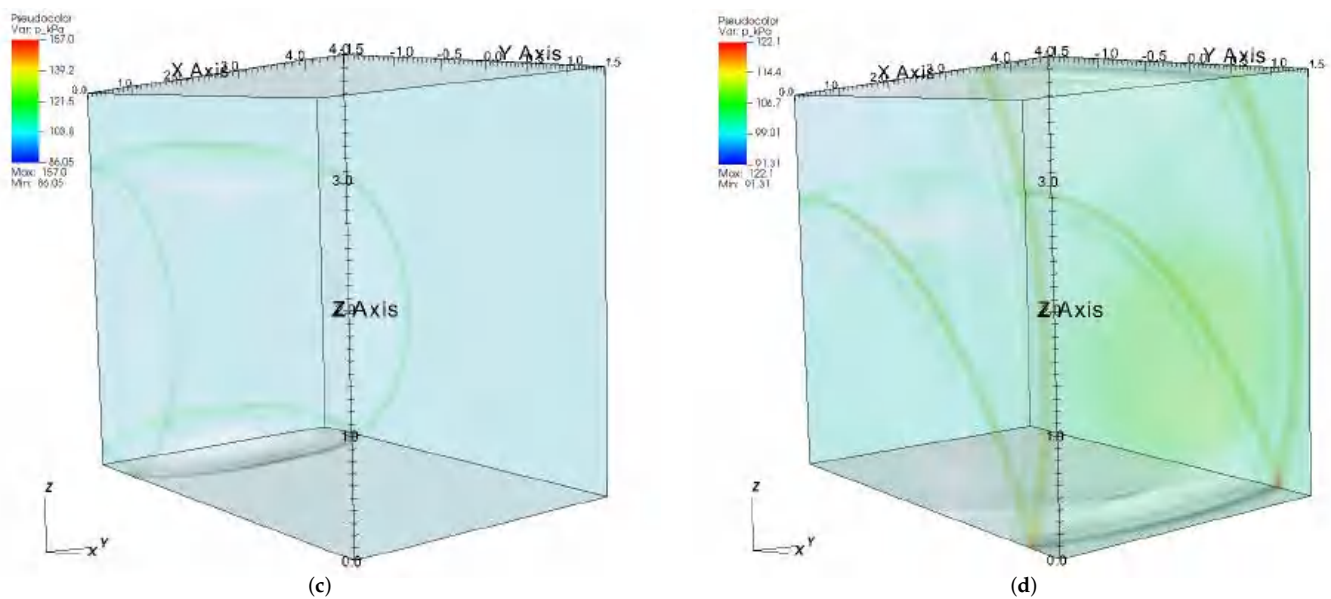


Figure 5. Snapshots of the pressure wave from explosion of a detonation cord (a) 0.27 ms, (b) 0.7 ms, (c) 4.6 ms, and (d) 12 ms after programmed detonation.

2.3. Blast-Barrier Interaction

Simulations of the interaction of incident overpressure waves and lightweight Lexan barriers were performed to gauge the effectiveness of simple modular structures to maintain “Public Withdrawal Distance” conditions where incident overpressures are already quite low. The 2D plane strain simulations were performed, given the assumption that multiple barriers could be placed alongside each other to minimize any edge effects. Further larger 3D cases of interest were explored to visualize and quantify the effects of lateral wraparound for standalone barriers.

Figure 6 presents a “cartoon” depiction of these simulations with labeled boundary conditions. Again the lower boundary is taken as a symmetry plane to estimate ground interactions as perfect reflections. The upper and outer boundaries have pressure continuous non-reflecting conditions. The $x = 0$ plane is given a pressure load curve corresponding to the pressure tracer time histories derived from the free-field blast simulations (Figure 4). It is assumed that in the far field the incident waves are planar. A problem arose in earlier simulations where reflections off of the barrier reached the $x = 0$ plane a re-reflected back into the problem domain before the relevant dynamic events could conclude, causing undesirable boundary effects. It was found that the non-reflecting boundary conditions did not coexist well with the pressure load curves and thus caused numerical issues with the incident pressure waves. To avoid these issues, the barrier was placed at a distance $d = \frac{1}{2}ct_{wave}$, where c is the speed of sound in air (approximately 343 m/s) and t_{wave} is the wavelength (in time) of the incident pressure wave, including positive and negative overpressure phases. Because the far-field waves are traveling at approximately the speed of sound, under these conditions the entire incident wave enters the domain before reflections can return to the boundary. Then, at time t_{wave} , the pressure load curve boundary conditions are replaced with pressure continuous, non-reflecting conditions which eliminate the problem of reflection. The 3D simulations were performed in half-symmetry, so that the $y = 0$ plane was a symmetry plane and the y_{max} also had pressure continuous and non-reflecting conditions.

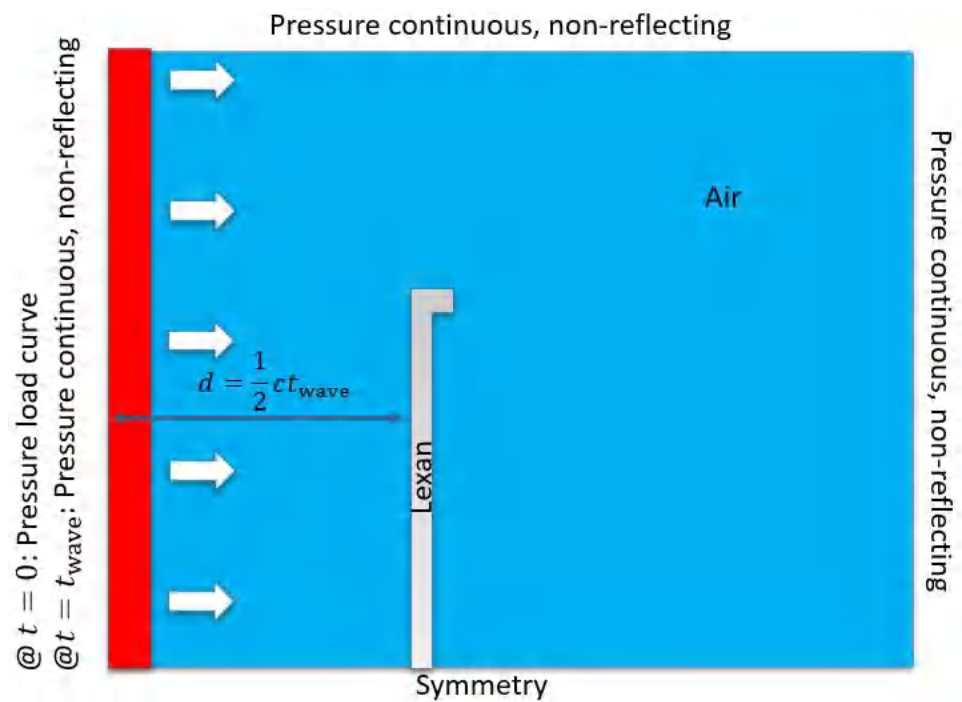


Figure 6. A “cartoon” depiction of the setup of the blast-structure interactions simulations with materials and boundary conditions labeled. (Not to scale)

Various simple designs of mitigation barriers were studied. These included three major types: single fairing, compound fairing, and deep-roof (Figure 7). The barriers are all 1.2 m wide, and 3.8 cm thick. The total height varies with the length and angle of the fairing, but the bases are approximately 2.2 m high.

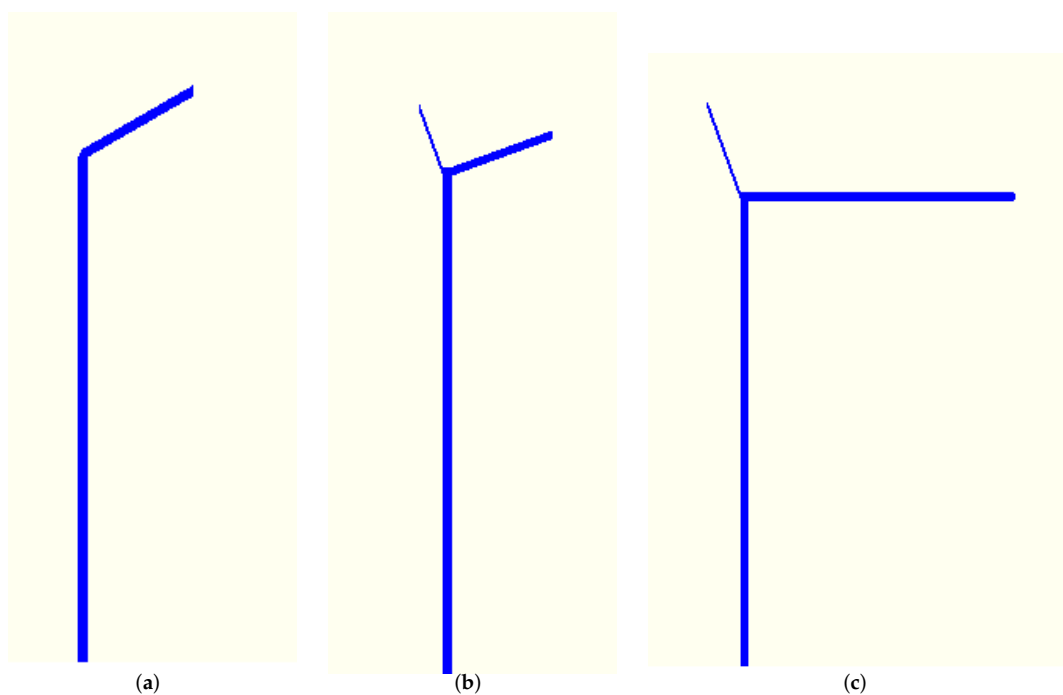


Figure 7. Representative cross-sections of the types of mitigation barriers studied: (a) Single-fairing barrier. (b) Compound-fairing barrier. (c) Barrier with deep roof.

All calculations utilized a graded mesh which was most refined in the area around the mitigation barrier. The 2D plane strain simulations ultimately contained around 1.2 million zones. The 3D simulations in general utilized a coarser mesh that was graded more aggressively, but still contained on the order of 10 million zones per simulation. Figures 8 and 9 show snapshots of the pressure fields in representative 2D and 3D simulations, respectively.

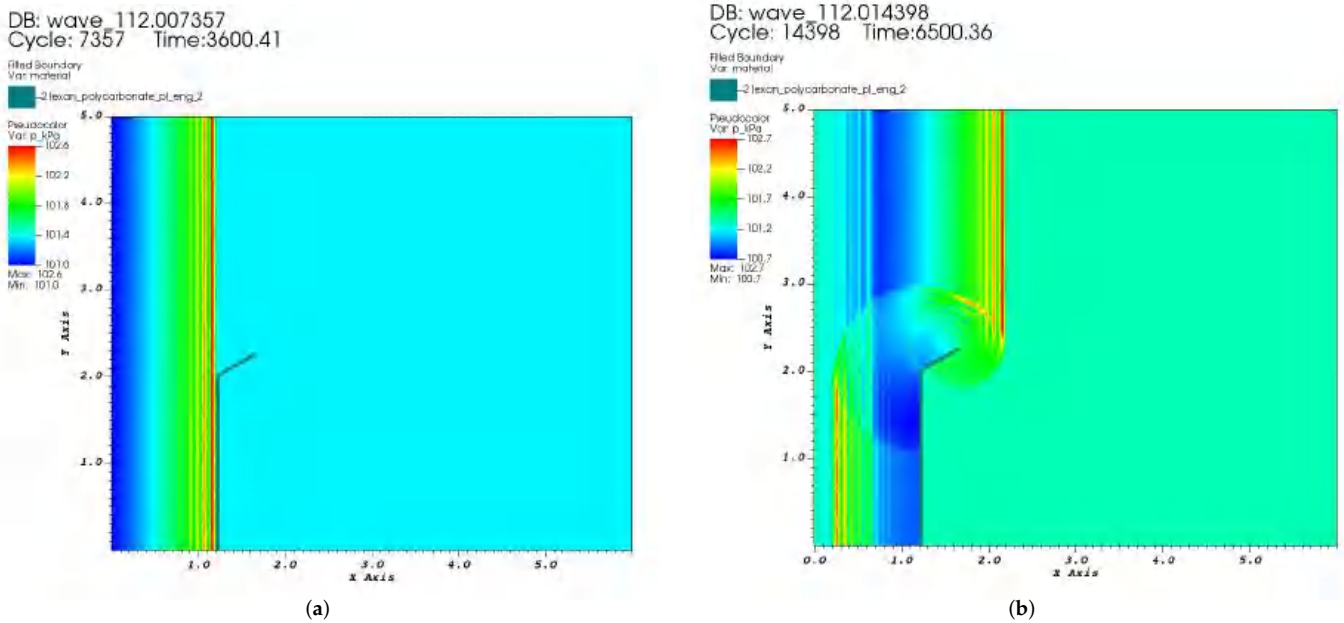


Figure 8. Images from a representative 2D plane strain blast-barrier mitigation simulation: (a) at arrival time of wave at barrier. (b) During dynamic interaction event.

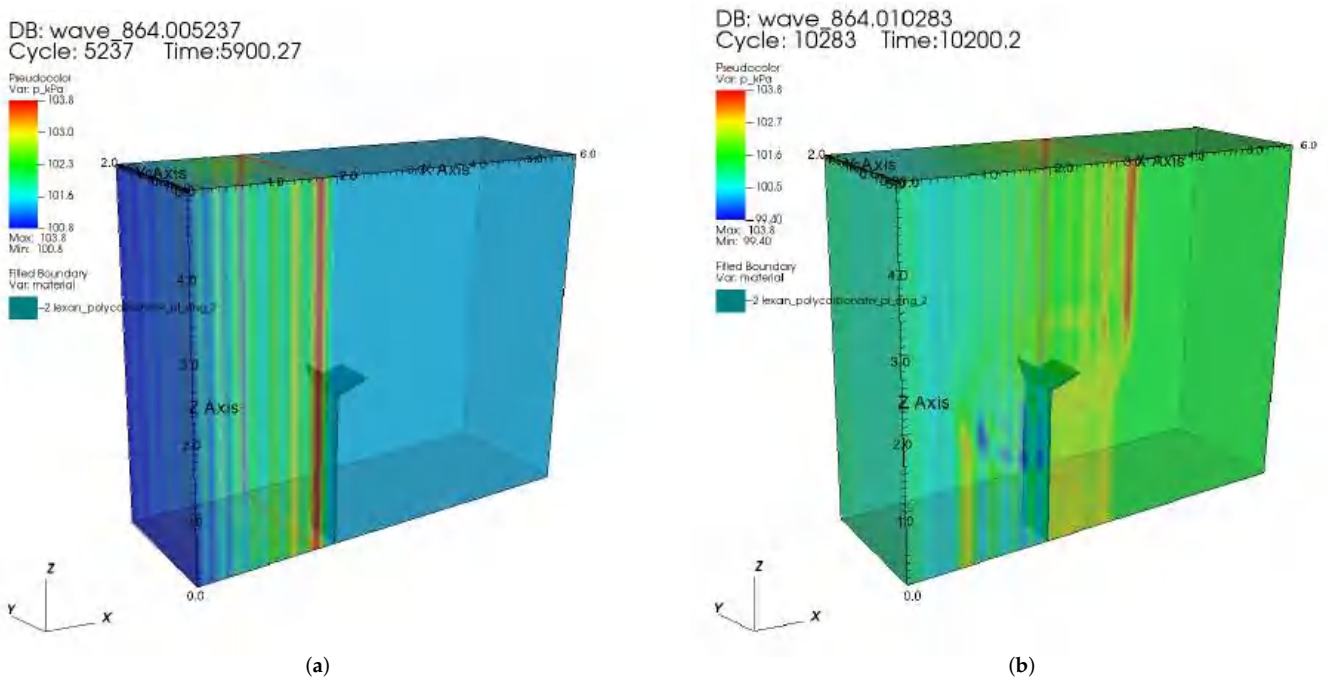


Figure 9. Images from a representative 3D blast-barrier mitigation simulation: (a) at arrival time of wave at barrier. (b) During dynamic interaction event.

3. Results

3.1. Comparison of Predicted and Simulated Blast Effects

Of particular interest is the comparison of numerical results with the classical Kingery-Blumash type empirical curves. The fits to these data are most conveniently given by Swisdak [4] in the following form:

$$\exp\left(A + B \ln K + C(\ln K)^2 + D(\ln K)^3 + E(\ln K)^4 + F(\ln K)^5 + G(\ln K)^6\right) \quad (7)$$

Here, K is the K factor given by Equation (1). The curve parameters $A - G$ for Equation (7) fitting peak incident overpressure and positive impulse are given in Tables 4 and 5, respectively.

Table 4. Parameters for Equation (7) for peak incident overpressure (from Swisdak).

<i>K</i> Values	<i>A</i>	<i>B</i>	<i>C</i>	<i>D</i>	<i>E</i>	<i>F</i>	<i>G</i>
0.2–2.9	7.2106	−2.1069	−0.3229	0.1117	0.0685	0.0	0.0
2.9–23.8	7.5938	−3.0523	0.40977	0.0261	−0.01267	0.0	0.0
23.8–198.5	6.0536	−1.4066	0.0	0.0	0.0	0.0	0.0

Table 5. Parameters for Equation (7) for incident impulse (from Swisdak).

<i>K</i> Values	<i>A</i>	<i>B</i>	<i>C</i>	<i>D</i>	<i>E</i>	<i>F</i>	<i>G</i>
0.2–0.96	5.522	1.117	0.6	−0.292	−0.087	0.0	0.0
0.96–2.38	5.465	−0.308	−1.464	1.362	−0.432	0.0	0.0
2.38–33.7	5.2749	−0.4677	−0.2499	0.0588	−0.00554	0.0	0.0
33.7–158.7	5.9825	−1.062	0.0	0.0	0.0	0.0	0.0

The results for blast overpressure are also compared with predictions from the Taylor–von Neumann–Sedov result. It is shown in [31] that from this solution, the blast radius and corresponding peak pressure are given as a function of time as:

$$R(t) = \beta \left(\frac{Et^2}{\rho_0} \right)^{1/5} \quad (8)$$

$$p(t) = \frac{2}{\gamma + 1} \rho_0 \left(\frac{2R}{5t} \right)^2 \quad (9)$$

Here, E is the energy of the explosion, ρ_0 the initial density of the air. γ is the same parameter appearing in Equation (3), and β is a corresponding parameter which has a value of 1.033 for air. Solving (8) for t and substituting into (9) yields an equation for pressure as a function of blast radius:

$$p(R) = \frac{8}{25(\gamma + 1)} ER^{-3} \beta^5 \quad (10)$$

This result is valid for a point source explosion in a zero-pressure medium expanding spherically from the origin. In order to compare with our hemispherical results, we compare to a blast having twice the energy of 1 kg TNT; this corresponds with the fact that the symmetry conditions on the floor of our free-field simulations make them numerically equivalent to spherical blasts of the same radius, i.e., twice the weight.

Figure 10 shows the comparisons for peak incident blast overpressure of the free field hemispherical and detonation cord simulations with Equations (7) and (10). Figure 11 shows the corresponding positive impulses calculated from the pressure tracers by numerically integrating the positive portions of the pressure tracers from the hemispherical simulations compared to Equation (7).

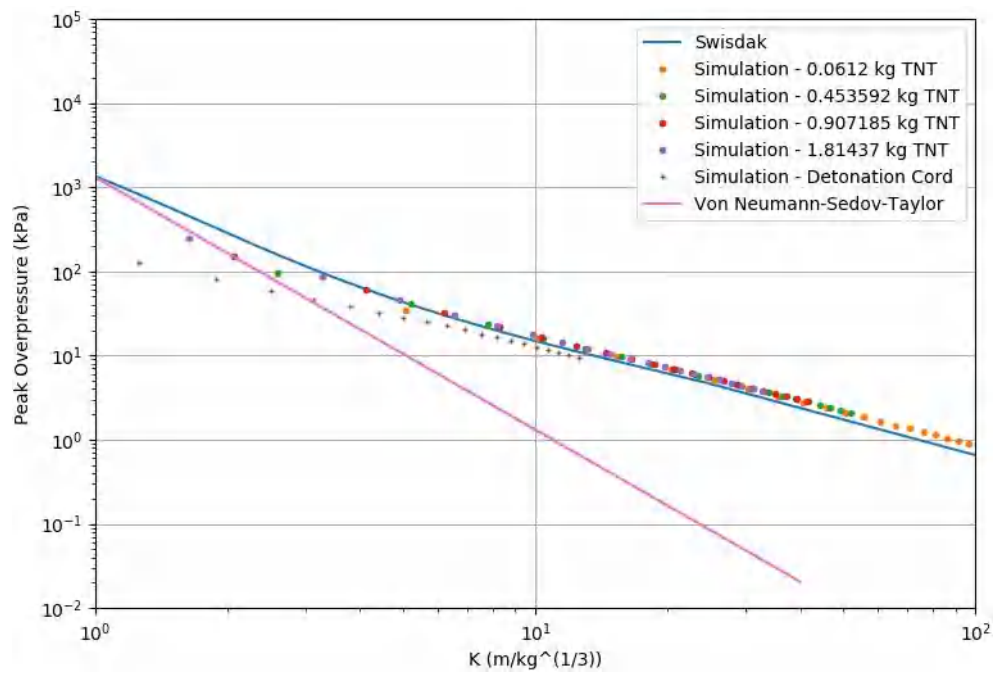


Figure 10. Peak incident blast overpressure versus K factor from the four TNT hemispherical simulations and the detonation cord simulation in comparison with the KB curve from Swisdak and the Taylor–von Neumann–Sedov prediction.

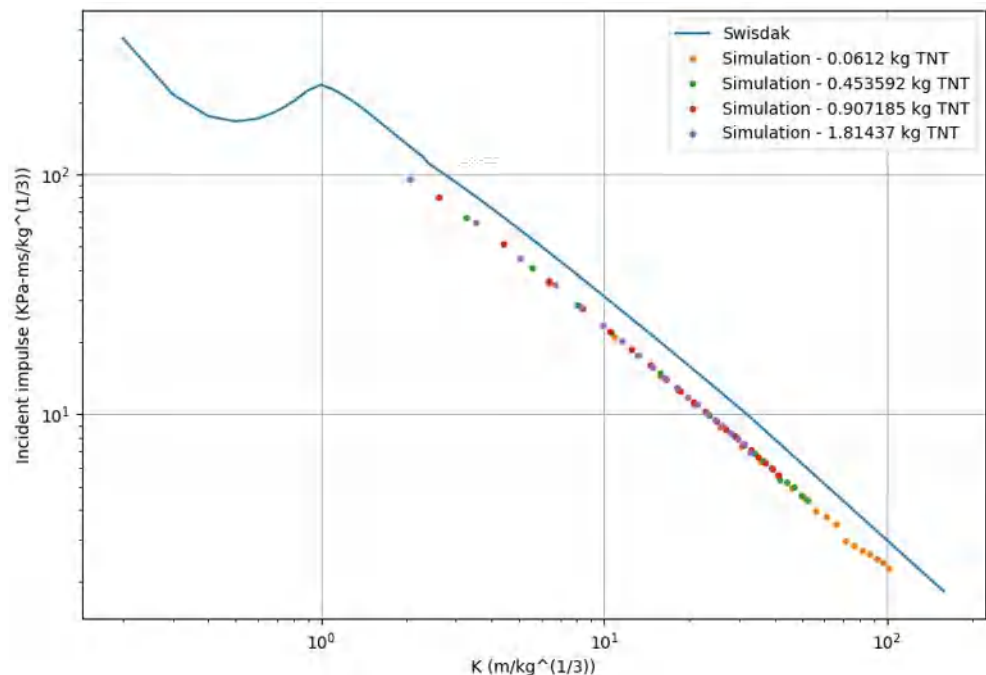


Figure 11. Positive impulse versus K factor from the four TNT hemispherical simulations in comparison with the KB curve from Swisdak.

3.2. Mitigation Effectiveness

The effectiveness of the simple Lexan barriers at mitigating incident pressure fields is investigated with particular emphasis on the so called “Public Withdrawal Distance”. In $m/kg^{1/3}$ units this corresponds to a K value of 130.12 and a blast overpressure of approximately 0.4516 kPa (0.0655 psi). To gauge mitigation effectiveness, pressure tracers were placed in a uniform grid behind the barriers in the present simulations; the pressure

time histories are then queried based on the aforementioned peak pressure criterion, and a “bubble” of space satisfying the maximum desired conditions can be plotted.

Figures 12 and 13 show the analysis of a single fairing mitigation barrier interacting with a wave from 0.06123 kg (0.135 lb) of TNT at approximately 36.576 meters (120 ft). The peak incident overpressure in this case is approximately 0.95 kPa (0.137 psi). Figure 12b shows that in the plane strain case, the pressure is effectively mitigated behind the barrier below 0.4516 kPa for a region over 2 m high and extent of almost 5 m. Figure 13b shows that in the 3D case with a barrier of finite width, there are small localized regions near the edges, center, and ground where edge wraparound and reflections exceed this pressure threshold.

Figures 14 and 15 show the results of plane strain analysis from a 0.45359 kg (1 lb) TNT charge at approximately 36.576 m (120 ft) interacting with a compound fairing and ‘deep roof’ type barrier. The peak incident overpressures in this case is approximately 2.38 kPa (0.345 psi). In both cases, the incident pressure wave is partially mitigated, so there are still large regions behind the barrier seeing pressures larger than 0.4516 kPa. The ‘deep roof’ style barrier provides a large ‘bubble’ for pressures under 0.4516 kPa. It is worth noting that in all cases, the largest pressures behind the barrier occur when the wave which passes over the top reflects back off the ground and the back of the barrier. The incident wave over the barrier has been mitigated below the target pressure, but the reflections exceed it.

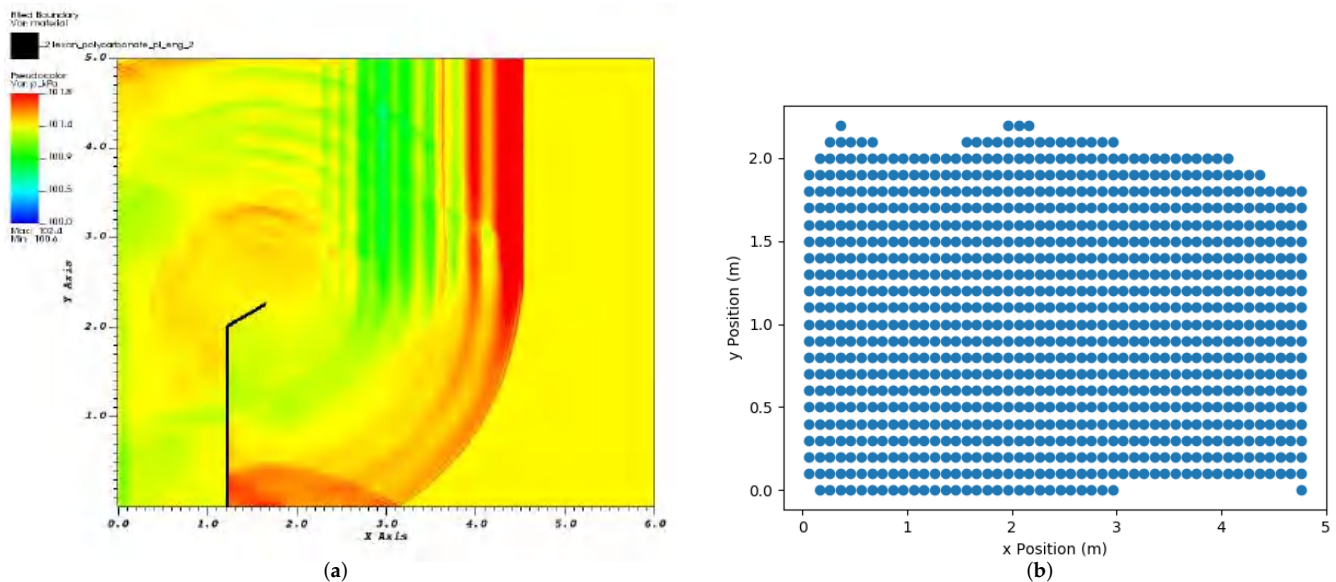


Figure 12. Results from a plane strain analysis of a single-fairing mitigation barrier loaded by a wave generated from 0.06123 kg of TNT at approximately 36.576 m. (a) A snapshot of the wave reflecting over the barrier. The color gradient is set so that max (red) values are above the 0.4516 kPa overpressure threshold. (b) The “bubble” behind the barrier for which max overpressure was beneath 0.4516 kPa.

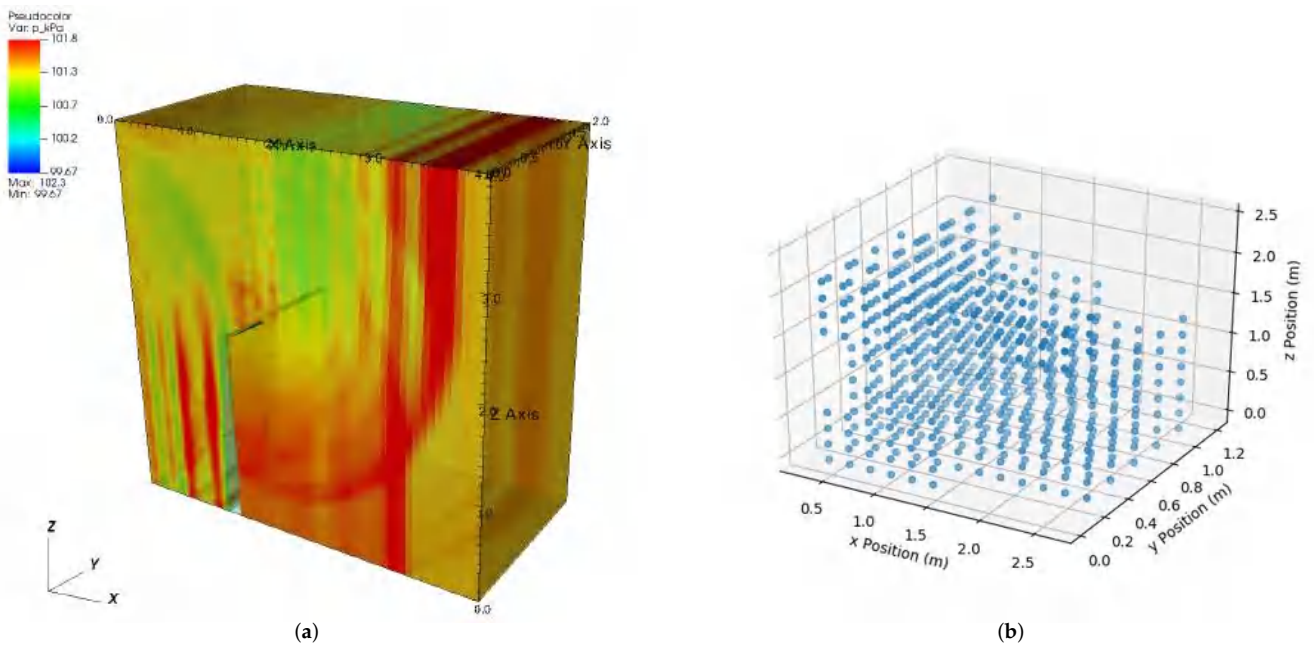


Figure 13. Results from a 3D analysis of a single-fairing mitigation barrier loaded by a wave generated from 0.06123 kg of TNT at approximately 36.576 m. (a) A snapshot of the wave reflecting over the barrier. The color gradient is set so that max (red) values are above the 0.4516 kPa overpressure threshold. (b) The “bubble” behind the barrier for which max overpressure was beneath 0.4516 kPa.

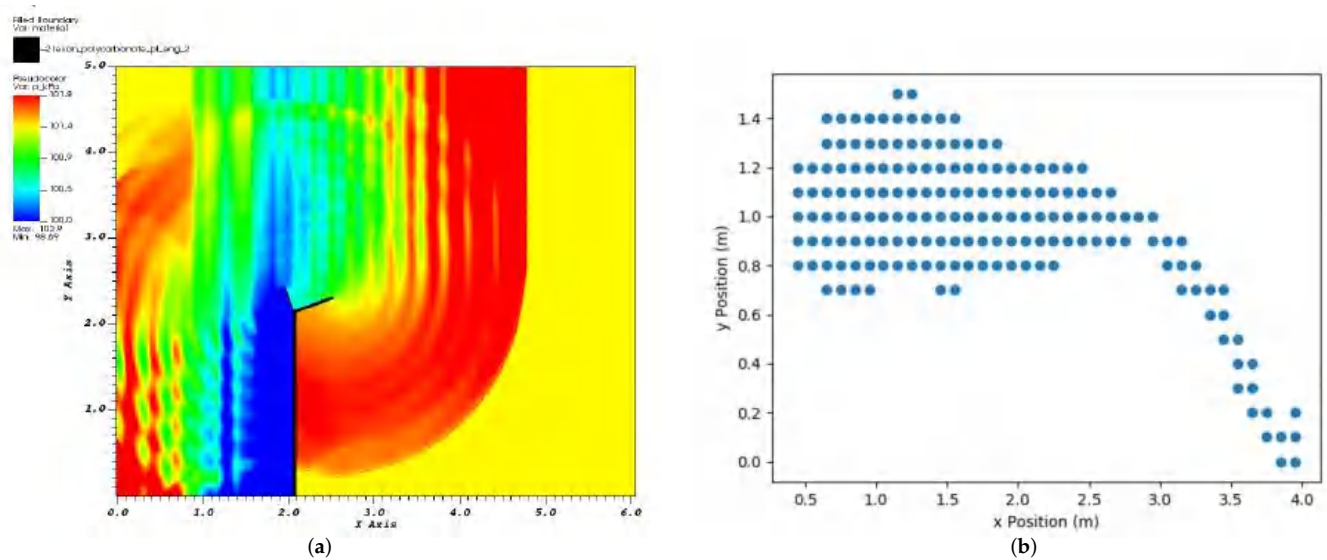


Figure 14. Results from a plane strain analysis of a compound-fairing mitigation barrier loaded by a wave generated from 0.45359 kg of TNT at approximately 36.576 m. (a) A snapshot of the wave reflecting over the barrier. The color gradient is set so that max (red) values are above the 0.4516 kPa overpressure threshold. (b) The “bubble” behind the barrier for which max overpressure was beneath 0.4516 kPa.

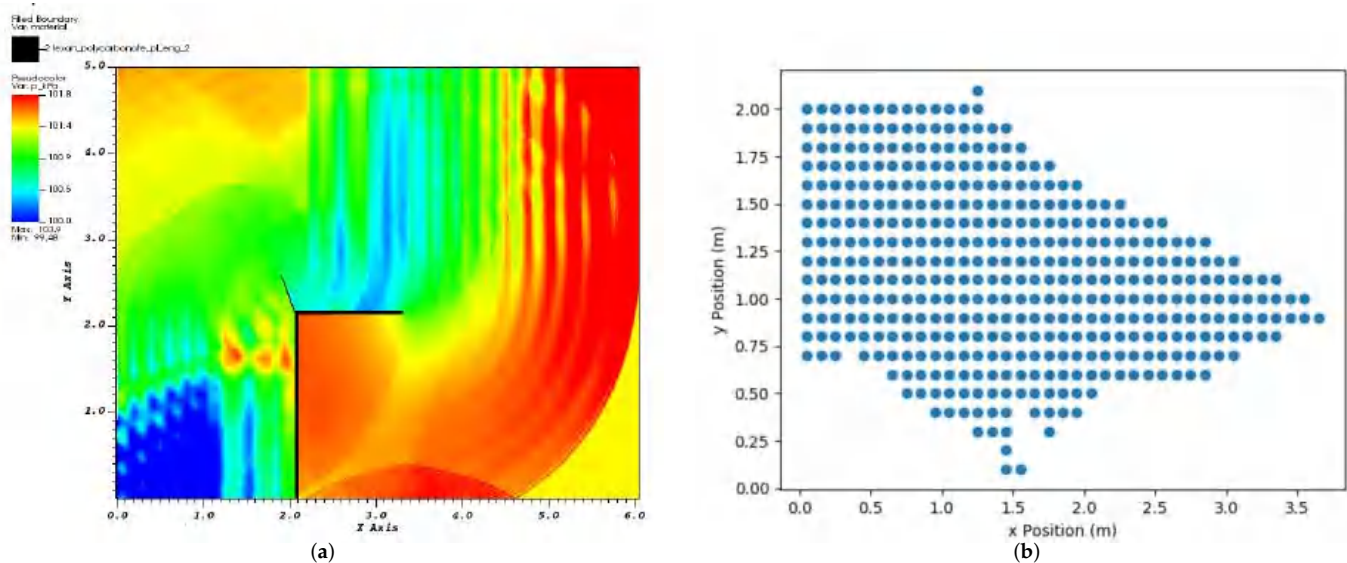


Figure 15. Results from a plane strain analysis of a ‘deep-roof’ type mitigation barrier loaded by a wave generated from 0.45359 kg of TNT at approximately 36.576 m. (a) A snapshot of the wave reflecting over the barrier. The color gradient is set so that max (red) values are above the 0.4516 kPa overpressure threshold. (b) The “bubble” behind the barrier for which max overpressure was beneath 0.4516 kPa.

4. Discussion

The calculated incident peak overpressures from the free-field hemispherical blast simulations show good agreement with the KB predictions in Figure 10. Interestingly, the largest deviation from the KB curve appears to be at the points closest to the explosions yielding the largest overpressure; these first three points lie closer to the von-Neumann-Taylor-Sedov prediction, which rapidly deviates from the Swisdak (KB) curve. The analytical prediction is only valid at an intermediate distance from large explosions; it breaks down near the explosion, as the point source assumption washes out details of the actual detonation event, but also in the very far-field, where the assumption that $p_0 = 0$ in the ambient gas begins to corrupt the results as the incident overpressure approaches the ambient atmospheric pressure. Since the deviation of the data points from the empirical curve is likely within the experimental errors of the original fits, the fact that the data seem to jump from the analytical to the empirical curves may be coincidental. In the very far-field, the KB predictions seem to be doing a reasonable job at predicting the calculated overpressures, despite the fact that it is fit to data from explosions that were orders of magnitude larger.

As expected, the KB predictions do not do well at predicting the overpressures near the detonation cord. The asymmetrical blast wave from a long, thin cylindrical cord lit at one end reaches a nearby point at different times, making the peak pressure smaller than that predicted from a localized (hemispherical) source. However, with greater distance this time delay becomes smaller and the data appears to converge onto the KB curve.

There is a larger discrepancy between the KB-predicted and calculated incident impulses in Figure 11. There is very good agreement in the slope of the data versus the curve, but the free-field simulations appear to uniformly under-predict the impulse relative to the KB curve by a relatively small amount. Given the better agreement in the peak overpressures, there may be some discrepancy in the shape or duration of the whole incident pressure wave. The source of this error could be numerical or physical. There may be low pressure effects to the waves which we not captured in the very large Kingery tests. Note the oscillations that appear in the smaller pressure time histories in Figure 3. These appear after the sharp shock-like pressure spikes decay into more smooth waves traveling at sound speed. While these oscillations could be numerical effects, subsequent calculations were

conducted to investigate this by changing mesh size and the position of the tracer nodes, which appeared to have no effects on the oscillations at distance. Thus it is possible that the oscillations in the far-field small pressure waves is in fact a physical phenomenon. This could in part explain the discrepancy in impulse when there is good agreement in the peak pressure magnitude. It is noted that similar but less pronounced oscillations also seem to appear in the farthest-field pressure histories in the works of Xue et al., Ding et al. [20,22]. There do not appear to be other curves available from similarly small charges at distance to compare with Figure 4. Taking experimental measurements of incident pressures and impulses much smaller than atmospheric pressure very far away from small explosives is quite difficult.

It is further noted that the overall predictive accuracy in the subsequent blast-mitigation dynamic simulations is in part dependent on the accuracy of the predicted incident waves. At 36.576 m (120 ft), only the wave from the smallest (0.06123 kg) charge was mitigated down below the “Public Withdrawal Distance” value of 0.4516 kPa consistency behind the barrier under plane strain conditions; a large bubble was confirmed under a larger 3D simulation of a single barrier, though there were small regions near the edge and center where pressure rose higher in this case. The practical suggestion gleaned from this is that when implementing this type of barrier it may be wise to include more than one side by side to approximate the plane strain condition.

It is noted that the relevant hydrodynamics effects are likely more accurately captured in the 3D simulations. For example, mixing and turbulence are fundamentally 3D phenomena. Furthermore, resolution of any smaller-scale effects is inherently limited by the resolution of the simulation at those scales. However, due to the relatively low velocities and pressures these factors are not thought to have much influence in the cases studied here. Recent work has shown that purposefully exploiting wave interference can be useful in blast mitigation for incident strong shocks [32].

Finally, the effectiveness of using TNT equivalence values to compare expected blast effects from different explosives depends on the situation [33]. The present work has employed only a simple model of TNT with the simplest numerical detonation/burn assumptions. This seemed appropriate when gauging effects in the far-field, when the incident waves are sufficiently decoupled from the nuances of the blast and the blast products. Further work should be conducted to verify the accuracy of the KB charts and the predictions made here with other types of explosive, as well as to simulations with more sophisticated burn models (e.g., ignition and growth [34]).

5. Conclusions

The present manuscript lays out two open problems (namely, what incident overpressure and impulses are felt at given distances from relatively small hemispherical ground charges, and how well can certain types of boundaries mitigate the incident overpressure below a certain threshold). It then describes the results of numerical investigations to attempt to answer these questions. A major motivating factor in this research is the uncertainty in the available empirical curve fits (e.g., Kingery–Bulmash). The source of this uncertainty is twofold: there is relatively large error between some of the original data and the available fitting curves, and the original data were taken for explosions that were many orders of magnitude larger than the charges investigated here. A major unknown remains the extent to which the assumed scaling described by Equation 1 (distance by the cubed root of charge weight) holds as weights become small. The free-field blast simulations presented here indicate that the strong shock of the initial blast smoothed out within the distance simulated and continued to propagate near the sound speed. The slowing of the wave speed is in fact predicted by the empirical Swisdak (KB) equations, but there remains uncertainty into how this change in the physics regime and the shape of the waveform effects the ultimate impulse at different scales. A benefit of the direct numerical calculations is the availability of the full waveforms in time at all distances in the simulation domain; this was further leveraged in the subsequent mitigation simulations. The ultimate shape of

the incident pressure wave may be another degree of freedom which is not fully captured by the K factor scaling. This may explain why the simulations agree well with the peak overpressure and the slope of the impulse curves from Swisdak, but seem to consistently predict slightly smaller impulse magnitudes.

It was never assumed that the empirical curves would or should be “exact” predictors of incident overpressure and impulse for a given case. While this was a primary motivator for the present attempts for a direct physics-based prediction, it is also not assumed that these predictions will correspond exactly to any field case. Ultimately, the analyst, engineer, or responsible person must weigh uncertainty and risk to assess a given scenario. It is hoped that the present simulations (or others like them) could be used in uncertainty quantification efforts for blasts effects in wider-varying scenarios.

The blast-barrier mitigation simulations presented here were also motivated by this desire to mitigate risk and uphold safety standards. The “Public Withdrawal Distance” or “K328” threshold was taken as a more-or-less arbitrary datum against which to gauge effectiveness. The findings of this work should not be used to indicate whether a given scenario is “safe”, but rather to elucidate some of the physical mechanisms of mitigation in a dynamic blast event. Safety standards and acceptable risk vary from scenario to scenario; this work provides a methodology of analyzing the effectiveness of hypothetical tools to decrease risk.

The specific barrier designs presented here were somewhat ad hoc and experimental. The fairings were designed to reflect incident waves and further mitigate overpressure from wraparound over the top. The double fairing was intended to facilitate mitigation further by partially reflecting the incident wave from the backward-facing fairing. The “deep roof” concept was designed to provide even further mitigation. Each subsequent design was found to enhance mitigation. The results indicate that these types of simple barriers are in fact effective at mitigating incident pressure and impulse. They do not, however, eliminate these risks. Ultimately, distance from the source is the surest form of mitigation.

All conclusions herein would be much strengthened by specific field test data taken from experiments with the same charge weights and at the same distances, both in the free-field and behind the proposed barriers. As far as the author knows, no data exists that is a direct match for the scenarios described here. Currently available state-of-the-art instrumentation may be able to reliably measure the small dynamic pressures considered in this study. The experimental verification of these scenarios is outside of the scope of the present work.

Funding: This research received no external funding.

Data Availability Statement: Not applicable.

Acknowledgments: This work was performed under the auspices of the U.S. Department of Energy by Lawrence Livermore National Laboratory under Contract DE-AC52-07NA27344. Special thanks to Mark M. Hart who posed the present problem and provided crucial expertise, intuition, and feedback. Further Thanks to Larry D. McMichael for guidance and expertise in setting up the numerical simulations.

Conflicts of Interest: The authors declare no conflict of interest.

Abbreviations

The following abbreviations are used in this manuscript:

1D	One-dimensional
2D	Two-dimensional
3D	Three-dimensional
ALE	Arbitrary Lagrangian/Eulerian
KB	Kingery–Bulmash

References

1. Kingery, C. *Air Blast Parameters Versus Scaled Distance for Hemispherical TNT Surface Burst*; Technical Report 1334; U.S. Army BRL: Harford County, MD, USA, 1966.
2. Kingery, C.; Pannill, B. *Peak Overpressures vs. Scaled Distance for TNT Surface Bursts (Hemispherical Charges)*; Technical Report BRL Memorandum Report 1518; U.S. Army BRL: Harford County, MD, USA, 1964.
3. Kingery, C.G.B. *Airblast Parameters from TNT Spherical Air Burst and Hemispherical Surface Burst*; Technical Report ARBRL-TR-02555; U.S. Army BRL: Harford County, MD, USA, 1984.
4. Swisdak, M. *Simplified Kingery Airblast Calculations*; Technical Report; Naval Surface Warfare Center Indian Head Div: Silver Spring, MD, USA, 1994.
5. Jeon, D.; Kim, K.; Han, S. Modified Equation of Shock Wave Parameters. *Computation* **2017**, *5*, 41. [CrossRef]
6. Karlos, V.; Solomos, G.; Larcher, M. Analysis of the blast wave decay coefficient using the Kingery–Bulmarsh data. *Int. J. Prot. Struct.* **2016**, *7*, 409–429. [CrossRef]
7. Karlos, V.; Solomos, G. *Calculation of Blast Loads for Application to Structural Components*; Technical Report EUR 26456EN, JRC Technical Report; Publications Office of the European Union: Luxembourg, 2013.
8. Karlos, V.; Solomos, G. *Analysis of Blast Parameters in the Near-Field for Spherical Free-Air Explosions*; Technical Report EUR 27823EN, JRC Technical Report; Publications Office of the European Union: Luxembourg, 2016.
9. Ullah, A.; Ahmad, F.; Jan, H.; Kim, S.; Hong, J. Review of analytical and empirical estimations for incident blast pressure. *KSCE J. Civ. Eng.* **2017**, *21*, 2211–2225. [CrossRef]
10. Stewart, M.G.; Netherton, M.D.; Baldacchino, H. Observed airblast variability and model error from repeatable explosive field trials. *Int. J. Prot. Struct.* **2020**, *11*, 235–257. [CrossRef]
11. Filice, A.; Mynarz, M.; Zinno, R. Experimental and Empirical Study for Prediction of Blast Loads. *Appl. Sci.* **2022**, *12*, 2691. [CrossRef]
12. Rigby, S.; Tyas, A.; Fay, S.; Clarke, S.; Warren, J. Validation of semi-empirical blast pressure predictions for far field explosions—Is there inherent variability in blast wave parameters? In Proceedings of the 6th International Conference on Protection of Structures against Hazards, Tianjin, China, 16–17 October 2014.
13. Taylor, G.I. The formation of a blast wave by a very intense explosion I. Theoretical discussion. *Proc. R. Soc. Lond. A* **1950**, *201*, 159–174. [CrossRef]
14. Taylor, G.I. The formation of a blast wave by a very intense explosion—II. The atomic explosion of 1945. *Proc. R. Soc. Lond. A* **1950**, *201*, 175–186. [CrossRef]
15. von Neumann, J. The point source solution. In *Collected Works*; Pergamon: New York, NY, USA, 1963; Volume 6; pp. 219–237.
16. Sedov, L. Propagation of strong shock waves. *J. Appl. Math. Mech.* **1946**, *10*, 241–250.
17. Brode, H. Numerical Solutions of Spherical Blast Waves. *J. Appl. Phys.* **1954**, *26*, 766–775. [CrossRef]
18. Brode, H. Blast Wave from a Spherical Charge. *Physicis Fluids* **1959**, *2*, 217–229. [CrossRef]
19. Goldstine, H.H.; von Neumann, J. Blast Wave Calculation. *Commun. Pure Appl. Math.* **1955**, *8*, 327–354. 1.1705911. [CrossRef]
20. Ding, Y.; Zhang, X.; Shi, Y.; Zhang, H. Prediction of far-field blast loads from large TNT-equivalent explosives on gabled frames. *J. Constr. Steel Res.* **2022**, *190*, 107120. [CrossRef]
21. Zhang, X.; Ding, Y.; Shi, Y. Numerical simulation of far-field blast loads arising from large TNT equivalent explosives. *J. Loss Prev. Process. Ind.* **2021**, *70*, 104432. [CrossRef]
22. Xue, Z.; Li, S.; Xin, C.; Shi, L.; Wu, H. Modeling of the whole process of shock wave overpressure of free-field air explosion. *Def. Technol.* **2019**, *15*, 815–820. [CrossRef]
23. Sung, S.H.; Chong, J.W. A fast-running method for blast load prediction shielding by a protective barrier. *Def. Technol.* **2020**, *16*, 308–315. [CrossRef]
24. Godio, M.; Williams Portal, N.; Flansbjerg, M.; Magnusson, J.; Byggnevi, M. Experimental and numerical approaches to investigate the out-of-plane response of unreinforced masonry walls subjected to free far-field blasts. *Eng. Struct.* **2021**, *239*, 112328. [CrossRef]
25. Vannucci, P.; Masi, F.; Stefanou, I. A Comparative Study on the Effects of Blast Actions on a Monumental Structure. Doctoral Dissertation, UVSQ, Versailles, France, 2017.
26. Draganić, H.; Varevac, D. Analysis of Blast Wave Parameters Depending on Air Mesh Size. *Shock Vib.* **2018**, *2018*, 3157457. [CrossRef]
27. Nichols, A.; Dawson, D. *ALE3D User's Manual*; Technical Report LLNL-SM-800962; Lawrence Livermore National Laboratory: Livermore, CA, USA, 2020.
28. Menikoff, R. *JWL Equation of State*; Technical Report LA-UR-15-29536; Los Alamos National Laboratory: Livermore, CA, USA, 2017.
29. Krauthammer, T.; Altenberg, A. Negative phase blast effects on glass panels. *Int. J. Impact Eng.* **2000**, *24*, 1–17. [CrossRef]
30. Rigby, S.E.; Tyas, A.; Bennett, T.; Clarke, S.D.; Fay, S.D. The Negative Phase of the Blast Load. *Int. J. Prot. Struct.* **2014**, *5*, 1–19. [CrossRef]
31. Landau, L.; Lifshitz, E. *Fluid Mechanics*; Course in Theoretical Physics 6. Translated from the Russian by JB Sykes and WH Reid; Pergamon: New York, NY, USA, 1987; pp. 403–406.

32. Zong, R.; Hao, H.; Shi, Y. Development of a New Fence Type Blast Wall for Blast Protection: Numerical Analysis. *Int. J. Struct. Stab. Dyn.* **2017**, *17*, 1750066. [CrossRef]
33. Cooper, P.W. Comments on TNT Equivalence. In Proceedings of the 20th International Pyrotechnics Seminar, Colorado Springs, CO, USA, 25–29 July 1994.
34. Lee, E.L.; Tarver, C.M. Phenomenological model of shock initiation in heterogeneous explosives. *Phys. Fluids* **1980**, *23*, 2362–2372. [CrossRef]

Article

Empirical Attenuation Law for Air Blast Waves Due to the Detonation of Explosives Outdoors

Juan Andrés Marín, Rafael Rodríguez *, María B. Díaz and Saray Antón

Department of Mining Exploitation and Prospecting, School of Mining, Energy and Materials Engineering, University of Oviedo, Independencia 13, 33004 Oviedo, Spain

* Correspondence: rrodrifer@uniovi.es

Abstract: The detonation of explosives in the open air was studied, analyzing different amounts of explosives detonated at different distances, monitoring the overpressure or air blast wave generated with the aim of determining a model, which allows to establish safety zones. A series of tests measuring the air wave with different loads and sensors placed at various distances from the origin of the explosion were carried out. The work was focused on designing full-scale trials that allowed to develop a predictive empirical method based on the calculation model of the equivalent mass of TNT. A total of 18 different gelatinous dynamite charges, placing the sensor at six different distances from the origin of the explosion, produced a total of 90 tests measuring the air wave produced by the detonation of gelatinous dynamite. Later, the outdoor detonation of 10 TNT explosive charges was analyzed to extend the model and improve its scope. With all this, it has been possible to develop a predictive model that allows assessing the overpressure generated by the detonation of a TNT-equivalent explosive charge. The results are useful to predict the air blast wave in common open-air blasts, such as those carried out with shaped charges to demolish metallic structures. On the other hand, the results are also useful to determine the air blast wave overpressure in the case of large explosive charges detonated in the open air, such as accidental explosive detonation or terrorist bombs. It is important to point out the relevance of the results achieved after the detonation of large explosive charges (more than 80 kg) simulating a type of bomb frequently used by terrorists. Reproducing the explosion on a real scale, the results are fully representative of the overpressure produced by an explosion of these characteristics without the need of extrapolating the results of tests with small loads. In addition, the detonation was carried out with TNT, which can serve as a standard to compare with any other type of explosive.

Citation: Marín, J.A.; Rodríguez, R.; Díaz, M.B.; Antón, S. Empirical Attenuation Law for Air Blast Waves Due to the Detonation of Explosives Outdoors. *Appl. Sci.* **2022**, *12*, 9139. <https://doi.org/10.3390/app12189139>

Academic Editors: Lina M. López, Ricardo Castedo and Anastasio P. Santos

Received: 20 July 2022

Accepted: 9 September 2022

Published: 12 September 2022

Publisher's Note: MDPI stays neutral with regard to jurisdictional claims in published maps and institutional affiliations.



Copyright: © 2022 by the authors. Licensee MDPI, Basel, Switzerland. This article is an open access article distributed under the terms and conditions of the Creative Commons Attribution (CC BY) license (<https://creativecommons.org/licenses/by/4.0/>).

Keywords: detonation; TNT; dynamite; air blast wave; overpressure

1. Introduction

1.1. Air Blast Wave

An explosion is a physical phenomenon in which there is a sudden, very rapid release of energy. The phenomenon lasts only some milliseconds, and it results in the production of gas with very high temperature and pressure. During detonation, the hot gases that are produced expand in order to occupy the available space, leading to wave-type propagation through space that is transmitted spherically through an unbounded surrounding medium. Along with the produced gases, the air around the blast (for air blasts) also expands, and its molecules pile up, resulting in what is known as a blast wave and shock front. The blast wave contains a large part of the energy that was released during detonation and moves faster than the speed of sound [1].

This shock wave is characterized by an abrupt pressure rise followed by a relatively slow decrease to a value below atmospheric pressure and with a subsequent return to the positive value [1,2]. This phenomenon, which initially takes a few milliseconds, depends

on the explosive mass and the distance to the initiation of the explosion. Subsequently, this waveform derived in a series of damped oscillations.

The study of the air wave produced by the detonation of explosives in the open air inevitably requires analyzing different controlled detonations and measuring the different parameters that characterize the air wave. This experimental level is not at all easy in the civil sphere, since the detonation of explosive substances involves having the availability of both the explosive and the initiator and the appropriate place to carry out the different detonations without affecting the surrounding environment—people, buildings, and communication ways.

The most characteristic effect of an explosion is the sudden increase in pressure that happens in the surrounding air, which propagates in the form of a spherical wave in all directions. The shape, characteristics, and magnitude of the wave depend on the type of explosion, the environment, and the distance from the origin where it was generated.

If the explosion takes place at a point far from the ground, the blast wave expands spherically, and its characteristics (maximum overpressure, duration, impulse, arrival time, etc.) are known as open-air explosion parameters. If the explosion occurs in the vicinity of the ground or on it, the parameters are known as surface explosion. In the first, any point will be affected by two shock waves: first, the incident one from the explosion and then the one reflected from the ground. In the second, the reflection on the ground is linked to the incident wave from the point of explosion, forming a single practically hemispherical wave, whose amplitude, for the same mass of explosive, is considerably greater than in the first case, since the energy must be distributed only in one hemisphere.

1.2. Negative Effects of Air Blast Wave

The air blast wave is an undesirable side effect that occurs in any explosive detonation and consequently has to be studied. The study of the air blast wave due to explosive detonation has been carried out in the last decades from two points of view.

One is the safety point of view, and the other is the environmental impact. The air blast wave is studied from the safety point of view because it has a great destructive effect within a radius that depends on the amount of explosive detonated.

During the second half of the 20th century, a considerable number of experimental and theoretical studies were conducted to understand the effects of blast on buildings and structures [3–7]. The aim was first to study the behavior of air blast waves including the determination of their characteristics and then to investigate the dominant factors influencing the incident waves. Another objective was to investigate the response of the building structure to blast loads [8–13].

The damage caused by the air waves on the structures depends on the overpressure, the impulse, and the formation of projectiles. The level of severity is also influenced by the orientation with respect to the direction of advance of the wave, the geometry of the structure (height/length ratio), and the construction materials. For emergency planning, it is interesting to consider inhabited buildings, due to the greater severity of the consequences.

When a shock wave reaches a structure, it is reflected, with an overpressure at least double that of the incident wave. The wave continues its propagation, reaching a moment in which the entire structure is encompassed by the wave. The explosions produced on the surface cause practically horizontal loads on the structures that they find in their path (except on the roof).

If the structure is small, with few openings, the load results in a homogeneous compression of it; if the structure is large, the load will be markedly different at the front and at the rear, with a greater potential for damage. The existence of openings or the breakage of some part of the structure will result in the homogenization of the pressure between the interior and the exterior of the structure. The calculation of the loads on a structure is carried out by combining the incident pressure and the dynamic pressure and their duration.

Actually, the response of a structure depends not only on the incident overpressure but also on the impulse (which takes into account the duration of the pressure pulse).

In the case of blasting in which the explosive is confined, it generates an air wave with a large proportion of low frequencies that can induce vibrations in buildings, although they are not heard because they are infrasonic. In any case, the effects of the air wave produced by a confined explosive are rarely harmful except in remote cases of glass breakage.

On the other hand, the air blast wave has been extensively studied from the environmental protection point of view. The air blast wave, even of a small intensity, can produce negative effects near the blasting areas. It is very typical of blasting related to mining (quarries or open-pit mines) or civil works (excavation or demolition). For example, the air blast wave can negatively influence the wildlife, which is critical in the case of protected animal species. In the same way, the air blast wave can produce different negative effects on population, from complaints of the neighbors of a village, to small damages to buildings, such as glass breakage or displacement of some tiles on the roof.

1.3. Empirical Prediction Models

Because of the importance of assessing the magnitude of the air blast wave, a lot of prediction models to determine explosion parameters, mainly overpressure, have been developed. These can be based on empirical (or analytical), semiempirical or numerical methods. Empirical methods are essentially correlations with experimental data. Most of these approaches are limited by the range of experiments carried out. The accuracy of all empirical correlations decreases with distance to the source of the explosion.

The use of empirical laws has been extensively studied and has been applied in various recommendations, mostly proposed by military authorities. After the first attempt due to Cranz [14], several methods were proposed [3–7], and due to the relevance of the topic recently, works about this topic have been published [15–17].

In the field of mining and civil engineering, several empirical models have also been proposed to estimate the magnitude of the air blast overpressure as for example [18–20].

In many cases, the air blast wave is given as a function of the scaled distance Z (in $\text{m}/\text{kg}^{1/3}$):

$$Z = \frac{R}{W^{1/3}} \quad (1)$$

R (m) is the distance from the explosion to the measurement point, and W (kg) is the amount of explosive detonated.

In order to be able to characterize the wave generated by any explosive substance and to be able to compare them with each other to assess their harmful effects after a detonation in the open air, it was important to establish a base explosive. The selected explosive was the Trinitrotoluene (TNT), which has well-known explosive properties. The TNT-equivalent mass is the mass of Trinitrotoluene (TNT) that would release an amount of energy equal to the explosive charge in question. If there is a mass W of a given explosive with an explosion heat Q , the equivalent TNT mass W_{eq} is:

$$W_{eq} = W \frac{Q}{Q_{eq}} \quad (2)$$

where Q_{eq} is the explosion heat of TNT $Q_{eq} = 4520 \text{ kJ/kg}$.

The relationship (2) is widely accepted for blast-resistant design. It is proposed in documents taken as a reference or guides, such as UFC 3-340-02 [21] or EUR 2645EN [22], which allow to determine the incident and reflected overpressures and impulses of a spherical or hemispherical TNT explosion.

1.4. Research and Objectives

The detonation of explosives in the open air has been studied, analyzing amounts of explosive material and distances at which it detonates, with the aim of establishing safety

zones, which implies previously determining the primary characteristic variables, as the air blast wave level.

Experimentation in this field presents great technical and economic difficulties, which is why most evaluations are carried out by extrapolation from small-scale experiences or from computer model results.

In the present study, two sets of full-scale tests were carried out. The first with small/medium explosive charges from 0.2 to 7 kg and the second trial with a large amount of explosive, from 25 to 84 kg (simulating terrorist bombs).

Two factors were taken into account that will fundamentally influence it: the explosive charge and the distance to the focus of the explosion.

To test the influence of these two factors, a campaign of air wave measurement tests was carried out with different charges and with sensors placed at different distances from the point of the explosion. With these tests, the intention was to obtain a model to predict the overpressure or magnitude of the air blast wave that is one of the factors influencing negatively on the environment and, in extreme cases, the main factor that affects the structures in outdoor detonations.

The works were focused on the design of a full-scale test procedure that would allow the development of a predictive empirical method based on the model for calculating the equivalent mass of TNT.

A total of 18 different Riodin explosive charges were formed, placing the sensor at six different distances from the focus of the explosion, with which a series of campaigns were carried out with a total of 90 air wave measurement tests produced by the detonation of gelatinous dynamite. With the results obtained, the pertinent adjustment of the TNT-equivalent mass calculation model was carried out, which was used to predict the effects generated by the air blast wave in the simulation processes of predefined scenarios.

Subsequently, the outdoor detonation of 10 TNT charges was analyzed in order to adjust the model and determine its range. Therefore, the results obtained in this work from the measurement of the air wave pressure peak in 100 full-scale tests are presented and analyzed, in which industrial and military explosives were detonated in the open air, without confinement, in different amounts, the highest that the environment allows without affecting people, communication routes, or buildings, which will conclude with the proposal of a calculation methodology based on the experience.

With all this, it was possible to develop a predictive model that allows assessing the overpressure generated by the detonation of a TNT-equivalent explosive charge. The results are useful to predict air blast waves in common open-air blasts, such as those carried out with shaped charges to demolish metallic structures. On the other hand, the results are also useful to determine the air blast wave overpressure in the case of large explosive charges detonated in the open air, such as accidental explosive detonation or terrorist bombs.

It is important to point out the relevance of the results achieved after the detonation of large explosive charges (more than 80 kg) simulating a type of bomb frequently used by terrorists. Reproducing the explosion on a real scale, the results are fully representative of the overpressure produced by an explosion of these characteristics without the need to extrapolate the results of tests with small loads. In addition, the detonation was carried out with TNT, which can serve as a standard to compare with any other type of explosive.

2. Materials and Methods

2.1. Equipment

For this research, the equipment used for data collection was an InstanTEL seismograph, Minimate Plus model, which has a channel for a microphone. It is a piece of equipment for monitoring vibrations and overpressure widely used in mining and civil works. Due to the wide range of acoustic pressure values measured, two different microphones were used for data collection. One is the microphone for air overpressure monitoring, which is supplied by default with the Minimate Plus seismograph; it is of the linear or A-weight type (see

Table 1). The other is a high-pressure microphone, which allows to measure pressure waves higher and can reach up to 69 kPa (Table 2).

Table 1. Instantel linear microphone characteristics used to measure air overpressure.

Scale type	Linear or A
Linear range	88 to 148 dB (500 Pa)
Linear resolution	0.25 Pa
Linear accuracy	+/-10% or +/-1 dB, whichever the higher, between 4 and 125 Hz
Linear frequency response	2 a 250 Hz between -3 dB points of roll off
A range	50–110 dBA
A resolution	0.1 dBA

Table 2. Instantel high-pressure microphone characteristics used to measure air overpressure.

Sensitivity	0.0233 V/kPa
Pressure range	0.0345 kPa to 69 kPa
Frequency response	5 to 1000 Hz

2.2. First Tests: Air Detonation of Dynamite Charges

The tests consisted of measuring the pressure wave or shock wave produced in a total of 90 explosions of different charges of a commercial explosive. These tests were carried out in the facilities of the Santa Bárbara Foundation, a public nonprofit foundation that works on training and R&D, always acting within the field of applied technology, safety, and technological progress. The foundation has several schools; one of them is located in the municipalities of Folgoso de la Ribera and Torre del Bierzo (León) where the trial was carried out.

For these first tests, gelatinous dynamite was used, specifically Riodin from the Maxam explosives manufacturer. The gum dynamite has a gelatinous consistency due to the greater amount of nitrogelatin in its composition (nitroglycerin/nitroglycol and nitrocellulose; >22%), and a predominant element is the ammonium nitrate. This mixture is even more energetic than nitroglycerin itself. This consistency of the explosive gives it, in general, an excellent resistance to water, as well as a high density. These characteristics, together with their high power and detonation speed, make them suitable for blasting rocks of a medium/high hardness, as well as for bottom loading holes and being essential for underwater blasting. Table 3 shows the main characteristics of Riodin. In order to obtain the amount of dynamite desired, cartridges of 26 mm and 32 mm in diameter (both 200 mm in length) were used in the tests.

Table 3. RIODIN main characteristics.

Packing density	1.45 g/cm ²
Detonation speed	6000 m/s
Heat of explosion at constant volume	4.09 MJ/kg
Gas volume produced	895 L/kg
Residual fume quality	Less than 2.27 L/100 g

To analyze the influence of the two more influencing factors, explosive dynamite charge and distance, a total of 90 airwave measurement tests were carried out. The distances and charges of Riodin-type gelatinous dynamite for each individual test are shown in Table 4.

Table 4. Riodin charge and distance for each test.

Num.	Distance (m)	Charge (kg)	Num.	Distance (m)	Charge (kg)	Num.	Distance (m)	Charge (kg)
1	25	0.238	31	25	3.571	61	15	3.571
2	25	0.714	32	25	4.286	62	25	3.571
3	25	1.190	33	25	4.762	63	40	3.571
4	25	1.190	34	25	5.476	64	50	3.571
5	25	1.190	35	25	5.952	65	75	3.571
6	25	2.381	36	25	6.667	66	15	4.762
7	25	3.571	37	25	7.143	67	15	5.952
8	25	4.762	38	75	2.381	68	15	7.143
9	25	5.952	39	75	1.190	69	15	5.952
10	25	7.121	40	75	0.714	70	15	4.762
11	25	4.762	41	50	2.381	71	10	3.571
12	10	2.381	42	50	1.190	72	10	2.381
13	10	3.571	43	50	0.714	73	10	1.190
14	15	3.571	44	40	2.381	74	10	4.762
15	15	4.762	45	40	1.190	75	25	2.381
16	15	5.952	46	40	0.714	76	25	3.571
17	25	2.381	47	25	2.381	77	10	4.762
18	25	2.381	48	25	1.190	78	10	1.190
19	25	3.571	49	25	0.714	79	15	1.667
20	25	3.571	50	15	2.381	80	15	2.381
21	25	4.762	51	15	1.190	81	25	1.905
22	25	4.762	52	15	0.714	82	25	3.095
23	25	3.550	53	25	0.714	83	25	3.571
24	25	0.238	54	25	1.190	84	25	3.571
25	25	0.476	55	25	2.381	85	25	4.762
26	25	0.714	56	15	1.667	86	25	5.714
27	25	1.190	57	25	1.905	87	25	5.714
28	25	1.905	58	40	1.905	88	25	5.714
29	25	2.381	59	50	1.905	89	25	5.714
30	25	3.095	60	75	1.905	90	25	4.286

2.3. Second Trial: Air Detonation of TNT Charges

The second tests consisted in measuring the pressure wave or shock wave produced in a total of 10 explosions with large charges of TNT.

The test was carried out at the “San Gregorio” Training Center, belonging to the Spanish Army (the General Military Academy, Zaragoza, Spain), which is located in the province of Zaragoza. It is the third largest training site in Europe.

The explosive chosen to be detonated in the open air was TNT. It is a light yellow, solid with a bitter taste, and it is less poisonous than other explosive substances. It has great chemical stability and very little sensitivity to shock. It is not affected by humidity, but by light, under whose action it acquires a dark color. Exposure to sunlight can cause sensitive alterations, and it burns without exploding, producing dense black smoke, unless stored in large quantities. It is the best of military explosives. It is used as a basic constituent of

a multitude of explosive mixtures in the loading of projectiles, firecrackers, and multipliers. Its detonation speed is around 7000 m/s.

The mass and configuration of the explosive charge were typical of bombs used by terrorists. The handcrafted geometry of the TNT explosive is very characteristic (Table 5, Figure 1), which provides higher explosive characteristics than a normal configuration, since it deals with directed charges.

Table 5. TNT charge and distance for each test.

Num.	Distance (m)	TNT Charge (kg)
91	25	84
92	50	84
93	50	84
94	30	84
95	25	84
96	25	84
97	25	42
98	25	25
99	25	42
100	25	84



Figure 1. Directed charges of 42 kg of TNT.

Different resistant element designs were subjected to the action of the explosive detonated in the open air. These loads were raised from the ground using wooden supports, the distances at which the loads were separated from the structures between 1.5 and 3 m apart (see Figure 2).



Figure 2. Charge locations in front of the different structures.

Each of the structures was designed to withstand the effects of overpressure of a shock wave generated by the detonation of a TNT charge, directed at a given distance and different charges and separation distances depending on the structural element. The analysis of the behavior of these resistant elements is confidential, and it is out of the scope of the present work.

Nevertheless, we can say that all the results were not satisfactory or as expected. The main problem attributed by most of the calculators was the lack of full-scale tests in sufficient quantity to validate the air wave characterization models used to carry out the different designs. The importance of this air blast wave study can be then understood.

3. Results and Discussion

3.1. Results of the First Tests and Attenuation Law for the Air Overpressure Due to Common Blasts

The detonation of the 90 charges of Riodin-type gelatinous dynamite located at different distances, detailed in Table 4, was carried out on different days. For each detonation, the value of the air overpressure of the detonation was measured in a straight line and was recorded without obstacles using the high-pressure microphone.

In order to analyze the air blast wave values measured in the full-scale tests, the variable scaled distance Z ($m/kg^{1/3}$) defined by Equation (1) was used. This variable includes the influence of the two independent variables that clearly affect the value of the detonation overpressure. The calculated scaled distance and the value of the air blast wave or air overpressure for each detonation are shown in Table 6.

Table 6. Values of scaled distances and air overpressure for each detonated charge.

N	Distance (m)	Charge (kg)	Scaled Distance (m/kg ^{1/3})	Overpressure (kPa)	N	Distance (m)	Charge (kg)	Scaled Distance (m/kg ^{1/3})	Overpressure (kPa)	N	Distance (m)	Charge (kg)	Scaled Distance (m/kg ^{1/3})	Overpressure (kPa)
1	25	0.238	40.35	2.84	31	25	2.571	16.36	9.85	61	15	3.571	9.81	16.80
2	25	0.714	27.95	4.70	32	25	4.286	15.39	10.50	62	25	3.571	16.36	12.10
3	25	1.190	23.59	5.95	33	25	4.762	14.86	11.40	63	40	3.571	26.17	5.91
4	25	1.190	23.59	5.95	34	25	5.476	14.18	11.50	64	50	3.571	32.17	5.12
5	25	1.190	23.59	6.57	35	25	5.952	13.79	13.20	65	75	3.571	49.07	2.73
6	25	2.381	18.72	9.79	36	25	6.667	13.28	10.50	66	15	4.762	8.92	21.90
7	25	3.571	16.36	11.40	37	25	7.143	12.98	14.30	67	15	5.952	8.28	16.40
8	25	4.762	14.86	11.60	38	75	2.381	56.17	2.63	68	15	7.143	7.79	20.20
9	25	5.952	13.79	14.90	39	75	1.190	70.77	1.80	69	15	5.952	8.28	26.10
10	25	7.121	12.99	11.50	40	75	0.714	83.9	1.42	70	15	4.762	8.92	16.30
11	25	4.762	14.86	12.30	41	50	2.381	37.44	3.63	71	10	3.571	6.54	23.90
12	10	2.381	7.49	24.96	42	50	1.190	47.18	2.73	72	10	2.381	7.49	27.10
13	10	6.571	6.54	24.10	43	50	0.714	55.93	2.07	73	10	1.190	9.44	23.40
14	15	3.571	9.81	21.12	44	40	2.381	29.96	5.15	74	10	4.762	5.94	32.20
15	15	4.762	8.92	22.86	45	40	1.190	37.74	3.53	75	25	2.381	18.72	10.20
16	15	5.952	8.28	26.54	46	40	0.714	44.75	2.73	76	25	3.571	16.36	12.90
17	25	2.381	18.72	7.85	47	25	2.381	18.72	10.10	77	10	4.762	5.94	32.04
18	25	2.381	18.72	9.58	48	25	1.190	23.59	6.98	78	10	1.190	9.44	21.14
19	25	3.571	16.36	9.30	49	25	0.714	27.97	5.32	79	15	1.667	16.65	14.17
20	25	3.571	16.36	10.10	50	15	2.381	11.23	17.80	80	15	2.381	11.23	16.01
21	25	4.762	14.86	12.10	51	15	1.190	14.15	13.70	81	25	1.905	20.17	9.44
22	25	4.762	14.86	8.47	52	15	0.714	16.78	9.65	82	25	3.095	17.15	11.20
23	25	3.550	16.39	10.70	53	25	0.714	27.97	5.32	83	25	3.571	16.36	12.50
24	25	0.238	40.34	2.46	54	25	1.190	23.59	7.09	84	25	3.571	16.36	12.40
25	25	0.476	32.01	3.67	55	25	2.381	18.72	9.06	85	25	4.762	14.86	15.60
26	25	0.714	27.97	4.50	56	15	1.667	12.65	14.50	86	25	5.714	13.98	15.00
27	25	1.190	23.59	6.46	57	25	1.905	20.17	8.30	87	25	5.714	13.98	16.00
28	25	1.905	20.17	7.40	58	40	1.905	32.27	5.05	88	25	5.714	13.98	16.60
29	25	2.381	18.72	8.71	59	50	1.905	40.34	3.60	89	25	5.714	13.98	15.90
30	25	3.095	17.15	9.16	60	75	1.905	60.50	1.76	90	25	4.286	15.39	13.90

All the cases are characterized by short overpressure pulses. To illustrate it, the overpressure records obtained in tests no. 17 ($S_b = 7.85$ kPa) and no. 37 ($S_b = 14.3$ kPa) are shown in Figure 3 (left and right, respectively). The duration of the positive phase is only a few milliseconds, 5–10 ms. They are in accordance with the results of recently published research [16], keeping in mind that in our case, the explosive charge is on the floor, and consequently the overpressure is approximately twice the overpressure measured by them.

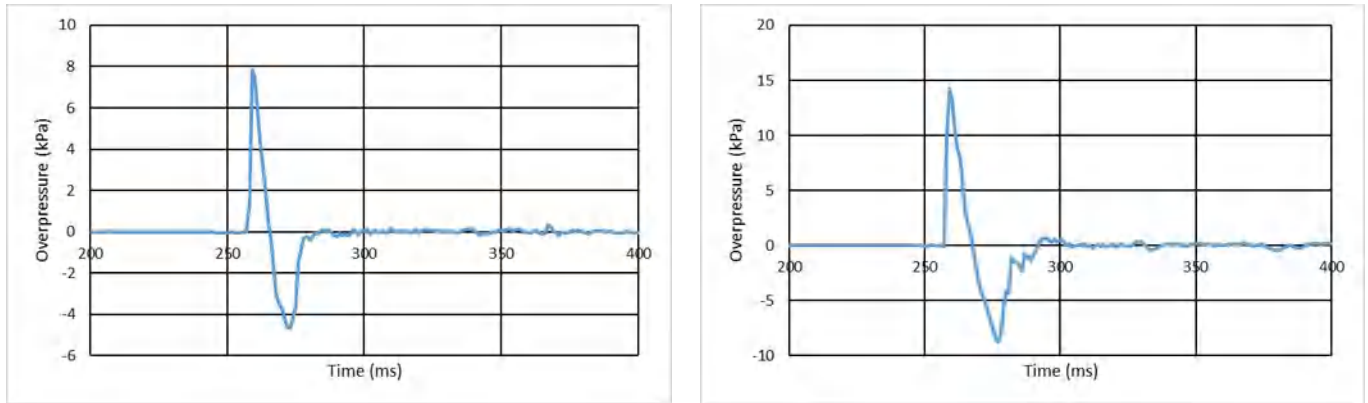


Figure 3. Air overpressure measured in tests no. 17 (left) and no. 37 (right).

The graph in Figure 4 was obtained by representing the overpressure measured at each detonation against the scaled distance in logarithmic scales. It is clear that there is a linear relationship between the $\log(S_b)$ and the $\log(Z)$, which means that there is a potential relationship between the variables S_b (kPa) and Z ($\text{m}/\text{kg}^{1/3}$). By applying logarithms and a least squares adjustment, the following relationship was found:

$$S_b = 309.33 \cdot Z^{-1.216} \tag{3}$$

with a high correlation coefficient $r^2 = 0.96$. This is in accordance with the first experiences in this field [10].

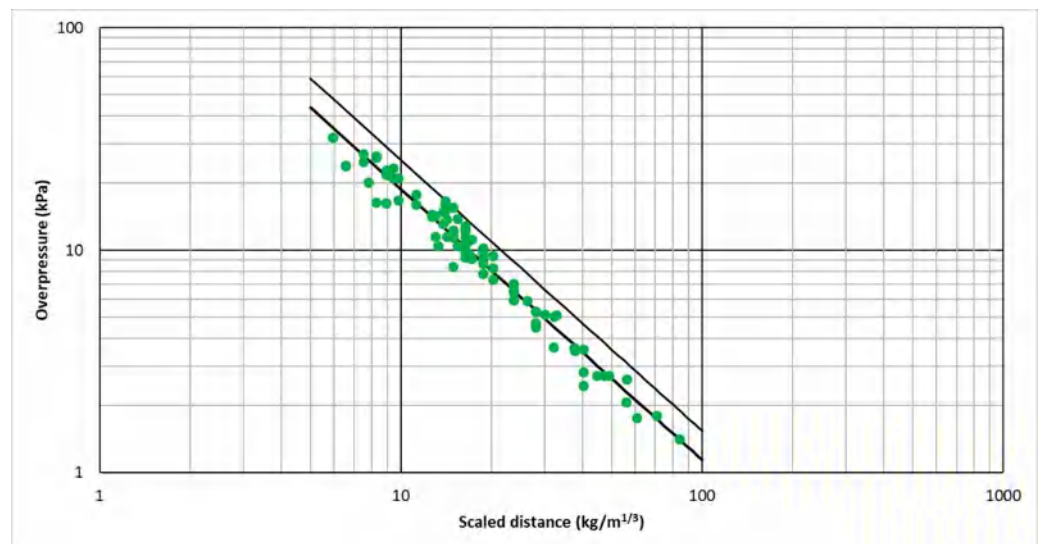


Figure 4. Air overpressure measured as a function of scaled distance with Riodin charges (dots are actual values while lower and upper lines correspond to Equation (3) and Equation (5) respectively).

On the other hand, the formula is quite similar to the prediction model proposed by the manufacturer of the explosive:

$$S_b = 322 \cdot W^{0.56} \cdot R^{-1.3} \quad (4)$$

although the latter gives results lower than the ones obtained from the experiences described here and it is useful only for $Z > 100$.

In the last years, different relationship between air peak overpressure S_b and scaled distance Z , mainly polynomial, have been proposed by several authors [3–5]. We propose the exponential function for coherence with the analysis of air blast wave due to blasting in civil engineering with which this study is most related. On the other hand, it is a simple formula that only needs two empirical parameters. The relationship between the logarithm of the air overpressure $\log(S_b)$ and the logarithm of the scaled distance $\log(Z)$ is linear, and these two parameters can be deduced easily from field data by means of a linear regression. In the present study, the correlation coefficient found is high, $r^2 = 96\%$, demonstrating that it is a sufficiently accurate approach for different analysis.

The point cloud and the regression line are represented in Figure 4. As can be deduced from the same figure, some actual values are higher than the predicted ones. Due to the fact that the aim of the research is safety, a coefficient can be used to assure that any predicted value is higher than the actual one with a given confidence level, i.e., 90% (the predicted value is higher than the actual one in more than 90% of the cases). By using the coefficient of 1.35, the predicted air overpressure fulfils this requirement. The expression deduced in this way is known as the attenuation law:

$$S_b = 417.59 \cdot Z^{-1.216} \quad (5)$$

Equation (4) corresponds to the lower line of the graph, while Equation (5) corresponds to the upper one.

With the values given by Formula (5), we have a predictive model that allows us to characterize the aerial wave generated by the detonation of Riodin-type gelatinous dynamite charges as a function of the distance to the detonation focus. It allows us to assess the overpressure generated by the detonation of a charge of this specific explosive and the possible effects on people or buildings that it will produce. Thus, protection and attenuation mechanisms are established and designed to greatly reduce the consequences of this detonation.

However, the reality is that explosive substances can be of a different nature and composition, not just gelatinous dynamites. For example, a typical blasting work, which produces high air overpressure, is the demolition of metallic structures with shaped charges (Figure 5). It is due to the fact that the explosive is not confined in a blast hole, but it detonates in the open air. In this case, the explosive is pentolite (Riocut), different from dynamite (Riodin), and then the deduced Formula (5) cannot be used directly.

So, in order to be able to characterize the wave generated by any explosive substance and to be able to compare them with each other to assess their harmful effects after a detonation in the open air, the equivalent TNT mass is used.

To apply this calculation method, it is necessary to know the heat of explosion, both of the TNT and of the explosive to be compared. The heat of explosion for TNT is 4520 kJ/kg, and from Table 3, there is a heat of explosion for this Riodin dynamite of 4090 kJ/kg. So, 1 kg of Riodin is equivalent to $1 \times 4090 / 4520 = 0.905$ kg of TNT. With these explosion heat values, the TNT equivalent of each charge used in the 90 detonations is determined, as well as the reduced distance for each of them with this resulting TNT-equivalent charge (Table 7).

The resulting values from Table 7 are shown in Figure 6 in which the measured overpressure is plotted against the TNT-equivalent scaled distance.



Figure 5. Demolition of metallic structures with shaped charges ((left) metallic silo; (right) large mining stacker).

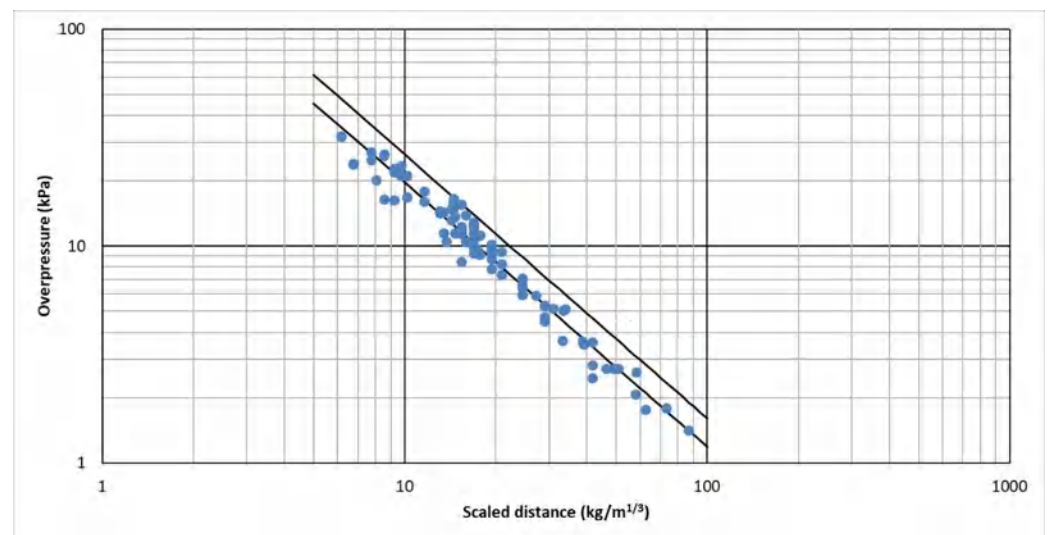


Figure 6. Overpressure measured as a function of scaled distance using the equivalent mass of TNT (dots are actual values while lower and upper lines correspond to Equations (6) and (7)).

Due to the proportionality between the Riodin and TNT explosion heats used, the expression deduced in this case by linear regression is similar to the previous one:

$$S_b = 322.13 \cdot Z^{-1.216} \quad (6)$$

where S_b is the overpressure generated by the wave in kPa, and Z is the reduced distance in $m/kg^{1/3}$. The correlation coefficient for this prediction model is also 96.06%.

By using the coefficient of 1.35, the predicted air overpressure will be higher than the actual one in more than 90% of the cases, and the formula represents the attenuation law of the air wave in the case of TNT explosive:

$$S_b = 434.87 \cdot Z^{-1.216} \quad (7)$$

Equation (6) corresponds to the lower line of the graph, while Equation (7) corresponds to the upper one.

Table 7. TNT-equivalent charge and scaled distance for each Riodin-detonated charge.

N	Distance (m)	Eq. TNT Charge (kg)	Scaled Distance (m/kg ^{1/3})	Overpressure (kPa)	N	Distance (m)	Eq. TNT Charge (kg)	Scaled Distance (m/kg ^{1/3})	Overpressure (kPa)	N	Distance (m)	Eq. TNT Charge (kg)	Scaled Distance (m/kg ^{1/3})	Overpressure (kPa)
1	25	0.215	41.70	2.84	31	25	3.232	16.91	9.85	61	15	3.232	10.15	16.80
2	25	0.646	28.91	4.70	32	25	3.878	15.91	10.50	62	25	3.232	16.91	12.10
3	25	1.077	24.39	5.95	33	25	4.309	15.36	11.40	63	40	3.232	27.06	5.91
4	25	1.077	24.39	5.95	34	25	4.955	14.66	11.50	64	50	3.232	33.82	5.12
5	25	1.077	24.39	6.57	35	25	5.386	14.26	13.20	65	75	3.232	50.73	2.73
6	25	2.154	19.36	9.79	36	25	6.032	13.73	10.50	66	15	4.309	9.22	21.90
7	25	3.232	16.91	11.40	37	25	6.463	13.42	14.30	67	15	5.386	8.56	16.40
8	25	4.309	15.36	11.60	38	75	2.154	58.07	2.63	68	15	6.463	8.05	20.20
9	25	5.386	14.26	14.90	39	75	1.077	73.16	1.80	69	15	5.386	8.56	26.10
10	25	6.444	13.43	11.50	40	75	0.646	86.74	1.42	70	15	4.309	9.22	16.30
11	25	4.309	15.36	12.30	41	50	2.154	38.71	3.63	71	10	3.232	6.76	23.90
12	10	2.154	7.74	24.96	42	50	1.077	48.78	2.73	72	10	2.154	7.74	27.10
13	10	2.331	6.76	24.10	43	50	0.646	57.83	2.07	73	10	1.077	9.76	23.40
14	15	3.231	10.15	21.12	44	40	2.154	30.37	5.15	74	10	4.309	6.15	32.20
15	15	4.309	9.22	22.86	45	40	1.077	39.02	3.53	75	25	2.154	19.36	10.20
16	15	5.386	8.56	26.54	46	40	0.646	46.26	2.73	76	25	3.232	16.91	12.90
17	25	2.154	19.36	7.85	47	25	2.154	19.36	10.10	77	10	4.309	6.15	32.04
18	25	2.154	19.36	9.58	48	25	1.077	24.39	6.98	78	10	1.077	9.76	21.14
19	25	3.232	16.91	9.30	49	25	0.646	28.91	5.32	79	15	1.508	13.08	14.17
20	25	3.232	16.91	10.10	50	15	2.154	11.61	17.80	80	15	2.154	11.61	16.01
21	25	4.309	15.36	12.10	51	15	1.077	14.63	13.70	81	25	1.724	20.85	9.44
22	25	4.309	15.36	8.47	52	15	0.646	17.35	9.65	82	25	2.801	17.74	11.20
23	25	3.212	16.94	10.70	53	25	0.646	28.91	5.32	83	25	3.232	16.91	12.50
24	25	0.215	41.7	2.46	54	25	1.077	24.39	7.09	84	25	3.232	16.91	12.40
25	25	0.431	33.1	3.67	55	25	2.154	19.36	9.06	85	25	4.309	15.36	15.60
26	25	0.646	28.91	4.50	56	15	1.508	13.08	14.50	86	25	5.171	14.46	15.00
27	25	1.077	24.39	6.46	57	25	1.724	20.85	8.30	87	25	5.171	14.46	16.00
28	25	1.724	20.85	7.40	58	40	1.724	33.36	5.05	88	25	5.171	14.46	16.60
29	25	2.154	19.36	8.71	59	50	1.724	41.7	3.60	89	25	5.171	14.46	15.90
30	25	2.801	17.74	9.16	60	75	1.724	62.55	1.76	90	25	3.878	15.91	13.90

3.2. Results of the Second Tests and Analysis of the Air Blast Wave Due to Bombs

Table 8 shows the parameters and results related to the ten explosions with a large amount of TNT explosive. Detonation number 91 was canceled because the microphone did not work properly.

Table 8. Values of scaled distances and air overpressure for each detonated TNT charge.

N	Distance (m)	TNT Charge (kg)	Scaled Distance (m/kg ^{1/3})	Overpressure (kPa)
91	25	84	5.71	-
92	50	84	11.42	16.00
93	50	84	11.42	21.90
94	30	84	6.85	45.30
95	25	84	5.71	63.80
96	25	84	5.71	57.60
97	25	42	7.19	36.30
98	25	25	8.55	33.00
99	25	42	7.19	57.00
100	25	84	5.71	54.10

In the case of detonation of TNT charges, two different behaviors can be seen. There is one test in which the air blast wave is moderate, and the shape of the overpressure pulse is similar to that described above. It is rather symmetrical, and the positive and negative parts are approximately of the same magnitude as can be seen in the overpressure record measured in test no. 92 ($S_b = 16.0$ kPa), Figure 7 (left).

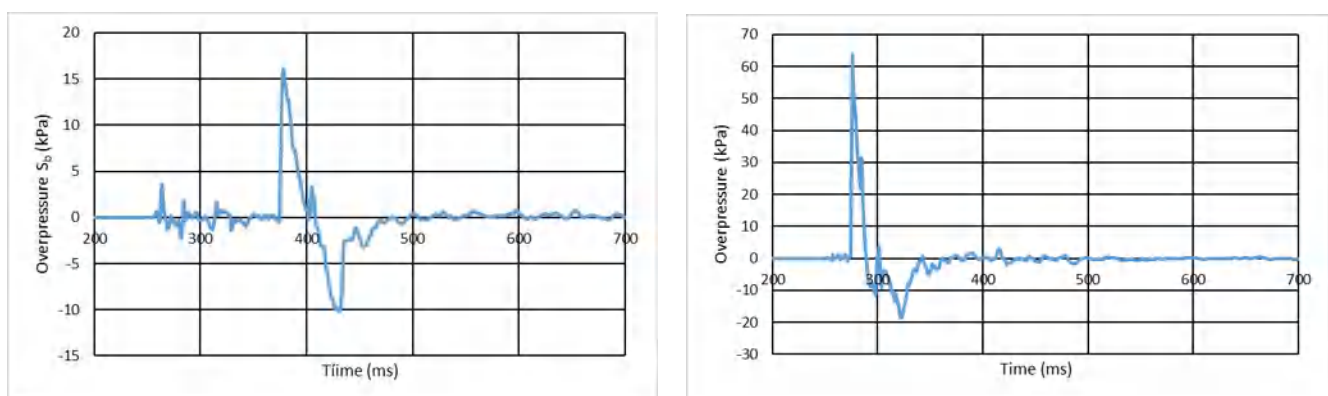


Figure 7. Air overpressure measured in tests no. 92 (left) and no. 95 (right).

Nevertheless, when the air blast wave is high, the shape of the pulse is equal to the ideal blast wave pressure with the positive part much higher than the negative one. On the other hand, the duration of the positive phase in these tests is significantly higher than in the others. For example, the overpressure measured in test no. 95 ($S_b = 63.8$ kPa) is shown in Figure 7 (right).

These overpressure results can be drawn together with the results obtained with the TNT explosive equivalent to Riodin dynamite. Then the graph of Figure 8 was obtained.

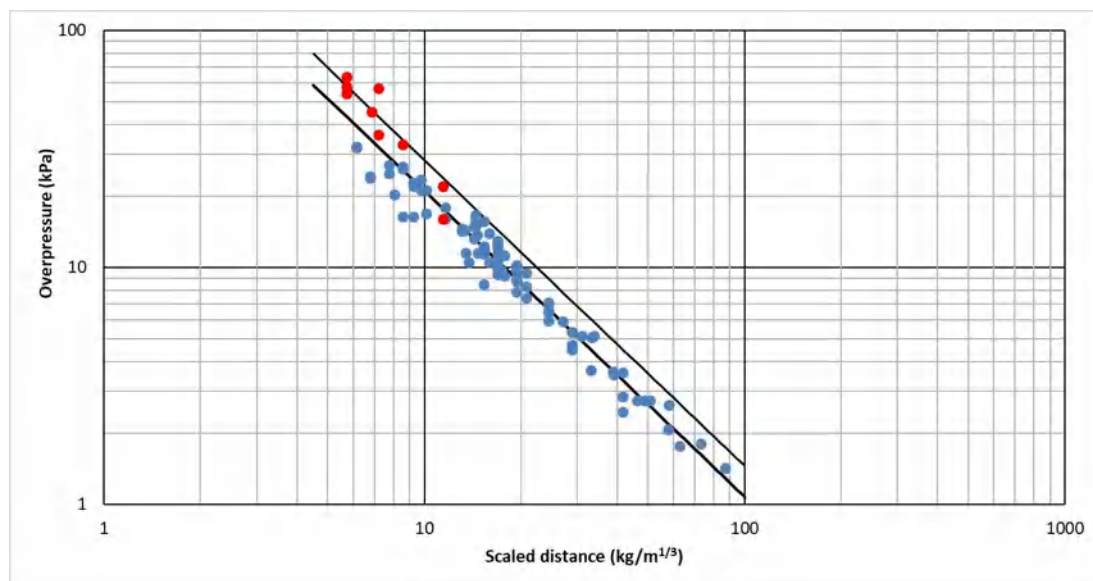


Figure 8. Overpressure measured as a function of scaled distance for the detonation of pure TNT and equivalent TNT (dots are actual values while lower and upper lines correspond to Equation (8) and Equation (9) respectively).

The expression derived from the data set is:

$$S_b = 396.27 \cdot Z^{-1.280} \quad (8)$$

With a correlation coefficient $r^2 = 95.9\%$.

By using the safety coefficient 1.35, the predicted air overpressure will be higher than the actual one in more than 90% of the cases, and the attenuation law of the air wave in the case of TNT explosive is:

$$S_b = 534.96 \cdot Z^{-1.280} \quad (9)$$

Formula (9), or alternatively the graphic of Figure 6, is useful to predict air blast wave overpressure near the explosion even in the case of detonation of a large amount of explosive.

4. Conclusions

The peak pressure value of the air blast wave from a total of 100 records corresponding to the detonation of different explosive charges in the open air was analyzed. These records can be separated into two basic groups: records from open-air detonations of a gelatinous dynamite-type explosive and records from open-air detonations of a TNT-type explosive.

The most important result achieved was the definition of an air wave attenuation law, overpressure S_b as a function of the scaled distance Z , for the determination of the overpressure peak due to the detonation of explosive charges in the outdoors. The law is simpler than others since it only requires the determination of two empirical parameters that can be determined with a smaller number of samples.

The model predicts the peak value of the air blast wave S_b (kPa) from the detonation of a given or equivalent TNT explosive charge in the open air that relates to the value of such variable, S_b , with the scaled distance Z ($m/kg^{1/3}$):

$$S_b = 396.27 \cdot Z^{-1.280}$$

where $Z = R/W_{eq}^{1/3}$, that is, the distance R (m) divided by the cubic root of the equivalent TNT mass W_{eq} (kg).

By using a safety coefficient of 1.35, the predicted S_b is higher than actual S_b in more than 90% of the cases:

$$S_b = 534.96 \cdot Z^{-1.280}$$

It has been demonstrated that this law is valid in a wide range of the reduced distance, with Z varying between 5.71 and 86.74 m/kg^{1/3}, and in a wide range of the air wave, with S_b between 1.42 and 63.8 kPa. In this way, the attenuation law is useful both for the prediction of the air blast wave due to the detonation of charges of a few kgs of explosives (such as the shaped charges used in civil works for the demolition of metallic structures) and for the prediction of the air wave in the case of the detonation of several tens of kgs of explosives (such as explosive detonations by accident or terrorist bombs).

The model proposed aims to serve as a basis for the design of protection and containment elements, but it is considered necessary to continue testing with full-scale explosives, in order to further limit other parameters involved in the propagation of the resulting wave of a detonation, tests that are difficult to carry out because they are of a destructive nature and because they are controlled materials for which there is authorization for consumption, qualification, and training.

Author Contributions: Conceptualization, R.R. and J.A.M.; methodology, J.A.M. and R.R.; investigation, J.A.M., R.R., M.B.D. and S.A.; data curation, J.A.M.; writing—original draft preparation, R.R., J.A.M. and S.A.; writing—review and editing, R.R. and J.A.M. All authors have read and agreed to the published version of the manuscript.

Funding: This research was carried out in the framework of the project “Especificaciones de diseño y estructurales para aparcamiento de terminales de transporte con riesgo de ataque terrorista” funded by the Spanish Ministry for Science and Innovation (No. Exp. 16-08).

Institutional Review Board Statement: Not applicable.

Informed Consent Statement: Not applicable.

Data Availability Statement: The article provides all data used in this research.

Conflicts of Interest: The authors declare no conflict of interest.

References

1. Baker, W.E. *Explosions in Air*; University of Texas Press: Austin, TX, USA, 1973.
2. Baker, W.E.; Cox, P.A.; Westine, P.S.; Kulesz, J.J.; Strehlow, R.A. *Explosion Hazards and Evaluation*; Elsevier Scientific Publishing Company: New York, NY, USA, 1983.
3. Henrych, J. *The Dynamics of Explosion and Its Use*; Elsevier: Amsterdam, The Netherlands, 1979.
4. Kingery, C.N.; Bulmash, G. *Airblast Parameters from TNT Spherical Air Burst and Hemispherical Surface Burst*; Technical Report ARBRL-TR-02555; U.S. Army BRL: Aberdeen, MD, USA, 1984.
5. Kinney, G.F.; Graham, K.J. *Explosive Shocks in Air*; Springer: Berlin/Heidelberg, Germany, 1985.
6. Mills, C.A. The design of concrete structures to resist explosions and weapon effects. In Proceedings of the 1st International Conference on Concrete for Hazard Protections, Edinburgh, UK, 27–30 September 1987.
7. Sadvoskiy, M.A. Mechanical effects of air shockwaves from explosions according to experiments. In *Geophysics and Physics of Explosion*; Sadvoskiy, M.A., Ed.; Selected Works; Nauka Press: Moscow, Russia, 2004.
8. Beshara, F.B. Modelling of blast loading on aboveground structures—I. General phenomenology and external blast. *Comput. Struct.* **1994**, *51*, 585–596. [CrossRef]
9. Brode, H.L. *Numerical Solution of Spherical Blast Waves*; American Institute of Physics: New York, NY, USA, 1955.
10. Remennikov, A.M. A review of methods for predicting bomb blast effects on buildings. *J. Battlef. Technol.* **2003**, *6*, 5–10.
11. Kocczaz, Z.; Sutcu, F.; Torunbalci, N. Architectural and structural design for blast resistant structures. In Proceedings of the 14th World Conference on Earthquake Engineering, Beijing, China, 12–17 October 2008.
12. Draganic, H.; Sigmund, V. Blast loading on structures. *Teh. Vjesn.* **2012**, *19*, 643–652.
13. Wu, C.; Hao, H.; Lu, Y.; Zhou, Y. Characteristics of wave recorded in small scale field blast tests in a layered rocksoil medium. *Geotechnique* **2003**, *53*, 587–599. [CrossRef]
14. Cranz, C. *Lehrbuch der Ballistic*; Springer: Berlin/Heidelberg, Germany, 1926.
15. Shirbhate, P.A.; Goel, M.D. A Critical Review of Blast Wave Parameters and Approaches for Blast Load Mitigation. *Arch. Comput. Methods Eng.* **2021**, *28*, 1713–1730. [CrossRef]

16. Filice, A.; Mynarz, M.; Zinno, R. Experimental and Empirical Study for Prediction of Blast Loads. *Appl. Sci.* **2022**, *12*, 2691. [CrossRef]
17. Ding, Y.; Zhang, X.; Shi, Y.; Zhang, H. Prediction of far-field blast loads from large TNT-equivalent explosives on gabled frames. *J. Constr. Steel Res.* **2022**, *190*, 107120. [CrossRef]
18. Siskind, D.E.; Stachura, V.J.; Stagg, M.S.; Kopp, J.W. *Structure Response and Damage Produced by Airblast from Surface Minin*; Report of Investigation 8485; U.S. Bureau of Mines: Washington, DC, USA, 1980.
19. Richards, A.B.; Moore, A.J. Airblast design concepts in open pit mines. In Proceedings of the 7th International Symposium on Rock Fragmentation by Blasting—Fragblast 7, Beijing, China, 11–15 August 2002; pp. 553–561.
20. Kuzu, C.; Fisne, A.; Ercelebi, S.G. Operational and geological parameters in the assessing blast induced airblast-overpressure in quarries. *Appl. Acoust.* **2020**, *70*, 404–411. [CrossRef]
21. UFC 3-340-02. *Structures to Resist the Effects of Accidental Explosions, Unified Facilities Criteria (UFC)*; Manual Number 3-340-02 (This Manual Supersedes US ARMY TM5-1300); US Department of Defense: Washington, DC, USA, 2008.
22. Karlos, V.; Solomos, G. *Calculation of Blast Loads for Application to Structural Components*; JRC Technical Report EUR 26456EN; European Union: Luxembourg, 2013.

Article

Forecast of Airblast Vibrations Induced by Blasting Using Support Vector Regression Optimized by the Grasshopper Optimization (SVR-GO) Technique

Lihua Chen ¹, Panagiotis G. Asteris ^{2,*}, Markos Z. Tsoukalas ², Danial Jahed Armaghani ³,
Dmitrii Vladimirovich Ulrikh ³ and Mojtaba Yari ⁴

¹ Department of Civil Engineering, Chongqing Vocational Institute of Engineering, Jiangjin District, Chongqing 402260, China

² Computational Mechanics Laboratory, School of Pedagogical and Technological Education, 15122 Maroussi, Greece

³ Department of Urban Planning, Engineering Networks and Systems, Institute of Architecture and Construction, South Ural State University, 76, Lenin Prospect, 454080 Chelyabinsk, Russia

⁴ Department of Mining Engineering, Faculty of Engineering, Malayer University, Malayer 65719-95863, Iran

* Correspondence: asteris@aspete.gr

Citation: Chen, L.; Asteris, P.G.; Tsoukalas, M.Z.; Armaghani, D.J.; Ulrikh, D.V.; Yari, M. Forecast of Airblast Vibrations Induced by Blasting Using Support Vector Regression Optimized by the Grasshopper Optimization (SVR-GO) Technique. *Appl. Sci.* **2022**, *12*, 9805. <https://doi.org/10.3390/app12199805>

Academic Editors: Ricardo Castedo, Lina M. López and Anastasio P. Santos

Received: 23 August 2022

Accepted: 13 September 2022

Published: 29 September 2022

Publisher's Note: MDPI stays neutral with regard to jurisdictional claims in published maps and institutional affiliations.



Copyright: © 2022 by the authors. Licensee MDPI, Basel, Switzerland. This article is an open access article distributed under the terms and conditions of the Creative Commons Attribution (CC BY) license (<https://creativecommons.org/licenses/by/4.0/>).

Abstract: Air overpressure (AOp) is an undesirable environmental effect of blasting. To date, a variety of empirical equations have been developed to forecast this phenomenon and prevent its negative impacts with accuracy. However, the accuracy of these methods is not sufficient. In addition, they are resource-consuming. This study employed support vector regression (SVR) optimized with the grasshopper optimizer (GO) algorithm to forecast AOp resulting from blasting. Additionally, a novel input selection technique, the Boruta algorithm (BFS), was applied. A new algorithm, the SVR-GA-BFS₇, was developed by combining the models mentioned above. The findings showed that the SVR-GO-BFS₇ model was the best technique ($R^2 = 0.983$, RMSE = 1.332). The superiority of this model means that using the seven most important inputs was enough to forecast the AOp in the present investigation. Furthermore, the performance of SVR-GO-BFS₇ was compared with various machine learning techniques, and the model outperformed the base models. The GO was compared with some other optimization techniques, and the superiority of this algorithm over the others was confirmed. Therefore, the suggested method presents a framework for accurate AOp prediction that supports the resource-saving forecasting methods.

Keywords: blasting; airblast; input selection; hybrid SVR model; prediction

1. Introduction

Air-overpressure (AOp) or airblast is an unwelcome outcome of blasting in mining operations. The blasting creates temporary air blast pressure waves that persist for some time [1,2]. More than 20% of the explosive energy is used to fracture and replace the rock fragments. More than 70% of this energy is dissipated, which causes AOp and other unwanted phenomena [1]. Various parameters, including terrain circumstances, blast design, and climate, are influential on AOp [2,3]. The enormous shock waves coming out of the blast spot toward the free facade create AOp. Hence, the AOp can be defined as a shock wave deflected laterally by density changes in the air. These AOp waves are released with some audible high- or low-frequency sounds. AOp can cause structural damage and harm to people in the vicinity of quarry sites [4].

Several studies attempted to establish associations for the AOp forecast using its influential factors. Kuzu et al. [5] ascertained an experimental association between AOp and interval among blast planes and monitoring spot and mass of explosive substances (32%). To reproduce ground shock and air explosion tensions deriving from facade explosions,

Wu and Hao [6] connected Autodyn2D to mathematical models, wherein properties of rock materials and free air were involved. A partial-empirical model for forecasting the airwave tension caused by blasting operations outside a tunnel was developed by Rodríguez et al. [7]. They claim that their model works in different situations. Rodríguez et al. [8] proposed a photometric curve and iso-attenuation curves to describe the phenomenon, as well as a proposed charge-distance curve to resolve the query.

Recently, various investigations have applied machine learning (ML) techniques to resolve science and engineering problems [9–19]. Such techniques were used to predict the AOp values and identify the most influential predictors [20–22]. These techniques are both time and cost-saving and can help both researchers and practitioners allocate resources to other necessary operations. Among the ML algorithms, artificial neural networks (ANNs) and an adaptive neuro-fuzzy inference system (ANFIS) were employed more frequently than other techniques in the investigations of AOp [23]. Some studies used tree-based techniques such as XGBoost, random forest (RF), and M5 [24]. Rare studies employed support vector regression to predict the AOp [25]. Additionally, some of these models were optimized with some techniques to improve accuracy and efficiency. Some of these optimization techniques include genetic algorithms (GA) and particle swarm optimization (PSO) [2]. Lastly, different methods, such as fuzzy Delphi methods, were used to choose the inputs before the model was built [26].

Despite the vast application of ML algorithms for AOp prediction, various efficient models for prediction, optimization, and input selection are neglected. In this study, the authors developed a novel prediction model that encompasses SVR as a prediction model, the Grasshopper algorithm for optimizing the SVR's hyperparameters, and the Boruta algorithm (BFS) for input selection. The Grasshopper algorithm is used in this study because it is easy to use, has a structure without gradients, avoids local optimums well, and treats problems as black boxes. SVR is rarely employed for AOp prediction, and to the best of the authors' knowledge, the Grasshopper and Boruta algorithms have not been applied in this domain. The rest of this paper is structured as follows: the next section discusses algorithms used in this study, including SVR, GO, and BFS. Additionally, the case study of this research will be explained in this section. The results and discussions' section describes the data preparations and performance criteria. The results of input selection and model optimization are reported in this section. The paper ends with a conclusion that sums up what was learned from this study and makes some suggestions for future research.

2. Material and Methods

This section thoroughly describes the methods used in this study. These methods include SVR as a well-known prediction technique, GO as a metaheuristic optimization technique and BFS as an input selection approach. The SVR-GO-BFS_n model, which is the result of combining the algorithms mentioned above, is adequately explained. Furthermore, four ML techniques and three optimization techniques were applied to verify the performance of the SVR-GO-BFS_n model.

2.1. Data Collection

Data for this study was collected from a published work by Hajihassani et al. [27]. According to their study, four granite mines were selected and considered for data collection in the Johor area, Malaysia. In total, 62 blasting operations were performed. The main substance of the explosion was ANFO, a widely used bulk industrial explosive, the stemming substance was granular gravel, and the diameters of the blast holes were 75, 89, and 115 mm. The specifications of rock quality designation (RQD) as well as the height of the bench are shown in Table 1. Various blasting parameters, including RQD, burden, hole depth, spacing, powder factor, and stemming length, were evaluated during the data collection.

Table 1. Some additional measurements in blasting sites.

Site	RQD (%)	Height of Bench (m)
Masai	60–84	15–20
Pasir Gudang	67–89	13–25
Pengerang	70–91	10–23
Ulu Tiram	65–88	10–15

The research team observed the AOp employing microphones (L type), which were linked to the AOp grooves of record-keeping elements. The AOp values ranged from 88 dB to 148 dB. To ensure an accurate measurement of overpressures, the operating frequency response of microphones was selected between 2 and 250 Hz. This frequency is suitable for measuring the overpressure for both human hearing and construction.

The minimum values of 10 m, 0.34 kg/m³, 60 kg, 1.7 m, 1.5 m, 2.65 m, 60%, 12, 300 m, and 89.1 dB were recorded for hole depth, powder factor, maximum charge per delay, stemming, burden, spacing, RQD, no. of hole, distance from the blast face, and AOp, respectively, while the values of 25 m, 0.76 kg/m³, 171 kg, 3.2 m, 4 m, 91%, 63, 600 m, and 126.3 dB were recorded as maximum amounts of the same variables. More information regarding the data used in this study can be found in the original study [27].

2.2. Preparation of Data

The min/max transformation technique was used to normalize the collected data. The objective of this transformation was to restrict the inputs’ possible advantages to those with noticeable numerical values, over those with small values. Handling large-value inputs can be challenging and complicated due to the fact that the kernel quantity relies on vectors’ internal multiplication of inputs. Therefore, conquering mathematical complications throughout calculation procedures is another crucial aspect of input normalization. The data were transformed using Equation (1) and the normalized data ranged from zero to one.

$$a_i^n = \frac{a_i - a_{min}}{a_{max} - a_{min}} \tag{1}$$

where the input vectors with the calculated observation points are denoted by a_i . a_{min} and a_{max} refer to the lowest and highest values that relate to the calculated data set. a_i^n is the transformed variant of a_i .

2.3. Support Vector Regression (SVR)

One of the most effective approaches for handling regression complications is SVM, which is a supervised technique [28]. The formation and optimization approach of SVM varies according to the nature of inputs, and ϵ -SVR is the regression form of SVM. The principal objective of SVR is to acquire a hypothesis whose entire errors of regression forecast are situated within a predetermined threshold, ϵ . The next aim of the learned function is that this function possesses an excellent achievable generalization capability. This aim is purposely attempted in order that a flat model can be established. The following equations enact the aforementioned aims, forming a typical convex quadratic optimization problem with linear constraints set. The above goals are met by the following equations, which, along with the set of linear constraints, make a typical curved quadratic optimization problem.

$$minimize \frac{1}{2} \|\omega\|^2 + c \sum_{i=1}^k (\vartheta_i + \vartheta_i^*) \tag{2}$$

$$subject \ to \ \begin{cases} b_i - \langle \omega, a_i + c \rangle \leq \vartheta_i + \epsilon, \forall n \\ \langle \omega, a_i + c \rangle - b_i \leq \vartheta_i^* + \epsilon, \forall n \\ \vartheta_i, \vartheta_i^* \geq 0, \forall n \end{cases} \tag{3}$$

where, for training points $(a_i, b_i), \dots, (a_n, b_n)$, k denotes the number of data samples, the vectors of a_i denote values of input, and b_i implies the corresponding output value for a_i . The upper and lower errors of training are represented by ϑ_i and ϑ_i^* , respectively. The errors are indifferent to a particular margin defined by ε ; afterwards, the cost function will be added by penalties. The normal vector is denoted by ω . The regularization parameter ($c > 0$) regulates the balance of the pair of goals enacted in the above equations. The authors employed Lagrange multipliers to ascertain the SVR's optimization problem expressed by the above equations. Some alterations were performed following that the Lagrangian is calculated until the next equation is obtained:

$$f(a, \beta_i, \beta_i^*) = \sum_{i=1}^n (\beta_i - \beta_i^*) l(a, a_i) - c \tag{4}$$

The equation obtained above is based on theories of optimality constraints, the kernel method, and Lagrange multipliers. While four renowned kernels, including sigmoid, polynomial, linear, and RBF, are available, this study employed RBF. This kernel was intentionally picked due to its computational capability. Typically, this kernel outperforms others [28]. RBF is extremely nonlinear, including possessing some inputs and an unlimited-dimensional space of mapping [29]. The RBF kernel is displayed in the following equation:

$$L(a_i, a_j) = e^{-\gamma(\|a_i - a_j\|^2)} \tag{5}$$

where $\gamma \in \mathbb{R}, \gamma > 0$ describes the expanse of the radial basis kernel function.

Figure 1 displays the structure of SVR based on Equation (3). This structure admits the requirements of Karush–Kuhn–Tucker for resolving a quadratic optimization query. The values of $(\beta_i - \beta_i^*)$ were used to obtain the decision function. It is worth mentioning that these values were non-null support vectors. One of the most vital steps to develop a profoundly accurate and stable prediction model is to optimize the pair of SVR's hyper-parameters, including C and γ . Adopting optimization methods for ascertaining these parameters' optimal conditions is considered in recent studies.

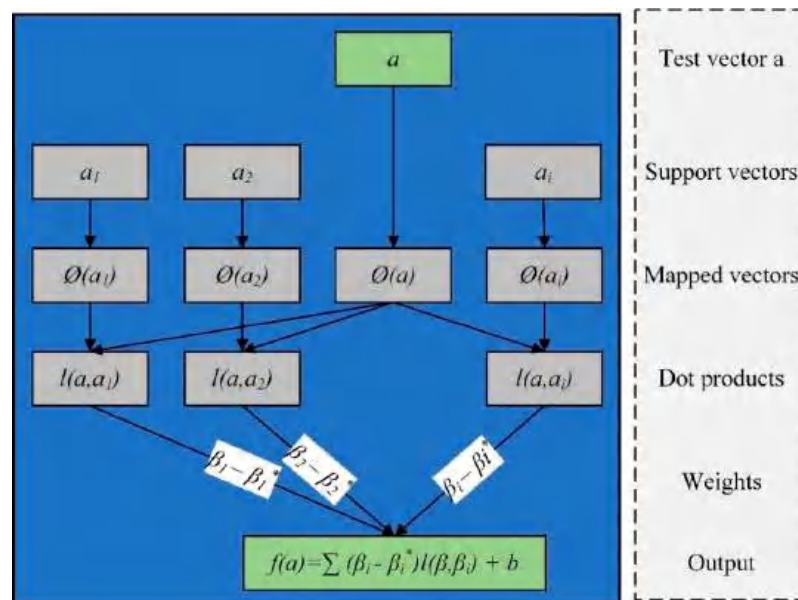


Figure 1. The SVR's structure SVR.

2.4. Grasshopper Optimization Algorithm (GO)

A recent swarm intelligence method, which is acknowledged as the grasshopper optimization (GO) algorithm, was employed in this study. Roles of nature are behind this method. This optimization technique was initially developed to deal with complicated

optimization queries [29]. GO mimics the behavior of grasshopper colonies for resolving the queries of optimization. The GO involves two search processes: exploitation and exploration. Nymph and adult grasshoppers execute the search procedure. Typically, long intervals are covered by adult grasshoppers. Hence, they can search a whole space (global) to discover more suitable areas, where more foods are provided. In fact, the exploration procedure is performed by them. On the other hand, nymph grasshoppers perform the exploitation task, which means that they aim for a specific or local region. The GO secures an equilibrium between exploitation and exploration. This balance may lead to a slightly more complex algorithm. Mathematically, Saremi et al. [30] achieved a method to represent the colony function of grasshoppers. The following formula shows the mathematical model of the grasshoppers' swarming function.

$$Y_i = A_i + B_i + C_i \tag{6}$$

where Y_i denotes the i th grasshopper's place. A_i indicates the idea of social interplay. So long as B_i expresses the strength of gravity forced on the i th grasshopper, the wind advection is demonstrated by C_i . Remarking that the formula was re-written $Y_i = m_1A_i + m_2B_i + m_3C_i$ to produce arbitrary behaviour, wherein m_1 , m_2 , and m_3 are accidentally picked figures between zero and one. The three steps of the implementation of GO algorithm are shown in Table 2.

Table 2. Implementation steps of GO algorithm.

1st STEP	$A_i = \sum_{j=1, j \neq i}^N a(f_{ij}) \cdot f_{ij}$	<ul style="list-style-type: none"> f_{ij} is a space, which divides the ith and jth grasshoppers, $f_{ij} = a_j - a_i$ $f_{ij} = (a_j - a_i)/ a_j - a_i$ means the unit vector between the ith and jth grasshoppers 	(7)
	$a(m) = z \cdot e^{-m \cdot d} - e^{-m}$	<ul style="list-style-type: none"> z is the attraction intensity d signifies the attractive length scale $m = d_{ij}$ 	(8)
2nd STEP	$B_i = -b \cdot e_b$	<ul style="list-style-type: none"> b is gravitational constant e_b stands for the unit vector heading to the globe center 	(9)
	$C_i = x \cdot e_\omega$	<ul style="list-style-type: none"> x is a constant drift e_ω refers to a unity vector in the wind direction N signifies the grasshoppers' number 	(10)
	$Y_i = \sum_{j=1, j \neq i}^N b \left(a_j - a_i \right) \cdot \frac{a_j - a_i}{ a_j - a_i } - t \cdot e_t + x \cdot e_\omega$		(11)
3rd STEP	$Y_i^f = c \left(\sum_{j=1, j \neq i}^N c \cdot \frac{ub_d - db_f}{2} \cdot a \left(a_j^d - a_i^d \right) \cdot \frac{a_j - a_i}{ a_j - a_i } \right) + O_f$	<ul style="list-style-type: none"> db_f and ub_d are lower and upper boundaries in the Fth dimension O_f is the location of the optimum solution it has found yet 	(12)
	$c = c_{max} - d \cdot \frac{c_{max} - c_{min}}{D}$	<ul style="list-style-type: none"> c_{min} and c_{max} refers to the minimum and the maximum values of the coefficient c d implies the existing iteration D represents the greatest iterations 	(13)

In the first step, the concepts of social interaction (A_i) and social forces ($a(m)$) were determined. The function “ a ” is able to divide the space amongst two grasshoppers into 3 areas: attraction, repulsion, and comfort. In the second step, the force of gravity imposed on the i th grasshopper was determined (B_i).

The wind advection (C_i) was established in the third step. It is worth mentioning that because the nymph grasshoppers do not have wings, the wind direction strongly impacts their movement. The elements of A_i , B_i , and C_i were replaced in Equations (6) and (11) was

formed. Typically, the grasshoppers reach their pleasure areas rapidly, and the group does not gather in particular spots. Thus, Equation (11) is unable to deal with the optimization queries immediately. This equation was amended to solve the optimization issue mentioned above, and Equation (12) was created. As shown in Equation (12), “ c ” is a lessening coefficient which is utilized on the way to decrease the comfort, attraction, and repulsion areas. In this Equation, the “ c ” enters double because of the following reasons:

- By expanding the abundance of iterations, the motion of marked grasshoppers is decreased by the initial “ c ”. This parameter equilibrates the whole exploration and exploitation of the target.
- The following “ c ” decreases the repulsion, attraction, and comfort areas amongst grasshoppers. The aforementioned decline is proportionate to the iterations’ abundance.

GO needs to be avoided by becoming stuck in the local optimum. Alternatively, it attempts to acquire a precise calculation of the global optima. Grasshoppers achieve progressive equilibrium between exploration and exploitation because of the diverse pleasure area parameter “ c ”. In each iteration, the “ c ” can be calculated by Equation (13). In this study, the authors employed great rates of repulsion since this is a crucial method in the GO to circumvent local solutions. The outcomes reveal that great repulsion rates limit grasshoppers to staying at a local optimum. To summarize, Algorithm 1 depicts the processes involved in executing the GO.

Algorithm 1 GO optimization

```

1: Initialize the swarm population (grasshoppers)  $Y_i$ , where  $i = (1, 2, \dots, N)$ 
2: Initialize the parameters:  $c_{min}, c_{max}, D$ 
3: Calculate the fitness value of each search agent
4: Assign  $O$  to the best search agent (the individual with highest fitness value)
5: while  $d < D$  do
6:   Use Equation (13) to update  $c$ 
7:   for each search agent
8:     Normalize the distance between grasshoppers within [1,4]
9:     Update the position of the current search agent by Equation (12)
10:    Bring the current search engine back when it exceeds the boundaries
11:   end for
12:   if there is a better solution, update  $O$ 
13:    $d = d + 1$ 
14: end while
15: Return  $O$ 

```

2.5. Boruta Feature Selection (BFS) Algorithm

The BFS is an ensemble-based input selection technique that follows the function system of RF with some extra tools to obtain better outcomes [31]. The BFS attempts to identify all the important inputs in both regression and classification queries. The principal concept of this technique is employing analytical measurements and executing various RFs to examine the significance of the original inputs and inputs with an expanded randomness degree. The additional randomness allows a greater understanding of what inputs are significant. Figure 2 shows the running steps of BFS.

The BFS determines all important inputs in the knowledge system and renders the inputs’ importance degree. This system also designates significant inputs with numerical rates indicating their significance. Therefore, this may assist scholars in building various input mixtures based on their relevance ranking to determine the optimal input collection. Detailed information about the Boruta input selection technique can be obtained from Kurasa and Rudnicki [31].

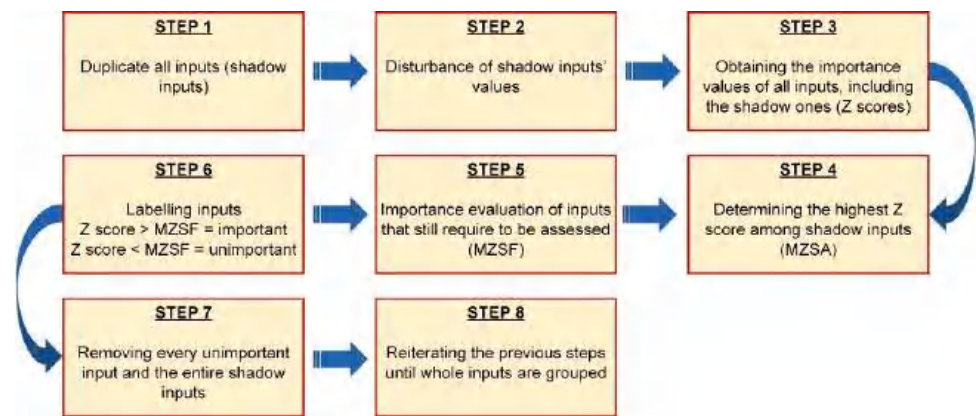


Figure 2. The execution steps of BFS.

2.6. SVR-GO-BFS_n Model Development

A hybrid model expressed by SVR-GO-BFS_n was developed to improve the performance of the AOp forecast. The effective algorithms are combined into SVR-GO-BFS_n: SVR, GO for optimizing parameters, and BFS for input choice. The parameterization of the SVR-GO-BFS_n model was based on “n”, which showed the abundance of inputs engaging in developing the model in line with the “n” greatest importance values assigned by BFS. The most important inputs were selected using BFS. Next, GO was utilized to train SVR and optimize a pair of its hyperparameters (γ and C). Finally, the developed model was used to predict the AOp values. Figure 3 shows a fundamental flowchart of the model developed, which includes the main four steps.

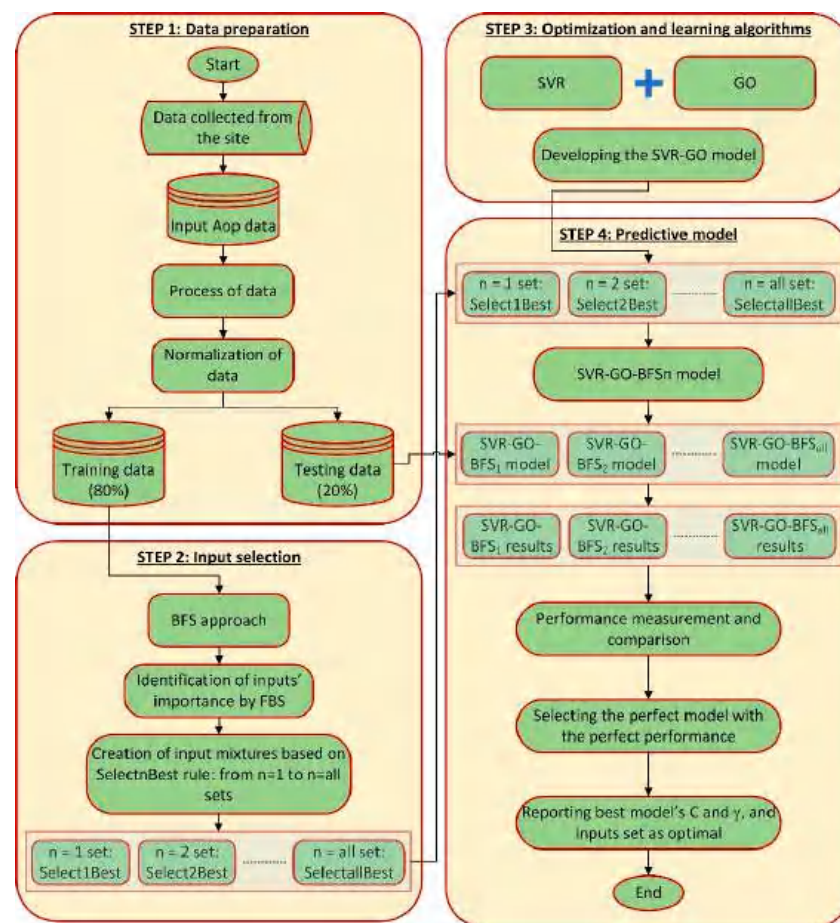


Figure 3. Flowchart of this study.

Step one involved the preparation of data. The dataset included nine candidate inputs. In this step, the data were also normalized as previously described. The second step involved the selection of inputs using the BFS technique. This method contributed to a fair and logical determination and ranking of significant and insignificant inputs from the AOP dataset. In line with the significant input ranking, various input mixtures were built and expressed as $n = 1, n = 2, \dots, n = \text{all}$. If the “n” is one, it means that the input collection simply includes one input (the most significant input). If the “n” is two, it refers to an input set that involves the two most significant ones. If “n” equals “all”, it means that an input assortment involves all significant ones. Obtaining the minimum optimal input’s collection was the main objective of this method.

Step three engaged in the optimization of SVR utilizing GO. A pair of SVR’s parameters, including C and γ , were optimized by applying GO. Ultimately, various regression models (SVR-GO-BFS_n) were developed based on various input mixtures.

Step four involved performing predictions using SVR-GO-BFS_n. Utilizing the testing set, the corresponding built predictive models were assessed, and the forecast outcomes were reported. The most suitable model was picked following its precision and error performance. Therefore, the most suitable input set was regarded as the optimal collection of inputs and its C and γ were the optimal SVR values.

2.7. Validation Scheme

The training data employ a different pre-process once the AOp dataset has been randomly partitioned into the training (80%) and test (20%) sets. We call this method the k-fold cross-validation approach. This technique improves the models’ flexibility and, consequently, their precision. Therefore, the statistical examination would generalize properly to a particular dataset. In comparison with holdout validation, cross-validation is more suitable for datasets with a small sample size. This method randomly divides the initial data into k equivalent sub-data sets. Following that, the k-1 sub-data are used for training, and one sub-data set is used for testing the model. This procedure is repeated k times. Finally, a single approximation is achieved by averaging the k results from the folds. In this study, the k value is 10 (Figure 4).

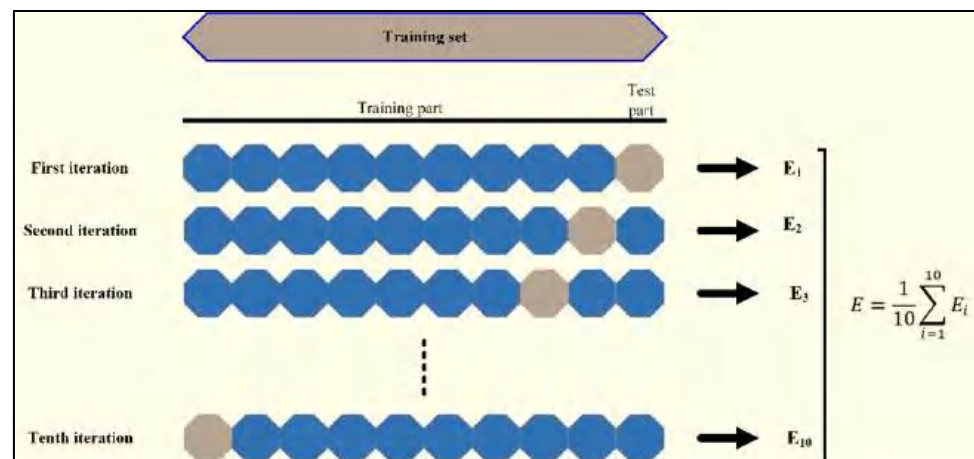


Figure 4. 10-fold cross validation schematic view.

3. Results and Discussion

3.1. Performance Criteria

Various performance criteria were utilized to gauge the performance of the models established in the present study. These metrics included squared correlation (R^2), root mean square error (RMSE), mean absolute error (MAE) and mean absolute percentage error (MAPE). The formulations of these criteria are presented by Equations (14)–(17). These

performance indices have been used by some other researchers as well in predictive and classification studies [32–37].

$$R^2 = 1 - \frac{\sum_{h=1}^N (z_h - \bar{b})^2}{\sum_{h=1}^N (b_h - \bar{b})^2} \tag{14}$$

$$RMSE = \sqrt{\frac{1}{N} \sum_{h=1}^N (z_h - b_h)^2} \tag{15}$$

$$MAE = \frac{1}{N} \sum_{h=1}^N |z_h - b_h| \tag{16}$$

$$MAPE = \frac{1}{N} \sum_{h=1}^N \left| \frac{z_h - b_h}{b_h} \right| \times 100\% \tag{17}$$

where N is the total quantity of samples; z_h and b_h signify predicted and real values; \bar{b} is the mean value of b .

3.2. Input Selection

The BFS was applied to evaluate the significance of inputs for predicting the AOp. In the beginning, the suggested approach examined nine inputs for the final selection of the inputs, and 100 iterations were used to execute the BFS. The authors did not notice any variations in the research results exceeding 100 runs. The findings of the BFS-based technique are presented in Figure 5.

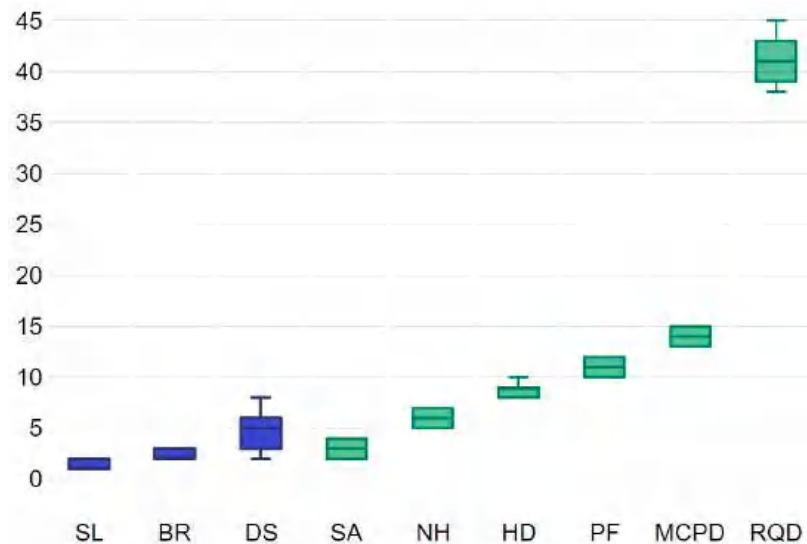


Figure 5. The results of the input selection study on the data.

Box plots in Figure 5 explain the significance of the inputs assessed through BFS. The green plots show those inputs that have more prominent predictability than those indicated by the blue colors. All inputs were classified as significant. Therefore, in developing various input mixtures for the AOp forecast, all nine inputs will be employed. Based on the suggested structure, nine predictive models will be proposed. This approach aims to determine the minimal optimal variable’s collection for overcoming the issues of underfitting and overfitting. Furthermore, the inputs indicated in red in the BFS results possess smaller informational potential compared with shadow traits. Hence, these inputs are eliminated from the final collection. Moreover, the yellow inputs show tentative ones. As a result, no inputs appeared tentative or unimportant.

The RQD, MCPD, and PF inputs were confirmed to be the most significant inputs, graded in the same descending form of value for the data obtained from the site. Following these inputs, the HD placed fourth in significance. These findings confirm that using the three characteristics of blasting improves the effectiveness of AOp predictability. Therefore, this study suggests that prospective scholars use these variables as inputs in their models. This algorithm is strong and can produce an unbiased and firm choice of significant and insignificant inputs from a dataset. Since combining more inputs can induce overfitting issues, the novel BFS's capacity to prioritize inputs in decreasing sequence of values can assist scholars in deciding which inputs apply to the AOp forecast. Hence, dropping unnecessary or less correlated inputs may reduce calculation complications and time linked with enhancing the suggested hyperparameters of the scheme.

3.3. SVR-GO-BFS_n Model Performance

Following recognizing the importance level of the inputs by BFS, an SVR model kernelized with RBF is employed to carry out the predictive analysis. During running the model, γ and C that are pair hyperparameters of SVR are optimized by the GO algorithm. Nine SVR-GO-BFS_n models (SVR-GO-BFS₁ to SVR-GO-BFS₉) are developed based on nine various inputs sets ($n = 1$ set to $n = 9$). The $n = 1$ set comprises just the first most significant input, while the $n = 9$ collection encompasses all nine vital inputs estimated by BFS. To choose among the SVR-GO-BFS_n model structures, this study uses MAPE as the primary criterion. In addition, the RMSE is used as GO's objective function. Prediction of the AOp values is the target of these models.

The AOp database is split into training (80%) and test (20%) sets at random throughout the experiment's run. The training set of data is utilized to develop the forecasting model, while the testing data are utilized to evaluate the predictability. Importantly, all generated models receive the same training and test sets on a regular basis. Following building numerous models, it has been evidenced that as the number of iterations rises, the model computation time grows. Small population sizes, on the other hand, generate inconsistent fitness values. Therefore, multiple groups of 50, 100, 150, 200, and 250 population numbers in the optimization model were chosen for the purposes of the current study, and their iteration curves were made based on the right fitness values.

Concerning the GO, the number of search agents was set as 40, as well as the largest iteration number of developed models was set as 100. Regarding SVR, the lower and upper bounds of γ and C were set to (0.01–50) and (0.01, 100). All inputs were normalized between zero and one for the estimation of performance criteria, as well as to decrease the calculation complications during searching for hyperparameters of models. Table 3 presents the best predictive fulfilment of the models developed in the current investigation. This table corresponds to SVR hyperparameter values optimized using GO and the smallest optimal collection of inputs. It can be seen that the model with seven inputs (SVR-GO-BFS₇) achieved the highest accuracy and lowest errors. Figure 6 depicts the outcomes of fitness values for SVR-GO-BFS₇ models in forecasting AOp, along with their iteration counts. Furthermore, to minimize the GO's cost function, the RMSE was chosen. This figure shows that the best population size for SVR-GO-BFS₇ is 200. Sizable errors in prediction are improbable to have occurred. Only average alternations were adopted up to iteration number 65; following this, no significant difference in the RMSE values was indicated. It should be noted that all models achieved the minimum RMSE in less than 70 iterations, which shows the power of GO in optimizing the SVR hyperparameters.

It was not required to have the full collection of significant inputs ($n = nine$) to obtain the most reliable predictive performance. Therefore, the authors can draw the conclusion that the effectiveness of SVR-GO-BFS_n in forecasting the AOp is excellent.

The performance of the SVR-GO-BFS_n models based on various mixtures of significant inputs ($n = 1$ set to $n = 9$ sets) is presented in Figure 7 through the stacked area. In Figure 7, it is obvious that the MAPE, RMSE, and MAE estimates obtained from all the SVR-GO-BFS_n models were essentially lower than 2.6953, 3.6637, and 3.3083, sequentially, even if only

one input was added to the model. For instance, the achieved values of MAPE, RMSE, and MAE were 2.6953, 3.2241, and 2.8476, sequentially, if just one input is employed for the model creation. Furthermore, the SVR-GO-BFS₂ model is associated with the poorest performance. This model achieved 0.9209 for R², 36637 for RMSE, 3.1152 for MAPE, and 3.3083 for MAE. Instead, the developed models become more precise through employing the three most significant inputs and beyond. For instance, the acquired RMSE varied from 2.1659 to 1.6092 for the models from SVR-GO-BFS₃ to SVR-GO-BFS₉. Therefore, the authors can assume that employing just the three most significant inputs from the dataset picked and rated by BFS would produce strong prediction outcomes. Moreover, comparable issues were found with R², MAPE, and MAE. The scatter plots of the real and predicted AOP values made by the developed models show this trend in Figure 8.

Table 3. Best model performance.

Performance Criterion	
Best model	SVR-GO-BFS ₇
Inputs No.	7
R ²	0.9826
RMSE	1.3315
MAE	1.2108
MAPE	1.1633
C	9.3119
γ	0.6363

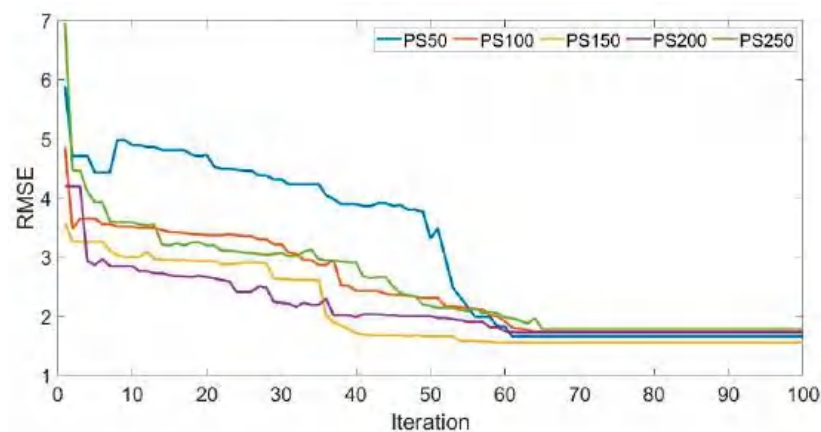


Figure 6. SVR-GO-BFS₇ optimization model for different population sizes (PSs).

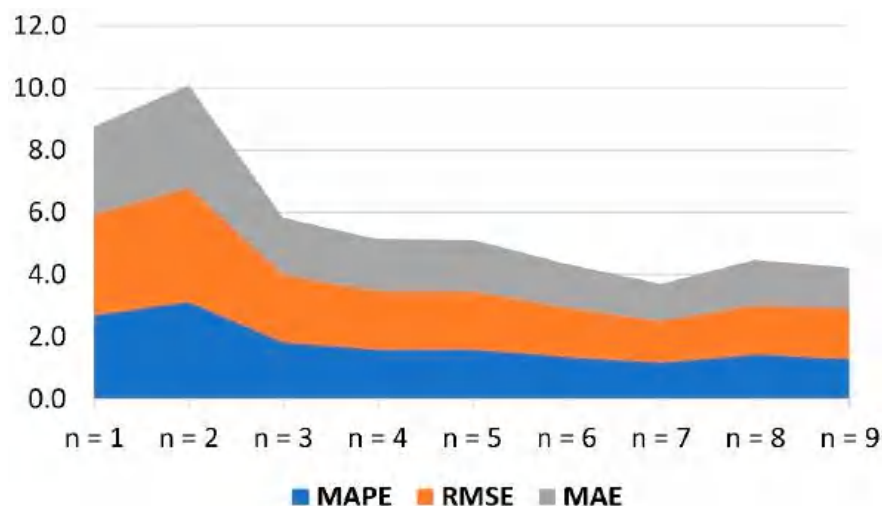


Figure 7. Cont.



Figure 7. Performance of the SVR-GO-BFS_n models with various inputs.

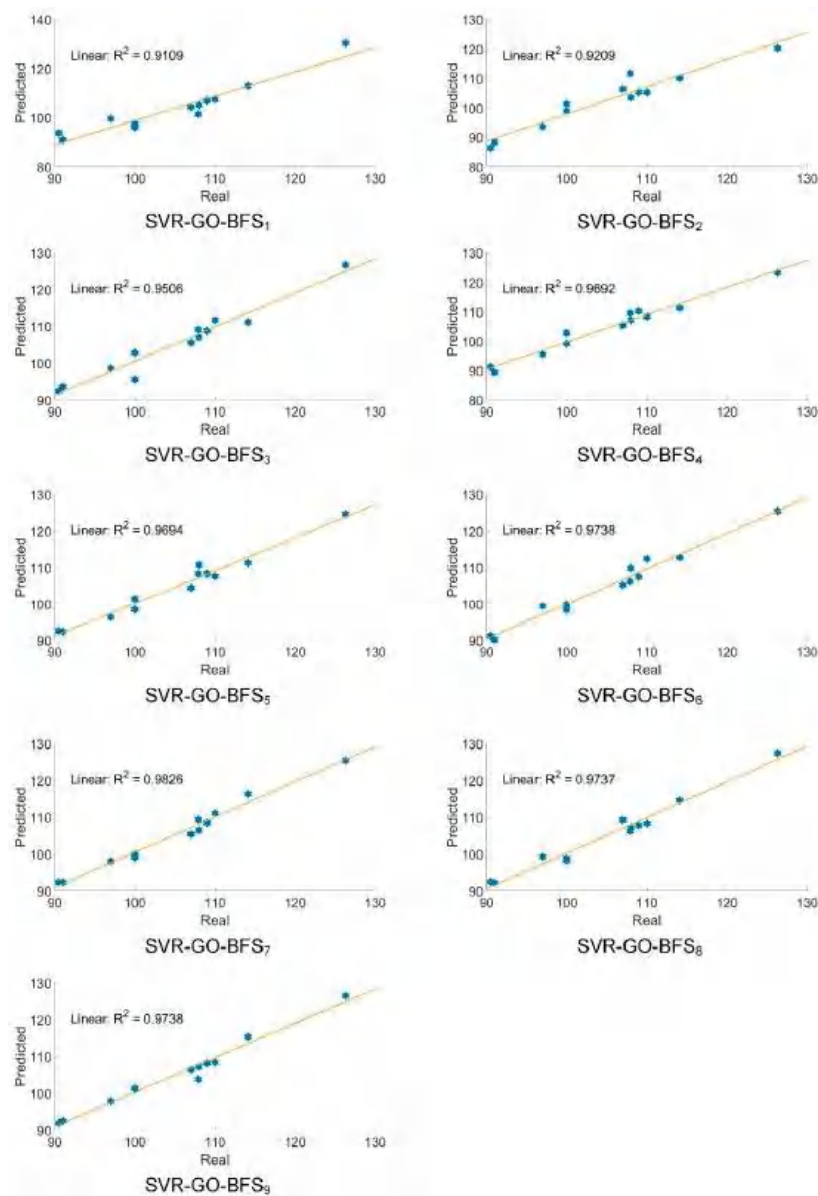


Figure 8. Real and predicted AOP values by various developed models, SVR-GO-BFS₇ is the best model.

3.4. Performance Comparison

The authors compared the performance of the developed SVR-GO-BFS₇ model with a single SVR model. All nine variables were used to train the single SVR model. The outcomes of this comparison are presented in Table 4. The SVR-GO-BFS₇ model achieved a notably lower MAPE value compared with the single SVR model. The value of MAPE improved by about 62% when the newly developed model was applied to the data. Furthermore, R² was enhanced by approximately 19%. RMSE and MAE were improved by 68.09% and 62.26%, respectively. Hence, for predictive precision, it can be assumed that SVR-GO-BFS₇ particularly beats the single SVR model for AOp forecasting in the selected granite quarry sites in Malaysia. The principal responsible for enhancing the prediction performance of the SVR-GO-BFS₇ model was SVR's parameter optimization by GO and employing BFS for input choice.

Table 4. Performance comparison between single SVR and SVR-GO-BFS₇.

Performance Criterion	SVR-GO-BFS ₇	Single SVR
R ²	0.9826	0.8245
RMSE	1.3315	4.1728
MAE	1.2108	3.2083
MAPE	1.1633	3.0527

This study also compared the achievement of the developed model with some well-known ML models, including Random Forest (RF), Artificial Neural Networks (ANN), Extreme Gradient Boosting Tree (XGBT), and Classification and Regression Trees (CART). Nevertheless, BFS and GO were not hybridized with these models. All models were trained using the full set of inputs (nine inputs). For XGBT, Eta and Lambada were set as 0.3, 1.0, and its objective function was reg:linear. For CART, the maximum tree depth was 7. Concerning ANN, a backpropagation procedure by the Levenberg–Marquardt training algorithm was employed for its optimization. Additionally, the ANN structure included a single hidden layer and 11 hidden nodes. Furthermore, the authors used a sigmoid activation function while the value of the learning rate was 0.2. Table 5 shows how these models compare to SVR-GO-BFS₇ in terms of how well they work.

Table 5. Comparison between the SVR-GO-BFS₇ and other models.

Performance Criterion	SVR-GO-BFS ₇	ANN	CART	RF	XGBT
R ²	0.9826	0.9767	0.5192	0.8874	0.9342
RMSE	1.3315	1.7206	7.0700	3.3300	2.5632
MAE	1.2108	1.4767	5.3168	2.9808	2.3600
MAPE	1.1633	1.3927	5.2427	2.8692	2.3240

The RMSE, MAPE, and MAE values of the developed SVR-GO-BFS₇ model were less than all benchmark models. Among benchmark models, ANN showed a better performance in terms of both accuracy and errors. Instead, the worst model was CART, which achieved the lowest accuracy and highest errors. While the XGBT obtained better accuracy than the RF, the RF outperformed the XGBT in terms of errors. The results of this comparison confirmed that the developed SVR-GO-BFS₇ was statistically better than the models developed for comparison. For a better explanation, the predictive effectiveness of the developed BA-GO-BFS₇ is demonstrated in Figure 9. The figure showed that the predicted data effectively track the real data with insignificant differences. The results of the performance criteria in Table 4 showed that the values of the error metrics were comparably low. The results of AOp predictions by SVR-GO-BFS₇ and other ML models are presented in Figure 10. The advantage of the developed SVR-GO-BFS₇ model was justified through the outcomes of the comparative evaluation. So, the importance of combining methods (SVR, GO, and BFS) is confirmed in the right way.

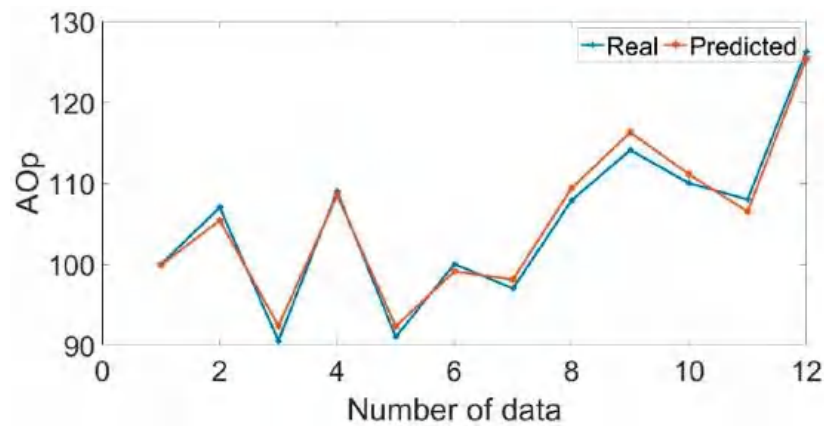


Figure 9. Real and predicted AOp values.

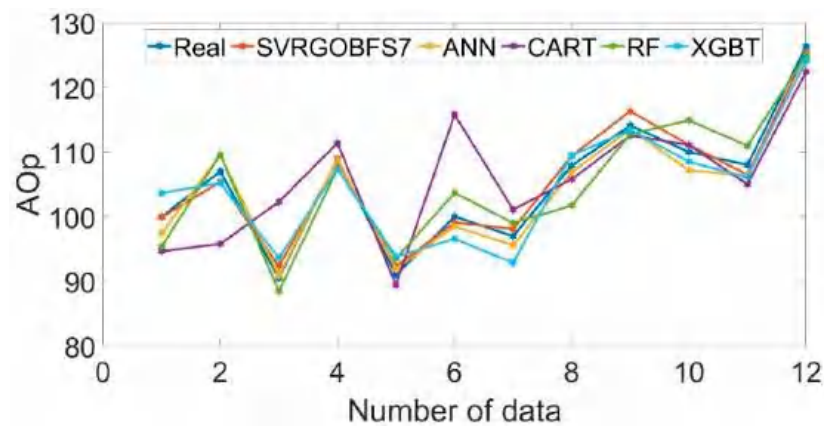


Figure 10. Results of predictions by various models.

3.5. Comparison with Other Optimization Models

In the current section, various examinations were carried out to confirm that the synthesis of BFS, SVR, and GO produces the most reliable returns. This experiment engaged three optimizers to obtain the hyperparameters of SVR. One of these techniques was PSO, which explains the regular optimization performance for adjusting the SVR’s hyperparameters. Another method was the Cuckoo Optimization Algorithm (COA), which was broadly employed for fine-tuning the parameters of ML algorithms [38]. The last optimizer was the Neural Network Algorithm (NNA), one of the most advanced optimization techniques [39]. The SVR model was optimized with PSO, COA, and NNA. Seven of the inputs that SVR-GO-BFS_n used were used again when the new optimized models were made.

The precision of the optimized models is presented in Figure 11. The performance results of the tuned SVR models by the optimized techniques are displayed in Table 6. For the granite quarry dataset, the precision of the SVR-GO-BFS₇ model was higher than that of the SVR-PSO-BFS₇, SVR-COA-BFS₇, and SVR-NNA-BFS₇ models. As a result, the capacity of the GO technique to search the SVR’s hyperparameters was more effective than NNA, PSO, and COA. Simply put, the SVR-GO-BFS₇ method achieves high accuracy for AOp forecasting and has the best efficiency and consistency among all basic techniques. Overall, the SVR-GO-BFS₇ technique obtained great precision for AOp prediction and had the greatest performance and cohesion amongst all basic methods. Consequently, in this research, the SVR-GO-BFS_n model is used for prediction, and further studies are suggested to utilize this method in other investigations based on the authors’ concerns.

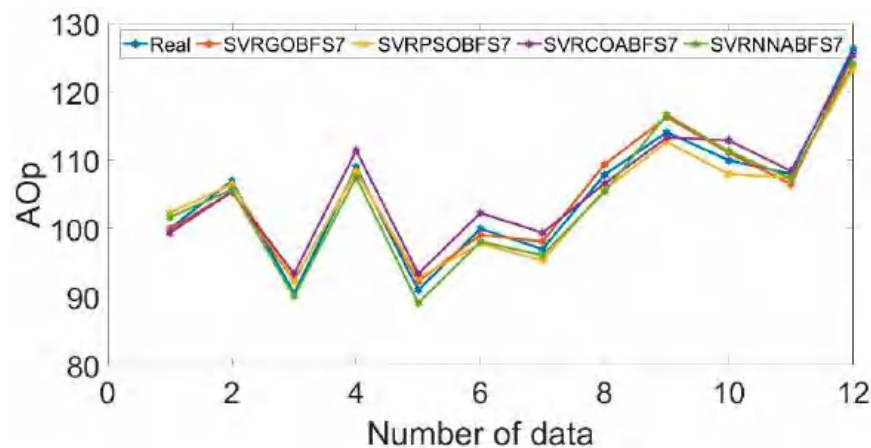


Figure 11. The outcomes of the developed model with various optimization methods.

Table 6. Comparison of various optimizers for AOp prediction.

Performance Criterion	SVR-GO-BFS ₇	SVR-PSO-BFS ₇	SVR-COA-BFS ₇	SVR-NNA-BFS ₇
R ²	0.9826	0.9796	0.9729	0.9747
RMSE	1.3315	1.8188	1.9547	1.6929
MAE	1.2108	1.6675	1.7475	1.5625
MAPE	1.1633	1.5997	1.7170	1.4740

In comparison with the previous work, the model developed in this study showed better performance. For instance, Hajihassani et al. [27] applied an ANN-PSO to the same inputs, and they did not utilize any input selection technique and only used their model for AOp estimation. The best R² that they achieved was 0.8836. The SVR-GA-BFS₇ model achieved a better R² while using a fewer number of inputs, which decreased the model complexity. The authors of this study believe that the current study and its process and results are able to add value to the available literature.

4. Conclusions and Future Works

Prediction of AOp values is vital because of their negative impacts on people and construction near the blasting zone. In this paper, a hybrid learning model, the SVR-GO-BFS_n, was developed to forecast the AOp values. A summary of the significant findings of this study is provided below:

- In incorporation with SVR, the BFS algorithm produced excellent forecasts on the dataset of this research concern.
- The GO algorithm was confirmed to efficiently function in exploring the optimal conditions of SVR's hyperparameters and achieving an accurate AOp prediction.
- The reason for this efficacy was that this algorithm possesses a compelling ability for finding and controlling the optimal answers to multi-scale issues.
- The developed model outperformed other established models in this study, including single SVR, CART, RF, ANN, and XGBT. Hence, the SVR-GO-BFS_n can be a useful procedure for forecasting AOp values. Among the various optimizers used in this study, the GO optimizer outperformed the alternative ones, i.e., PSO, NNA, and COA.

As shown by the findings of the present study, the performance of the model developed was better than others. This approach is usable by other studies in different domains. Nevertheless, the regression issue is to be resolved by the developed model and is confined to the AOp forecast. Moreover, it is vital to note that the outcomes of this model are limited to quarries with similar characteristics. Although GO is a powerful optimizer, this study only used it to tune the SVR hyperparameters. We used only one dataset, which may be a limitation of this study. Future studies should use more datasets to test our proposed model.

Following this discussion, the authors suggest that further investigations could be carried out. Further studies should implement this developed method to deal with other issues in the blasting and mining analysis. Supplementary analysis of AOp predictions in various areas is required to assure the generalization of the outcomes of the developed system. The employment of GO as an input selection technique should be examined, and, subsequently, its efficiency should be analyzed against the BFS.

Author Contributions: L.C. Methodology, Software, Formal analysis, Writing—original draft. P.G.A. Methodology, Writing—review and editing, Supervision. M.Z.T. Writing—review and editing, Supervision. D.J.A., Conceptualization, Software, Formal analysis, Writing—review and editing, Supervision. D.V.U. Writing—review and editing. M.Y., Conceptualization, Writing—review and editing. All authors have read and agreed to the published version of the manuscript.

Funding: Supported by the Science and Technology Research Program of Chongqing Municipal Education Commission (Grant No. KJQN202103415).

Institutional Review Board Statement: Not applicable.

Informed Consent Statement: Not applicable.

Data Availability Statement: The data is available from the corresponding author upon reasonable request.

Conflicts of Interest: The authors declare no conflict of interest.

References

- Hagan, T.N. Rock breakage by explosives. In *Gasdynamics of Explosions and Reactive Systems*; Elsevier: Amsterdam, The Netherlands, 1980; pp. 329–340.
- Harandizadeh, H.; Armaghani, D.J. Prediction of air-overpressure induced by blasting using an ANFIS-PNN model optimized by GA. *Appl. Soft Comput.* **2020**, *99*, 106904. [CrossRef]
- Khandelwal, M.; Kankar, P. Prediction of blast-induced air overpressure using support vector machine. *Arab. J. Geosci.* **2011**, *4*, 427–433. [CrossRef]
- Konya CJ, W.E. *Surface Blast Design*; Prentice Hall: Englewood Cliffs, NJ, USA, 1990.
- Kuzu, C.; Fisne, A.; Ercelebi, S.G. Operational and geological parameters in the assessing blast induced airblast-overpressure in quarries. *Appl. Acoust.* **2009**, *70*, 404–411. [CrossRef]
- Wu, C.; Hao, H. Modeling of simultaneous ground shock and airblast pressure on nearby structures from surface explosions. *Int. J. Impact Eng.* **2005**, *31*, 699–717. [CrossRef]
- Rodríguez, R.; Torano, J.; Menéndez, M. Prediction of the airblast wave effects near a tunnel advanced by drilling and blasting. *Tunn. Undergr. Space. Technol.* **2007**, *22*, 241–251. [CrossRef]
- Rodríguez, R.; Lombardía, C.; Torno, S. Prediction of the air wave due to blasting inside tunnels: Approximation to a ‘phonometric curve’. *Tunn. Undergr. Space. Technol.* **2010**, *25*, 483–489. [CrossRef]
- Hosseini, S.; Monjezi, M.; Bakhtavar, E.; Mousavi, A. Prediction of Dust Emission Due to Open Pit Mine Blasting Using a Hybrid Artificial Neural Network. *Nat. Resour. Res.* **2021**, *30*, 4773–4788. [CrossRef]
- Khandelwal, M.; Singh, T. Evaluation of blast-induced ground vibration predictors. *Soil Dyn. Earthq. Eng.* **2007**, *27*, 116–125. [CrossRef]
- Yang, H.; Song, K.; Zhou, J. Automated Recognition Model of Geomechanical Information Based on Operational Data of Tunneling Boring Machines. *Rock Mech. Rock Eng.* **2022**, *55*, 1499–1516. [CrossRef]
- Yang, H.; Wang, Z.; Song, K. A new hybrid grey wolf optimizer-feature weighted-multiple kernel-support vector regression technique to predict TBM performance. *Eng. Comput.* **2020**, *38*, 2469–2485. [CrossRef]
- Kardani, N.; Bardhan, A.; Samui, P.; Nazem, M.; Asteris, P.G.; Zhou, A. Predicting the thermal conductivity of soils using integrated approach of ANN and PSO with adaptive and time-varying acceleration coefficients. *Int. J. Therm. Sci.* **2022**, *173*, 107427. [CrossRef]
- Asteris, P.G.; Rizal, F.I.M.; Koopialipoor, M.; Roussis, P.C.; Ferentinou, M.; Armaghani, D.J.; Gordan, B. Slope Stability Classification under Seismic Conditions Using Several Tree-Based Intelligent Techniques. *Appl. Sci.* **2022**, *12*, 1753. [CrossRef]
- Barkhordari, M.; Armaghani, D.; Asteris, P. Structural Damage Identification Using Ensemble Deep Convolutional Neural Network Models. *Comput. Model. Eng. Sci.* **2022**. [CrossRef]
- Asteris, P.G.; Lourenço, P.B.; Roussis, P.C.; Adami, C.E.; Armaghani, D.J.; Cavaleri, L.; Chalioris, C.E.; Hajihassani, M.; Lemonis, M.E.; Mohammed, A.S. Revealing the nature of metakaolin-based concrete materials using artificial intelligence techniques. *Constr. Build. Mater.* **2022**, *322*, 126500. [CrossRef]
- Zhou, J.; Qiu, Y.; Khandelwal, M.; Zhu, S.; Zhang, X. Developing a hybrid model of Jaya algorithm-based extreme gradient boosting machine to estimate blast-induced ground vibrations. *Int. J. Rock Mech. Min. Sci.* **2021**, *145*, 104856. [CrossRef]

18. Zhou, J.; Dai, Y.; Khandelwal, M.; Monjezi, M.; Yu, Z.; Qiu, Y. Performance of Hybrid SCA-RF and HHO-RF Models for Predicting Backbreak in Open-Pit Mine Blasting Operations. *Nat. Resour. Res.* **2021**, *30*, 4753–4771. [CrossRef]
19. Zhou, J.; Chen, C.; Wang, M.; Khandelwal, M. Proposing a novel comprehensive evaluation model for the coal burst liability in underground coal mines considering uncertainty factors. *Int. J. Min. Sci. Technol.* **2021**, *31*, 799–812. [CrossRef]
20. Zhang, R.; Li, Y.; Gui, Y.; Zhou, J. Prediction of blasting induced air-overpressure using a radial basis function network with an additional hidden layer. *Appl. Soft Comput.* **2022**, *127*, 109343. [CrossRef]
21. Zeng, J.; Jamei, M.; Nait Amar, M.; Hasanipanah, M.; Bayat, P. A novel solution for simulating air overpressure resulting from blasting using an efficient cascaded forward neural network. *Eng. Comput.* **2022**, *38*, 2069–2081. [CrossRef]
22. Hosseini, S.; Poormirzaee, R.; Hajihassani, M. Application of reliability-based back-propagation causality-weighted neural networks to estimate air-overpressure due to mine blasting. *Eng. Appl. Artif. Intell.* **2022**, *115*, 105281. [CrossRef]
23. Hasanipanah, M.; Jahed Armaghani, D.; Khamesi, H.; Bakhshandeh Amnieh, H.; Ghoraba, S. Several non-linear models in estimating air-overpressure resulting from mine blasting. *Eng. Comput.* **2016**, *32*, 441–455. [CrossRef]
24. Murlidhar, B.; Bejarbaneh, B.; Armaghani, D.; Mohammed, A.; Mohamad, E. Application of Tree-Based Predictive Models to Forecast Air Overpressure Induced by Mine Blasting. *Nat. Resour. Res.* **2020**, *30*, 1865–1887. [CrossRef]
25. Hasanipanah, M.; Shahnazar, A.; Bakhshandeh Amnieh, H.; Jahed Armaghani, D. Prediction of air-overpressure caused by mine blasting using a new hybrid PSO–SVR model. *Eng. Comput.* **2017**, *33*, 23–31. [CrossRef]
26. He, Z.; Armaghani, D.J.; Masoumnezhad, M.; Khandelwal, M.; Zhou, J.; Murlidhar, B.R. A Combination of Expert-Based System and Advanced Decision-Tree Algorithms to Predict Air—Overpressure Resulting from Quarry Blasting. *Nat. Resour. Res.* **2021**, *30*, 1889–1903. [CrossRef]
27. Hajihassani, M.; Jahed Armaghani, D.; Sohaei, H.; Tonnizam Mohamad, E.; Marto, A. Prediction of airblast-overpressure induced by blasting using a hybrid artificial neural network and particle swarm optimization. *Appl. Acoust.* **2014**, *80*, 57–67. [CrossRef]
28. Vapnik, V. *The Nature of Statistical Learning Theory*; Springer Science & Business Media: Berlin, Germany, 2013; ISBN 1475732643.
29. Dreyfus, G. *Neural Networks: Methodology and Applications*; Springer: Berlin/Heidelberg, Germany, 2005.
30. Saremi, S.; Mirjalili, S.; Lewis, A. Grasshopper optimisation algorithm: Theory and application. *Adv. Eng. Softw.* **2017**, *105*, 30–47. [CrossRef]
31. Kursu, M.B.; Rudnicki, W.R. Feature selection with the Boruta package. *J. Stat. Softw.* **2010**, *36*, 1–13. [CrossRef]
32. Lu, S.; Koopialipour, M.; Asteris, P.G.; Bahri, M.; Armaghani, D.J. A Novel Feature Selection Approach Based on Tree Models for Evaluating the Punching Shear Capacity of Steel Fiber-Reinforced Concrete Flat Slabs. *Materials* **2020**, *13*, 3902. [CrossRef]
33. Asteris, P.G.; Argyropoulos, I.; Cavaleri, L.; Rodrigues, H.; Varum, H.; Thomas, J.; Lourenço, P.B. Masonry compressive strength prediction using artificial neural networks. In Proceedings of the International Conference on Transdisciplinary Multispectral Modeling and Cooperation for the Preservation of Cultural Heritage, Athens, Greece, 10–13 October 2018; pp. 200–224.
34. Huang, J.; Asteris, P.; Pasha, S.; Mohammed, A.; Hasanipanah, M. A new auto-tuning model for predicting the rock fragmentation: A cat swarm optimization algorithm. *Eng. Comput.* **2020**, *38*, 2209–2220. [CrossRef]
35. Asteris, P.G.; Gavriilaki, E.; Touloumenidou, T.; Koravou, E.; Koutra, M.; Papayanni, P.G.; Pouleres, A.; Karali, V.; Lemonis, M.E.; Mamou, A. Genetic prediction of ICU hospitalization and mortality in COVID-19 patients using artificial neural networks. *J. Cell. Mol. Med.* **2022**, *26*, 1445–1455. [CrossRef]
36. Asteris, P.G.; Douvika, M.G.; Karamani, C.A.; Skentou, A.D.; Chlichlia, K.; Cavaleri, L.; Daras, T.; Armaghani, D.J.; Zaoutis, T.E. A novel heuristic algorithm for the modeling and risk assessment of the COVID-19 pandemic phenomenon. *Comput. Model. Eng. Sci.* **2020**, *125*, 815–828. [CrossRef]
37. Psyllaki, P.; Stamatiou, K.; Iliadis, I.; Mourlas, A.; Asteris, P.; Vaxevanidis, N. Surface treatment of tool steels against galling failure. In *Proceedings of the MATEC Web of Conferences*; EDP Sciences: Les Ulis, France, 2018; Volume 188, p. 4024.
38. Rajabioun, R. Cuckoo optimization algorithm. *Appl. Soft Comput.* **2011**, *11*, 5508–5518. [CrossRef]
39. Sadollah, A.; Sayyaadi, H.; Yadav, A. A dynamic metaheuristic optimization model inspired by biological nervous systems: Neural network algorithm. *Appl. Soft Comput.* **2018**, *71*, 747–782. [CrossRef]

Article

Experimental and Empirical Study for Prediction of Blast Loads

Anselmo Filice ^{1,2,*} , Miroslav Mynarz ³ and Raffaele Zinno ² 

¹ Department of Computer Science, Modeling, Electronics and Systems Engineering, DIMES, University of Calabria, 87036 Arcavacata, Italy

² Department of Environmental Engineering, DIAM, University of Calabria, 87036 Arcavacata, Italy; raffaele.zinno@unical.it

³ Faculty of Safety Engineering, VSB, Technical University of Ostrava, 70833 Ostrava, Czech Republic; miroslav.mynarz@vsb.cz

* Correspondence: anselmo.filice@unical.it; Tel.: +39-333-1371258

Abstract: This paper presents the issue of determining the blast load on an engineering structure. In cases of industrial accidents or terrorist attacks, in many cases it is necessary to determine the necessary explosion parameters to determine the response of the structure, preferably in a simple and time-saving manner. In such a way, the empirical relationships can be used to estimate the selected parameters of the explosion load. Many empirical relationships have been derived in the past, but not all are suitable for different types of explosions. This article compares and validates experimentally determined selected explosion parameters for the chosen explosive with empirical relationships. For comparison, three already verified and frequently used calculation procedures (Kingery, Kinney, Henrych) and one newly derived procedure (PECH) were used. As part of the experimental measurements, blast wave explosion parameters for small charges were determined for near-field explosions. The general-purpose plastic explosive Semtex 10-SE was used for the experiments. The results of the comparative study presented in this article demonstrate the importance of taking these procedures into account for a reliable determination of the effects of blast actions on buildings.

Keywords: blast loads; engineering structures; prediction; validation; Semtex

Citation: Filice, A.; Mynarz, M.; Zinno, R. Experimental and Empirical Study for Prediction of Blast Loads. *Appl. Sci.* **2022**, *12*, 2691. <https://doi.org/10.3390/app12052691>

Academic Editors: Lina M. López, Ricardo Castedo and Anastasio P. Santos

Received: 30 January 2022

Accepted: 2 March 2022

Published: 4 March 2022

Publisher's Note: MDPI stays neutral with regard to jurisdictional claims in published maps and institutional affiliations.



Copyright: © 2022 by the authors. Licensee MDPI, Basel, Switzerland. This article is an open access article distributed under the terms and conditions of the Creative Commons Attribution (CC BY) license (<https://creativecommons.org/licenses/by/4.0/>).

1. Introduction

The effects of explosions were studied more extensively after World War II, mainly because many explosives were developed during this period and are still in use today. For many explosives, demands are made for high stability, safety and effectiveness. Most aromatic nitroates and a much smaller number of nitric acid esters and nitroamines meet these criteria. The most commonly used explosive is the well-known Trinitrotoluene (tritol or TNT).

To estimate or calculate the response of an object or structure to the effects of an explosion, it is necessary to know the explosion parameters. Of these parameters needed to determine the response, the most important are usually the peak overpressure, the positive phase duration and the positive phase impulse. The positive phase impulse can usually be calculated from the blast curve and is dependent on the overpressure and positive duration. Knowledge of the blast parameters then defines the basic load of buildings or structures. A variety of methods can be used to determine explosion parameters. These can be based on empirical (or analytical), semi-empirical or numerical methods. Empirical methods are essentially correlations with experimental data. Most of these approaches are limited by the range of experiments carried out. The accuracy of all empirical correlations decreases with distance to the source of the explosion. Semi-empirical methods are based on simplified models of physical phenomena. They try to use the essential physical processes in a simplified way. These methods rely on extensive experimental data. Their predictive accuracy is generally better than that of empirical methods.

Numerical methods are based on mathematical equations that describe the basic laws of the phenomena being solved. These methods consider the conservation of mass, momentum and energy, or the physical behaviour of materials by means of constitutive relations. It is the empirical methods in the initial assessment of objects in the context of prevention or severe consequence assessment that can be a very useful tool. When rapid estimates of explosion parameters are needed, often for a large number of objects, these methods are essential. For a more in-depth analysis of the load of a building or to refine the initial load values of a structure, numerical methods are much more suitable.

During the second half of the 20th century, a considerable number of experimental and theoretical studies were conducted to understand the effects of blast on buildings and structures [1–5]. The aim was first to study the behaviour of air blast waves including the determination of their characteristics and then to investigate the dominant factors influencing the incident waves. Another objective was to investigate the response of the building structure to blast load [6,7], based on the analysis of several experimental data, which presented the formulae to compute peak positive overpressure, positive phase duration and positive phase impulse [2,4], and utilised both experimental and theoretical means to obtain the parameters of the blast wave such as overpressure, positive phase duration, blast wave arrival time and positive phase impulse [1]. In 1984, Kingery and Bulmash presented the parameters for air burst in terms of high order polynomials [4,8] and presented the same results as were produced by Kingery, in terms of simplified polynomials functions.

The use of empirical laws has been extensively studied and has been applied in various recommendations, mostly proposed by military authorities. In particular, the two most commonly used empirical models are based upon different but related studies of the U.S. Army Corps of Engineers (USACE): the document [9], containing the model CONWEP, and the Technical Manual TM5-1300 [10], completed by successive documents [11]. In 2013, the Joint Research Centre of the European Union produced a Technical Report [12], substantially referring to these two last documents and to another Technical Report of the U.S. Army [4]. In [12], all the empirical laws of [10] are reproduced using the International System of Units. Most available publications concerning the effects of an explosion on a civil structure regard reinforced concrete structures, and usually the geometries considered are really simple, normally a squared building [13–18], or in some cases bridges, e.g., [19]. Analyses of complex and structurally advanced objects are not published to any great extent. These analyses require the use of sophisticated computational software, usually based on CFD or FEM methods. These methods require a high level of computational expertise and are also very time consuming, both in terms of model building and computational time.

2. Materials and Methods

2.1. Ideal Blast Wave Characteristics

An explosion is a physical phenomenon in which there is a sudden, very rapid release of energy. The phenomenon lasts only some milliseconds, and it results in the production of very high temperatures and pressures. During detonation the hot gases that are produced expand in order to occupy the available space, leading to wave-type propagation through space that is transmitted spherically through an unbounded surrounding medium. Along with the produced gases, the air around the blast (for air blasts) also expands and its molecules pile-up, resulting in what is known as a blast wave and shock front. The blast wave contains a large part of the energy that was released during detonation and moves faster than the speed of sound [20].

Figure 1 illustrates the idealised profile of the pressure in relation to time for the case of a free air blast wave, which reaches a point at a certain distance from the detonation. The pressure surrounding the element is initially equal to the ambient pressure P_0 , and it undergoes an instantaneous increase to a peak pressure P_{S0} at the arrival time t_A , when the shock front reaches that point. The time needed for the pressure to reach its peak value is very small and for design purposes it is assumed to be equal to zero. The peak pressure

P_{S0} is also known as side-on overpressure. The peak overpressure $P_{S0} - P_0$ is marked as P_{ti} in the following sections. The value of the peak overpressure as well as the velocity of propagation of the shock wave decrease with increasing distance from the detonation centre. After its peak value, the pressure decreases with an exponential rate until it reaches the ambient pressure at $t_A + t_0$, where t_0 is called the positive phase duration. After the positive phase of the pressure–time diagram, the pressure becomes smaller (referred to as negative) than the ambient value, and finally returns to it. The negative phase is longer than the positive one, its minimum pressure value is denoted as P_{S0}^- and its duration as t_0^- . During this phase the structures are subjected to suction forces, which is the reason why sometimes during blast loading glass fragments from failures of facades are found outside a building instead of in its interior. This specific type of failure is usually due to a primary failure of the glass filling by the positive phase, or a situation may occur where the negative phase has a significantly higher negative impulse value i_s^- [21].

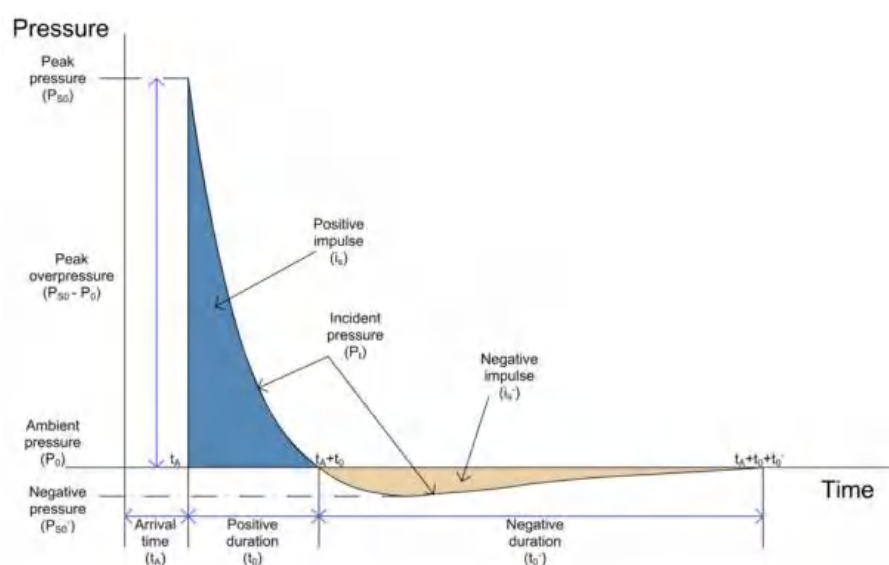


Figure 1. Ideal blast wave's pressure time course.

2.2. Positive Phase/Shock Wave

The positive (expanding) phase of a shock wave is created when the very hot expanding gases produced by the detonation compress the surrounding air. These compressed layers of air are sometimes visible as white, rapidly expanding rings called a shock front. The width of the shock front is only very small and represents that part of the atmosphere which is compressed just before it sets itself in motion and thus becomes part of the positive or expanding phase of a shock wave. If a strong shock front hits a solid obstacle, it is reflected or passes through (when the obstacle is destroyed), but its energy is reduced [22].

2.3. Experiments

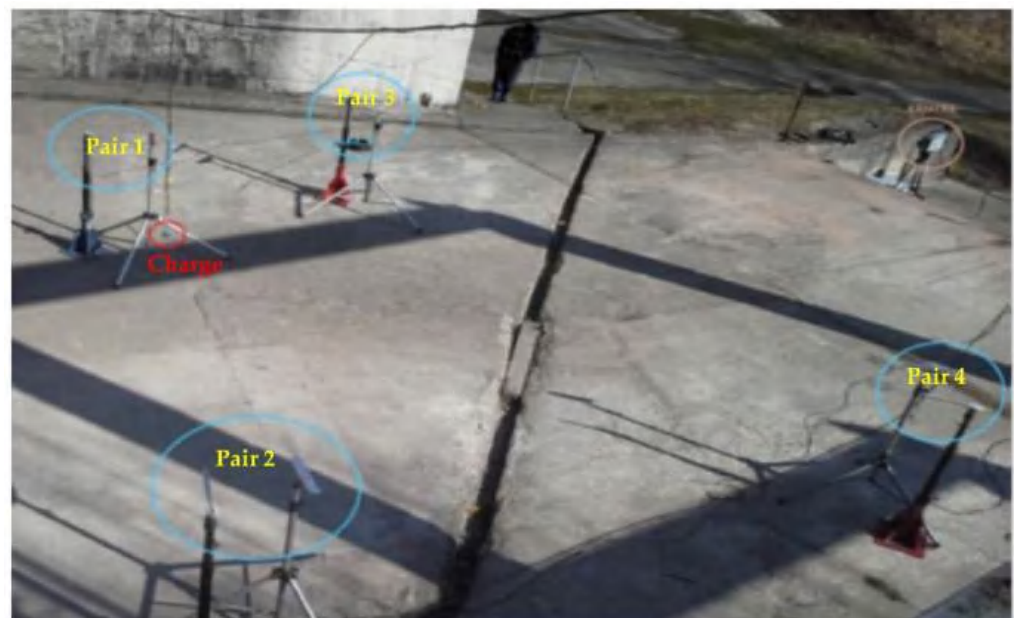
A set of 20 tests was made in the experiments carried out, with five measurements (repeated trials) for each charge. During the measurements, the propagation of the shock wave was recorded, and the individual explosive parameters were evaluated based on the observed propagations. These were mainly peak overpressure and positive phase duration. Charges of 100, 200, 300 and 400 g were used in the experiments. The charges were placed at a height of 1.25 m above the ground surface (terrain). With respect to the air shock wave, this is a hemispherical blast, which occurs when the charge is placed on or near the ground surface.

To prevent the shock wave from being affected (e.g., by obstacles), the charge was suspended. The ignition coil was attached to the charge along the suspension (from above). The atmospheric conditions during the experiments carried out are shown in Table 1.

Table 1. The atmospheric conditions during the experiments.

Temperature (°C)	Air Density (kg/m ³)	Ambient Pressure (kPa)	Relative Air Humidity (%)	Height above Sea Level (m)	Sound Speed (m/s)
15	1.225	101.385	55	415	340

The recording of the blast wave was carried out using two types of transducers. PCB Piezotronics type 113B28 transducers in pencil probe or knife probe design were used. The transducers have a measuring range of 344.7 kPa, rise time less than 1 μ s and natural frequency greater than 500 kHz. Pressure transducers were arranged in pairs (pencil and knife probes) around the charge at predetermined distances so as not to interfere with the measurements of the other pairs. The measurement distances were set at 2, 3, 4 and 5 m. The transducers were placed at the same height above the ground as the charge, i.e., 1.25 m. The arrangement of the pairs of transducers and their distances are presented in Figure 2 (the pairs of transducers are marked as pair). The positions of the suspended charge and the HS camera are also seen in the figure.

**Figure 2.** Arrangement of charges and measuring equipment.

2.4. The Explosive Used

The explosive used in the experiments was labelled Semtex 10-SE. Semtex 10-SE is a plastic, industrial waterproof white explosive that is classified as a special purpose explosive. This type of Semtex contains a non-explosive plasticizer. Highly explosive pentrite (PETN) is its main and effective component. It is supplied in a leaf charge form. It is mainly used for blast hardening of metallic materials. Selected parameters of the explosive are specified in Table 2.

Table 2. Selected properties of explosive Semtex 10-SE.

Detonation Velocity (m/s)	Density (g/cm ³)	Heat of Combustion (kJ/kg)	Temperature of Detonation (°C)	Gas Volume (dm ³ /kg)	Oxygen Balance (% O ₂)	Brisance by Hess (mm)
6700	1.45	2709	1975	1100	−62.6	20

The initiation of the charges was carried out with an electric detonator marked 0-ZB-S from the manufacturer Austin Detonator, which is instantaneous with medium resistance to the effects of external sources of electricity. The tube material is copper. The primary charge is quicksilver. The secondary charge of the detonator is 720 mg (PETN). It has a relatively high initiating capability. The Semtex 10-SE charges used were shaped into spheres of 100, 200, 300 and 400 g. The design of the experiment was based on the authors' interest in detecting near-field blast effects. The course of the explosive transformation when using a 300 g charge in defined time periods is presented in Figure 3. In addition, the propagation of the shock wave including the reflection from the ground level (blue line) is shown.

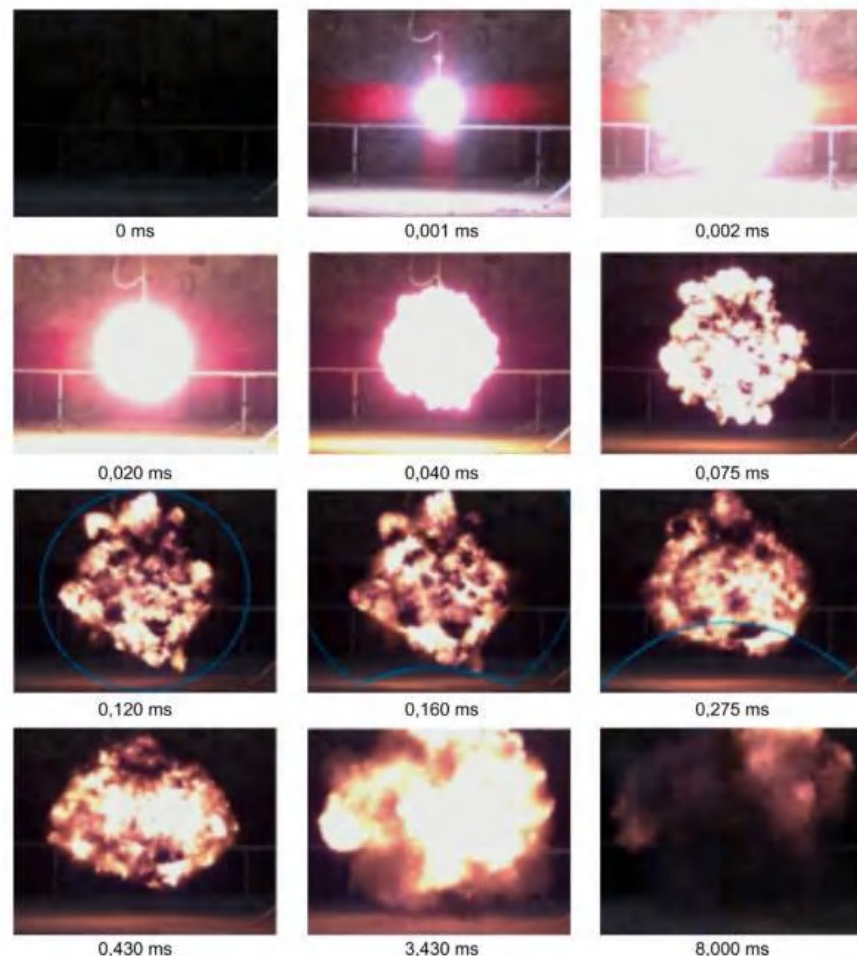


Figure 3. Detonation sequence of a 300 g Semtex 10-SE spherical charge with shock wave propagation marked.

2.5. Predictive Models

This section deals with predictive calculation methods for individual shock wave parameters. Based on many literature sources, there are a large number of computational relationships for individual parameters of blast. To verify their applicability to the case of small near-field charges, the most appropriate ones have been selected.

The concept of reducing the distance is based on the complexity of determining the values of shock wave effects. In the case of one type of explosive, it would be necessary to measure the parameters for all explosive masses at different distances in the experiment, which would be very difficult for large charges, for example. It can therefore be assumed that, at the same reduced distance, the magnitude of a particular shock wave parameter induced by a particular type of explosive is the same for all explosive masses. The reduced distance makes it possible to determine the correlation between the different distances

and masses of explosives and to simplify the possibilities of determining their explosion parameters [22,23].

Thus, the reduced distance is a basic calculation relationship that is used to derive shock wave parameters based on the knowledge of the explosive mass and the distance between the point of exposure to the shock wave and the epicentre of the explosion, as given in Relation (1).

$$Z = \frac{R}{\sqrt[3]{W}}, \tag{1}$$

In this relationship, Z represents the reduced distance in $m \cdot kg^{-1/3}$, R is the actual distance of the charge in m , and W is the mass of the charge, usually the equivalent mass of TNT in kilograms.

2.5.1. Kingery and Bulmash

A single polynomial function is applied for calculations of all shock wave parameters. The calculation of the corresponding parameter consists in the appropriate assignment of the corresponding constants to the specified coefficients. These constants differ from each other according to the type of the parameter to be searched and belong to the corresponding interval of reduced distances. The general notation of the polynomial function according to Kingery and Bulmash is provided by Relation (2) [4].

$$f = e^{A+B \cdot \ln Z + C \cdot (\ln Z)^2 + D \cdot (\ln Z)^3 + E \cdot (\ln Z)^4 + F \cdot (\ln Z)^5 + G \cdot (\ln Z)^6}, \tag{2}$$

In this relation, f is the result variable of the calculation, characterising the parameter being searched for. This relation can be used to calculate the peak overpressure P_{S0} , the arrival time of the shock wave t_A , the duration of the positive phase t_0 , the shock wave velocity v , the positive impulse of the explosion i_s , the reflected pressure p_r and the reflected impulse of the explosion i_r . A, B, C, D, E, F and G are the coefficients to which values from the constants corresponding to the parameter of interest are assigned. The values of these coefficients can be found in Table 3.

Table 3. Simplified Kingery air blast coefficients for blast overpressure.

Z ($m \cdot kg^{-1/3}$)	A	B	C	D	E	F	G
0.2–2.9	7.2106	−2.1069	−0.3229	0.1117	0.0685	0	0
2.9–23.8	7.5938	−3.0523	0.4098	0.0261	−0.0127	0	0
23.8–198.5	6.0536	−1.4066	0	0	0	0	0

This relation is suitable due to its complexity, as many parameters can be determined using it. In addition, it enables calculation for a relatively wide range of reduced distances, especially for peak overpressure (0.2–198.5 $m \cdot kg^{-1/3}$).

2.5.2. Kinney and Graham

The Kinney and Graham relations were chosen as one of the alternative calculation relations, which provide the calculation of the maximum overpressure, impulse and the positive phase duration [1]. The individual relations are not constrained by the range of reduced distances. For comparison purposes, only the relationships for peak overpressure (Relation (3)) and positive phase duration (Relation (4)) are presented:

$$\Delta p_f = P_0 \cdot \frac{808 \cdot \left[1 + \left(\frac{Z}{4.5} \right)^2 \right]}{\sqrt{1 + \left(\frac{Z}{0.048} \right)^2} \cdot \sqrt{1 + \left(\frac{Z}{0.32} \right)^2} \cdot \sqrt{1 + \left(\frac{Z}{1.35} \right)^2}}, \tag{3}$$

$$t_{p+} = \sqrt[3]{W} \cdot \frac{980 \cdot \left[1 + \left(\frac{Z}{0.54}\right)^{10}\right]}{\left[1 + \left(\frac{Z}{0.02}\right)^3\right] \cdot \left[1 + \left(\frac{Z}{0.74}\right)^6\right] \cdot \sqrt{1 + \left(\frac{Z}{6.9}\right)^2}}, \tag{4}$$

2.5.3. Henrych and Major

The calculation relations according to Henrych and Major are not intended for such large ranges of reduced distances as the relations of Kingery and Bulmash, but they provide possibilities of calculation of certain parameters of shock waves for the range of sufficiently low reduced distances, when the Kingery and Bulmash relations in some cases (e.g., peak overpressure) do not allow the calculation [2].

As with the other relationships, these relationships allow the calculation of peak overpressure, positive phase impulse and the positive phase duration. In order to apply each formula, the condition that the reduced distance must fall within a specified interval for which the relation holds, must be met—as it is found in Relations (5)–(7).

$$\Delta p_f = \frac{1.380}{Z} + \frac{0.543}{Z^2} - \frac{0.035}{Z^3} + \frac{0.000613}{Z^4} \text{ for } (0.05 \leq Z \leq 0.3), \tag{5}$$

$$\Delta p_f = \frac{0.607}{Z} - \frac{0.032}{Z^2} + \frac{0.209}{Z^3} \text{ for } (0.3 \leq Z \leq 1.0), \tag{6}$$

$$\Delta p_f = \frac{0.0649}{Z} + \frac{0.397}{Z^2} + \frac{0.322}{Z^3} \text{ for } (1.0 \leq Z \leq 1.0). \tag{7}$$

Only one formula is defined for the positive phase duration, Relation (8).

$$t_{p+} = \sqrt[3]{W} \cdot (0.107 + 0.444 Z + 0.264 Z^2 - 0.129 Z^3 + 0.0335 Z^4) \text{ for } (0.05 < Z \leq 3.0). \tag{8}$$

2.5.4. PECH

The derived PECH calculation relation does not primarily use reduced distance values and is applicable to a wide range of actual distances. The calculation relation allows only the peak overpressure (Relation (9)) to be determined. A formula for the positive phase duration has not yet been derived.

$$\Delta p_f = 0.84 \cdot \left(\frac{W}{R^3}\right)^{\frac{1}{3}} + 2.7 \cdot \left(\frac{W}{R^3}\right)^{\frac{2}{3}} + 7 \cdot \left(\frac{W}{R^3}\right), \tag{9}$$

The above computational relations were used to determine selected explosion parameters (peak overpressure and the positive phase duration of the explosion) during the initiation of charges with varying mass. To verify the applicability of the computational relations, a comparison with experimentally determined values was made. Based on the comparison, it was then possible to deduce the most suitable computational procedure for the required shock wave parameters under the given conditions of the realised experiments.

3. Results

The experimental measurements included five repeated trials for each charge weight. The charge weights were determined in the range of 100 to 400 g. Table 4 presents the values of selected explosion parameters (peak overpressure and positive phase duration) for each charge weight and scaled distance. Since the peak overpressure values from the repeated trials for each charge varied only slightly (only in tenths of kPa), the averaged values are presented. In the case of the positive phase duration values, the variations were quite negligible.

Table 4. Measured peak overpressures and positive phase durations.

Blast Parameters	Charge Weight (g)	Distance (m)			
		2	3	4	5
Peak incident overpressure P_{ti} (kPa)	100	44.1	23.4	14.3	10.5
	200	66.6	31.1	20.1	13.6
	300	81.3	41.6	25.9	17.9
	400	93.4	46.2	28.0	20.4
Positive phase duration t_0 (ms)	100	1.2	1.5	1.7	1.8
	200	1.2	1.6	1.7	1.9
	300	1.4	1.5	1.9	2.0
	400	1.4	1.6	1.7	1.8

Figure 4 shows the blast curves for each distance for a 100 g charge. From the graph it is possible to read the values of peak overpressure, positive phase duration and possibly other explosion parameters. The value “0” on the horizontal axis indicates the moment of initiation of the charge.

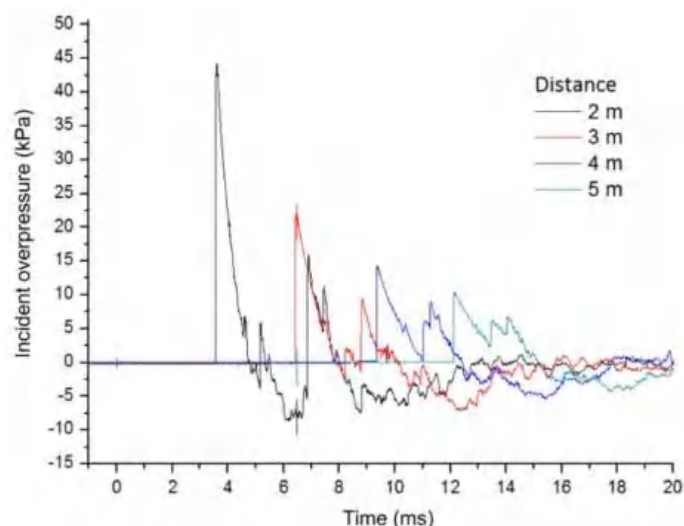


Figure 4. Pressure time course for a 100 g charge.

The values calculated according to the individual predictive models for a 100 g charge are provided in Table 5. For some models, it was not possible to calculate positive phase duration values, either because the scaled distance values were outside the range of applicability of the formulas, or the method used did not allow this calculation.

Table 5. Values of empirical relations for a 100 g charge.

Semtex 100 g	Scaled Distance Z ($m \cdot kg^{-1/3}$)	Blast Parameters	Kingery and Bulmash	Kinney and Graham	Henrych and Major	PECH
Distance (m)	2	P_{ti} (kPa)	54.8	37.6	39.4	40.8
		t_0 (ms)	1.6	1.0	-	-
	3	P_{ti} (kPa)	27.6	18.4	20.2	21.1
		t_0 (ms)	1.9	1.3	-	-
	4	P_{ti} (kPa)	17.9	12.0	13.1	13.9
		t_0 (ms)	2.1	1.5	-	-
	5	P_{ti} (kPa)	13.2	8.9	-	10.3
		t_0 (ms)	2.3	1.6	-	-

Table 6 summarises the relative deviations of the calculated and measured values for a charge of 100 g. The relative deviations are calculated for the individual scaled distances for both blast parameters. Positive values of the relative deviations indicate an overestimation of the blast parameters compared to the experimentally determined values, and conversely, negative values of the relative deviations indicate an underestimation. For a more comprehensive evaluation of the applicability of the computational relationships, all relative deviations were averaged within one model, separately for each observed explosion parameter.

Table 6. Values of relative deviations from experiment for a 100 g charge.

Semtex 100 g	Scaled Distance Z ($m \cdot kg^{-1/3}$)	Blast Parameters	Kingery and Bulmarsh	Kinney and Graham	Henrych and Major	PECH
			Relative Deviation (%)			
Distance (m)	2	P_{ti} (kPa)	24.3	−14.7	−10.7	−7.5
		t_0 (ms)	33.3	−16.7	-	-
	3	P_{ti} (kPa)	17.9	−21.4	−13.7	−9.8
		t_0 (ms)	26.7	−13.3	-	-
	4	P_{ti} (kPa)	25.2	−16.1	−8.4	−2.8
		t_0 (ms)	23.5	−11.8	-	-
	5	P_{ti} (kPa)	25.7	−15.2	-	−1.9
		t_0 (ms)	27.8	−11.1	-	-
Arithmetic mean (%)		P_{ti} (kPa)	23.3	−16.9	−10.9	−5.5
		t_0 (ms)	28.4	−12.9	-	-

Figure 5 illustrates the blast curves for each distance for a 200 g charge.

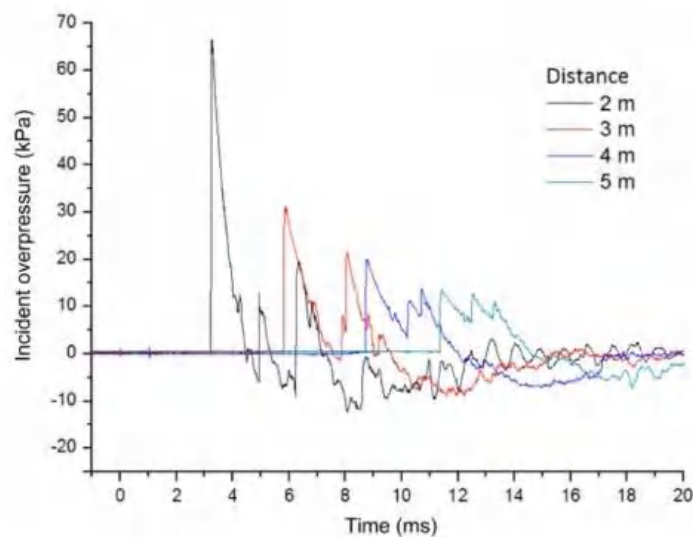


Figure 5. Pressure time course for a 200 g charge.

The values calculated according to the individual predictive models for a 200 g charge are presented in Table 7. Table 8 lists the relative deviations of the calculated and measured values for a 200 g charge.

Table 7. Values of empirical relations for a 200 g charge.

Semtex 200 g	Scaled Distance Z (m·kg ^{-1/3})	Blast Parameters	Kingery and Bulmash	Kinney and Graham	Henrych and Major	PECH
Distance (m)	2	P_{ti} (kPa) t_0 (ms)	85.5 1.8	60.0 1.1	59.2 -	62.0 -
	3	P_{ti} (kPa) t_0 (ms)	40.6 2.2	27.1 1.5	29.4 -	30.4 -
	4	P_{ti} (kPa) t_0 (ms)	25.2 2.5	16.8 1.7	18.5 -	19.4 -
	5	P_{ti} (kPa) t_0 (ms)	18.1 2.6	12.1 1.9	13.2 -	14.0 -

Table 8. Values of relative deviations from experiment for a 200 g charge.

Semtex 200 g	Scaled Distance Z (m·kg ^{-1/3})	Blast Parameters	Kingery and Bulmash	Kinney and Graham	Henrych and Major	PECH
			Relative Deviation (%)			
Distance (m)	2	P_{ti} (kPa) t_0 (ms)	28.4 50.1	-9.9 -8.3	-11.1 -	-6.9 -
	3	P_{ti} (kPa) t_0 (ms)	30.5 37.5	-12.9 -6.3	-5.5 -	-2.3 -
	4	P_{ti} (kPa) t_0 (ms)	26.0 47.1	-16.0 0.0	-7.5 -	-3.0 -
	5	P_{ti} (kPa) t_0 (ms)	33.1 30.0	-11.0 -5.0	-2.9 -	2.9 -
Arithmetic mean (%)		P_{ti} (kPa) t_0 (ms)	29.5 41.2	-12.5 -4.9	-6.8 -	-2.3 -

Figure 6 gives the blast curves for each distance for a 300 g charge.

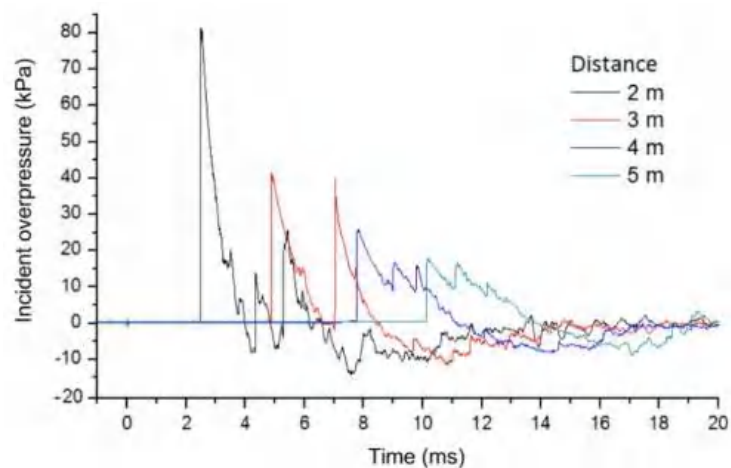


Figure 6. Pressure time course for a 300 g charge.

The values calculated according to the individual predictive models for a 300 g charge are shown in Table 9.

Table 9. Values of empirical relations for a 300 g charge.

Semtex 300 g	Scaled Distance Z (m·kg ^{-1/3})	Blast Parameters	Kingery and Bulmash	Kinney and Graham	Henrych and Major	PECH
Distance (m)	2	P_{ti} (kPa) t_0 (ms)	112.9 1.9	80.3 1.1	76.0 -	80.5 -
	3	P_{ti} (kPa) t_0 (ms)	51.1 2.4	34.8 1.5	36.8 -	38.2 -
	4	P_{ti} (kPa) t_0 (ms)	31.2 2.7	20.9 1.8	22.9 -	23.8 -
	5	P_{ti} (kPa) t_0 (ms)	22.1 2.9	14.7 2.1	16.2 -	17.0 -

Table 10 contains the relative deviations of the calculated and measured values for a 300 g charge.

Table 10. Values of relative deviations from experiment for a 300 g charge.

Semtex 300 g	Scaled Distance Z (m·kg ^{-1/3})	Blast Parameters	Kingery and Bulmash	Kinney and Graham	Henrych and Major	PECH
			Relative Deviation (%)			
Distance (m)	2	P_{ti} (kPa) t_0 (ms)	38.9 26.7	-1.2 -26.0	-6.5 -	-1.0 -
	3	P_{ti} (kPa) t_0 (ms)	22.8 71.4	-16.3 7.1	-11.5 -	-8.2 -
	4	P_{ti} (kPa) t_0 (ms)	20.5 42.1	-19.3 -5.3	-11.6 -	-8.1 -
	5	P_{ti} (kPa) t_0 (ms)	23.5 31.8	-17.9 -4.5	-9.5 -	-5.0 -
Arithmetic mean (%)		P_{ti} (kPa) t_0 (ms)	26.4 43.0	-13.7 -7.2	-9.8 -	-5.6 -

Figure 7 represents the blast curves for each distance for a 400 g charge.

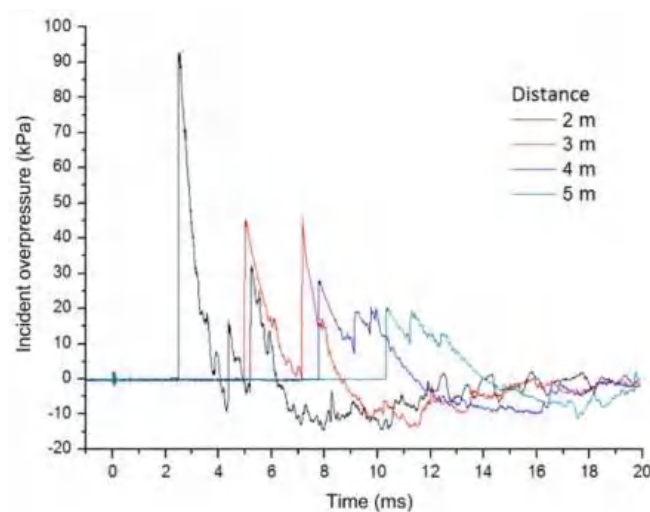


Figure 7. Pressure time course for a 400 g charge.

The values calculated according to the individual predictive models for a 400 g charge are presented in Table 11.

Table 11. Values of empirical relations for a 400 g charge.

Semtex 400 g	Scaled Distance Z ($\text{m} \cdot \text{kg}^{-1/3}$)	Blast Parameters	Kingery and Bulmash	Kinney and Graham	Henrych and Major	PECH
Distance (m)	2	P_{ti} (kPa) t_0 (ms)	138.5 1.9	99.4 1.1	91.1 -	97.5 -
	3	P_{ti} (kPa) t_0 (ms)	60.9 2.5	42.0 1.6	43.5 -	45.1 -
	4	P_{ti} (kPa) t_0 (ms)	36.6 2.9	24.6 1.9	26.7 -	27.7 -
	5	P_{ti} (kPa) t_0 (ms)	25.5 3.1	17.0 2.2	18.8 -	19.6 -

Table 12 sets out the relative deviations of the calculated and measured values for a 400 g charge.

Table 12. Values of relative deviations from experiment for a 400 g charge.

Semtex 400 g	Scaled Distance Z ($\text{m} \cdot \text{kg}^{-1/3}$)	Blast Parameters	Kingery and Bulmash	Kinney and Graham	Henrych and Major	PECH
			Relative Deviation (%)			
Distance (m)	2	P_{ti} (kPa) t_0 (ms)	48.3 35.7	6.4 −21.4	−2.5 -	4.4 -
	3	P_{ti} (kPa) t_0 (ms)	31.8 47.1	−9.1 −5.9	−5.8 -	−2.4 -
	4	P_{ti} (kPa) t_0 (ms)	30.7 70.6	−12.1 11.8	−4.6 -	−1.1 -
	5	P_{ti} (kPa) t_0 (ms)	25.0 82.4	−16.7 29.4	−7.8 -	−3.9 -
Arithmetic mean (%)		P_{ti} (kPa) t_0 (ms)	34.0 59.0	−7.9 3.5	−5.2 -	−0.8 -

4. Discussion

When evaluating the results of experiments carried out with Semtex 10-SE spherical charges, which differed in mass, the assumption that the peak overpressure increases with increasing charge mass was confirmed. This is verified by theoretically calculated and experimentally obtained results. Based on the comparison of experimentally measured and theoretically calculated values of peak overpressures, it can be concluded that the different predictive calculation models are applicable for load estimation, but the degree of uncertainty varies from one relation to another. Percentage relative deviations, following the authors' calculation formulas, were interpreted in Tables 6, 8, 10 and 12. From the average values of the relative deviations between the calculated and measured values, it can be concluded that the calculated values according to Kinney and Graham, Henrych and Major and PECH are always on average lower than the experimentally measured values. On the other hand, the calculated results according to Kingery and Bulmash are in all cases larger than the measured values.

All the calculations of peak overpressures mentioned so far are roughly the same in comparison with the measured values, with differences of units or a few tens of percent at most (the most extreme difference found was in the case of comparison of the Kingery and Bulmash result with the measured value at a distance of 2 m for a 400 g Semtex charge, which was 48.3%). The largest differences occurred in the case of the Kingery and Bulmash calculations, with differences in the tens of percent range. It appears that as the distance from the charge reduces and the mass of the charge increases, higher differences

between the measured and calculated values arise. This is due to the lower sensitivity of the computational relations for the close surroundings of the explosive. From a practical point of view, this is not a major complication, since the parameters of the explosive loads are usually more relevant for larger distances, where the accuracy of the calculation relations is already considerably higher. The overall intercomparison of the results of these relations with measured values shows that the smallest average differences between the theoretical calculations and experimentally measured values of peak overpressures are in the case of using the PECH calculation relation.

Theoretical calculations of positive phase duration show that this time increases with increasing mass of the explosive and with increasing distance from the explosion site. Although some increase is evident from the graphs and from the indicative positive phase durations within the measurement results for a given mass, there are exceptions where the duration decreases or does not change. These variations may arise from the passing of a shock wave related to the measuring equipment used. The measurement of these values was already at the limit of the accuracy of the measuring setup used, which could have affected values in the order of hundredths of milliseconds. The same phenomenon was observed in the case of increasing mass of the explosive used, where some increase in the positive phase duration is noticeable, but inconsistent with the theoretical results.

In general, the measured positive phase durations are roughly around similar values, but this results in increasing average percentage differences between the measured and calculated values according to Kingery and Bulmash. The calculations according to Kinney and Graham were initially lower than the measured values, therefore the average difference in values first decreases and then increases again with increasing mass of the charge. In the case of the calculation of the duration of the positive phase according to Henry and Major, the values could not be determined because the values of the reduced distances were outside the range of validity of the calculation relationship. From the above facts it follows that the calculation relations for the positive phase durations are of limited applicability in the context of the experimental conditions.

5. Conclusions

The subject of the investigation of the magnitude of the explosive load on objects or building structures was the chosen type of explosive, namely the industrial explosive Semtex, which, due to its known properties, served as a reference sample in this case. At the theoretical level of determining the selected blast wave parameters, there are many different calculation relationships. The calculations by these different relations differ from each other; this is due to the differences in the conditions for which the calculation relation was constructed. In general, one of the most important blast wave parameters is the peak overpressure, since it is the parameter that has a major influence on the action of the pressure wave on the building structure. Based on extensive research, predictive relationships have also been traced that can be applied more universally. The limitations for these relationships arise from their applicability to specific situations. Due to the applicability of the computational relations, only the relations for peak overpressure and positive phase duration were used in the theoretical calculations of blast wave parameters.

Two types of pressure probes were used in the experimental measurements, but with the same pressure transducers used. The values of the measured overpressures differed only minimally between the single transducers at the same distance (in the same pair), within a maximum of one percent. From the recorded blast curves, the peak overpressure and the duration of the positive phase can be read off, as well as other important blast wave parameters. The overpressure curves also showed the reflection of the blast wave from the bedrock (or other obstacles), which can affect their course and distort the measured values under certain circumstances.

Comparing the experimentally measured and theoretically calculated peak overpressures, it was found that the smallest differences occurred in the case of using the predictive model according to PECH, whose deviations from the measured values differed at most

in units of percent. On this basis, it can be determined that this was the most appropriate computational relationship under the conditions of the experiment.

Author Contributions: Conceptualization, A.F. and M.M.; methodology, M.M.; software, A.F. and M.M.; validation, M.M., A.F. and R.Z.; formal analysis, A.F. and M.M.; investigation, M.M. and A.F.; resources, M.M.; data curation, A.F.; writing—original draft preparation, M.M.; writing—review and editing, A.F.; visualization, A.F.; supervision, R.Z.; project administration, R.Z.; funding acquisition, A.F. and R.Z. All authors have read and agreed to the published version of the manuscript.

Funding: This research was funded by University of Calabria, SMART Lab (Structural Monitoring, Structural Advanced Materials, Structural Rehabilitation, Structural Testing Laboratory).

Institutional Review Board Statement: Not applicable.

Informed Consent Statement: Not applicable.

Data Availability Statement: The article provides all data used in this research.

Acknowledgments: Special thanks for organizing and conducting the experimental studies is given to the Faculty of Safety Engineering, VŠB Technical University of Ostrava, Czech Republic.

Conflicts of Interest: The authors declare no conflict of interest.

References

1. Kinney, G.F.; Graham, K.J. *Explosive Shocks in Air*; Springer: Berlin, Germany, 1985.
2. Henrych, J. *The Dynamics of Explosion and Its Use*; Elsevier: Amsterdam, The Netherlands, 1979.
3. Mills, C.A. The design of concrete structures to resist explosions and weapon effects. In Proceedings of the 1st International Conference on Concrete for Hazard Protections, Edinburgh, UK, 27–30 September 1987.
4. Kingery, C.N.; Bulmash, G. *Airblast Parameters from TNT Spherical Air Burst and Hemispherical Surface Burst*; Technical Report ARBRL-TR-02555; U.S. Army BRL: Aberdeen Proving Ground, MD, USA, 1984.
5. Sadovskiy, M.A. Mechanical effects of air shockwaves from explosions according to experiments. In *Geophysics and Physics of Explosion*; Selected Works; Sadovskiy, M.A., Ed.; Nauka Press: Moscow, Russia, 2004.
6. Beshara, F.B. Modelling of blast loading on aboveground structures—I. General phenomenology and external blast. *Comput. Struct.* **1994**, *51*, 585–596. [CrossRef]
7. Brode, H.L. *Numerical Solution of Spherical Blast Waves*; American Institute of Physics: New York, NY, USA, 1955.
8. Swisdak, M.M., Jr. Simplified Kingery Airblast Calculations. In *Minutes of the Twenty Sixth DOD Explosives Safety Seminar*; DTIC Document; U.S. Department of Defense, Explosives Safety Board: Indian Head, MD, USA, 1994.
9. U.S. Department of the Army. *Design and Analysis of Hardened Structures to Conventional Weapons Effects*; Technical Manual 5-855-1; U.S. Department of the Army: Arlington, VA, USA, 1986.
10. U.S. Department of the Army. *Structures to Resist the Effects of Accidental Explosions*; Technical Manual 5-1300; U.S. Department of the Army: Arlington, VA, USA, 1990.
11. U.S. Department of the Army. *Structures to Resist the Effects of Accidental Explosions*; Technical Report UFC 3-340-02; U.S. Department of the Army: Arlington, VA, USA, 2008.
12. Karlos, V.; Solomos, G. *Calculation of Blast Loads for Application to Structural Components*; JRC Technical Report, EUR 26456EN; European Union: Luxembourg, 2013.
13. Remennikov, A.M. A review of methods for predicting bomb blast effects on buildings. *J. Battlef. Technol.* **2003**, *6*, 5–10.
14. Ngo, T.; Mendis, P.; Gupta, A.; Ramsay, J. *Blast Loading and Blast Effects on Structures—An Overview*; EJSE Special Issue: Loading on Structures; The University of Melbourne: Parkville, VIC, Australia, 2007.
15. Koccaz, Z.; Sutcu, F.; Torunbalci, N. Architectural and structural design for blast resistant structures. In Proceedings of the 14th World Conference on Earthquake Engineering, Beijing, China, 12–17 October 2008.
16. Draganić, H.; Sigmund, V. Blast loading on structures. *Teh. Vjesn.* **2012**, *19*, 643–652.
17. Ding, Y.; Zhang, X.; Shi, Y.; Zhang, H. Prediction of far-field blast loads from large TNT-equivalent explosives on gabled frames. *J. Constr. Steel Res.* **2022**, *190*, 107120. [CrossRef]
18. Shirbhate, P.A.; Goel, M.D. A Critical Review of Blast Wave Parameters and Approaches for Blast Load Mitigation. *Arch. Comput. Methods Eng.* **2021**, *28*, 1713–1730. [CrossRef]
19. Birhane, T.H. Blast Analysis of Railway Masonry Bridges. Master's Thesis, University of Minho, Braga, Portugal, 2009.
20. Baker, W.E. *Explosions in Air*; University of Texas Press: Austin, TX, USA, 1973.
21. Baker, W.E.; Cox, P.A.; Westine, P.S.; Kulesz, J.J.; Strehlow, R.A. *Explosion Hazards and Evaluation*; Elsevier Scientific Publishing Company: New York, NY, USA, 1983.
22. Hopkinson, B. *British Ordnance Board Minutes*; Report 13565; British Ordnance Office: London, UK, 1915.
23. Cranz, C. *Lehrbuch der Ballistic*; Springer: Berlin, Germany, 1926.

Article

Assessment of the Sympathetic Detonation of Blasting Caps

Eugen Trană , Marin Lupoae , Bogdan Iftimie and Alexandru Cătălin Casapu

Faculty of Integrated Armament Systems, Military Engineering and Mechatronics, Military Technical Academy "Ferdinand I", 050141 Bucharest, Romania

* Correspondence: marin.lupoae@mta.ro

Abstract: The neutralization of improvised explosive devices (IEDs) involves the use of disrupting agents propelled explosively. Due to the special nature of such materials, a proper investigation of the parts most susceptible to sympathetic detonation is in order. The initiation of IEDs is caused by detonation products, shock waves, and propelled disruptive agents. In this paper, initiation of IED composition (acceptor charge) due to the neutralization system's (donor charge's) explosive charge detonation is evaluated based on the influence of the first two of the three above-mentioned factors. One of the most susceptible components of IEDs to sympathetic initiation is the blasting cap. Based on an experimental and numerical mix approach, blasting cap tendency to sympathetic detonation in open field had been investigated. The suitability of critical energy fluence and Chapman–Jouguet threshold criteria to the sympathetic detonation tendency of blasting caps was investigated. Experimental and numerical/analytical results describing the phenomenon are in agreement.

Keywords: improvised explosive device; sympathetic detonation; blasting cap; numerical simulation

Citation: Trană, E.; Lupoae, M.; Iftimie, B.; Casapu, A.C. Assessment of the Sympathetic Detonation of Blasting Caps. *Appl. Sci.* **2022**, *12*, 12761. <https://doi.org/10.3390/app122412761>

Academic Editors: Ricardo Castedo, Lina M. López and Anastasio P. Santos

Received: 4 November 2022

Accepted: 7 December 2022

Published: 12 December 2022

Publisher's Note: MDPI stays neutral with regard to jurisdictional claims in published maps and institutional affiliations.



Copyright: © 2022 by the authors. Licensee MDPI, Basel, Switzerland. This article is an open access article distributed under the terms and conditions of the Creative Commons Attribution (CC BY) license (<https://creativecommons.org/licenses/by/4.0/>).

1. Introduction

Sympathetic detonation involves the initiation (usually unwanted) of an explosive charge called the acceptor due to the detonation of another charge called the donor. The initiation of the acceptor can be induced by detonation products and/or shock waves, depending on the distance between the two explosive charges.

The issue of sympathetic detonation is encountered in both military and civilian applications. In the military domain, avoiding sympathetic detonation is important, among other things, in the process of neutralizing IEDs or unexploded ordnance (UXO). In order to determine the critical distances at which the neutralization system can be placed, the possibility of sympathetic initiation of the IED load must also be taken into account since it is very important to avoid the effects that are produced by an unwanted initiation of the IED.

Starting from the principle of IED neutralization, namely preventing its operation (detonation of the explosive charge) and separating the component elements so that its functioning can no longer be triggered by the subsequent handling or interacting with the environment, the requirement of the neutralization system's performance can be formulated as the ability to induce a high enough shock in the IED to separate its parts, but at the same time to avoid the initiation of the explosive charge caused by the effects of the donor charge's detonation.

In both military and civilian fields, the storage, transportation, handling, and the production of explosives or items that include explosives involve risks due to the sensitivity and reactivity of such materials. As history has proven, one of the main risks is associated with the tendency of energetic materials to react to a nearby stimulus, such as an explosion or a kinetic impact. Over time, the above-mentioned tendency led to several catastrophic accidents in military facilities as well as in civil mining and industrial sites. Due to these tragic events, regulations regarding the design and use of items containing explosives were

imposed. Among these regulations, sympathetic detonation evaluation tests are mandatory and can be seen as the backbone of safety program tests.

The evaluation of the tendency of an energetic material toward sympathetic detonation is assessed using the gap test. Basically, the gap test is a widely used test that aims to evaluate the sensitivity of explosives to blast waves. The gap test and other associated tests have been performed numerically and experimentally for different types of explosives, both on land and underwater, by several researchers throughout history. Thus, Yang et al. [1] numerically investigated Composition B's susceptibility to sympathetic detonation based on a Direct Numerical Simulation (DNS) scheme, which was also validated experimentally. They concluded that the probability of sympathetic detonation is related not only to the type of explosive and distance but also to the size of the charge. Zhang et al. [2] experimentally evaluated the underwater sympathetic detonation of TNT and analyzed the energy, pressure, and pulsing cycle. Kubota et al. [3,4] investigated using high-speed photography the sympathetic detonation of Composition B both in air and underwater and also investigated it numerically by using Lee and Tarver's phenomenological reaction-rate law. An experimental study by Becuwe and Delclos [5] on the sympathetic detonation of low-sensitivity explosive compounds (NTO and HMX-based PBX) showed that the shock insensitivity of the studied explosive mixture is combined with very good behavior under fire, slow heating, and a ball impact. Keshavarz et al. [6] studied the possibility of using a small-scale gap test to evaluate the sympathetic detonation of CaHbNcOd explosives and proposed a simple procedure for the analytical calculation of the shock sensitivity of energetic compounds. Ko et al. [7] investigated experimentally and numerically the shock sensitivity of a shaped charge underwater and showed that in an underwater explosion, the index of the sympathetic detonation is slightly higher than in the air. Along with the previously mentioned research teams, several others can easily be named, including researchers/teams that approached the subject in a theoretical manner, such as M.H. Keshavarz, E.N. Ferm, H.R. James, and A.C. Victor [6,8–10].

When an explosive charge (explosive bars) is subjected to the action of a shock wave, this shock wave will produce the initiation of the acceptor charge only if the energy of the shock wave is greater than the critical energy. The critical energy considers not only the pressure level (shock amplitude) but also the pulse duration and the acceptor impedance as stated by Walker and Wasley [11]. The formula for energy calculation is given in Equation (1).

$$E_c = P^2 t / \rho_0 U \quad (1)$$

where P is the shock amplitude, t indicates the pulse duration, ρ_0 denotes the acceptor's initial density, and U is the shock velocity that travels through the acceptor. The term E_c has the dimension of energy per unit area and is therefore referred to as energy fluence. Through experimental tests carried out with different explosives subjected to the square-wave shock produced by the impact of the flyer test, it was found that each explosive has a range of energy fluence in which a stable detonation is produced, called critical energy fluence [12]. Additionally, for the evaluation of the initiation of an explosive under the action of the shock wave, the "Pop-plot" [12] can be considered, which represents the graphic representation in logarithmic coordinates of the run distance as a function of pressure for the acceptor explosive.

The application of Equation (1) used to evaluate the initiation of detonation of an explosive charge requires the determination, by numerical analysis, of the amplitude and duration of the applied shock. In the absence of numerical analysis, the relationship developed by Yadav [13] takes into account detonation parameters, which are easier to measure and can be used to determine the energy transmitted to the explosive charge. This relation is specified in Equation (2).

$$E_c = \frac{\rho_0 D_j \delta \left[\frac{D_j - a_x}{2b_x} + \frac{D_j}{2(r+1)} \right]^2}{D_j - \left[\frac{D_j - a_x}{2b_x} + \frac{D_j}{2(r+1)} \right]} \quad (2)$$

where ρ_0 is the initial density, D_j is the velocity of detonation, δ is the thickness of reaction, r denotes the specific heat ratio of detonation products, and a_x and b_x are Hugoniot constants.

In line with the sympathetic detonation issue, yet in a less conventional manner, the current paper focuses on the investigation of the sympathetic detonation tendency of the blasting cap, containing pentaerythritol tetranitrate (PETN) charges. The main focus is targeted on investigating the applicability of critical energy fluence for a particular configuration with an air gap between donor and acceptor explosive charges.

For the assessment of the detonation initiation potential of a blasting cap, in this paper, we will use Equation (1) because, when using numerical analysis, the parameters in this equation are determined much faster. The relevance of the study is obvious when one considers the specific way in which the neutralization of suspicious packages is carried out. Basically, the disruption of such packages is performed by propelling a disrupting agent (metallic/plastic bolts or water) with the use of small explosive charges. The blast wave generated by the detonation of an explosive charge has the potential, in certain conditions, to lead to unwanted package detonation due to the initiation of explosive charge and/or blasting caps.

2. Experimental Investigation

In order to experimentally evaluate the sensitivity of blasting caps to blast waves, several tests have been performed. The experiments involved the use of 100 g of TNT as donor charge and $\phi 7 \times 69$ mm blasting cap as an acceptor. TNT was chosen as a donor because it is considered a reference explosive. Although the amount of 100 g of explosive is not common for neutralization systems, it was used to better capture the influence that the detonation products and the shock wave can have on the sympathetic detonation of a blast initiator. The experimental setup illustrated in Figure 1 aims to identify a critical distance, in terms of air thickness, between the acceptor and the donor that will end in a no-go reaction for the acceptor.

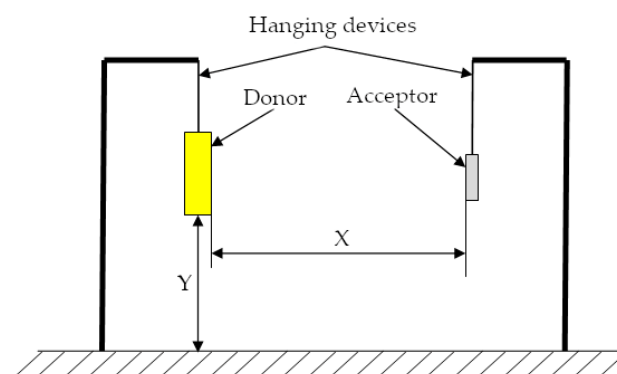


Figure 1. Experimental set-up (side-on configuration).

The blasting cap type used in these experiments is based on 0.6 g PETN charge with a density of 1.75 gm/cm^3 . The donor charge was detonated using the same type of blasting cap as the detonator as the one used as the acceptor.

The tests were performed in an open space configuration, imposing a higher y value (donor/ground distance) than the x value (donor/acceptor distance). Using this approach, the incident blast wave was allowed to arrive first at the acceptor position instead of a one reflected. The post-test recovery of target blasting caps, when possible, was the criterion for

identifying a possible detonation of the acceptor. A witness plate was not used due to the chosen test setup (the TNT charge was parallel to the blasting caps in order to have a larger contact surface; this represents the most unfavorable situation in relation to the position that a disruption load can have towards an acceptor load from the components of an IED). In this situation, the presence of a witness plate could have influenced the initiation of the blast cap from the shock wave that is reflected from the plate.

Table 1 lists the experimental results regarding blasting cap sympathetic detonation tendency.

Table 1. Gap test experimental results.

Air Gap Thickness X (mm)	Go/No Go
100	Go
200	Go
350	No go
500	No go

A fast image recording camera (Photron, FASTCAM SA-Z), set to an acquisition rate of 30,000 fps, was used as part of the testing setup. Thus, the blast wave position and fireball dimension during experimental tests were traced. Table 2 contains the results that were extracted from image analysis, and the detonation of 100 g TNT is illustrated in Figure 2.

Table 2. Blast wave position and fireball dimension.

Time (s)	Blast Wave Position (mm)	Fireball Dimension (mm)
0	0	0
0.0003000	608.39	623.04
0.0005330	715.52	798.26
0.0006670	749.59	900.48
0.0009670	827.45	1061.09
0.0016330	851.79	1406.67
0.0036670	992.94	1596.58
0.0050330	1017.28	N/A
0.0067670	1065.96	N/A
0.0114330	1168.17	N/A

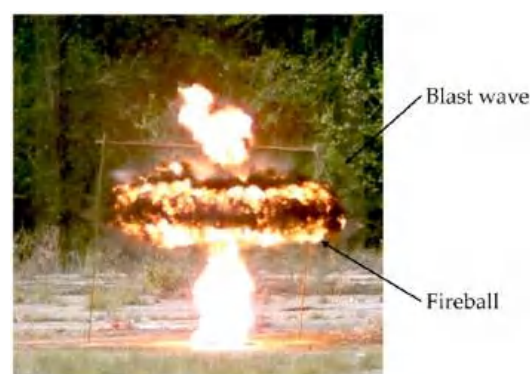


Figure 2. Typical image of 100 g TNT detonation.

3. Numerical Approach

While experimental testing is the most suitable method to evaluate sympathetic detonation, the numerical approach has proved to be a valuable tool in deciphering the process specifics. Thus, important aspects of the detonation propagation process (pressure level in the donor/acceptor charge or run distance for a stable detonation) can be investigated using a low-cost and reasonable-time scenario. For the proposed experimental tests, numerical models have been defined using Autodyn 2021[®] software [14].

3.1. Preprocessing

In order to corroborate the experimental results with the numerical ones, one simple approach was considered. The numerical model is based on a 2D planar symmetrical geometry and the use of multi-material Euler part.

Since the mesh sensitivity is a well-known characteristic of commercial software based on the Finite Element Method (FEM), special attention was given to this aspect. Considering Ko's observation [7] regarding the recommended mesh dimension as a function of the distance for the free air blast wave and also the distances involved in experimental tests, a graded mesh was imposed. The mesh dimension varies in both directions from 0.1 mm in the blasting cap region to 1 mm in the donor charge area, as shown in Figure 3.

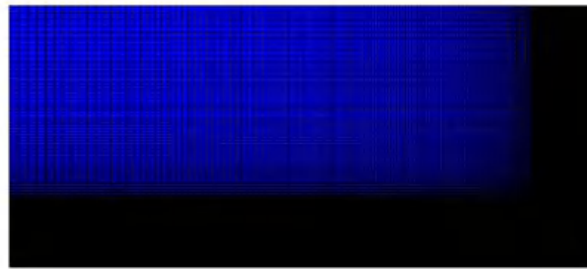


Figure 3. Typical mesh example.

In addition to the above-mentioned aspects, it must be pointed out that two rows of six gauges, 1 mm apart on the X axis and 5 mm apart on the Y axis, were used for numerical calculus to record the peak pressure in the acceptor charge. The position of the gauges, the material location, and the edges on which boundary condition were imposed, as shown in Figure 4. Additionally, in order to reduce the simulation time, the pressure contours generated by 100 g TNT detonation have been remapped in the current simulation using the fill option from a separate Autodyn 2021[®] file.

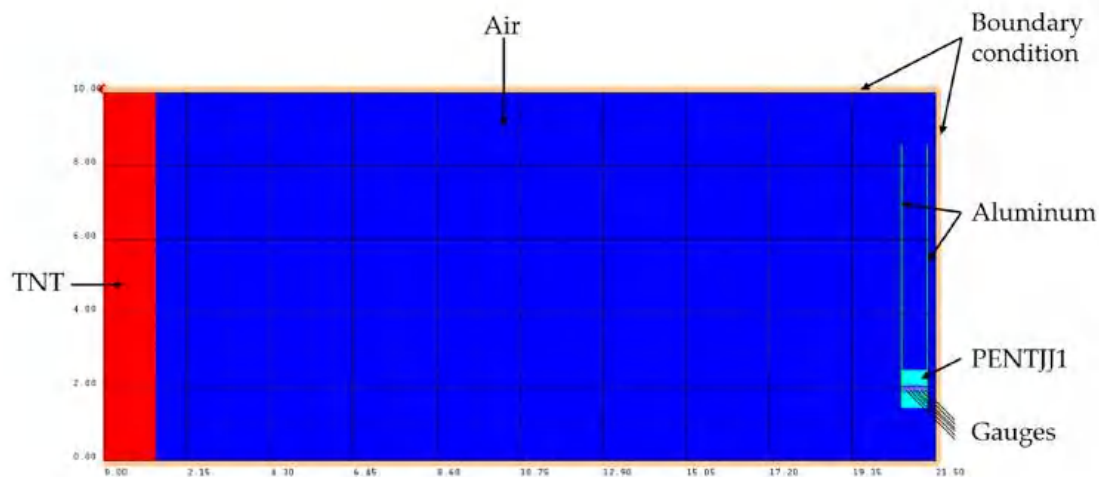


Figure 4. Materials location and gauges position.

3.2. Material Models

The basic properties of any substance, explosives included, are usually identified through a mathematical relation that correlates pressure, volume, and internal energy/temperature. The relation is called an equation of state (EOS).

In the process of numerical analysis of the sympathetic detonation, it was found that the choice of the equation of state that describes the behavior of the donor and acceptor charges plays a very important role.

Over time, numerous attempts to define an EOS that accurately predicts the behavior of explosive gas products have been made. In fact, the number of proposed equations was high enough to classify them into two distinct categories: one considers the chemistry explicitly and the other does not [15].

Unfortunately, all of the above-mentioned equations have limited the applicability and variable accuracy. Despite this shortcut, their use in numerical calculus is extremely beneficial since different particular situations can be investigated in a reasonable time frame and an almost costless manner.

When explosive detonation applications are numerically investigated, one EOS is usually involved, namely Jones–Wilkins–Lee (JWL) [16]. In fact, the use of the JWL EOS is so common that by now almost all hydrocodes have implemented it and several forms can be identified in the literature. However, the most known form of equation is the form of a family of isentropes [17], which is illustrated in Equation (3).

$$p(S, V) = Ae^{-R_1V} + Be^{-R_2V} + C^*(S)V^{-(\omega+1)} \quad (3)$$

where p is the pressure; S refers to the entropy per unit initial volume (s/v_0); V is the volume relative to the undetonated state (v/v_0); A , B , R_1 , and R_2 are constant fitting parameters; ω is an assumed-constant material parameter (Grüneisen function); and $C^*(S)$ is a parameter dependent only upon the entropy S .

Based on the previously mentioned JWL EOS and ideal gas EOS assumptions, the pressure in the front of a traveling blast wave can be accurately evaluated when hydrodynamic simulations are employed. Even though the equation's versatility is impressive, the application of JWL EOS by itself cannot deliver crucial data regarding the initiation of the explosive when subjected to blast wave stimulus. Thus, in order to investigate the blasting cap sympathetic detonation susceptibility, a slightly different EOS was chosen, the Lee–Tarver equation of state [18]. In fact, the Lee–Tarver EOS is basically a JWL EOS that has been upgraded with a supplementary equation, Equation (4), that allows the evaluation of the burning fraction based on the pressure level acting on/inside the explosive [18].

$$\frac{\partial F}{\partial t} = I(1 - F)^b \left(\frac{\rho}{\rho_0} - 1 - a \right)^x + G_1(1 - F)^c F^d p^y + G_2(1 - F)^e F^g p^z \quad (4)$$

where F is the explosive burning fraction which has a value between 0 and 1.

The importance of JWL EOS and Lee–Tarver EOS for the current blast cap sympathetic detonation study is correlated with the Chapman–Jouguet pressure level that can be used as the Go/No-Go criterion.

The materials used in the numerical simulation are TNT for the donor charge, PETNJJ1 for the acceptor charge, aluminum for the blasting cap walls, and air for the space between the donor and the acceptor. All the equations of state (EOS) and strength models of the materials were adopted from the library of the Autodyn 2021[®] software.

3.3. Numerical Results

The obtained numerical results are presented in Table 3. In Figure 5, the pressure levels recorded by two different gauges located inside the acceptor charge are illustrated for two cases. Figure 5a shows the pressure levels in the case of a 200 mm gap between the donor and acceptor, while Figure 5b shows the results for a distance of 500 mm. The peak overpressure was directly measured from the gauges. The pressure wave speed was determined from graphs of pressure in time, for consecutive sensors. By dividing the distance between the sensors by the values of the times at which the maximum values of the pressures were obtained, the shock wave velocities were determined for each case of the acceptor–donor charge. The critical energy fluence was determined by using the maximum pressure value, speed, and the pulse duration of the shock wave. For the calculation of the shock wave pulse duration, the area under the pressure–time curve was numerically evaluated and then approximated with a square-shaped pulse (rectangle with a height

given by the maximum pressure value and length given by the value of pressure-acting time that equals the previously calculated impulse).

Table 3. Virtually measured data in acceptor charge.

Air Gap Thickness, X (mm)	Peak Overpressure (Mbar)	Pressure Wave Speed (mm/ms)	Critical Energy Fluence (J/m^2)
100	4.02×10^{-3}	3162	1.69×10^5
200	3.55×10^{-3}	2881	1.51×10^5
350	1.58×10^{-5}	2840	97.38
500	0.91×10^{-5}	2739	37.46

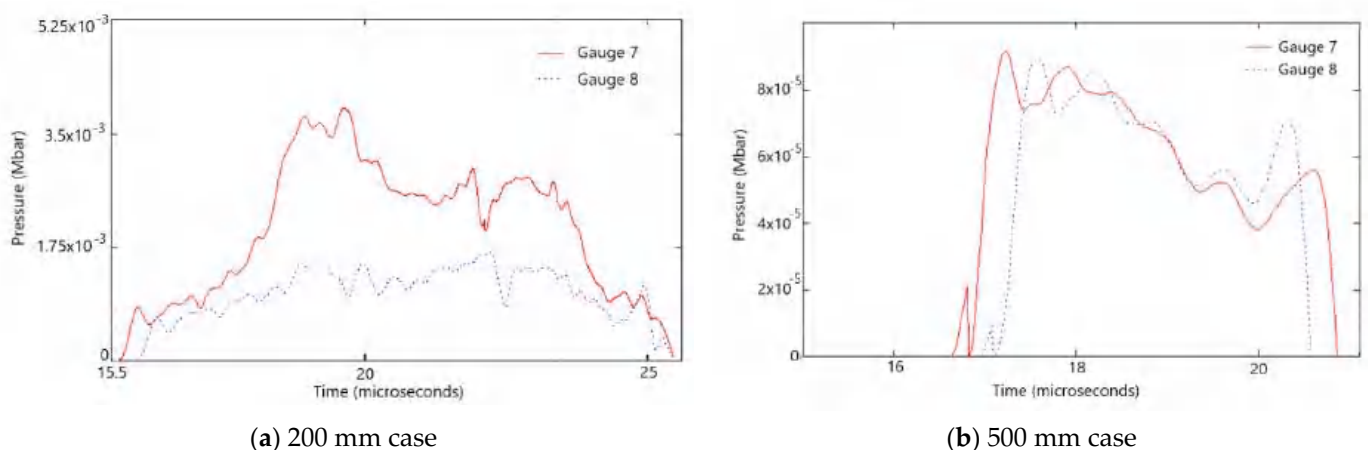


Figure 5. Typical examples of numerically recorded pressure history in PETNJJ1 material (gauges 7 and 8 are the first and second gauges from the upper row).

4. Discussion

As the main goal of the present study is to evaluate the sympathetic detonation tendency of blasting caps, the main focus is on the correlation of experimental and numerical results.

If the experimental approach is a straight forward method that clearly points out the presence of acceptor detonation, the numerical approach is somehow trickier.

As previously mentioned, the numerical simulation is based on the use of Lee–Tarver EOS [19]. The Lee–Tarver EOS points mainly at the Chapman–Jouguet [19,20] findings that were later included in von Neumann’s work [21]. Basically, a stable detonation is achieved when the pressure level reaches a certain value that is specific to each explosive (0.327 Mbar for PETN). Considering this approach, the blasting cap will not be susceptible to sympathetic detonation (in a range of a 0.1 to 0.5 m clearance distance) as long as the pressure recorded by the gauges indicates significantly lower levels (see Table 3). Nevertheless, as experimental tests have proved, the blasting cap detonation manifested at both 100 mm and 200 mm, where, according to numerical simulation, the peak overpressure is less than 0.327 Mbar.

Acknowledging the hypothesis involved in the critical energy fluence theory (step pulse shape and constant impedance, mainly) and the $1.5 \times 10^5 \text{ J}/\text{m}^2$ threshold value for the energy fluence of PETN ($1.75 \text{ gm}/\text{cm}^3$) [22], the calculus based on the numerical data (Figure 5) indicates a very good match with the experimental observation (see Tables 1 and 3). Thus, it is found that for distances of 100 mm and 200 mm, the critical energy values are close to the threshold value for the initiation of the acceptor explosive. On the other hand, the recorded pressures are lower than those corresponding to the C–J state, which indicates a weak detonation. The values of the maximum pressure and the duration of the positive phase of the phenomenon shown in Figure 5a fall within the values presented in the literature for the initiation of solid explosives [23]. Moreover, the shape of

the pressure–time curve in Figure 5a is similar to the ones in Walker and Wasley’s work [24] at the point that the initiation of the explosive occurs. Additionally, by analyzing Figure 5, it can be observed that the pressure wave shape acting on the blasting cap has a much different profile from the ones usually recorded during a standard gap test.

Due to the mismatch between the shock wave’s front velocity and donor gas products’ front velocity, the first to act on the blast cap is the blast wave, and the gas products pressure shortly afterward, depending on the relative position between the donor and acceptor charges, as can be deduced from Figure 6. The pressure wave profile is also shaped by the reflected blast wave, which is clearly indicated by the numerical simulation.

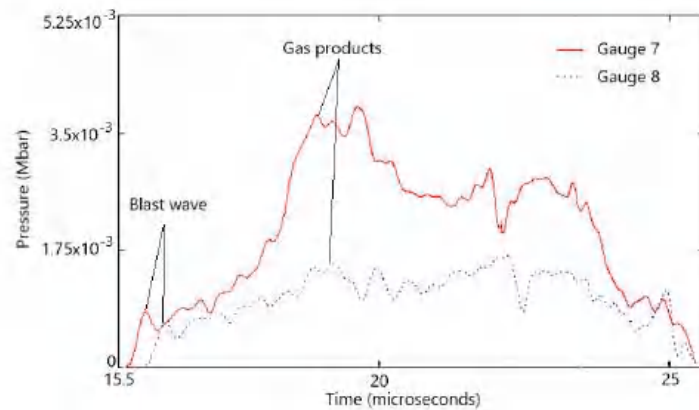


Figure 6. Pressure wave profile (200 mm case).

The same outcome can be underlined by theoretical means as well. Therefore, using far-field experimental data (images recorded when the blast wave has already traveled over a 0.6 m distance), the Sedov-Taylor model [25,26], and Gilev’s observations [27], one can predict the distance between the incident blast wave and the gas products’ border. Useful data regarding the position of the blast wave and the gas products’ border can be extracted by solving Equations (5)–(10) [25–29]. In Figure 7, a comparison between experimental results and the application of Equations (5)–(10) for two values of the expansion dimensionality factor is presented.

$$R_s(t) = at^b \tag{5}$$

$$a = \left[\frac{E_d / (\tau_0^s l_0^{3-n})}{\rho} \right]^{1/(n+2)} \tag{6}$$

$$b = \frac{s+2}{n+2} \tag{7}$$

$$l_0 = \left(\frac{3m}{2\pi\rho} \right)^{1/3} \tag{8}$$

$$\tau_0 = \frac{l_0}{v_{TNT}} \tag{9}$$

$$R_f(t) = R_{max} \left(1 - e^{-kt} \right) \tag{10}$$

where $R_s(t)$ indicates the shock front radii; a and b are coefficients; E_d is the TNT release energy during detonation (usually 4.1 MJ/kg); l_0 denotes a length scale; τ_0 denotes a time scale; m is the TNT mass; ρ is the TNT mass density; v_{TNT} denotes the TNT detonation velocity (6940 m/s); s indicates a factor characterizing the rate of energy release: instantaneous energy release ($s = 0$) and constant-rate energy release ($s = 1$); n is the expansion dimensionality: planar expansion ($n = 1$), cylindrical expansion ($n = 2$), and spherical

expansion ($n = 3$); $R_f(t)$ indicates the fireball radii; R_{max} is the fireball stopping radii (0); and k denotes the drag coefficient.

It must be stated that the Sedov–Taylor equation can be applied only to the mid-field region according to Equation (11) [28].

$$\left(\frac{3m}{2\pi\rho}\right)^{1/3} \ll R_s \ll \left(\frac{\Delta H_d}{p}\right)^{1/3} \tag{11}$$

where ΔH_d indicates the total energy released during detonation, afterburning included, (up to 10.1 MJ/kg [30]), and p denotes the ambient pressure.

Using high-speed camera imaging, R_s radii can be identified for different time values. Since the TNT charge has a cylindrical shape, a factor $n = 2$ was considered. Additionally, due to the fact that the distances between the TNT charge and the blasting cap are small (less than 0.5 m) for the experimental setup, an instantaneous energy release ($s = 0$) was set. However, the experimental results plotted against the results provided by Equation (5), which are presented in Figure 7a, show some considerable differences.

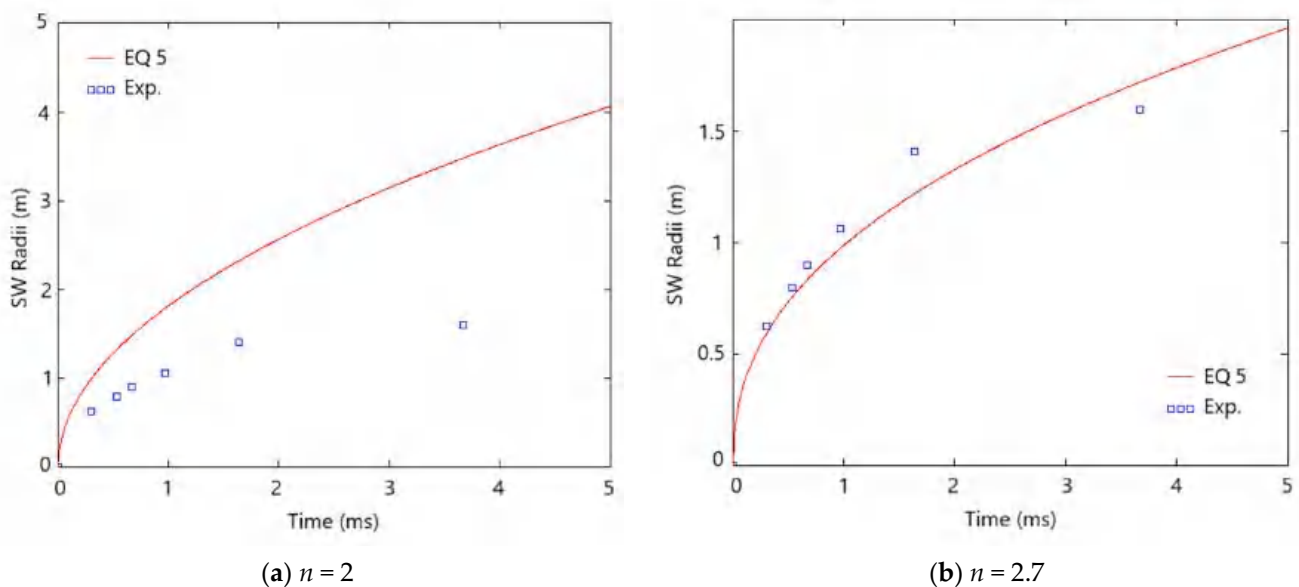


Figure 7. Experimental vs. Equation (5) results.

By closely analyzing the footage in Figure 8, it can be observed that the blast wave shape presents itself neither as a cylindrical shape nor as a spherical one. The mismatch is probably due to the ratio between the length and the diameter of the TNT blast charge, which has a value of 3.57, and also due to the overall small dimensions of the charge. Considering the experimental blast’s wave shape, which is more like an ellipsoid, a different value for n factor was chosen, namely 2.7. A comparison between predicted and experimental results for the modified value of the n factor is presented in Figure 7b, and it is clear that the use of this value leads to a much better approximation of the experimental data.

The R_f radii can also be calibrated with the use of the camera footage and finally plotted against R_s values, as shown in Figure 9. Predictions using Equation (11) are plotted in the same figure. With the use of Figure 9, one can easily see that the blast wave gradually moves away from the fireball border, which is consistent with the data provided by the numerical simulation.



Figure 8. Blast wave shape (perfect sphere (blue) and real (black)).

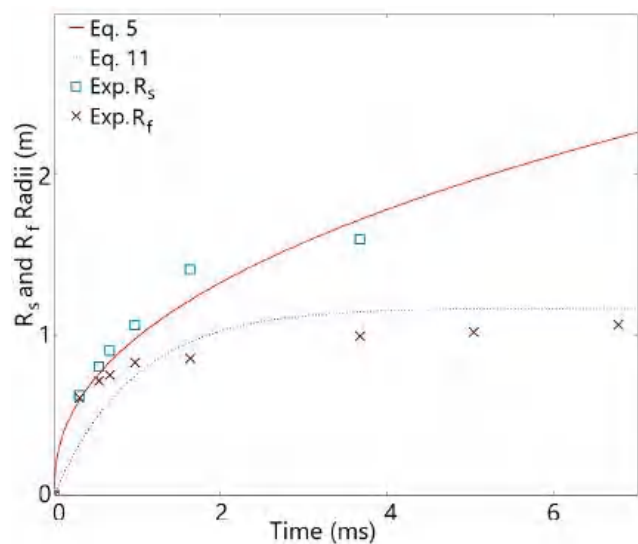


Figure 9. Blast wave vs. Fireball Radii.

The analytical calculus based on Equations (5)–(10) is confirmed by a numerical approach, as shown in Figure 10. According to Figure 10, the blast wave front gradually speeds up, leaving behind the front of the donor gas products.

As mentioned in Section 3.1, two rows of gauges (six gauges/row) were used for pressure recording in the acceptor charge. This particular choice was due to the close distance between the donor and acceptor charges which resulted in a curved shock wave front, as depicted in Figure 10. As a result of the curved shock wave front, the first susceptible area to interact with the blast wave is the upper front of the acceptor charge. This can be clearly seen in Figure 5, where the higher-pressure values are recorded by gauges no. 7 and 8.

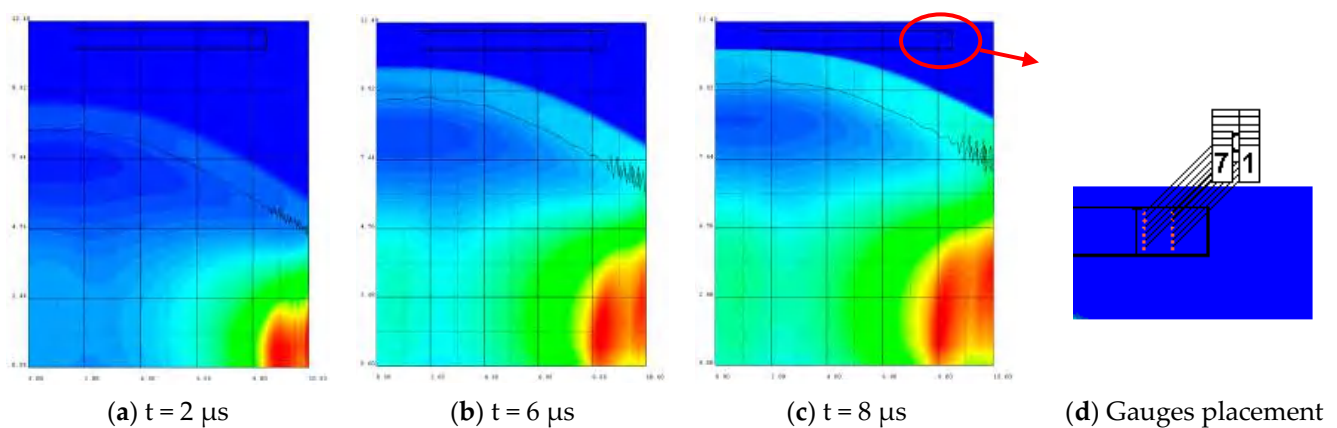


Figure 10. Blast wave front vs. TNT gas products front for 100 mm air gap thickness case.

5. Conclusions

Sympathetic detonation tendency of the blasting cap for different scenarios is mandatory when the disrupting equipment is used on suspicious packages (IEDs). While experimental tests easily allow the evaluation of blasting cap sensitivity to blast waves, the mix between numerical and experimental approaches can enhance the understanding of the phenomenon.

Based on the relations of the mathematical model, it can be concluded that the shock wave detaches gradually from the donor gas products, the complete detachment being completed at a greater distance than the ones characterized by the blast cap initiation. In the nearby distance of the donor charge, both the shock waves' and the gas products' overpressure act on and initiate the blasting caps, even though not simultaneously, as proved in Figure 6. It is also clearly pointed out that the presence of gas products favors reaching the critical value for sympathetic detonation, according to the critical energy fluence criterion.

The analysis of sympathetic detonation tendency of blasting caps in close vicinity shows that the critical energy fluence criterion is preferable to the Chapman–Jouguet pressure threshold. The critical energy fluence criterion can be applied to test configurations that include not only a dense matter gap but also an air gap.

Author Contributions: Conceptualization, M.L. and E.T.; methodology, E.T. and M.L.; software, E.T. and A.C.C.; validation, E.T., M.L. and A.C.C.; formal analysis, E.T., M.L. and B.I.; investigation, M.L., B.I., E.T. and A.C.C.; resources, M.L. and B.I.; data curation, E.T.; writing—original draft preparation, E.T. and B.I.; writing—review and editing, M.L., E.T. and A.C.C.; visualization, E.T., B.I. and A.C.C.; supervision, E.T.; project administration, M.L.; funding acquisition, M.L. All authors have read and agreed to the published version of the manuscript.

Funding: The paper was partially supported by a grant of the Romanian Ministry of Innovation and Research, UEFISCDI, project number 33SOL/2021 within PNCDI III.

Institutional Review Board Statement: Not applicable.

Informed Consent Statement: Not applicable.

Data Availability Statement: Not applicable.

Conflicts of Interest: The authors declare no conflict of interest.

References

1. Yang, T.; Wang, C.; Li, T. Numerical simulation study of sympathetic detonation in stages. *Def. Technol.* **2021**, *18*, 1382–1393. [CrossRef]
2. Zhang, Z.; Wang, C.; Hu, H.; Yang, T. Investigation of underwater sympathetic detonation. *Prop. Explos. Pyrotech.* **2020**, *45*, 1736–1744. [CrossRef]

3. Kubota, S.; Shimada, H.; Matsui, K.; Liu, Z.-Y.; Itoh, S. High-speed photography of underwater sympathetic detonation of high explosives. In Proceedings of the 24th International Congress on High-Speed Photography and Photonics, Sendai, Japan, 24–29 September 2000; Volume 4183, pp. 763–770.
4. Kubota, S.; Liu, Z.Y.; Otsuki, M.; Nakayama, Y.; Ogata, Y.; Yoshida, M. A Numerical study of sympathetic detonation in gap test. *Mater. Sci. Forum* **2004**, *465–466*, 163–168. [CrossRef]
5. Becuwe, A.; Deldos, A. Low-sensitivity explosive compounds for low vulnerability warheads. *Prop. Explos. Pyrotech.* **1993**, *18*, 1–10. [CrossRef]
6. Keshavarz, M.H.; Motamedoshariati, H.; Pouretedal, H.R.; Tehrani, M.K.; Semnani, A. Prediction of shock sensitivity of explosives based on small-scale gap test. *J. Hazard. Mater.* **2007**, *145*, 109–112. [CrossRef] [PubMed]
7. Ko, Y.-H.; Kim, S.-J.; Yang, H.-S. Assessment for the sympathetic detonation characteristics of underwater shaped charge. *Geosystem Eng.* **2017**, *20*, 286–293. [CrossRef]
8. Ferm, E.N.; Ramsay, J.B. Spherical projectile impact on explosives. In Proceedings of the Ninth Symposium (International) on Detonation, Portland, OR, USA, 28 August–1 September 1989; Volume 2, pp. 1427–1431.
9. James, H.R. Critical energy criterion for the shock initiation of explosives by projectile impact. *Prop. Explos. Pyrotech.* **1988**, *13*, 35–41. [CrossRef]
10. Victor, A.C. A Simple method for calculating sympathetic detonation of cylindrical, cased explosive charges. *Prop. Explos. Pyrotech.* **1996**, *21*, 90–99. [CrossRef]
11. Walker, F.E. A Comparison of the Classical and a Modern Theory of Detonation. *J. Phys. IV Proc.* **1995**, *5*, C4-231–C4-257.
12. Cooper, P.W. *Explosives Engineering*; Wiley: New York, NY, USA, 1996.
13. Yadav, H.S.; Asthana, S.N.; Subhananda, A. Critical Shock Energy and Shock and Detonation Parameters of an Explosive. *Def. Sci. J.* **2009**, *59*, 436–440. [CrossRef]
14. ANSYS Inc. *AUTODYN User Manual*, version 14.0; ANSYS Inc.: Beijing, China, 2013.
15. Fickett, W.; Davis, W.C. *Detonation: Theory and Experiment*; Dover Publications: Mineola, NY, USA, 2011; p. 25.
16. Kubota, S.; Saburi, T.; Nagayama, K. Unified Form EOS for Detonation Products Based on Relationship between Initial Density and Detonation Velocity. *AIP Conf. Proc.* **2020**, *2272*, 030012.
17. Seglets, S.B. *An Examination of the JWL Equation of State*; ARL-TR-8403; US Army Research Laboratory: Adelphi, MD, USA, 2018.
18. McIntosh, G.W.J. *Explosive Modelling Using Ls-Dyna—A User Guide*; Technical Memorandum; Defence R&D Canada: Valcartier, QC, Canada, 2014.
19. Chapman, D.L. VI. On the rate of explosion in gases. *Philos. Mag.* **1899**, *47*, 90–104. [CrossRef]
20. Jouguet, E. Sur la propagation des réactions chimiques dans les gaz. *J. Math. Pures Appl.* **1905**, *1*, 347–425.
21. Von Neumann, J. Theory of detonation waves. In *Collected Works*; Taub, A.H., Ed.; Pergamon Press Ltd.: Oxford, UK, 1963; Volume 6, pp. 178–218.
22. Schwarz, A.C. *New Technique for Characterizing an Explosive for Shock Initiation Sensitivity*; SAND75-0314 Report; Sandia Labs.: Albuquerque, NM, USA, 1975.
23. Walker, F.E.; Wasley, R.J. A general model for the shock initiation of explosives. *Prop. Explos. Pyrotech.* **1976**, *1*, 73–78. [CrossRef]
24. Walker, F.E.; Wasley, R.J. Initiation of nitromethane with relatively long-duration, low-amplitude shock waves. *Combust. Flame* **1970**, *15*, 233–246. [CrossRef]
25. Sedov, L.I. *Similarity and Dimensional Methods in Mechanics*, 1st ed.; Academic Press: New York, NY, USA; London, UK, 1959.
26. Taylor, G.I. The formation of a blast wave by a very intense explosion. *Proc. Roy. Soc. A* **1950**, *201*, 159–174.
27. Gilev, S.D.; Anisichkin, V.F. Interaction of aluminum with detonation products. *Combust. Explos. Shock Waves* **2006**, *42*, 107–115. [CrossRef]
28. Gordon, J.M.; Gross, K.C.; Perram, G.P. Fireball and shock wave dynamics in the detonation of aluminized novel munitions. *Combust. Explos. Shock Waves* **2013**, *49*, 450–462. [CrossRef]
29. Aouad, C.J.; Chemissany, W.; Mazzali, P.; Temsah, Y.; Jahami, A. Beirut explosion: TNT equivalence from the fireball evolution in the first 170 milliseconds. *Shock Waves* **2021**, *31*, 813–827. [CrossRef]
30. Kim, H.J.; Hwang, K.; Yoon, Y.H.; Lee, H.-J. Numerical analysis of the effect of afterburning on damage to the concrete structure under interior explosion. *Int. J. Concr. Struct. Mater.* **2022**, *16*, 6. [CrossRef]

Article

Behavior of Sedimentary Rock Tunnel against Rigid Projectile Impact

Abdullah H. Alsabhan ^{1,*}, Md. Rehan Sadique ^{2,*} , Ali S. Alqarni ¹, Shamshad Alam ¹  and Wonho Suh ³ ¹ Department of Civil Engineering, College of Engineering, King Saud University, Riyadh 11421, Saudi Arabia² Civil Engineering Department, Z.H. College of Engineering & Technology, Aligarh Muslim University, Aligarh 202002, India³ Department of Smart City Engineering, Hanyang University ERICA Campus, Ansan 15588, Korea

* Correspondence: aalsabhan@ksu.edu.sa (A.H.A.); rehan.sadique@zhcet.ac.in (M.R.S.)

Abstract: The tunnels in present-day cities are experiencing varying degrees of loading conditions ranging from static to extreme loading. Therefore, the stability of underground tunnels needs to be analyzed and understood for safer and strengthened design. The present study was conducted to simulate the impact loading conditions due to a missile traveling at a velocity of 5 Mach for different rock tunnels. The nonlinear continuum finite element analysis has been carried out through Abaqus and Explicit. The four different types of sandstones considered in the present study include Kota, Jamrani, Singrauli, and Jhingurda sandstones. An elastoplastic Mohr–Coulomb constitutive material model has been considered to model the behavior of rock surrounding the tunnel opening. The tunnel has an opening of 7 m in diameter (d), and 50 m in height and breadth, with 50 m of longitudinal length. The deformation and stress in the rock and the damage to the concrete lining have been compared in different cases. The Concrete–Damage–Plasticity (CDP) model and the Johnson–Cook model were considered for modelling of the RC lining and steel reinforcement. It was concluded that Jhingurda sandstone has maximum deformations due to impacts caused by missiles.

Citation: Alsabhan, A.H.; Sadique, M.R.; Alqarni, A.S.; Alam, S.; Suh, W.

Behavior of Sedimentary Rock Tunnel against Rigid Projectile Impact. *Appl. Sci.* **2022**, *12*, 9595.

<https://doi.org/10.3390/app12199595>

Academic Editors: Ricardo Castedo, Lina M. López and Anastasio P. Santos

Received: 7 March 2022

Accepted: 19 September 2022

Published: 24 September 2022

Publisher's Note: MDPI stays neutral with regard to jurisdictional claims in published maps and institutional affiliations.



Copyright: © 2022 by the authors. Licensee MDPI, Basel, Switzerland. This article is an open access article distributed under the terms and conditions of the Creative Commons Attribution (CC BY) license (<https://creativecommons.org/licenses/by/4.0/>).

Keywords: numerical modeling; rock tunnel; sandstone; missile impact

1. Introduction

Due to the rapid migration of the population from rural to urban cities, the demand for better, faster, and safer modes of transportation arises. In addition, the horizontal expansion of residential construction has created a need for subsurface construction. Therefore, the need for the design and research of tunnels and other underground structures has arisen. A number of studies have been carried out by researchers to understand the different aspects of tunnel stability [1–12].

Subsurface structures, especially tunnels and caverns, have been an integral part of the defense strategy of the country. The stability and equilibrium of these structures need to be studied for extreme loading events such as seismic loading, blast, and impact loading. Therefore, a number of researchers have studied the behavior of tunnels under varying types of loading conditions [13–17]. However, there are few studies that depict the performance of underground tunnels constructed in rock when subjected to impact load.

The numerical tools for computation and modelling have been used by researchers to study the stability of tunnels under varying impact loading conditions. Gao et al. [18] studied the behavior of intact rocks under an impact load using a commercial tool, LS-DYNA. They proposed a relationship and a model to study the behavior of intact rocks under impact loads. The model was validated with high accuracy using experimental results. Experimental and numerical simulations have been carried out by Aziznejad et al. [19] using a distinct element code to study the response of rock mass under an impact load. The propagation of cracks in the rock tunnel was studied by Zhou et al. [20] under the impact loading condition, and it was found that the speed of crack propagation is

non-uniform; therefore, cracks may stop propagating suddenly. Zhou et al. [21] considered the change in orientation of the impact with respect to the tunnel model. They categorized different types of failure modes in tunnels under impact loading conditions. Zhou et al. [22] had concluded that the tunnel experiences different types of failure modes due to impact load and found that radial cracks propagate in the tunnel from the edge of the tunnel.

Therefore, it may be summarized that the strength of tunnels in rocks under impact loads has been rarely studied in the open literature. However, there is still a significant scope and a need for further study. Sedimentary rocks cover the majority of metropolitan areas in different countries of the world. However, the impact resistance of these rocks against soft and hard missiles has received little attention from previous researchers. Moreover, sandstone is found in significant areas near the borders of strong military countries like India, Pakistan, and China. Hence, it needs to be studied for impact loading conditions. Consequently, the present paper has considered four different types of sandstone: Jhingurda, Singrauli, Jamrani, and Kota. A missile having 100 kg of weight and a velocity of 5 Mach has been considered to simulate the impact loading conditions for different rock tunnels. The nonlinear elastoplastic continuum FE (finite element) method has been adopted to understand the adverse effects of impact loading on rock tunnels.

2. Impact Loading Simulation

The impact resistance of four different sandstone rock tunnels has been studied in the present paper. A missile has been modelled based on the description given by Vidanović et al. [23]. The missile has a 0.7637 m length and a mass of 100 kg, modelled as a discrete part. The commercial software Abaqus has been used, and explicit mode has been selected for the simulation. The missile had a 5 Mach velocity before it hit the ground surface above the rock through which a tunnel has been constructed. The geometry of the tunnel has been considered based on the DMRC design specifications and published articles [24–26]. A dynamic explicit analysis has been carried out in the finite element tool Abaqus. In Abaqus, a step is time allotted for a particular analysis. However, according to the demand of output frame, it breaks the overall time allotted in small increments. In the present analysis, the step time is 0.035.

2.1. Geometry

The rock surrounding the tunnels has been modelled as a bigger size element having a three-dimensional size of 50 m × 50 m × 50 m and 12.5 m of overburden depth. The tunnel has an opening of 7 m in diameter and has been supported by a reinforced concrete liner of 0.35 m in thickness. The liner has an M30 grade of concrete. The concrete liner has reinforcement of steel bars of Weldox 460E grade in the longitudinal and circular directions. The details of the reinforcement and tunnel geometry are presented in Figure 1.

2.2. Input Properties of Materials

The rock mass surrounding the tunnel has been considered as a nonlinear elastoplastic material. The Mohr–Coulomb failure model has been used to incorporate the nonlinearity of four different types of sandstones. The four sandstone rocks considered in the present paper are Jhingurda, Singrauli, Jamrani, and Kota. The input parameters are taken from Rao et al. [27]. Table 1 represents the different physical and mechanical properties of rocks used in the present simulation.

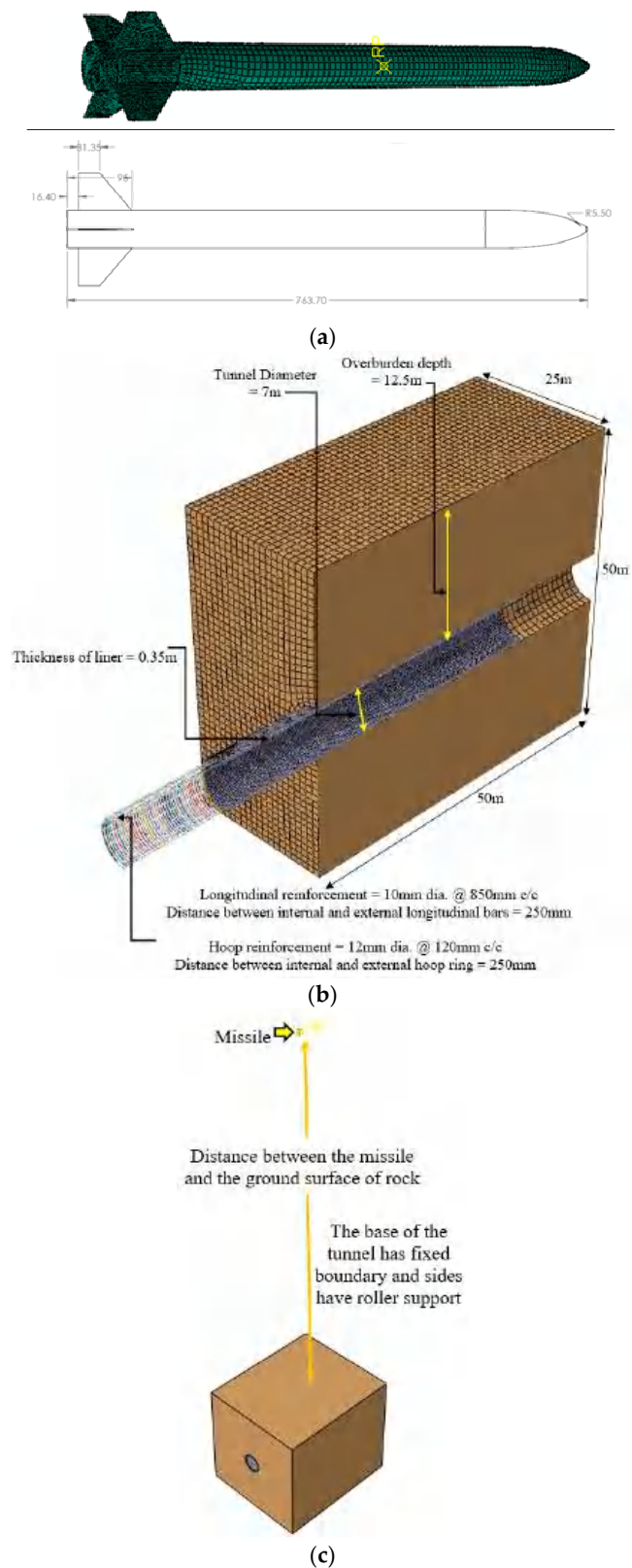


Figure 1. Geometry of finite element model for impact loading simulation. (a) Abaqus model of Missile, 0.7637 m in length and a mass of 100 kg with 5 Mach velocity (b) Tunnel with an opening of 7 m in diameter and supported by a reinforced concrete(M30) liner of 0.35 m in thickness. (c) The rock surrounding the tunnels of 50 m × 50 m × 50 m and 12.5 m of overburden depth.

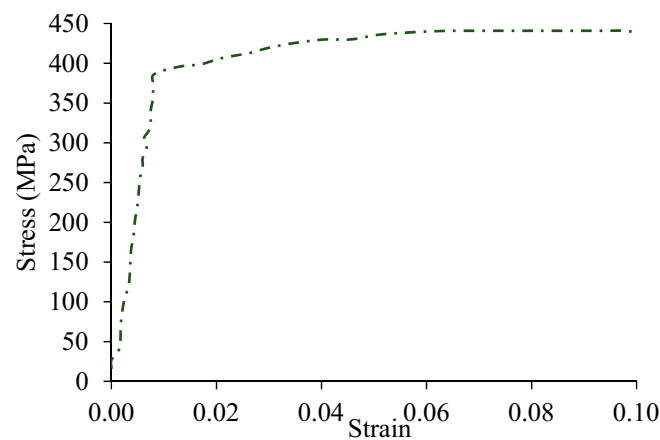
Table 1. Four different sandstone rock surrounding the tunnel opening.

Rock	Mass Density (kg/m ³)	Young's Modulus (GPa)	Poisson's Ratio	Friction Angle (Degree)	Cohesion (MPa)
Jhingurda	1670	2.84	0.25	21.34	3.68
Singrauli	2310	4.31	0.29	27.11	10.47
Jamrani	2480	5.29	0.22	37.79	11.17
Kota	2310	14.02	0.21	43.42	20.93

Similarly, the nonlinear behavior has been considered for steel bars by providing the elastoplastic properties of steel. Table 2 and Figure 2 show the properties of steel reinforcement used in this study. The interaction between the steel bars and concrete of the liner is achieved by embedding the circular and longitudinal reinforcement. The embedment constraint in the interaction module applied the proper bond between the steel and concrete, creating a reinforced concrete liner for the rock tunnel. The Johnson–Cook model [28] has been used for modelling the steel bars and properties are taken from Borvik et al. [29]. Borvik et al. [29] had performed a series of experiments on the steel under different strain rate and at varying temperature range.

Table 2. Elastoplastic properties of reinforced steel with Wieldox 460 E grade.

(ρ) (kg/m ³)	(E) (GPa)	(ν)	A (MPa)	B (MPa)	n	C	Rate (s ⁻¹)
7850	200	0.33	490	807	0.73	0.0114	100

**Figure 2.** Plastic behavior of steel reinforcement material.

Moreover, the concrete liner has been considered as M30 grade and its nonlinear elastoplastic behavior has been simulated through the Concrete Damage Plasticity model. It also incorporated the damage characteristic of the concrete and, therefore, proved to be useful in studying the overall failure of the internal lining.

The M30 grade of concrete has a mass density of 2500 kg/m³ and a Young's modulus of 26.6 GPa, with a 0.20 Poisson's ratio. Moreover, the dilation angle and eccentricity of 31 degrees and 0.1, respectively, have been considered. The variation in stress and damage corresponding to strain for the M30 grade of concrete are shown in Figures 3 and 4, respectively.

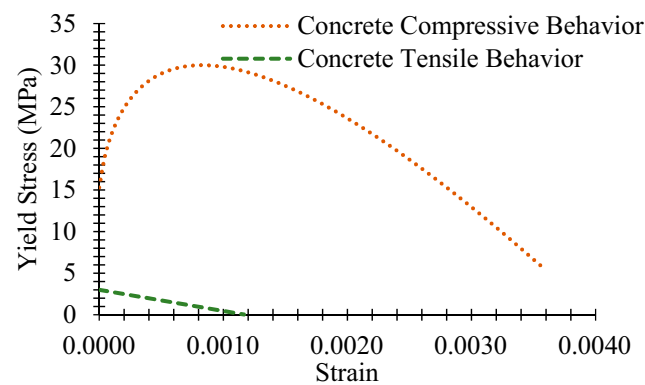


Figure 3. Input of stress–strain variation for M30 grade of concrete liner used in tunnel.

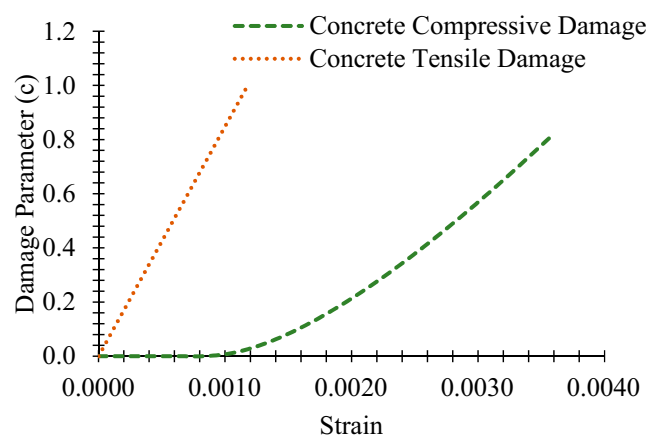


Figure 4. Damage parameter variation with strain for M30 grade of concrete.

2.3. Meshing, Loading, Boundary and Interaction Conditions

The rock mass surrounding the tunnel has been meshed as C3D8R (Continuum Three-dimensional eight-nodded reduced integration solid Brick element), as suggested and used by Zaid and Sadique [30,31], Zaid and Shah [32] and Zaid et al. [33–37]. The element size of 0.7 has been used based on mesh convergence, and this type of mesh is defined as brick-type element, which has eight nodes. The steel bars are modelled as beam-type element, i.e., B31, as suggested and used by Zaid and Sadique [38–40]. The steel bars elements have an element size of 0.05. The missile has been meshed by the R3D4 element type to make it rigid and discrete. The general hard contact and frictionless tangential contact has been assigned to the whole model. The embedment interaction has been used to model the reinforced concrete liner by embedding the steel bars in concrete liner. The base of the rock has a fixed support as the rock mass extends to infinite depth, and the sides of the model have roller supports, which allow vertical movement but restrain other directional movement of rock mass. One set of simulation takes around six and a half CPU hours on a 64GB RAM system with a Dell Precision Tower 7810. General hard contact and frictionless tangential contact have been assigned to the whole model. The embedment interaction has been used to model the reinforced concrete liner by embedding the steel bars in the concrete liner.

3. Validation of Dynamic Loading

In order to validate the present finite element simulation, an experimental study has been simulated using the present methodology and numerical results are compared with the experimental study by Andersson [41], as shown in Table 3. A steel mass weighing 600 kg was considered for impact loading on $0.2 \text{ m} \times 0.2 \text{ m}$ area in the middle of a slab. The height of fall was varied from 1 m to 2 m on the concrete slab having a $1.75 \text{ m} \times 1.75 \text{ m}$

cross section and a 0.12 m thickness. The size of the slab, loading conditions, and the properties of the model have been adopted as per the report by Andersson [41].

Table 3. Comparison of results of properties of reinforced steel.

Slab No.	Height (m)	Deformation (mm)		% Cent Error
		Experimental Study	FE Study	
S4	1.0	46	44.39	3.5
S5	1.5	63	61.74	2.0
S6	1.5	50	47.00	6.0
S8	1.0	60	57.00	5.0
S9	1.2	61	59.17	3.0
S10	2.0	77	73.15	5.0

4. Results and Discussion

Commercial software based on the finite element method, i.e., Abaqus/Explicit, has been used for modelling and analysis. Four different sandstone rocks, Jhingurda, Singrauli, Jamrani, and Kota, were considered. A generally used design specification for metro tunnels has been used based on Delhi Metro Rail Corporation designs. A missile having a 5 Mach velocity and weighing 100 kg has been considered. The simulation has been run for 30 milliseconds, which is the time required by a missile to hit the rock ground from 100 m away.

Figure 5 has been plotted to compare the deformation variation with time when a missile hits the ground surface for all the sandstone rocks considered in the present study. It has been observed that the amplitude of deformation for Jhingurda sandstone is the maximum, having a magnitude of 2.45 m. Maximum deformations of 1.35 m, 1.03 m, and 0.76 m have been observed for Singrauli, Jamrani, and Kota rocks prospectively at the ground surface. Therefore, Kota sandstone has shown maximum resistance to missile penetration, while Jhingurda sandstone has the least resistance to missile penetration.

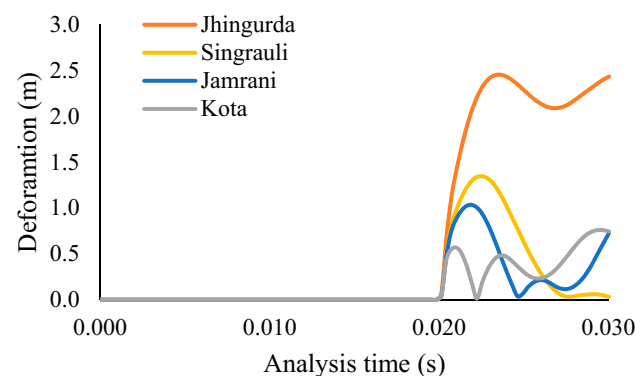


Figure 5. Variation in deformation with time to compare the ground surface behavior under impact loading of 100 kg missile.

The deformation profile is one of the important output results for understanding the internal behavior of a tunnel. Figure 6 shows the comparison of the deformation profiles of four sandstone rocks. The deformation profile for Jhingurda sandstone follows a smooth curvature, while the curvature becomes distorted and non-uniform for other types of sandstone. It has also been observed that as the strength of sandstone increases, the peak deformation gets decreased, while the length of tunnel under disturbance increases with the increase in the strength of sandstone. Moreover, a slight bulging has been observed in all the sandstones except for Jhingurda sandstone. Therefore, it may be concluded that weaker sandstone requires strengthening for a smaller area after an impact loading event, while high-strength sandstone will require repair for a longer portion of the tunnel.

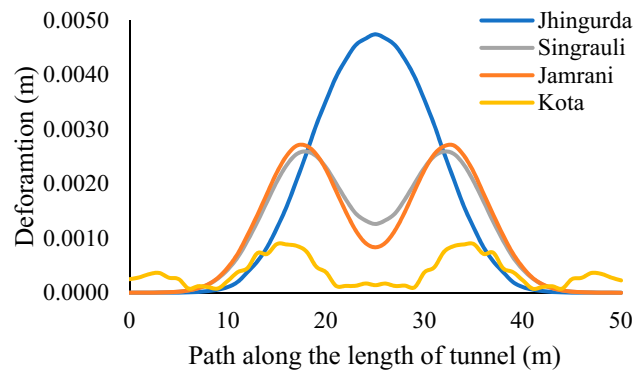


Figure 6. Comparison of deformation profile generated under the response of impact load.

Particle velocity is one of the significant output results in the dynamic loading analysis of rock tunnels. Therefore, the peak velocity at the ground surface of different sandstone rocks is shown in Figure 7 for comparison. The peak of the particle velocity graph has been observed at 20.41 milliseconds in each case of sandstone rock. However, the variation of particle velocity follows a separate path for different rocks, but the pattern of the particle velocity plot remains similar in all the cases. Figure 8 represents the peak acceleration at the ground surface when a missile hits the different sandstone rocks. In the case of Jhingurda sandstone, the magnitude of peak velocity and acceleration is greatest. Moreover, the pattern of variation in acceleration and velocity remains similar, and therefore, it is independent of the type of sandstone.

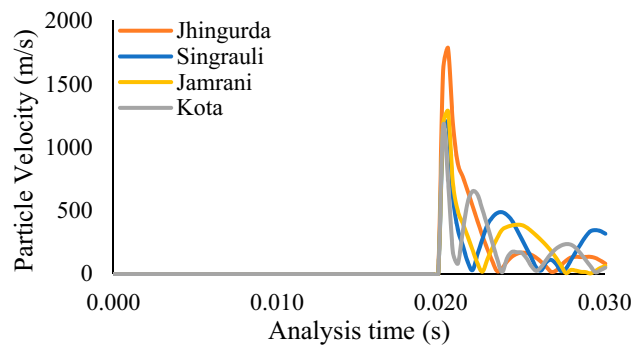


Figure 7. Comparison of particle velocity at ground surface under present impact loading condition.

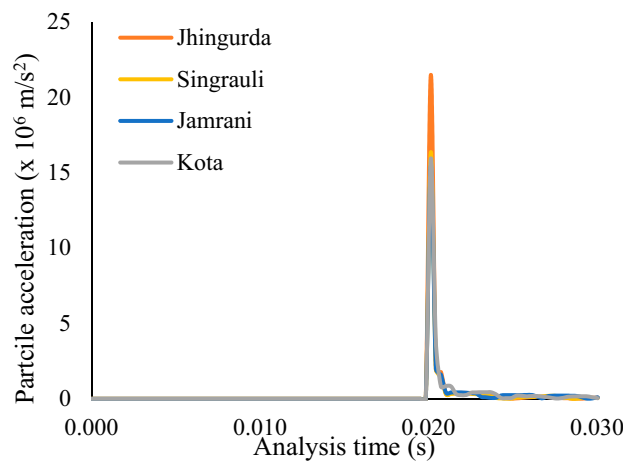


Figure 8. Comparison of particle acceleration at ground surface under present impact loading condition.

Figure 9 shows the deformation contours of Jhingurda, Singrauli, Jamrani, and Kota sandstone when a 100 kg missile moving at the velocity of 5 Mach hits the ground surface of the rock-containing tunnel. It has been observed that the brittleness and strength of rock have a significant influence on the deformation zone. In the cases of Jhingurda, Singrauli, Jamrani, and Kota, the maximum deformation at the crown is 4.94 mm, 2.75 mm, 2.61 mm, and 1.04 mm, respectively. It can be concluded that Kota sandstone has minimum deformation, and therefore, it is the safest sandstone rock under impact loading conditions. However, the area of disturbance is maximum in the case of Kota sandstone, and vibrations may reach the tunnel crown in a shorter time as compared to other sandstones.

Figure 10 has been plotted to compare the serviceability of reinforced concrete liners under impact loading conditions in the case of different types of sandstone. Tension damage has been observed in each type of sandstone. However, the area of the damaged zone increases with the strength and brittleness of sandstone. Therefore, reinforced concrete liner has maximum tensile damage in Kota sandstone (0.99) and less tension damage in the case of Jhingurda sandstone (0.017). It has been concluded that the consequences of an impacting projectile reach the tunnel lining when constructed in strong and brittle sandstone, or vice-versa. In addition, the tensile damage in all the different types of sandstones considered in the present study remains concentrated at the outer periphery of the liner.

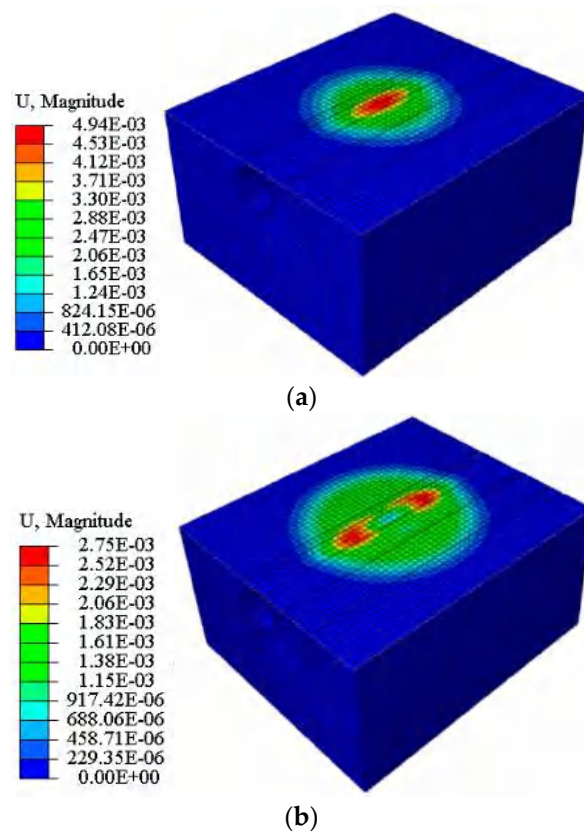


Figure 9. Cont.

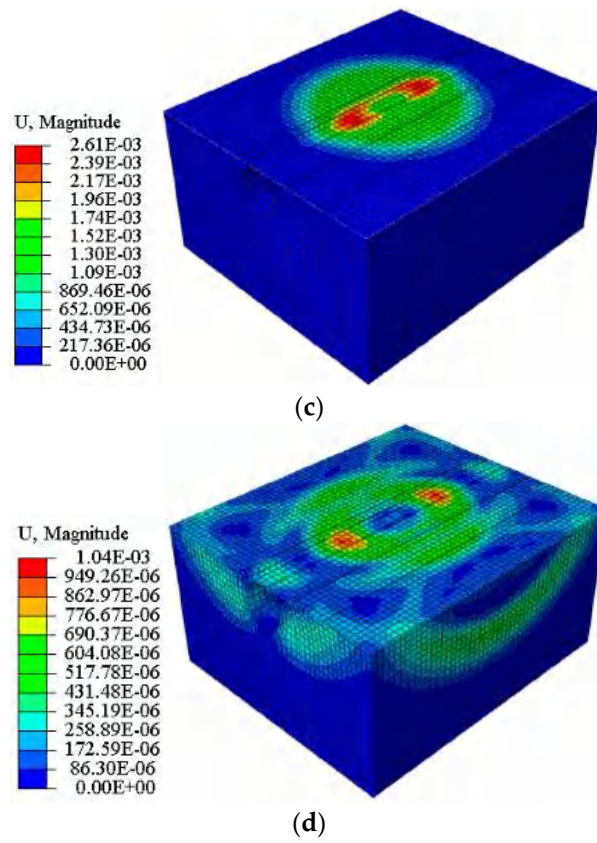


Figure 9. Deformation contours of (a) Jhingurda, (b) Singrauli, (c) Jamrani and (d) Kota when an impact loading occurs due to 100 kg missile.

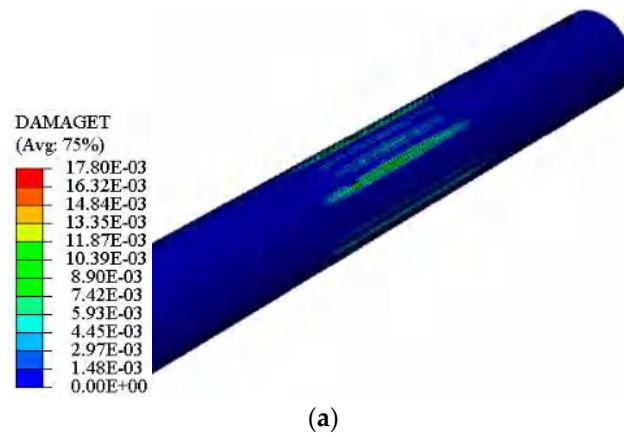


Figure 10. Cont.

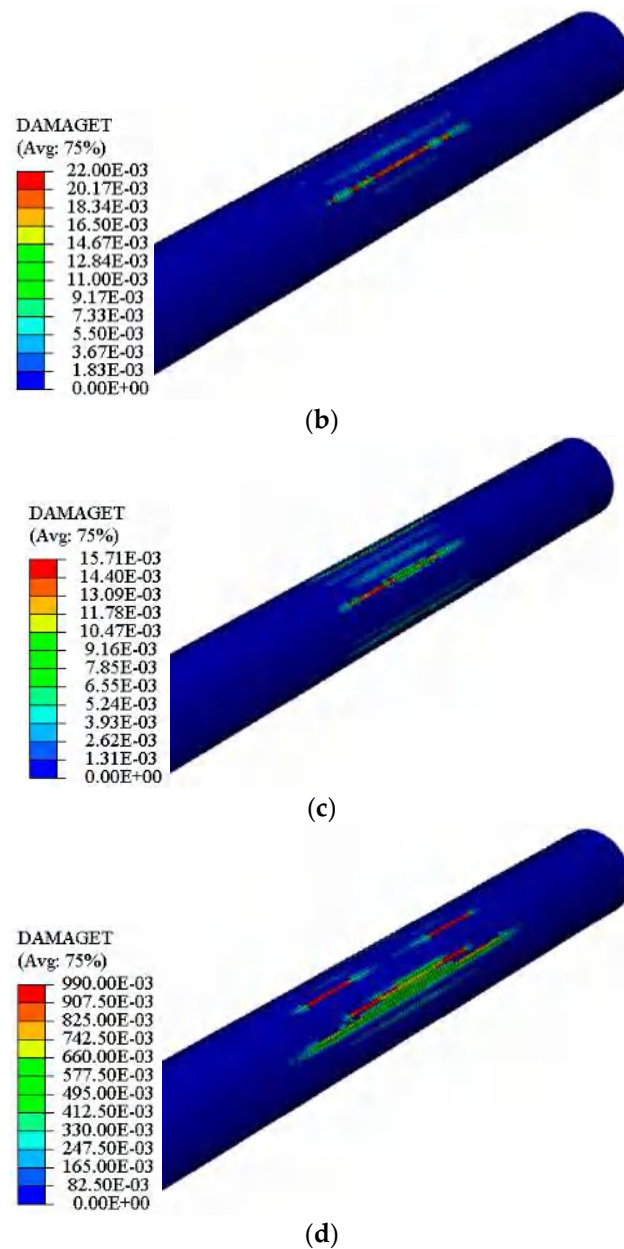


Figure 10. Tension damage contours of (a) Jhingurda, (b) Singrauli, (c) Jamrani, and (d) Kota sandstone tunnel when an impact loading occurs due to a 100 kg missile.

The in-depth view of lining performance has been studied by comparing the deformation at the reinforcement cage of steel bars in the case of different rocks, as shown in Figure 11. The maximum value of deformation has been noted for Jhingurda sandstone, while the maximum value of deformation remains concentrated at the crown of the tunnel.

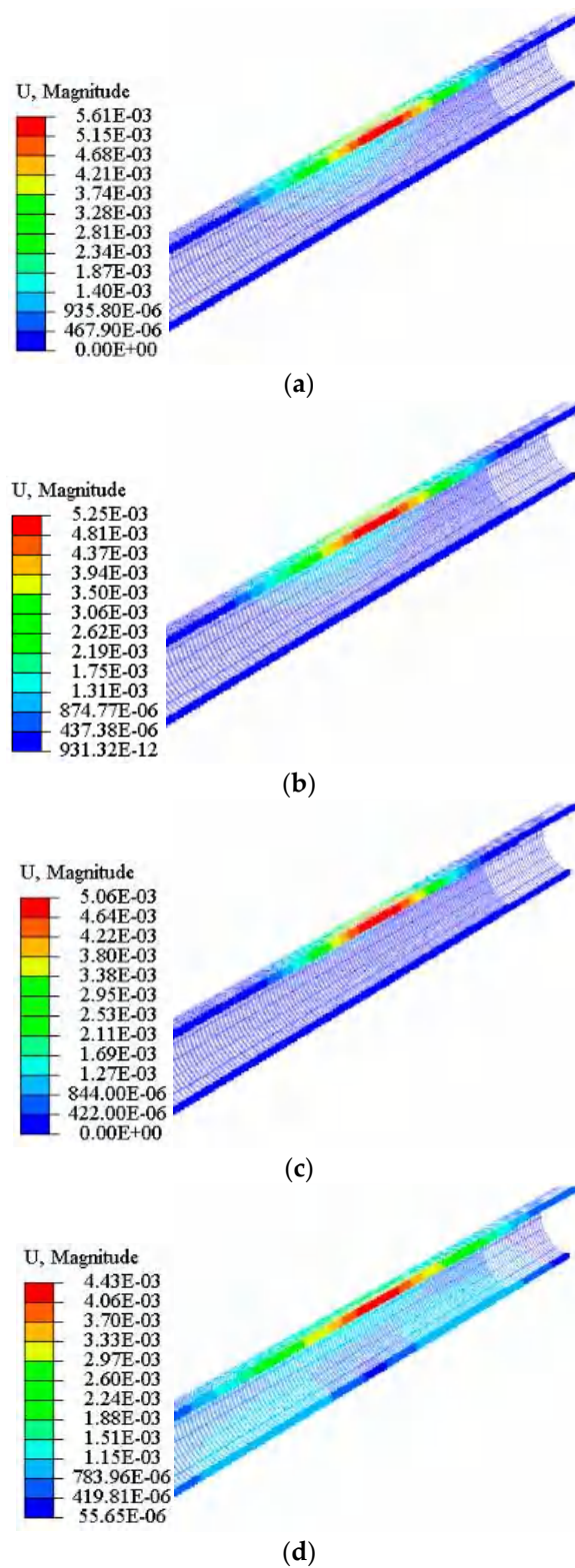


Figure 11. Deformation contours of steel bar reinforcement cage for (a) Jhingurda, (b) Singrauli, (c) Jamrani, and (d) Kota sandstone tunnel when an impact loading occurs due to a 100 kg missile.

5. Conclusions

The present study of finite element simulation for rock tunnel resistance against impact loading has four different sandstone rocks surrounding a 5 m diameter reinforced concrete tunnel lining. The major conclusions drawn from the present study are as follows:

1. The Kota sandstone has 2.22-times, 0.77-times, 0.35-times more impact resistance than Jhingurda, Singrauli and Jamrani sandstone, respectively. Therefore, the impact resistance of a rock tunnel is a function of cohesion and friction angle.
2. The deformation profile for Jhingurda sandstone follows a smooth curvature while the curvature becomes distorted and non-uniform for other types of sandstone. It has also been observed that as the strength of sandstone increases, the peak deformation decreases, while the length of tunnel under disturbance increases with the increase in the strength of sandstone. In addition, it has been concluded that weaker sandstone requires strengthening for a smaller area after an impact loading event while high-strength sandstone will require repair for a longer portion of the tunnel.
3. The magnitude of peak velocity and acceleration is maximum in case of Jhingurda sandstone at 20.41 milliseconds. Moreover, the pattern of variation in acceleration and velocity remains similar, and therefore, it is independent of the type of sandstone.
4. It can be concluded that Kota sandstone has minimum deformation and is therefore the safest sandstone rock under impact loading conditions. However, the area of disturbance is greatest in the case of Kota sandstone, and vibrations may reach the tunnel crown in a shorter time in comparison to other rocks.
5. The effect of impact loading has reached the tunnel lining when constructed in strong and brittle sandstone, or vice versa. In addition, the tensile damage in all the different types of sandstones considered in the present study remains concentrated at the outer periphery of the liner. The steel reinforcement cage experiences maximum deformation at the crown position in all the cases, while the maximum magnitude of deformation occurred in the case of Jhingurda sandstone.

Author Contributions: M.R.S.: drafting—data collection and preparation of the manuscript, writing review and editing, S.A.: drafting—preparation of the manuscript, revision and correction; A.H.A.: composing—reviewing, fund acquisition and modifying; A.S.A.: composing—reviewing, and modifying; W.S.: reviewing and modifying. All authors have read and agreed to the published version of the manuscript.

Funding: The authors acknowledge the support provided by Researchers Supporting. Project Number (RSP2022R473), King Saud University, Riyadh, Saudi Arabia.

Institutional Review Board Statement: Not applicable.

Informed Consent Statement: Not applicable.

Data Availability Statement: Not applicable.

Acknowledgments: Authors acknowledge the support provided by King Saud University, Saudi Arabia, and Aligarh Muslim University, India, to carry out this study.

Conflicts of Interest: The authors declare no conflict of interest.

References

1. Do, N.A.; Oreste, P.; Dias, D.; Antonello, C.; Djeran-Maigre, I.; Livio, L. Stress and strain state in the segmental linings during mechanized tunnelling. *Geomech. Eng.* **2014**, *7*, 75–85. [CrossRef]
2. Do, N.A.; Dias, D.; Oreste, P.; Djeran-Maigre, I. 2D numerical investigations of twin tunnel interaction. *Geomech. Eng.* **2014**, *6*, 263–275. [CrossRef]
3. Eskandari, F.; Goharrizi, K.G.; Hooti, A. The impact of EPB pressure on surface settlement and face displacement in intersection of triple tunnels at Mashhad metro. *Geomech. Eng.* **2018**, *15*, 769–774. [CrossRef]
4. Ghasemi, S.H.; Nowak, A.S. Reliability analysis of circular tunnel with consideration of the strength limit state. *Geomech. Eng.* **2018**, *15*, 879–888. [CrossRef]
5. Mazek, S.A. Evaluation of surface displacement equation due to tunnelling in cohesionless soil. *Geomech. Eng.* **2014**, *7*, 55–73. [CrossRef]
6. Miranda, T.; Dias, D.; Pinheiro, M.; Eclaircy-Caudron, S. Methodology for real-time adaptation of tunnels support using the observational method. *Geomech. Eng.* **2015**, *8*, 153–171. [CrossRef]
7. Fahimifar, A.; Ghadami, H.; Ahmadvand, M. The ground response curve of underwater tunnels, excavated in a strain-softening rock mass. *Geomech. Eng.* **2015**, *8*, 323–359. [CrossRef]

8. Nawel, B.; Salah, M. Numerical modeling of two parallel tunnels interaction using three-dimensional finite elements method. *Geomech. Eng.* **2015**, *9*, 775–791. [CrossRef]
9. Nikadat, N.; Marji, M.F. Analysis of stress distribution around tunnels by hybridized fsm and ddm considering the influences of joints parameters. *Geomech. Eng.* **2016**, *11*, 269–288. [CrossRef]
10. Khezri, N.; Mohamad, H.; Fatahi, B. Stability assessment of tunnel face in a layered soil using upper bound theorem of limit analysis. *Geomech. Eng.* **2016**, *11*, 471–492. [CrossRef]
11. Aalianvari, A.; Soltani-Mohammadi, S.; Rahemi, Z. Estimation of geomechanical parameters of tunnel route using geostatistical methods. *Geomech. Eng.* **2018**, *14*, 453–458. [CrossRef]
12. Zidan, A.F.; Ramadan, O.M. A hybrid MC-HS model for 3D analysis of tunnelling under piled structures. *Geomech. Eng.* **2018**, *14*, 479–489. [CrossRef]
13. Khan, M.A.; Sadique, M.R.; Harahap, I.H.; Zaid, M.; Alam, M.M. Static and Dynamic Analysis of the Shielded Tunnel in Alluvium Soil with 2D FEM Model. *Transp. Infrastruct. Geotechnol.* **2022**, *9*, 73–100. [CrossRef]
14. Sadique, R.M.; Zaid, M.; Naqvi, M.W.; Akhtar, M.F. Analysis of Underground Renewable Energy Storage Tunnels Subjected to Capricious Superstructures. In *Renewable Power for Sustainable Growth, Proceedings of the International Conference on Renewal Power (ICRP 2020), Rajouri, India, 17–18 April 2020*; Lecture Notes in Electrical Engineering; Springer: Singapore, 2021; Volume 723.
15. Sadique, M.R.; Ali, A.; Zaid, M.; Masroor Alam, M. Experimental and Numerical Modeling of Tunneling-Induced Ground Settlement in Clayey Soil. In *Advances in Geotechnics and Structural Engineering, Proceedings of the TRACE 2020, Noida, India, 20–21 August 2020*; Lecture Notes in Civil Engineering; Springer: Singapore, 2021; Volume 143.
16. Sadique, M.R.; Zaid, M.; Alam, M.M. Rock Tunnel Performance Under Blast Loading Through Finite Element Analysis. *Geotech. Geol. Eng.* **2022**, *40*, 35–56. [CrossRef]
17. Zaid, M.; Mishra, S. Numerical Analysis of Shallow Tunnels Under Static Loading: A Finite Element Approach. *Geotech. Geol. Eng.* **2021**, *39*, 2581–2607. [CrossRef]
18. Gao, F.; Hou, A.; Yang, X. Numerical Analysis of Dynamic Mechanical Properties for Rock Sample under Strong Impact Loading. *Int. J. Inf. Eng. Electron. Bus.* **2010**, *2*, 10–16. [CrossRef]
19. Aziznejad, S.; Esmaili, K.; Hadjigeorgiou, J.; Labrie, D. Responses of jointed rock masses subjected to impact loading. *J. Rock Mech. Geotech. Eng.* **2018**, *10*, 624–634. [CrossRef]
20. Zhou, L.; Zhu, Z.; Wang, M.; Ying, P.; Dong, Y. Dynamic propagation behavior of cracks emanating from tunnel edges under impact loads. *Soil Dyn. Earthq. Eng.* **2018**, *105*, 119–126. [CrossRef]
21. Zhou, L.; Zhu, Z.; Dong, Y.; Fan, Y.; Zhou, Q.; Deng, S. The influence of impacting orientations on the failure modes of cracked tunnel. *Int. J. Impact Eng.* **2019**, *125*, 134–142. [CrossRef]
22. Zhou, L.; Zhu, Z.; Dong, Y.; Ying, P.; Wang, M. Study of the fracture behavior of mode I and mixed mode I/II cracks in tunnel under impact loads. *Tunn. Undergr. Space Technol.* **2019**, *84*, 11–21. [CrossRef]
23. Vidanović, N.; Rašuo, B.; Kastratović, G.; Maksimović, S.; Čurčić, D.; Samardžić, M. Aerodynamic–structural missile fin optimization. *Aerosp. Sci. Technol.* **2017**, *65*, 26–45. [CrossRef]
24. DMRC. *Design Specifications of DMRC*; DMRC: New Delhi, India, 2015.
25. Zaid, M. Dynamic stability analysis of rock tunnels subjected to impact loading with varying UCS. *Geomech. Eng.* **2021**, *24*, 505–518. [CrossRef]
26. Zaid, M. Three-dimensional finite element analysis of urban rock tunnel under static loading condition: Effect of the rock weathering. *Geomech. Eng.* **2021**, *25*, 99–109. [CrossRef]
27. Rao, K.; Rao, G.; Ramamurthy, T. Strength Behaviour of Some Indian Sandstones. In *Proceedings of the Asian Regional Conference on Geotechnical Problems and Practices in Foundation Engineering, Colombo, Sri Lanka, 25–27 February 1986*; pp. 1–6.
28. Johnson, G.R.; Cook, W.H. A Constitutive modeling and data for metals subjected to large strain rates and high temperatures. In *Proceedings of the 7th International Symposium on Ballistics, The Hague, The Netherlands, 19–21 April 1983*.
29. Borvik, T.; Hopperstad, O.S.; Berstad, T.; Langseth, M. A computational model of viscoplasticity and ductile damage for impact and penetration. *Eur. J. Mech. A Solids* **2001**, *20*, 685–712. [CrossRef]
30. Zaid, M.; Rehan Sadique, M. Dynamic analysis of tunnels in western ghats of indian peninsula: Effect of shape and weathering. In *Recent Trends in Civil Engineering*; Springer: Singapore, 2021; Volume 77.
31. Zaid, M.; Rehan Sadique, M. A Simple Approximate Simulation Using Coupled Eulerian–Lagrangian (CEL) Simulation in Investigating Effects of Internal Blast in Rock Tunnel. *Indian Geotech. J.* **2021**, *51*, 1038–1055. [CrossRef]
32. Zaid, M.; Shah, I.A. Blast-Resistant Stability Analysis of Triple Tunnel. In *Advances in Geotechnics and Structural Engineering, Proceedings of the TRACE 2020, Noida, India, 20–21 August 2020*; Lecture Notes in Civil Engineering; Springer: Singapore, 2021; Volume 143.
33. Zaid, M.; Athar, M.F.; Sadique, M.R. Effect of Rock Weathering on the Seismic Stability of Different Shapes of the Tunnel. In *Lecture Notes in Civil Engineering, Proceedings of the Indian Geotechnical Conference, 2019, Surat, India, 19–21 December 2021*; Springer: Singapore, 2021; Volume 137.
34. Zaid, M.; Faraz Athar, M.; Rehan Sadique, M. Interaction of Transmission Tower Footing with Twin Rock Tunnel. In *Advances in Geotechnics and Structural Engineering, Proceedings of the TRACE 2020, Noida, India, 20–21 August 2020*; Lecture Notes in Civil Engineering; Springer: Singapore, 2021; Volume 143.

35. Zaid, M.; Naqvi, M.W.; Sadique, M.R. Stability of Arch Tunnel in Different Magnitude of Earthquake with Effect of Weathering in Western Ghats of India. In *Lecture Notes in Civil Engineering, Proceedings of the Indian Geotechnical Conference 2019, Surat, India, 19–21 December 2021*; Springer: Singapore, 2021; Volume 138.
36. Zaid, M.; Sadique, M.R.; Alam, M.M. Blast Resistant Analysis of Rock Tunnel Using Abaqus: Effect of Weathering. *Geotech. Geol. Eng.* **2021**, *40*, 809–832. [CrossRef]
37. Zaid, M.; Sadique, M.R.; Alam, M.M. Blast analysis of tunnels in Manhattan-Schist and Quartz-Schist using coupled-Eulerian–Lagrangian method. *Innov. Infrastruct. Solut.* **2021**, *6*, 69. [CrossRef]
38. Zaid, M.; Sadique, M.R. Effect of joint orientation and weathering on static stability of rock slope having transmission tower. In *Proceedings of the 7th Indian Young Geotechnical Engineers Conference 2019, Silchar, India, 15–16 March 2019*; Volume 5, pp. 414–422.
39. Zaid, M.; Sadique, M.R. Numerical modelling of internal blast loading on a rock tunnel. *Adv. Comput. Des.* **2020**, *5*, 417–443. [CrossRef]
40. Zaid, M.; Sadique, M.R. The response of rock tunnel when subjected to blast loading: Finite element analysis. *Eng. Rep.* **2021**, *3*, e12293. [CrossRef]
41. Andersson, A. *Impact Loading on Concrete Slabs: Experimental Tests and Numerical Simulation*; KTH: Stockholm, Sweden, 2014.

Article

Blast Hole Pressure Measurement and a Full-Scale Blasting Experiment in Hard Rock Quarry Mine Using Shock-Reactive Stemming Materials

Younghun Ko ^{1,*} , Chanhwi Shin ², Youngjun Jeong ³ and Sangho Cho ^{2,4,*}

¹ Department of Geotechnical Engineering Research, Korea Institute of Civil Engineering and Building Technology, 283 Goyang-daero, Ilsanseo-gu, Goyang-si 10223, Korea

² Department of Energy Storage & Conversion Engineering of Graduate School, Jeonbuk National University, 567 Baekje-Daero, Deokjin-gu, Jeonju-si 54896, Korea

³ Seokseong Blasting Construction Co., Ltd., Wolgye-ro 37-gil, Gangbuk-gu, Seoul 01226, Korea

⁴ Department of Mineral Resources and Energy Engineering, Jeonbuk National University, 567 Baekje-Daero, Deokjin-gu, Jeonju-si 54896, Korea

* Correspondence: younghunko@kict.re.kr (Y.K.); chosh@jbnu.ac.kr (S.C.)

Abstract: By increasing the effectiveness of the energy generated by the explosive charge inserted into a blast hole, stemming increases rock fragmentation. Missing or improper stemming, which can lead to the detonation gas escaping from the blast hole in advance, results not only in the waste of explosive energy and poor fragmentation but also in environmental problems, such as ground vibration, noise, flying rocks, back breaks, and air blasts. In this study, a stemming material based on a shear thickening fluid (STF) that reacts to dynamic pressure was developed. Two blasting experiments were conducted to verify the performance of the STF-based stemming material. In the first experiment, the pressure inside the blast hole was directly measured based on the application of the stemming material. In the second experiment, full-scale bench blasting was performed, and the blasting results of sand stemming and the STF-based stemming cases were compared. The measurement results of the pressure in the blast hole showed that when the STF-based stemming material was applied, the pressure at the top of the blast hole was lower than in the sand stemming case, and the stemming ejection was also lower. Full-scale bench blasting was conducted to compare the two types of stemming materials by evaluating the size of the rock fragments using image processing. The results of the two blasting experiments helped to verify that the blockage performance of the STF-based stemming material in the blast hole was superior to that of the sand stemming material.

Keywords: blasting experiment; stemming material; shear thickening fluid; sand; blockage performance

Citation: Ko, Y.; Shin, C.; Jeong, Y.; Cho, S. Blast Hole Pressure Measurement and a Full-Scale Blasting Experiment in Hard Rock Quarry Mine Using Shock-Reactive Stemming Materials. *Appl. Sci.* **2022**, *12*, 8629. <https://doi.org/10.3390/app12178629>

Academic Editors: Ricardo Castedo, Lina M. López and Anastasio P. Santos

Received: 2 August 2022

Accepted: 26 August 2022

Published: 29 August 2022

Publisher's Note: MDPI stays neutral with regard to jurisdictional claims in published maps and institutional affiliations.



Copyright: © 2022 by the authors. Licensee MDPI, Basel, Switzerland. This article is an open access article distributed under the terms and conditions of the Creative Commons Attribution (CC BY) license (<https://creativecommons.org/licenses/by/4.0/>).

1. Introduction

Stemming is a process applied to blast holes to prevent gases from escaping during detonation. A stemming material helps confine the explosive energy for a longer duration. Without stemming, up to 50% of the explosive energy can escape through the borehole [1]. Proper stemming has been shown to improve explosive efficiency by over 41% [2]. Further, employing even the least efficient stemming materials can boost the usable energy of an explosion by 60%, while the most efficient stemming materials can increase it by up to 93% [3].

Missing or improper stemming, which can lead to the detonation gas escaping from the blast hole in advance, results not only in the waste of explosive energy and poor rock fragmentation but also in environmental problems, such as ground vibration, noise, flying rocks, back breaks, and air blasts [4].

Smaller amounts of explosives may be used to produce the same blasting effects if explosive energy was used more effectively [5,6]. Improvements in fragmentation will

result in lower second breaking work costs. Proper stemming can reduce costs and improve the productivity and profitability of a mining operation. The main objective of rock-blasting is fragmentation by explosive. The loading and hauling operations of a mining operation, particularly the crushing line, profit greatly from good fragmentation [7]. Additionally, cracks are generated over a larger area in the rock mass using proper stemming. These cracks propagate, interconnect, and cut the rock mass; thus, the block size and distribution after blasting satisfy the construction or mining requirements. Therefore, reasonably selecting the stemming material is of particular importance for improving the blasting effect, increasing the efficiency of explosives, and obtaining ideal blasting fragmentation.

In the mining industry, blast holes are sealed with three different sorts of stemming materials: colloidal, liquid, and solid. Additional research on the performance of stemming materials is required. Li et al. [8] used a water stemming technique that involves putting water-filled polyvinyl plastic bags within blast holes. A water-silt composite-stemmed blasting method for tunnels was proposed [9] to increase rock breakage, reduce dust, and use fewer explosives.

In most cases, using fluid-type stemming inside a blast hole as a stemming material produced good results. Fluid has a higher density than air, and even at extremely high pressures, the compression of water is significantly lower than that of air [10].

Under dynamic loading, Zhu et al. [11] performed an AUTODYN numerical analysis using a variety of stemming materials, such as fluid (water), sand, and air, placed in the area between the internal explosives and the hollow wall inside the blast hole. The water stemming case, which was also the best medium for shockwave transmission, produced the largest fracture area. Additionally, the presence of fluid (water), which results in the deformation and displacement of the rock, causes the shock wave to reflect and bubble pulse, which contributes to the high stress exerted during this process.

The most effective method to evaluate the stemming effect is to conduct field experiments. A stemming performance test of a small-scale model was developed, and the results showed that different stemming materials have different functionalities, which can significantly influence the efficiency of rock breaking [12].

Kopp [13] suggested a simple physical model for predicting the time required to eject stemming. This model depends only on the inertia of the stemming material. The frictional forces that resist the movement were omitted. The stemming performance of the stemming material can be evaluated using the initial ejection velocity of the stemming part at the entrance of the blast hole [14].

The momentum of the stemming structure based on the explosive load can be calculated using the mass of the stemming structure and the initial velocity of the stemming part when the stemming is ejected into the orifice.

As a highly capable method in the mining industry, image analysis techniques have been used to predict rock fragmentation by blasting. These techniques are capable of visual processing, thereby serving as an appropriate alternative to low-accuracy methods [15]. Over the past few decades, various image analysis software packages, such as Split-Online, Split-desktop, Gold-Size, and Wip-Frag, have been developed, and their applications in the mining industry and mineral processing have been reported. The main advantages of these software packages are their integration and lack of disruption [16].

The specific charge is mainly used as an indicator to predict the blasting effect, but the amount of powder used per unit volume of crushed rock cannot properly reflect the influence of energy change in the blasting hole; therefore, the pressure in the blasting hole must be estimated and used to understand this [17]. However, the blasting pressure has relied on calculations rather than direct measurement. Recently, the blasting pressure has been estimated through a numerical analysis approach, but it is difficult to predict the explosion reaction of explosives acting on rocks, an anisotropic material. Therefore, the concepts of abnormal explosion and ideal sealing are used to calculate the pressure in the blast hole, assuming that there is no external influence [18]. Therefore, field experiments are being conducted to directly measure the pressure in the blast hole. However, the pressure

probe used is very expensive, and the sensor is only used once because of the extreme conditions generated by the blast, thereby requiring a significant financial investment. Therefore, in most cases, a pressure measurement sensor is inserted into the dummy hole, and the blasting pressure is indirectly measured based on the impact pressure propagated through the rock [19].

In recent years, a new intelligent material named shear thickening fluid (STF) has been widely used in energy absorption research [20–25]. STF exhibits an intense viscosity jump under shock load; as a result, it has been used in various applications, such as liquid body armor [26]. However, limited research on the application of STF for industrial blasting or as a stemming material is currently available.

In this study, a shock-reactive stemming material was developed that behaves similar to water in terms of shockwave propagation and has a high shear strength for dynamic shocks. The STF is characterized by its reversible energy absorption behavior under impulse loading. Its remarkable energy absorption capacity is attributed to viscous dissipation during shear and compression thickening. The STF-based stemming material was developed based on the following advantages. (1) STF has excellent sealing properties as it is a fluid-based material. (2) Its viscosity rapidly changes because of external shock, while material compaction or deformation is minimal with respect to the dynamic gas pressure in the blast hole. (3) Using starch as the main base material reduces costs.

Two blasting experiments were conducted to compare and contrast the blast effects of the developed stemming material and those of commonly used blasting stemming materials. The first is an experiment in which the blast hole pressure and stemming ejection are directly measured, and the second is an experiment to verify the stemming performance by analyzing the assessment of rock fragmentation through a full-scale blasting experiment.

2. Materials and Methods

2.1. STF-Based Stemming Material Rheology Tests

A dense colloidal dispersion of solid nanoparticles in a carrier fluid is known as an STF [27]. When a shear force is applied, the random distribution of particles in the dispersion initially emerges in an ordered fashion because the hydrodynamic forces are greater than the repulsive forces operating between the interstitial gaps the particles have generated. The order–disorder theory, put forth by Hoffmann in 1972 [28], is represented by this arrangement of particles. Large hydrodynamic forces tend to push out the fluid between the interstitial spaces with rising shear rates, leading to the production of hydroclusters. The hydroclustering mechanism proposed by Brady and Bossis in 1985 is comprised of this phenomenon [29]. These clusters are stress-bearing elements that lead to particle jamming, when additional shearing pressures are applied.

STFs behave by increasing the dynamic viscosity under the application of shear stress. When tightly packed particles combine with enough liquid to cover the spaces between the particles, dilatancy occurs. The fluid serves as a lubricant at low speeds, facilitating easy movement of the dilatant substance.

Because of the increased friction caused by the inability of the liquid to fill the gaps left by the particles at greater velocities, the viscosity also increases. The STF is also non-Newtonian in nature because its viscosity depends on the shear rate or shear rate history. This behavior is a type of deviation from Newton's law and is controlled by factors, such as particle size, shape, and distribution. Empirical studies have also shown that shear thickening effects vary with different particles and additive concentrations, as well as with the molecular chain of the additives [30].

Shear thickening is a reversible phenomenon governed by a power law model. Generally, a non-Newtonian fluid is described using the power law model expressed in Equations (1) and (2).

$$\tau = K \left(\frac{\partial \mu}{\partial y} \right)^n = K(\gamma)^n = \tau = K(\gamma)^{n-1} (\gamma)^1, \quad \tau = \mu_{apparent}(\gamma), \quad (1)$$

$$\mu_{\text{apparent}} = K(\dot{\gamma})^{n-1} \quad (2)$$

where τ is the shear stress exerted by the fluid, K is the fluid viscosity, μ is the shear deformation, y is the distance from the reference layer, $\frac{\partial \mu}{\partial y}$ is the strain rate, n is the flow behavior index, and μ_{apparent} is the apparent viscosity.

As shown in Figure 1, the fluid behaves as a Newtonian fluid at $n = 1$ and exhibits shear thinning properties when $0 < n < 1$. Moreover, several dispersions and liquid polymers exhibit shear thinning behavior for n values between 0.3 and 0.7. However, this depends on the particle concentration and molecular weight of the carrier fluid.

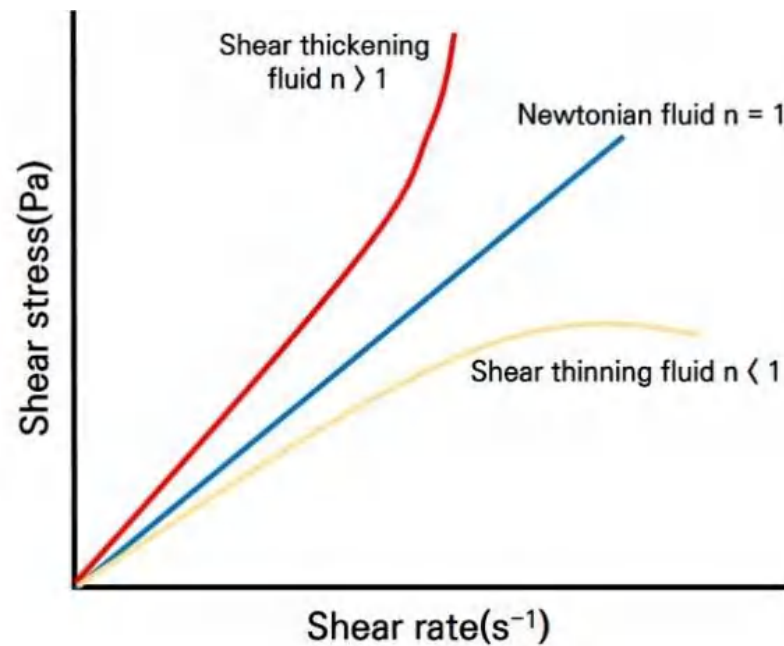


Figure 1. The shear thickening process of a shear thickening fluid.

The shear thickening effect of STF is demonstrated by the lower rate of increase in the shear stress in the low-shear-strain-rate regions and a higher rate of increase in the high-shear-strain-rate regions (Figure 1). Figure 1 also depicts the relationship between the shear stress and shear strain rate of the STF. The potential of a STF to improve the effectiveness of body armor against ballistic impacts and stab resistance has been thoroughly researched [31,32]. Further research is necessary, nevertheless, to fully understand the potential impact of STF on the stemming of blast holes. The motivation of this study is to harness the strength of the STF through flexible deployment and relatively easy stemming, which can help dissipate pressure wave loading around the rock mass during an explosion. The rheological behavior of the non-Newtonian fluid was measured using a rheometer.

In this study, the STF-based stemming material was mainly based on corn starch, while xanthan gum and guar gum were blended to increase the viscosity. Sodium benzoate was used to prevent the putrefaction of starch, and nitroglycol and salt were added to prevent freezing in winter.

The STF samples were sandwiched between a cone plate and the foundation support of a rheometer (Anton-Paar MCR301 rheometer) for rheological experiments. During the studies, the shear rate applied to the sample was increased from 0 to 100 s^{-1} , and all of the tests were carried out at a temperature of $25 \text{ }^\circ\text{C}$.

A schematic of the rheometer and the results of the rheological tests conducted on the STF-based stemming material are shown in Figures 2 and 3. The rheology tests were performed on the STF samples of 30, 45, and 55 wt.% corn starch suspensions. In the case of the 30 wt.% corn starch suspension, no significant shear thickening is observed. However, as the starch content increases, the particle content exceeds the ratio of the dispersion

medium; therefore, the distance between the corn starch particles decreases, and the shear thickening effect increases. For the sample made up of 55 wt.%, a shear thickening effect is attained at a critical shear rate of 85 s^{-1} . The STF initially experiences marginal shear thinning, which then grows with the shear rate. In particular, the viscosity of the STF suddenly increases as the shear rate reaches a critical value, indicating a shear thickening phenomenon. However, the viscosity of the STFs sharply decreases after a period of shear thickening. The critical shear rate of the STF sample is approximately 85 s^{-1} , and the maximum viscosity of the STF samples is 543 Pa.

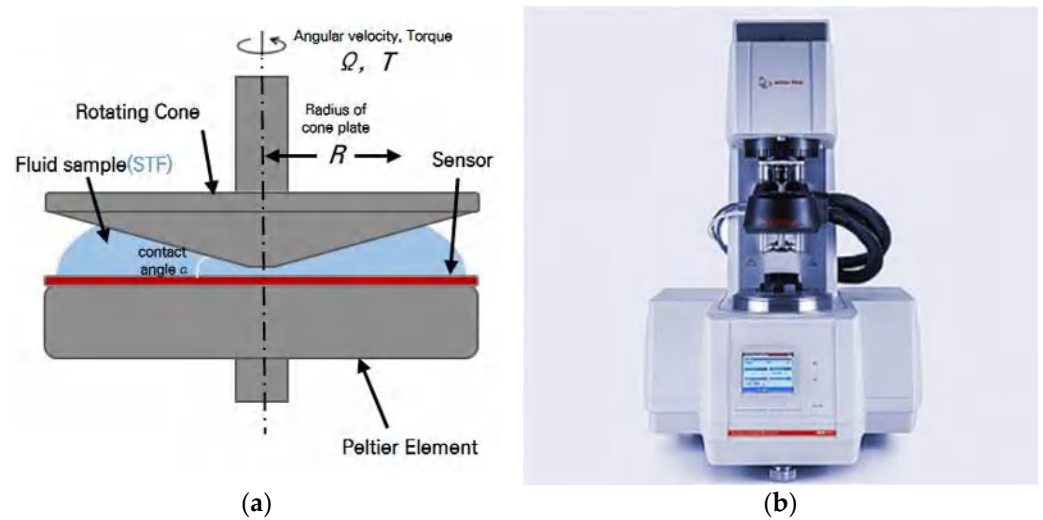


Figure 2. (a) Rheometer schematic and (b) Anton-Paar MCR301 rheometer.

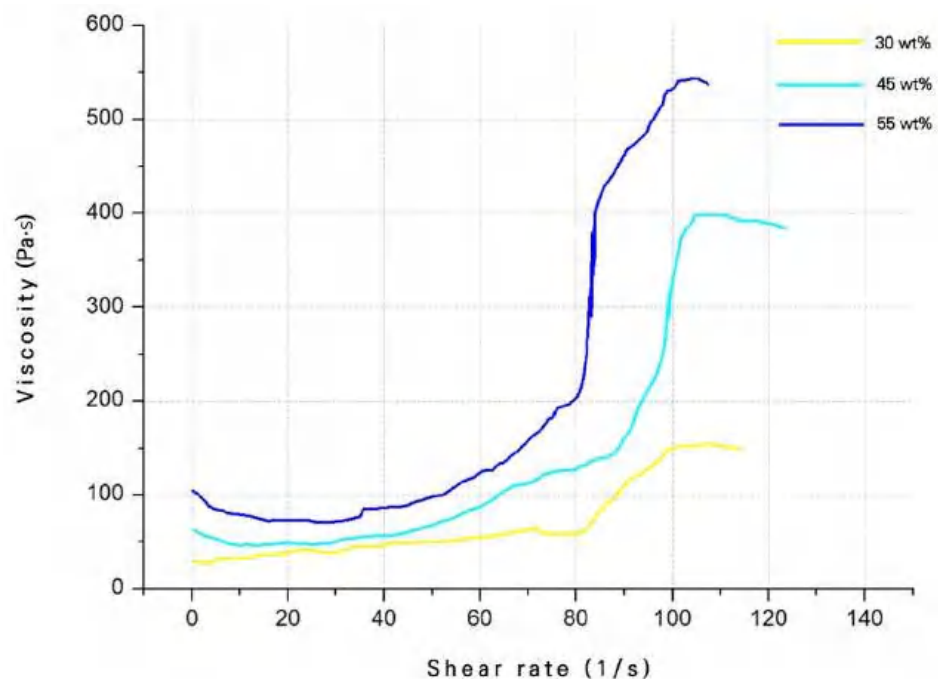


Figure 3. Results of the shear thickening fluid based stemming material’s rheological tests.

The STF-based stemming material image and package products are shown in Figure 4. The hammer recoils upon impact with the STF suspension surface, similar to hitting a true solid interface. It is a suspension of starch powder with a diameter range of $5\text{--}20 \mu\text{m}$ in water. The STF was created using a mixture of mechanical and ultrasonic mixing at a concentration of 55 wt.%. This weight percentage was chosen to preserve a viable solution,

while ensuring the shear thickening tendency [33]. According to previous experimental results [34] for 52.5–55 wt.% corn starch, after the impact of rock falling on the suspension surface, the rock recoiled, similar to hitting a true solid interface.



Figure 4. (a) Shear thickening fluid-based stemming material image and (b) package products.

2.2. Overview of the Blast Hole Pressure Measurements

In blasting, stemming constrains the blasting pressure in the blasting hole, leads to crack propagation through the behavior inside the blasting hole under the explosive pressure, and ultimately plays an important role in crushing the rock. Therefore, the behavior and control of the explosive pressure acting on the blast hole are important for effective blasting.

Laboratory- and field-scale experiments were conducted to measure the pressure inside the blast hole. However, because the sensor that measures the pressure inside the blast hole is expensive, there is a risk of failure owing to a strong impact. Therefore, the explosive pressure is measured using a one-time polyvinylidene fluoride (PVDF) sensor [35] or by drilling a dummy hole [36].

In this study, instead of using a one-time sensor or drilling a dummy hole to measure the pressure inside the blast hole, nylon tubes and water pressure measurement sensors that can be used multiple times were employed. Thus, the pressure generated by blasting was measured in the blasting hole without sensor damage or additional drilling.

2.3. Assessment for Rock Fragmentation of Bench Blasting

In this study, full-scale bench blasting was performed for each stemming material (sand or STF), and an image-based blast fragmentation method was applied to compare and evaluate the performance of each stemming material.

Sieving or screening is a direct and accurate method for evaluating the size distribution of particles or their fragmentation. This method is feasible for small-scale blasts or operations; however, it is costly and time-consuming. Rock fragments are screened through sieves of different mesh numbers for different fragment sizes, and the screened fragments are grouped based on their size. The nature of the blast was predicted by counting the number of fragments of each size [37].

WipFrag is an image analysis system for sizing materials, such as blasted or crushed rocks [38]. It has also been used to measure other materials, such as ammonium nitrate prills, glass beads, and zinc concentrates. WipFrag accepts images from a variety of sources, such as roving camcorders, fixed cameras, images, or digital files. It uses automatic algorithms to identify individual blocks and to create an outline “net” using state-of-the-art edge detection. If desired or necessary, manual intervention (editing the image net) can be performed to improve the fidelity. WipFrag measures a 2D net and reconstructs a 3D distribution using the principles of geometric probability. WipFrag supports two methods: Rossin Rammler and Swebrec. Two parameters were used by Rammler as key performance indicators (KPIs); X_c , known as the characteristic size of the distribution and more specifically $D_{63.2}$, and n , the value of which is the measure of uniformity [39].

Analyzing every fragment in the rock muck pile is fortunately not necessary because it is widely accepted that the mass percentage of fragments smaller than any given size varies linearly with the fragment size when plotted in the Rosin–Rammler domain. By measuring only a sufficient number of particles, the slope and intercept of the Rosin–Rammler line can be confidently defined [40]. A Rosin–Rammler line can be expressed as in Equation (3).

$$R(X) = 1 - \exp \left[- \left(\frac{X}{X_c} \right)^n \right] \tag{3}$$

Here,

$R(X)$ = Cumulative fraction by weight undersize in relation to size x .

X_c = Size modulus, which defines the characteristic size of the distribution.

n = Distribution modulus, which defines the spread of the distribution.

For $R(X) = 0.5$ (i.e., 50% of the fragments passing through the sieve), the value of X_c can be measured as follows:

$$X_c = \frac{X_{50}}{0.693^{1/n}} \tag{4}$$

3. Blast Hole Pressure Measurement Experiment

3.1. Explosion Pressure Sensor Calibration

In this study, it was necessary to calibrate the pressure sensor to measure the explosive pressure inside the blast hole. Therefore, prior to this experiment, explosive pressure sensor calibration using water pressure was performed. The explosive pressure sensor was calibrated under the same installation conditions as those of the blasting site.

Calibration of the explosion pressure sensor was performed by filling the nylon tube connected to the explosion pressure sensor with water, connecting it with a water pump, and pressurizing the pressure port of the explosion pressure sensor under the conditions of 0 MPa, 25 MPa, and 50 MPa three times each. The average and standard deviation of the results for three calibration tests was 0.984 (± 0.0033) Voltage at 0 MPa, 2.98 (± 0.0082) Voltage at 25 MPa, and 4.98 Voltage (± 0.0144) at 50 MPa. In addition, Nonlinearity was 0.137% FS (Full Scale), and Accuracy was 0.86% FS. The results of the experiments performed are specified in Table 1, and the Voltage to pressure (MPa) correction equation is shown in Figure 5.

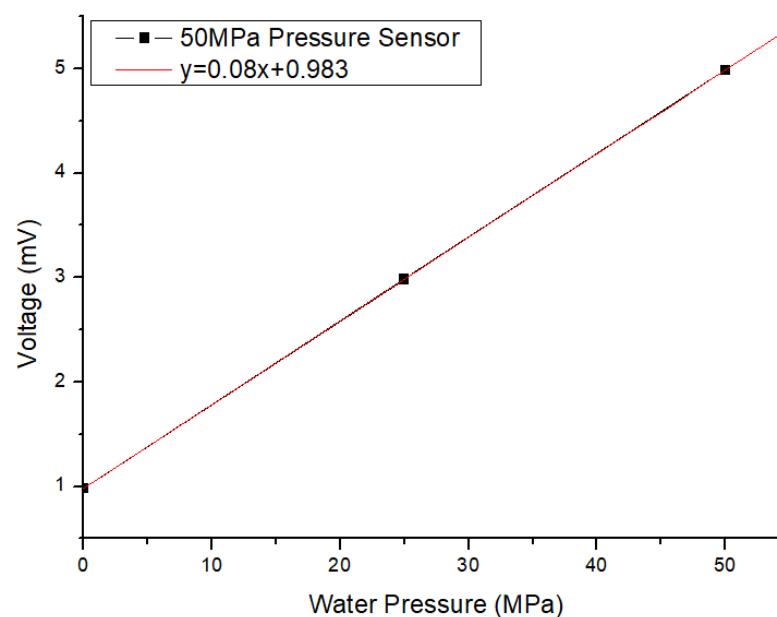


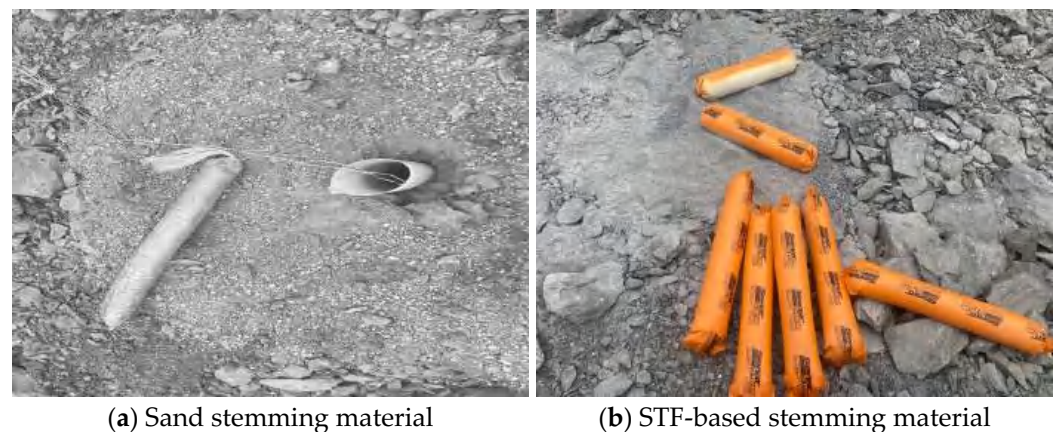
Figure 5. Explosive pressure bar calibration results.

Table 1. Results of the Explosion Pressure sensor calibration.

No.	Pressure Range (MPa)	Analog Output (V)
1	0	0.985
2	25	2.98
3	50	4.984
4	0	0.988
5	25	2.97
6	50	4.955
7	0	0.98
8	25	2.99
9	50	4.987

3.2. Blast Hole Pressure Measurement System

The purpose of the experiment was to measure the explosion pressure in a blast hole for each string material and to evaluate the pressure resistance of the stemming material. Conventional sand and STF-based stemming materials were applied to evaluate their resistance capability under explosive pressure. Figure 6 shows the shape of each stemming material.

**Figure 6.** Stemming materials used in blast hole pressure measurement experiment.

To measure the explosive pressure data from the blast hole, a pressure meter with cerabar (PMC) model of manufacturer Sensys capable of instantaneous dynamic shock pressure measurement was applied, and the MREL's MicroTrap was used to collect the data and set the detonation time trigger. The hydraulic shock pressure sensor had a pressure measurement range of 0–50 MPa. To measure the explosive pressure in the blast hole, the sensor was connected to a nylon tube filled with water using a coupling connector, placed in a water tube. To measure the explosive pressure in the blast hole, the sensor was connected to a nylon tube filled with water using a coupling connector, placed in a water tube. An explosive pressure-measuring device through hydraulic pressure was manufactured. Additionally, the manufactured water tube was protected with an industrial hose made of piezoelectric material to prevent damage when inserted into the blasting hole. Figure 7 shows the measuring tool applied to the blast pressure measuring system in the blast hole through hydraulic pressure. To collect the corresponding explosive pressure data as a time history at the same time as detonation using MicroTrap, a trigger line was attached to the explosion in the blast hole, and the break circuit trigger method was applied in which the connection signal was cut by the detonation of the explosive, and the measurement was finally started.



(a) Newmite Plus 1 with trigger line



(b) MREL's MicroTrap



(c) Water tube for hydraulic pressure measurement



(d) Piezoelectric tube for water tube protection

Figure 7. Measuring tool applied to blast pressure measuring system.

The length of the blast holes drilled for measuring the impact pressure of the stemming material was 3.2 m, and the explosives charge length was 1 m. The emulsion series Newmite Plus 1 ($\Phi 50$ mm, 2.5 kg) manufactured by Hanhwa with an explosion speed of 5700 m/s were applied to the experiment. On top of the explosive, a test stemming material (sand or STF) of 0.6 m was applied; a 0.5 m water tube was inserted to measure the pressure caused by the explosion as the water pressure; and in the 1.1 m remaining at the top of the blast hole, general sand stemming was inserted. Figure 8 shows a schematic of the blast hole measurement system.

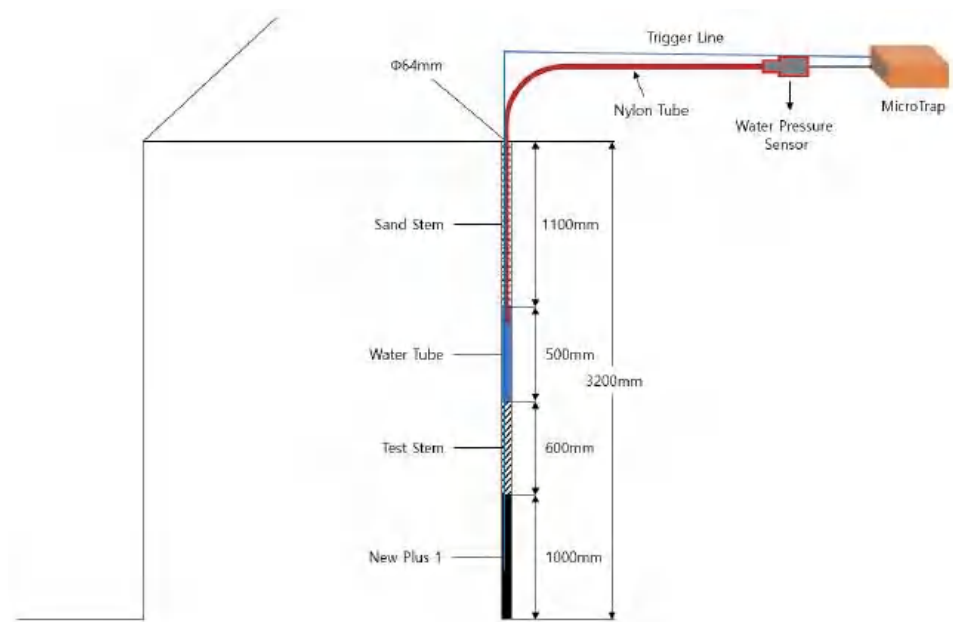


Figure 8. Schematic of the blast hole measurement system.

3.3. Experimental Results

In this experiment, a hydraulic explosive pressure propagation data measurement system was used to measure the pressure in the blast hole, and a comparative analysis was conducted on the blasting pressure behavior of the sand- and STF-based stemming materials. Table 2 presents the results of the blast hole pressure measurements.

Table 2. Result of the explosion pressure measurement in blast hole.

	Peak Pressure in Blasting Hole (MPa)	Explosive Pressure Arrival Time after Trigger (ms)	Explosive Pressure Duration in Blasting Hole (ms)
Sand Stemming	5.84	12.24	16.82
STF-based stemming	2.80	31.82	21.81

The pressure in the blasting hole is 5.84 MPa for the sand stemming material and 2.80 MPa for the STF-based stemming material. Further, the blasting pressure by sand is two times higher than by STF-based stemming material. This is the pressure transferred to the water tube located above the test stemming material; therefore, a lower measured pressure value means that the loss of explosive pressure in the blast hole due to stemming transfer is lower.

The time taken from detonation to explosion pressure transfer is 12.24 ms in the sand stemming material and 31.82 ms in the STF-based stemming material; the measured value is significantly lower than that of the sand stemming material. This is the explosive pressure transfer time from the lower part of the blasting hole to the upper part of the blasting hole for the explosive detonation of the stemming material. Thus, the longer the measured explosive pressure delay time, the better the ejection resistance. In addition, the duration of the explosive pressure in the blast hole is 16.82 ms when using the sand stemming material and 21.81 ms when using the STF-based stemming material, an improvement of approximately 5 ms. This implies that the explosive pressure acted longer inside the blast hole, as long as the duration of the explosive pressure. Figure 9 shows the time-pressure hysteresis curve inside the blast hole.

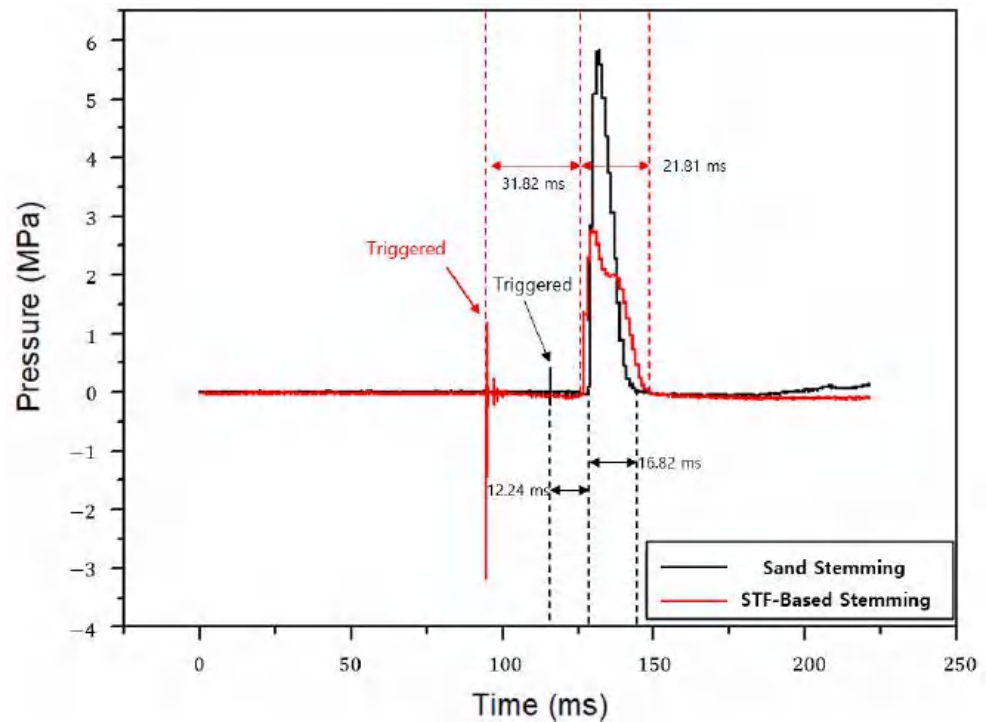
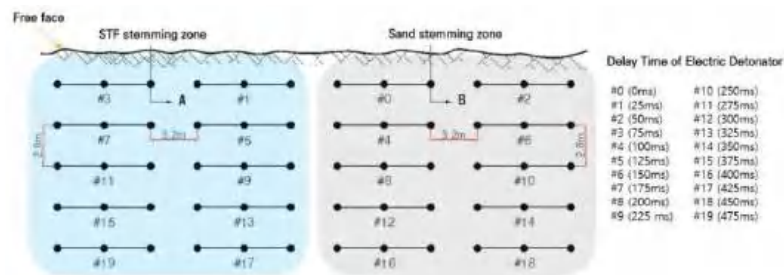


Figure 9. Time-pressure hysteresis curve inside the blast hole.

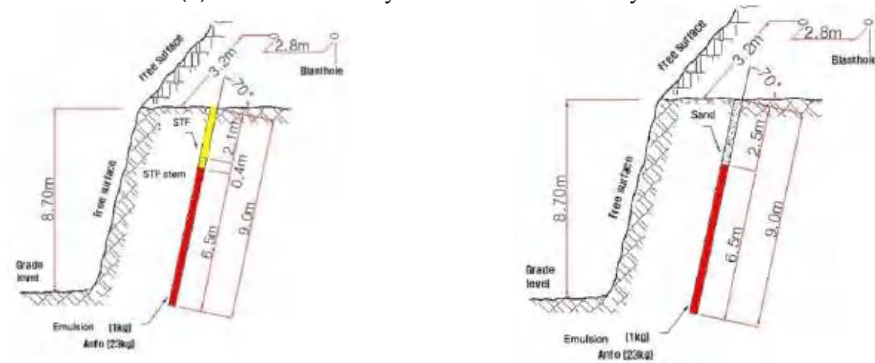
4. Full-Scale Blasting Experiment

4.1. Bench Blasting

The aggregate production step comprises blasting, a vibration feeder, a primary crusher, a secondary crusher, belt conveyors, and vibrating screens. The feed size of the jaw crusher operating in the A-aggregate mine requires a rock fragment size of at least 1000 mm or less. Therefore, to input the jaw crusher for primary crushing, it is necessary to perform secondary work on fragments by hydraulic rock breakers after blasting the rock, which incurs additional costs. Approximately \$25,000 US dollars per month are required to operate large hydraulic rock breakers, and mine A has ten of such equipment. Figure 10 shows the bench blasting design applied to aggregate mine A, and the blasting results are compared by applying sand and STF-based stemming materials to each different bench part. Table 3 lists the main parameters of the full-scale bench blasting experiment. In the blasting experiment, the STF-based stemming was applied to the left part, and general sand stemming was applied to the right part.



(a) Blast hole array and detonator delay time



(b) Bench section (STF stemming)

(c) Bench section (sand stemming)

Figure 10. Bench blasting design of full-scale blasting experiment.

Table 3. Main parameters of the full-scale bench blasting experiment.

Parameter	Unit	Value
Hole diameter	mm	75
Hole length	m	9.0
Burden	m	2.8
Hole spacing	m	3.2
Charge per hole	kg/hole	24.0
Charge per delay	kg/delay	72.0
Charge type	-	Emulsion 1.0 kg ANFO 23.0 kg
Specific charge	kg/m ³	0.308
Rock fracture per hole	m ³ /hole	77.95
Number of holes	ea	30
Stemming length	M	2.5
Stemming type	-	STF or Sand
Total charge	kg	720

The properties of the rock mass condition can have a significant influence on the fragmentation outcomes of the blast. Rock properties, such as compressive strength, porosity, Young’s modulus, Poisson’s ratio, and rock fracturing and jointing, can all influence fragmentation. In this experiment, by performing blasting at the same experimental area, the variation in results due to the rock mass condition difference was reduced as much as possible. The type of rock in this quarry mine is gneiss, and the uniaxial compressive strength is approximately 130–160 MPa. The rock density is approximately 2.6 g/cm³, and the porosity is less than 0.15%. As shown in Figure 11a, a bench slope with a discontinuity direction and similar region was selected as the experimental site. The spacing of the discontinuities was observed to be approximately 1.2–1.5 m each, and they were under completely dry conditions. Figure 11b,c show the resulting image after the blasting. Under the same blasting conditions, the rock fragments in the STF-applied part are generally smaller than in the sand stemming part.



(a) Bench slope image of the experimental area



(b) Shear thickening fluid stemming



(c) Sand stemming

Figure 11. Bench blasting results obtained by applying different stemming materials.

4.2. Evaluation of Rock Fragmentation

Muck piles of fragmented rocks were photographed using a single camera from the top surface of the bench and the front. In the images, a reference scale was used for single-scale factor analysis by applying a square marker target of 18 cm in width and height. Table 4 shows the image-based sieving analysis results of the rock fragmentation of the muck pile after full-scale bench blasting. Figures 12–15 show the analysis of the rock fragment size distribution. Larger rock fragments are displayed in red in the resulting image.

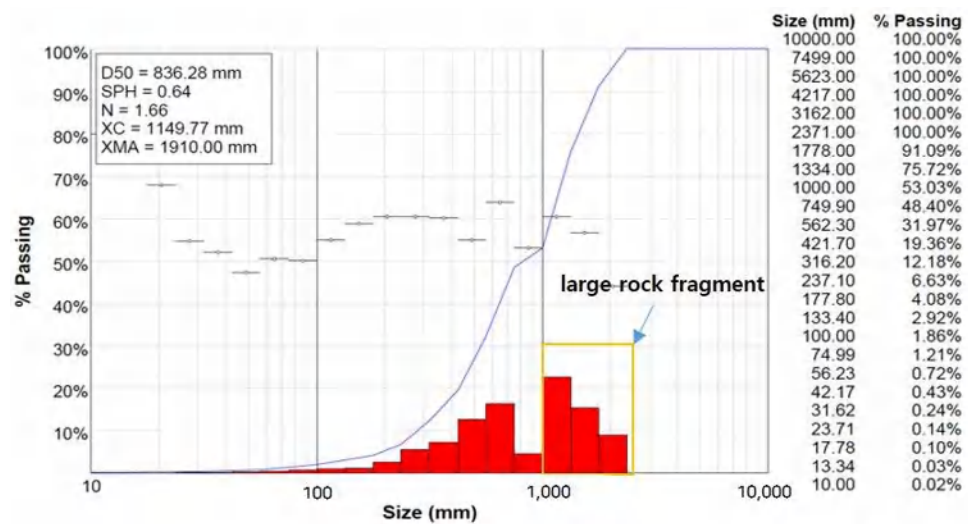
Table 4. Results of rock fragmentation analysis.

Location from Which the Image Was Captured	Stemming Type	Characteristic Size (X_c , mm)	Uniformity Index (n)	Average Fragment Size (X_{50} , mm)	Maximum Fragment (X_{ma} , mm)
Top of rock pile	Sand	1149	1.66	836	1910
	STF	419	1.93	345	1.100
Front of rock pile	Sand	1234	2.07	1020	2610
	STF	938	2.01	772	2010

Images taken from the top of the bench muck pile are compared. In the bench region to which sand stemming was applied, the characteristic size (X_c) for evaluating the fragment size is approximately 2.7 times larger than that in the region to which STF-based stemming material was applied. Moreover, the uniformity index (n) for evaluating the particle size distribution of the fragment rocks of the muck pile is 1.66 for the sand stemming region and 1.93 for the STF-based stemming. A higher uniformity index indicates a more uniform distribution of the fragmented rock.

Similarly, images taken from the front of the bench muck pile are compared. In the bench region to which sand stemming was applied, the characteristic size (X_c) for evaluating the fragment size is approximately 1.3 times larger than that of the region to which the STF-based stemming material was applied; however, the uniformity index shows no significant difference between the two cases. This is expected to affect the uniformity index as a large rock fragment falls to the front of the muck pile after blasting. These large fragments fell from the top of the outermost bench and had relatively little effect on the explosive force. Moreover, it is for this reason that the average fragment size compared, respectively, at the front and top of the bench muck pile image shows a significant difference

The WipFrag 3 program automatically generates the histogram graph. The x-axis is a log graph showing the size distribution of the rock fragments. The y-axis is the rate of passing. Large fragments are marked with boxes in Figures 12–15. The size of the large fragments that must be subjected to secondary breaking with a breaker machine before being placed in the jaw crusher line is approximately 1000 mm or more in diameter. When STF is applied as a stemming, the average fragment size decreases, and the number of large fragments that require second breaking work is greatly reduced.



(a) WipFrag Graph from the top of the muck pile

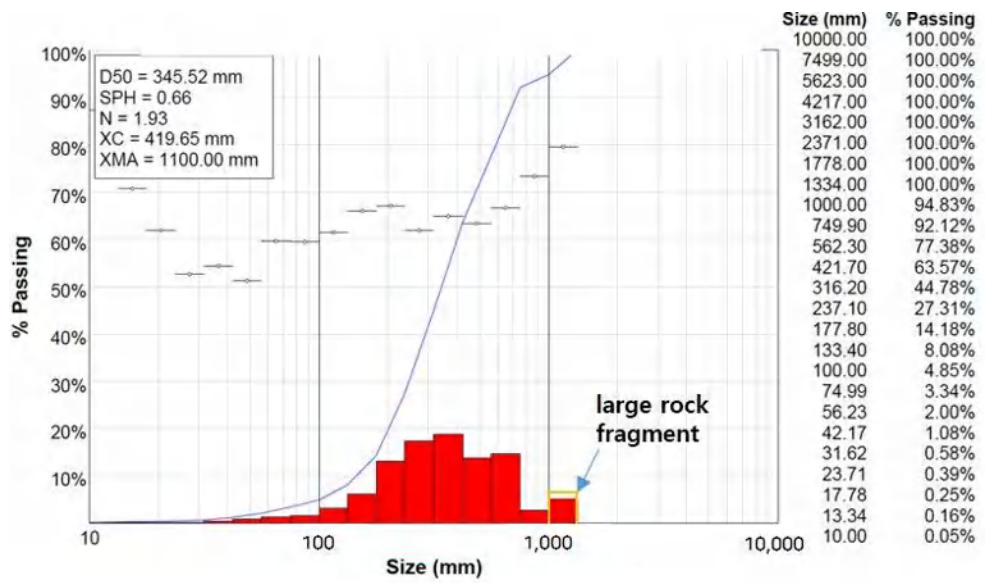


(b) Fragmented rock pile



(c) WipFrag Net Image

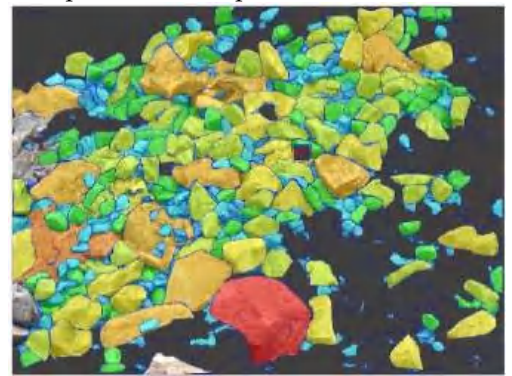
Figure 12. Rock pile image, contouring, histogram, and cumulative size curve of the fragmented block (bench top image of sand stemming case after blasting).



(a) WipFrag Graph from the top of the muck pile

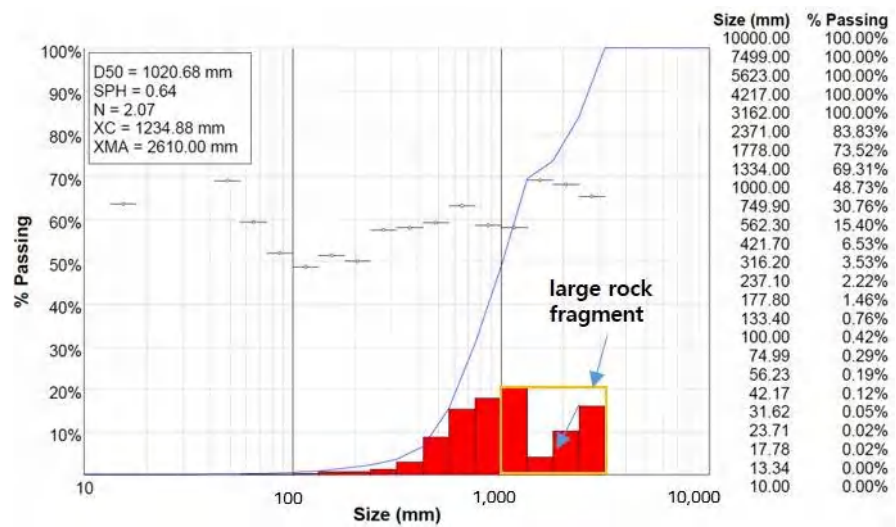


(b) Fragmented rock pile



(c) WipFrag Net Image

Figure 13. Rock pile image, contouring, histogram, and cumulative size curve of the fragmented block (bench top image of STF stemming case after blasting).



(a) WipFrag Graph from the front of the muck pile

Figure 14. Cont.

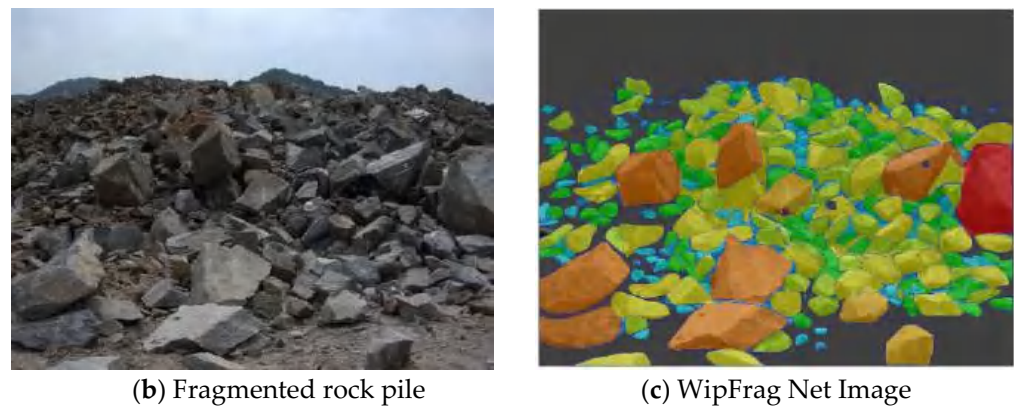
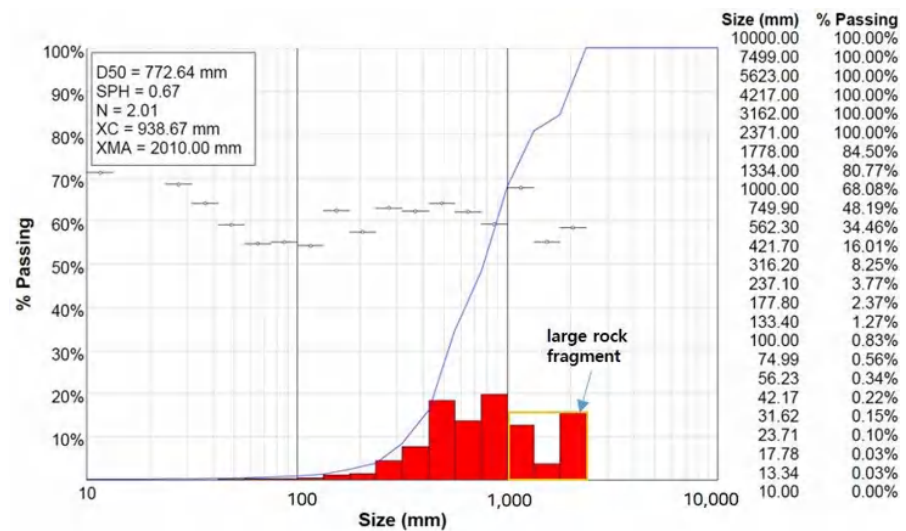


Figure 14. Rock pile image, contouring, histogram, and cumulative size curve of the fragmented block (bench front image of sand stemming case after blasting).



(a) WipFrag Graph from the front of the muck pile

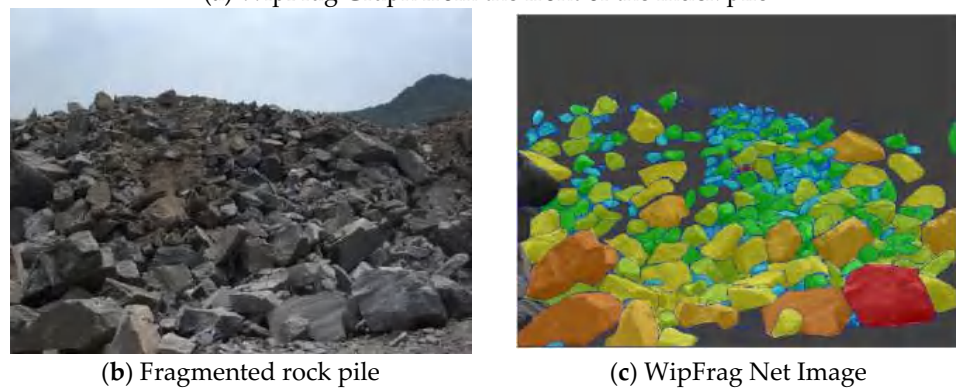


Figure 15. Rock pile image, contouring, histogram, and cumulative size curve of fragmented block (bench front image of STF stemming case after blasting).

5. Discussion

In this study, a material that instantaneously changes from shock load was developed as a blast stemming material and its performance was verified. Then, the pressure in the upper part of the stemming area was directly measured inside the blast hole. There are limited case studies that directly measure the pressure in the blast hole during bench blasting.

Previous research showed that stemming could increase the action time of the dynamic gas pressure in the blast hole and the efficiency of the explosives, reducing explosive consumption, as shown in Figure 16 [5,6]. Figure 16 depicts the time–pressure concept curves according to the stemming condition. In cases of missing or improper stemming, the pressure rapidly attenuates in the blast hole (Figure 16a), but proper stemming can increase the action time of the detonation gas inside the blast hole (Figure 16b). It is estimated that the shock pressure in the blast hole could be sustained for a longer time compared with that in the sand cases owing to the unique characteristics of STF. This is because STF is a smart-fluid type exhibiting an intense viscosity jump when subjected to loading.

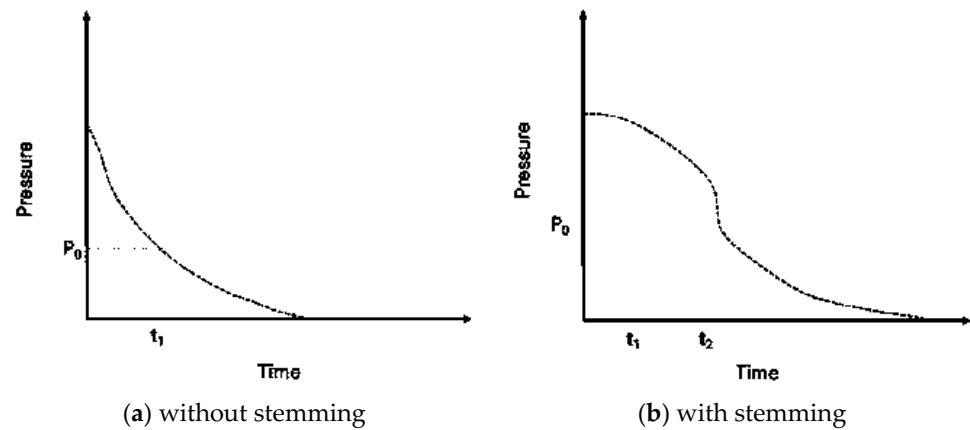


Figure 16. Concept curves of pressure and time: (a) without stemming, and (b) with stemming.

Figure 17 shows the time–pressure results according to the direct measurement of blast hole pressure, where sand- or STF-stemming materials were applied in each experiment. Since the pressure was measured at the upper part of the stemming area, a lower measured peak pressure transmits enough energy to the rock mass around the blast hole and below the stemming area. Stage I indicates detonation durations. When the shock front arrives at the gauge point, the gauge outputs a peak pressure. Stage II indicates the pressure variation as detonation propagates from gauge point to blast hole. Note that during this time, the stemming material begins initial ejection from the blast hole. Finally, in stage III the pressure curve rapidly decreases to atmospheric pressure when the stemming part is completely ejected.

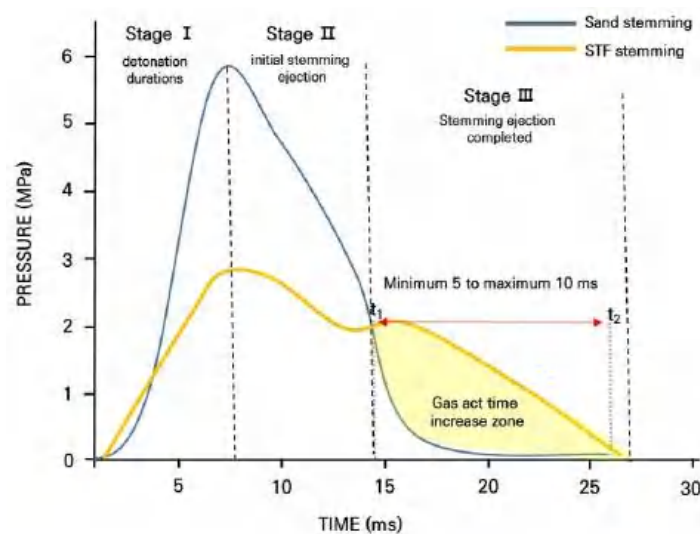


Figure 17. The time–pressure curves of the experimental results according to sand or shear thickening fluid (STF) stemming.

In the case of STF-based stemming, the pressure attenuates more slowly than in the sand stemming case. The pressure acts approximately 5–10 ms longer than the blasting gas pressure for the STF-based stemming than for the sand stemming. Eloranta et al. [41] verified that 1 ms of increased gas retention time in a blast hole increased the fragment work done on the rock mass and reduced waste energy. Therefore, an increase in the gas retention time of approximately 5 ms has a significant impact on rock fragmentation.

The purpose of stemming is to increase blasting efficiency by extending the duration of the explosion gas and forming more cracks in the crushing area. Therefore, the ability to resist the gas pressure emitted in the direction of the blast hole inlet implies the stemming performance, which is directly related to the blast efficiency. In this study, after crushing and cracking under the effect of detonation, the pressure applied to the elastic area was measured using a water pressure sensor from a nylon tube inserted into the water tube, and the pressure acting in the elastic area was measured, as shown in Figure 18.

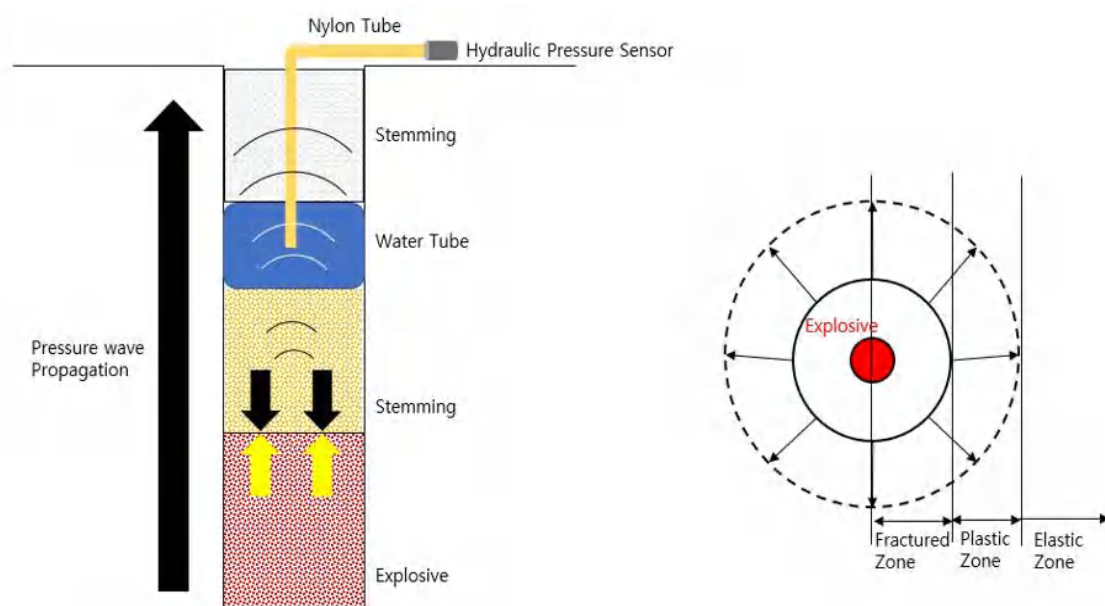


Figure 18. Schematic of the measured pressure wave in the blast hole.

Therefore, the pressure behavior in the blast hole owing to the explosive detonation measured through the hydraulic pressure measurement sensor is the pressure value at which the pressure ejected to the upper part of the blast hole by the explosion is attenuated by the stemming material and not by the direct blast pressure. The low peak pressure measured by the hydraulic sensor implies that the stemming material has an excellent pressure constraint against the explosive pressure ejected to the upper part of the blast hole. This suggests that the explosive pressure applied to the lower part of the blast hole is high. In addition, because the explosive pressure delay time measured by the hydraulic pressure sensor is from the trigger to the pressure wave measurement, the longer the delay time from the detonation to the pressure measurement, the more continuous the pressure behavior of the stemming material under the blast hole. Finally, the time at which the explosion pressure returns to atmospheric pressure after the increase indicates the duration of the explosive pressure in the blast hole. This suggests that, the longer the duration of the explosive pressure, the longer the crack propagation time owing to the gas pressure behavior in the blast hole.

The measured pressure behavior in the blast hole correlates with the resistance characteristics of the stemming material. It is judged that the STF-based stemming material will effectively achieve the purpose of the stemming material by resisting the blasting pressure and maintaining relatively high pressure in the blast hole for a longer time compared to the conventional sand stemming material.

6. Conclusions

By conducting two blasting experiments, we compared the stemming effects of the developed STF-based stemming material and those of commonly used sand stemming material. The conclusions drawn from the blasting experiments are as follows:

- (1) The measured pressure was 2.80 MPa for the STF-based stemming case and 5.84 MPa for the sand stemming case based on the direct dynamic pressure measurement at the top of the blast hole. The lower the measured pressure value, the lower the loss of explosive pressure in the blast hole owing to stemming transfer. In addition, the explosive gas pressure action time in the STF stemming case was 5 ms longer than the sand-stemming case. The longer the duration of the explosive pressure, the greater the energy that can be used to fracture the rock;
- (2) The measured pressure behavior in the blast hole correlated with the resistance characteristics of the stemming material. It is judged that the STF-based stemming material can effectively resist the blasting pressure and maintain a relatively high pressure in the blast hole for a longer duration compared to the conventional sand stemming material;
- (3) The hydraulic pressure measurement system was developed to measure blasting pressure in a blast hole. This was done by improving the method of measuring the blasting pressure by drilling a dummy hole, which was mainly performed for the explosion pressure measurements. The pressure behavior depending on the voltage of pressure meter with cerabar (PMC) was set through the sensor calibration performed before the blasting experiment, the test method to evaluate the pressure constraint capacity of the stemming material was presented, and the validity of the pressure measurement system in the blasting hole was verified;
- (4) As a full-scale bench blasting experiment, a rock pile fragmentation analysis was performed after blasting, and it was confirmed that the average fragment size was reduced by an approximate minimum of 25% to a maximum of 60%, when using STF-based stemming material. This suggests that the secondary crushing work in aggregate quarry mines can be reduced.

Author Contributions: Conceptualization, Y.J.; Investigation, C.S.; Methodology, Y.K.; Supervision, S.C.; Writing—original draft, Y.K. All authors have read and agreed to the published version of the manuscript.

Funding: This research was supported by a grant from the project “Development of new stemming material and blasting method using shear thickening fluid by high shock-wave reaction”, funded by the Korea Institute of Civil Engineering and Building Technology (KICT).

Institutional Review Board Statement: Not applicable.

Informed Consent Statement: Not applicable.

Data Availability Statement: Not applicable.

Conflicts of Interest: The authors declare no conflict of interest regarding the publication of this paper.

References

1. Brinkmann, J.R. An experimental study of the effects of shock and gas penetration in blasting. In Proceedings of the 3th International Symposium on Rock Fragmentation by Blasting, Brisbane, Australia, 26–31 August 1990; pp. 55–66.
2. Konya, C.J.; Konya, A. Effect of hole stemming practices on energy efficiency of comminution. In *Energy Efficiency in the Minerals Industry*; Awuah-Offei, K., Ed.; Springer: Cham, Switzerland, 2018; pp. 31–53.
3. Snelling, W.O.; Hall, C. *The Effect of Stemming on the Efficiency of Explosives*; United States Government Printing Office: Washington, DC, USA, 1912.
4. Floyd, J.L. Explosive energy relief—The key to Control. Over break. In Proceedings of the Explosion, Kalgoorlie, WA, USA, October 1999; pp. 147–153.
5. Zong, Q. Theoretical discussion of movement rule of stemming in blast holes. *Blasting* **1996**, *13*, 8–11.
6. Luo, Y.; Wu, S. Study on length of stemming material and its effect in hole-charged blasting. *Mech. Eng.* **2006**, *28*, 48–52.

7. Phamotse, K.M.; Nhleko, A.S. Determination of optimal fragmentation curves for a surface diamond mine. *J. S. Afr. Inst. Min. Metall.* **2019**, *119*, 613–619. [CrossRef] [PubMed]
8. Li, Y.L.; Shi, X.Z.; Liu, B.; Zhao, J.P. Experimental research on reasonable length of water stemming. *Blasting* **2015**, *32*, 11–16.
9. Cui, Z.D.; Yuan, L.; Yan, C.L. Water–silt composite blasting for tunnelling. *Int. J. Rock Mech. Min. Sci.* **2010**, *47*, 1034–1037. [CrossRef]
10. Wang, Z.; Li, Y. Numerical simulation on effects of radial water-decoupling coefficient in engineering blast. *Yantu Lixue/Rock Soil Mech.* **2005**, *26*, 1926.
11. Zhu, Z.; Xie, H.; Mohanty, B. Numerical investigation of blasting-induced damage in cylindrical rocks. *Int. J. Rock Mech. Min. Sci.* **2008**, *45*, 111–121. [CrossRef]
12. Boshoff, D.; Webber-Youngman, R.C.W. Testing stemming performance, possible or not? *J. S. Afr. Inst. Min. Metall.* **2011**, *111*, 871–874.
13. Kopp, J.W. *Stemming Ejection and Burden Movements from Small Borehole Blasts*; United States Department of the Interior, Bureau of Mines: Twin Cities, MN, USA, 1987.
14. Wang, C. The action of the blasthole plug. *J. Univ. Hydr. Electric. Eng.* **1999**, *21*, 45–49.
15. Hunter, G.C.; McDermott, C.; Miles, N.J.; Singh, A.; Scoble, M.J. A review of image analysis techniques for measuring blast fragmentation. *Min. Sci. Technol.* **1990**, *11*, 19–36. [CrossRef]
16. Sudhakar, J.; Adhikari, G.R.; Gupta, R.N. Comparison of fragmentation measurements by photographic and image analysis techniques. *Rock Mech. Rock Eng.* **2006**, *39*, 159–168. [CrossRef]
17. Jung, M. A Study on the Estimation of Non-Ideal Blasthole Pressure of Bulk Blend Explosives. Ph.D. Thesis, Seoul National University, Seoul, Korea, 2019.
18. Cunningham, C. Blasthole Pressure: What it really means and how we should use it. *Proc. Annu. Conf. Explos. Blasting Tech.* **2006**, *32*, 255.
19. Raina, A.K.; Murthy, V.M.S.R.; Soni, A.K. Estimating flyrock distance in bench blasting through blast induced pressure measurements in rock. *Int. J. Rock Mech. Min. Sci.* **2015**, *76*, 209–216. [CrossRef]
20. Majumdar, A.; Laha, A.; Bhattacharjee, D.; Biswas, I. Tuning the structure of 3D woven aramid fabrics reinforced with shear thickening fluid for developing soft body armour. *Compos. Struct.* **2017**, *178*, 415–425. [CrossRef]
21. Daelemans, L.; Cohades, A.; Meireman, T.; Beckx, J.; Spronk, S.; Kersemans, M.; De Baere, I.; Rahier, H.; Michaud, V.; Van Paepegem, W.; et al. Electrospun nanofibrous interleaves for improved low velocity impact resistance of glass fibre reinforced composite laminates. *Mater. Des.* **2018**, *141*, 170–184. [CrossRef]
22. Majumdar, A.; Butola, B.S.; Srivastava, A. Development of soft composite materials with improved impact resistance using Kevlar fabric and nano-silica based shear thickening fluid. *Mater. Des. 1980–2015* **2014**, *54*, 295–300. [CrossRef]
23. Wei, M.; Lin, K.; Liu, H. Experimental investigation on hysteretic behavior of a shear thickening fluid damper. *Struct. Contr. Health Monit.* **2019**, *26*, e2389. [CrossRef]
24. Gürgen, S.; Sofuoğlu, M.A. Experimental investigation on vibration characteristics of shear thickening fluid filled CFRP tubes. *Compos. Struct.* **2019**, *226*, 111236. [CrossRef]
25. Lim, J.; Kim, S.-W. Enhanced damping characteristics of carbon fiber reinforced polymer-based shear thickening fluid hybrid composite structures. *J. Intell. Mater. Syst. Struct.* **2020**, *31*, 2291–2303. [CrossRef]
26. Gürgen, S.; Kushan, M.C. The effect of silicon carbide additives on the stab resistance of shear thickening fluid treated fabrics. *Mech. Adv. Mater. Struct.* **2017**, *24*, 1381–1390. [CrossRef]
27. Boersma, W.H.; Laven, J.; Stein, H.N. Shear thickening (dilatancy) in concentrated dispersions. *AIChE J.* **1990**, *36*, 321–332. [CrossRef]
28. Hoffman, R.L. Discontinuous and dilatant viscosity behavior in concentrated suspensions. I. Observation of a flow instability. *Trans. Soc. Rheol.* **1972**, *16*, 155–173. [CrossRef]
29. Brady, J.F.; Bossis, G. The rheology of concentrated suspensions of spheres in simple shear flow by numerical simulation. *J. Fluid Mech.* **1985**, *155*, 105–129. [CrossRef]
30. Xu, Y.; Gong, X.; Peng, C.; Sun, Y.; Jiang, W.; Zhang, Z. Shear thickening fluids based on additives with different concentrations and molecular chain lengths. *Chin. J. Chem. Phys.* **2010**, *23*, 342–346. [CrossRef]
31. Lee, Y.S.; Wetzel, E.D.; Wagner, N.J. The ballistic impact characteristics of Kevlar woven fabrics impregnated with a colloidal shear thickening fluid. *J. Mater. Sci.* **2003**, *38*, 2825–2833. [CrossRef]
32. Decker, M.J.; Halbach, C.J.; Wetzel, E.D.; Nam, C.H.; Wagner, N.J. Stab resistance of shear thickening fluid (STF)-treated fabrics. *Compos. Sci. Technol.* **2007**, *67*, 565–578. [CrossRef]
33. Ko, Y.; Kwak, K. Blast effects of a shear thickening fluid-based stemming material. *Mining* **2022**, *2*, 330–349. [CrossRef]
34. Bischoff White, E.E.; Chellamuthu, M.; Rothstein, J.P. Extensional rheology of a shear-thickening cornstarch and water suspension. *Rheol. Acta* **2010**, *49*, 119–129. [CrossRef]
35. Chi, L.Y.; Zhang, Z.X.; Aalberg, A.; Yang, J.; Li, C.C. Measurement of shock pressure and shock-wave attenuation near a blast hole in rock. *Int. J. Impact Eng.* **2019**, *125*, 27–38. [CrossRef]
36. Raina, A.K.; Trivedi, R. Exploring rock-explosive interaction through cross blasthole pressure measurements. *Geotech. Geol. Eng.* **2019**, *37*, 651–658. [CrossRef]

37. Palangio, T.C. WipFrag—A new tool for blast evaluation. In Proceedings of the 11th Annual ISEE Symposium on Blasting Research, Nashville, TN, USA, 5–9 February 1985; pp. 269–285.
38. WipFrag. WipFrag 3 Operating Manual. Available online: <https://wipware.com> (accessed on 15 July 2022).
39. Singh, P.K.; Sinha, A. Rock fragmentation by blasting. In Proceedings of the 10th International Symposium on Rock Fragmentation by Blasting, New Delhi, India, 26–29 November 2012; CRC Press: Boca Raton, FL, USA, 2013; pp. 10–18.
40. Scott, A.; McKee, D.J. The inter-dependence of mining and mineral beneficiation processes on the performance of mining projects. In Proceeding of the Australian Institute of Mining and Metallurgy Annual Conference, Melbourne, Australia, 5–9 August 1994; pp. 5–9.
41. Eloranta, J. Stemming selection for large diameter blast holes. In Proceedings of the 20th Annual Conference on Explosive and Blasting Techniques, ISEE, Austin, TX, USA, 30 January–3 February 1994; pp. 1–11.

Article

A Numerical Simulation of Blasting Stress Wave Propagation in a Jointed Rock Mass under Initial Stresses

Qian Dong ^{1,2,*}, Xinping Li ³, Yongsheng Jia ^{1,2} and Jinshan Sun ^{1,2} 

¹ Hubei Key Laboratory of Blasting Engineering, Jianghan University, Wuhan 430056, China; sinoblaster_jia@jhun.edu.cn (Y.J.); sunjinshan@cug.edu.cn (J.S.)

² Hubei (Wuhan) Institute of Explosion Science and Blasting Technology, Jianghan University, Wuhan 430056, China

³ Hubei Key Laboratory of Road-Bridge and Structure Engineering, Wuhan University of Technology, Wuhan 430070, China; whutxinpingli@sina.com

* Correspondence: dongqian@jhun.edu.cn

Abstract: The initial stresses have a strong effect on the mechanical behavior of underground rock masses, and the initial stressed rock masses are usually under strong dynamic disturbances such as blasting and earthquakes. The influence mechanism of a blasting excavation on underground rock masses can be revealed by studying the propagation of stress waves in them. In this paper, the improved Mohr-Coulomb elasto-plastic constitutive model of the intact rock considering the initial damage was first established and numerically implemented in Universal Distinct Element Code (UDEC) based on the variation of the experimental stress wave velocity in the initial stressed intact rock, and the feasibility of combining the established rock constitutive model and the BB (Bandis-Barton) model which characterizes the nonlinear deformation of the joints to simulate stress waves across jointed rock masses under initial stress was validated by comparing the numerical and model test results subsequently. Finally, further parameter studies were carried out through the UDEC to investigate the effect of the initial stress, angle, and number of joints on the transmission of the blasting stress wave in the jointed rock mass. The results showed that the initial stress significantly changed the propagation of the stress waves in the jointed rock mass. When the initial stress was small, the transmission coefficients of the stress waves in the jointed rock were vulnerable to be influenced by the variation of the angle and the number of joints, while the effect of the angle and the number of joints on the stress wave propagation gradually weakened as the initial stress increased.

Keywords: numerical modeling; blasting stress wave; underground rock masses; initial stress; transmission coefficient

Citation: Dong, Q.; Li, X.; Jia, Y.; Sun, J. A Numerical Simulation of Blasting Stress Wave Propagation in a Jointed Rock Mass under Initial Stresses. *Appl. Sci.* **2021**, *11*, 7873. <https://doi.org/10.3390/app11177873>

Academic Editor: Ricardo Castedo

Received: 29 July 2021

Accepted: 24 August 2021

Published: 26 August 2021

Publisher's Note: MDPI stays neutral with regard to jurisdictional claims in published maps and institutional affiliations.



Copyright: © 2021 by the authors. Licensee MDPI, Basel, Switzerland. This article is an open access article distributed under the terms and conditions of the Creative Commons Attribution (CC BY) license (<https://creativecommons.org/licenses/by/4.0/>).

1. Introduction

Underground rock masses are inevitably in a certain geological and tectonic environment, and are subject to initial stresses such as gravitational stress, tectonic stress, temperature stress, etc. The initial stresses have a strong effect on the mechanical behavior of the underground rock masses and the stability of the underground engineering [1–3]. Meanwhile, the drill-and-blast method is the most widely used technique for tunnel excavation and underground mining. In this process, the initial stressed underground rock masses are under strong dynamic disturbances, and the underground structure can be damaged by the stress waves generated during the excavation process. Hence, it is of great practical significance to study the propagation of stress waves in underground rock masses under initial stress for the optimal design of underground rock mass blasting excavation parameters and the dynamic stability analysis of underground engineering.

Rock masses contain various types of discontinuous interfaces such as joints and fractures and so on, which have a noticeable effect on the mechanical response of the rock mass [4,5]. Discontinuous interfaces in natural rock mass are usually distributed

in groups, such as a stratified rock mass, and it is particularly important to study the propagation of blasting stress waves in the layered rock mass and to monitor the vibrations generated during the blasting of the stratified rock masses [6]. Intensive studies have been conducted to investigate the propagation of stress waves across jointed rock masses via various theoretical and experimental methods. In terms of theoretical research, the displacement discontinuity model (DDM) proposed by Schoenberg [7] has been widely applied to study stress wave propagation through a jointed rock mass [8,9]. The DDM was also combined with other analysis methods, e.g., the method of characteristics (MC) [10], the scattering matrix method [11], and the time-domain recursive method (TDRM) [12] to study the stress waves passing through linear and nonlinear joints [13,14], one single joint and a set of parallel joints [15,16], and even intersecting rock joints [17]. By experimental means to date, the split Hopkinson pressure bar (SHPB) apparatus has been mainly used to study stress wave propagation across rock masses [18,19].

In contrast, the numerical simulation method is an economical and feasible alternative to survey the stress wave propagation across a jointed rock mass. Based on the discrete element method (DEM) proposed by Cundall [20], the universal distinct element code (UDEC) has been widely used to calculate the propagation problems of stress waves in a jointed rock mass [21–23]. Furthermore, other numerical methods and software have been adopted to solve the problems involving the stress wave propagation in a rock mass, e.g., the particle manifold method (PMM) [24,25], the numerical manifold method (NMM) [26,27], the particle flow code (PFC) [28,29], and the three-dimensional element code (3DEC) [30]. However, the above theoretical, experimental, and numerical methods have mainly focused on the effect of the parameters of the joints, e.g., joint stiffness, joint spacing, joint number, and the parameters of the stress wave, e.g., waveform, amplitude, frequency, and the incident angle of stress wave on the stress wave propagation pattern, and have proposed that the attenuation of the stress wave only occurs at the joints, while it has been assumed that the intact rock is elastic. Few works have been conducted that investigate the effect of initial stresses on the stress wave propagation in the jointed rock mass, and studies considering the initial damage of intact rocks in the rock mass under initial stresses are much rarer.

On the other hand, besides discontinuous interfaces, intact rocks are the other part of the rock mass. Due to their long geological age and various complex tectonic effects, intact rocks inevitably contain a certain number of defects such as microcracks and micropores; therefore, intact rock can be considered as an initial damaged medium [31–33]. Considerable studies have revealed that in the process of static loading, the microcracks in the intact rock experience the stages of closure, development, extension, and interactive penetration [34–36], and the wave impedance of intact rocks is strongly affected by the initial stress given the stress sensitivity of the wave velocity and density. Consequently, microcracks within the intact rock enter different evolution stages under different initial stresses, leading to changes in wave impedance, which in turn have an influence on the stress wave propagation.

The variation in the quantity of microcracks inside the intact rock under initial stress causes changes in the macroscopic mechanical properties of the rocks, which is usually named initial damage [37,38]. In the progressive destruction process of rocks under static loading, the closure effect of the microcracks at the initial loading stage can significantly affect the deformation characteristics of rocks, and the current research on the damage of intact rocks has rarely considered the compaction stage of the initial void. For a porous medium with natural defects such as rocks, when the porosity of rocks is high, the compaction stage of the initial microcracks is even more non-negligible. However, related research has been rarely reported.

This paper presents a numerical exploration of blasting stress wave propagation in the initial stressed jointed rock mass. Firstly, based on the variation of the stress wave velocity in the intact rock under different equal biaxial static loading in the model test, the initial damage variable was determined, and the Mohr-Coulomb elasto-plastic constitutive model

of the rock considering initial damage was established and subsequently implemented in the UDEC. Then, the feasibility of combining the developed model and the BB (Bandis-Barton) model which characterizes the nonlinear deformation of the joints to simulate stress waves across the jointed rock mass under initial stress was validated by comparing the numerical results with the model test results. Finally, further parameter studies were carried out through the UDEC to investigate the effect of the initial stress, angle, and number of joints on the transmission of blasting stress waves in the jointed rock mass.

2. A Brief Introduction of the Model Test

The detailed model test process is referred to in another two papers [39,40], and is only briefly described in this paper, as follows:

- (1) For the instrument providing the biaxial static loads in the model test, the corresponding size of the specimen was 1.6 m (length) \times 1.3 m (height) \times 0.4 m (thickness), as shown in Figure 1.

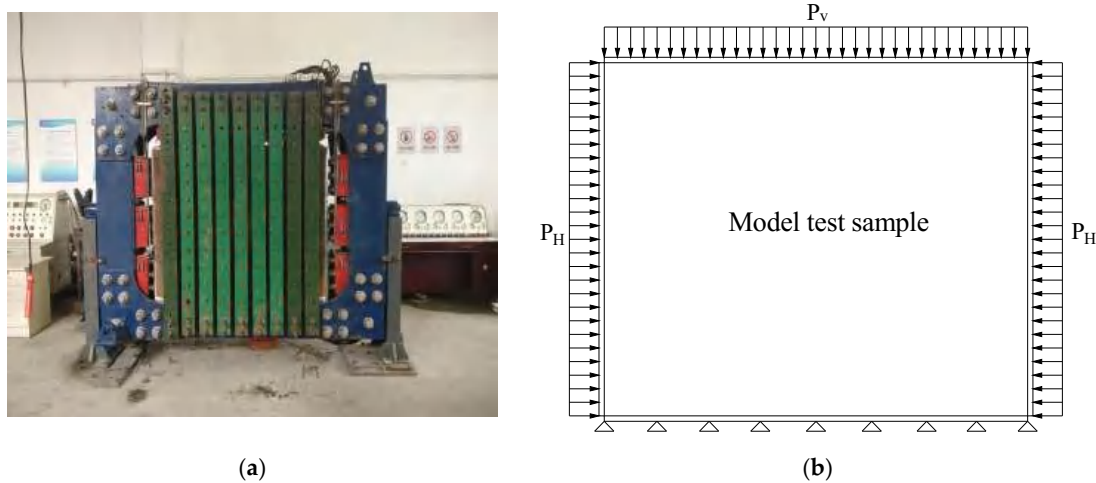


Figure 1. Multifunctional testing machine for the rock and soil: (a) test equipment; (b) static loading schematic.

- (2) The prototype of the model test was the deep-buried underground engineering surrounding rock, and the physical and mechanical parameters of the prototype are shown in Table 1. The corresponding intact rock simulation material was low strength cement mortar containing cement, sand, water, and a plasticizer. Meanwhile, the stress similarity coefficient C_σ between the prototype and simulation material was 20. Through a series of tests, the mechanical parameters of the cement mortar material were obtained and are shown in Table 1. In addition, the joints in the model test samples were simulated by the mica plates, and their normal and tangential stiffnesses were 12 GPa/m and 7.53 GPa/m, respectively, and were obtained through laboratory tests.

Table 1. Physical and mechanical parameters of similar materials and the prototype of the intact rock.

Type	R_c /MPa	σ_t /MPa	E /GPa	φ ($^\circ$)	C /MPa	μ	ρ /kg/m ³
Prototype	120	12	50	30	30	0.223	2600
Similar material	5.864	0.613	5.226	23.2	1.49	0.203	1980

Where, R_c , σ_t , E , φ , C , μ and ρ are the uniaxial compressive strength, tensile strength, elastic modulus, internal friction angle, cohesion, poisson ratio, and density of the prototype and similar material, respectively.

- (3) According to the number and the angle of the joints, a total of three model test samples were made, named T1, T2, and T3 respectively, as shown in Figure 2. Due to the

structural characteristics of the cylindrical charge, two test sections were uniformly arranged along the thickness direction in each model test sample. Four measuring lines were arranged on each section to measure the stress and strain at different distances from the explosion source. Sixteen strain measuring points were arranged on the strain testing section, ranging from 1 to 16, and eight stress measuring points were arranged on the stress testing section, ranging from 17 to 24.

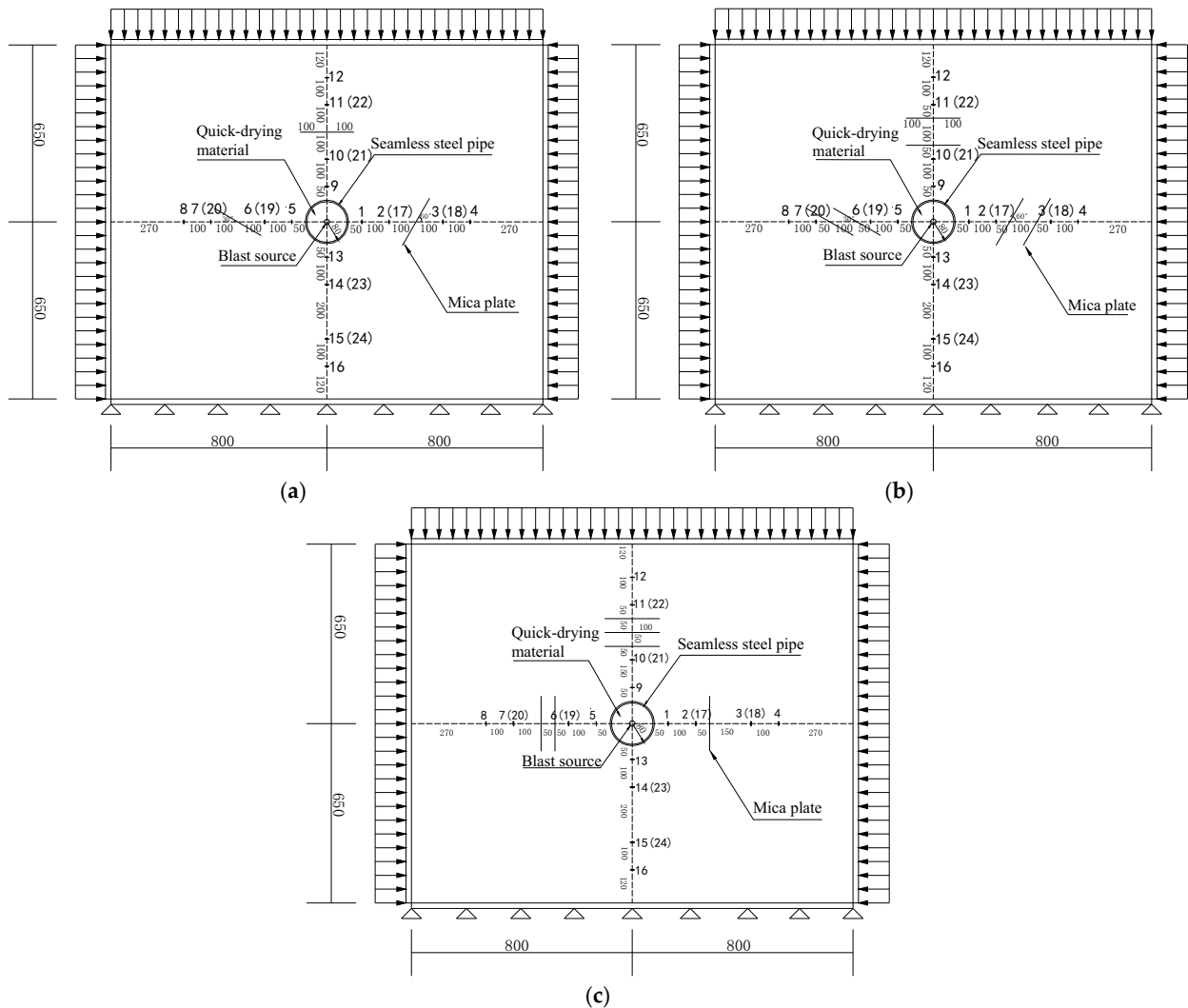


Figure 2. Layout of the measuring points and the joints of the model test samples (unit: mm): (a) T1 sample; (b) T2 sample; (c) T3 sample.

- (4) The T1 and T2 samples were designed to study the propagation of the blasting stress waves in intact rock, and the normal or oblique impact of the blasting stress wave on the rock mass containing joints with a different number and angle, and the corresponding research objects of the T1 and T2 test samples were intact rock and single-joint and double-joints rock masses of 30°, 60°, and 90°, respectively. Meanwhile, the T3 sample was designed to study the propagation of the blasting stress waves in intact rock and the normal jointed rock mass. According to the number of joints in the four measuring lines, the corresponding research objects were intact rock, 90° single-joint rock mass, 90° double-joints rock mass, and 90° three-joints rock mass.

- (5) In the model test, detonating cords with a total length of 1.6 m and TNT (Trinitrotoluene) with an equivalence of 17.6 g were used as the explosive sources to generate the blasting stress wave, and the detonating cords were fixed in the seamless steel pipe in the center of the test samples through the wooden centering stent. Subsequently, the quick-drying materials were poured into the pipes as the loading core in the samples, as shown in Figure 3. At the same time, seamless steel tubes were arranged to reduce the damage of the blasting loads, and repeated dynamic loading was realized by replacing the crushed quick-drying materials in the seamless steel tubes. In the model test, the vertical static load P_V and horizontal static load P_H applied on the model specimens were equal and were 0, 0.75 MPa, 1.5 MPa, and 3 MPa, respectively, and the corresponding initial in situ stresses were 0, 15 MPa, 30 MPa, and 60 MPa, respectively.

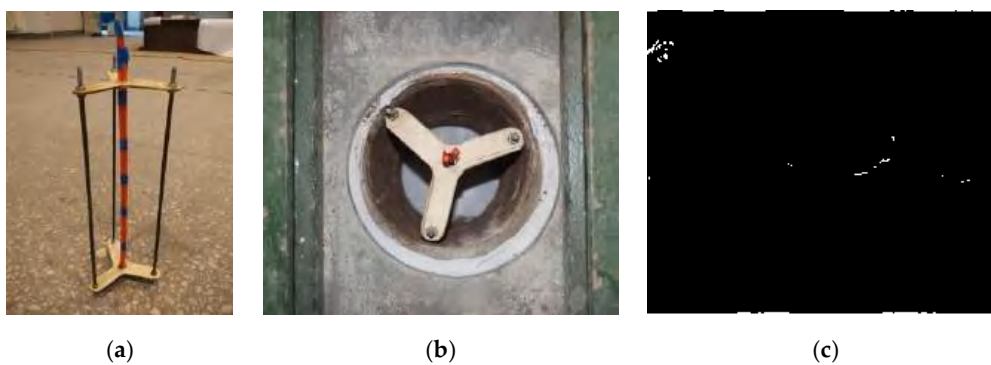


Figure 3. Schematic diagram of the charge structure in the model test samples: (a) detonating cords fixed in the wooden centering stent; (b) wooden centering stent in the model samples; (c) the pouring of quick-drying materials.

3. Establishment of the Mohr-Coulomb Elasto-Plastic Constitutive Model of the Rock Considering Initial Damage

Under different initial static loads, the microcracks in rocks enter different stages of evolution, so the physical and mechanical properties of rocks change correspondingly, leading to different propagation laws of stress waves in the rocks. Therefore, it is necessary to establish a constitutive model that can consider the initial damage of rocks caused by initial static stresses. Based on this, the influence of the change of initial stress on the propagation law of stress waves in rocks can be considered in a numerical simulation.

In the model test, the initial stresses applied on the test samples were the biaxial static loads, but in the test process, only the uniaxial compressive strength R_c of the rock simulation material was obtained as 5.864 MPa. Intensive studies have shown that the biaxial compressive strength R_{bc} of brittle materials such as rock and concrete was improved compared with the uniaxial compressive strength. The ratio of the biaxial compressive strength R_{bc} to the uniaxial compressive strength R_c of the brittle materials as β was defined by Papanikolaou et al. [41] and Huang [42], and through considerable test data, the fitting formula of β changing with the uniaxial compressive strength was obtained as the followed equation:

$$\beta = 1.493R_c^{-0.0634} \quad (1)$$

The above equation shows that the relationship between β and the uniaxial strength R_c of the rock meets a negative exponential relationship, and β decreases with the increase in the uniaxial strength R_c , indicating that the difference between the biaxial strength R_{bc} and the uniaxial strength R_c of the rock gradually decreases with the increase in the uniaxial strength R_c , and β is greater than 1 in the conventional uniaxial strength range of the rock. Substituting the uniaxial compressive strength R_c of the rock simulation material into Equation (1), the biaxial compressive strength R_{bc} of the rock simulation material can be obtained as 7.826 MPa.

The propagation velocity in the material is an important part of the propagation characteristics of stress waves, which can reflect the evolution of microcracks and the damage degree of the medium [43]. Based on this, to study the initial damage evolution of the intact rock under different static loads, the stress wave velocities of the intact rock in each model test sample under different biaxial static loads were calculated, and the initial damage variation of the intact rock was obtained through the change in the wave velocities. Specifically, the stress wave propagation velocity can be calculated by the arrival time difference in the stress wave recorded by the sensors arranged in the intact rock at different distances from the explosion source. In the three model test samples, the number of strain sensors in the intact rock area was more than that of the stress sensors, and the range of the strain sensors was also larger. Therefore, the strain time history curves recorded at the strain measuring points at different distances from the explosion source were used to calculate the stress wave velocity through the arrival time difference of the waves.

In each model test sample under different biaxial static loads, based on the time difference Δt corresponding to the jumping point in the time history curves of strain measuring points 13 and 16 in the intact rock, and the distance between the two measuring points Δl , the value of the stress wave velocity c of the intact rock can be calculated by the following equation:

$$c = \frac{\Delta l}{\Delta t} \quad (2)$$

Through the above equation, the average propagation velocities of stress waves in the intact rock section of each model test sample under different biaxial static loads were calculated, which were 1990 m/s, 2077 m/s, 2099 m/s, and 1898 m/s when the static loads were 0, 0.75 MPa, 1.5 MPa, and 3 MPa. The reason for this phenomenon was that when the static load was small, the initial microcracks in the intact rock started to close with the growth of the static load, resulting in the increase in the wave velocity with the elastic modulus. When the static load was raised to a critical value, the initial microcracks in the intact rock were completely closed, and when the static load continued to rise, new microcracks were initiated, resulting in the decrease in the wave velocity, and this critical value of the static load can be obtained by a subsequent analysis. Meanwhile, it can be seen that when the static load was 0 MPa, the average stress wave velocity in the intact rock was about 1990 m/s. Meanwhile, the ultrasonic wave velocity of the intact rock, similar to the material measured in the model test, was 1980 m/s. The results showed that when the amplitude of the stress wave was not large enough, its propagation speed in the rocks was about the same as that of an elastic wave, which is consistent with the conclusion that when the stress wave amplitude is small under the combined action of dynamic and static, the initial damage to the rock is mainly caused by the application of the static load [40].

To derive the variation law of stress wave velocities in the rocks under biaxial static loading, the average stress wave velocities in the intact rock under different static loads were plotted, as seen in Figure 4. It should be noted that for the subsequent initial damage analysis, the stress wave velocity in the intact rock was assumed to drop to zero when the biaxial static load reached the biaxial compressive strength of 7.826 MPa.

From the above Figure 4, it can be seen that the stress wave velocity in the intact rock increased and then decreased with the increase in the static load, which was also similar to the variation law of the physical attenuation of stress waves in the intact rock with the biaxial static load derived from the model test results, reflecting the stress sensitivity of the evolution of the microcracks in rocks. Numerous studies have shown that there is a close connection between the wave velocity and the intrinsic damage of a medium, so the damage evolution of the propagation medium can be described by the change of wave velocity. Combining the fitted static load versus the stress wave velocity curve in Figure 4, the maximum wave velocity of the intact rock was 2109 m/s, and the corresponding biaxial static load was 1.23 MPa, which was about 15.7% of the biaxial compressive strength, indicating that the microcracks inside the rocks were in the fully compacted stage at this static load level. Meanwhile, the new microcracks had not yet started to initiate.

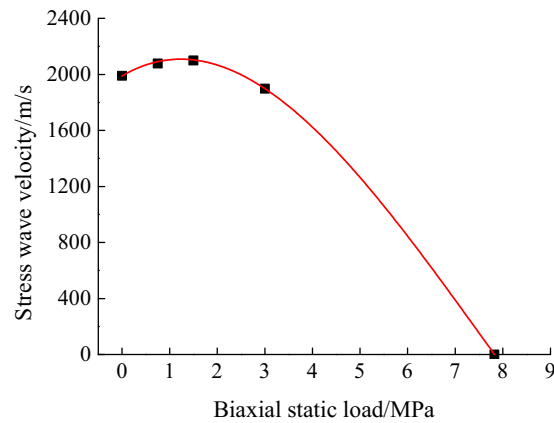


Figure 4. Relationship between the stress wave velocity and the static load of the intact rock.

The maximum wave velocity v_0 was defined as the wave velocity of the undamaged rock, so the initial damage variable D_0 of the rock can be defined by the following equation, when the value of D_0 is 0 and 1, respectively, indicating that the rocks are in an undamaged and fully damaged stage.

$$D_0 = 1 - \left(\frac{v_1}{v_0}\right)^2 \tag{3}$$

where, v_1 is the stress wave velocity under different static loads. Therefore, through Figure 4, the initial damage variable D_0 variation curve of the rock under different biaxial static loads can be derived, as shown in Figure 5, while the initial damage value of the rock was considered to be 1 when the biaxial static load reached the biaxial compressive strength.

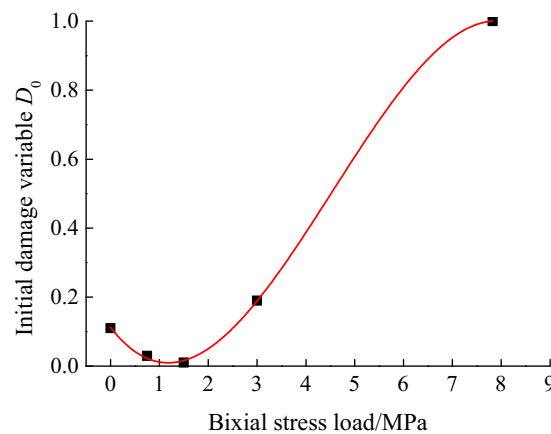


Figure 5. Relationship between the initial damage variable and the static load of the intact rock.

Based on the five data samples in Figure 5, including four experimental data points and one data point that characterized the failure of the intact rock obtained by mechanical analysis, the fitting equation was obtained by the least square polynomial fitting as shown in Equation (4), and the adjusted R-square and residual sum of squares of the equation were 0.994 and 1.034×10^{-4} , respectively.

$$D_0 = 0.11253 - 0.18321\sigma_b + 0.08918\sigma_b^2 - 0.00655\sigma_b^3 \tag{4}$$

The above equation is the initial damage evolution equation considering the compaction effect of the microcracks inside the rocks under different biaxial static loads. In addition, since the object studied in this section is the intact rock without macroscopic fractures, the initial damage evolution within the rocks can be assumed to be isotropic.

After the evolution equation of the initial damage variable D_0 was determined, it was coupled with the internal Mohr-Coulomb elasto-plastic model in UDEC to establish the improved model considering the initial damage for the intact rock. Based on the Lemaite strain equivalence principle, the principal stress tensor σ_i and the effective principal stress tensor $\tilde{\sigma}_i$, the bulk modulus K and the initial damage bulk modulus \bar{K} , the shear modulus G , and the initial damage shear modulus \bar{G} should satisfy the following relationships:

$$\begin{cases} \tilde{\sigma}_i = \sigma_i / (1 - D_0) \\ \bar{K} = (1 - D_0)K \\ \bar{G} = (1 - D_0)G \end{cases} \quad (5)$$

After the bulk modulus \bar{K} and the shear modulus \bar{G} containing the initial damage factor D_0 were obtained, the relationship between the stress increment $\Delta\sigma_i$ and the strain increment $\Delta\varepsilon_i$ in the Mohr-Coulomb elastic-plastic model of the rocks was given by:

$$\Delta\sigma_i = \bar{\lambda}\delta_i\Delta\varepsilon_i + 2\bar{G}\Delta\varepsilon_i \quad (6)$$

where, $\bar{\lambda}$ is the Lamé constant of the damaged rock and δ_i is the Kronecker symbol. Meanwhile, both the rock yield damage function and the plastic flow law within the Mohr-Coulomb elasto-plastic constitutive model were changed to functions based on the effective principal stress tensor $\tilde{\sigma}_i$, and the Mohr-Coulomb elasto-plastic constitutive model considering the initial damage was established. Based on the internal Fish language in UDEC, the relevant parameters in the calculation process of the constitutive model were modified through the custom functions and variables to establish the user-defined constitutive model, and the calculation procedure of the established Mohr-Coulomb elasto-plastic constitutive model considering the initial damage is shown in Figure 6.

Combined with Figure 6, the detailed calculation process was as follows: The initial damage variable D_0 was first calculated based on the biaxial static load σ_b of the numerical model using Equation (4), and the physical and mechanical parameters of the rock considering the initial damage such as \bar{K} and \bar{G} , as well as the total strain increment $\Delta\varepsilon_i$ of the element under the initial static load were derived. Then, based on the Lemaite strain equivalence principle and combined with the initial damage variable D_0 , the effective principal stress increment $\Delta\tilde{\sigma}_i$ was derived by Equation (6), and finally the effective principal stress $\tilde{\sigma}_i$ of the element was obtained by an iterative calculation.

When the effective principal stress $\tilde{\sigma}_i$ of the element reached the yield condition and entered the plastic phase, the updated stress state of the element was obtained by the plastic flow law, and the above process was divided into two cases: The first case was when $h(\tilde{\sigma}_1, \tilde{\sigma}_3) \leq 0$, the shear failure occurred in the element, through the shear yield function f^s expressed by the effective principal stress and the shear plastic flow method, the new effective principal stress increment $\Delta\tilde{\sigma}_i$ was calculated by the total strain increment $\Delta\varepsilon_i$, and finally the effective principal stress $\tilde{\sigma}_i^N$ of the element was obtained. The other was when $h(\tilde{\sigma}_1, \tilde{\sigma}_3) \geq 0$, the element underwent tensile damage, and the new effective principal stress $\tilde{\sigma}_i^N$ of the element was calculated by the tensile yield function f^t and the tensile plastic flow law according to the same steps of the first case.

It is worth noting that the established rock constitutive model was based on the model test results and the damage mechanics theory, which can take into account the initial damage of intact rock under different biaxial equal static loads. For an underground rock mass with caverns, blast holes, and stress relief holes, numerical modeling can be carried out based on the established model as long as the initial boundary static load condition can be simplified to biaxial equal static loading.

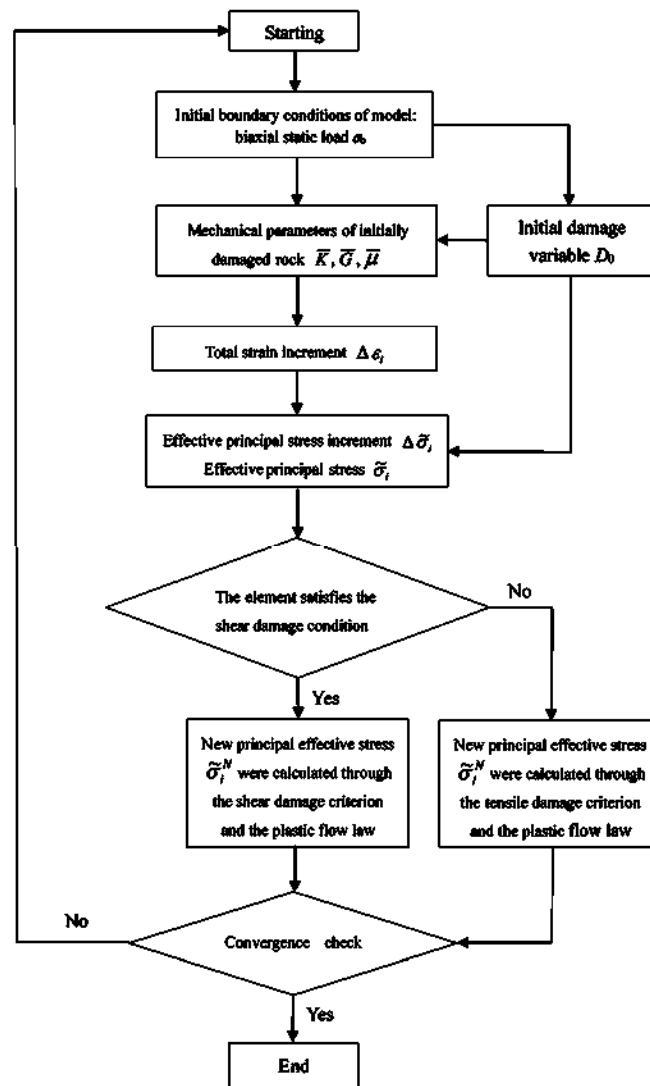


Figure 6. Calculation flow of the Mohr-Coulomb elasto-plastic constitutive model of the rock considering the initial damage.

4. Verification of the Established Rock Constitutive Model

In order to verify the accuracy of the established rock constitutive model based on this model and the widely adopted BB (Bandis-Barton) model which describes the nonlinear deformation characteristics of the joints [4], the model tests were numerically reproduced by the UDEC, and the experimental and numerical results were compared to analyze and verify the feasibility of the established rock constitutive model.

4.1. Numerical Model and Calculation Procedure

According to the three test samples designed in the model test as shown in Figure 2, the corresponding discrete element numerical models based on UDEC were established as shown in Figure 7. The dimensions of the numerical models were identical to the model test samples, whose length and width were 1600 mm and 1300 mm, respectively, while the lengths and spatial locations of the joints in the different numerical models were consistent with the model test samples. Due to the high mechanical strength of the seamless steel pipe, its deformation under static loads was approximately negligible, so it was not necessary to consider the quick-drying material inside the seamless steel pipe in the numerical model. The interior of the steel pipe was blank and the equivalent blast loads were applied directly to the inner wall of the steel pipes.

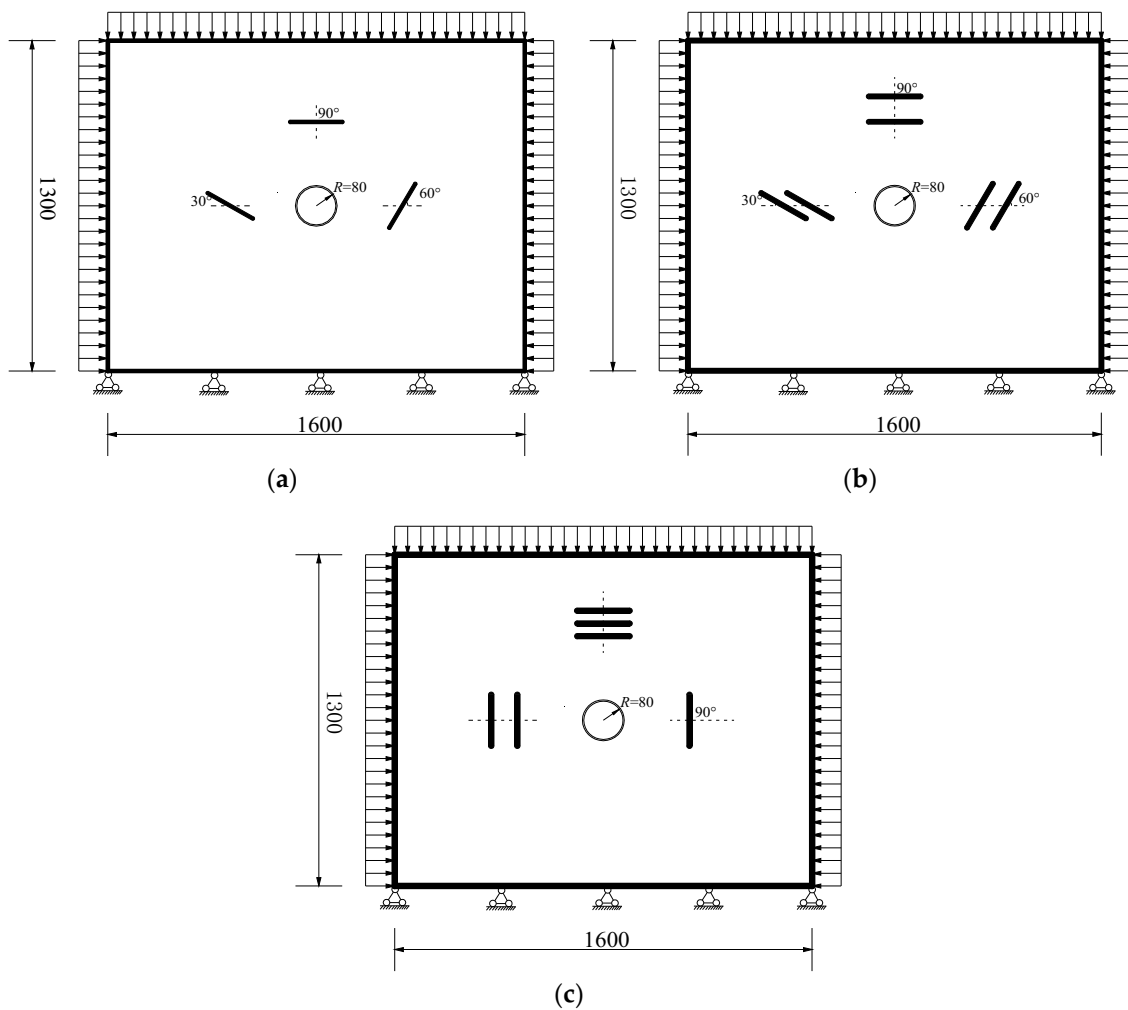


Figure 7. Numerical model of the different model test samples (unit: mm): (a) T1 sample; (b) T2 sample; (c) T3 sample.

After meshing, the established numerical models all contained intact rock, joint, and seamless steel pipe elements, and the number of degrees of freedom of the element was 3, including the translation in the x and y directions, and the rotation in the x-y plane. According to the statistics, the number of seamless steel pipe elements in the T1, T2, and T3 test blocks was 40, while the number of intact rock and joint elements were 25,510 and 84, 36,752 and 178, and 32,536 and 148, respectively. The static loading and constraints of the numerical models were the same as that of the model test samples. The fixed constraint was applied at the lower end of the model, and the uniformly distributed load was applied on the other three sides. The magnitude of the static loads applied on the numerical models was the same as the biaxial static loads in the model test. In reference to the physical and mechanical parameters of the rock and the joint simulated materials in the model test, the corresponding mechanical parameters of the rock, joint, and seamless steel pipe in the numerical simulation are shown in Table 2.

Only the elastic modulus and Poisson’s ratio of the simulated rock material were derived in the model tests, while the mechanical parameters used in the established rock constitutive model were the bulk modulus K and shear modulus G , which can be converted by the following equation.

$$\begin{cases} K = \frac{E}{3(1-2\mu)} \\ G = \frac{E}{2(1+\mu)} \end{cases} \quad (7)$$

Table 2. Physical and mechanical parameters of the intact rock, joint, and seamless steel pipe.

Parameters	Intact Rock	Joint	Seamless Steel Pipe
Compressive strength/MPa	5.864	/	645
Tensile strength/MPa	0.613	/	400
Elastic modulus/GPa	5.226	/	206
Internal friction angle/°	23.2	/	/
Cohesion/MPa	1.49	/	/
Poisson ratio	0.203	/	0.3
Initial normal stiffness/GPa/m	/	12	/
Initial shear stiffness/GPa/m	/	7.53	/

In the numerical model, the developed Mohr-Coulomb elasto-plastic constitutive model considering the initial damage was used to simulate the intact rock. According to the results of the model test, the nonlinear BB model could express the mechanical response of the joints under dynamic loading in the presence of the initial static loading, so the joints were simulated in the numerical simulation using the BB model in UDEC. Meanwhile, the strength of the seamless steel pipe was relatively higher compared to the rock and joints simulation materials as seen in Table 2, so the linear elastic model in UDEC was chosen for the simulation. The detailed numerical calculation process was as follows:

- (1) The initial static loads were first applied on the numerical model, where the applied static loads in the horizontal and vertical directions were of equal magnitude. To compensate for the insufficient static load conditions in the model test and considering the biaxial compressive strength of the rock material of 7.826 MPa, the number of static load conditions was increased in the numerical simulation, and there were 11 different static load conditions, namely 0, 0.75 MPa, 1.5 MPa, 2.25 MPa, 3 MPa, 3.75 MPa, 4.5 MPa, 5.25 MPa, 6 MPa, 6.75 MPa, and 7.5 MPa.
- (2) After the static loads were applied, an equivalent blast load curve was applied to the inner wall of the seamless steel tubes in the numerical model. The equivalent blast load was determined as follows: In the T3 test sample, an additional stress sensor was arranged in the quick-drying material inside the seamless steel pipe, and the sensor was arranged close to the inner wall of the steel pipe to record the time history curve of the blasting load generated during the detonation of the detonating cords. The measured blasting load is shown in Figure 8a below. Figure 8a shows that the measured blast load curve was roughly triangular, with a peak value of 47.59 MPa, a duration of 0.24 ms, and a rise time of about 0.11 ms. After the measured blast load curve was derived, it was applied to the inner wall of the steel pipe as shown in Figure 8b below. The totally computational time of the T1, T2, and T3 numerical models was 327 s, 539 s, and 473 s, respectively.

4.2. Comparison of the Numerical and Model Test Results

In order for a comparison with the model test results, the nodes near the stress measurement points in the corresponding model test samples were selected in each numerical model, and the radial stress time history curves at this point were obtained under the combined effect of different biaxial pressures and blasting loads. The waveforms of the measured and numerical stress time history curves at the same locations in different model test samples were firstly compared, and the measured and numerical stress time curves of the stress measurement points 17 and 18 in the T1, T2, and T3 test samples were selected under the biaxial pressure conditions of 0, 0.75 MPa, 1.5 MPa, and 3 MPa in both the model tests and numerical simulations as shown in Figure 9.

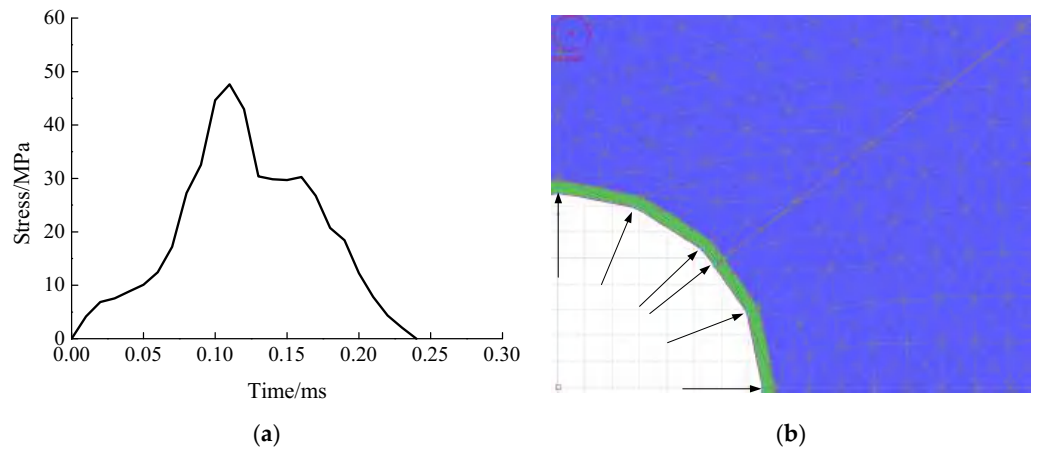


Figure 8. Measured blast load and applied schematic: (a) measured blasting load time curve; (b) blasting load application.

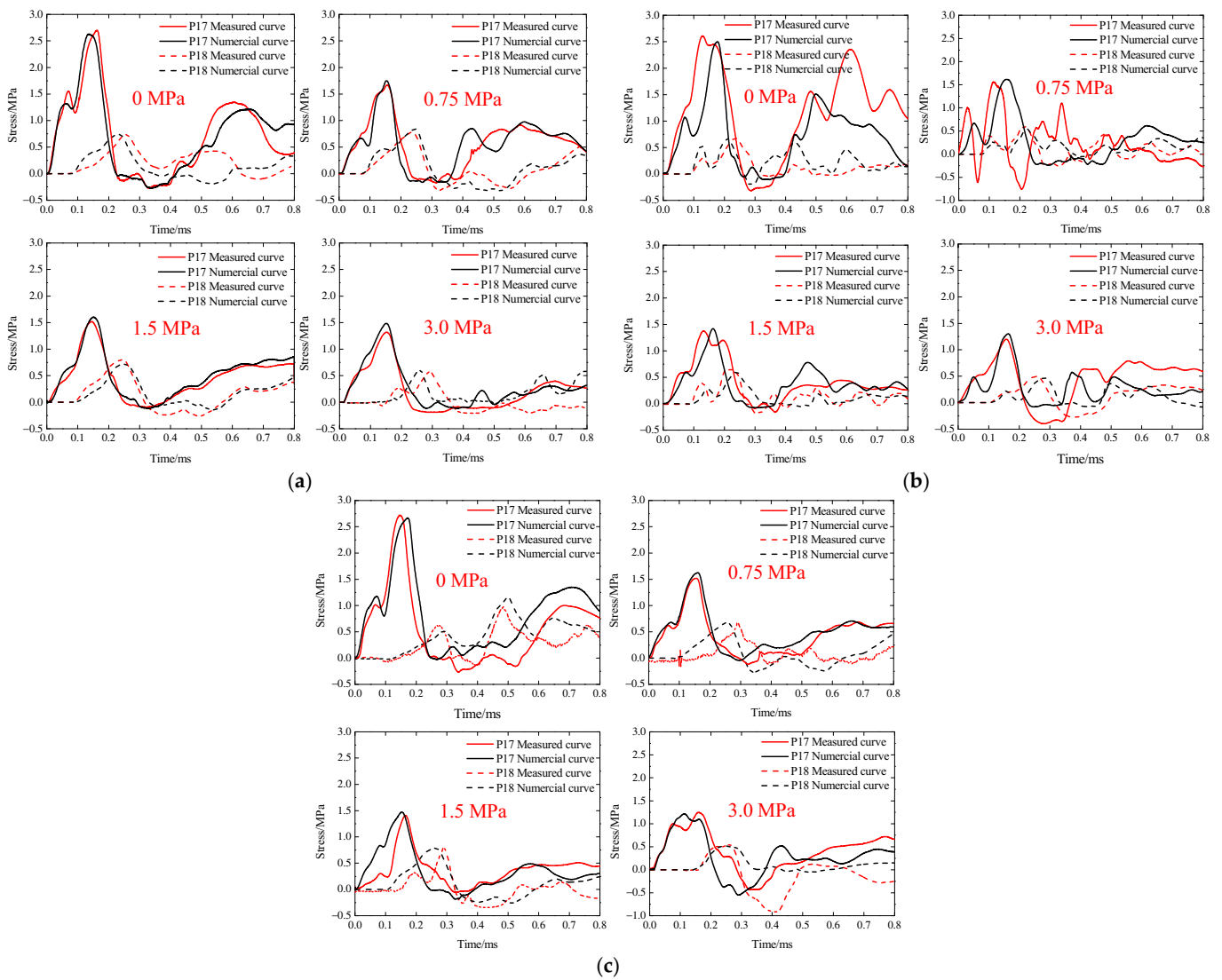


Figure 9. Measured and numerical stress wave curve at P17 and P18 points in each sample under different static loads: (a) T1 sample; (b) T2 sample; (c) T3 sample.

As seen in Figure 9, the measured and numerical stress wave curves recorded at P17 and P18 stress measurement points in each model test sample under different biaxial pressures were relatively similar in form and amplitude, and the stress wave amplitude decreased as the biaxial pressure increased. The above phenomena demonstrate the feasibility and accuracy of the numerical calculations based on a combination of the BB model describing the nonlinearity of the joints and the established Mohr-Coulomb elasto-plastic rock constitutive model considering the initial damage.

In order to verify the rationality of the established rock constitutive model from the perspective of stress wave propagation, the stress wave transmission coefficients of the jointed rock masses contained in each numerical model under different biaxial pressures were used for comparing the numerical and experimental results, as shown in Figure 10. It should be noted that the stress wave transmission coefficients of rock masses with a different number and angle joints in the model test were determined by the incident wave and the transmitted wave collected by the stress sensors arranged before and after the rock masses, which was the ratio of the amplitude of the transmitted stress wave to the incident wave. For example, for the T1, T2, and T3 test samples in Figure 2, the amplitude ratios of the stress wave recorded by the stress measuring points 22 and 21 were the stress wave transmission coefficients of the 90° single-joint rock mass, the 90° double-joints rock mass, and the 90° three-joints rock mass, respectively. In the numerical modeling, the nodes corresponding to the stress measuring points in the model test samples were selected in the numerical model to determine the incident and transmitted stress wave of the rock mass, and the numerical transmission coefficients were obtained. Meanwhile, the applied confining pressures in the model tests were 0, 0.75 MPa, 1.5 MPa, and 3 MPa, respectively, but the range of confining pressures was increased in the numerical calculations, which were from 0 to 7.5 MPa, with an interval of 0.75 MPa, for a total 11 different confining pressures. For a comparative analysis, the numerical results were expressed as smoothed curves of numerical transmission coefficients under different biaxial loads.

Figure 10 shows that the measured and numerical transmission coefficients of the jointed rock mass contained in each numerical model under different static loads were relatively close to each other, and when the static load increased from 0, the measured and numerical transmission coefficients both showed a trend of increasing first and then decreasing. Based on the numerical simulation results in Figure 10, the stress wave transmission coefficient of the jointed rock mass containing different angles and numbers reached its maximum value when the static load was about 2.2 MPa, which was about 28.1% of the biaxial compressive strength.

It can also be seen in Figure 10 that the measured and numerical transmission coefficients of the jointed rock masses within different numerical models were relatively close in the ascending part of the curve, while a certain deviation occurred in the descending part. The reason was that in the model test when the static load increased to 3 MPa, which was about 38.3% of the biaxial compressive strength, the closed microcracks within the intact rock started to expand, and new microcracks were initiated, resulting in a decrease in the transmission coefficient [40]. However, in the numerical calculation, the expansion of the microcracks within the intact rock was not considered, which led to the larger numerical results.

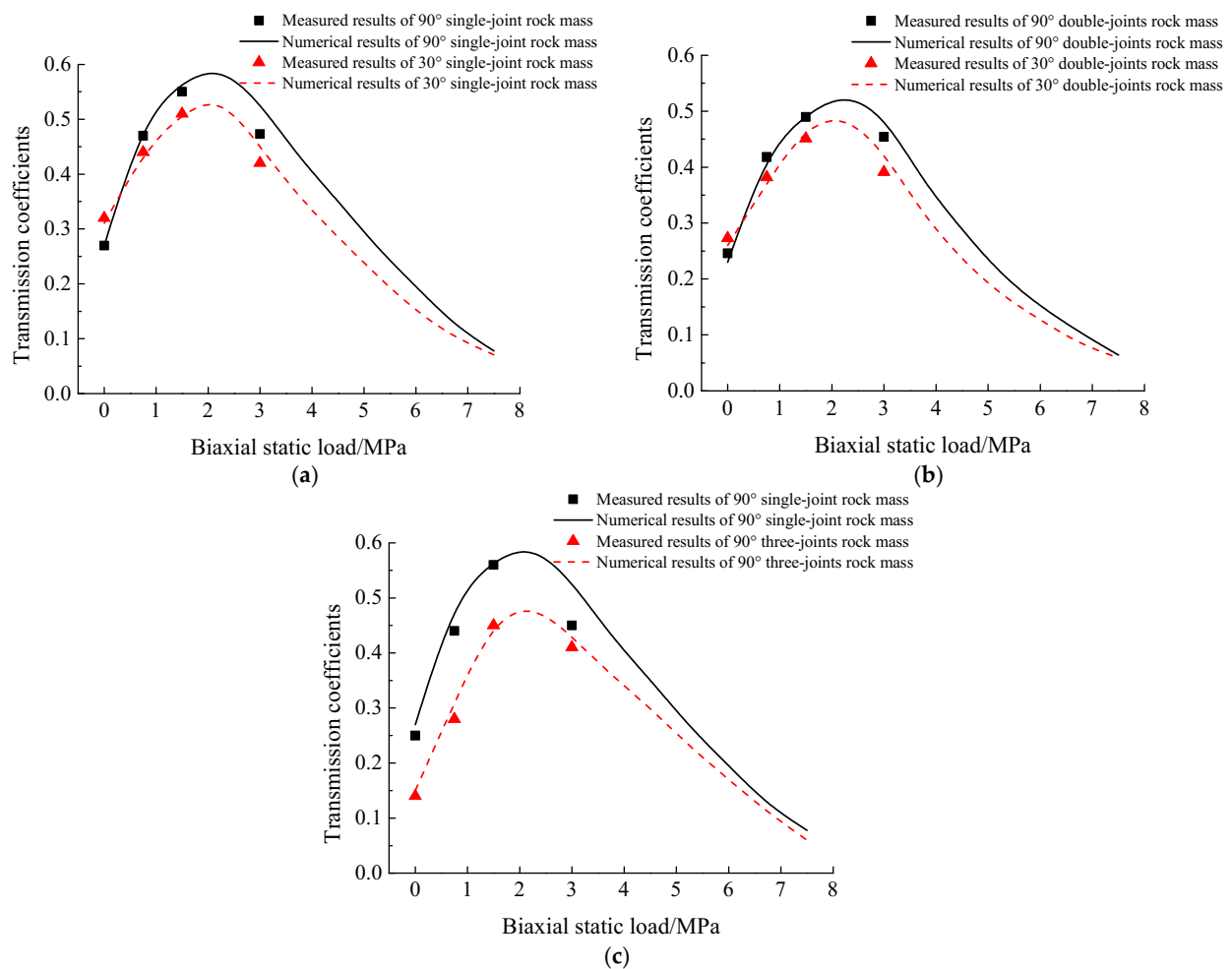


Figure 10. Measured and numerical transmission coefficients of jointed rock masses under different static loads: (a) T1 sample; (b) T2 sample; (c) T3 sample.

5. Numerical Calculation of the Effect of the Angle and the Number of Joints on the Stress Wave Propagation

The last section obtained a high agreement between the numerical and experimental results, which verified the accuracy of the established rock constitutive model considering the initial damage and the feasibility of the adopted numerical simulation method. Due to the limited angle and number of joints set in the model test, a numerical calculation of the stress wave propagation in rock masses with various angles and numbers of joints under different biaxial static loads was carried out based on the same numerical simulation method in Section 4 for a more thorough study of the effect of the angle and number of joints on the stress wave propagation. The physical and mechanical parameters of the rocks and joints in the numerical calculations are shown in Table 2.

5.1. Effect of the Angle of Joints

The angles of the joints selected in the model tests were 30°, 60°, and 90°, while the selection range of the joint angles was expanded in the numerical calculations, with nine different joint angles selected ranging from 10° to 90° and with an interval of 10°. In order to eliminate the effect of the number of joints, only one single joint was selected for the study, and appropriate simplifications were made on the basis of the single-joint model test sample T1.

According to the symmetry of the model test sample, the numerical model was developed as shown in Figure 11 with the size of 800 mm (length) × 1300 mm (width), and

a penetration joint was contained in the numerical model. A fixed restraint was applied at the bottom of the numerical model, and biaxial static loads were applied to the remaining three outlines. During the numerical calculation, the applied biaxial static loads were the same as in Section 3, from 0 to 7.5 MPa for total eleven conditions, and the applied blast stress wave load $P(t)$ is shown in Figure 8a.

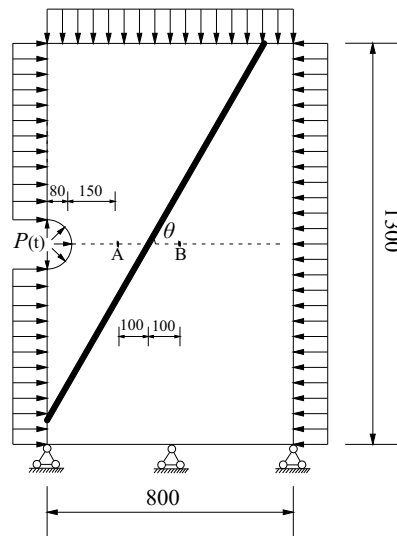


Figure 11. Numerical model containing one single joint with different angles (unit: mm).

According to the actual positions of the stress measurement points P17 and P18 arranged before and after the joint in the single-joint model test sample T1, nodes A and B near the same position before and after the joint were selected in the numerical model as shown in Figure 11, and the stress wave transmission coefficients were calculated from the stress wave amplitudes recorded by the measurement points A and B in the numerical model. The variation of the stress wave transmission coefficient with the angle of the joint under different biaxial static loads was compiled and is shown in Figure 12 below.

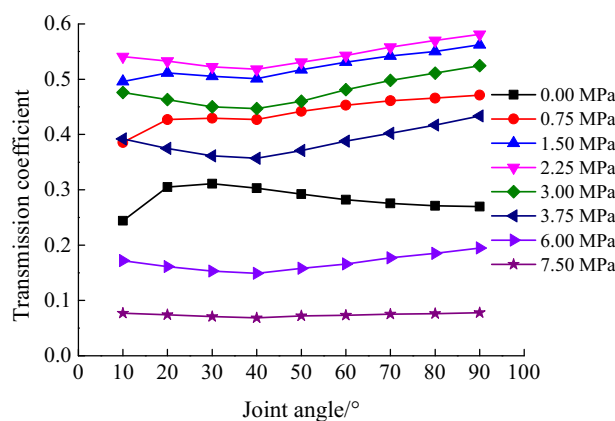


Figure 12. Effect of the joint angle on the transmission coefficient under different biaxial static loads.

As seen in Figure 12, the transmission coefficient increased and then decreased with the increase in the joint angle when the circumferential pressure was 0. The transmission coefficient was at a maximum when the joint angle was close to 30° and decreased with the increase in the joint angle when the joint angle was greater than 30°, which was also consistent with the measured results [40]. The transmission coefficient increased, then slightly decreased, and finally increased with the increase in the joint angle at the biaxial static load of 0.75 MPa and 1.5 MPa and showed an overall trend of increasing. When the

biaxial static load was greater than 2.25 MPa, the transmission coefficient decreased and then increased with the increase in the joint angle, and the transmission coefficient was the smallest when the joint angle was about 40° . In addition, it can be seen from Figure 12 that the overall transmission coefficient of rock masses containing one single joint with different angles showed a pattern of increasing and then decreasing with the increase in the biaxial static load, which was also consistent with the results shown in Figure 10.

5.2. Effect of the Number of Joints

In order to investigate the effect of the number of joints on the transmission coefficient of stress waves under different biaxial static loads, numerical calculations were conducted on the cases of jointed rock masses with vertical incidence (i.e., the angle of joints was 90°) and oblique incidence (the angle of joints was 60°) of stress waves propagation. Based on this, the numerical models of rock masses containing a different number of 90° and 60° joints were established. In the numerical calculation, six different number of joints were selected, which were 1, 2, 3, 5, 7, and 9, respectively. At the same time, according to the joint spacing in the three-joints test sample T3 in the model test, the joint spacing selected in the numerical model was also 50 mm. According to the number of joints, the size of the numerical model established was 1300 mm (length) \times 1300 mm (width), and the numerical models including five joints with angles of 90° and 60° are shown in Figure 13.

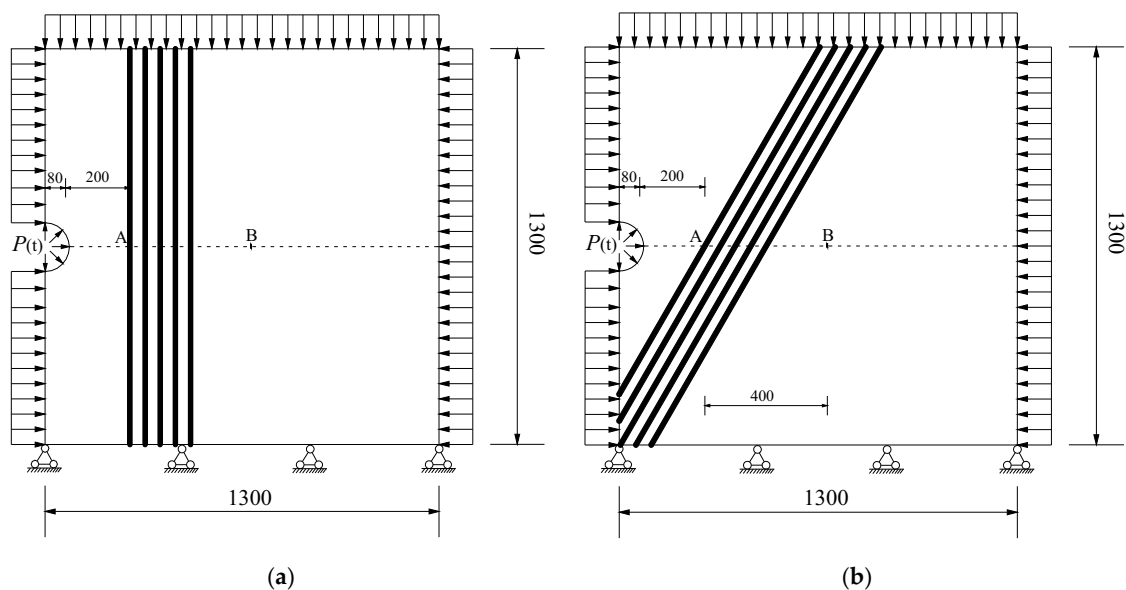


Figure 13. Numerical calculation model of the rock mass containing five joints with different angles (unit: mm): (a) joint angle of 90° ; (b) joint angle of 60° .

The applied biaxial static loads in the numerical simulation were somewhat different from those in Section 4.1, which were 0 MPa, 0.75 MPa, 1.5 MPa, 2.25 MPa, 4.5 MPa, and 6.75 MPa, for a total of six conditions, while the applied stress wave load $P(t)$ remained the same as in Section 4.1. To eliminate the effects of the geometric and physical attenuation of the stress waves, the selected measurement points in the numerical model were node A located on the measurement line near the left side of the first joint and node B located on the measurement line near the right side of the ninth joint when the number of joints was nine, as shown in Figure 13 above, which was slightly different from the arrangement of the measurement points in the T2 test sample in the model test. The variation of the transmission coefficient with the number of joints for vertical and oblique incidence of stress waves under different biaxial static loads was sorted out as shown in Figure 14.

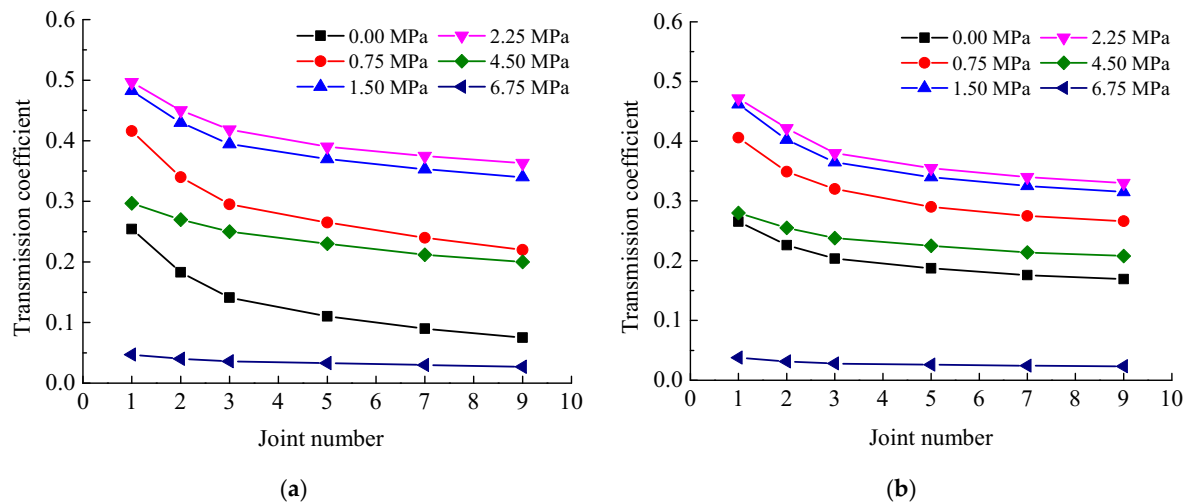


Figure 14. Transmission coefficient of the rock mass containing different numbers of 90° and 60° joints under biaxial static loads: (a) 90° jointed rock mass; (b) 60° jointed rock mass.

As can be seen from Figure 14 above, the transmission coefficients of both the 90° and 60° joint rock masses showed a decreasing trend with an increase in the number of joints under the same static load, and the decreasing increment gradually became smaller, especially after the number of joints reached a certain number (more than five), the attenuation effect of the increase in the number of joints on the stress wave propagation gradually weakened.

At the same time, the reduction in the transmission coefficient for the 90° joint rock mass was 70.5%, 47.1%, 34.2%, 32.6%, 29.1%, and 26.8% when the number of joints was increased from 1 to 9 with biaxial static loads of 0 MPa, 0.75 MPa, 1.5 MPa, 2.25 MPa, 4.5 MPa, and 6.75 MPa, respectively, and the corresponding reduction in the transmission coefficient for the 60° joint rock mass was 36.3%, 34.4%, 31.7%, 30.0%, 25.7%, and 22.6%, respectively. The above results showed that when the static load was small, such as 0 MPa and 1.5 MPa, the decrease in the transmission coefficient of the 90° jointed rock masses caused by increasing the number of joints was significantly larger than that of the 60° jointed rock masses, and the larger the static load was, the smaller the decrease in the stress waves transmission coefficient caused by increasing the number of joints for both 90° and 60° jointed rock masses, indicating that the attenuation effect of the number of joints on stress wave propagation became weaker as the static load increased.

6. Conclusions

In this paper, the variation of the initial damage variable was firstly determined based on the change in the stress wave velocity in the intact rock under different equal biaxial static loads in the model test, and the Mohr-Coulomb elasto-plastic constitutive model of the rock considering initial damage was established by combining the Mohr-Coulomb strength criterion. The developed rock constitutive model was then numerically implemented using the Fish language in discrete element software UDEC, and the model tests were numerically reproduced in conjunction with the BB model characterizing the nonlinear deformation properties of the joints. Finally, further numerical studies on the effects of the biaxial static load, the angle, and the number of joints on the propagation of stress waves in the jointed rock mass were carried out, and the following conclusions were drawn.

- (1) The numerical and experimental results of the propagation law of stress waves in the jointed rock masses under different biaxial static loads were compared and analyzed from the perspectives of the waveform, amplitude, and the transmission coefficient of

- stress waves, which were relatively consistent, verifying the feasibility of the adopted numerical calculation method.
- (2) The initial damage variation in the intact rock with the biaxial static load increased first and then decreased. When the biaxial static load was 1.23 MPa, which was about 15.7% of the biaxial compressive strength of the intact rock, the stress wave velocity reached its maximum value while the initial damage was the smallest, indicating that the internal microcracks in the intact rock were in a fully compacted state under this static load.
 - (3) As the biaxial static loads increased, the measured and numerical transmission coefficients of the rock masses containing different angles and numbers of joints all showed a trend of first increasing and then decreasing, and the transmission coefficient was the largest when the static load was about 2.2 MPa, which was about 28.1% of the biaxial compressive strength of the intact rock.
 - (4) The transmission coefficient increased and then decreased with the increase in the joint angle without the static load and was the largest when the joint angle was close to 30°. The transmission coefficient continuously increased with the increase in the joint angle when the static load was relatively small, such as 0.75 MPa and 1.5 MPa, i.e., less than 20% of the biaxial compressive strength of the intact rock. The transmission coefficient decreased and then increased with the increase in the joint angle when the static load was greater than 2.25 MPa (28.7% biaxial compressive strength of the intact rock) and was the smallest at the joint angle of about 40°.
 - (5) Under the same static loading, the transmission coefficients of the jointed rock masses all showed a tendency to decrease with the increase in the number of joints, and the decreasing increment gradually became smaller. The larger the static load, the smaller the decrease in the transmission coefficients caused by the increase in the number of joints, indicating the effect of the number of joints on the transmission coefficients which decreased as the static load increased.
 - (6) In the blasting excavation of the underground rock mass, the in situ stress and the spatial distribution of the joints significantly affected the propagation of the blasting stress wave. When the blasting stress wave vertically impacted the initial stressed rock mass, the transmission coefficient was the largest. Therefore, the connection line of blast holes should be perpendicular to the dominant joints in an underground rock mass to ensure the efficient transmission of explosive energy, so that the rock mass can be efficiently and adequately fragmented.

Author Contributions: Conceptualization, Q.D.; methodology, Q.D. and X.L.; software, Q.D.; validation, Y.J. and J.S.; formal analysis, Q.D.; investigation, Q.D.; resources, X.L.; data curation, Q.D.; writing—original draft preparation, Q.D.; writing—review and editing, Q.D.; visualization, Q.D.; supervision, Y.J.; project administration, Q.D.; funding acquisition, X.L., Y.J. and J.S. All authors have read and agreed to the published version of the manuscript.

Funding: This research was funded by the Natural Science Foundation of Hubei Province, China (2020CFB428), the Innovation Group Project of the Natural Science Foundation of Hubei Province, China (2020CFA043), the Key Research and Development Project of Hubei Province, China (2020BCA084), the National Natural Science Foundation of China (51774222), and the Research Start-Up Foundation of Jiangnan University (1027-06020001).

Institutional Review Board Statement: Not applicable.

Informed Consent Statement: Not applicable.

Data Availability Statement: The data used to support the findings of this study are available from the corresponding author upon request.

Acknowledgments: Special thanks for organizing and conducting the experimental studies to the faculty of the Hubei Key Laboratory of Blasting Engineering, Jiangnan University.

Conflicts of Interest: The authors declare no conflict of interest.

References

1. Fan, L.F.; Sun, H.Y. Seismic wave propagation through an in-situ stressed rock mass. *J. Appl. Geophys.* **2015**, *121*, 13–20. [CrossRef]
2. Yi, C.P.; Johansson, D.; Greberg, J. Effects of in-situ stresses on the fracturing of rock by blasting. *Comput. Geotech.* **2018**, *104*, 321–330. [CrossRef]
3. Tao, J.; Yang, X.G.; Li, H.T.; Zhou, J.; Fan, G.; Lu, G. Effects of in-situ stresses on dynamic rock responses under blast loading. *Mech. Mater.* **2020**, *145*, 103374. [CrossRef]
4. Bandis, S.C.; Lumsden, A.C.; Barton, N.R. Fundamentals of rock joint deformation. *Int. J. Rock Mech. Min. Sci. Geomech. Abstr.* **1983**, *20*, 249–268. [CrossRef]
5. Babanouri, N.; Mansouri, H.; Nasab, S.K.; Bahaadini, M. A coupled method to study blast wave propagation in fractured rock masses and estimate unknown properties. *Comput. Geotech.* **2013**, *49*, 134–142. [CrossRef]
6. Skrzypkowski, K.; Korzeniowski, W.; Zagórski, K.; Zagórska, A. Adjustment of the Yielding System of Mechanical Rock Bolts for Room and Pillar Mining Method in Stratified Rock Mass. *Energies* **2020**, *13*, 2082. [CrossRef]
7. Schoenberg, M. Elastic wave behavior across linear slip interfaces. *J. Acoust. Soc. Am.* **1980**, *68*, 1516–1521. [CrossRef]
8. Pyrak-Nolte, L.J.; Myer, L.R.; Cook, N.G.W. Transmission of seismic waves across single natural fractures. *J. Geophys. Res. Solid Earth* **1990**, *95*, 8617–8638. [CrossRef]
9. Zhao, J.; Cai, J.G. Transmission of Elastic P-waves across Single Fractures with a Nonlinear Normal Deformational Behavior. *Rock Mech. Rock Eng.* **2001**, *34*, 3–22. [CrossRef]
10. Zhao, J.; Cai, J.G.; Zhao, X.B.; Li, H.B. Dynamic Model of Fracture Normal Behaviour and Application to Prediction of Stress Wave Attenuation Across Fractures. *Rock Mech. Rock Eng.* **2008**, *41*, 671–693. [CrossRef]
11. Perino, A.; Orta, R.; Barla, G. Wave Propagation in Discontinuous Media by the Scattering Matrix Method. *Rock Mech. Rock Eng.* **2012**, *45*, 901–918. [CrossRef]
12. Li, J.C.; Li, H.B.; Ma, G.W.; Zhao, J. A time-domain recursive method to analyse transient wave propagation across rock joints. *Geophys. J. Int.* **2012**, *188*, 631–644. [CrossRef]
13. Zhao, X.B.; Zhao, J.; Cai, J.G. P-wave transmission across fractures with nonlinear deformational behaviour. *Int. J. Numer. Anal. Methods Geomech.* **2006**, *30*, 1097–1112. [CrossRef]
14. Li, J.C.; Ma, G.W. Analysis of Blast Wave Interaction with a Rock Joint. *Rock Mech. Rock Eng.* **2010**, *43*, 777–787. [CrossRef]
15. Cai, J.G.; Zhao, J. Effects of multiple parallel fractures on apparent attenuation of stress waves in rock masses. *Int. J. Rock Mech. Min. Sci.* **2000**, *37*, 661–682. [CrossRef]
16. Li, J.C. Wave propagation across non-linear rock joints based on time-domain recursive method. *Geophys. J. Int.* **2013**, *193*, 970–985. [CrossRef]
17. Chai, S.B.; Li, J.C.; Zhang, Q.B. Stress Wave Propagation across a Rock Mass with Two Non-parallel Joints. *Rock Mech. Rock Eng.* **2016**, *49*, 4023–4032. [CrossRef]
18. Ju, Y.; Sudak, L.; Xie, H.P. Study on stress wave propagation in fractured rocks with fractal joint surfaces. *Int. J. Solids Struct.* **2007**, *44*, 4256–4271. [CrossRef]
19. Feng, J.J.; Wang, E.Y.; Chen, L.; Li, X.; Xu, Z.; Li, G. Experimental study of the stress effect on attenuation of normally incident P-wave through coal. *J. Appl. Geophys.* **2016**, *132*, 25–32. [CrossRef]
20. Cundall, P.A. A computer model for simulating progressive large-scale movements in blocky rock systems. In Proceedings of the Symposium of the International Society for Rock Mechanics, Nancy, France, 4–6 October 1971; pp. 11–18.
21. Zhu, J.B.; Deng, X.F.; Zhao, X.B.; Zhao, J. A Numerical Study on Wave Transmission Across Multiple Intersecting Joint Sets in Rock Masses with UDEC. *Rock Mech. Rock Eng.* **2013**, *46*, 1429–1442. [CrossRef]
22. Li, H.B.; Liu, T.T.; Liu, Y.Q.; Li, J.; Xia, X.; Liu, B. Numerical Modeling of Wave Transmission across Rock Masses with Nonlinear Joints. *Rock Mech. Rock Eng.* **2015**, *49*, 1115–1121. [CrossRef]
23. Zheng, Y.; Chen, C.X.; Liu, T.T.; Zhang, W. Numerical Study of P-Waves Propagating across Deep Rock Masses Based on the Hoek-Brown Model. *Int. J. Geomech.* **2020**, *20*, 04019152. [CrossRef]
24. Sun, L.; Zhao, G.F.; Zhao, J. Particle manifold method (PMM): A new continuum-discontinuum numerical model for geomechanics. *Int. J. Numer. Anal. Methods Geomech.* **2012**, *37*, 1711–1736. [CrossRef]
25. Zhao, J.; Sun, L.; Zhu, J.B. Modelling P-wave transmission across rock fractures by particle manifold method (PMM). *Geomech. Geoenviron. Int. J.* **2012**, *7*, 175–181. [CrossRef]
26. Fan, L.F.; Yi, X.W.; Ma, G.W. Numerical manifold method (NMM) simulation of stress wave propagation through fractured rock mass. *Int. J. Appl. Mech.* **2013**, *5*, 1350022. [CrossRef]
27. Zhou, X.; Fan, L.; Wu, Z. Effects of Microfracture on Wave Propagation through Rock Mass. *Int. J. Geomech.* **2017**, *17*, 04017072. [CrossRef]
28. Huang, X.; Qi, S.; Williams, A.; Zhou, Y.; Zheng, B. Numerical simulation of stress wave propagating through filled joints by particle model. *Int. J. Solids Struct.* **2015**, *69–70*, 23–33. [CrossRef]
29. Zhou, H.; He, C. Propagation law of stress wave and cracks in non-penetrating jointed rock mass: A numerical study based on particle flow code. *Geotech. Geol. Eng.* **2020**, *38*, 3967–3981. [CrossRef]
30. Babanouri, N.; Fattahi, H. Evaluating orthotropic continuum analysis of stress wave propagation through a jointed rock mass. *Bull. Eng. Geol. Environ.* **2018**, *77*, 725–733. [CrossRef]

31. Heidari, M.; Khanlari, G.R.; Torabi-Kaveh, M. Effect of Porosity on Rock Brittleness. *Rock Mech. Rock Eng.* **2014**, *47*, 785–790. [CrossRef]
32. Patrick, B.; Wong, T.F.; Zhu, W. Effects of porosity and crack density on the compressive strength of rocks. *Int. J. Rock Mech. Min. Sci.* **2014**, *67*, 202–211.
33. Jin, J.F.; Yuan, W.; Wu, Y.; Guo, Z. Effects of axial static stress on stress wave propagation in rock considering porosity compaction and damage evolution. *J. Cent. South Univ.* **2020**, *27*, 592–607. [CrossRef]
34. Martin, C.D.; Chandler, N.A. The progressive fracture of Lac du Bonnet granite. *Int. J. Rock Mech. Min. Sci. Geomech. Abstr.* **1994**, *31*, 643–659. [CrossRef]
35. Cai, M.; Kaiser, P.K.; Tasaka, Y.; Maejima, T.; Morioka, H.; Minami, M. Generalized crack initiation and crack damage stress thresholds of brittle rock masses near underground excavations. *Int. J. Rock Mech. Min. Sci.* **2004**, *41*, 833–847. [CrossRef]
36. Wang, X.; Ge, H.; Wang, J.; Wang, D.; Chen, H. Evaluation of the Micro-cracks in Shale from the Stress Sensitivity of Ultrasonic Velocities. *Rock Mech. Rock Eng.* **2016**, *49*, 4929–4934. [CrossRef]
37. Hou, R.; Zhang, K.; Tao, J.; Xue, X.; Chen, Y. A Nonlinear Creep Damage Coupled Model for Rock Considering the Effect of Initial Damage. *Rock Mech. Rock Eng.* **2018**, *52*, 1275–1285. [CrossRef]
38. Du, M.; Su, J.; Wang, X.; Zhang, S.; Zhang, Y. Dynamic response and crack propagation law of tunnel invert with initial damage. *Eng. Fail. Anal.* **2021**, *119*, 104939.
39. Dong, Q. Model test study on propagation law of plane stress wave in jointed rock mass under different in-situ stresses. In Proceedings of the IOP Conference Series: Earth and Environmental Science, Singapore, 22–25 December 2017; p. 012009.
40. Dong, Q.; Li, X.P.; Huang, J.H. Model test study on cylindrical blasting stress wave propagation across jointed rock mass with different initial stresses. *Adv. Civ. Eng.* **2020**, *2020*, 8881302. [CrossRef]
41. Papanikolaou, V.K.; Kappos, A.J. Confinement-sensitive plasticity constitutive model for concrete in triaxial compression. *Int. J. Solids Struct.* **2007**, *44*, 7021–7048. [CrossRef]
42. Huang, H. Experimental Study on Biaxial-to-Uniaxial Strength Ratio of Concrete at Early Age. Master's Thesis, Dalian University of Technology, Dalian, China, 2013. (In Chinese).
43. Yin, S.; Wang, S. Relation of stresses with elastic modulus and velocities and its application. *Rock Soil Mech.* **2003**, *24*, 597–601. (In Chinese)

Article

Predictive Modelling for Blasting-Induced Vibrations from Open-Pit Excavations

Yo-Hyun Choi and Sean Seungwon Lee * 

Department of Earth Resources and Environmental Engineering, Hanyang University, Seoul 04763, Korea; netisen@hanyang.ac.kr

* Correspondence: seanlee@hanyang.ac.kr; Tel.: +82-2220-2243

Abstract: Reliable estimates of peak particle velocity (PPV) from blasting-induced vibrations at a construction site play a crucial role in minimizing damage to nearby structures and maximizing blasting efficiency. However, reliably estimating PPV can be challenging due to complex connections between PPV and influential factors such as ground conditions. While many efforts have been made to estimate PPV reliably, discrepancies remain between measured and predicted PPVs. Here, we analyzed various methods for assessing PPV with several key relevant factors and 1191 monitored field blasting records at 50 different open-pit sites across South Korea to minimize the discrepancies. Eight prediction models are used based on artificial neural network, conventional empirical formulas, and multivariable regression analyses. Seven influential factors were selected to develop the prediction models, including three newly included and four already formulated in empirical formulas. The three newly included factors were identified to have a significant influence on PPV, as well as the four existing factors, through a sensitivity analysis. The measured and predicted PPVs were compared to evaluate the performances of prediction models. The assessment of PPVs by an artificial neural network yielded the lowest errors, and site factors, K and m were proposed for preliminary open-pit blasting designs.

Citation: Choi, Y.-H.; Lee, S.S. Predictive Modelling for Blasting-Induced Vibrations from Open-Pit Excavations. *Appl. Sci.* **2021**, *11*, 7487. <https://doi.org/10.3390/app11167487>

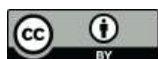
Academic Editor: Ricardo Castedo

Received: 14 May 2021

Accepted: 13 August 2021

Published: 15 August 2021

Publisher's Note: MDPI stays neutral with regard to jurisdictional claims in published maps and institutional affiliations.



Copyright: © 2021 by the authors. Licensee MDPI, Basel, Switzerland. This article is an open access article distributed under the terms and conditions of the Creative Commons Attribution (CC BY) license (<https://creativecommons.org/licenses/by/4.0/>).

Keywords: peak particle velocity; blasting-induced vibration; prediction; artificial neural networks; site factors K and m; open-pit blasting

1. Introduction

Drilling and blasting is typically used to fragment rock masses at various building and civil construction sites because it is the most economical means of breaking rock for excavation. However, blasting at construction sites is accompanied by undesirable environmental side effects, such as vibration, noise, and scattering of debris. According to Korea's Office of National Environmental Conflict Resolution Commission, 3840 (approximately 84%) of the 4557 environmental dispute cases on record involve noise and vibration, primarily from construction sites [1]. Blasting vibrations occurring at a construction site account for the majority of these environmental disputes because they result in damage to nearby structures and present various safety concerns. Every country specifies a limit on the peak particle velocity (PPV) of the induced vibrations to minimize damage to nearby structures. According to DIN 4150-3 [2], the limits on PPV are 2 cm/s for buildings used for commercial purposes, 0.5 cm/s for dwellings, and 0.3 cm/s for buildings under preservation orders at a frequency of 1 to 10 Hz. Siskind et al. [3] proposed that 1.9 and 1.3 cm/s are safe levels of blasting vibration for drywall and plaster under 10 Hz conditions. In South Korea, the limits on PPV are 0.2 cm/s for cultural assets and 0.5 cm/s for apartments. Blasting engineers try to accurately predict PPVs that will be induced by blasting and apply the predicted PPVs to the design of blasting patterns to comply with these regulations. Many researchers have studied and proposed various empirical formulas to predict and control PPV [4]. Among the various empirical formulas, a conventional empirical formula

developed by U.S. Bureau of Mines (USBM) researchers, Duvall and Petkof [5] has been widely used to predict PPV and design blasting patterns. The current design approach consists of two steps. First, several test blastings are conducted to determine site factors K and m , which represent geological characteristics, before massive blasting. At each test, the distances between blasting and monitoring points, the charge weights per delay, and the PPVs are monitored and recorded. Based on these factors, K and m are calculated. Second, PPV is predicted using an empirical formula with K , m , the distance between blasting and monitoring points, and the charge weight per delay. However, this empirical formula often results in significant discrepancies between measured and predicted PPVs. Due to the discrepancies, blasting engineers are forced to use a high factor of safety (FoS) to prevent problems resulting from excessive vibration velocity. A high FoS typically requires the use of a more conservative charge weight per delay than the maximum allowable weight would accommodate. The conservative charge weight per delay can decrease blasting efficiency and increase construction time and total cost. A more accurate method of predicting PPV is vital to protect the environment and increase the efficiency of blasting.

The artificial neural network (ANN) has been applied in various fields such as renewable energy systems [6], atmospheric science [7], and civil engineering [8,9] to predict targets. In addition, research is also ongoing on predicting PPVs using ANN. To develop an ANN model for PPV prediction, Nguyen et al. [10] gathered 185 blasting datasets from a limestone mine in Vietnam, Azimi et al. [11] collected 70 blasting datasets from a copper mine in Iran, and Bui et al. [12] obtained 83 blasting datasets from a quarry mine in Vietnam. Every result of the research showed good agreement with the measured and predicted PPVs. ANN is generally not limited by any assumptions such as linearity or normality, thus ANN has the modeling power to derive excellent results even with irregular datasets and complex phenomena [13,14]. However, in the previous studies, the largest number of datasets was only 185 and the datasets were obtained from a limited local region. Each ANN model developed in the previous studies is only strictly applicable to the site where the study was conducted due to the limited region. Therefore, it is necessary to develop the global prediction model and to select influential factors which can be obtained easily from every blasting site. In this paper, an ANN was selected as one of the prediction methods due to its strengths. Its performance for predicting PPVs was compared with the performances of conventional empirical formulas and multivariate regression analyses to find the best prediction methods for predicting PPVs with numerous datasets of field blasting records from various sites.

2. Methodology

Figure 1 shows the process for this study, which consists of three steps; acquisition and pre-processing of blasting datasets, development of prediction models using three other methods, and testing and comparison of the prediction models.

2.1. Artificial Neural Network

An ANN is a prediction method based on causes and effects obtained through experience. It can be used as a tool for training, remembering, and analyzing using the computational power of a computer [15]. The network calculates non-linear and complex connections with an input layer, a hidden layer, and an output layer. Each layer has a node for calculation, and their weights and biases act as interlayer connections. The input and output layers consist of causal and result parameters, respectively. The training algorithm of the ANN used in this study was back-propagation, which is the most efficient ANN training algorithm available [16,17]. In back-propagation, the output values calculated in the forward direction through weights and biases are used to calculate training errors from the true values. Through these errors, weights and biases are corrected to minimize the errors in the reverse direction. These sequences repeat until the errors meet the convergence tolerance or other limit conditions. After the ANN model meets the conditions, it can be used as a prediction model with final weights and biases.

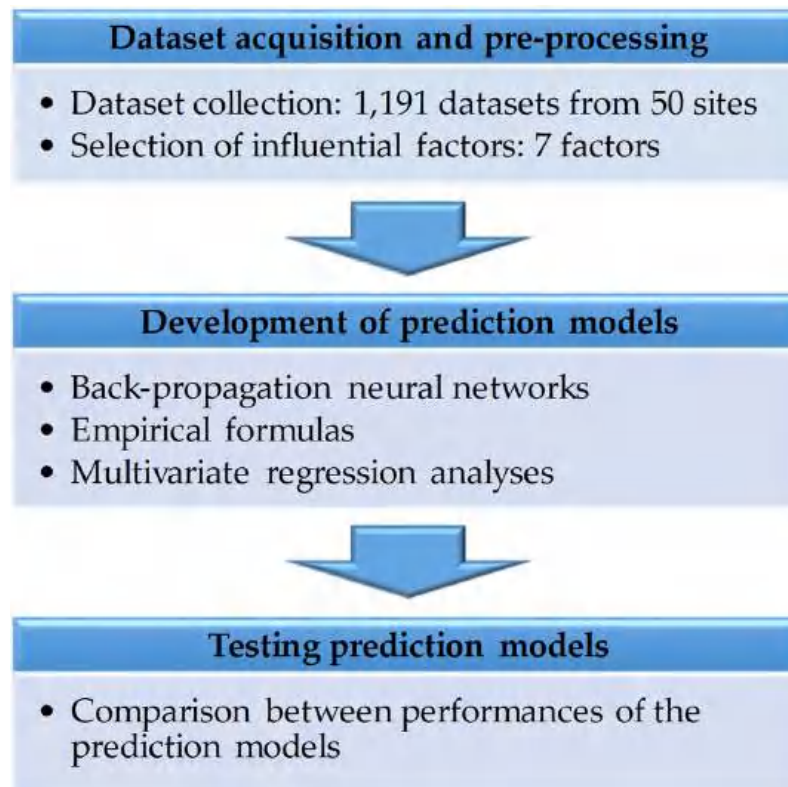


Figure 1. Three steps of the research process.

The ANN requires activation and normalization functions. The former converts the sum of the input signals into the output signal in the nodes of a hidden layer. A non-linear function should be used to determine a non-linear relationship between input and output parameters. Generally, sigmoid, hyperbolic tangent, and rectified linear unit (ReLU) functions, which are non-linear and represented by Equations (1)–(3), respectively, are used as an activation function.

$$f(x) = \frac{1}{1 + e^{-x}} \tag{1}$$

$$f(x) = \frac{e^x - e^{-x}}{e^x + e^{-x}} \tag{2}$$

$$f(x) = \begin{cases} 0, & x < 0 \\ x, & x \geq 0 \end{cases} \tag{3}$$

A normalization function converts all input values which have on different scales into a common scale. It is necessary because the degrees of influence on the output parameter can vary depending on the range of the input parameters. Usually, min-max scaling and standard scaling are used as a normalization function represented by Equations (4) and (5), respectively. In Equation (4), x_{Max} and x_{min} are the maximum and minimum values for each data type, respectively. In Equation (5), \bar{x} and S_x are the mean and standard deviation values for each data type, respectively.

$$N(x) = \frac{x - x_{min}}{x_{Max} - x_{min}} \tag{4}$$

$$N(x) = \frac{x - \bar{x}}{S_x} \tag{5}$$

2.2. Empirical Formula

As mentioned, various PPV prediction techniques are available but only the empirical formula of Equation (6) has been used to predict PPVs for blasting designs in South Korea [18]. Therefore, in this study, the empirical formula developed by USBM was selected to assess ground vibration and identify the optimal prediction method. In Equation (6), the values of K and m are obtained through linear regression of the blasting datasets consisting of PPV and the scaled distance (SD) expressed in Equation (7) [19]. Here, W is a charge weight per delay, and D is the distance between blasting and monitoring points.

$$\text{PPV} = K(\text{SD})^m \quad (6)$$

$$\text{SD} = D/\sqrt{W} \quad (7)$$

2.3. Multivariate Regression Analysis

Multivariate regression analysis is defined as a regression analysis in which two or more independent variables are used to account for changes in the dependent variable [20]. It is called multivariate linear regression analysis (MLRA) and the relationships between the independent and the dependent variables are expressed linearly. The MLRA is expressed as follows:

$$y = \beta_0 + \beta_1 x_1 + \dots + \beta_p x_p \quad (8)$$

In Equation (8), y is the dependent variable, x_1 to x_p are the independent variables, β_0 to β_p are regression coefficients, and p is the number of independent variables. The regression coefficients, which make the summation of all square errors minimum, are obtained through the method of least squares.

We defined expressing non-linearly the relationships between independent and dependent variables as multivariate non-linear regression analysis (MnLRA). Among the various forms of MnLRA, an exponential form was employed in this study and it is expressed as follows:

$$y = \beta_0 (x_1)^{\beta_1} (x_2)^{\beta_2} \dots (x_p)^{\beta_p} \quad (9)$$

After both sides of Equation (9) are logged, it is equivalent to the same form as Equation (8), so MnLRA can be generated in the same way. Besides, since the empirical formula of Equation (6) is also in exponential form, MnLRA was chosen as the exponential form in this study. It is important to confirm that the model is statistically significant through F and p -values of the results of an analysis of variance (ANOVA) and p -value of a partial regression coefficient in the multivariate regression analysis.

3. Datasets

The authors collected 1191 blasting datasets, which are more than six times the datasets used in the previous studies, from 50 diverse construction sites, representing each region of South Korea. The locations of 50 diverse construction sites by 28 administrative districts are depicted in Figure 2. The number of construction sites that were conducted in the same administrative district is expressed in the circle. Even though the construction sites are located in the same administrative district, they are different construction sites. Building and road construction were the main site activities, and open-pit blasting was used at all 50 construction sites. Of the total 1191 datasets, 714 (60%) and 179 (15%) were used for prediction model development as training and validation datasets, respectively. The remaining 298 (25%) were used to test the models. The datasets were randomly designated for Training, Validation, and Testing via PYTHON code.

Predicting PPV requires a selection of influential factors. Since this study aims to predict the PPV accurately and easily at any open-pit blasting site, the influential factors should not only affect the PPV but also be easily obtained by untrained field staff.

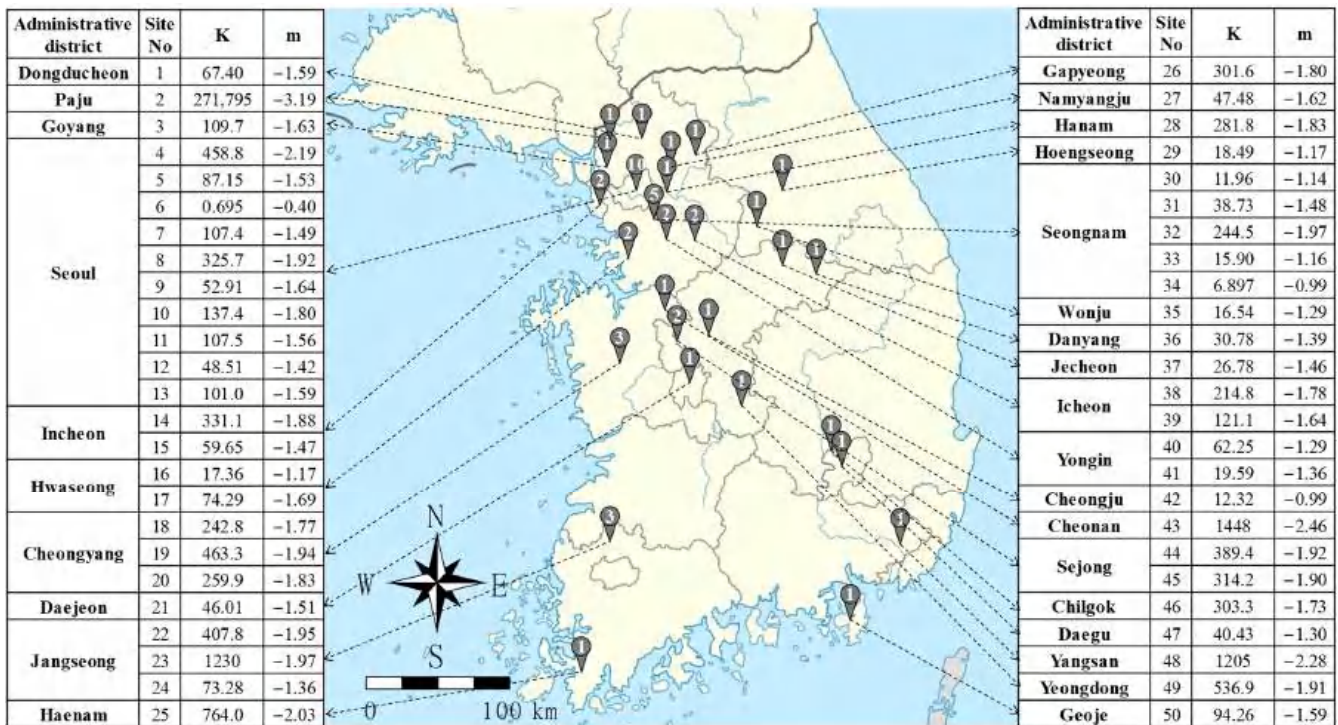


Figure 2. Locations of 50 diverse construction sites by administrative district.

Eleven common initial influential factors satisfied these conditions from 1191 blasting datasets: type of explosive (TE), charge weight per delay (W), specific weight (SW), length of drilling hole (LH), the height of the bench (HB), burden spacing (BS), hole spacing (HS), type of rock (TR), the distance between blasting and monitoring points (D), site factor K, and site factor m. To use an influential factor as quantitative data, the TE and the TR must be converted to values that express the velocity of detonation (VoD) and the velocity of the P-wave (VoP). The explosive types used at the 50 sites were Megamex, New emulate, Newmite, and Lovex manufactured by Hanwha Corporation [21]. The eight types of rock were gneiss, granite, limestone, schist, shale, andesite, rhyolite, and tuff. The conversion values are summarized in Tables 1 and 2.

It is necessary to remove or change the initial influential factors to avoid multicollinearity that negatively affects prediction due to the high correlations between independent variables [22]. As shown in Figure 3, factors W, LH, HB, BS and HS are strongly correlated (>0.88) with each other. To remove a strong correlation between influential factors, we removed the LH, HB, BS and HS since W is the most important factor to PPV among the five factors. Finally, we selected seven influential factors relevant to PPV. The units and ranges of the selected factors and PPV are shown in Table 3.

Table 1. Input values for types of explosive.

Explosive Type	Megamex	New Emulite	NewMITE	LoVEX
Velocity of Detonation (m/s)	6000	5900	5700	3400

Table 2. Input values for types of rock.

Rock Type	P-Wave Velocity (m/s)	Reference
Gneiss	5500	[23]
Granite	5300	[23]
Limestone	5470	[23]
Schist	4550	[23]

Table 2. Cont.

Rock Type	P-Wave Velocity (m/s)	Reference
Shale	3500	[23]
Andesite	5121	[24]
Rhyolite	4100	[25]
Tuff	2750	[26]

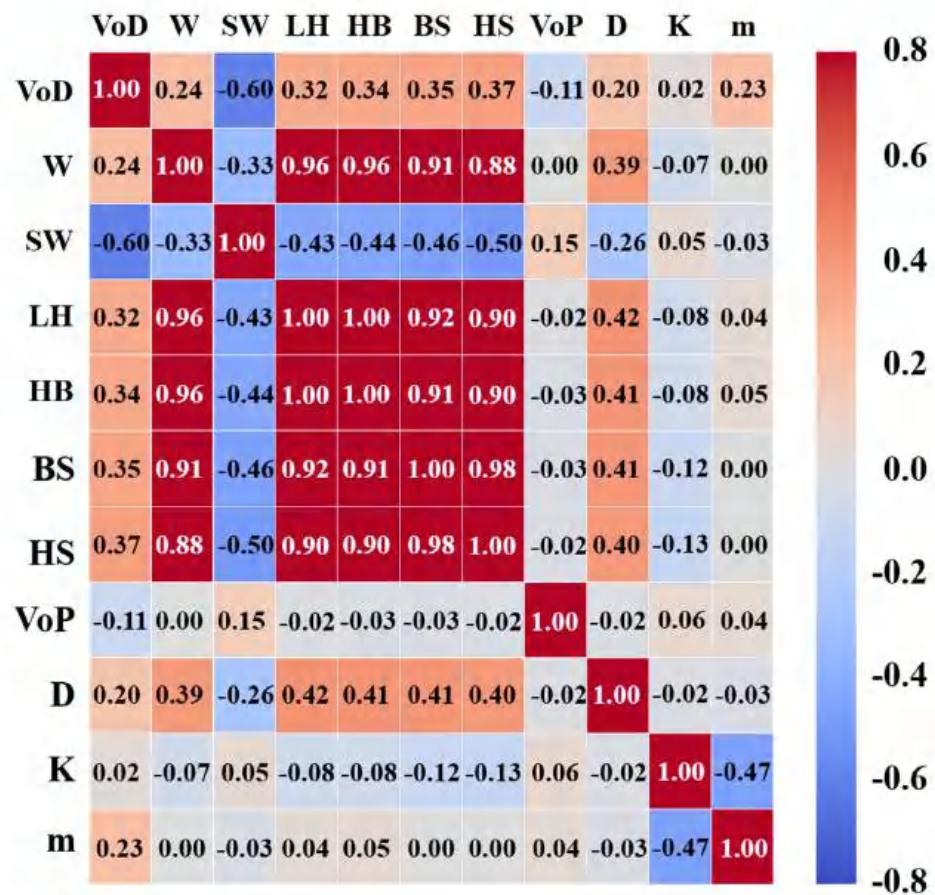


Figure 3. Correlations between initial influential factors.

Table 3. Characteristics of influential factors and peak particle velocity (PPV).

Type	Parameters	Symbol	Unit	Range of Datasets
Input	Velocity of detonation	VoD	m/s	3400–6000
	Charge weight per delay	W	kg	0.1–10
	Specific weight	SW	kg/m ³	0.25–0.56
	Velocity of P-wave	VoP	m/s	2750–5500
	Distance between blasting and monitoring points	D	m	5–650
Output	K	K	-	0.7–271,795
	m	m	-	−3.19 to −0.40
	Peak Particle Velocity		cm/s	0.005–6.514

4. Prediction Models

4.1. Artificial Neural Network

Trial-and-error analysis of hyper-parameters is required to obtain the optimal prediction model which has the lowest validation loss. In this analysis, it was carried out with a different number of hidden layers, nodes, normalization methods, and activation

functions; one and two hidden layers; 3, 5, 7, 11, 14, 15, 21, 28 and 35 nodes for the hidden layer; min-max and standard scalings; and three activation functions, sigmoid, hyperbolic tangent, and ReLU. In other words, 54 ($2 \times 9 \times 3$) and 486 ($2 \times 9 \times 9 \times 3$) structures were assessed on 1 and 2 hidden layers, respectively. The number of nodes was determined by Table 4. Here, N_i and N_o mean number of input and output parameters, respectively. We added some equations in the final row of Table 4 to analyze many structures. The Adam optimizer [27] was used to reduce the loss with a learning rate of 0.001. Also, we used an early stopping to avoid overfitting and to obtain the best-fitted model. Every structure of the ANN model was trained with the 714 training datasets and validated by the 179 validation datasets. Every ANN model was developed with the software PYTHON Version 3.7.6.

Table 4. Equations for determination of the number of nodes.

Equation	Number of Nodes	Reference
$\sqrt{N_i \times N_o}$	3	[28]
$(4N_i^2 + 3) / (N_i^2 - 8)$	5	[29]
$3N_i / 2$	11	[30]
$2N_i + 1$	15	[31]
$3N_i$	21	[32]
$N_i, 2N_i, 4N_i, 5N_i$	7, 14, 28, 35	-

In the results of trial-and-error analysis, the average validation loss of 540 structures was 0.126 cm/s. Among the 540 ANN models, the structure composed of two hidden layers with 21 and 28 nodes, normalized by min-max scaling and combined with ReLU showed the lowest validation loss of 0.115 cm/s. Therefore, we selected the ANN model, which has the 7-21-28-1 structure depicted in Figure 4 as an optimal ANN model for a PPV prediction. The training of this model was stopped at 4208 epochs by early stopping. Table 5 summarizes the characteristics of the selected ANN model. This model is represented by Equations (10)–(12). PPV is calculated by Equation (10). Equations (11) and (12) represent hidden layers 1 and 2, respectively.

$$PPV = [H_2] \cdot [W_3] + [b_3] \tag{10}$$

$$[H_2] = R([H_1] \cdot [W_2] + [b_2]) \tag{11}$$

$$[H_1] = R([m[I]] \cdot [W_1] + [b_1]) \tag{12}$$

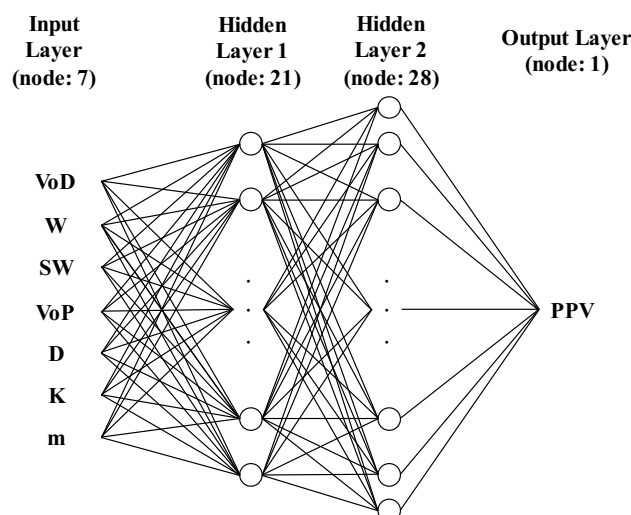


Figure 4. Structure of the artificial neural network (ANN) model developed.

Table 5. Characteristics of the ANN model.

	Characteristics	Details
Datasets	Total datasets	1191
	Training and validation datasets	714, 179
	Test datasets	298
Structure	Number of input parameters	7
	Number of output parameter	1
	Number of hidden layers	2
	Number of nodes	21, 28
Training parameters	Activation function	ReLU
	Optimization	Adam
	Normalization	Standard scaling
	Regularization	Early-stopping
	Number of epochs	4208
	Training algorithm	Back-propagation

In these equations, [I] is the matrix of input data sets, [W] is the matrix of weights, and [b] is the matrix of biases. The weight and bias matrices are constants that were obtained from the ANN training. Here, [W₁], [W₂], [W₃], [b₁], [b₂], and [b₃] are 7 × 21, 21 × 28, 28 × 1, 1 × 21, 1 × 28, and 1 × 1 matrices. When predicting *i* PPVs, [I] is an *i* × 7 matrix. R is a ReLU function expressed by Equation (3), m is a min-max scaling expressed by Equation (4).

4.2. Empirical Formula

Each empirical formula of the 50 construction sites was generated using Equation (6) with the site factors, K and m. For instance, Equation (13) represents the empirical formula of Site 1 with K and m values of 67.4 and −1.59, respectively. The site factors of each site are represented in Figure 2. Through this method, 50 empirical formulas were generated and defined as EF-1. Each of the formulas included in EF-1 can only be applied to the PPV prediction at the site where it was generated. The K of Site 2, which is far higher than the rest, seems to be noise. In geotechnical engineering, some noise could have happened due to uncertainties. Thus, datasets obtained from Site 2 should also be analyzed with other datasets.

$$V = 67.4(SD)^{-1.59} \quad (13)$$

Test blasting is required to obtain site factors K and m, used in empirical formulas such as EF-1. However, it is difficult to perform test blastings at the preliminary design stage, and representative values of K and m are needed to compensate for this weakness. Representative K and m values of 200 and −1.6 were proposed based on Design and Construction Guidelines for Open-pit blasting in Road construction published by the Ministry of Land, Infrastructure, and Transport in South Korea [33]. We defined Equation (14) as EF-2 using the K and m. Many engineers have designed preliminary blasting patterns, applying Equation (14).

$$PPV = 200(SD)^{-1.6} \quad (14)$$

To derive one representative empirical formula for the 50 sites, we calculated K and m values of 74.9 and −1.535 using datasets of 50 open-pit blasting construction sites. Equation (15) expresses the representative empirical formula and it was defined as EF-3. Since this is a representative equation of 50 sites, it will show lower prediction accuracy than EF-1. However, it could be used at the preliminary design stage like EF-2. Figure 5 shows EF-3 (solid line) and the 893 datasets (circles) on a log-log plot where the vertical axis is PPV and the horizontal axis is SD. As mentioned in Section 2.2, EF-3 was obtained from the linear regression of the 893 blasting datasets.

$$PPV = 74.9(SD)^{-1.535} \quad (15)$$

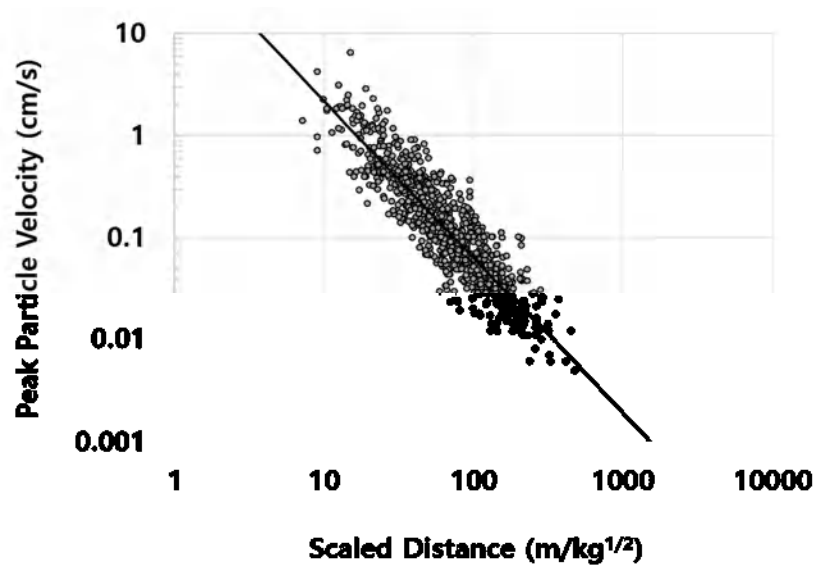


Figure 5. Peak particle velocity versus scaled distance for 893 datasets.

Equations (16) and (17) are prediction models proposed by the International Society of Explosives Engineers (ISEE) [34] and USBM [35], respectively. These two equations have been widely used to predict PPVs. We defined Equations (16) and (17) as the ISEE model and USBM model, respectively.

$$PPV = 172.5(SD)^{-1.6} \tag{16}$$

$$PPV = 71.4(SD)^{-1.6} \tag{17}$$

4.3. Multivariable Regression Analysis

Multivariable regression analyses were carried out using IBM SPSS Statistics Version 26.0 (SPSS), which is a powerful statistical software package [36] that generates a simple equation for estimating output. Many researchers have performed multivariable regression analyses with ANN to compare the performance of prediction methods [15,16,37]. In this study, two types of multivariable regression analysis were carried out using training and validation datasets from 50 open-pit blasting construction sites to identify linear or non-linear relationships between influential factors and PPV. One was multivariable linear regression analysis (MLRA) and the other was multivariable non-linear regression analysis (MnLRA). The developed MLRA is represented by Equation (18). From seven influential factors, SW and VoP were excluded, since their partial regression coefficients had higher *p*-values than the significant level, 0.05. After the two factors were removed, the F and *p*-values of the MLRA model showed approximately 49 and 0, respectively. In addition, constant and five influential factors had *p*-values that were near 0. These F and *p*-values mean that the MLRA model is statistically significant. However, this model showed a low R of 0.495. The developed MnLRA is represented by Equation (19). This equation has been developed in exponential form following the form of the conventional empirical formula. *p*-values of all partial regression coefficients except for VoP were shown to be lower than the significant level, 0.05. Therefore, we removed the VoP from the input parameters. F and *p*-values of the MnLRA model showed approximately 898 and 0, respectively. Besides, the R of this model was high, 0.927. Here, the influential factor *m* was converted to $-m$ in Equation (19) because all influencing factors and PPV are positive, while *m* is negative.

$$PPV = -0.588 + 1.2 \times 10^{-4}VoD + 0.092W - 0.003D - 1.45 \times 10^{-6}K - 0.193m \tag{18}$$

$$PPV = 0.034VoD^{0.79}W^{0.741} SW^{-0.37}D^{-1.602}K^{0.375} (-m)^{-2.248} \tag{19}$$

Note that test datasets were never used prior to the performance evaluation of the prediction methods. This means only the training and validation datasets were used to develop the ANN model, EF-1, 2 (K and m), MLRA, and MnLRA.

5. Prediction Results

5.1. Performance Comparisons of the Six Prediction Models

The 298 test datasets, which account for 25% of the total datasets obtained, were predicted using the eight predictive analysis methods, ANN, EF-1, EF-2, EF-3, ISEE model, USBM model, MLRA, and MnLRA, described in Chapter 4. First, the PPVs were predicted using the weights and biases matrices of the optimal ANN model. Here, all seven influential factors, VoD, W, SW, VoP, D, K, m were used as input parameters. Second, we used EF-1 which grouped 50 empirical formulas to predict PPVs of the test datasets. Here, each test dataset was predicted by the empirical formula of the site where they were obtained. W and D were used as input parameters. Finally, the test datasets were predicted by EF-2, 3, ISEE model, USBM model, MLRA, and MnLRA expressed as Equations (14)–(19), respectively, using input parameters of each method. In this study, three performance indicators, mean absolute error (MAE), root mean square error (RMSE), and mean absolute percent error (MAPE), were used to analyze prediction results. These performance indicators are listed in Table 6.

Table 6. Equations of performance indicators.

Performance Indicator	Equation
MAE	$MAE = \frac{1}{n} \sum_i^n V_{mi} - V_{pi} $
RMSE	$RMSE = \sqrt{\frac{1}{n} \sum_i^n (V_{mi} - V_{pi})^2}$
MAPE	$MAPE = \frac{1}{n} \sum_i^n \left \frac{V_m - V_p}{V_m} \right \times 100$

Here, V_{mi} and V_{pi} are the i -th measured and predicted values, respectively, and n is the total number of test datasets. Table 7 summarizes the performances of the eight prediction models on the predicted PPVs. The developed ANN model achieved the lowest MAE of 0.064 cm/s, RMSE of 0.161 cm/s, and MAPE of 23.2%. These results were approximately 30%, 56%, and 11% lower than those from EF-1, which is currently the most commonly used method to predict PPVs when designing blasting patterns for construction. However, the EF-2 deduced the highest MAE of 0.305 cm/s and RMSE of 0.731 cm/s.

Table 7. Performances of the six prediction models.

Method	MAE (cm/s)	RMSE (cm/s)	MAPE (%)
ANN	0.064	0.161	23.2
EF-1	0.092	0.370	26.1
EF-2	0.305	0.731	146.5
EF-3	0.123	0.309	47.8
ISEE model	0.244	0.601	115.7
USBM model	0.123	0.308	40.7
MLRA	0.202	0.370	175.1
MnLRA	0.108	0.298	39.1

Linear regression analyses were performed with a coefficient of determination known as R^2 to explain the correlation and similarity between the predicted PPVs from the six predictive analysis methods and measured PPVs of the test datasets. The value of R^2 can

be found using Equation (20), where V_m and V_p are measured and predicted PPV values, Cov is the covariation between two factors, and Var is the variation of a factor.

$$R^2 = \frac{\text{Cov}^2(V_m, V_p)}{\text{Var}(V_m) \times \text{Var}(V_p)} \quad (20)$$

Each predicted PPV by the six prediction methods is plotted as a small circle in Figure 6a to 6h respectively according to prediction methods. The x and y axes represent the measured and predicted PPV, respectively, in cm/s. There are two lines in each figure. The dashed line is the Measured PPV = Predicted PPV (1:1) line and the solid line is the linear regression line. In the lower right corner of each figure, it shows the equation of the linear regression line and R^2 . The linear regression line resulting from the ANN shows the best result in terms of similarity to the 1:1 line as shown in Figure 6. The linear regression line resulting from the MLRA displays the greatest distance between the two lines.

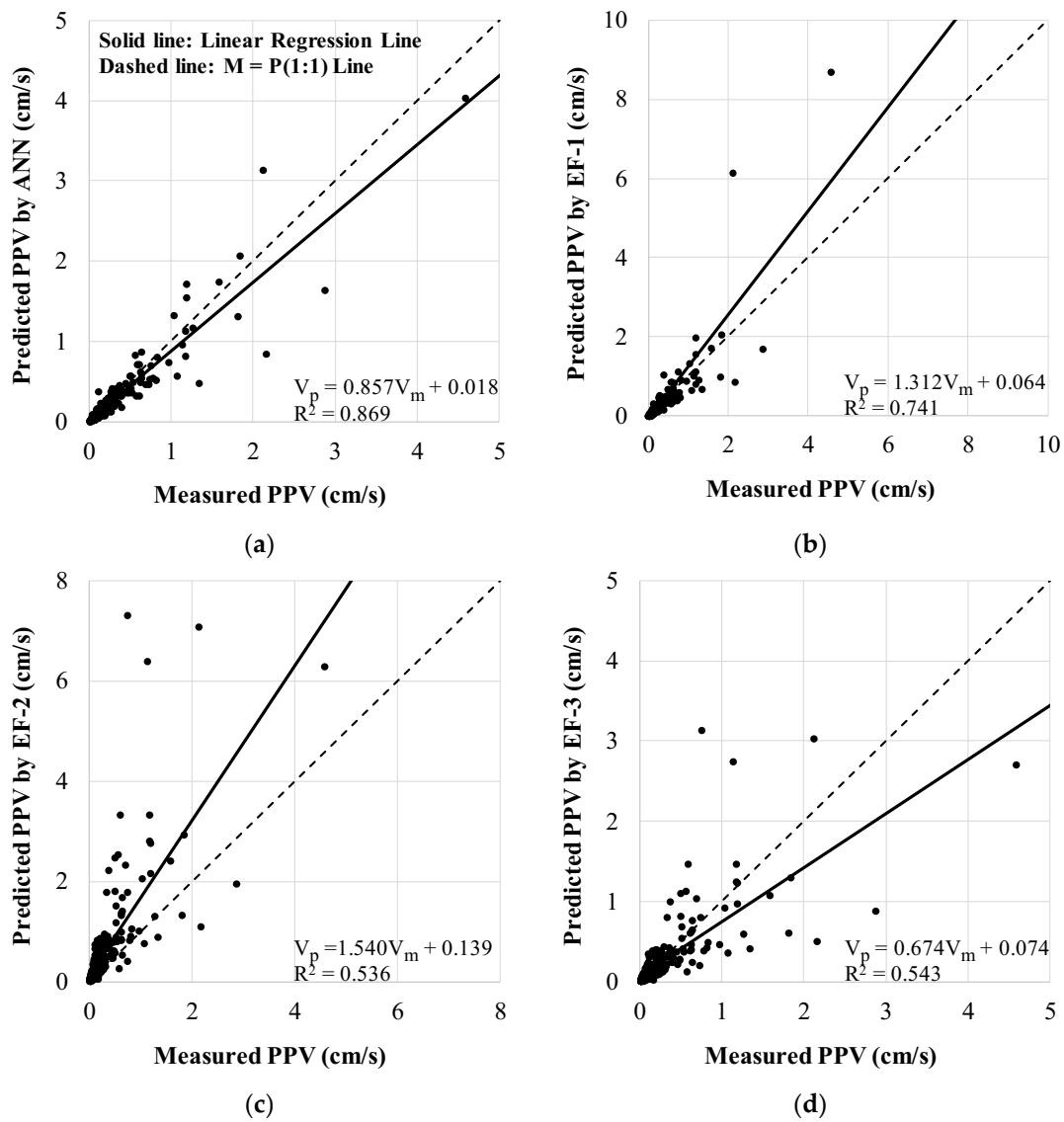


Figure 6. Cont.

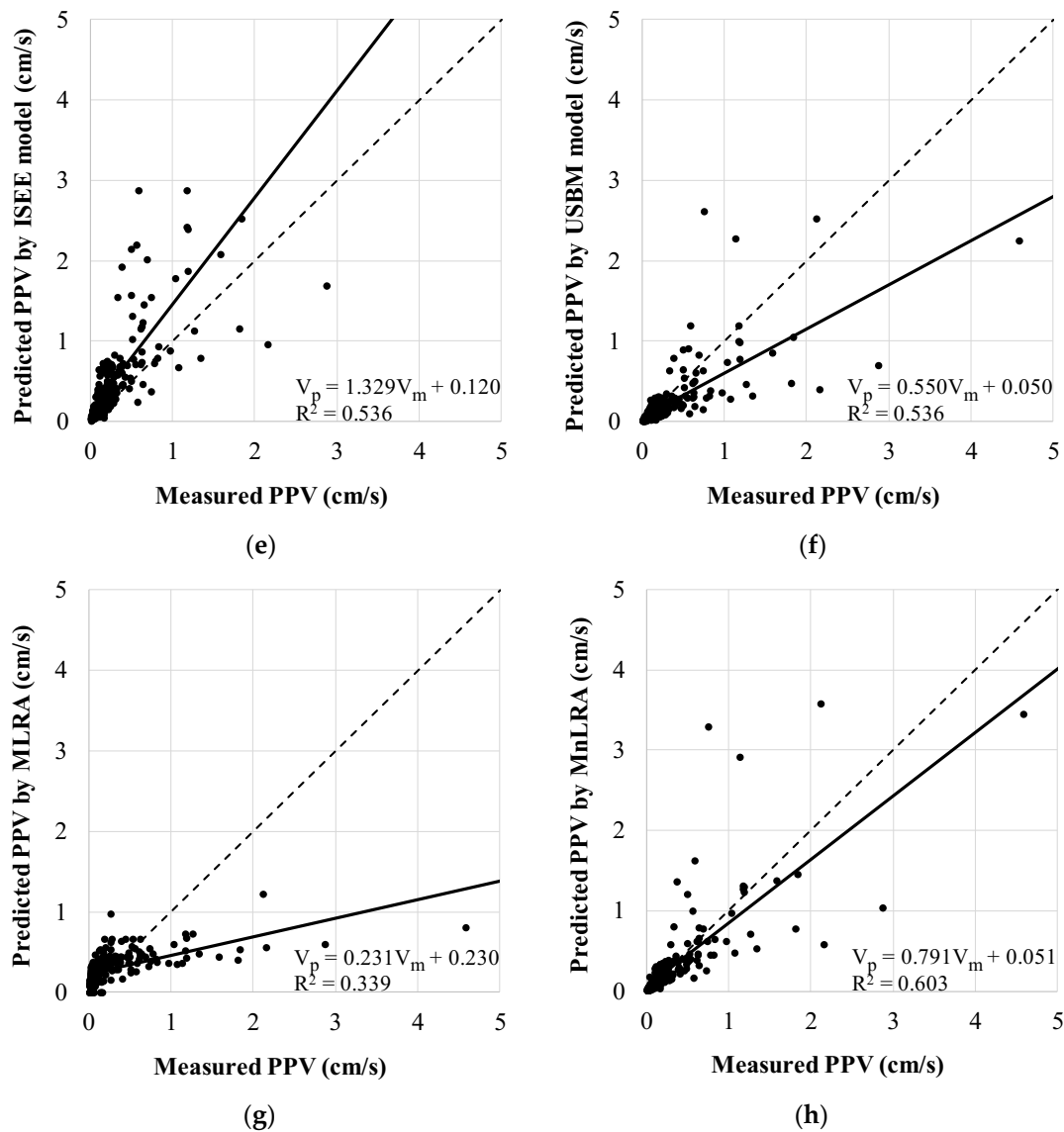


Figure 6. Predicted PPV versus measured PPV by the six prediction methods. The graphs in (a–h) were made using predicted PPVs by the ANN, EF-1, EF-2, EF-3, ISEE model, USBM model, MLRA, and MnLRA, respectively.

5.2. Sensitivity Analysis

A sensitivity analysis was performed using the cosine amplitude method for all seven influential factors. This method has been applied previously [4,15,38] to determine the relative significance of each factor on PPV. It calculates a relation, r_{ij} , and provides results from a pairwise comparison of two factors, x_i and x_j , using Equation (21) [39].

$$r_{ij} = \frac{\left| \sum_{k=1}^m x_{ik}x_{jk} \right|}{\sqrt{\left(\sum_{k=1}^m x_{ik}^2 \right) \left(\sum_{k=1}^m x_{jk}^2 \right)}} \quad (21)$$

The influential factors and PPV of the 1191 datasets, which consist of both training and test datasets, were logged and analyzed using Equation (21). The relative significances of the seven influential factors are depicted in Figure 7. The relative significances between VoD, W, SW, VoP, D, K, m, and PPV were deduced to be approximately 0.885, 0.729, 0.876, 0.886, 0.932, 0.844, and 0.833, respectively.

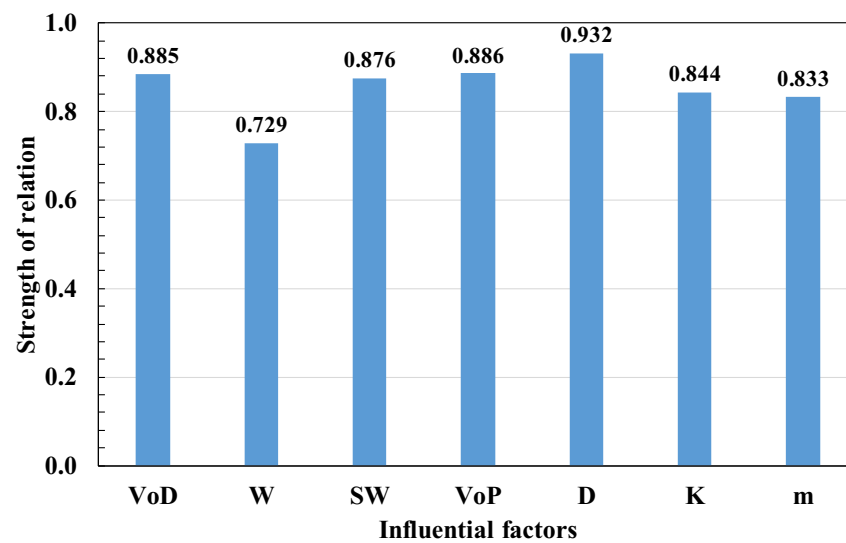


Figure 7. Sensitivity analysis of the influential factors.

6. Discussion

The ANN model showed the best agreement with measured PPVs among eight prediction methods, including the globally used ISEE and USBM models. It would be due to using the most influential factors, which has the ability to reproduce and model the non-linear connections between input and output parameters, and to deal with noise. As shown in Figure 7, the seven influential factors have similar strengths of relation. It indicates that using these seven factors is more effective than using the only four factors which are included in the conventional empirical formula to predict PPVs. The complex connections between PPV and influential factors could be found in the comparison between the MLRA and MnLRA. When we developed these two models, they showed a statistical significance; however, the MLRA had a low R (0.495) while the MnLRA had a high R (0.927). The MAE from the MLRA showed about twice that of the MnLRA. These two models differ in their use of linear and non-linear relationships to explain PPV from influencing factors. Because of this difference, the MnLRA showed better predictive performance than the MLRA. It means that the relationships between the influential factors and PPV are non-linear. The ability to deal with noise could be verified by the prediction results about the biggest measured PPV, 4.58 cm/s, which is over 17 times the average measured PPVs, 0.26 cm/s. The prediction results from the ANN, EF-1, EF-2, EF-3, ISEE model, USBM model, MLRA, and MnLRA were 4.04, 8.7, 6.3, 2.72, 5.43, 2.25, 0.81 and 3.45 cm/s, respectively. The prediction results from the ANN model showed the closest to the measured PPV. It implies that the ANN has an excellent ability to deal with noise.

EF-2 showed the worst performances at MAE and RMSE and it would be due to its applicability. EF-2 is suitable for road construction sites because it was developed using only blasting datasets from road construction sites. These results mean that applying the conventional representative formula for a preliminary blasting design from road constructions has a limitation in applying it to other open-pit blastings. Therefore, a new alternative prediction equation is required. EF-3 which was developed using datasets from 50 diverse open-pit blasting construction sites would be suitable as the alternative prediction equation since it has the same form as EF-2, and it showed better predictive performances than EF-2.

The proposed model has been applied only to open-pit blasting construction sites. Future studies of PPV prediction models such as ANN model and EF-3 will include blasting records from underground caverns, tunnels, and mines as well to ensure the prediction models be generally applicable to any region and type of blasting.

7. Conclusions

In this study, the prediction of PPV using eight predictive analysis methods of ANN, EF-1, EF-2, EF-3, ISEE model, USBM models, MLRA, and MnLRA with 1191 datasets, which are more than six times the maximum datasets used in the previous studies, was carried out to assess PPV prediction methods at an open-pit construction site.

Seven key factors relevant to PPV were considered in the prediction models. The seven key factors were selected according to the ease of obtaining them and their influence on PPV. They consist of three factors, VoD, SW, and VoP, newly proposed in this study, and four key factors, W, D, and the site factors K and m, currently included in the conventional empirical formula. The use of three additional influential factors played a significant role in identifying the prediction model that produced the lowest error. Their significant roles were confirmed through a comparison of the performances of the ANN and others. These roles were also apparent in the results of the sensitivity analysis. The seven key factors have similar strengths of relations with PPV. It implies that not only are the previously used factors important in predicting PPV but also the newly added factors.

The PPV prediction based on the ANN model achieved the lowest values at MAE, RMSE, and MAPE among the eight prediction models. Even the ANN, which was generalized for application to all sites, produced lower errors than those from the EF-1, which can apply to only a specific site. In addition, the prediction accuracy of the ANN model was higher than that of the ISEE and USBM models. It would be attributed to the ability of ANN to express complex and non-linear relationships between influential factors and PPV, and the ability of ANN to deal with noise. It is necessary to perform a grid search for structures and hyper-parameters and early stopping to obtain an optimal prediction model. In this study, we compared 540 ANN models, to which were applied the early stopping method. These models have one or two hidden layers with the number of nodes calculated using the number of input and output parameters and three activation functions. Finally, a structure consisting of two hidden layers with 21 and 28 nodes using a ReLU as an activation function was determined as the optimal model. Other hyper-parameters were chosen following the previous studies. As a result, we generated the prediction model showing the lowest errors among the six prediction methods. Therefore, we recommend using an ANN for predicting PPVs whose hyper-parameters are selected from a grid search and literature research.

The EF-2 was proposed by the Ministry of Land, Infrastructure, and Transport in South Korea for designing preliminary blasting patterns. However, the MAE, RMSE, and MAPE associated with the EF-2 were over two times higher than those associated with the EF-3, which is newly proposed in this study. This difference might be a result of different construction types in the datasets. EF-3 was developed by analyzing data from 50 open-pit construction sites, including building construction sites in downtowns, road construction sites, aggregate extraction sites, and restoration work sites while EF-2 was developed by analyzing only datasets at road construction sites. Using the newly proposed EF-3, which proposes a K value of 74.9 and an m value of -1.535 , for a preliminary design of open-pit blasting would be more accurate and reliable than using the EF-2.

The ANN model with the seven key factors and EF-3, proposed in this paper, can predict PPVs more accurately and will help blasting pattern design to be more reliable. The reliable blasting patterns will reduce environmental problems significantly and maximize the efficiency of blasting in construction. Moreover, the use of the newly proposed prediction methods will lessen civil complaints, and improve the efficiency in the construction schedule, and reduce the overall construction budgets. These advantages will lead to greater safety and sustainable urban development.

Author Contributions: Data curation, Y.-H.C.; Formal analysis, Y.-H.C.; Investigation, Y.-H.C.; Methodology, Y.-H.C.; Project administration, Y.-H.C.; Validation, Y.-H.C.; Writing—original draft preparation, Y.-H.C.; Conceptualization, S.S.L.; Funding acquisition, S.S.L.; Project administration, S.S.L.; Supervision, S.S.L.; Writing—review & editing, S.S.L. All authors have read and agreed to the published version of the manuscript.

Funding: This work is supported by the Korea Agency for Infrastructure Technology Advancement (KAIA) grant funded by the Ministry of Land, Infrastructure and Transport (Grant 21UUTI-B157786-02).

Institutional Review Board Statement: Not applicable.

Informed Consent Statement: Not applicable.

Data Availability Statement: Not applicable.

Acknowledgments: This work was supported by the Korea Agency for Infrastructure Technology Advancement (KAIA) grant funded by the Ministry of Land, Infrastructure and Transport (Grant 21UUTI-B157786-02) and by the National Research Foundation of Korea (NRF) grant funded by the Korea government (MSIT) (NRF-2020R1A6A3A13077513).

Conflicts of Interest: The authors declare no conflict of interest. The funders had no role in the design of the study; the collection, analyses, or interpretation of data; the writing of the manuscript; or the decision to publish the results.

References

- National Environmental Dispute Resolution Commission. Statistical Data, Such as Handling Environmental Disputes (31 December 2020). Available online: <https://ecc.me.go.kr/front/user/main.do> (accessed on 15 February 2021).
- German Standards Organization. *DIN 4150-3: Structural Vibration—Part 3: Effects of Vibration on Structures*; Deutsches Institut für Normung e.V.: Berlin, Germany, 1999.
- Siskind, D.E.; Stagg, M.S.; Kopp, J.W.; Dowding, C.H. *Structure Response and Damage Produced by Ground Vibration from Surface Mine Blasting*; US Department of the Interior, Bureau of Mines: New York, NY, USA, 1980.
- Hajihassani, M.; Armaghani, D.J.; Monjezi, M.; Mohamad, E.T.; Marto, A. Blast-induced air and ground vibration prediction: A particle swarm optimization-based artificial neural network approach. *Environ. Earth Sci.* **2015**, *74*, 2799–2817. [CrossRef]
- Duvall, W.I.; Petkof, B. *Spherical Propagation of Explosion-Generated Strain Pulses in Rock*; US Department of the Interior, Bureau of Mines: New York, NY, USA, 1959.
- Liu, Q.; Li, N.; Duan, J.; Yan, W. The Evaluation of the Corrosion Rates of Alloys Applied to the Heating Tower Heat Pump (HTHP) by Machine Learning. *Energies* **2021**, *14*, 1972. [CrossRef]
- Perera, A.; Azamathulla, H.; Rathnayake, U. Comparison of different Artificial Neural Network (ANN) training algorithms to predict atmospheric temperature in Tabuk, Saudi Arabia. *Mausam* **2020**, *71*, 551–560.
- Ahmadi, M.; Naderpour, H.; Kheyroddin, A. ANN Model for Predicting the Compressive Strength of Circular Steel-Confining Concrete. *Int. J. Civ. Eng.* **2016**, *15*, 213–221. [CrossRef]
- Kim, M.-S.; Lee, J.-K.; Choi, Y.-H.; Kim, S.-H.; Jeong, K.-W.; Kim, K.-L.; Lee, S.S. A Study on the Optimal Setting of Large Uncharged Hole Boring Machine for Reducing Blast-induced Vibration using Deep Learning. *Explos. Blasting* **2020**, *38*, 16–25.
- Nguyen, H.; Drebenstedt, C.; Bui, X.-N.; Bui, D.T. Prediction of Blast-Induced Ground Vibration in an Open-Pit Mine by a Novel Hybrid Model Based on Clustering and Artificial Neural Network. *Nat. Resour. Res.* **2019**, *29*, 691–709. [CrossRef]
- Azimi, Y.; Khoshrou, S.H.; Osanloo, M. Prediction of blast induced ground vibration (BIGV) of quarry mining using hybrid genetic algorithm optimized artificial neural network. *Measurement* **2019**, *147*, 106874. [CrossRef]
- Bui, X.-N.; Choi, Y.; Atrushkevich, V.; Nguyen, H.; Tran, Q.-H.; Long, N.Q.; Hoang, H.-T. Prediction of Blast-Induced Ground Vibration Intensity in Open-Pit Mines Using Unmanned Aerial Vehicle and a Novel Intelligence System. *Nat. Resour. Res.* **2019**, *29*, 771–790. [CrossRef]
- Tufféry, S. *Data Mining and Statistics for Decision Making*; John Wiley & Sons: Chichester, UK, 2011.
- Singh, A.; Thakur, N.; Sharma, A. A review of supervised machine learning algorithms. In Proceedings of the 2016 3rd International Conference on Computing for Sustainable Global Development (INDIACom), New Delhi, India, 16–18 March 2016; pp. 1310–1315.
- Khandelwal, M.; Singh, T. Prediction of blast-induced ground vibration using artificial neural network. *Int. J. Rock Mech. Min. Sci.* **2009**, *46*, 1214–1222. [CrossRef]
- Monjezi, M.; Ghafurikalajahi, M.; Bahrami, A. Prediction of blast-induced ground vibration using artificial neural networks. *Tunn. Undergr. Space Technol.* **2011**, *26*, 46–50. [CrossRef]
- Kim, Y.; Lee, S.S. Application of Artificial Neural Networks in Assessing Mining Subsidence Risk. *Appl. Sci.* **2020**, *10*, 1302. [CrossRef]
- Lee, C.-W.; Park, S.-Y. Prediction of Blasting-induced Vibration at Sintanjin Area, Daejeon using Borehole Test Blasting. *J. Korean Soc. Agric. Eng.* **2018**, *60*, 55–62.
- Morhard, R.C. *Explosives and Rock Blasting*; Atlas Powder Company: Wilmington, DE, USA, 1987.
- Suh, H.; Yang, K.; Kim, N.; Kim, H.; Kim, M. *SPSS (PASW) Regression Analysis*, 3rd ed.; Hannarae: Seoul, Korea, 2009.
- Hanwha Corporation. *Hanwha Corporation Explosive Products Guide*; Hanwha Corporation: Seoul, Korea, 2017.
- Matignon, R. *Data Mining Using SAS Enterprise Miner*; John Wiley & Sons: Hoboken, NJ, USA, 2007; Volume 638.
- Barton, N. *Rock Quality, Seismic Velocity, Attenuation and Anisotropy*; Taylor and Francis Group: London, UK, 2006.

24. Fathollahy, M.; Uromeihy, A.; Riahi, M. Evaluation of P-wave velocity in different joint spacing. *Bollettino di Geofisica Teorica ed Applicata* **2017**, *58*, 157–168.
25. Mielke, P.; Bär, K.; Sass, I. Determining the relationship of thermal conductivity and compressional wave velocity of common rock types as a basis for reservoir characterization. *J. Appl. Geophys.* **2017**, *140*, 135–144. [CrossRef]
26. Vinciguerra, S.; Trovato, C.; Meredith, P.; Benson, P.; Troise, C.; De Natale, G. Understanding the Seismic Velocity Structure of Campi Flegrei Caldera (Italy): From the Laboratory to the Field Scale. *Pure Appl. Geophys. PAGEOPH* **2006**, *163*, 2205–2221. [CrossRef]
27. Kingma, D.P.; Ba, J. Adam: A method for stochastic optimization. *arXiv* **2014**, arXiv:1412.6980.
28. Kaastra, I.; Boyd, M. Designing a neural network for forecasting financial and economic time series. *Neurocomputing* **1996**, *10*, 215–236. [CrossRef]
29. Sheela, K.G.; Deepa, S.N. Review on Methods to Fix Number of Hidden Neurons in Neural Networks. *Math. Probl. Eng.* **2013**, *2013*, 1–11. [CrossRef]
30. Mamaqani, B.H.M.H. *Numerical Modeling of Ground Movements Associated with Trenchless Box Jacking Technique*; The University of Texas at Arlington: Arlington, TX, USA, 2014.
31. Hecht-Nielsen, R. Kolmogorov's mapping neural network existence theorem. In Proceedings of the International Conference on Neural Networks, San Diego, CA, USA, 21–24 July 1987; pp. 11–14.
32. Hush, D.R. Classification with neural networks: A performance analysis. In Proceedings of the IEEE 1989 International Conference on Systems Engineering, Fairborn, OH, USA, 24–26 August 1989; pp. 277–280.
33. The Ministry of Land, Infrastructure and Transport in Korea. Open-Pit Blasting Design and Construction Guideline for Road Construction. Available online: http://www.molit.go.kr/USR/BORD0201/m_34879/DTL.jsp?mode=view&idx=28896 (accessed on 23 February 2021).
34. Hopler, R.B. *ISEE Blasters' Handbook*; International Society of Explosives Engineers (ISEE): Cleveland, OH, USA, 1998.
35. Nicholls, H.R.; Johnson, C.F.; Duvall, W.I. *Blasting Vibration and Their Effects on Structures*; US Department of the Interior, Bureau of Mines: New York, NY, USA, 1971.
36. IBM SPSS Software. Available online: <https://www.ibm.com/analytics/spss-statistics-software> (accessed on 21 April 2021).
37. Khandelwal, M.; Singh, T. Prediction of blast induced ground vibrations and frequency in opencast mine: A neural network approach. *J. Sound Vib.* **2006**, *289*, 711–725. [CrossRef]
38. Monjezi, M.; Hasanipanah, M.; Khandelwal, M. Evaluation and prediction of blast-induced ground vibration at Shur River Dam, Iran, by artificial neural network. *Neural Comput. Appl.* **2012**, *22*, 1637–1643. [CrossRef]
39. Ross, T.J. *Fuzzy Logic with Engineering Applications*; John Wiley & Sons: Chichester, UK, 2004.

Article

Study on Rock Damage Mechanism for Lateral Blasting under High In Situ Stresses

Xiaofeng Huo ¹, Xiuzhi Shi ¹, Xianyang Qiu ^{1,*}, Hui Chen ², Jian Zhou ¹, Shian Zhang ¹ and Dijun Rao ¹

¹ School of Resources and Safety Engineering, Central South University, Yuelu District, Changsha 410083, China; huoxiaofeng@csu.edu.cn (X.H.); baopo@csu.edu.cn (X.S.); csujzhou@hotmail.com (J.Z.); zhangshian@csu.edu.cn (S.Z.); raodijun@csu.edu.cn (D.R.)

² School of Geological and Mining Engineering, Xinjiang University, Tianshan District, Urumqi 830000, China; chenhui@xju.edu.cn

* Correspondence: qiuxianyang_csu@163.com

Abstract: A 3D numerical model was presented to investigate the blast-induced damage characteristics of highly stressed rock mass. The RHT (Riedel, Hiermaier, and Thoma) model in LS-DYNA was used to simulate the blast-induced damage and its parameters were calibrated by a physical model test. Based on the calibrated numerical model, the influences of confining pressure and free surface span on the blast-induced damage characteristics were investigated. The results show that under uniaxial loading, the crater volume increases with confining pressure increases. The uniaxial static load can change the optimal burden and the critical embedding depth of charge. In stressed rock, the variation law of the crater shape affected by radial tensile fractures is opposite to that affected by reflected tensile fractures. Under the biaxial static load, the crater volume of the borehole placed on the side of the max static load is greater than the other side. The explosion crater can be improved by increasing the free surface span on the same side. Finally, it is suggested that the blasting efficiency can be improved by preferentially detonating the charge on the side of the max static load, and then the charge on the other side can be detonated with a wider free surface span.

Keywords: blast-induced damage; explosion crater; lateral blasting; in situ stress; lateral free surface

Citation: Huo, X.; Shi, X.; Qiu, X.; Chen, H.; Zhou, J.; Zhang, S.; Rao, D. Study on Rock Damage Mechanism for Lateral Blasting under High In Situ Stresses. *Appl. Sci.* **2021**, *11*, 4992. <https://doi.org/10.3390/app11114992>

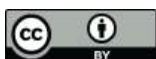
Academic Editor: Ricardo Castedo

Received: 11 May 2021

Accepted: 24 May 2021

Published: 28 May 2021

Publisher's Note: MDPI stays neutral with regard to jurisdictional claims in published maps and institutional affiliations.



Copyright: © 2021 by the authors. Licensee MDPI, Basel, Switzerland. This article is an open access article distributed under the terms and conditions of the Creative Commons Attribution (CC BY) license (<https://creativecommons.org/licenses/by/4.0/>).

1. Introduction

With the increase of excavation depth, the in situ stress increases gradually and plays an increasingly important role in the rock breaking by blasting. Due to the existence of in situ stress, blast-induced damage characteristics are different from those in surface and shallow sub-surface rock blasting, especially considering the role of lateral free surface in production blasting. In order to determine the parameters of borehole layout and blasting parameters in highly stressed rock mass as well as for safe and efficient production, it is necessary to investigate the blast-induced damage characteristics in the static-dynamic stress field.

A lot of studies have been done in the area of rock breaking due to blasting considering the effect of in situ stress. Kutter et al. [1] analytically and experimentally investigated the influence of in situ stress on the blast-induced rock fracture. The results showed that the cracks induced by blasting stress wave and gas pressure grow preferably in the direction of maximum principal stress of superimposed stress fields. Zhang and Peng [2–5] studied the crater blasting under different confining pressures via theoretical analysis and physical model tests. The outcomes showed that the crater shape becomes oval with the long axis aligned on the loading direction, and the open angle in this direction and the crater volume is greater with the increase of confining pressure under uniaxial static load. Based on the fracture mechanics and the rock damage failure criterion, Xiao et al. [6] calculated rock fragmentation induced by blasting under high stress. It is concluded that the release of strain energy in the highly stressed rock mass is helpful to improve the breaking effect.

Yang et al. [7] conducted caustics experiments to investigate the propagation characteristics of blast-induced cracks in the dynamic-static stress field. The results indicated that the in situ stress has an important effect on crack propagation induced by blasting and the crack propagation is restrained when the crack propagation direction is perpendicular to the direction of in situ stress. Hu and Lu [8,9] studied the formation and propagation of crack induced by presplitting blasting in highly stressed rock mass via a mathematical model and concluded that the in situ stress can restrain the development of cracks between the presplitting holes when the in situ stress is perpendicular to the crack face. Yang and He [10,11] experimentally investigated the influence of confining pressure and ratios of horizontal-to-vertical pressure on the blast-induced rock fracture. The results showed that the direction of crack growth was largely controlled by the hoop tensile stress and biaxial pre-pressure ratio.

As a research tool, the numerical modeling method has been widely used to investigate the blast-induced damage characteristics of rock. Donzé et al. [12] used the discrete element method (DEM) to study the blast-induced radial fractures under confining pressure and found that the radial fractures induced by blasting tend to grow in the direction of maximum principal stress. Yilmaz et al. [13] investigated the blast-induced damage characteristics under different in situ stresses via a 3D FLAC (Fast Lagrangian Analysis of Continua) analysis. The results indicated that the development of fractures around the borehole is governed by the maximum principal stress and it is more obvious with the increase of the difference between the two principal stresses. Xie [14] used LS-DYNA to study the damage characteristics in cutting blasting under different in situ stresses. The results showed that with the increase of in situ stress, the damage zone becomes smaller. With the increase of the lateral pressure coefficient, the extending direction of the tensile damage zone becomes more obvious, which causes a great challenge to the cutting blasting excavation in deep rock masses. Yi, Jayasinghe, Ma and Li [15–18] used LS-DYNA to investigate the influence of in situ stress on the blast-induced cracks. Their results showed that the crack propagation trends towards the direction of maximum compressive pressure. Han, Wei and Deng [19] used a numerical model to study the contour control blasting under different in situ stresses. The result indicated that the in situ stress could affect the crack evolution and direction, and the quality of the contour surface is hard to control in highly stressed rock masses.

The studies mentioned above mainly focus on the plane problems of blasting under static load. However, the three-dimension propagation of stress wave induced by explosives, the charge length, and the detonation velocity of explosive cannot be considered in these 2D plane strain models. The above factors can be involved in a 3D model analysis to obtain more realistic results. Additionally, the key factor of the free surface is rarely considered, especially the lateral free surface, which plays an important role in the rock breaking by blasting. In this study, a 3D blasting model of coupling static and dynamic loads is developed in LS-DYNA and the model parameters are calibrated by the physical model test. Subsequently, the calibrated numerical model is used to simulate the blast-induced damage considering the roles of in situ stress and lateral free surface. Based on the damage distribution, the blast-induced damage characteristics and the explosion craters under different static loads and free surface spans are analyzed.

2. Numerical Modeling

2.1. Constitutive Model Parameters and Validation

2.1.1. Numerical Model for Physical Model Test

To verify the material model and apply it to the subsequence simulation of lateral blasting under static load, a physical single-hole crater blasting model test was conducted firstly to calibrate the material parameter, as shown in Figure 1a. The whole model is $400 \times 400 \times 200$ mm. A borehole with a diameter of 8.0 mm and a length (L) of 40 mm is drilled in the center and the explosive with a diameter (d) of 8.0 mm and a length (l) of 12 mm is charged in the borehole. The cemented sand, which is composed of ordinary

Portland cement (PC32.5), uniform-grained sand and water in the mass ratio of 3:3:1, is used as the model material to study the blast-induced damage of rock. The material mechanical parameters are determined by averaging the measured data from six mortar cubic blocks. The density ρ_0 is 2456 kg/m³; the compressive strength f_c is 48.3 MPa and the elastic modulus E is 32.36 GPa; Poisson's ratio μ is 0.24; P-wave velocity v_p is 3828 m/s. According to the physical model, the single-hole crater blasting numerical model was developed for comparison with the test results, as shown in Figure 1b. The model consists of rock, explosive, and stemming. The size of the numerical model is same as the physical model and the total number of the meshed elements is 0.56 million, where the numerical convergence tests has been carried out and the calculation results of the model are convergent and accurate.

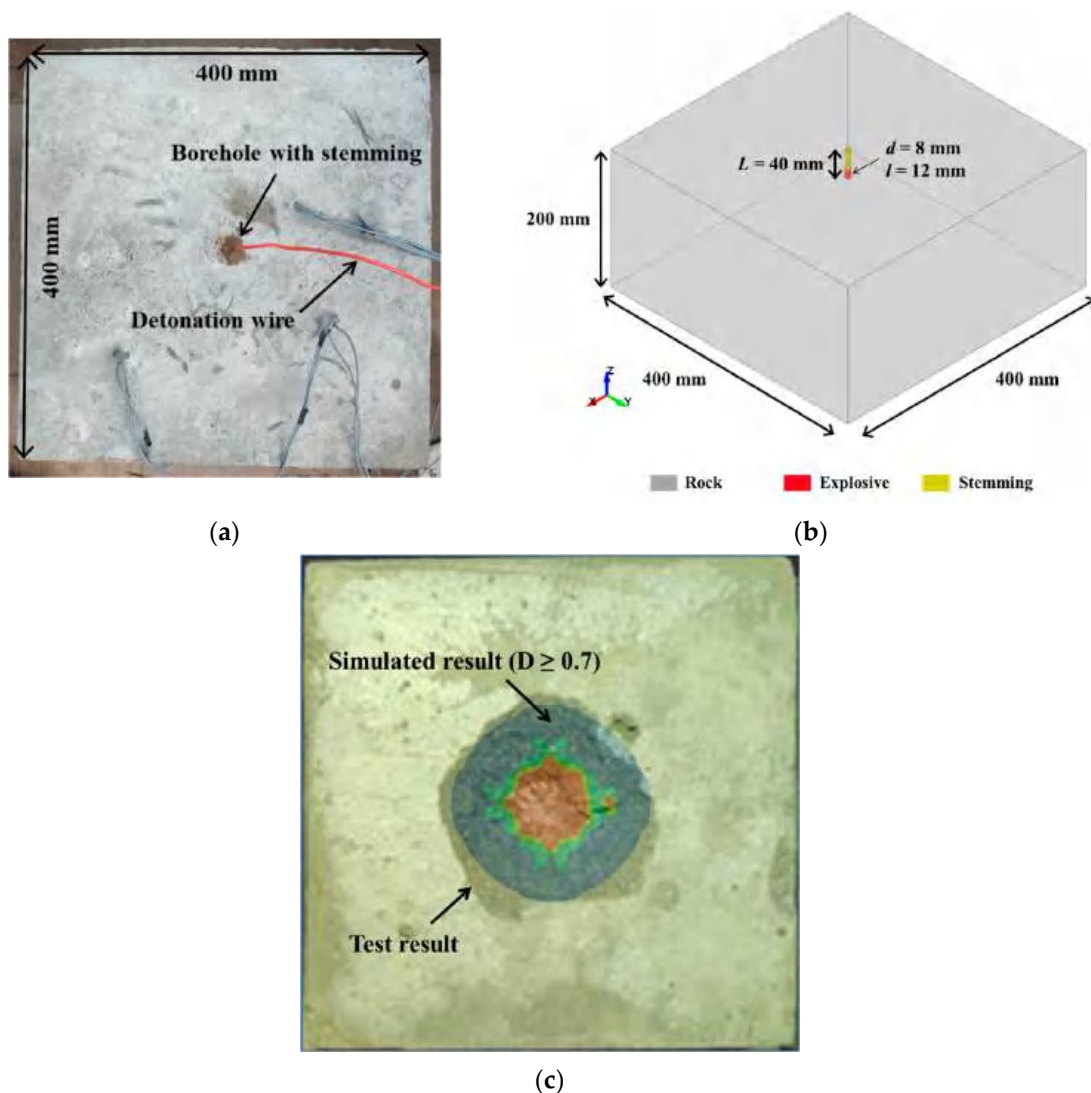


Figure 1. Single-hole crater blasting model and the comparison of explosion craters: (a) physical model; (b) numerical model; (c) the comparison of experimental and simulation results.

2.1.2. RHT Material Model for Rock

In this study, the dynamic response and damage process of rock mass were simulated by Riedel, Hiermaier, and Thoma (RHT) in LS-DYNA, which were widely used in the numerical simulation of concrete and rock [3,20–25]. The damage degree of the RHT material model is given by $D = \sum \frac{\Delta \epsilon^p}{\epsilon^f}$, in which $\Delta \epsilon^p$ is the accumulated plastic strain and ϵ^f is the failure strain. The detailed introduction of the RHT constitutive model can be

found in [20]. Based on the tested mechanical parameter, the following sections obtain the other material parameters through empirical formulas or related literatures.

1. Strain rate parameters

The effect of strain rate on the rock strength is clear. The strain rate strength factor $F_r(\dot{\epsilon}_p)$ is expressed as [21]:

$$F_r(\dot{\epsilon}_p) = \begin{cases} (\dot{\epsilon}_p/\dot{\epsilon}_0^c)^{\beta_c} & P \geq f_c/3 \\ \frac{P+f_t/3}{f_c/3+f_t/3}(\dot{\epsilon}_p/\dot{\epsilon}_0^c)^{\beta_c} - \frac{P-f_c/3}{f_c/3+f_t/3}(\dot{\epsilon}_p/\dot{\epsilon}_0^t)^{\beta_t} & -f_t/3 < P < f_c/3 \\ (\dot{\epsilon}_p/\dot{\epsilon}_0^t)^{\beta_t} & P \leq -f_t/3 \end{cases} \quad (1)$$

where $\dot{\epsilon}_p$ is the strain rate; $\dot{\epsilon}_0^c$ and $\dot{\epsilon}_0^t$ are the compressive and tensile reference strain rates, which are $3 \times 10^{-5} \text{ s}^{-1}$ and $3 \times 10^{-6} \text{ s}^{-1}$, respectively; P is the hydrostatic pressure; f_c and f_t are the uniaxial strengths in compression and tension. The strain rates in compression (β_c) and in tension (β_t) are constant for the material and can be calculated by

$$\beta_c = \frac{4}{20 + 3f_c}, \beta_t = \frac{2}{20 + f_c} \quad (2)$$

where the unit is MPa, and then β_c and β_t are determined as 0.024 and 0.029.

2 Failure surface parameters

A and N are the constants in the failure surface and can be obtained by:

$$\sigma_f^*(P^*, F_r) = A \left(P^* - F_r/3 + (A/F_r)^{-1/N} \right)^N \quad 3P^* \geq F_r \quad (3)$$

where $\sigma_f^*(P^*, F_r)$ is the normalized strength and can be calculated by $\sigma_f^* = \frac{\sigma_f}{f_c}$; P^* is the normalized hydrostatic pressure and can be calculated by $P^* = \frac{P}{f_c}$; F_r is the strain rate strength factor.

When the rock is in a quasi-static state, $\dot{\epsilon}_p = 3.0 \times 10^{-5} \text{ s}^{-1}$, and then $F_r = 1$ can be calculated by Equation (1). The rock strength under different confining pressures can be calculated by empirical equation of Hoek-Brown [26] and the fitting equations for rock material are as follows [27]:

$$\sigma_1 = \sigma_3 + 48.3 \left(24 \frac{\sigma_3}{48.3} + 1 \right)^{1/2} \quad (4)$$

The axial stress at failure (σ_1) under different confining pressures ($\sigma_2 = \sigma_3$) can be calculated by Equation (4). The results are shown in Table 1. Subsequently, the pressure $P = \frac{1}{3}(\sigma_1 + \sigma_2 + \sigma_3)$, equivalent stress at failure $\sigma_f = \sqrt{\frac{1}{2}[(\sigma_1 - \sigma_2)^2 + (\sigma_2 - \sigma_3)^2 + (\sigma_3 - \sigma_1)^2]}$, P^* , and σ_f^* can be obtained and are shown in Table 1. Based on Equation (3), $A = 2.439$ and $N = 0.7528$ can be obtained by substituting the values of P^* and σ_f^* corresponding to the confining pressures of 5 MPa and 30 MPa.

Table 1. Mechanical parameters under different confining pressures.

$\sigma_2=\sigma_3/\text{MPa}$	σ_1/MPa	P/MPa	σ_f/MPa	P^*	σ_f^*
0	48.3	16.1	48.3	0.33	1.00
5	95	35	90	0.73	1.87
10	128	49	118	1.02	2.44
20	180	73	160	1.52	3.31
30	223	94	193	1.95	3.99
50	296	132	246	2.73	5.08

3 P - α compaction EOS (Equation of State) parameters

The P - α compaction of RHT is given by

$$P(\rho, e) = \frac{1}{\alpha} \left((B_0 + B_1 \mu_0) \alpha \rho e + A_1 \mu_0 + A_2 \mu_0^2 + A_3 \mu_0^3 \right) \mu_0 > 0 \tag{5}$$

where B_0 and B_1 are the material constants; α and ρ are the initial porosity and density; e is the specific internal energy; μ_0 is the volumetric strain; A_1, A_2, A_3 are the polynomial coefficients.

$A_1, A_2,$ and A_3 can be calculated by formulas in [24],

$$A_1 = \alpha \rho c^2 A_2 = \alpha \rho c^2 (2k - 1) A_3 = \alpha \rho c^2 [(3k - 1)(k - 1)] \tag{6}$$

where c is the wave speed; k is the material constant. A_1, A_2 and A_3 can be calculated as 36.0, 40.4 and 4.8 GPa, respectively.

The minimum damaged residual strain (ϵ_p^m) can be determined by the calibration of the physical model test. The remaining model parameters in this study, which are not sensitive to the numerical results, are referred to the cemented sand parameters in the literatures [28,29]. The determined RHT parameters are listed in Table 2.

Table 2. RHT parameters for rock mass.

Parameter	Value	Parameter	Value
Density ρ_0	2456 kg/m ³	Compressive strain rate β_c	0.024
Shear modulus G	13 GPa	Tensile strain rate β_t	0.029
ONEMPA ¹	1.0×10^6	Pressure influence on plastic flow in tension PTF	0.001
Eroding plastic strain EPSF	2.0	Compressive yield surface g_c^*	0.53
Polynomial EOS B_0	1.22	Tensile yield surface g_t^*	0.7
Polynomial EOS B_1	1.22	Shear modulus reduction factor ζ	0.5
Polynomial EOS T_1	35 GPa	Damage parameter D_1	0.04
Failure surface A	2.439	Damage parameter D_2	1
Failure surface N	0.7528	Minimum damaged residual strain ϵ_p^m	12×10^{-3}
Compressive strength f_c	48.3 MPa	Residual surface parameter A^f	1.6
Relative shear strength f_s^*	0.18	Residual surface parameter n^f	0.61
Relative tensile strength f_t^*	0.1	Gruneisen gamma GAMMA	0
Lode angle Q_0	0.681	Hugoniot polynomial coefficient A_1	3.6×10^{10}
Lode angle B	0.0105	Hugoniot polynomial coefficient A_2	4.04×10^{10}
Polynomial EOS T_2	0	Hugoniot polynomial coefficient A_3	0.48×10^{10}
Ref. compressive strain rate ϵ_0^c	3.0×10^{-5}	Crush pressure P_{cl}	16.1 MPa
Ref. tensile strain rate ϵ_0^t	3.0×10^{-6}	Compaction pressure P_{co}	6 MPa
Break compressive strain rate ϵ^c	3.0×10^{25}	Porosity exponent N_p	3
Break tensile strain rate ϵ^t	3.0×10^{25}	Initial porosity α_0	1

¹ ONEMPA is the unit conversion factor defining 1 MPa in the pressure units used.

2.1.3. Material Identifications of Charge, Air and Stemming

The charge is modeled by MAT_HIGH_EXPLOSIVE_BURN in LS-DYNA [30]. The JWL(Jones–Wilkins–Lee) EOS are given by:

$$P = A \left(1 - \frac{\omega}{R_1 V} \right) e^{-R_1 V} + B \left(1 - \frac{\omega}{R_2 V} \right) e^{-R_2 V} + \frac{\omega E}{V} \tag{7}$$

where P is the pressure, $A, B, R_1, R_2,$ and ω are constants, V is the specific volume, and E is the internal energy with an initial value of E_0 .

In this study, the explosive is a mixture of RDX (Hexogen), PETN, DDNP, et al. The estimation of JWL parameters of explosive is complex and costly [31], so the parameters refer to similar explosive parameters [32]: $A = 524$ GPa, $B = 7.68$ GPa, $R_1 = 4.2, R_2 = 1.1,$ $\omega = 0.34, E_0 = 8.5$ GPa. The charge density is 1.6×10^3 kg/m³ and the detonation velocity is 6950 m/s.

The air is modeled by MAT_NULL in LS-DYNA, and the corresponding EOS is given by [30]:

$$P = C_0 + C_1u + C_2u^2 + C_3u^3 + (C_4 + C_5u + C_6u^2)e \quad (8)$$

where $C_0, C_1, C_2, C_3, C_4, C_5$ and C_6 are polynomial coefficients; $\mu = \frac{\rho}{\rho_0} - 1$ is specific volume; e is the internal energy per volume and has the unit of pressure, Pa. In this study, the air is modeled as an ideal gas by setting $C_0 = C_1 = C_2 = C_3 = C_4 = 0$ and $C_5 = C_6 = 0.4$, and the initial internal energy per volume is set to 0.25 J/cm^3 [25].

The stemming is modeled by MAT_SOIL_AND_FOAM in LS-DYNA and its parameters are shown in Table 3.

Table 3. Parameters for stemming.

Density ρ'	Poisson's Ratio ν	Shear Modulus E_T	Cohesive Force c	Friction Coefficient μ	Internal Friction Angle φ
2600 kg/m ³	0.19	16 GPa	0.018 MPa	0.7	35°

2.2. Constitutive Model Parameters and Validation

Figure 1c shows the comparison of explosion craters between the physical test results and the simulated results. In the simulated results, the critical damage is set to 0.6 or 0.7 according to the previous studies [15,22,23,33]. In this study, a critical value D of 0.7 is reasonable for the consistency between the physical test results and the numerical results. It can be found that the crater boundary in the simulated results is similar to that in the test results. Therefore, the calibrated numerical model is able and feasible to study the blast-induced damage characteristics.

2.3. Numerical Model for Lateral Blasting under Static Load

A numerical model with dimensions of $400 \times 400 \times 200 \text{ mm}$ was built to simulate the dynamic response and damage evolution of lateral blasting, as shown in Figure 2. It is commonly seen that rectangular cavern is usually generated by production boreholes with an excavation method of lateral caving with large-diameter long-hole blasting or by tunneling excavation for its advantages of simple procedures, high excavation efficiency and convenient support measures [22,34]. Therefore, the cavern prototype was set as a rectangle in this study, which also has important enlightening significances for other shapes. In the center of the model, a rectangular cavern with a size of span $X \times$ span $Y \times 200 \text{ mm}$ is placed to form the lateral free surface and a borehole with a diameter of 8.0 mm is placed near the cavity with a distance of W . It should be noted that the span X and span Y are no more than $1/3$ of the model size of 400 mm to decrease the influence of boundary on the stress distribution. The explosive with a diameter of 6.3 mm and a length of 20 mm is charged in the hole centrally. The ends of the borehole are filled with stemming. Static stresses, P1 and P2, are applied to the four external boundaries of the model in X and Y directions respectively using a dynamic relaxation scheme, and the four sides inside the model are specified as free surfaces. After the stress initialization, the charge is loaded in the model and detonated. The numerical model is meshed by hexahedral elements, with a size of 4 mm, which is small enough to avoid any wave distortion [22]. The total number of meshed elements is 0.5 million. In this study, in order to monitor the damage distribution in the rock mass, cut Y1 and cut Z1 are selected, as shown in Figure 2. The evolution process of blast-induced damage is completed before $100 \mu\text{s}$, which is set to the calculation termination time.

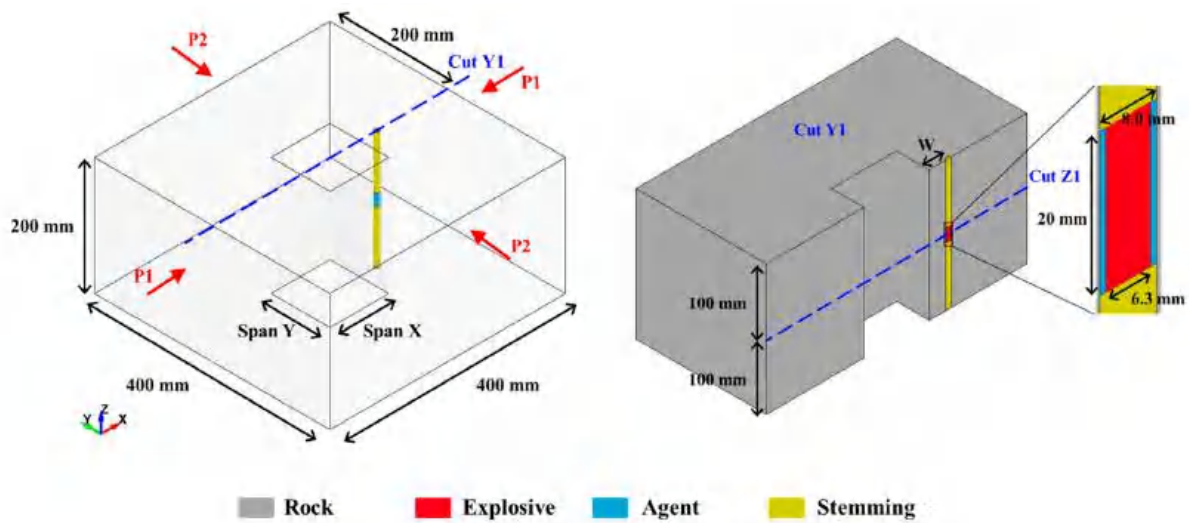


Figure 2. Numerical model of single hole blasting with a lateral free surface.

3. Results and Analysis

3.1. Influence of Uniaxial Static Load on the Damage Distribution under Different Burdens

In this section, a span X of 100 mm and a span Y of 100 mm are applied to the numerical model, and then the simulations of uniaxial loading of P1, uniaxial loading of P2, and biaxial loading were conducted. The damage contours of cut Z1 at 100 μ s were extracted from the numerical results. The variation characteristics of damage distribution, the volume V and the shape of the crater were studied in detail in this section.

According to the elastic mechanics, on the right side of the rectangle cavern, the X-direction stress is small, and the stress field is governed by the Y-direction stress, especially near the free surface. Therefore, the blast-induced damage is mainly affected by the original Y-direction stress field. Figure 3 shows the Y-direction elastic stress fields (σ_y) under different static loads ($W = 4$ cm). For the stress σ_y , its sign is positive in tension and negative in compression. As seen from the Y-direction stress contours, the rectangle cavern induces stress concentration near the free surface. For $P1 = 5$ MPa, as shown in Figure 3a, there is a large tensile stress zone on the left side of the borehole, especially near the free surface, and a small tensile stress zone on the right side of the borehole. The maximum tensile stress is 6.6 MPa near the free surface and σ_y decreases to around 2 MPa on the left side of the borehole. For $P2 = 5$ MPa, as shown in Figure 3b, the excavation zone is in a compressive stress field. The σ_y is maximum around the free surface (around 12 MPa), and it decreases to around 7 MPa on the left side of the borehole. For $P1 = P2 = 5$ MPa, as shown in Figure 3c, the excavation zone is also in a compressive stress field, but the compressive stress field is weakened, and the distribution changes a lot. The maximum σ_y transfers from the free surface, where the σ_y decreases to around 4 MPa, to the four corners of the cavern. The above static stress field analysis is beneficial to understanding the coupling mechanism of static load and blasting stress wave load on the rock damage characteristics in the subsequent dynamic analysis.

To evaluate the influence of P1 on the damage distribution due to blasting, five cases of uniaxial static loads, $P1 = 0, 2, 5, 8,$ and 10 MPa, were first conducted in this section. Figure 4 shows the damage contours for different P1 with different burdens at cut Z1. As mentioned in Section 2.2, the elements with a damage level above 0.7 are regarded as severe damage zone and form the explosion crater. In the case of $P1 = 0$ MPa, blast-induced severe damage zones ($D \geq 0.7$) are widely distributed and can form craters from the charge center to the free surface when the burden W is no more than 4 cm. When W is more than 5 cm, the blast-induced severe rock damage ($D \geq 0.7$) mainly distributes around the explosive and little severe damage zone covers the free surface, but the two zones are not connected. Thus, in the cases of $W = 5$ cm and $W = 6$ cm, only blasting cavities are formed around the

charge but no crater is formed by the blasting. Therefore, the burden should be no more than 4 cm to form an explosion crater in the case of $P_1 = 0$ MPa. In the case of $P_1 = 2$ MPa, the damage zones are enlarged for each burden, but the severe damage zone ($D \geq 0.7$) around the charge and the damage zone near the free surface are still separated when $W = 5$ cm and $W = 6$ cm, which indicates no crater is formed. When P_1 increases to 5 MPa, the damage zones are further enlarged, and the two zones begin to connect for $W = 5$ cm but not for $W = 6$ cm. In the case of $P_1 = 8$ MPa and 10 MPa, with the increase of static load, the damage zones become larger. Especially for $W = 5$ cm, the severe damage zone is clearly enlarged near the free surface, thus a crater is formed. It should be noted that there is still a large low-level damage zone ($D < 0.7$) between the blasting cavity and the free surface for $W = 6$ cm, as a result, the explosion crater cannot be formed.

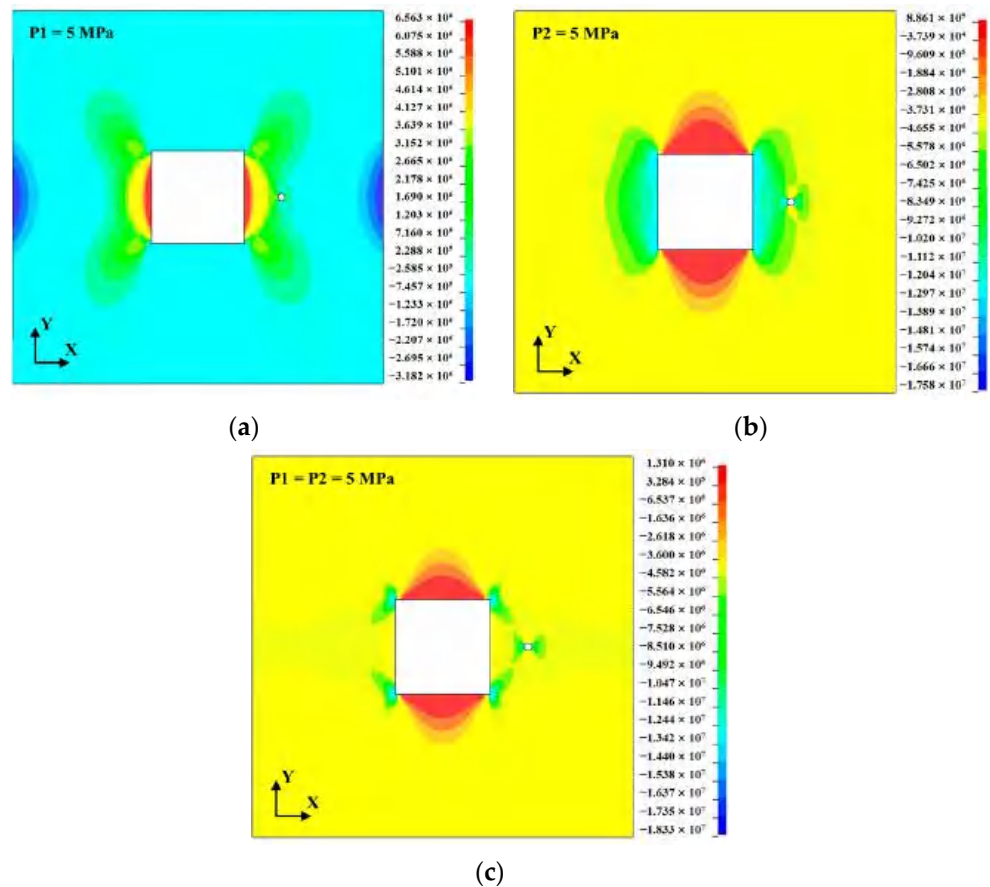


Figure 3. Y-direction elastic stress fields (σ_y) under different static loads ($W = 4$ cm): (a) $P_1 = 5$ MPa; (b) $P_2 = 5$ MPa; (c) $P_1 = P_2 = 5$ MPa.

In order to evaluate the explosion crater clearly, the crater volume V is measured by counting the high-level damage elements ($D \geq 0.7$) and summing their volumes. The crater volumes for each burden under different static loads are shown in Figure 5. It can be found that with P_1 increases, the volume of explosion crater tends to increase. When P_1 is less than 8 MPa, the V for $W = 2$ cm is the smallest (no crater for $W = 5$ and 6 cm, as shown in Figure 4) due to excessive dissipation of the explosion energy into the atmosphere and the V for $W = 3$ cm is the largest, which indicates that the optimal burden is 3 cm. However, when P_1 is more than 8 MPa, the burden of 4 cm is optimal because its corresponding crater volume is the largest. It can be clearly seen that the V for $W = 2$ cm is not sensitive to the static load, but the others vary greatly with changing P_1 , especially for $W = 4$ cm, $W = 5$ cm and $W = 6$ cm when $P_1 \geq 5$ MPa. The above results are due to the rapid expansion of the damage zone near the free surface for $W = 5$ cm and $W = 6$ cm (as shown in Figure 4). It should be noted that the V for $W = 6$ cm is the volume sum of the blasting cavity and the

damage zone near the free surface, but not the crater volume (as shown in Figure 4). It can be concluded that the P1 can change the optimal burden of charge and increase the critical embedding depth of the charge.

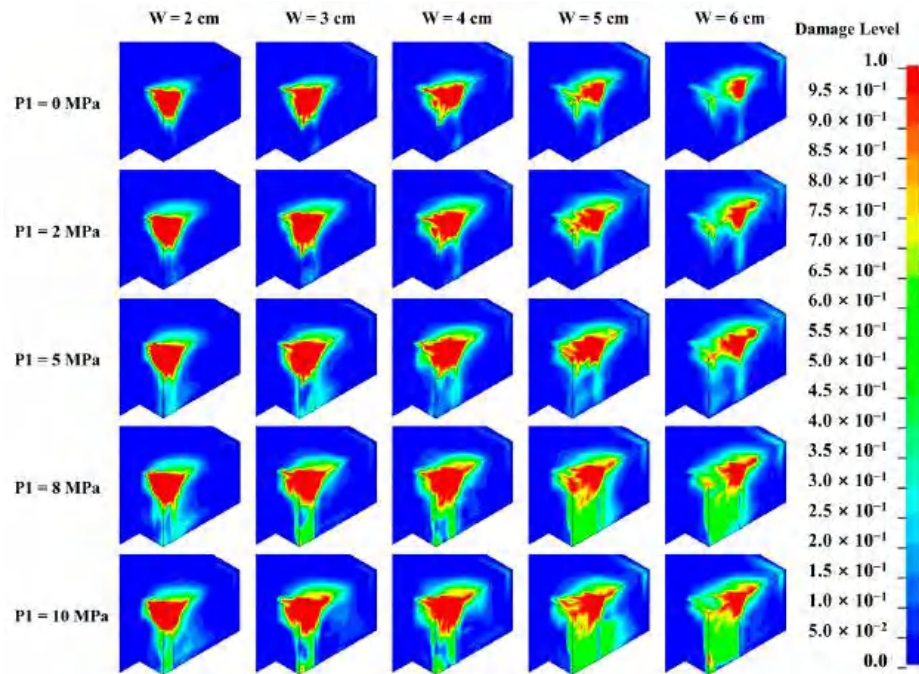


Figure 4. Damage contours for each burden under different static loads (P1) at cut Z1.

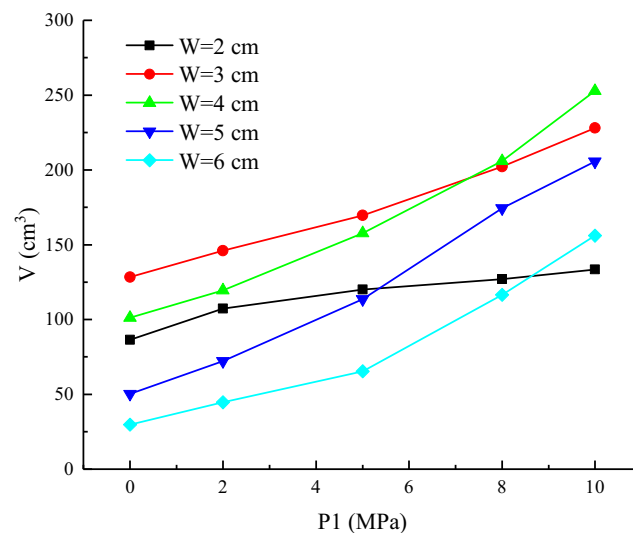


Figure 5. Crater volumes for each burden under different static loads (P1).

In order to investigate the variation in the shape of the explosion crater, the craters (formed by the elements with $D \geq 0.7$) for $W = 4$ cm under different P1 are plotted in Figure 6. In the XY plane, the shape of the explosion craters is similar to a triangle and expands with the increase of P1. The diameter of the crater in the Y direction also becomes larger with the increase of P1 at different depths (X direction), especially in the top of the crater, where a new damage zone is generated. The above results are induced by the combined effect of the Y-direction tensile component of the stress wave and the Y-direction tensile stress field (as shown in Figure 3a). In the XZ plane, there is a clear trend that with the increase of P1, the diameter in the Z direction becomes larger, especially when

$P1 = 8$ MPa. This is because with the increase of Y-direction stress field (σ_{y1}) induced by $P1$, the combined effect of the Y-direction tensile component of incident stress wave (σ_{yI}) and Y-direction stress field (σ_{y1}) is intensified and promotes the initiation and propagation of radial tensile fracture at point A, as shown in Figure 7a. Besides, some damage zones appear in the left side of the borehole due to the stress concentration, but they expand little in the Y direction, as shown in the YZ plane. In the YZ plane, when $P1 = 5$ MPa, the long axis of the bottom circle of the crater is in the Y direction. This is because the superposition of the Y-direction component of reflected tensile stress (σ_{yR}) and Y-direction stress field (σ_{y1}) at point B (as shown in Figure 7b) increases the Y-direction dimension of reflected tensile damage zone around the free surface, which is also shown in the XY plane. However, with the increase of $P1$, the long axis of the bottom circle of the crater transfers from Y direction to Z direction due to the faster growth of the diameter in the Z direction, which is consistent with the results in the XZ plane and can be illustrated by Figure 7a. The result is also consistent with the law that the long axis of blast-induced damage is parallel to the max principal compressive stress (Z direction). It can be concluded that the crater shape is governed by the reflected tensile fractures when $P1 \leq 5$ MPa, but governed by the radial tensile fractures when $P1 \geq 8$ MPa.

Another five cases of uniaxial static loads, $P2 = 0$ MPa, $P2 = 2$ MPa, $P2 = 5$ MPa, $P2 = 8$ MPa and $P2 = 10$ MPa, were simulated to investigate the effect of load direction on damage distribution. Figure 8 shows the damage contours at cut Z1 and the crater volumes for different burdens under different $P2$. In the case of $P2 = 2$ MPa, the crater volumes are enlarged for $W = 2$ cm, 3 cm, and 4 cm, but shrunk for $W = 5$ and 6 cm, as shown in Figure 8b. There is still no crater formed by the blasting for $W = 5$ and 6 cm, as shown in Figure 8a. The increase of the crater volumes for $W = 2, 3,$ and 4 cm is mainly induced by the increase of reflected tensile fractures around the free surface, where the combined effect of the X-direction component (σ_{xR}) of reflected tensile wave and the compressive stress field (σ_{y2}) induced by $P2$ promotes the damage development at point C and D, and the increase of radial tensile damage zone, where the combined effect of the Z-direction tensile component (σ_{zL}) of incident wave and σ_{y2} promotes the damage development at point B, as shown in Figure 9. However, the reductions of the crater volumes for $W = 5$ cm and 6 cm are induced by the reduction of radial damage zones distributed around the charge, where the volumes of blasting cavities are mainly restrained by σ_{y2} , especially at point A, as shown in Figure 9. In the case of $P2 = 5$ MPa, the crater volumes are increased when $W = 2$ cm, 4 cm, 5 cm, and 6 cm but reduced when $W = 3$ cm. For $W = 3$ cm, this may be because the increase of reflected tensile fractures around the free surface is smaller than the reduction of the radial tensile damage zone around the charge. There is a clear increase of the damage zones for $W = 4, 5,$ and 6 cm, which is induced by the great increase of fractures around the free surface. Especially for $W = 5$ cm, the fractures around the free surface are clearly enlarged and begin to connect with the blasting cavity formed by the damage zone around the charge. For $W = 6$ cm, the combined effect of σ_{xR} and σ_{y2} is enhanced due to the intensification of the latter, and some damage zones extend from the free surface to the borehole. However, the damage zones only distribute along the Y direction but expand little in the Z direction, so the crater is hard to form. In the case of $P2 = 8$ MPa and 10 MPa, with the increase of static load, the damage zones become larger, except for $W = 3$ cm, where the damage zone distribution along the Z direction is reduced, as shown in Figure 8a. It should be noted that the crater is still not formed for $W = 6$ cm. For each W , the fractures tend to extend along the Y direction with $P2$ increases, which is consistent with the law that the long axis of the blast-induced damage zone is parallel to the max principal stress (Y direction).

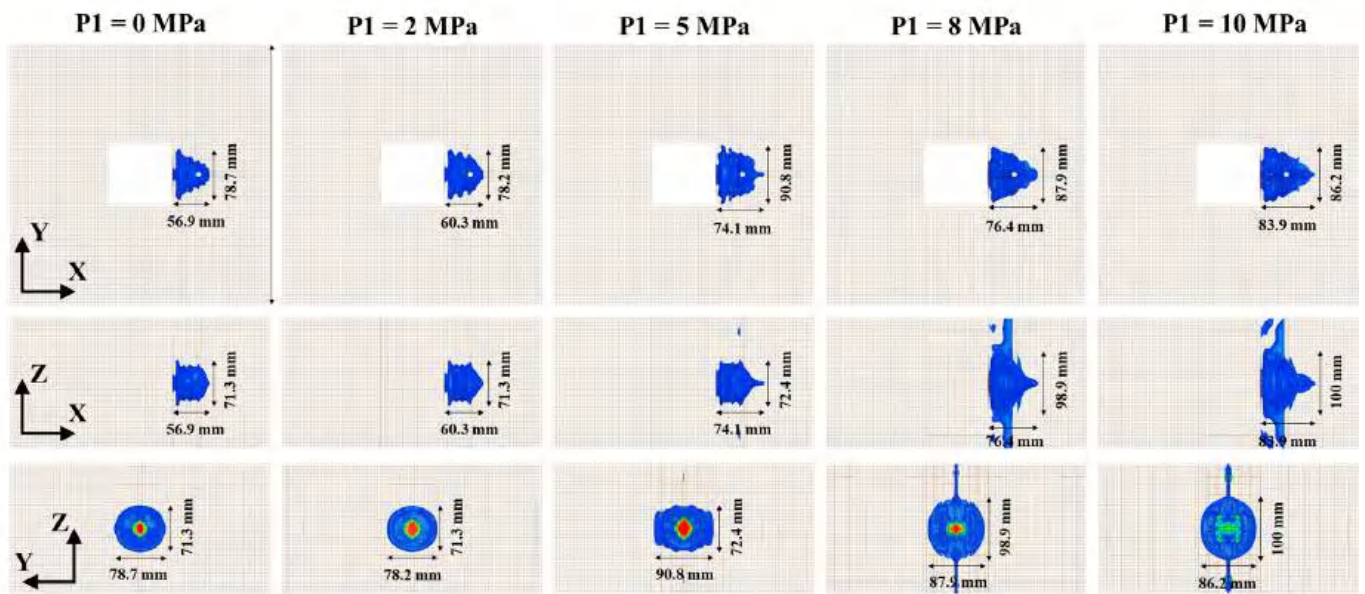


Figure 6. The craters for $W = 4$ cm under different P_1 .

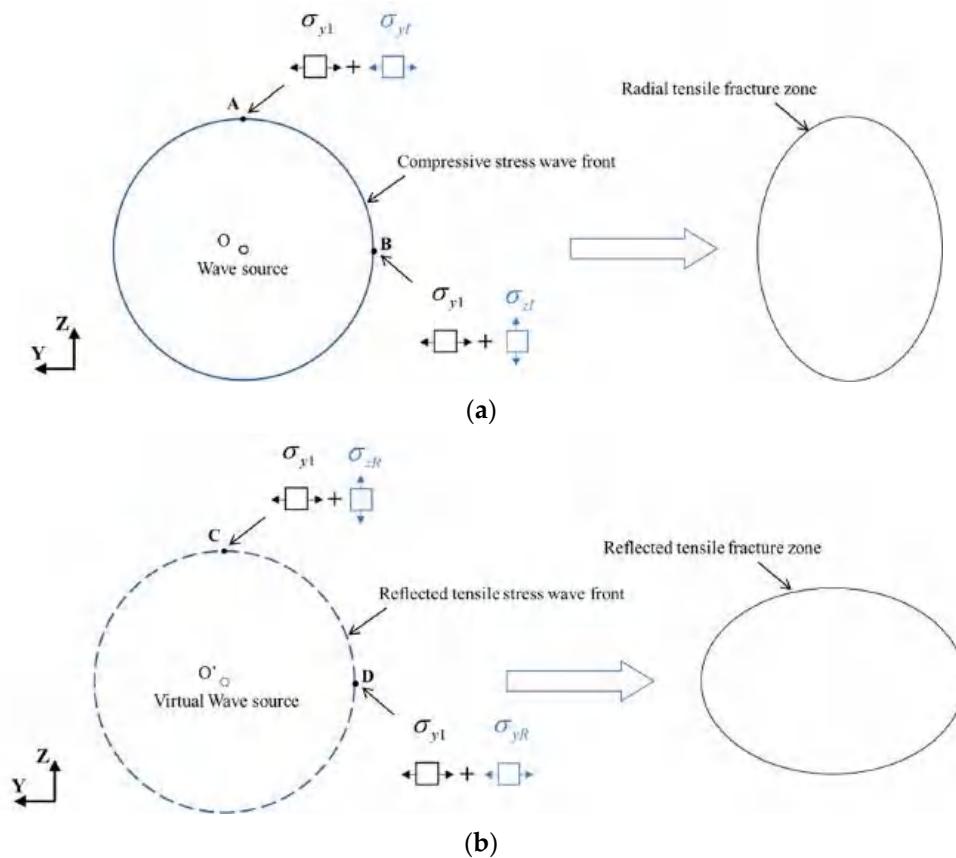
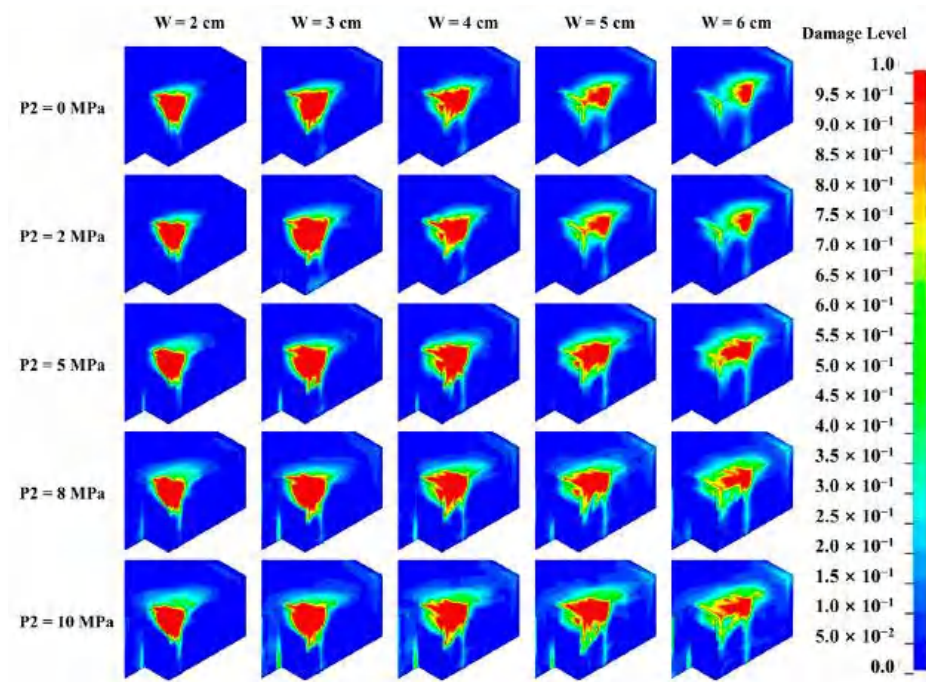
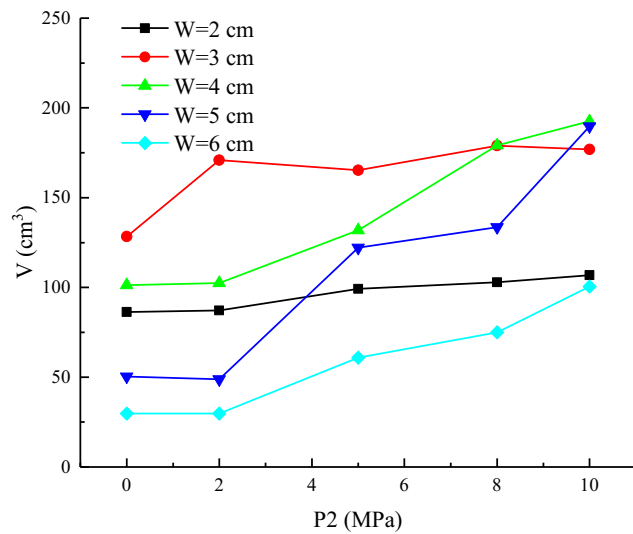


Figure 7. Schematics of superposition of original stress field (P_1) and stress wave and its influence on the crater shape: (a) radial tensile fracture induced by incident compressive stress wave; (b) reflected tensile fracture induced by reflected tensile stress wave.



(a)



(b)

Figure 8. Damage contours at cut Z1 and crater volumes for each burden under different P2: (a) damage contours; (b) crater volumes.

With the increase of P1 or P2, the crater volume can be enlarged. However, the increase of V with P1 is more than that with P2. For example, when W = 4 cm, the V for P1 increases by 17.1, 25.8, 26.8 and 60.3 cm³ compared with that for P2 when the stress level is 2, 5, 8 and 10 MPa, respectively. In other words, when the static load values are the same, the V is increased by 15–31% for P1 compared with P2. The results show that the effect of P1 on the increase of V is greater than that of P2.

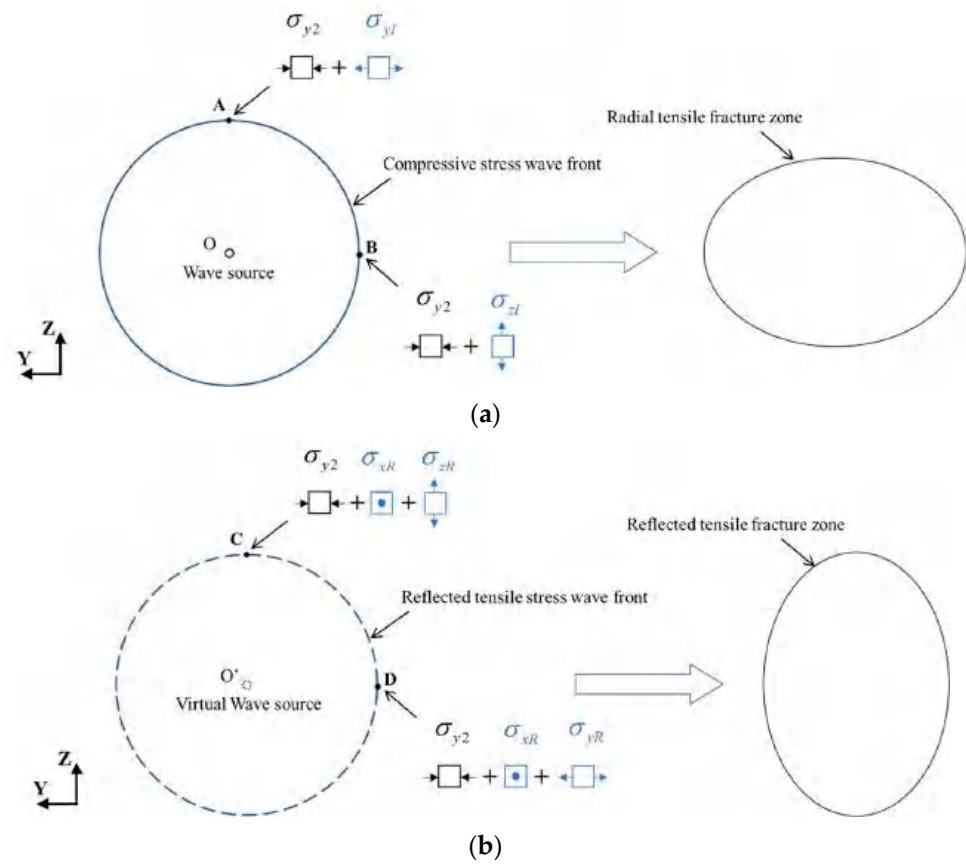


Figure 9. Schematics of superposition of original stress field (P2) and stress wave and its influence on the crater shape: (a) radial tensile fracture induced by incident compressive stress wave; (b) reflected tensile fracture induced by reflected tensile stress wave.

The shapes of the craters for $W = 4$ cm under different P2 are plotted in Figure 10a. In the XY plane, the shape of the explosion crater gradually changes from a triangle to a trapezoid and has a significant expansion in the Y direction at different depths due to the directional effect of the Y-direction compressive stress field. However, the depth of the explosion crater is reduced a little due to the volume shrink at the top of the crater, especially in the case of $P2 = 10$ MPa, where the crater is mainly distributed on the left side of the borehole. In the XZ plane, near the free surface, the Z-direction diameter gradually increases under the combined effect of reflected tensile wave and σ_{y2} . In the YZ plane, the shape of the crater becomes an oval and its long axis is in the Y direction for $P2 = 2$ MPa, which obeys the law that the long axial of blast-induced damage zone is parallel to the max principal stress. However, when $P2 \geq 5$ MPa, the shape tends to expand in the Z direction. This is because the reflected tensile fracture zone becomes the dominant factor affecting the crater shape. As shown in Figure 9b, σ_{y2} is perpendicular to σ_{xR} and Z-direction tensile stress component (σ_{zR}) of reflected wave at point C and point D, and it is conducive to the growth of reflected tensile fractures induced by σ_{xR} . However, it is opposite to the Y-direction tensile stress component (σ_{yR}) at point D and it will restrain the formation of reflected tensile fractures induced by σ_{yR} . As a result, the Z-direction reflected tensile fractures are easier to propagate. To study the effect of P2 on the radial tensile fracture zone distribution, as shown in Figure 10a, section A-A at 1 cm to the left side of the borehole is selected, which is away from the free surface, and its damage zone is mainly governed by radial tensile fractures.

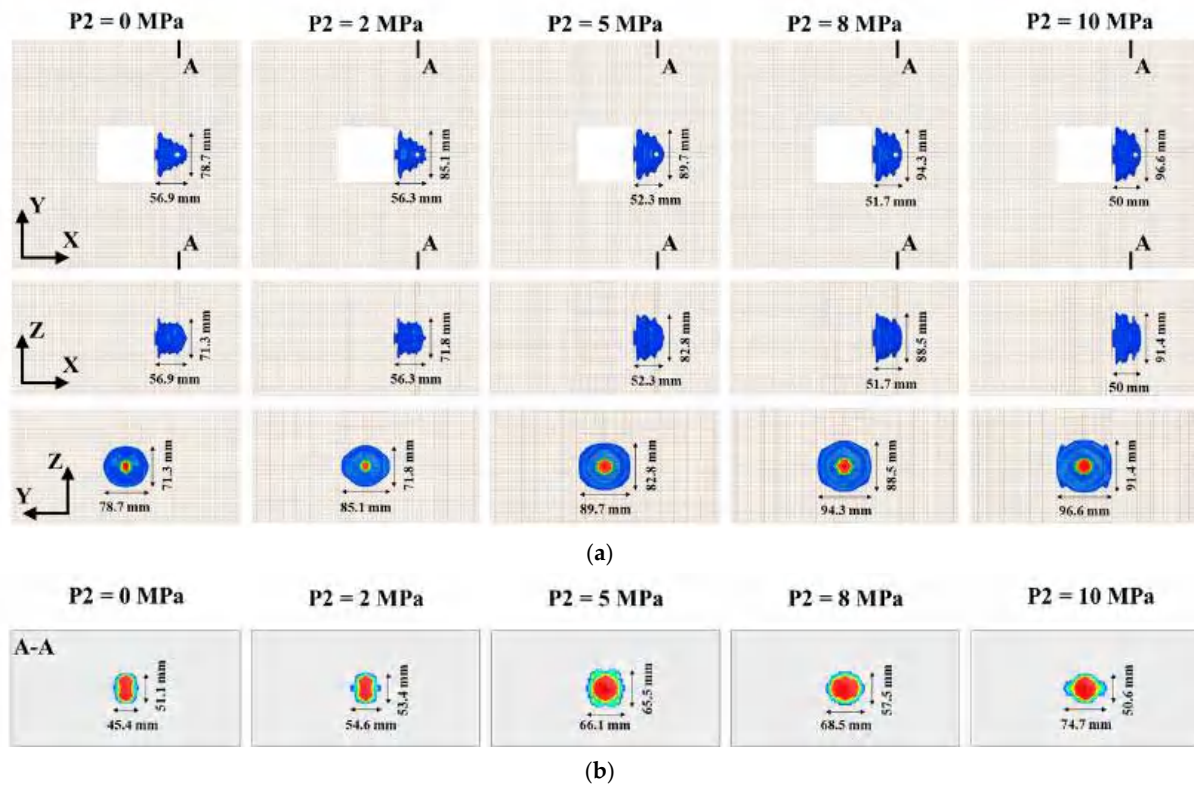


Figure 10. The craters for $W = 4$ cm under different P2: (a) perspective view of craters at different planes; (b) section A-A.

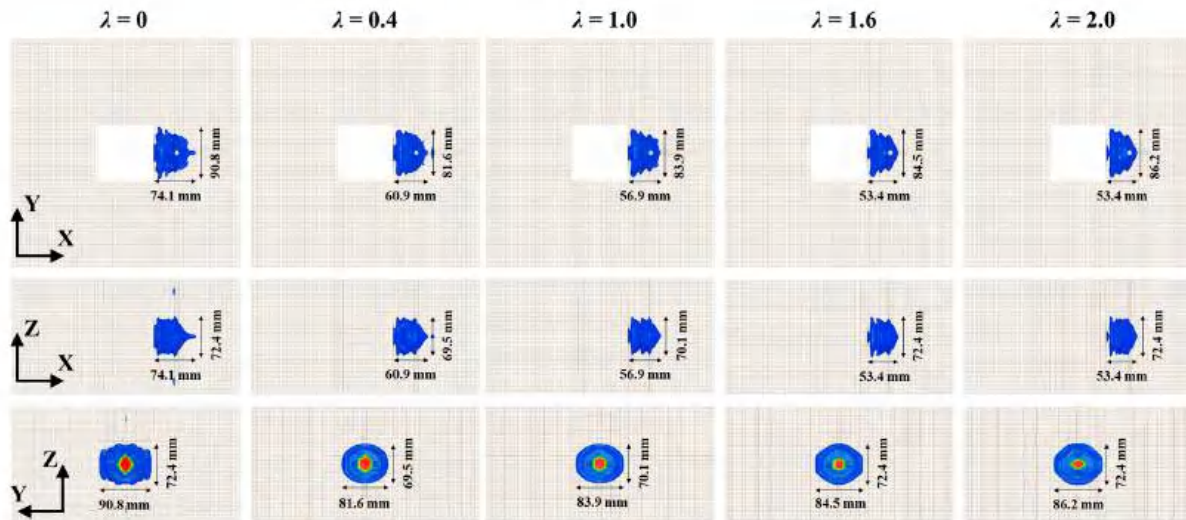
In section A-A, it can be clearly found with P2 increases, the Z-direction dimension of the crater reduces ($P2 \geq 5$ MPa) and the Y-direction dimension of the crater increases gradually, as shown in Figure 10b. The above results are caused by the coupling mechanism of σ_{y2} and the incident compressive stress wave, which is illustrated by Figure 9a. At point A, the original static compressive stress field (σ_{y2}) is opposite to the Y-direction tensile stress component (σ_{y1}) and it will prevent the formation of radial tensile fractures induced by σ_{y1} . However, at point B, σ_y is perpendicular to σ_{z1} , and it is conducive to the growth of reflected tensile fractures induced by σ_{z1} . Therefore, the radial tensile fracture zone is an ellipse with a long axis in the Y direction.

3.2. Influence of Biaxial Static Load on the Damage Distribution

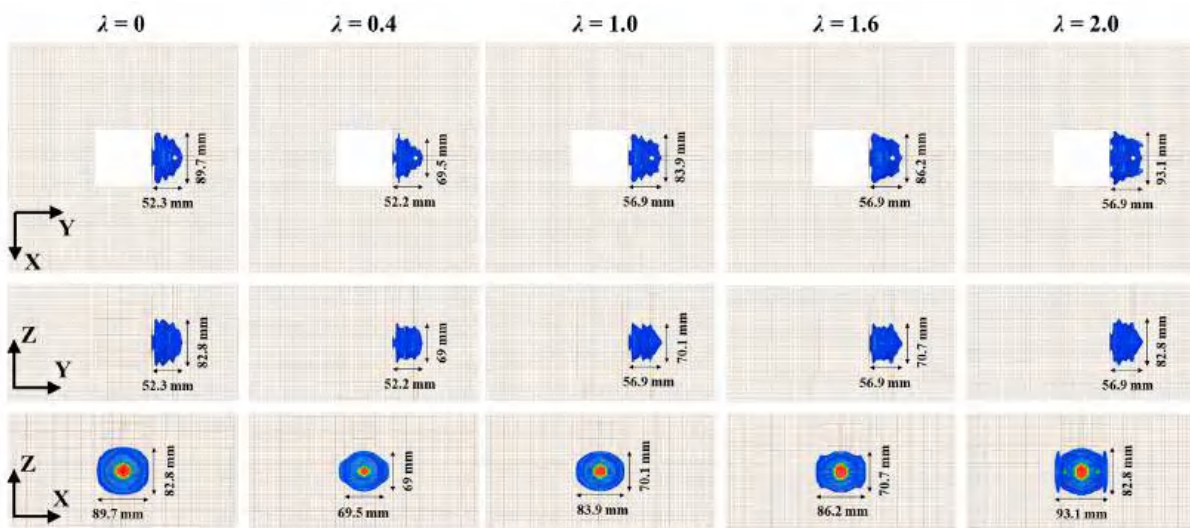
To investigate the characteristic of damage distribution under biaxial loading, $W = 4$ cm and $P1 = 5$ MPa were kept, 11 cases of P2, 0, 1, 2, 3, 4, 5, 6, 7, 8, 9, and 10 MPa, were simulated to investigate the effect of the pressure coefficient $\lambda = \frac{P2}{P1}$ on damage distribution. The borehole is placed on the right side of the cavern, named as case I, or the top side of the cavern, named as case II.

Figure 11a shows the shapes of craters for $W = 4$ cm under biaxial loads with different λ for case I. With the λ increases, the shapes in the three planes are shrinking in the overall trend. In the XY plane, the shape transforms from a trapezoid to a triangle, and the X-direction dimension reduces much to cause the decrease of the depth of the crater. In the XZ plane, away from the free surface, the Z-direction and X-direction dimensions are both reduced due to the increasing Y-direction compressive stress field. In the YZ plane, two damage zones distribute the leftmost side and the rightmost side along the Z direction for $\lambda = 0$, but they disappear for $\lambda = 0.4$. For $\lambda = 0$, the two damage zones are formed by the combined effect of σ_{yR} and σ_{y1} induced by P1. However, for $\lambda = 0.4$, the addition of the new Y-direction compressive stress field (σ_{y2}) induced by P2 will neutralize part of the tensile stress and prevent the formation of the two damage zones. When $\lambda \geq 0.4$, the shape is getting flatter due to the increase of the additional compressive stress field. For case I, the crater volume V reduces monotonically with the increase of λ , as shown in Figure 11c.

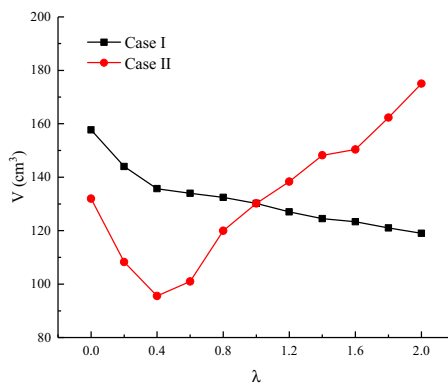
It should be noted that the law only applies to the case of small λ . When λ is large enough, the Y-direction compressive stress field induced by lateral pressure P2 will govern the damage distribution around the surface and away from the charge, and the crater volume may be increased with the increase of λ , as described in the uniaxial loading case of P2.



(a)



(b)



(c)

Figure 11. The shapes and the volumes of craters for $W = 4$ cm under biaxial loads with different λ ($P_1 = 5$ MPa): (a) case I; (b) case II; (c) volume with λ .

Figure 11b shows the shapes of craters for $W = 4$ cm under biaxial loads with different λ for case II. The shape of the explosion crater is the smallest in each plane when $\lambda = 0.4$. In the XY plane, the dimension in the X direction reduces first when $\lambda = 0.4$. This is because the X-direction compressive stress field, which is beneficial for the damage development along the X direction, is weakened by the X-direction tensile stress field induced by P2. When $\lambda = 1.0$, the dimension in the X direction increases instead, especially the damage zones on the upside and downside of the borehole. This is because that the damage mechanism has changed, and the damage zones are mainly formed by the combined effect of the X-direction tensile stress, which is caused by the rock rebound, and the Y-direction compressive stress field induced by P2. Compared with the case of $\lambda = 0.4$, the compressive stress field reduces in the X direction but enhances in the Y direction, which is beneficial for the evolution of the damage zones on the upper and lower sides of the borehole. Therefore, the X-direction crater dimension increases at the top of the crater. When $\lambda = 1.6$ and 2.0, the crater shape is enlarged further due to the increase of P2. In the YZ plane, the variation characteristics of the crater shape are similar to those in the XY plane, and the shape tends to be a triangle, which is consistent with the characteristics in the uniaxial loading cases of P1. In the XZ plane, when $\lambda = 0$, the damage zone near the free surface is induced by the coupling effect of the reflected tensile stress wave and the X-direction compressive stress field. When $\lambda = 0.4$, the combined effect is weakened by the addition of the X-direction tensile stress field induced by P2. Afterwards, with the increase of λ , the P2 becomes the dominant factor affecting the crater shape and the damage mechanism begins to change. When $\lambda = 1.6$ and 2.0, two damage zones appear on the left side and the right side along the Z direction, which are formed by the coupling effect of the X-direction tensile component of the reflected wave and the X-direction tensile stress field. It can be seen that when $\lambda \geq 0.4$, the variation characteristics of crater shape at each plane are similar to these in the uniaxial loading cases of P1. For case II, as shown in Figure 11c, the crater volume V reduces first before λ increases to 0.4 and then increases with λ increases. The turning point of V is mainly caused by the change of the dominant damage mechanism, as described in the above analysis. It can be found that $\lambda = 1$ is a demarcation point. The crater volume V is greater for case I (the borehole is placed on the right side of the rectangular cavity) when $\lambda < 1$, but greater for case II (the borehole is placed on the top side of the rectangular cavity) when $\lambda > 1$. There is a common feature that the V is greater when the borehole is placed on the side of the max static load. Taking the demarcation point of $\lambda = 1$ as the reference point, the increase of V with the increase of the static load on the side of the borehole is greater than that with the reduction of the static load on the other side. The result indicates that the crater volume is more sensitive to the variation of static load on the same side than the other side, which is consistent with the uniaxial load numerical result in Section 3.1 that the effect of P1 on the increase of V is greater than that of P2.

3.3. Influence of Span Ratio on the Damage Distribution

In this section, the span X of 100 mm, $W = 4$ cm, and $P1 = 5$ MPa were kept, and the span $Y = 100, 110, 120$ and 130 mm were considered to investigate the characteristic of the damage distribution with different span ratios $k = \frac{\text{span } Y}{\text{span } X}$. Considering that the static stress field on the top side is less influenced by the variation of span Y , the borehole layout placed on the top side is not considered in this section.

Figure 12 shows the Y-direction elastic stress fields with different k under $P1 = P2 = 5$ MPa. It can be found that with span Y increases, the σ_y on the right side of the rectangle cavern reduces from around 6 MPa to around 2 MPa, but varies little on the top side. The results indicate that the Y-direction compressive stress field on the right side is weakened with the increase of k . Figure 13a shows the explosion crater with different k under $P1 = P2 = 5$ MPa. In the XY plane, the crater Y-direction dimensions near the free surface are enlarged with the increase of k , which is similar to the characteristics of case II when $\lambda \geq 0.4$ in Section 3.2. The expanded damage zones are also induced by the combined effect of the Y-direction rock rebound and the X-direction compressive stress field. When k increases, the Y-direction

compressive stress field reduces, and the X-direction compressive stress field increases, which can intensify the combined effect and improve the X-direction damage development. In the XZ plane, the crater shape is enlarged with the increase of k , and the variation characteristic is also consistent with the results of case II when $\lambda \geq 0.4$ in Section 3.2. In the YZ plane, the crater shape changes from an ellipse to a circle with the increase of k , which is induced by the weakening of the Y-direction compressive field. Figure 13b shows the explosion crater with different k under $P1 = 5$ MPa and $P2 = 10$ MPa. The results show that the shape variation characteristics are similar to those under $P1 = P2 = 5$ MPa. The crater volumes under different k are listed in Table 4. It can be found that the crater volume increases with k increases. The results indicate that in the stressed rock mass, the explosion crater can be improved by increasing the free surface span on the side of the borehole. Especially for the case of unequal biaxial loading, the rock on the side of the maximum principle stress should be excavated first, where the rock breaking efficiency is higher than the other side with the same span, and then the span on the other side can be increased, which is beneficial to improving the explosion crater on this side. In the view of strain energy density, Yang [35] pointed out that the rock mass with a poor strain energy density should be excavated first to release the high strain energy of the adjacent rock, and then the release intensity of strain energy can be effectively controlled and the vibration induced by the instantaneous unloading can be reduced. In our study, the borehole on the side of $P2$, where the strain energy density is poor (as shown in Figure 14), should also be detonated firstly to improve the crater volume and the critical embedding depth of the charge. Besides, as shown in Figure 14, with the excavation of rock mass on the side of $P2$, the strain energy density on the other side ($P1$) will be reduced. The result is beneficial to the control of vibration induced by the instantaneous unloading and the increase of the rock breaking efficiency in the high strain energy zone.

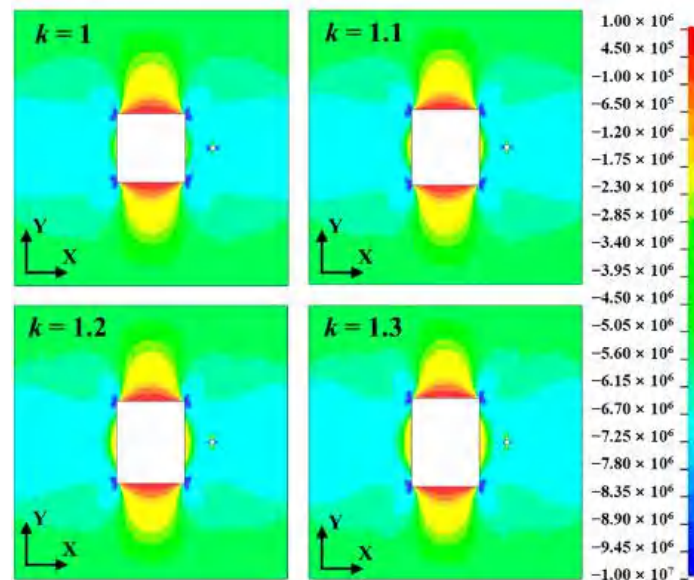
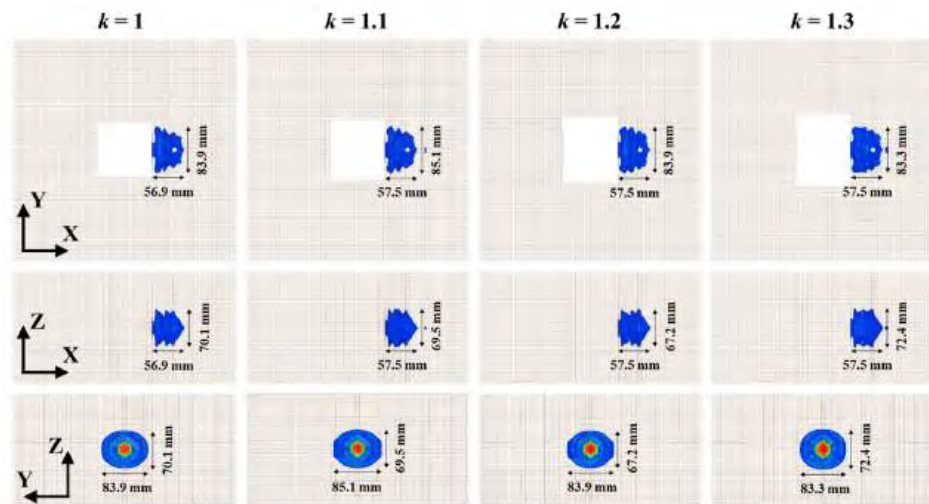


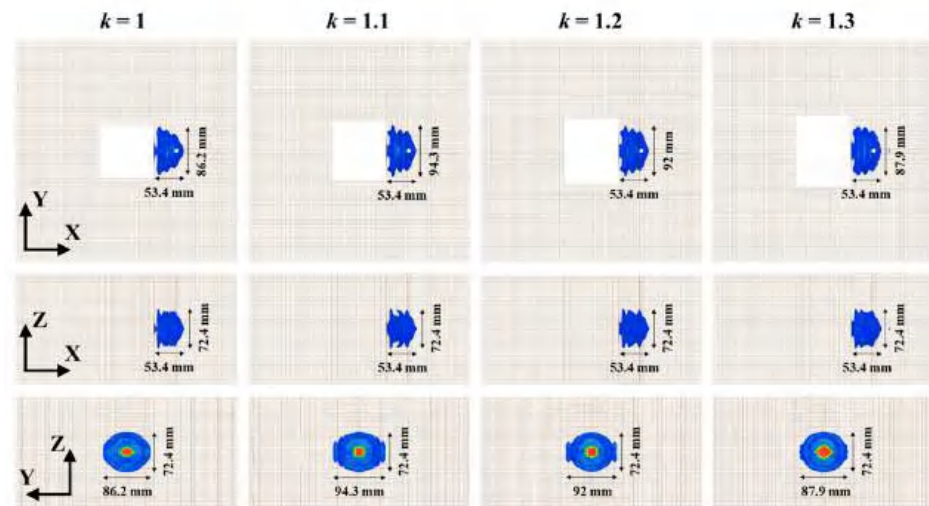
Figure 12. Y-direction elastic stress fields (σ_y) with different k under $P1 = P2 = 5$ MPa.

Table 4. The crater volumes under different k .

k	V/cm ³	
	P1 = 5 MPa P2 = 5 MPa	P1 = 5 MPa P2 = 10 MPa
1.0	130.2	119.0
1.1	139.0	128.1
1.2	141.1	135.0
1.3	150.0	143.2



(a)



(b)

Figure 13. The explosion crater with different k : (a) $P_1 = P_2 = 5$ MPa; (b) $P_1 = 5$ MPa; $P_2 = 10$ MPa.

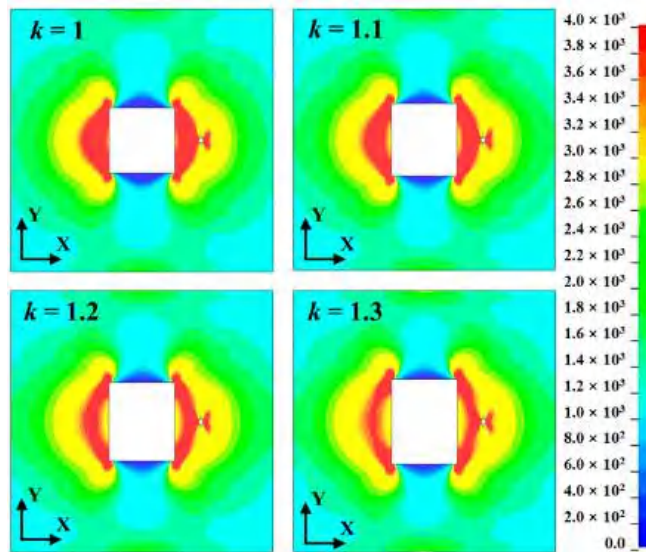


Figure 14. Strain energy density with different k under $P_1 = 5$ MPa and $P_2 = 10$ MPa.

4. Discussion and Conclusions

This study mainly investigates the blast-induced damage characteristics considering the lateral free surface in highly stressed rock mass by using a 3D numerical model. Firstly, the numerical model is calibrated by comparing the results of single-hole crater blasting model test and the numerical simulation. The results of the test and simulation are in good agreement in the upper part of the crater boundary, but the test result gives a slightly larger contour in the lower part. This may be due to the existence of an uneven weakening part in the lower part during the pouring process of cemented sand, which is more likely to be damaged and not considered in the numerical simulation. On the whole, the numerical model is reasonably accurate to study the blast-induced damage characteristics. And then, the influence of uniaxial static load under different burdens, biaxial static load and span ratio on the damage distribution were evaluated with the calibrated numerical model. When the free surface exists, the damage mechanisms are clearly different from these of the plane problem without considering the free surface and the 3D stress state. The development of the blast-induced damage away from the charge is governed by the static load, especially near the free surface.

For uniaxial loading, the damage zone and the crater volume V increase with the increase of uniaxial static load $P1$ or $P2$. The V is greater when the borehole is placed on the side of the static load. For example, when $W = 4$ cm, compared with $P2$, the V is increased by 15–31% for $P1$ with the same static load value. The variations of crater volume also show that the uniaxial static load can change the optimal burden of charge and increase the critical embedding depth of the charge, especially for $P1$.

Static load significantly affects the blast-induced damage distribution, especially for the radial tensile fractures zone and the reflected tensile fractures zone. For the radial tensile fractures zone, the long axis of the bottom circle of the crater turns parallel to the max principal compressive stress, which has been proposed by many researchers [2–4,8,13–15]. However, the law only applies to the radial tensile fractures but not to the reflected tensile fractures. For the latter, the opposite law that the long axis of the reflected tensile fracture zone is perpendicular to the max principal compressive stress will be obtained.

The variation law of the crater volume is different for the case of the biaxial static load. When $P1 = 5$ MPa is kept and the borehole is placed on the side of $P1$, the V reduces monotonously with the increase of $P2$ before λ increases to 2.0. When the borehole is placed on the other side, the V first reduces until λ increases to 0.4 and then increases with the increase of $P2$ before λ increases to 2.0. The turning point at $\lambda = 0.4$ is mainly caused by the transformation of the dominant factor affecting the crater shape and the damage mechanism from $P1$ to $P2$. The crater volume is greater when the borehole is placed on the side of the max static load, where the strain energy density is lower. Meanwhile, the V is also more sensitive to the variation of static load on the same side than the other side.

The crater volume increases with k increases, which indicates that in the stressed rock mass, the explosion crater can be improved by increasing the free surface span on the side of the borehole. Especially for the case of unequal biaxial loading with the same span ($\lambda \neq 1$ and $k = 1$), the rock on the side of max principle stress should be excavated first, where the rock breaking efficiency is higher than the other side, and then the span on the other side can be increased (k increases), which is beneficial to improving the blasting efficiency on this side. Meanwhile, when the charge on the side of the max static load (lower strain energy density) is detonated first and the charge on the other side (higher strain energy density) is detonated later, the transient unloading induced vibration can be reduced [35].

Author Contributions: Investigation, Software, Writing—Original Draft, X.H. and X.Q.; Project Administration, Supervision, X.S.; Writing—Review and Editing, H.C. and J.Z.; Investigation, S.Z. and D.R. All authors have read and agreed to the published version of the manuscript.

Funding: This research was funded by the National Natural Science Foundation Project of China, grant number 51874350 and 52004329 and the National Key Research and Development Program of China, grant number 2017YFC0602902.

Institutional Review Board Statement: Not applicable.

Informed Consent Statement: Not applicable.

Data Availability Statement: The data presented in this study are available on request from the corresponding author.

Conflicts of Interest: The authors declare no conflict of interest.

References

1. Kutter, H.K.; Fairhurst, C. On the fracture process in blasting. *Int. J. Rock Mech. Min. Sci.* **1971**, *8*. [CrossRef]
2. Zhang, F.; Peng, J.; Qiu, Z.; Chen, Q.; Li, Y.; Liu, J. Rock-like brittle material fragmentation under coupled static stress and spherical charge explosion. *Eng. Geol.* **2017**, *220*, 266–273. [CrossRef]
3. Peng, J.; Zhang, F.; Du, C.; Yang, X. Effects of confining pressure on crater blasting in rock-like materials under electric explosion load. *Int. J. Impact Eng.* **2020**, *139*, 103534. [CrossRef]
4. Peng, J.; Zhang, F.; Yan, G.; Qiu, Z.; Dai, X. Experimental study on rock-like materials fragmentation by electric explosion method under high stress condition. *Powder Technol.* **2019**, *356*, 750–758. [CrossRef]
5. Zhang, F.; Yan, G.; Peng, J.; Qiu, Z.; Dai, X. Experimental study on crack formation in sandstone during crater blasting under high geological stress. *Bull. Eng. Geol. Environ.* **2020**, *79*, 1323–1332. [CrossRef]
6. Xiao, S.Y.; Su, L.J.; Jiang, Y.J.; Liu, Z.X. Numerical analysis of hard rock blasting unloading effects in high in situ stress fields. *Bull. Eng. Geol. Environ.* **2019**, *78*, 867–875. [CrossRef]
7. Yang, R.; Ding, C.; Li, Y.; Yang, L.; Zhao, Y. Crack propagation behavior in slit charge blasting under high static stress conditions. *Int. J. Rock Mech. Min. Sci.* **2019**, *119*, 117–123. [CrossRef]
8. Hu, Y.; Lu, W.; Wu, X.; Liu, M.; Li, P. Numerical and experimental investigation of blasting damage control of a high rock slope in a deep valley. *Eng. Geol.* **2018**, *237*, 12–20. [CrossRef]
9. Lu, W.; Chen, M.; Geng, X.; Shu, D.; Zhou, C. A study of excavation sequence and contour blasting method for underground powerhouses of hydropower stations. *Tunn. Undergr. Space Technol.* **2012**, *29*, 31–39. [CrossRef]
10. Yang, L.; Xie, H.; Huang, C.; Zhang, D.; Chao, Y.J. Experimental study on notched directional blasting in tensile stress field. *J. Eng. Sci. Technol. Rev.* **2020**, *13*, 106–113. [CrossRef]
11. He, C.; Yang, J.; Yu, Q. Laboratory study on the dynamic response of rock under blast loading with active confining pressure. *Int. J. Rock Mech. Min. Sci.* **2018**, *102*, 101–108. [CrossRef]
12. Donzé, F.V.; Bouchez, J.; Magnier, S.A. Modeling fractures in rock blasting. *Int. J. Rock Mech. Min. Sci.* **1997**, *34*, 1153–1163. [CrossRef]
13. Yilmaz, O.; Unlu, T. Three dimensional numerical rock damage analysis under blasting load. *Tunn. Undergr. Space Technol.* **2013**, *38*, 266–278. [CrossRef]
14. Xie, L.X.; Lu, W.B.; Zhang, Q.B.; Jiang, Q.H.; Wang, G.H.; Zhao, J. Damage evolution mechanisms of rock in deep tunnels induced by cut blasting. *Tunn. Undergr. Space Technol.* **2016**, *58*, 257–270. [CrossRef]
15. Yi, C.; Johansson, D.; Greberg, J. Effects of in-situ stresses on the fracturing of rock by blasting. *Comput. Geotech.* **2018**, *104*, 321–330. [CrossRef]
16. Jayasinghe, L.B.; Shang, J.; Zhao, Z.; Goh, A.T.C. Numerical investigation into the blasting-induced damage characteristics of rocks considering the role of in-situ stresses and discontinuity persistence. *Comput. Geotech.* **2019**, *116*. [CrossRef]
17. Ma, G.W.; An, X.M. Numerical simulation of blasting-induced rock fractures. *Int. J. Rock Mech. Min. Sci.* **2008**, *45*, 966–975. [CrossRef]
18. Li, X.; Liu, K.; Yang, J. Study of the Rock Crack Propagation Induced by Blasting with a Decoupled Charge under High In Situ Stress. *Adv. Civ. Eng.* **2020**, *2020*, 1–18. [CrossRef]
19. Han, H.; Fukuda, D.; Liu, H.; Salmi, E.F.; Sellers, E.; Liu, T.; Chan, A. Combined finite-discrete element modelling of rock fracture and fragmentation induced by contour blasting during tunnelling with high horizontal in-situ stress. *Int. J. Rock Mech. Min. Sci.* **2020**, *127*. [CrossRef]
20. Riedel, W.; Thorna, K.; Hiermaier, S.; Schmolinske, E. Penetration of reinforced concrete by BETA-B-500, numerical analysis using a new macroscopic concrete model for hydrocodes. In Proceedings of the Proceedings of the 9th International Symposium on Interaction of the Effects of Munitions with Structures, Berlin, Germany, 3–7 May 1999; pp. 315–322.
21. Borrvall, T.; Riedel, W. The RHT concrete model in LS-DYNA. In Proceedings of the 8th European LS-DYNA Users Conference, Strasbourg, France, 23–24 May 2011.
22. Huo, X.; Shi, X.; Qiu, X.; Zhou, J.; Gou, Y.; Yu, Z.; Ke, W. Rock damage control for large-diameter-hole lateral blasting excavation based on charge structure optimization. *Tunn. Undergr. Space Technol.* **2020**, *106*, 1–21. [CrossRef]
23. Yi, C.; Sjöberg, J.; Johansson, D. Numerical modelling for blast-induced fragmentation in sublevel caving mines. *Tunn. Undergr. Space Technol.* **2017**, *68*, 167–173. [CrossRef]

24. Xie, L.X.; Lu, W.B.; Zhang, Q.B.; Jiang, Q.H.; Chen, M.; Zhao, J. Analysis of damage mechanisms and optimization of cut blasting design under high in-situ stresses. *Tunn. Undergr. Space Technol.* **2017**, *66*, 19–33. [CrossRef]
25. Liu, K.; Li, Q.; Wu, C.; Li, X.; Li, J. A study of cut blasting for one-step raise excavation based on numerical simulation and field blast tests. *Int. J. Rock Mech. Min. Sci.* **2018**, *109*, 91–104. [CrossRef]
26. Hoek, E.; Brown, E.T. *Underground Excavations in Rock*; CRC Press: Boca Raton, FL, USA, 1980.
27. Dehghan Banadaki, M.M.; Mohanty, B. Numerical simulation of stress wave induced fractures in rock. *Int. J. Impact Eng.* **2012**, *40*, 16–25. [CrossRef]
28. Grunwald, C.; Schaufelberger, B.; Stolz, A.; Riedel, W.; Borrvall, T. A general concrete model in hydrocodes: Verification and validation of the Riedel—Hiermaier—Thoma model in LS-DYNA. *Int. J. Prot. Struct.* **2017**, *8*, 58–85. [CrossRef]
29. Yang, G.; Wang, G.; Lu, W.; Yan, P.; Chen, M. Combined effects of penetration and explosion on damage characteristics of a mass concrete target. *J. Vibroeng.* **2018**, *20*, 1632–1651. [CrossRef]
30. Livermore Software Technology Corporation (LSTC) LS-DYNA Keyword User’s Manual, Version R 10.0. p. 2017. Available online: <http://www.lstc.com/> (accessed on 16 October 2017).
31. Castedo, R.; Natale, M.; López, L.M.; Sanchidrián, J.A.; Santos, A.P.; Navarro, J.; Segarra, P. Estimation of Jones-Wilkins-Lee parameters of emulsion explosives using cylinder tests and their numerical validation. *Int. J. Rock Mech. Min. Sci.* **2018**, *112*, 290–301. [CrossRef]
32. Yuan, P.; Xu, Y.; Zheng, Z. Time-frequency analyses of blasting vibration signals in single-hole blasting model experiments. *J. Vibroeng.* **2017**, 363–375. [CrossRef]
33. Yi, C.; Sjöberg, J.; Johansson, D.; Petropoulos, N. A numerical study of the impact of short delays on rock fragmentation. *Int. J. Rock Mech. Min. Sci.* **2017**, *100*, 250–254. [CrossRef]
34. Huo, X.; Shi, X.; Gou, Y. Simulation of Crack Growth in Sidewall Controlled Blasting and Parameter Optimization. *Blasting* **2019**, *36*, 21–28. (In Chinese)
35. Yang, J.; Wu, Z.; Jiang, S.; Yao, C.; Lu, W.; Zhou, C. Study on controlling methods for transient unloading inducing rock vibration due to blasting excavation of deep tunnels. *Chin. J. Rock Mech. Eng.* **2019**, *37*, 2751–2761. (In Chinese)

MDPI
St. Alban-Anlage 66
4052 Basel
Switzerland
www.mdpi.com

Applied Sciences Editorial Office
E-mail: applsci@mdpi.com
www.mdpi.com/journal/applsci



Disclaimer/Publisher's Note: The statements, opinions and data contained in all publications are solely those of the individual author(s) and contributor(s) and not of MDPI and/or the editor(s). MDPI and/or the editor(s) disclaim responsibility for any injury to people or property resulting from any ideas, methods, instructions or products referred to in the content.



Academic Open
Access Publishing

mdpi.com

ISBN 978-3-0365-8976-3